

---

Proceedings of

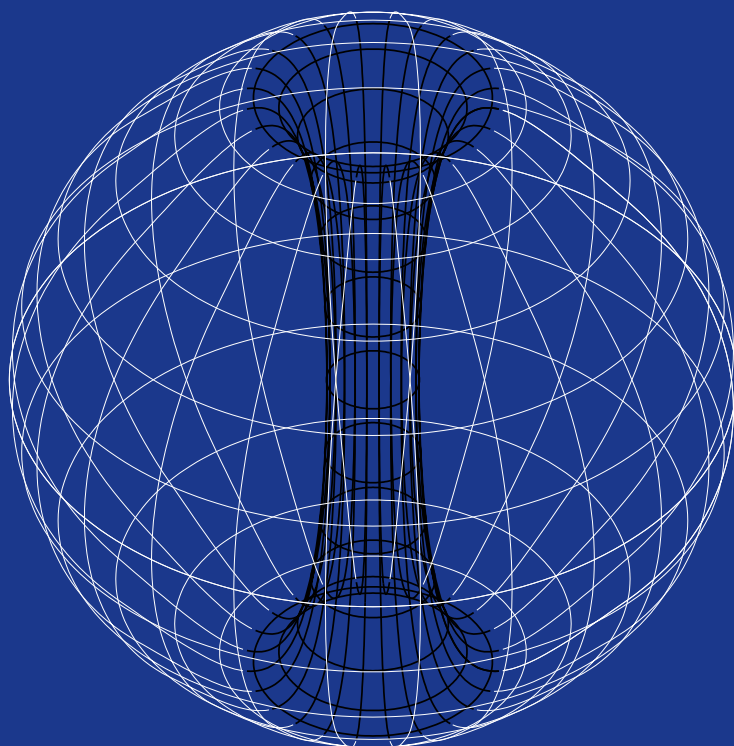
RAGtime 4/5:  
Workshops  
on black holes  
and  
neutron stars

14–16/13–15 October '02/'03  
Opava, Czech Republic

and

neutron stars

Editors  
S. Hledík  
Z. Stuchlík



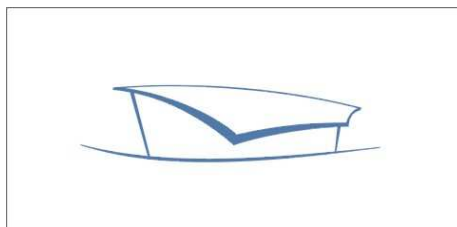
SILESIA UNIVERSITY IN OPAVA

Publications of the Institute of Physics No. 3

Sponsored by



<http://www.sarai.cz/>



Víceúčelová hala v Opavě  
Multi-purpose hall Opava

<http://www.hala-opava.cz/>

H O T E L

---

O P A V A

<http://www.hotel-opava.cz/>

Proceedings of RAGtime 4/5:  
Workshops on black holes and neutron stars  
14–16/13–15 October 2002/2003  
Opava, Czech Republic

S. Hledík and Z. Stuchlík, editors

Opava 2004

Editorial Board: prof. RNDr. Zdeněk Stuchlík, CSc.  
prof. Marek Abramowicz  
RNDr. Stanislav Hledík, Ph.D.

Annotation: In this Proceedings, the talks presented during workshops RAGtime 4 (14–16 October 2002, Opava, Czech Republic) and RAGtime 5 (13–15 October 2003, Opava, Czech Republic) are collected.

Copyright © 2004 Silesian University in Opava

## PREFACE

Relativistic Astrophysics Group (RAG) at the Institute of Physics, the Faculty of Philosophy and Science of the Silesian University in Opava, started a series of Workshops on Black Holes and Neutron Stars called *RAGtime* in 1999. The purpose of the workshops was to enable presentation and discussion on recent developments in the field of relativistic astrophysics related to accretion processes onto black holes and neutron stars, and to general physical phenomena connected to the properties of black holes, and the internal structure of neutron stars or quark stars, as they were obtained by collaborating research groups at the Silesian University, the Faculty of Mathematics and Physics of the Charles University in Prague, the International School for Advanced Studies in Trieste, the Institute of Astrophysics at University of Oxford, the Department of Astrophysics of Chalmers University, Göteborg, the Institute of Physics at the University of Trondheim, the Institute of Physics at the University of Bergen, the Institute of Astronomy of the Polish Academy of Science, and other remarkable institutes.

The *RAGtime* workshops are also vitally important for students of theoretical physics and astrophysics of the Silesian University, because they have a regular opportunity to be in a direct contact with the most recent results of relativistic astrophysics and yet they have a possibility to discuss problems with leading (worldwide) astrophysicists like Prof. Marek Abramowicz, Prof. John Miller, Prof. Antonio Lanza, Prof. Luciano Rezzolla, Prof. Bożena Czerny, Doc. Vladimír Karas, Dr. Petr Hadrava, Dr. Jiří Grygar and others.

We would like to thank all the authors for careful preparation of their contributions.

Opava, December 2004

S. Hledík and Z. Stuchlík  
editors

## CONTENTS

<i>M. A. Abramowicz, W. Kluźniak, Z. Stuchlík and G. Török</i> Twin peak QPOs frequencies in microquasars and Sgr A*. The resonance and other orbital models . . . . .	1
<i>M. Bursa</i> Variability of accreting sources at very high time resolution . . . . .	25
<i>M. Dovčiak, V. Karas, A. Martocchia, G. Matt and T. Yaqoob</i> An XSPEC model to explore spectral features from black-hole sources . . . . .	33
<i>S. Hledík, Z. Stuchlík and K. Mrázová</i> Comparison of general relativistic polytropic and adiabatic fluid spheres with a repulsive cosmological constant . . . . .	75
<i>J. Horák</i> General aspects of nonlinear resonance 3 : 2 in QPO context . . . . .	91
<i>J. Kovář and Z. Stuchlík</i> Inertial forces in Kerr–de Sitter spacetimes . . . . .	111
<i>P. Nováček</i> Astrophysical clouds in galactic nuclei. Monte Carlo simulations . . . . .	135
<i>T. Pecháček and V. Karas</i> Decaying orbits near a rotating black hole . . . . .	147
<i>L. Rezzolla</i> Nonlinear dynamics of thick discs in Schwarzschild–de Sitter spacetimes . . . . .	151
<i>Z. Stuchlík and K. Plšková</i> Optical appearance of isotropically radiating sphere in the Schwarzschild–de Sitter spacetime . . . . .	167
<i>Z. Stuchlík and J. Schee</i> Influence of relict vacuum energy on the Rees–Sciama effect . . . . .	187
<i>Z. Stuchlík and P. Slaný</i> Accretion disks in the Kerr–de Sitter spacetimes . . . . .	205
<i>Z. Stuchlík, P. Slaný and G. Török</i> Marginally stable thick discs with gradient inversion of orbital velocity measured in locally non-rotating frames. A mechanism for excitation of oscillations in accretion discs? . . . . .	239
<i>Z. Stuchlík, G. Török and S. Hledík</i> Trapping of neutrinos in extremely compact stars . . . . .	257
<i>L. Šubr and V. Karas</i> Stellar orbits in the gravitational field of a massive torus near a galactic centre . . . . .	271

# Twin peak QPOs frequencies in microquasars and Sgr A\*

## The resonance and other orbital models

Marek A. Abramowicz<sup>1,2,5</sup>, Włodek Kluźniak<sup>1,3,4</sup>,  
Zdeněk Stuchlík<sup>5</sup> and Gabriel Török<sup>1,2,5</sup>

<sup>1</sup>UKAFF supercomputer facility, Dept. of Physics and Astronomy, University of Leicester, England

<sup>2</sup>Theoretical Physics, Chalmers University S-412-96 Göteborg, Sweden, marek@fy.chalmers.se

<sup>3</sup>Institute of Astronomy, Zielona Góra University ul. Lubuska 2, PL-65-265 Zielona Góra, Poland

<sup>4</sup>Copernicus Astronomical Centre, Warszawa, Poland, wlodek@camk.edu.pl

<sup>5</sup>Institute of Physics, Bezručovo nám. 13, CZ-746 01 Opava, Czech Republic,  
zdenek.stuchlik@jpf.slu.cz

### ABSTRACT

In all four microquasars which show twin peak kHz QPOs, the ratio of the two frequencies is 3:2. This rather strongly supports the suggestion by [Abramowicz and Kluźniak, 2001] that twin peak kHz QPOs are due to a resonance between some modes of accretion disk oscillations. Detailed studies of this suggestion revealed that several such non-linear resonances are present in nearly Keplerian disks in strong gravity. Here, we fit to observations predictions of the resonance hypothesis for two particular types of non-linear resonances between vertical and radial epicyclic frequencies. For three microquasars with known masses, the fits give an accurate estimate of the spin.

**Keywords:** LMXRB and Galactic Centre black holes – X-ray variability – observations – theory

## 1 INTRODUCTION

Many Galactic black hole and neutron star sources in low X-ray mass binaries show both chaotic and quasi periodic variability in their observed X-ray fluxes. Some of the quasi periodic oscillations (QPOs) are in the kHz range and often come in pairs ( $\nu_{\text{up}}$ ,  $\nu_{\text{down}}$ ) of *twin peaks* in the Fourier power spectra (e.g., [van der Klis, 2000], [McClintock and Remillard, 2003]). There is no general agreement on a physical mechanism exciting QPOs. We follow here a suggestion by [Abramowicz and Kluźniak, 2001] that twin peak kHz QPOs are due to a resonance in accretion disk oscillation modes. The resonance model is based on fundamental features of strong gravity, and motivated by observations that sharply illuminate physical nature of QPOs:

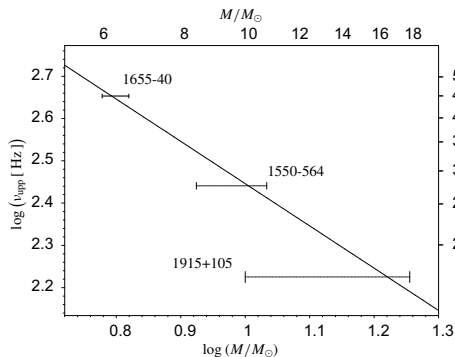


**Figure 1.** The best fit for the frequency–mass scaling for microquasars’ kHz twin peak QPOs,  $\nu_{\text{upp}} = 2793/M$  [Hz/ $M_{\odot}$ ], adopted from [McClintock and Remillard, 2003] who pointed out the scaling. The scaling proves that oscillations are relativistic, i.e., they occur at a radius fixed in terms of the gravitational radius  $r_G = GM_0/c^2$ .

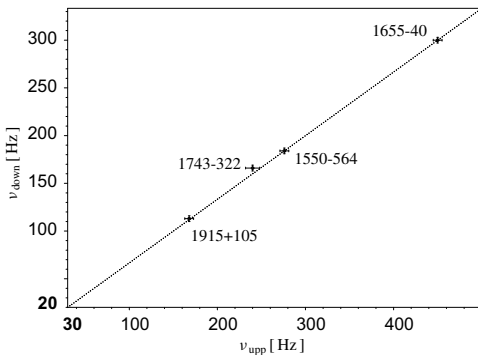


**Figure 2.** The 3:2 correlation for this microquasars. More on that in Section 3 (error bars are discussed in subsection 7.1).

**Table 1.** Frequencies of twin peak kHz QPOs in microquasars.

Source	$\nu_{\text{upp}}$ [Hz]	$\Delta\nu_{\text{upp}}$ [Hz]	$\nu_{\text{down}}$ [Hz]	$\Delta\nu_{\text{down}}$ [Hz]	$2\nu_{\text{upp}}/3\nu_{\text{down}} - 1$	Mass [ $M_{\odot}$ ]
(a) XTE 1550–564	276	$\pm 3$	184	$\pm 5$	0.00000	8.4 – 10.8
(a) GRO 1655–40	450	$\pm 3$	300	$\pm 5$	0.00000	6.0 – 6.6
(a) GRS 1915+105	168	$\pm 3$	113	$\pm 5$	0.00885	10.0 – 18.0
(b) H 1743–322	240	$\pm 3$	166	$\pm 8$	-0.03614	not measured

(a) From [McClintock and Remillard, 2003].

(b) From [Homan et al., 2003].

(i) A correlation  $\nu_{\text{low}} = 0.08\nu_{\text{high}}$  was found between low and high frequency QPOs in black hole and neutron stars sources by [Psaltis et al., 1999], and extended to white dwarfs by [Mauche, 2002] and [Warner et al., 2003]. It proves that in general the QPOs phenomenon is due to accretion disk oscillations, and not to kinematic effects like, e.g., Doppler modulation of fluxes from isolated hot spots: QPOs are waves, not particles (more on this in Section 6).

(ii) The frequencies of twin peak kHz QPOs in microquasars scale with mass,  $\nu \sim 1/M$  (Fig. 1). This proves a relativistic origin of them.

(iii) In all four microquasars with twin peak kHz QPOs pairs,  $\nu_{\text{upp}}/\nu_{\text{down}} = 3/2$  (Table 1, Fig. 2), suggesting a resonance (Section 3).

## 2 THE ORBITAL MOTIONS IN BLACK HOLE'S STRONG GRAVITY. THE $1/M$ SCALING

Consider a black hole<sup>1</sup> with the mass  $M_0$  and angular momentum  $J_0$ . According to the standard Shakura–Sunyaev accretion disk model, matter spirals down the central black hole along streamlines that are located almost on the equatorial plane  $\theta = \theta_0 = \pi/2$ , and that locally differ only slightly from a family of concentric circles  $r = r_0 = \text{const}$ . The small deviations,  $\delta r = r - r_0$ ,  $\delta\theta = \theta - \theta_0$  are governed, with accuracy to linear terms, by

$$\delta\ddot{r} + \omega_r^2 \delta r = \delta a_r, \quad \delta\ddot{\theta} + \omega_\theta^2 \delta\theta = \delta a_\theta. \quad (1)$$

Here dot denotes time derivative. For purely Keplerian (free) motion  $\delta a_r = 0$ ,  $\delta a_\theta = 0$  and the above equations describe two uncoupled harmonic oscillators with the eigenfrequencies  $\omega_\theta$ ,  $\omega_r$  equal, in Kerr geometry (e.g., [Abramowicz et al., 1999]),

$$\begin{aligned} \omega_\theta^2 &= \Omega_K^2 \left( 1 - 4ax^{-3/2} + 3a^2x^{-2} \right), \\ \omega_r^2 &= \Omega_K^2 \left( 1 - 6x^{-1} + 8ax^{-3/2} - 3a^2x^{-2} \right), \\ \Omega_K &= \left( \frac{GM_0}{r_G^3} \right)^{1/2} \left( x^{3/2} + a \right)^{-1}, \end{aligned} \quad (2)$$

where  $x = r/M$ . The two epicyclic frequencies, vertical  $\nu_\theta = \omega_\theta/2\pi$  and radial  $\nu_r = \omega_r/2\pi$ , are shown in Fig. 3 together with the Keplerian orbital frequency  $\nu_K = \Omega_K/2\pi$  for a non rotating ( $a = 0$ ) black hole, and for a moderately rotating ( $a = 0.8$ ) black hole. Figs 4 and 5 show these frequencies in the whole range of  $a$ , from a maximally co-rotating black hole ( $a = 1$ ) to a maximally counter-rotating black hole ( $a = -1$ ).

In Newton's theory with the  $-GM_0/r$  potential it is  $GM_0/r^{3/2} = \nu_K = \nu_r = \nu_\theta$ , but in the strong gravity of a rotating black hole,  $\nu_K > \nu_\theta > \nu_r$ . The radial epicyclic frequency  $\nu_r$  goes to zero at  $r_{\text{ISCO}}$ , the Innermost Stable Circular Orbit for the Keplerian (free) motion, and has a maximum at a particular circular orbit with the radius  $r > r_{\text{ISCO}}^2$ , depending on the black hole spin [Okazaki et al., 1987]. Note that all three orbital frequencies in (2) have the general form,

$$\nu = \left( \frac{GM_0}{r_G^3} \right)^{1/2} f(x, a) = 32293 \left( \frac{M_0}{M_\odot} \right)^{-1} f(x, a) \text{ [Hz]}, \quad (3)$$

with  $f(x, a)$  being a dimensionless function. For several relativistic effects radius is fixed in terms of gravitational radius, which means that also  $x = x(a)$  is fixed. In this case the above formula predicts that frequencies scale as  $1/M$ , with some scatter induced by the spin of the black hole  $a$ . In particular, each orbital resonance  $n : m$  discussed here occurs at its own resonance radius  $x_{n:m}(a)$ . The scatter for the particular 3:2 resonance is not very large because, as we shall see in the next Section, this resonances occurs at  $x_{3:2}(a) > 4$ , where

<sup>1</sup> We rescale mass with  $M = GM_0/c^2 = r_G$ , and angular momentum with  $a = J_0c/GM_0^2$ . We use Boyer–Lindquist coordinates,  $t, r, \theta, \phi$ .

<sup>2</sup> Analogically – marginally bound circular orbit  $r_{\text{RISCO}}$  is the limit of stable nongeodesic orbits in thick accretion disks with pressure suffering their balance (see also discussion in subsection 4.1)

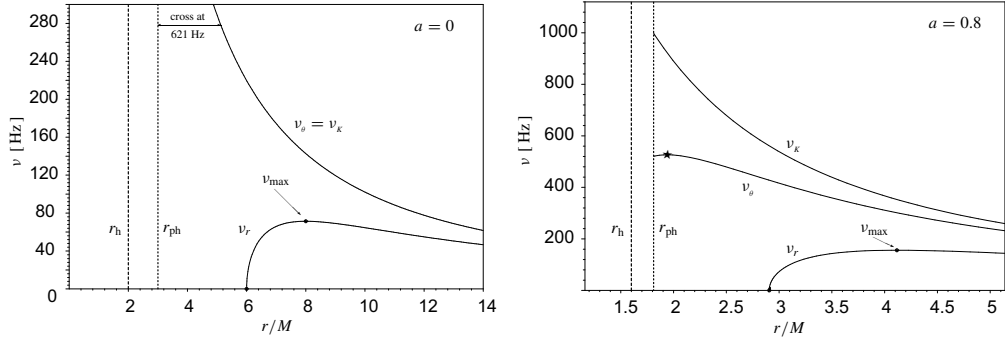


**Figure 3.** Orbital frequency  $\nu_K$ , and the two epicyclic frequencies, radial  $\nu_r$ , and vertical  $\nu_\theta$  for Keplerian circular orbits around a  $10 M_\odot$  black hole. Such orbits are possible only for radii larger than the radius of the circular photon orbit  $r_{\text{ph}}$ . This limit is labelled here and in other Figures by the subscript “ph”. Left panel for non-rotating black hole, right panel for a moderately ( $a = 0.8$ ) rotating one. In Newton’s theory with the  $1/r$  potential, all the three frequencies are equal:  $\nu_K = \nu_\theta = \nu_r$ . Strong Einstein’s gravity makes  $\nu_K \geq \nu_\theta > \nu_r$ .

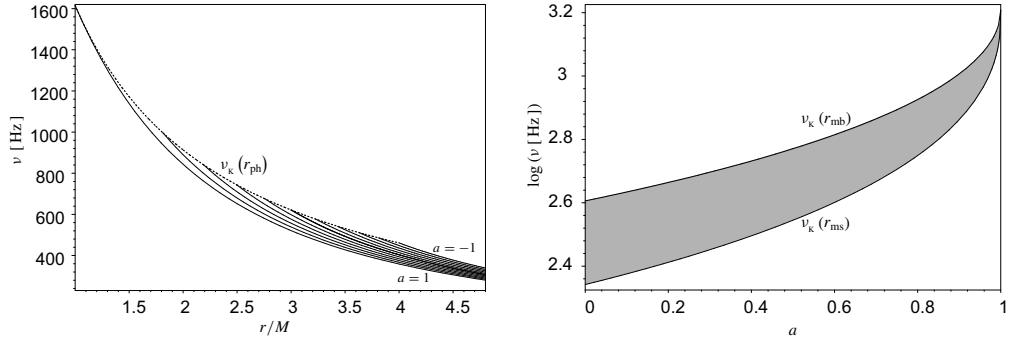


**Figure 4. Left:** The Keplerian orbital frequency for  $10 M_\odot$  mass black hole. **Right:** RISCO and ISCO frequencies for  $10 M_\odot$  mass black hole. The accretion disk inner edge must be located between RISCO and ISCO, depending on disk’s efficiency. If efficiency is not known, one may only argue that the maximal possible orbital frequency is somewhere in the shaded region, but not necessarily on the  $\nu_K(r_{\text{ms}})$  line.

the influence of  $a$  is not dominant. The  $1/M$  scaling of the twin peak QPOs frequencies with the 3:2 ratio was proposed by [Abramowicz et al., 2004] as a method for estimating black hole masses in AGNs and ULXs, based on [Mirabel and Rodríguez, 1998] analogy between microquasars in our Galaxy and distant quasars. Indeed, if the analogy is also valid for accretion disk oscillations, then discovering in ULXs the twin peak QPOs frequencies with the 3:2 ratio, would resolve the controversy about their mass: if ULXs black holes have the same masses as microquasars, the frequencies will be  $\sim 100$  Hz; if ULXs black holes are  $\sim 1000$  times more massive, the frequencies will be  $\sim 0.1$  Hz instead.

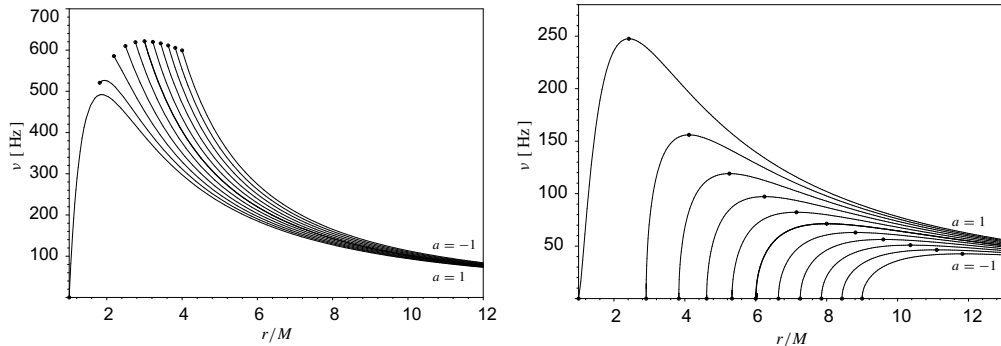


**Figure 5. Left:** The vertical epicyclic frequency for  $10 M_{\odot}$  mass black hole. **Right:** the radial epicyclic frequency for  $10 M_{\odot}$  mass black hole.

### 3 NON-LINEAR, RELATIVISTIC ORBITAL RESONANCES

#### 3.1 Importance of the non-linear effects

The effective potential  $\mathcal{U}(r, \theta; \ell)$  for orbital motion of a particle with a fixed angular momentum  $\ell > \ell_{\text{ms}}$  has a minimum at  $r_0(\ell)$ , corresponding to the location of a stable circular orbit. Its Taylor expansion (for simplicity we write it on the equatorial plane  $\theta = \pi/2$ ),

$$\mathcal{U}(r, \ell) = \frac{1}{2} \left( \frac{\partial^2 \mathcal{U}}{\partial r^2} \right)_0 (r - r_0)^2 + \frac{1}{6} \left( \frac{\partial^3 \mathcal{U}}{\partial r^3} \right)_0 (r - r_0)^3 + \dots \quad (4)$$

contains higher than quadratic terms, which means that small oscillations around the minimum at  $r - r_0$  are described by non-linear differential equations (e.g., [Landau and Lifshitz, 1973, Nayfeh and Mook, 1979]). Non-linear resonances that may be excited in these non-linear oscillations have several characteristic properties that closely resemble those observed in QPOs:

- (i) Resonance occurs in a region with a finite and often large width  $\delta\nu$ .
- (ii) The frequencies of oscillations  $\nu_i$  depend on amplitude and for this reason they may be time dependent and may differ from the fixed eigenvalue frequencies  $\nu_{i(0)}$  of the system,  $\nu_i(t) = \nu_{i(0)} + \delta\nu_i(t)$ .
- (iii) Combination frequencies,  $\nu_{i(0)} \pm \nu_{k(0)}$  may be present.
- (iv) Subharmonic frequencies may be present.

In this Section we shall describe two particularly important non-linear, relativistic resonances, starting from the 3:2 parametric resonance which in our opinion is the best candidate to explain twin peak kHz QPOs in Galactic black hole sources.

#### 3.2 The 3:2 parametric resonance

We shall start with an argument appealing to physical intuition and showing that the resonance now discussed is a very natural, indeed necessary, consequence of strong gravity.

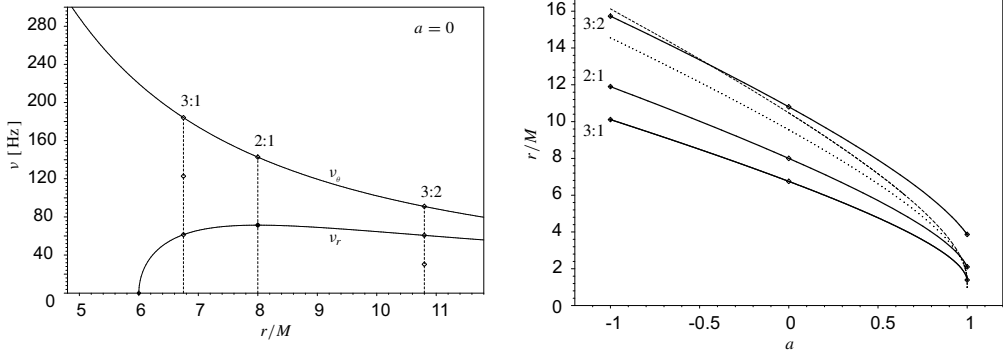


**Figure 6.** **Left:** locations of the three resonances: the 3:2 parametric, and 2:1 and 3:1 forced for Schwarzschild case. **Right:** these locations depending on the black hole spin. Also shown is the radius  $r_F$  (dotted line) at which the standard relativistic Shakura–Sunyaev disk [Page and Thorne, 1974] emits locally the maximal flux, and the radius  $r_C$  (dashed line) corresponding to the pressure centre of the maximally thick torus, i.e., the torus with constant angular momentum equal to the Keplerian value at RISCO.

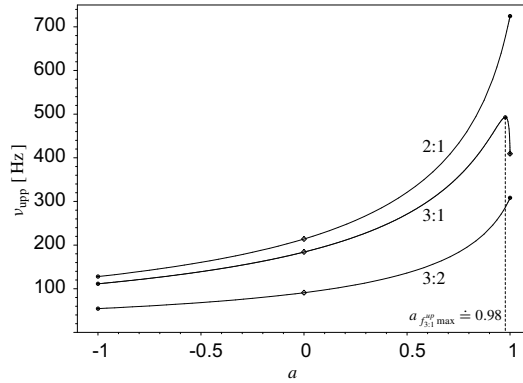


**Figure 7.** Generally non-monotonic dependence  $\nu_{\text{upp}}(a)$  for 3:2 parametric, 3:1 and 2:1 forced resonance in example for ten solar masses black hole.

In thin disks, random fluctuations have  $\delta r \gg \delta \theta$ . Thus,  $\delta r \delta \theta$  is a first order term in  $\delta \theta$  and should be included in the first order equation for vertical oscillations (1). The equation now takes the form,

$$\delta \ddot{\theta} + \omega_\theta^2 [1 + h \delta r] \delta \theta = \delta a_\theta, \quad (5)$$

where  $h$  is a known constant. The first order equation for  $\delta r$  has the solution  $\delta r = A_0 \cos(\omega_r t)$ . Inserting this in (5) together with  $\delta a_\theta = 0$ , one arrives at the Mathieu equation ( $A_0$  is absorbed in  $h$ ),

$$\delta \ddot{\theta} + \omega_\theta^2 [1 + h \cos(\omega_r t)] \delta \theta = 0, \quad (6)$$

that describes the *parametric resonance*. From the theory of the Mathieu equation one knows that when

$$\frac{\omega_r}{\omega_\theta} = \frac{\nu_r}{\nu_\theta} = \frac{2}{n}, \quad n = 1, 2, 3, \dots \quad (7)$$

the parametric resonance is excited [Landau and Lifshitz, 1973]. The resonance is strongest for the smallest possible value of  $n$ . Because near black holes  $\nu_r < \nu_\theta$ , the smallest possible value for resonance is  $n = 3$ , which means that  $2\nu_\theta = 3\nu_r$ . This explains the observed 3:2 ratio, because, obviously,

$$\nu_{\text{upp}} = \nu_\theta, \quad \nu_{\text{down}} = \nu_r. \quad (8)$$

Of course in real disks neither  $\delta r = A_0 \cos(\omega_r t)$ , nor  $\delta a_\theta = 0$  exactly, but one may expect that because these equations are approximately obeyed for thin disks, the parametric resonance will also be excited in realistic situations. And this is indeed the case. The parametric resonance of the type discussed above was found in numerical simulations of oscillations in a nearly Keplerian accretion disk by [Abramowicz et al., 2003a]. Their numerical results were reproduced in an exact analytic solutions first by [Rebusco, 2003] and later confirmed and generalised by [Horák, 2004]. The analytic solution is accurate up to third order terms in  $\delta r$ ,  $\delta \theta$ , and based on the method of multiple scales (see, e.g., [Nayfeh and Mook, 1979]). Existence of the 3:2 parametric resonance is therefore a mathematical property of thin, nearly Keplerian disks. It was found that the resonance is excited only in the non-Keplerian case, with some weak forces  $\delta a_\theta \neq 0$  and  $\delta a_r \neq 0$  present. Their origin is certainly connected to stresses (pressure, magnetic field, viscosity), but exact details remain to be determined – at present  $\delta a_\theta$  and  $\delta a_r$  are not calculated from first principles but described by an ansatz<sup>3</sup>.

The parametric resonance occurs at a particular radius  $r_{3:2}(a)$ , determined by the condition  $3\omega_r(r_{3:2}, a) = 2\omega_\theta(r_{3:2}, a)$  and equation (2). We show the function  $r_{3:2}(a)$  in Fig. 6. In Fig. 8 we fit the 3:2 resonance theoretically predicted frequencies to the observational data for the three microquasars with the known masses.

### 3.3 The forced 3:1 and 2:1 resonances – possible combination of frequencies

A direct resonant forcing of vertical oscillations by the radial ones through a pressure coupling, and with  $\delta a_r \sim \cos(\omega_r t)$ , was evident in recent numerical simulations of oscillations of a perfect fluid torus [Lee et al., 2003]. This supports an idea [Abramowicz and Kluźniak, 2001] for another possible model for the twin peak kHz QPOs: a forced non-linear oscillator,

$$\delta \ddot{\theta} + \omega_\theta^2 \delta \theta + [\text{non linear terms in } \delta \theta] = h(r) \cos(\omega_r t), \quad \omega_\theta = n\omega_r. \quad (9)$$

Obviously, there is no value for  $n$  such that  $\omega_\theta$  and  $\omega_r$  could be in the 3:2 ratio. However, the non-linear terms allow the presence of combination frequencies in a resonant solutions for  $\delta \theta(t)$  (see, e.g., [Landau and Lifshitz, 1973]),

<sup>3</sup> While the lack of a full physical understanding is obviously not satisfactory, the experience tells that such a situation is not uncommon for non-linear systems. Examples are known of mathematically possible resonances causing damage in bridges, aeroplane wings etc., for which no specific physical excitation mechanism could have been pinned down [Nayfeh and Mook, 1979].

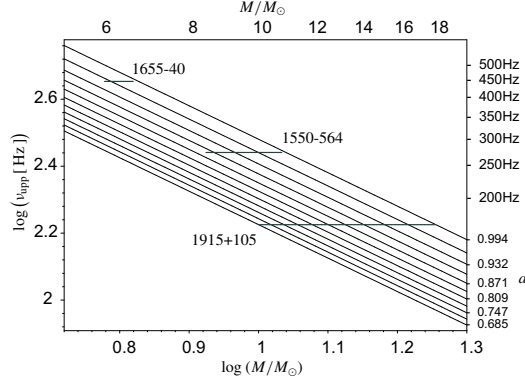


**Figure 8.** Fit of the frequency  $\nu_{\text{upp}} = \nu_{\theta}(M, a)$  predicted by the 3:2 parametric resonance model to the frequencies observed in three microquasars with known masses. The spin parameter  $a$  is not known from observations, and the lines  $a = \text{const}$  are calculated from the model. One should notice that the deduced black hole spins are rather high, which is expected if microquasars' jets are a signature of large spin of the centre black hole.

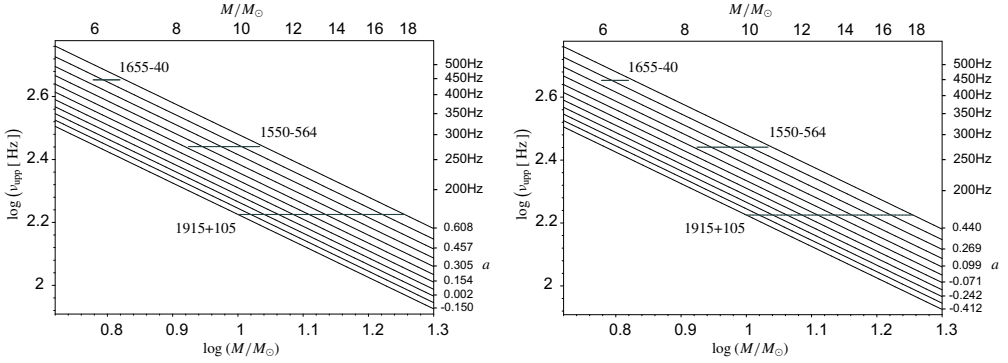


**Figure 9. Left:** Fit of the predictions of the 3:1 forced resonance model to observations. **Right:** the same for the 2:1 forced resonance. Both resonances are between vertical and radial epicyclic oscillations.

$$\omega_- = \omega_{\theta} - \omega_r, \quad \omega_+ = \omega_{\theta} + \omega_r. \quad (10)$$

As noticed by [Abramowicz and Kluźniak, 2001], these combination frequencies may be in the 3:2 ratio for  $n = 2$ , or  $n = 3$  forced resonances (for the detailed discussion of other possibilities, see [Török et al., 2004]). Simple arithmetic shows that in these two cases the observed frequencies  $\nu_{\text{down}} = \omega_{\text{down}}/2\pi$  and  $\nu_{\text{upp}} = \omega_{\text{upp}}/2\pi$  are uniquely given by,

$$\omega_{\text{down}} = \omega_- = 2\omega_r, \quad \omega_{\text{upp}} = \omega_{\theta} = 3\omega_r \quad \text{for } n = 3 \text{ f. epicycl. res.} \quad \omega_{\theta} = 3\omega_r, \quad (11)$$

$$\omega_{\text{upp}} = \omega_+ = 3\omega_r, \quad \omega_{\text{down}} = \omega_{\theta} = 2\omega_r \quad \text{for } n = 2 \text{ f. epicycl. res.} \quad \omega_{\theta} = 2\omega_r. \quad (12)$$

We fit observed QPOs to those predicted by the forced epicyclic 3:1 and 2:1 resonances in Fig. 9.

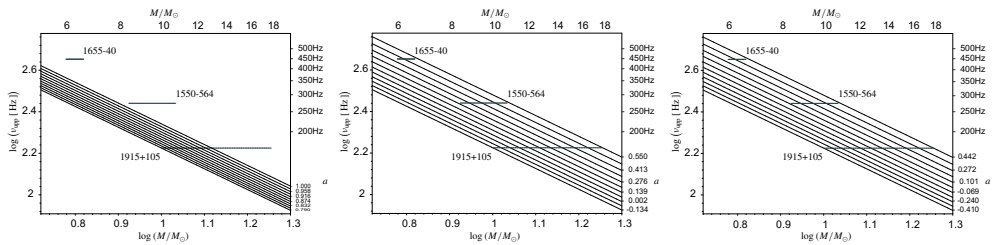


**Figure 10.** From left: fit of the predictions of the hypothetical 3:2, 3:1 and 2:1 “Keplerian” resonance to observations. Resonances are between radial epicyclic oscillations and some hypothetical (and physically unlikely) oscillations at Keplerian frequency.

### 3.4 “Keplerian” resonances

The resonances discussed so far were due to a coupling between epicyclic oscillations – radial and vertical. Such a coupling exists in variety of realistic physical situations. One may also imagine a physical coupling between radial epicyclic oscillations and the orbital Keplerian motion. For example, [Abramowicz and Kluźniak, 2001] noticed that it is possible for the radial epicyclic frequency to be in a resonant relation with the orbital frequency,  $n\nu_r = m\nu_K$ , with  $n, m$  integer. The case (Table 2)  $\nu_K/\nu_r = 3/2$  is excluded by observations – see left panel of Fig. 10. The remaining possibilities are that the upper frequency  $\nu_{\text{upp}} = \nu_K$ , with  $\nu_K/\nu_r = 3$ , or  $\nu_{\text{upp}} = \nu_K + \nu_r$ , with  $\nu_K/\nu_r = 2/1$  (Fig. 10 – middle and right panel).

[Kato, 2001a] considered a particular case of the g-modes with frequencies (14). In this case, the co-rotation resonance with  $\nu_m = \nu_K$  may occur. However, the co-rotation resonance leads to damping, and not excitation, of modes [Kato, 2001b].

Another possibility for a physical coupling between radial epicyclic oscillations and the orbital Keplerian motion is provided by the Spiegel’s vortex idea [Abramowicz et al., 1992]. When the potential vorticity is conserved, coherent vortices tend to form in pairs with opposite vorticity [Bracco et al., 1998]. One may imagine that because the spatial distance between the two structures that oscillate with the epicyclic radial frequency depends on the velocity profile of the disk, i.e., also on the oscillations of orbital velocity, a resonance between these two frequencies is possible.

In Fig. 10 we plot the prediction of the only three possible “Keplerian” cases corresponding to  $\omega_{\text{upp}}/\omega_{\text{down}} = 3/2$ .

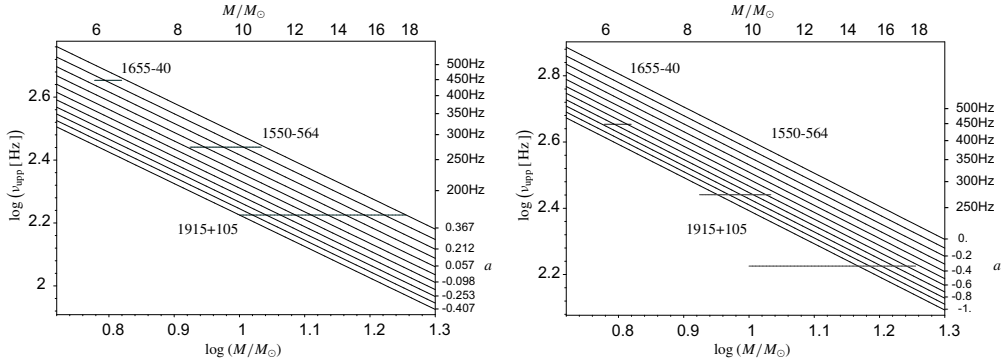
## 4 NON-RESONANT FREQUENCIES THAT SCALE WITH $1/M$

### 4.1 The highest possible orbital frequency, ISCO and RISCO

Matter moves, roughly, on circular orbits in the region  $r > r_{\text{in}}$  and free-falls in the region  $r < r_{\text{in}}$ . The radius  $r = r_{\text{in}}$  is often called the inner radius of accretion disk. It is located between the marginally stable  $r_{\text{ms}}$ , i.e., ISCO and marginally bound  $r_{\text{mb}}$ , i.e., RISCO circular orbits [Kozłowski et al., 1978, Krolik and Hawley, 2002], depending on efficiency. Thin, standard Shakura-Sunyaev disk have high efficiencies and their inner edge is located almost exactly at ISCO. Adafs, with their very low efficiencies, have the inner edges almost exactly

**Table 2.** Summary of relation for observed frequencies  $\nu_{\text{upp}}$ ,  $\nu_{\text{down}}$  for “standard” ( $\nu_{\text{v}} = \nu_{\theta}$ ) and “Keplerian” ( $\nu_{\text{v}} = \nu_{\text{K}}$ ) resonances.

		Theory		Observed frequencies	
Type of resonance		$n\nu_{\text{rad}} = m\nu_{\text{v}}$		$\nu_{\text{upp}}$	$\nu_{\text{down}}$
		$n$	$m$		
standard	parametric	3	2	$\nu_{\theta}$	$\nu_{\text{rad}}$
	3:1 forced	3	1	$\nu_{\theta}$	$\nu_{\theta} - \nu_{\text{rad}}$
	2:1 forced	2	1	$\nu_{\theta} + \nu_{\text{rad}}$	$\nu_{\theta}$
Keplerian	parametric	3	2	$\nu_{\text{K}}$	$\nu_{\text{rad}}$
	3:1 forced	3	1	$\nu_{\text{K}}$	$\nu_{\text{K}} - \nu_{\text{rad}}$
	2:1 forced	2	1	$\nu_{\text{K}} + \nu_{\text{rad}}$	$\nu_{\text{K}}$

**Figure 11.** Left: ISCO frequencies compared with the observed kHz twin peak QPOs. Right: the same for RISCO.

at RISCO [Abramowicz et al., 1996]. The same is true for super-Eddington slim and thick disks [Abramowicz et al., 1988, Jaroszyński et al., 1980]. In Fig. 4 we compare ISCO and RISCO frequencies for  $10 M_{\odot}$  black holes with different spins. For a non-rotating black hole one has  $r_{\text{RISCO}} = 4M$ ,  $\nu_{\text{RISCO}} = 4037 (M/M_{\odot})^{-1}$  [Hz], and  $r_{\text{ISCO}} = 6M$ ,  $\nu_{\text{ISCO}} = 2197 (M/M_{\odot})^{-1}$  [Hz]. Comparing ISCO and RISCO frequencies with the twin peak kHz QPOs upper frequency is only of formal interest. It is done in Fig. 11.

## 4.2 Dragging of inertial frames and the c-mode

The “corrugation” c-mode [Silbergleit et al., 2001] is a non-axisymmetric, vertically incompressible wave near the inner edge of the disk that exists only for co-rotating disks  $a > 0$ . It precesses around the angular momentum of the black hole. Its frequency coincides with

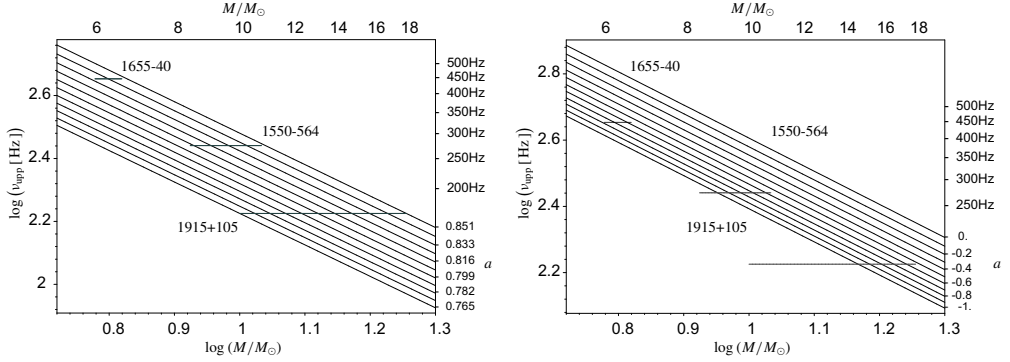


**Figure 12.** Left: c-mode ISCO frequencies compared with the observed kHz twin peak QPOs. Right: the same at RISCO.

the Lense–Thirring frequency produced by the dragging of inertial frames. In Fig. 12 we compare with observations the highest frequency connected to the c-mode, assuming that the mode is located at ISCO or RISCO:

$$\nu_{\text{upp}} = \nu_{\text{LT}}(r_{\text{ms}}), \quad \text{or} \quad \nu_{\text{upp}} = \nu_{\text{LT}}(r_{\text{mb}}), \quad \text{where (in units SI)} \quad \nu_{\text{LT}} = \frac{GM_0}{\pi c^2 r^3} a. \quad (13)$$

### 4.3 The trapped modes

One of the characteristic properties of the oscillations of relativistic disks is the presence of trapped mode oscillations [Okazaki et al., 1987, Nowak and Wagoner, 1992, Perez et al., 1997]. The physical reason for the trapping is that the radial epicyclic frequency,  $\nu_r$ , is not monotonic but has a maximum value,  $\nu_{\text{trapp}}$ , at a radius  $r_{\text{trapp}}$  slightly larger than the ISCO. For the non-rotating black hole  $r_{\text{trapp}} = 8M$  [Kato and Fukue, 1980]. The g-mode (inertial-gravity) oscillations [Perez et al., 1997] can be characterised by a restoring force that is typically dominated by the net gravitational-centrifugal force. The axisymmetric ( $m = 0$ ) g-modes are centred at  $r_{\text{trapp}}$ . Non-axisymmetric trapped g-modes with the azimuthal wave-number  $m = 1$  have frequencies [Kato, 2001b]

$$\nu \sim \nu_{\text{K}}(r_{\text{trapp}}) \pm \nu_{\text{trapp}}, \quad \text{and} \quad \nu \sim \nu_{\text{K}}(r_{\text{trapp}}). \quad (14)$$

In Fig. 13 we show the highest frequency connected to these oscillations,  $\nu_{\text{upp}} = \nu_{\text{K}}(r_{\text{trapp}}) + \nu_{\text{trapp}}$ , and compare it with observations.

## 5 IMPORTANCE OF THE $1/M$ SCALING. ULX AND INTERMEDIATE BLACK HOLES.

If [Mirabel and Rodríguez, 1998] analogy between microquasars in our Galaxy and distant quasars is valid also for the properties of accretion disks oscillations in those black-hole sources, one would expect the radiation from AGNs to be modulated quasi-periodically at a frequency in the microhertz range for a billion solar mass black hole. Discovering the counterpart of microquasar’s 3:2 twin peak kHz QPOs in AGNs would convincingly

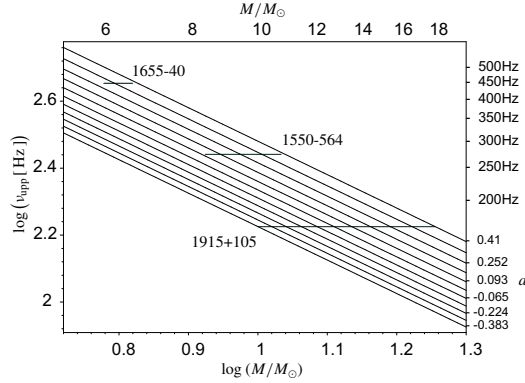


**Figure 13.** The highest trapped g-mode frequencies compared with the observed kHz twin peak QPOs.

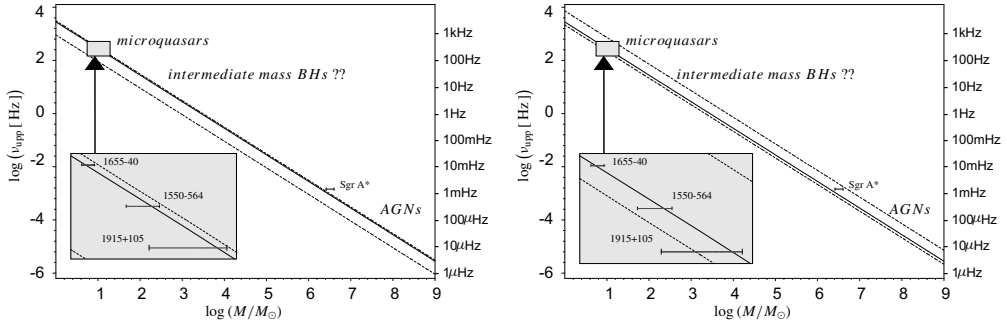


**Figure 14. Left:** the observed twin peak 3:2 QPOs in microquasars and their yet to be discovered counterparts in ULXs and AGNs: the importance of the  $1/M$  scaling. The solid line is the best fit  $\nu_{\text{ripp}}$  vs.  $1/M$  found by [McClintock and Remillard, 2003] and described by equation  $\nu_{\text{ripp}} \doteq 2.8 (M_{\odot}/M) \text{ kHz}$ . Dotted lines for the case of the 3:2 parametric resonance are for  $a = 0$  (lower line) and  $a = 1$  (upper line). Mass range for Sgr A\* corresponds to the range given by inequality (15). Vertical error bar for Sgr A\* is given by Table 3. **Right:** the same, only dotted lines are for 2:1 forced resonance.

test this theory which, if true, would provide a new method of estimating the central black-hole mass. [Abramowicz et al., 2004] pointed out that determination of the (as yet undetected) frequencies of the twin QPOs in the recently discovered ULX (ultra-luminous X-ray) sources, would resolve the controversy about their mass – twin QPOs in a 2:3 frequency ratio would have a frequency of about 0.1 Hz, instead of the 100 Hz value in the microquasars, if the black hole mass were about 1000 times larger than is usual for stellar-mass black holes. The idea of the 3:2 resonance frequency  $1/M$  scaling is illustrated in Figs 14 and 15. One should notice that the lack of a priori knowledge of black hole’s angular momentum is of relatively minor importance.

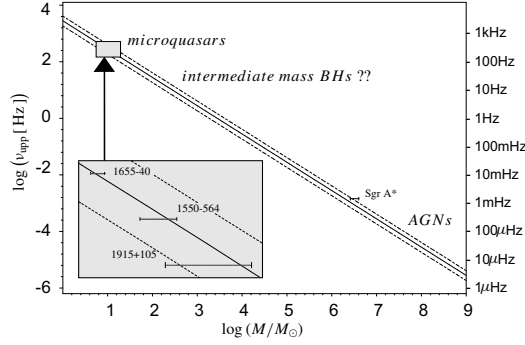


Figure 15. The same for 3:1 forced resonance.

### 5.1 Double peak QPOs with the 3:2 ratio in Sgr A\* ?

From the best current analysis of stellar orbits within 10-100 light hours of Sgr A\*, obtained independently by the MPI Garching group [Schoedel, 2002, Schoedel et al., 2003, Eisenhauer et al., 2003] and the UCLA group [Ghez, 2003, Ghez, 2004], the best estimate of the central mass is  $3.6 \pm 0.4 \times 10^6 M_\odot$ , where the error bars represent both statistical and systematic errors. Earlier lower statistical mass estimates based on proper motions of stars further away gave somewhat lower masses ( $2.6 \times 10^6 M_\odot$ ) but in the light of new information on stellar distribution and anisotropies these earlier data would now also lead to masses near  $3.5 \times 10^6 M_\odot$  (see the discussion in [Schoedel et al., 2003]). This well constrained mass must be contained within a few light hours, which is still several hundred Schwarzschild radii, of course. The analysis of the spatial distribution of the stellar cusp centred on the BH suggests that most likely no more than  $1 \times 10^3 M_\odot$  of that is in form of stars or stellar remnants (the latter is less well constrained: [Genzel et al., 2003]). From the lack of motion of the radio source itself and a theoretical comparison of the stochastic motions of a BH of different masses with surrounding stars, a lower limit of the mass contained within the radius of the radio source (10 light minutes, 20 Schwarzschild radii) is about  $\sim 10^5 M_\odot$  [Reid et al., 1999, Reid et al., 2003, Backer and Sramek, 1999, Schoedel et al., 2003].

From these papers one concludes that the most likely mass of the BH in Sgr A\* is in the interval

$$2.6 \times 10^6 M_\odot < M < 4.4 \times 10^6 M_\odot, \quad (15)$$

and that a very conservative lower limit is  $\sim 10^5 M_\odot$ <sup>4</sup>. [Genzel et al., 2003] measured a clear periodicity of 17 min (1020 sec) in Sgr A\* variability during a flaring event. This period is in the range of Keplerian orbital periods at a few gravitational radii away from a black hole with the mass constrained by (15). More recently, [Aschenbach et al., 2004] have reported three other QPOs periodicities, 692 sec, 1130 sec, 2178 sec, roughly in the orbital Keplerian range, and two much shorter periods of 100 sec and 219 sec. [Aschenbach et al., 2004] gave not enough information to convince the reader that periodicities found by them

<sup>4</sup> We thank Reinhard Genzel for providing updated information on the Sgr A\* mass measurements that is discussed here.

**Table 3.** Frequencies of twin peak mHz QPOs in Galaxy centre black hole.

Source	$\nu_{\text{upp}}$ [mHz]	$\Delta\nu_{\text{upp}}$ [mHz]	$\nu_{\text{down}}$ [mHz]	$\Delta\nu_{\text{down}}$ [mHz]	$2\nu_{\text{upp}}/3\nu_{\text{down}} - 1$	Mass [ $10^6 M_{\odot}$ ]
(a) Sgr A*	1.445	$\pm 0.16$	0.886	$\pm 0.04$	0.08728	2.6 – 4.4

(a) From [Aschenbach et al., 2004].

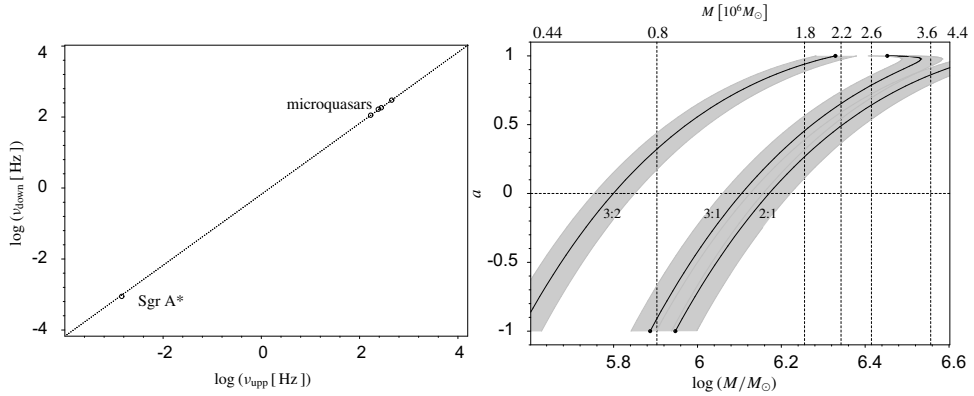


**Figure 16. Left:** The same 3:2 ratio as for microquasars (Fig. 1) seems to be present in double peak QPOs in Sgr A\*. The accuracy is so high that the error bars cannot be shown in this logarithmic plot. **Right:** Spin dependence for 3:2 parametric, 3:1 and 2:1 forced resonance in Sgr A\* implied by measured period 692 s, shadows respect accuracy of measuring.

are significant and real. It is also difficult to judge their estimates of errors in the frequency determination. This is a serious problem, because quality of the time series used by them is not impressively high, and their PDS appear rather messy. Their value of 1130 sec differ by 10% from the 1020 sec period found by [Genzel et al., 2003] and may correspond to the same real periodicity of the source, but again it is difficult to be firmly convicted. Having these serious uncertainties in mind<sup>5</sup>, we note nevertheless that

$$(1/692) : (1/1130) : (1/2178) \approx 3 : 2 : 1, \quad (16)$$

i.e., that the “Keplerian” frequencies found in Sgr A\* form ratios that are very close to be an exact commensurable sequence, 3:2:1. The data for Sgr A\* are picked-up in Table 3. Corresponding spin calculations for five representative values of the Sgr A\* mass are summarised in Table 6, and illustrated in Figs 16, 14 and 15.

<sup>5</sup> We thank several X-ray observers and data analysts who have discussed this point with us.

## 6 DISCUSSION: WHAT NEEDS TO BE DONE

### 6.1 Physics of X-ray flux modulation

The analytic resonance model predicts twin peak kHz QPOs frequencies with values and ratios corresponding to those observed. However, it is rather vague in explaining how the X-ray flux is actually modulated by the resonant disk oscillations. One has here an interesting and promising prediction, but without much of supporting physics. Situation with numerical simulations is exactly opposite – they provide a very detailed description of physics, but fail to predict twin peak kHz QPOs. Indeed, although the recent sophisticated 3-D MHD simulations of accretion disks performed independently by several groups (e.g., [Igumenshchev et al., 2003, Villiers et al., 2003]) reveal a very complex time-dependent accretion flow structure, no twin peak kHz QPOs resembling those observed have ever been found in these simulations.

The apparent lack of agreement between the analytic and numerical models may have its source in the fact that all analytic models describe thin, nearly Keplerian, disks while numerical simulations deal with far more thicker disks and adafs. This may reflect a genuine physical difference, and suggest that twin peak kHz QPOs originate only in thin, nearly Keplerian disks, but not in the thick non-Keplerian ones. However, a possible counterexample to that may emerge from studies of oscillations of tori in the QPOs context, indicated by [Rezzolla et al., 2003] and further developed by [Kluźniak et al., 2003], and [Lee et al., 2003]. Such tori at present are not yet physically realistic – are assumed to be adiabatic, constant angular momentum, inviscid and axisymmetric. It is therefore impossible to formulate a firm opinion about their possible relevance to the QPOs phenomenon. In this respect, it would be crucially important to develop 3-D, time dependent, non-axisymmetric and not equatorial plane symmetric numerical codes to study wrapped, non steady slim disks in Kerr geometry. It is a difficult task. The existing time dependent slim accretion disk numerical codes which are an obvious starting point for further developments (e.g., [Szuszkiewicz and Miller, 2001]) are far behind of what is needed.

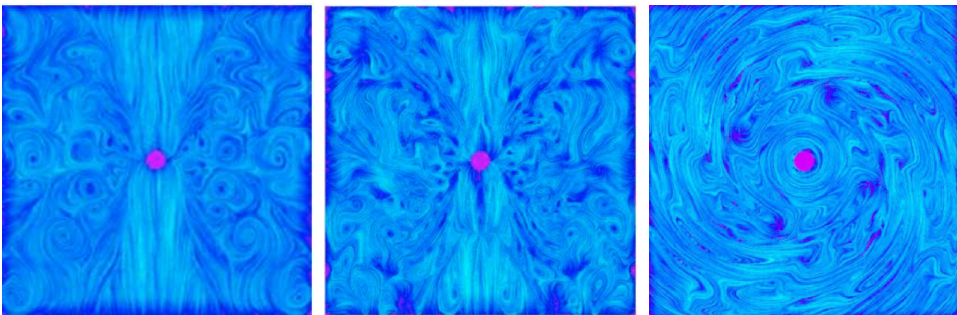


**Figure 17.** Three snapshots of accretion disk from 3-D MHD simulation by [Igumenshchev et al., 2003] (reproduced with permission) show a very complex behaviour dominated by vigorous convection, but not kHz QPOs. This is typical for all recent 3-D MHD simulations, also by other authors.

## 6.2 X-ray flux modulation by Doppler, light bending and lensing in Kerr geometry

X-ray flux must also be modulated by the relativistic Doppler effect, light bending and lensing. [Schnittman and Bertschinger, 2003] assumed that the 3:2 parametric resonance produces a “hot spot”, a coherent non-axisymmetric structure at  $r = r_{3:2}$  that corotates with the disk. They then determined, by directly calculating light trajectories from the spot to an observer very far away (at infinity), X-ray flux modulation by the disk rotation and by relativistic effects on light propagation. They concluded that relativistic effects in light trajectories are very strong, in fact dominant, for high inclinations,  $i > 60^\circ$ , in accord with the results obtained for spots orbiting the Schwarzschild black holes (see, e.g., [Bao and Stuchlík, 1992]). By matching the calculated variability power spectra with those observed, [Schnittman and Bertschinger, 2003] restricted several free parameters of the hot spot, in particular its size and shape.

A different model for modulation by general relativistic Doppler effect, light bending and lensing was developed by Bursa, Abramowicz, Karas and Kluźniak (2003, in preparation). They assumed that an optically thin and geometrically slender torus located at the parametric resonance radius,  $r = r_{3/2}$  oscillates with the epicyclic frequencies  $\nu_r, \nu_\theta$ . Then, by ray tracing, they constructed the observed light curve of the torus. An interesting result of this calculation is that a significant modulation may be obtained also in a situation which is almost axially symmetric. Details may be found in M. Bursa’s contribution to these Proceedings [Bursa, 2004].

## 6.3 The Psaltis–Belloni–van der Klis–Mouche correlation. The 13th wave?

It was noticed by [Psaltis et al., 1999] that a correlation exists between the high ( $\sim$ kilohertz) QPOs frequencies  $\nu_{\text{high}}$ , and the low ( $\sim$ hertz) QPOs frequencies  $\nu_{\text{low}}$  for neutron star and black hole sources,

$$\nu_{\text{low}} = 0.08\nu_{\text{high}} \quad (17)$$

[Mauche, 2002] extended this correlation to cataclysmic variables and show that it is obeyed by high frequency quasi-coherent “dwarf nova oscillations” and the low frequency “horizontal branch” oscillations.

This is a *very* serious problem to *any* relativistic model of kHz QPOs including the resonance model discussed here. Indeed, one may assume that the correlation (17) indicates the same physical origin of high frequency oscillations in black hole, neutron stars and white dwarf accretion disks. However, this immediately excludes relativistic mechanisms because, obviously, correlation (17) is incompatible with the relativistic  $1/M$  scaling.

[Abramowicz et al., 2003b], suggested a possible way to resolve the problem. In turbulent accretion disks around black holes, neutron stars and white dwarfs alike, most of the high frequency variability should be connected to transient oscillatory phenomena that occur at random locations in disks. Because they are not connected to any particular location fixed in terms of gravitational radius, they do not scale with  $1/M$ . These locally excited high frequency waves are subject to the side-band [Benjamin and Feir, 1967] instability, well known in oceanography. Suppose that a deep water wave pulse contains initially waves of identical length. Non-linearities will cause the crests of waves with the larger amplitude  $a$

to travel more quickly,  $\omega^2 \sim k(1 + k^2 a^2)$ . Thus, wave number  $k$  will tend to increase in the front of the pulse and decrease at the end of the pulse. The shorter waves in the front of the pulse and the longer waves behind the pulse cause energy to approach the centre of the pulse, resulting in an increase of the amplitude in the centre. This feeds the instability. As a result, about every  $n$ -th wave has a higher amplitude, and this creates a low frequency quasi-periodicity, with  $\omega/n$ . The value of  $n$  depends on particular details, and there is not a general agreed theory to explain why the “9th wave” seems to be the most common in oceans and seas. If the side band instability is also behind the correlation, then in accretion disks, for some reason,  $1/0.08 \sim 13 = n$ , i.e., “13th wave” is most common.

Among these random high frequency phenomena, only double peak kHz QPOs with rational ratios originate due to a relativistic effect: strong gravity’s orbital epicyclic parametric resonance. They of course may also be accompanied by the low frequency “13th wave” and therefore fit the correlation (17). However, they are unique to black hole and neutron stars accretion disks. And this is the point here. Because it is likely that finding the reason for accretion disks’ “13th wave” could be similarly unsuccessful as finding the reason for the “9th wave” in oceanography, one may argue that the discussion above has a little predictive power. However, it obviously makes one clear, testable prediction: there should be no twin peak dwarf nova oscillations.

#### 6.4 Models without the $1/M$ scaling

Some of the twin peak kHz QPOs theoretical models based not on relativistic orbital motion but instead on hydrodynamical oscillations [Rezzolla et al., 2003] or magnetohydrodynamical ones [Li and Narayan, 2003] may predict rational ratios of frequencies (and in particular the 3:2 ratio), but without making some ad hoc assumptions they do not naturally explain the  $1/M$  relativistic orbital scaling.

## 7 CONCLUSIONS

### 7.1 Orbital resonance model for microquasars

In Table 4 we summarise results of our estimates of the black hole spin for the three microquasars with known masses. The uncertainty in the spin estimate is due to uncertainty in the present knowledge of the black hole mass. In this respect we note that in the case of GRO 1655–40, the possible spin ranges given in Table 2 for 3:1 and 2:1 Keplerian resonances are, respectively, 0.45–0.53, and 0.31–0.42. They are more precise than the corresponding estimates by Abramowicz & Kluźniak (2001), i.e., 0.36–0.67 and 0.2–0.6. The improvement in the accuracy is due to the improvement in the knowledge of the mass of GRO 1655–40. In 2001 the mass was known to be in the range  $5.5 < M/M_{\odot} < 7.9$ , while in 2003 the accuracy increased to  $6.0 < M/M_{\odot} < 6.6$ .

The resonance model is rather sensitive to observational constraints: the data already excludes the 3:2 Keplerian resonance as a possible explanation of twin peak QPOs in case of two microquasars. All other resonances discussed in the paper are consistent with the existing data, but it is plausible that future observations may narrow down the choice of a resonance. Future developments in accretion disk theory could also narrow down the

**Table 4.** Summary of angular momentum estimates for resonance models (Figs 8–10).

Model	Interval of possible spin implicated for given source:		
	1550–564	1655–40	1915+105
3:2 [ $\nu_\theta, \nu_r$ ] parametric	+0.89 – +0.99	+0.96 – +0.99	+0.69 – +0.99
2:1 [ $\nu_\theta, \nu_r$ ] forced	+0.12 – +0.42	+0.31 – +0.42	–0.41 – +0.44
3:1 [ $\nu_\theta, \nu_r$ ] forced	+0.32 – +0.59	+0.50 – +0.59	–0.15 – +0.61
3:2 [ $\nu_K, \nu_r$ ] “Keplerian” p.			+0.79
2:1 [ $\nu_K, \nu_r$ ] “Keplerian” f.	+0.12 – +0.43	+0.31 – +0.42	–0.41 – +0.44
3:1 [ $\nu_K, \nu_r$ ] “Keplerian” f.	+0.29 – +0.54	+0.45 – +0.53	–0.13 – +0.55

Table contain pure values of dimensionless spin computed from exact upper observed frequency, additional error  $\Delta a(\Delta\nu_{\text{upp}})$  resulting from uncertainty of frequency measurement (Table 1) is for microquasars XTE 1550–564 (GRO 1655–40, GRS 1915+105) given by relation:  $\Delta a(\Delta\nu_{\text{upp}}) \sim \pm 0.03$  (0.01, 0.05).

**Table 5.** Summary of angular momentum estimates for some other models (Figs 11–13).

Model	Interval of possible spin implicated for given source:		
	1550–564	1655–40	1915+105
Marginally stable (ISCO)	+0.07 – +0.35	+0.25 – +0.35	–0.41 – +0.37
Marginally bound (RISCO)	– –0.56	–0.78 – –0.58	– –0.53
C-mode at ISCO	+0.81 – +0.85	+0.84 – +0.85	+0.76 – +0.85
C-mode at RISCO	+0.63 – +0.68	+0.66 – +0.68	+0.56 – +0.68
Highest g-mode	+0.11 – +0.40	+0.29 – +0.39	–0.38 – +0.41

choice. For example, it is often argued that the presence of relativistic jet is a signature of large black hole spin [Blandford and Znajek, 1977], see however [Ghosh and Abramowicz, 1997]. Because microquasars do have jets, one would expect that  $a \approx 1$  for their black holes. This argument, if proven true, would uniquely point to the 3:2 parametric resonance, as the only possible choice for this microquasars.

## 7.2 Implications for other black hole sources

If commensurability of double peak QPOs frequencies in Sgr A\* is confirmed, this together with the already established  $1/M$  scaling, would give a very strong support for the suggestion that the double peak QPOs physics, the same in microquasars and in Sgr A\*, is due to a non-linear orbital resonance in strong gravity. It would be interesting to see whether other

**Table 6.** Sgr A\* spin estimates from observed 3:2 QPOs, calculated for five representative values of mass from large spectrum above lower conservative limit include the best mass estimate  $3.6 \times 10^6 M_\odot$ .

Mass [ $10^6 M_\odot$ ]:	0.8	1.8	2.2	2.6	3.6
<b>Resonances</b>					
3:2 [ $\nu_\theta, \nu_r$ ] parametric	0.32	0.94	(b)	(a)	(a)
2:1 [ $\nu_\theta, \nu_r$ ] forced	(b)	0.28	0.49	0.64	0.86
3:1 [ $\nu_\theta, \nu_r$ ] forced	-0.91	0.46	0.65	0.79	(b)
3:2 [ $\nu_K, \nu_r$ ] “Keplerian” p.	0.37	(a)	(a)	(a)	(a)
2:1 [ $\nu_K, \nu_r$ ] “Keplerian” f.	(c)	0.27	0.49	0.65	0.88
3:1 [ $\nu_K, \nu_r$ ] “Keplerian” f.	-0.82	0.41	0.59	0.71	0.89

(a) marking no solution with  $-1 < a < 1$

(b) marking no solution with  $-1 < a < 1$  but see Fig. 16 (left panel) – there is some possibility because of frequency measurement errors

(c) marking no solution with  $-1 < a < 1$  but there is some possibility because of frequency measurement error

Because in the case of Galaxy centre black hole the error bar of measured upper frequency is much smaller than of down frequency ( $1.5\Delta a(\nu_{\text{down}}) < \Delta a(\nu_{\text{upp}})$ ) is more correct to compute spin estimate from down frequency. This is already fixed in [Török, 2004].

black hole sources, ULXs and AGNs, as was described in Section 5, show the same phenomenon [Abramowicz et al., 2004].

For black hole sources with known mass that display the double peak QPOs, one may measure the black hole spin, but the spin estimate depends on which of the theoretically possible resonance, 2:1, 3:1, or 3:2, is actually excited in the source. At present, neither observations, nor the resonance theory could firmly determine this.

Different resonances occur at very different resonance radii. Fig. 6 shows that accretion disk physics at these radii is also very different. The 3:2 parametric resonance is located at a very outer part of the innermost region of the disk, the 2:1 resonance is located in the middle of this region, and the 3:1 resonance most close to the inner edge. A physical excitation mechanism (still unknown) may be very different for different resonances.

## ACKNOWLEDGEMENTS

We thank Ron Remillard, Jeff McClintock, R. V. Wagoner, Tomek Bulik, Reinhard Genzel, Vladimír Karas, Jean-Pierre Lasota, Jeff McClintock, Ramesh Narayan, Bohdan Paczyński and Luciano Rezzolla for discussion. Most of the work reported here was done at the UK

Astrophysical Fluids Facility (UKAFF) and supported through the European Commission *Access to Research Infrastructure action of the Improving Human Potential Program*. Z. S. and G. T. were supported by the Czech GAČR grants 202/02/0735 and 205/03/H144, and M. A. A. and W. K. by the Polish KBN grant 2P03D01424.

## REFERENCES

- [Abramowicz et al., 1992] Abramowicz, M. A., A., A. L., Spiegel, E. A., and Szuszkiewicz, E. (1992). Vortices on accretion disks. *Nature*, 356:41.
- [Abramowicz et al., 1999] Abramowicz, M. A., Björnsson, G., and Pringle, J. E. (1999). *Theory of Black Hole Accretion Disks*. Cambridge University Press, Cambridge.
- [Abramowicz et al., 1996] Abramowicz, M. A., Chen, X.-M., Granath, M., and Lasota, J.-P. (1996). Advection-dominated Accretion Flows around Kerr Black Holes. *Astrophys. J.*, 471(2):762.
- [Abramowicz et al., 1988] Abramowicz, M. A., Czerny, B., Lasota, J. P., and Szuszkiewicz, E. (1988). *Astrophys. J.*, 332:646.
- [Abramowicz et al., 2003a] Abramowicz, M. A., Karas, V., Kluźniak, W., Lee, W., and Rebusco, P. (2003a). Non-Linear Resonance in Nearly Geodesic Motion in Low-Mass X-Ray Binaries. *Publ. Astronom. Soc. Japan*, 55(2):467.
- [Abramowicz and Kluźniak, 2001] Abramowicz, M. A. and Kluźniak, W. (2001). A precise determination of black hole spin in GRO J1655-40. *Astronomy and Astrophysics*, 374:L19.
- [Abramowicz et al., 2003b] Abramowicz, M. A., Kluźniak, W., Barret, D., Lee, W., and Spiegel, E. (2003b). In preparation.
- [Abramowicz et al., 2004] Abramowicz, M. A., Kluźniak, W., McClintock, J. E., and Remillard, R. A. (2004). The importance of discovering a 3:2 twin-peak QPO in a ULX or how to solve the puzzle of intermediate mass black holes. *Submitted to Astrophys. J.* arXiv: astro-ph/0402012.
- [Aschenbach et al., 2004] Aschenbach, B., N., N. G., Porquet, D., and Predehl, P. (2004). X-ray flares reveal mass and angular momentum of the Galactic Center black hole. astro-ph/0401589.
- [Backer and Sramek, 1999] Backer, D. C. and Sramek, R. A. (1999). Proper Motion of the Compact, Nonthermal Radio Source in the Galactic Center, Sagittarius A\*. *Astrophys. J.*, 524(2):805–815.
- [Bao and Stuchlík, 1992] Bao, G. and Stuchlík, Z. (1992). *Astrophys. J.*, 400:163.
- [Benjamin and Feir, 1967] Benjamin, T. B. and Feir, J. E. (1967). The disintegration of wave trains in deep water, Part1. Theory. *J. Fluid Mech.*, 27:417–430.
- [Blandford and Znajek, 1977] Blandford, R. D. and Znajek, R. L. (1977). *Monthly Notices Roy. Astronom. Soc.*, 197:433.
- [Bracco et al., 1998] Bracco, A., Provenzale, A., Spiegel, E. A., and Yecko, P. (1998). Cambridge University Press.
- [Bursa, 2004] Bursa, M. (2004). Variability of accreting sources at very high time resolution. In Hledík, S. and Stuchlík, Z., editors, *Proceedings of RAGtime 4/5: Workshops on*

- black holes and neutron stars, Opava, 14–16/13–15 October 2002/03*, Opava. Silesian University in Opava. This volume.
- [Eisenhauer et al., 2003] Eisenhauer, F., Schödel, R., Genzel, R., Ott, T., Tecza, M., Abuter, R., Eckart, A., and Alexander, T. (2003). A Geometric Determination of the Distance to the Galactic Center. *Astrophys. J. Lett.*, 597(2):L121.
- [Genzel et al., 2003] Genzel, R., Schödel, R., Ott, T., Eisenhauer, F., Hofmann, R., Lehnert, M., Eckart, A., Alexander, T., Sternberg, A., Lenzen, R., Clénet, Y., Lacombe, F., Rouan, D., Renzini, A., and Tacconi-Garman, L. E. (2003). The Stellar Cusp around the Supermassive Black Hole in the Galactic Center. *Astrophys. J.*, 594(2):812–832.
- [Ghez, 2003] Ghez, A. M. (2003). The First Measurement of Spectral Lines in a Short-Period Star Bound to the Galaxy’s Central Black Hole: A Paradox of Youth. *Astrophys. J. Lett.*, 586(2):L127–L132.
- [Ghez, 2004] Ghez, A. M. (2004). astro-ph.
- [Ghosh and Abramowicz, 1997] Ghosh, P. and Abramowicz, M. A. (1997). Electromagnetic extraction of rotational energy from disc-fed black holes: the strength of the Blandford-Znajek process. *Monthly Notices Roy. Astronom. Soc.*, 292(4):887.
- [Homan et al., 2003] Homan, J., Miller, J. M., Wijnands, R., Steeghs, D., Belloni, T., van der Klis, M., and Lewin, W. H. G. (2003). Atel 16 (<http://integral.rssi.ru/atelmirror/>).
- [Horák, 2004] Horák, J. (2004). General aspects of nonlinear resonance 3 : 2 in QPO context. In Hledík, S. and Stuchlík, Z., editors, *Proceedings of RAGtime 4/5: Workshops on black holes and neutron stars, Opava, 14–16/13–15 October 2002/03*, Opava. Silesian University in Opava. This volume.
- [Igumenshchev et al., 2003] Igumenshchev, I. V., Narayan, R., and Abramowicz, M. A. (2003). Three-dimensional Magnetohydrodynamic Simulations of Radiatively Inefficient Accretion Flows. *Astrophys. J.*, 592(2):1042–1059.
- [Jaroszyński et al., 1980] Jaroszyński, M., Abramowicz, M. A., and Paczyński, B. (1980). *Acta Astronom.*, 30:1.
- [Kato, 2001a] Kato, S. (2001a). Trapping of Non-Axisymmetric g-Mode Oscillations in Thin Relativistic Disks and kHz QPOs. *Publ. Astronom. Soc. Japan*, 53(5):L37.
- [Kato, 2001b] Kato, S. (2001b). Trapping of Non-Axisymmetric g-Mode Oscillations in Thin Relativistic Disks and kHz QPOs. *Publ. Astronom. Soc. Japan*, 53(5):L39.
- [Kato and Fukue, 1980] Kato, S. and Fukue, J. (1980). Trapped Radial Oscillations of Gaseous Disks around a Black Hole. *Publ. Astronom. Soc. Japan*, 32(3):377–388.
- [Kluźniak et al., 2003] Kluźniak, W., Abramowicz, M. A., Kato, S., Lee, W. H., and Stergioulas, N. (2003). Non-linear resonance in the accretion disk of a millisecond pulsar. *Astrophys. J.* arXiv: astro-ph/0308035.
- [Kozłowski et al., 1978] Kozłowski, M., Jaroszyński, M., and Abramowicz, M. A. (1978). The analytic theory of fluid disks orbiting the Kerr black hole. *Astronomy and Astrophysics*, 63:209–220.
- [Krolik and Hawley, 2002] Krolik, J. H. and Hawley, J. F. (2002). Where Is the Inner Edge of an Accretion Disk around a Black Hole? *Astrophys. J.*, 573(2):754–763.
- [Landau and Lifshitz, 1973] Landau, L. D. and Lifshitz, J. M. (1973). *Mechanika*, volume I of *Teoretičeskaja fizika*. Nauka, Moskva, 3rd edition.
- [Lee et al., 2003] Lee, W. H., Abramowicz, M. A., and Kluźniak, W. (2003). In preparation.

- [Li and Narayan, 2003] Li, L.-X. and Narayan, R. (2003). Quasi-Periodic Oscillations from Rayleigh-Taylor and Kelvin-Helmholtz Instability at a Disk-Magnetosphere Interface. arXiv: astro-ph/0310081.
- [Mauche, 2002] Mauche, C. W. (2002). Correlation of the Quasi-Periodic Oscillation Frequencies of White Dwarf, Neutron Star, and Black Hole Binaries. *Astrophys. J.*, 580(1):423–428.
- [McClintock and Remillard, 2003] McClintock, J. E. and Remillard, R. A. (2003). Black Hole Binaries. arXiv: astro-ph/0306213.
- [Mirabel and Rodríguez, 1998] Mirabel, I. F. and Rodríguez, L. F. (1998). Microquasars in our Galaxy. *Nature*, 392:673–676.
- [Nayfeh and Mook, 1979] Nayfeh, A. H. and Mook, D. T. (1979). *Nonlinear Oscillations*. Wiley-interscience, New York.
- [Nowak and Wagoner, 1992] Nowak, M. A. and Wagoner, R. V. (1992). *Astrophys. J.*, 393:697.
- [Okazaki et al., 1987] Okazaki, A. T., Kato, S., and Fukue, J. (1987). Global Trapped Oscillations of Relativistic Accretion Disks. *Publ. Astronom. Soc. Japan*, 39(3):457–473.
- [Page and Thorne, 1974] Page, D. N. and Thorne, K. S. (1974). *Astrophys. J.*, 191:499P.
- [Perez et al., 1997] Perez, C. A., Silbergleit, A. S., Wagoner, R. V., and Lehr, D. E. (1997). Relativistic Diskoseismology. I. Analytical Results for Gravity Modes. *Astrophys. J.*, 476(2):589.
- [Psaltis et al., 1999] Psaltis, D., Belloni, T., and van der Klis, M. (1999). Correlations in Quasi-periodic Oscillation and Noise Frequencies among Neutron Star and Black Hole X-Ray Binaries. *Astrophys. J.*, 520(1):262–270.
- [Rebusco, 2003] Rebusco, P. (2003). In preparation.
- [Reid et al., 2003] Reid, M. J., Menten, K. M., Genzel, R., Ott, T., Schoedel, R., Eckart, A., and Brunthaler, A. (2003). The Position, Motion, and Mass of Sgr A\*.
- [Reid et al., 1999] Reid, M. J., Readhead, A. C. S., Vermeulen, R. C., and Treuhaft, R. N. (1999). The Proper Motion of Sagittarius A\*. I. First VLBA Results. *Astrophys. J.*, 524(2):816–823.
- [Rezzolla et al., 2003] Rezzolla, L., Yoshida, S., Maccarone, T. J., and Zanotti, O. (2003). A new simple model for high-frequency quasi-periodic oscillations in black hole candidates. *Monthly Notices Roy. Astronom. Soc.*, 344(3):L37–L41.
- [Schnittman and Bertschinger, 2003] Schnittman, J. D. and Bertschinger, E. (2003). A Hot Spot Model for Black Hole QPOs. In Kaaret, P., Lamb, F. K., and Swank, J. H., editors, . American Institute of Physics.
- [Schoedel, 2002] Schoedel, R. (2002). A star in a 15.2-year orbit around the supermassive black hole at the centre of the Milky Way. *Nature*, 419:694.
- [Schoedel et al., 2003] Schoedel, R., Ott, T., Genzel, R., Eckart, A., Mouawad, N., and Alexander, T. (2003). Stellar Dynamics in the Central Arcsecond of Our Galaxy. *Astrophys. J.*, 596(2):1015–1034.
- [Silbergleit et al., 2001] Silbergleit, A. S., Wagoner, R. V., and Ortega-Rodríguez, M. (2001). Relativistic Diskoseismology. II. Analytical Results for C-modes. *Astrophys. J.*, 548(1):335–347.

- [Szuszkiewicz and Miller, 2001] Szuszkiewicz, E. and Miller, J. C. (2001). Non-linear evolution of thermally unstable slim accretion discs with a diffusive form of viscosity. *Monthly Notices Roy. Astronom. Soc.*, 328(1):36.
- [Török, 2004] Török, G. (2004). A possible 3:2 orbital epicyclic resonance in QPOs frequencies of Sgr A\*. *astro-ph/0412500*.
- [Török et al., 2004] Török, G., Abramowicz, M. A., and Kluźniak, W. (2004). The resonance model for twin peak QPOs in microquasars.
- [van der Klis, 2000] van der Klis, M. (2000). Millisecond Oscillations in X-ray Binaries. *Annual Review of Astronomy and Astrophysics*, 38:717–760.
- [Villiers et al., 2003] Villiers, J.-P. D., Hawley, J. F., and Krolik, J. H. (2003). Magnetically Driven Accretion Flows in the Kerr Metric I: Models and Overall Structure. *arXiv: astro-ph/0307260*.
- [Warner et al., 2003] Warner, B., Woudt, P. A., and Pretorius, M. L. (2003). Dwarf nova oscillations and quasi-periodic oscillations in cataclysmic variables - III. A new kind of dwarf nova oscillation, and further examples of the similarities to X-ray binaries. *Monthly Notices Roy. Astronom. Soc.*, 344:1193.



# Variability of accreting sources at very high time resolution

Michal Bursa

*Faculty of Mathematics and Physics, Charles University, Prague, Czechia;  
Astronomical Institute, Academy of Sciences, Prague, Czechia*

## ABSTRACT

We are carrying out a project to study rapid variability of radiation originating from accreting compact objects. Our goal is to examine fluctuations of the radiation flux occurring on the light-crossing time scales, taking into account effects of strong gravitational field. The assumption of a geometrically thin, optically thick disc has been often imposed in previous works, but here it is relaxed. Instead, we construct a toy model of an oscillating torus in the slender approximation, we assume thermal bremsstrahlung for the intrinsic emissivity of the medium, and we compute observed (predicted) radiation signal including the contribution of indirect (higher-order) images and caustics.

## 1 INTRODUCTION

In the past decade, missions such as XMM, RXTE, BeppoSAX and others have opened an X-ray window to the deep universe and allowed us to observe sources of energetic radiation in details we have never seen before. In many active galactic nuclei as well as in cataclysmic variables and low-mass X-ray binaries we observe rapid temporal changes of flux and of individual spectral features. In the widely accepted scenario, these sources contain a compact object surrounded by an accretion flow in the form of a disc or a torus (see, e.g., [Ulrich et al., 1997, van der Klis, 2000]). The strong gravity near these objects introduces distinctive deviations from Newtonian physics including bending of light rays, gravitational red shift and existence of the inner-most stable circular orbit. All these effects of general relativity affect profiles of observed light curves and have impact on the power spectra.

To address these issues I have developed a new three-dimensional modular ray-tracing code which can be used to study light curve profiles and power spectra of luminous, spatially extensive astrophysical objects, such as thick accretion flows or tori, as well as radiation from 2D patterns, such as hot spots, belts, thin disks, etc.

## 2 DESCRIPTION OF THE CODE

Various numerical and semi-analytical approaches have been developed in order to tackle the problem of light ray-tracing in a curved spacetime. Some of them are focused on solving

a special kind of problems, often they are limited to 2D geometry of a sphere or a disk. Therefore the need for a general, efficient and 3D ray-tracing computational tool has arisen which motivates the development of a new code, called `sim4`.

Code `sim4` is a MPI-parallel modular ray-tracer written in the C language. It is modular in the sense that certain parts of the code (modules) can be easily modified or replaced. There are modules for a metric, a topology and for a model. Each module provides a small set of functions which are called by the core and to which a user may put its own implementation of a problem. This concept of modularity makes the code to be very versatile and powerful – with several changes in the code it is possible to turn focus to completely different problems.

## 2.1 Ray-tracing

For our calculations we adopt the approximation of geometrical optics in a vacuum space-time. The integration begins with division of the image plane into a number of pixels of equal solid angle on the observer's sky, each pixel corresponding to a single light ray. Following the method proposed by [Rauch and Blandford, 1994] and further developed by [Dovčiak et al., 2004] and using given spacetime metric function, for each ray the code determines the initial position and 4-velocity and integrates the geodesic equation

$$\frac{d^2x^\mu}{d\lambda^2} = -\Gamma_{\alpha\beta}^\mu \frac{dx^\alpha}{d\lambda} \frac{dx^\beta}{d\lambda} \quad (1)$$

back in time, i.e., from the observer to the source. Note that both in the above equation and throughout, geometrised units  $G = c \equiv 1$  are used. This approach has the advantage that only photons which hit the target are actually integrated. On the other hand it puts a constraint on a metric function which must be stationary. Since in most astrophysical cases the distribution of matter is, in the first approximation, spherical, rays for not all pixels on the rectangular image plane are integrated, but only those which have impact parameter less than a certain value.

The determination of the gravitational lensing effect is performed by construction of two unit vectors  $U$  and  $V$  that, at the beginning, are perpendicular to the photon's 4-velocity and they are perpendicular to one another as well, so they enclose an area of a unit size. These vectors are transported along with the light ray by integrating the geodesic deviation equation if the form

$$\frac{d^2U^\mu}{d\lambda^2} = -2\Gamma_{\alpha\beta}^\mu u^\alpha \frac{dU^\beta}{d\lambda} - \Gamma_{\alpha\beta,\gamma}^\mu u^\alpha u^\beta U^\gamma, \quad (2)$$

where  $u$  stands for the photon's 4-velocity, and the same equation for  $V$ . The lensing factor, defined as the ratio of the photon tube cross-section area in infinity and at the point of emission, is given by

$$l \equiv \frac{S_{\text{inf}}}{S_{\text{em}}} = \frac{1}{U \times V} = \frac{1}{\sqrt{(U^\mu U_\mu)(V^\nu V_\nu) - (U^\mu V_\mu)^2}}. \quad (3)$$

After certain number of integration steps the code collects the actual photon position, momentum and corresponding lensing factor, passes these information to the topology module which decides whether to save (and eventually dumps the data to an output file)

and whether to stop the integration. It allows the user to specify exactly what data will be recorded and for how long the ray will be integrated. The recording condition can be either two or three dimensional and also allows to select several distinct regions. How often the data are recorded depends on chosen precision and also on the integration step. As the integration goes on, the code watches the step size and adjusts the saving frequency: when the step is small it saves more often, when it is large it saves less often and conserves resources.

All data are stored in the file which can be small or huge depending on the resolution, recording condition and chosen precision. This data file is then used to computation of the light curve and, in fact, if the recording condition is made general enough it can be reused many times even for completely different set of problems.

## **2.2 Light curve**

In the next step the information from the photon data file is used to construct the light curve. The code reads the set of recorded points for each photon from the file and using spline interpolation it reconstructs its whole trajectory. Then by making small spatial steps it follows the trajectory back in time from its end to where it starts and always asks the model module to return the amount of radiation flux (with respect to the observer at infinity) which is produced at that place. Knowing the time delay it can then determine the exact instant of time when this amount of flux reaches the observer.

The model module is where all the physics is stored and “where the radiation comes from”. It can be as much complex and involve as much physics as one wish including access to external data (for instance from MHD simulations). An example of a possible model is given in the following section.

## **2.3 Visualisation**

Visualisation is very similar process to construction a light curve and it follows almost the same procedure. The difference is that while to make a light curve we require very good time resolution and need no spatial resolution, to make an image or a movie we need no or little time resolution but require the information about spatial resolution. So instead of summing the flux carried by each photon to one number, the code records the numbers separately to corresponding pixels of the projection plane making an actual image of the observed object at that point of time.

## **3 TOY TORUS MODEL**

As an example of the code usage and capabilities I present, without explaining any motivation or astrophysical background, the model of a toy torus. While real tori that exist or may exist as a part of an accretion flows near the central objects can be very complex, the toy torus is an abstraction that should be as simple as possible, but still keeping basic properties of the real situation. Simplified physics will then help to uncover and isolate effects of general relativity on the light curve.

We consider a part of an accretion flow with constant distribution of specific angular momentum  $\ell = \ell_K(r_0) = (Mr_0^3)^{1/2}/(r_0 - 2M)$  in the Schwarzschild spacetime, where  $M$  is the mass of the central object and  $r_0$  is the distance of the equilibrium point. The solution of the relativistic Euler equation

$$\frac{\partial_\mu p}{p + \epsilon} = -\partial_\mu (\ln u_t) + \frac{\Omega \partial_\mu \ell}{1 - \Omega \ell} \quad (4)$$

can be given by determining surfaces of a constant potential  $W(r, \theta)$  by relations [Abramowicz et al., 1978]

$$\Delta W \equiv W - W_{\text{in}} = - \int_0^p \frac{dp}{p + \epsilon} \quad (5)$$

and

$$W = \ln u_t = \frac{1}{2} \ln \left[ \frac{-g_{tt}}{1 + \frac{g_{tt}}{g_{\phi\phi}} \ell^2} \right]. \quad (6)$$

Here  $u$  is the fluid 4-velocity,  $\Omega = -\ell g_{tt}/g_{\phi\phi}$  is the angular velocity field,  $p$  and  $\epsilon$  denote the pressure and the total energy density of the fluid and the subscript “in” refers to the inner edge of the torus. The equipotential surfaces are determined by the condition  $\Delta W(r, \theta) = \text{const}$  and the surfaces of constant pressure are given by Eq. (5). For a polytropic gas, where

$$p = K\rho^\gamma, \quad (7)$$

$$\epsilon = \rho + \frac{p}{\gamma - 1}, \quad (8)$$

we can integrate Eq. (5) and obtain the mass density profile  $\rho$ . Here  $\gamma = \frac{5}{3}$  is the polytropic index and  $K$  is the polytropic constant. We fix  $K$  by specifying the density and temperature in the torus centre.

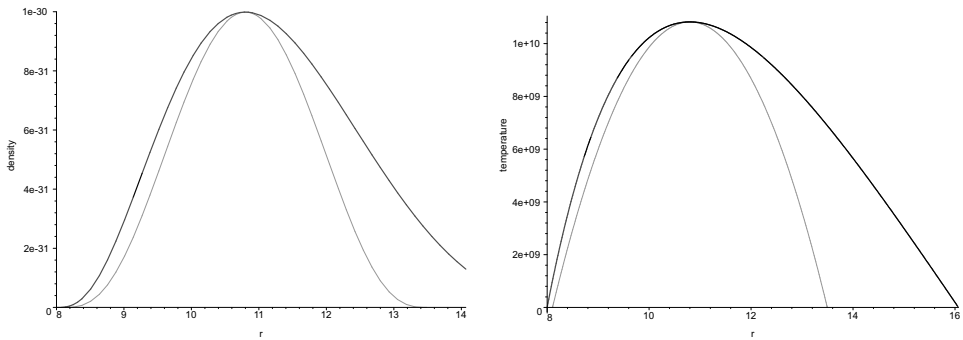


**Figure 1.** Mass density  $\rho$  (left) and temperature  $T$  (right) profile inside the torus in the  $\theta = \pi/2$  plane. Thick line corresponds to the real potential  $W$ , thin line to the toy potential  $W_{\text{toy}}$ .

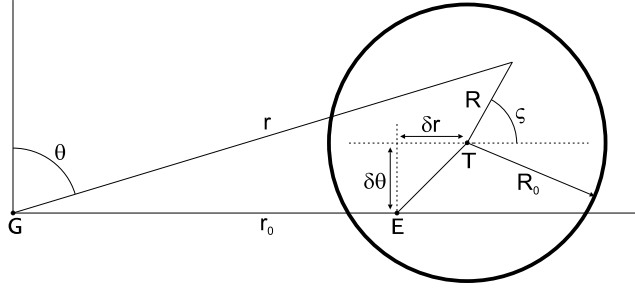


**Figure 2.** Configuration: The equilibrium centre of the torus E is in the distance  $r_0$  from the centre of gravity G. The real centre of the torus T, i.e., point where pressure and density are maximal, is displaced from E by  $\delta r$  in radial and  $\delta\theta$  in vertical direction.

Using the equation of state we can then express all basic thermodynamical quantities in terms of  $W$  in this way

$$\rho = \left[ \frac{\gamma - 1}{K\gamma} (e^{\Delta W} - 1) \right]^{\frac{1}{\gamma-1}}, \quad (9)$$

$$p = K\rho^\gamma, \quad (10)$$

$$T = K\rho^{\gamma-1} \frac{\mu m_u}{k_B}. \quad (11)$$

Constants  $\mu$ ,  $m_u$  and  $k_B$  are mean molecular weight, atomic mass unit and the Boltzmann constant respectively. For hydrogen-helium ratio 75 : 25,  $\mu = \frac{7}{4}$ .

Instead of considering the real profile of equipotentials given by Eq. (6), we make an abstraction to the slender torus of a circular cross-section. We introduce a toroidal coordinate system  $(R, \zeta, \phi)$ , where  $R$  is the distance from the torus centre (the point of maximal pressure T),  $\zeta$  is an angular distance measured from the plane parallel to the equatorial plane and  $\phi$  is an angular position in azimuthal direction (see Fig. 2). In terms of the standard spherical Schwarzschild coordinates  $(r, \theta, \phi)$  they are defined as

$$R^2 = (r \cos \theta - \delta\theta)^2 + (r \sin \theta - r_0 - \delta r)^2, \quad (12)$$

$$\sin \zeta = \frac{r \cos \theta - \delta\theta}{R}, \quad (13)$$

$$\phi = \phi. \quad (14)$$

In this coordinate system we expand the potential  $W$  around point  $R = 0$  in the vertical direction and keep only quadratic terms in  $R$ . The toy potential is then

$$W_{\text{toy}} = \frac{1}{2} \ln \left[ \frac{(r_0 - 2M)^2}{r_0(r_0 - 3M)} \right] + \frac{R^2}{2r_0^2(r_0 - 3M)} \quad (15)$$

and

$$\Delta W_{\text{toy}} \equiv (W_{\text{toy}})_{\text{in}} - W_{\text{toy}} = \frac{R_0^2 - R^2}{2r_0^2(r_0 - 3M)}, \quad (16)$$

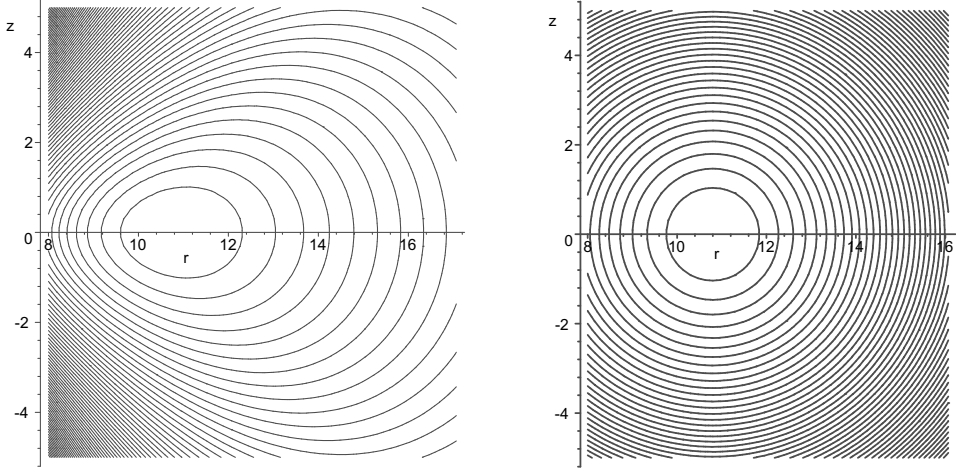


**Figure 3.** Contours of equipotential surfaces of the real potential  $W$  (left) and the toy potential  $W_{\text{toy}}$  (right) in the  $r$ - $z$  cross-section plane.

where  $R_0$  is the torus cross-section radius with respect to the Schwarzschild radial coordinate.

Now we impose periodic radial and vertical oscillations on the torus centre with frequencies  $\omega_r$  and  $\omega_\theta$ , so it will travel around the equilibrium point  $\mathbf{E}$  being displaced at the time  $t$  by

$$\delta r = \delta r_0 \cos(\omega_r t) , \quad (17)$$

$$\delta \theta = \delta \theta_0 \cos(\omega_\theta t) . \quad (18)$$

To complete the set of equations for the model suppose the flow is advection-dominated, optically thin and radiates by thermal bremsstrahlung. In the local frame the emissivity (here in CGS units) is [Abramowicz et al., 1996]

$$f = 5.698 \times 10^{20} \rho^2 T^{\frac{1}{2}} \text{ ergs cm}^{-3} \text{ s}^{-1} . \quad (19)$$

Here  $\rho$  and  $T$  are given by equations (9) and (11) with  $W$  replaced by  $W_{\text{toy}}$ . The overall intensity observed at infinity is an integration of the emissivity  $f$  over the path length along geodesics and it can be written down as

$$I_{\text{obs}}(t) = \int f(r, \theta, \phi, t - \Delta t) \sqrt{-g_{tt}} k^t g^4 d\lambda . \quad (20)$$

The integration along the light ray that is parametrised by an affine parameter  $\lambda$ .  $S_{\text{inf}}$  is the area subtended by the ray at infinity,  $l$  is the lensing factor,  $k^t = dt/d\lambda$  is the time component of photon's 4-momentum,  $g$  is the red-shift factor and  $\Delta t$  is the photon time delay.

Results of numerical simulations are shown in Fig. 4. In this setup the torus cross-section radius is  $R_0 = 2M$ , oscillations amplitudes are  $\delta\theta_0 = \delta r_0 = 1M$  and frequencies are  $\omega_\theta = \Omega_K$  and  $\omega_r = \frac{2}{3}\Omega_K$ . All relativistic effects including light bending, formation of Einstein's rings and Doppler boosting can be clearly seen. As different effects become

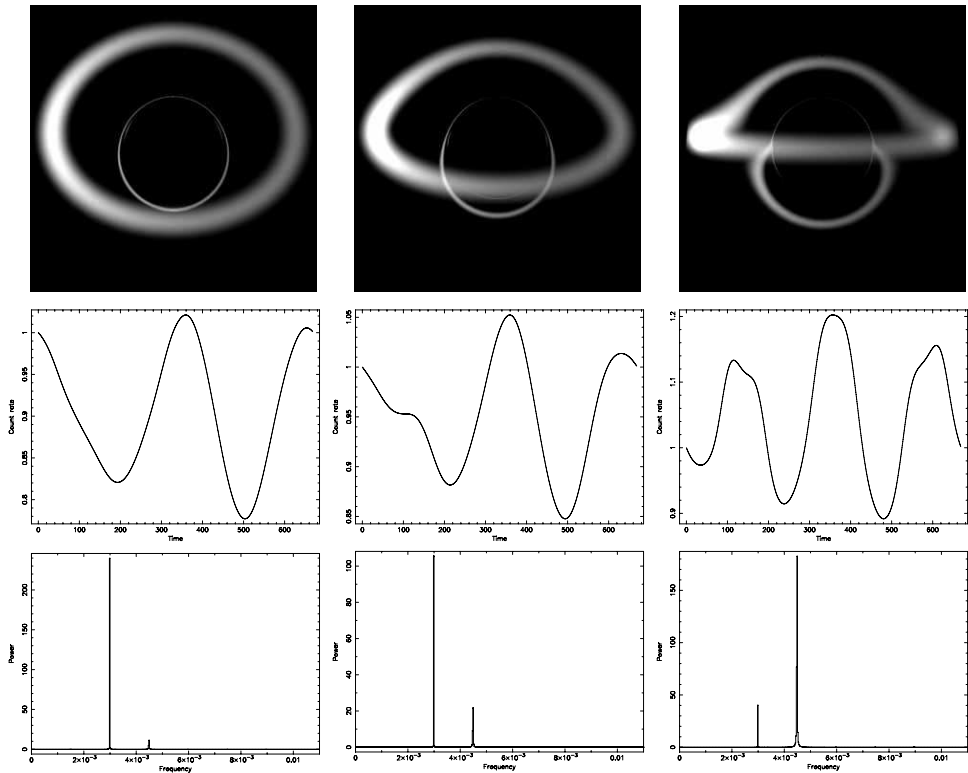


**Figure 4.** Results of numerical simulations of the oscillating toy torus. Its cross-section radius is  $R_0 = 2M$ , distance of equilibrium point  $r_0 = 10.8M$ , oscillation amplitudes  $\delta\theta_0 = \delta r_0 = 1M$  and frequencies  $\omega_\theta = \Omega_K$ ,  $\omega_r = \frac{2}{3}\Omega_K$ . The snapshot of an instant image, as viewed by a distant observer (on the top), the computed light curve (in the middle) and the corresponding power spectrum (at the bottom) are shown for three different viewing angles 45 (left), 65 (middle) and 85 (right) degrees.

more important at certain inclinations (e.g., Doppler boosting is strongest in the edge-on view), the profile of light curves is also changing and although the amplitudes of oscillations keep the same, the power spectrum shows that relative power of the two frequencies changes with inclinations.

## 4 CONCLUSIONS

The new three-dimensional general relativistic ray-tracing code has been presented here. It is parallel high performance solver of geodesic equation which can be run on both shared and distributed memory systems. Based on the given metric, topology and model the code is capable of integrating radiative transfer equations along photon trajectories and calculates light curves and photo-realistic images of the examined object. Its modularity allows to use a set of light trajectories for multiple light curve calculations.

**ACKNOWLEDGEMENTS**

I wish to thank to the organisers of the Opava RAGtime conference and acknowledge the support of the European Commission through grant number HPRI-CT-1999-00026 (the TRACS Programme at EPCC). This work was also supported by the GAČR Grant No. 205/03/0902 and GAUK 2004.

**REFERENCES**

- [Abramowicz et al., 1996] Abramowicz, M. A., Chen, X.-M., Granath, M., and Lasota, J.-P. (1996). Advection-dominated Accretion Flows around Kerr Black Holes. *Astrophys. J.*, 471(2):762.
- [Abramowicz et al., 1978] Abramowicz, M. A., Jaroszyński, M., and Sikora, M. (1978). Relativistic accreting disks. *Astronomy and Astrophysics*, 63(1–2):221–224.
- [Dovčiak et al., 2004] Dovčiak, M., Karas, V., Martocchia, A., Matt, G., and Yaqoob, T. (2004). An XSPEC model to explore spectral features from black-hole sources. In Hledík, S. and Stuchlík, Z., editors, *Proceedings of RAGtime 4/5: Workshops on black holes and neutron stars, Opava, 14–16/13–15 October 2002/03*, Opava. Silesian University in Opava. This volume.
- [Narayan and Yi, 1994] Narayan, R. and Yi, I. (1994). *Astrophys. J.*, 428:L13.
- [Rauch and Blandford, 1994] Rauch, K. P. and Blandford, R. D. (1994). Optical caustics in a Kerr space-time and the origin of rapid X-ray variability in active galactic nuclei. *Astrophys. J.*, 421:46.
- [Ulrich et al., 1997] Ulrich, M. H., Maraschi, L., and Urry, C. M. (1997). Variability of active galactic nuclei. *Annual Review of Astronomy and Astrophysics*, 35:445–502.
- [van der Klis, 2000] van der Klis, M. (2000). Millisecond Oscillations in X-ray Binaries. *Annual Review of Astronomy and Astrophysics*, 38:717–760.

# An XSPEC model to explore spectral features from black-hole sources

M. Dovčiak<sup>1,2</sup>, V. Karas<sup>1,2</sup>, A. Martocchia<sup>3</sup>,  
G. Matt<sup>4</sup> and T. Yaqoob<sup>5,6</sup>

<sup>1</sup>*Astronomical Institute, Academy of Sciences, Prague, Czech Republic*

<sup>2</sup>*Faculty of Mathematics and Physics, Charles University Prague, Czech Republic*

<sup>3</sup>*Observatoire Astronomique, Strasbourg, France*

<sup>4</sup>*Dipartimento di Fisica, Università degli Studi “Roma Tre”, I-00146 Roma, Italy*

<sup>5</sup>*Department of Physics and Astronomy, Johns Hopkins University, Baltimore, MD 21218*

<sup>6</sup>*Laboratory for High Energy Astrophysics, NASA/Goddard Space Flight Center, Greenbelt, MD 20771*

## ABSTRACT

We report on a new general relativistic computational model enhancing, in various respects, the capability of presently available tools for fitting spectra of X-ray sources. The new model is intended for spectral analysis of black-hole accretion discs. Our approach is flexible enough to allow easy modifications of intrinsic emissivity profiles. Axial symmetry is not assumed, although it can be imposed in order to reduce computational cost of data fitting. The main current application of our code is within the XSPEC data-fitting package, however, its applicability goes beyond that: the code can be compiled in a stand-alone mode, capable of examining time-variable spectral features and doing polarimetry of sources in the strong-gravity regime. Basic features of our approach are described in a separate paper (Dovčiak, Karas & Yaqoob [Dovčiak et al., 2004]). Here we illustrate some of its applications in more detail. We concentrate ourselves on various aspects of line emission and Compton reflection, including the current implementation of the lamp-post model as an example of a more complicated form of intrinsic emissivity.

## 1 INTRODUCTION

Regions of strong gravitational field are most usually explored via X-ray spectroscopy, because very hot X-ray emitting material is commonly believed to be present in regions near a neutron star surface or a black-hole horizon. Accretion plays crucial role in the process of energy liberation and mass accumulation that takes place in this kind of objects [Kato et al., 1998, Krolik, 1999]. In particular, disc-type accretion represents an important mode which is realized under suitable circumstances, given by the global geometrical arrangement and local microphysics of the fluid medium. A central compact body, undetectable via its own radiation, resides in galactic nuclei where it is surrounded by a rather dense population of stars and gaseous environment. Photons emerging from the accretion disc and its corona

are influenced by gravity of the black hole, so they bear various imprints of the gravitational field structure. This concerns especially X-rays originating very near the core and, for this reason, spectral analysis with X-ray satellites is particularly relevant for astronomical study of strong gravitational fields around black holes. For a general discussion, see review articles [Fabian et al., 2000, Reynolds and Nowak, 2003] and further references cited therein.

In this paper we describe a newly developed computational model aimed for the spectral analysis of line profiles and continuum originating in a geometrically thin, planar accretion disc near a rotating (Kerr) black hole. Such analysis has been routinely performed via XSPEC package [Arnaud, 1996], which performs deconvolution of observed spectra for the effective area and energy redistribution of the detector. Previously, several routines were developed and linked with this package in order to fit data to a specific model of a black-hole accretion disc [Laor, 1991, Martocchia et al., 2000]. However, a substantially improved variant of the computational approach has been desirable because previous tools have various limitations that may be critical for analyses of present-day and forthcoming high-resolution data.

We describe the layout and usage of the new code and we show some examples and comparisons between new model components. Our present contribution provides information complementary to the basic description which can be found in [Dovčiak et al., 2004]. We suggest the reader to consult that paper as well as further details in Thesis [Dovčiak, 2004], as they give more examples and citations to previous works. Here we concentrate our attention to technical issues of the code structure and its performance when computing and fitting spectra. Different perspectives and applications of general relativistic computations for black-hole accretion discs have been considered by various authors. In particular, it is very useful to consult recent papers of Gierliński, Maciolek-Niedźwiecki & Ebisawa [Gierliński et al., 2001] and Schnittman & Bertschinger [Schnittman and Bertschinger, 2004]. Very recently, a new independent code has been developed by Beckwith & Done [Beckwith and Done, 2004]. Their approach also allows to study accretion disc spectra including strong gravity effects of a Kerr black hole. This is also one of the applications of our code, and so relatively accurate comparisons between both tools are possible. We performed several such comparisons and found a very good agreement in the shape of predicted line profiles.

Given a limited space for this contribution, we cannot describe all aspects of the new code: capability of the code with respect to timing and polarimetry are discussed elsewhere. Nonetheless, it may be good to bear in mind that such capability has been already implemented and tested, taking into account all strong-gravity effects on time-delays and the Stokes parameters.

## 2 TRANSFER FUNCTIONS

We concentrate on geometrically thin and optically thick accretion discs and we point out that general relativity effects can play a role if the configuration is sufficiently dense in a limited region, typically a few tens of gravitational radii. Nevertheless, our computational domain extends up to about  $\approx 10^3$  gravitational radii in a non-uniform spatial grid.

In order to calculate the final spectrum that an observer at infinity measures when local emission from the accretion disc is given, one must first specify the intrinsic emissivity in

frame co-moving with the disc medium and then perform transfer of photons to a distant observer. Here we concentrate on the latter part of this task.

Six functions need to be computed across the source: (i) energy shift affecting the photons (i.e., gravitational and Doppler  $g$ -factor, needed to account for spectral redistribution), (ii) gravitational lensing (for the evaluation of radiation flux or count rate), (iii) direction of emission with respect to the disc normal (for the limb darkening effect), (iv) relative time-delay of the light signal (i.e., the mutual delay between photons arriving from different regions of the source, needed for the proper account of the light-time effect in timing analysis), (v) change of the polarization angle due to photon propagation in the gravitational field (for polarimetry), and (vi) azimuthal direction of emission (also for polarimetry). While the first three quantities are always necessary, the time-delay factor is required only when local emission is not stationary (e.g., the case of orbiting spots) and the change of the polarization angle with the azimuthal direction of emission are essential for calculating the overall

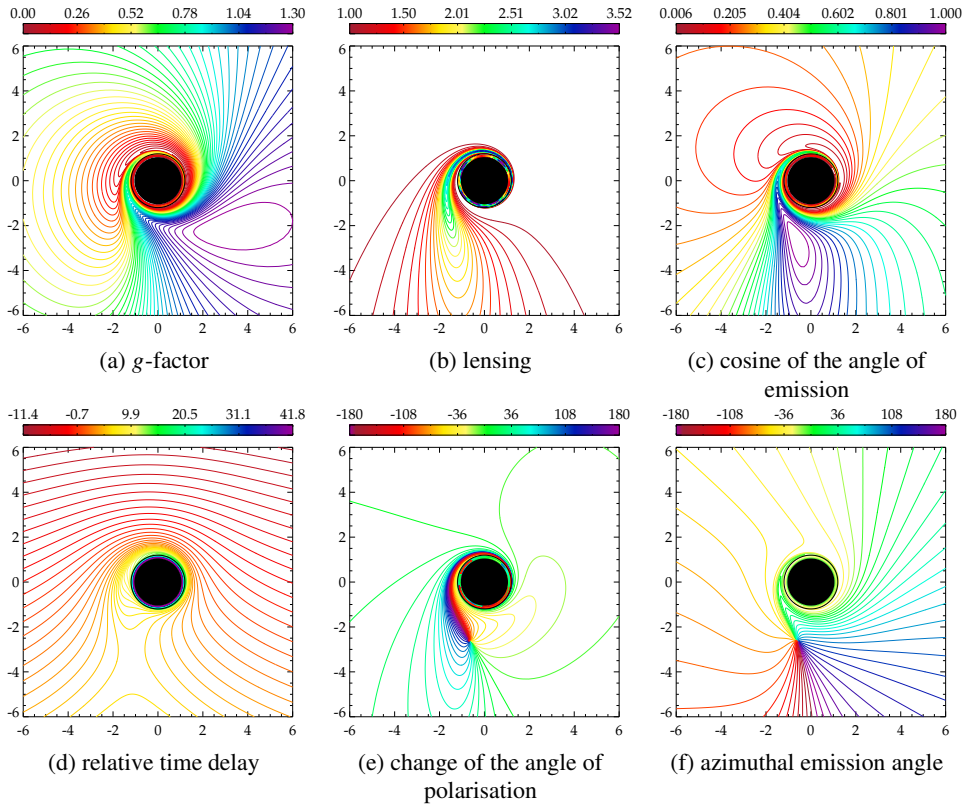


**Figure 1.** Six transfer functions are shown in the equatorial plane of a Kerr black hole with  $a \doteq 0.9987$  (horizon  $r_h = 1.05$ ). The black hole rotates counter-clockwise. The observer is located upwards at the inclination  $\theta_o = 70^\circ$ . The values of transfer functions are encoded by a colour scale, as indicated above each graph. For mathematical formulae defining these functions see eqs. (A13), (A14)–(A19) and (A26) in Appendix A1.

degree and angle of polarization, as observed at infinity. In the adopted approximation of geometrical optics, light rays follow null geodesics (in curved space-time) and spectral computations are reduced to a text-book problem [Chandrasekhar, 1992] which, however, may be rather demanding computationally on practical level of data fitting. Useful form of light-ray equations and further references can be found in various papers [Dovčiak et al., 2004, Fanton et al., 1997, Rauch and Blandford, 1994]. We summarize the basic equations in Appendix A1.

In order for our new model to be fast and practical, we pre-calculated the transfer functions for 21 values of the angular momentum of the black hole and 20 values of the inclination angle of the observer. The choice of the grid appears sufficiently fine to ensure high accuracy. We have stored the transfer functions in the form of tables – i.e., as binary extensions of a FITS file. For a technical description of the files layout see Appendix A3.1. Values of the transfer functions are interpolated when integrating the spectrum for a given angular momentum of the black hole and inclination angle of the observer.

The graphical representation of the tables is shown in Fig. 1. Six frames of contour plots correspond to individual transfer functions, which are necessary in computations. This figure captures equatorial plane for given values of  $a$  and  $\theta_o$ . The radius extends up to  $r = 10^3 r_g$  in the tables, but here we show only the central region,  $r \leq 6r_g$ , where relativistic effects are most prominent.<sup>1</sup> Clock-wise distortion of the contours is due to frame-dragging near a rapidly rotating Kerr black hole, and it is clearly visible in the Boyer–Lindquist coordinates here. Notice that this dramatic distortion appears in the graphical representation only. In order to achieve high accuracy of the tables the dragging effect has been largely eliminated in computations by means of appropriate transformation of coordinates, as described below.

### 3 PHOTON FLUX FROM AN ACCRETION DISC

Properties of radiation are described in terms of photon numbers. The source appears as a point-like object for a distant observer, so that the observer measures the flux entering the solid angle  $d\Omega_o$ , which is associated with the detector area  $dS_o \equiv D^2 d\Omega_o$  (see Fig. 2a). This relation defines distance  $D$  between the observer and the source. We denote the total photon flux received by a detector,

$$N_o^S(E) \equiv \frac{dn(E)}{dt dS_o} = \int d\Omega N_1(E/g) g^2, \quad (1)$$

where

$$N_1(E_1) \equiv \frac{dn_1(E_1)}{d\tau dS_1 d\Omega_1} \quad (2)$$

is a local photon flux emitted from the surface of the disc,  $dn(E)$  is the number of photons with energy in the interval  $\langle E, E + dE \rangle$  and  $g = E/E_1$  is the redshift factor. The local flux,  $N_1(E_1)$ , may vary over the disc as well as in time, and it can also depend on the local

<sup>1</sup> Spheroidal coordinates have been employed. We denote  $r_g = GM_\bullet/c^2 \approx 1.5 \times 10^5 (M_\bullet/M_\odot)$  cm and we use geometrized units with  $c = GM_\bullet = 1$  hereafter, which means that we scale lengths with  $M_\bullet$ . Therefore, all quantities are dimensionless.

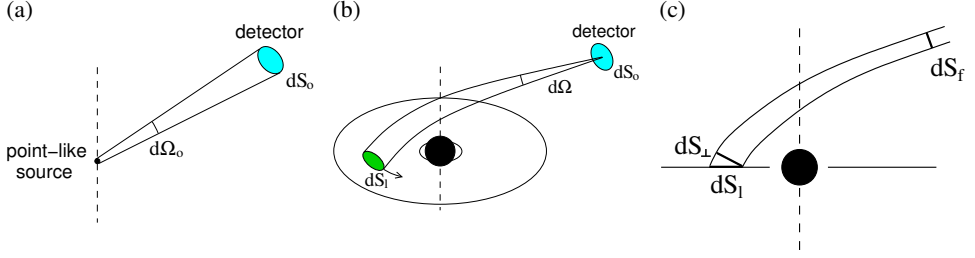


**Figure 2.** Denomination of various elements of solid angles and areas defined in the text: a) the light source appears to the observer to be point-like; b) the light rays received by the detector are coming from different parts of the disc (closer view of the disc than in previous figure); c) area of a light tube changes as the light rays travel close to the black hole (the disc is edge on).

emission angle. This dependency is emphasised explicitly only in the final formula (11), otherwise it is omitted for brevity.

The emission arriving at the detector within the solid angle  $d\Omega$  (see Fig. 2b) originates from the proper area  $dS_1$  on the disc (as measured in the rest frame co-moving with the disc). Hence, in our computations we want to integrate the flux contributions over a fine mesh on the disc surface. To achieve this aim, we adjust Eq. (1) to the form

$$N_o^S(E) = \frac{1}{D^2} \int dS \frac{D^2 d\Omega}{dS} N_1(E/g) g^2 = \frac{1}{D^2} \int dS \frac{dS_\perp}{dS} \frac{dS_f}{dS_\perp} N_1(E/g) g^2. \quad (3)$$

Here  $dS_f$  stands for an element of area perpendicular to light rays corresponding to the solid angle  $d\Omega$  at a distance  $D$ ,  $dS_\perp$  is the proper area measured in the local frame of the disc and perpendicular to the rays, and  $dS$  is the coordinate area for integration. We integrate in a two-dimensional slice of a four-dimensional space-time, which is specified by coordinates  $\theta = \pi/2$  and  $t = t_0 - \Delta t$  with  $\Delta t$  being a time delay with which photons from different parts of the disc (that lies in the equatorial plane) arrive to the observer (at the same coordinate time  $t_0$ ). Therefore, let us define the coordinate area by (we employ coordinates  $t', \theta, r, \varphi$  with  $t' = t - \Delta t$  and  $\Delta t = \Delta t(r, \theta, \varphi)$ )

$$dS \equiv |d^2S_{t',\theta}| = \left| \frac{\partial x^\mu}{\partial t'} d^2S_{\mu,\theta} \right| = |d^2S_{t,\theta}| = |g^{\theta\mu} d^2S_{t\mu}|. \quad (4)$$

We define the tensor  $d^2S_{\alpha\beta}$  by two four-vector elements  $dx_1^\mu \equiv (dt_1, dr, 0, 0)$  and  $dx_2^\mu \equiv (dt_2, 0, 0, d\varphi)$  and by Levi-Civita tensor  $\varepsilon_{\alpha\beta\gamma\delta}$ . The time components of these vectors,  $dt_1$  and  $dt_2$ , are such that the vectors  $dx_1^\mu$  and  $dx_2^\mu$  lie in the tangent space to the above defined space-time slice. Then we obtain

$$dS = |g^{\theta\theta} \varepsilon_{t\theta\alpha\beta} dx_1^\alpha dx_2^\beta| = g^{\theta\theta} \sqrt{-\|g_{\mu\nu}\|} dr d\varphi = dr d\varphi, \quad (5)$$

where  $g_{\mu\nu}$  is the metric tensor and  $\|g_{\mu\nu}\|$  is the determinant of the metric. The proper area,  $dS_\perp$ , perpendicular to the light ray can be expressed covariantly in the following way:

$$dS_\perp = -\frac{U^\alpha p^\beta d^2S_{\alpha\beta}}{U^\mu p_\mu}. \quad (6)$$

Here,  $dS_{\perp}$  is the projection of an element of area, defined by  $d^2S_{\alpha\beta}$ , on a spatial slice of an observer with velocity  $U^{\alpha}$  and perpendicular to light rays.  $U^{\alpha}$  is four-velocity of an observer measuring the area  $dS_{\perp}$ , and  $p^{\beta}$  is four-momentum of the photon. The proper area  $dS_{\perp}$  corresponding to the same flux tube is identical for all observers. This means that the last equation holds true for any four-velocity  $U^{\alpha}$ , and we can express it as

$$p^{\beta} d^2S_{\alpha\beta} + p_{\alpha} dS_{\perp} = 0, \quad \alpha = t, r, \theta, \varphi. \quad (7)$$

For  $\alpha = t$  (note that  $d^2S_{tr} = d^2S_{t\varphi} = 0$ ) we get

$$\frac{dS_{\perp}}{dS} = \left| \frac{1}{g^{\theta\theta}} \frac{dS_{\perp}}{d^2S_{t\theta}} \right| = \left| -\frac{p_{\theta}}{p_t} \right| = \frac{r\mu_e}{g}. \quad (8)$$

In the last equation we used the formula for the cosine of local emission angle  $\mu_e$ , see Eq. (A15), and the fact that we have chosen such an affine parameter of the light geodesic that  $p_t = -1$ . From eqs. (3), (4) and (8) we get for the observed flux per unit solid angle

$$N_{\circ}^{\Omega}(E) \equiv \frac{dn(E)}{dt d\Omega_{\circ}} = N_0 \int_{r_{\text{in}}}^{r_{\text{out}}} dr \int_{\phi}^{\phi+\Delta\phi} d\varphi N_1(E/g) g l \mu_e r, \quad (9)$$

where  $N_0$  is a normalisation constant and

$$l = \frac{dS_{\text{f}}}{dS_{\perp}} \quad (10)$$

is the lensing factor in the limit  $D \rightarrow \infty$  (the limit is performed while keeping  $D^2 d\Omega$  constant, see Fig. 2c).

For the line emission, the normalisation constant  $N_0$  is chosen in such a way that the total flux from the disc is unity. In the case of a continuum model, the flux is normalised to unity at a certain value of the observed energy (typically at  $E = 1$  keV, as in other XSPEC models).

Finally, the integrated flux per energy bin,  $\Delta E$ , is

$$\begin{aligned} \Delta N_{\circ}^{\Omega}(E, \Delta E, t) &= \int_E^{E+\Delta E} d\bar{E} N_{\circ}^{\Omega}(\bar{E}, t) \\ &= N_0 \int_{r_{\text{in}}}^{r_{\text{out}}} dr \int_{\phi}^{\phi+\Delta\phi} d\varphi \int_{E/g}^{(E+\Delta E)/g} dE_1 N_1(E_1, r, \varphi, \mu_e, t - \Delta t) g^2 l \mu_e r, \end{aligned} \quad (11)$$

where  $\Delta t$  is the relative time delay with which photons arrive to the observer from different parts of the disc. The transfer functions  $g$ ,  $l$ ,  $\mu_e$  and  $\Delta t$  are read from the FITS file `KBHtablesNN.fits` described in Appendix A3.1. This equation is numerically integrated for a given local flux  $N_1(E_1, r, \varphi, \mu_e, t - \Delta t)$  in all hereby described new general relativistic *non-axisymmetric models*.

Let us assume that the local emission is stationary and the dependence on the axial coordinate is only through the prescribed dependence on the local emission angle  $f(\mu_e)$  (limb darkening/brightening law) together with an arbitrary radial dependence  $R(r)$ , i.e.,

$$N_1(E_1, r, \varphi, \mu_e, t - \Delta t) \equiv N_1(E_1) R(r) f(\mu_e). \quad (12)$$

The observed flux  $N_{\circ}^{\Omega}(E)$  is in this case given by

$$N_0^{\Omega}(E) = \int_{-\infty}^{\infty} dE_1 N_1(E_1) G(E, E_1), \quad (13)$$

where

$$G(E, E_1) = N_0 \int_{r_{\text{in}}}^{r_{\text{out}}} dr R(r) \int_0^{2\pi} d\varphi f(\mu_e) g^2 l \mu_e r \delta(E - gE_1). \quad (14)$$

In this case, the integrated flux can be expressed in the following way:

$$\begin{aligned} \Delta N_0^{\Omega}(E, \Delta E) &= \int_E^{E+\Delta E} d\bar{E} N_0^{\Omega}(\bar{E}) \\ &= \int_E^{E+\Delta E} d\bar{E} N_0 \int_{r_{\text{in}}}^{r_{\text{out}}} dr R(r) \int_0^{2\pi} d\varphi f(\mu_e) N_1(\bar{E}/g) g l \mu_e r \int_{-\infty}^{\infty} dE_1 \delta(E_1 - \bar{E}/g) \\ &= N_0 \int_{r_{\text{in}}}^{r_{\text{out}}} dr R(r) \int_{-\infty}^{\infty} dE_1 N_1(E_1) \int_{E/E_1}^{(E+\Delta E)/E_1} d\bar{g} F(\bar{g}), \end{aligned} \quad (15)$$

where we substituted  $\bar{g} = \bar{E}/E_1$  and

$$F(\bar{g}) = \int_0^{2\pi} d\varphi f(\mu_e) g^2 l \mu_e r \delta(\bar{g} - g). \quad (16)$$

Eq. (15) is numerically integrated in all *axially symmetric models*. The function  $dF(\bar{g}) \equiv d\bar{g} F(\bar{g})$  has been pre-calculated for several limb darkening/brightening laws  $f(\mu_e)$  and stored in separate files, `KBHlineNN.fits` (see Appendix A3.2).

#### 4 STOKES PARAMETERS IN STRONG GRAVITY REGIME

For polarisation studies, Stokes parameters are used. Let us define specific Stokes parameters in the following way:

$$i_\nu \equiv \frac{I_\nu}{E}, \quad q_\nu \equiv \frac{Q_\nu}{E}, \quad u_\nu \equiv \frac{U_\nu}{E}, \quad v_\nu \equiv \frac{V_\nu}{E}, \quad (17)$$

where  $I_\nu$ ,  $Q_\nu$ ,  $U_\nu$  and  $V_\nu$  are Stokes parameters for light with frequency  $\nu$ ,  $E$  is energy of a photon at this frequency. Further on, we drop the index  $\nu$  but we will always consider these quantities for light of a given frequency. We can calculate the integrated specific Stokes parameters (per energy bin), i.e.,  $\Delta i_o$ ,  $\Delta q_o$ ,  $\Delta u_o$  and  $\Delta v_o$ . These are the quantities that the observer determines from the local specific Stokes parameters  $i_1$ ,  $q_1$ ,  $u_1$  and  $v_1$  on the disc in the following way:

$$\Delta i_o(E, \Delta E) = N_0 \int dS \int dE_1 i_1(E_1) Fr, \quad (18)$$

$$\Delta q_o(E, \Delta E) = N_0 \int dS \int dE_1 [q_1(E_1) \cos 2\Psi - u_1(E_1) \sin 2\Psi] Fr, \quad (19)$$

$$\Delta u_o(E, \Delta E) = N_0 \int dS \int dE_1 [q_1(E_1) \sin 2\Psi + u_1(E_1) \cos 2\Psi] Fr, \quad (20)$$

$$\Delta v_o(E, \Delta E) = N_0 \int dS \int dE_1 v_1(E_1) Fr. \quad (21)$$

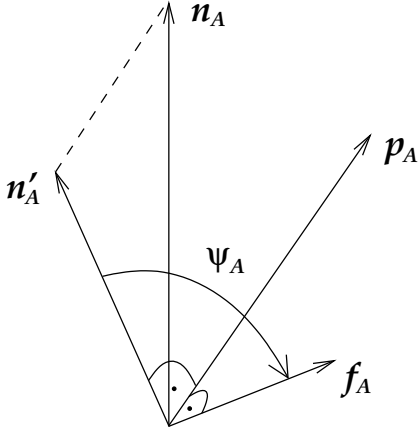


**Figure 3.** Definition of the change of polarisation angle  $\Psi$ .

(i) Let three-vectors  $\mathbf{p}_A$ ,  $\mathbf{n}_A$ ,  $\mathbf{n}'_A$  and  $\mathbf{f}_A$  be the momentum of a photon, normal to the disc, projection of the normal to the plane perpendicular to the momentum and a vector which is parallelly transported along the geodesic (as four-vector), respectively;

(ii) let  $\Psi_A$  be an angle between  $\mathbf{n}'_A$  and  $\mathbf{f}_A$ ;

(iii) let the quantities in (i) and (ii) be evaluated at the disc for  $A = 1$  with respect to the local rest frame co-moving with the disc, and at infinity for  $A = 2$  with respect to the stationary observer at the same light geodesic;

(iv) then the change of polarisation angle is defined as  $\Psi = \Psi_2 - \Psi_1$ .

Here,  $F \equiv F(r, \varphi) = g^2 l \mu_e$  is a transfer function,  $\Psi$  is the angle by which a vector parallelly transported along the light geodesic rotates. We refer to this angle also as a change of the polarisation angle, because the polarisation vector is parallelly transported along light geodesics. See Fig. 3 for an exact definition of the angle  $\Psi$ . The integration boundaries are the same as in Eq. (11). As can be seen from the definition, the first specific Stokes parameter is equal to the photon flux, therefore, eqs. (11) and (18) are identical. The local specific Stokes parameters may depend on  $r$ ,  $\varphi$ ,  $\mu_e$  and  $t - \Delta t$ , which we did not state in the eqs. (18)–(21) explicitly for simplicity.

The specific Stokes parameters that the observer measures may vary in time in the case when the local parameters also depend on time. In eqs. (18)–(21) we used a law of transformation of the Stokes parameters by the rotation of axes (eqs. (I.185) and (I.186) in [Chandrasekhar, 1960]).

An alternative way for expressing polarisation of light is by using the degree of polarisation  $P_o$  and two polarisation angles  $\chi_o$  and  $\xi_o$ , defined by

$$P_o = \sqrt{q_o^2 + u_o^2 + v_o^2} / i_o, \quad (22)$$

$$\tan 2\chi_o = u_o / q_o, \quad (23)$$

$$\sin 2\xi_o = v_o / \sqrt{q_o^2 + u_o^2 + v_o^2}. \quad (24)$$

## 5 NEW MODEL FOR XSPEC

We have developed several general relativistic models for line emission and Compton reflection continuum. The line models are supposed to be more accurate and versatile than the LAOR model [Laor, 1991], and substantially faster than the KERRSPEC model [Martocchia et al., 2000]. Several models of intrinsic emissivity were employed, including the lamp-post model [Matt et al., 1992]. Among other features, these models allow various parameters to be fitted such as the black-hole angular momentum, observer inclination, accretion disc size and some of the parameters characterising disc emissivity and primary illumination

properties. They also allow a change in the grid resolution and, hence, to control accuracy and computational speed. Furthermore, we developed very general convolution models. All these models are based on pre-calculated tables described in Section 2 and thus the geodesics do not need to be calculated each time one integrates the disc emission. These tables are calculated for the vacuum Kerr space-time and for a Keplerian co-rotating disc plus matter that is freely falling below the marginally stable orbit. The falling matter has the energy and angular momentum of the matter at the marginally stable orbit. It is possible to use different pre-calculated tables if they are stored in a specific FITS file (see Appendix A3.1 for its detailed description).

There are two types of new models. The first type integrates the local disc emission in both of the polar coordinates on the disc and thus enables one to choose non-axisymmetric area of integration. This option is useful for example when computing spectra of spots or partially obscured discs. One can also choose the resolution of integration and thus control the precision and speed of the computation. The second type of models is axisymmetric – the axially dependent part of the emission from rings is pre-calculated and stored in a FITS file (the function  $dF(\bar{g}) = d\bar{g} F(\bar{g})$  from (16) is integrated for different radii with the angular grid having 20 000 points). These models have less parameters that can be fitted and thus are less flexible even though more suited to the standard analysis approach. On the other hand they are fast because the emission is integrated only in one dimension (in the radial coordinate of the disc). It may be worth emphasising that the assumption about axial symmetry concerns only the form of intrinsic emissivity of the disc, which cannot depend on the polar angle in this case, not the shape of individual light rays, which is always complicated near a rotating black hole.

There are several parameters and switches that are common for all new models (see Table 1):

`a/M` – specific angular momentum of the Kerr black hole in units of  $GM/c$  ( $M$  is the mass of the central black hole),

`theta_o` – the inclination of the observer in degrees,

`rin-rh` – inner radius of the disc relative to the black-hole horizon in units of  $GM/c^2$ ,

`ms` – switch for the marginally stable orbit,

`rou-rh` – outer radius of the disc relative to the black-hole horizon in units of  $GM/c^2$ ,

`zshift` – overall redshift of the object,

**Table 1.** Common parameters for all models.

Parameter	Unit	Default value	Minimum value	Maximum value
<code>a/M</code>	$GM/c$	0.9982	0.	1.
<code>theta_o</code>	deg	30.	0.	89.
<code>rin-rh</code>	$GM/c^2$	0.	0.	999.
<code>ms</code>	–	1.	0.	1.
<code>rou-rh</code>	$GM/c^2$	400.	0.	999.
<code>zshift</code>	–	0.	-0.999.	10.
<code>ntable</code>	–	0.	0.	99.

`ntable` – number of the FITS file with pre-calculated tables to be used.

The inner and outer radii are given relative to the black-hole horizon and, therefore, their minimum value is zero. This becomes handy when one fits the  $a/M$  parameter, because the horizon of the black hole as well as the marginally stable orbit changes with  $a/M$ , and so the lower limit for inner and outer disc edges cannot be set to constant values. The `ms` switch determines whether we intend to integrate also emission below the marginally stable orbit. If its value is set to zero and the inner radius of the disc is below this orbit then the emission below the marginally stable orbit is taken into account, otherwise it is not.

The `ntable` switch determines which of the pre-calculated tables should be used for intrinsic emissivity. In particular, `ntable = 0` for files `KBHtables00.fits` (`KBHline00.fits`), `ntable = 1` for `KBHtables01.fits` (`KBHline01.fits`), etc., corresponding to non-axisymmetric (axisymmetric) models.

The following set of parameters is relevant only for non-axisymmetric models (see Table 2):

`phi` – position angle of the axial sector of the disc in degrees,

`dphi` – inner angle of the axial sector of the disc in degrees,

`nrad` – radial resolution of the grid,

`division` – switch for spacing of radial grid (0 – equidistant, 1 – exponential),

`nphi` – axial resolution of the grid,

`smooth` – switch for performing simple smoothing (0 – no, 1 – yes),

`Stokes` – switch for computing polarisation (see Table 3).

The `phi` and `dphi` parameters determine the axial sector of the disc from which emission comes (see Fig. 4). The `nrad` and `nphi` parameters determine the grid for numerical integration. If the `division` switch is zero, the radial grid is equidistant; if it is equal to unity then the radial grid is exponential (i.e., more points closer to the black hole).

If the `smooth` switch is set to unity then a simple smoothing is applied to the final spectrum. Here  $N_0^{\Omega}(E_i) = [N_0^{\Omega}(E_{i-1}) + 2N_0^{\Omega}(E_i) + N_0^{\Omega}(E_{i+1})]/4$ .

If the `Stokes` switch is different from zero, then the model also calculates polarisation. Its value determines, which of the Stokes parameters should be computed by XSPEC, i.e., what will be stored in the output array for the photon flux `photar`; see Table 3. (If `Stokes`  $\neq 0$  then a new `ascii` data file `stokes.dat` is created in the current directory,

**Table 2.** Common parameters for non-axisymmetric models.

Parameter	Unit	Default value	Minimum value	Maximum value
<code>phi</code>	deg	0.	-180.	180.
<code>dphi</code>	deg	360.	0.	360.
<code>nrad</code>	–	200.	1.	10000.
<code>division</code>	–	1.	0.	1.
<code>nphi</code>	–	180.	1.	20000.
<code>smooth</code>	–	1.	0.	1.
<code>Stokes</code>	–	0.	0.	6.

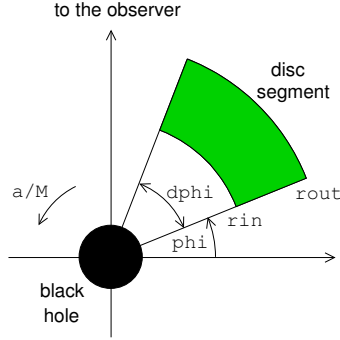


**Figure 4.** Segment of a disc from which emission comes (view from above).

**Table 3.** Definition of the `Stokes` parameter.

Value	Photon flux array <code>pho<sub>tar</sub></code> contains <sup>†‡</sup>
0	$i = I/E$ , where $I$ is the first Stokes parameter (intensity)
1	$q = Q/E$ , where $Q$ is the second Stokes parameter
2	$u = U/E$ , where $U$ is the third Stokes parameter
3	$v = V/E$ , where $V$ is the fourth Stokes parameter
4	degree of polarisation, $P = \sqrt{q^2 + u^2 + v^2}/i$
5	angle $\chi$ [deg] of polarisation, $\tan 2\chi = u/q$
6	angle $\xi$ [deg] of polarisation, $\sin 2\xi = v/\sqrt{q^2 + u^2 + v^2}$

<sup>†</sup> the `photar` array contains values described in the table and multiplied by width of the corresponding energy bin

<sup>‡</sup>  $E$  is energy of observed photons

where values of energy  $E$  together with all Stokes parameters  $i$ ,  $q$ ,  $u$ ,  $v$ ,  $P$ ,  $\chi$ [deg] and  $\xi$ [deg] are stored, each in one column.)

A realistic model of polarisation has been currently implemented only in the `KYL1CR` model (see Section 7.1 below). In other models, a simple assumption is made – the local emission is assumed to be linearly polarised in the direction perpendicular to the disc (i.e.,  $q_1 = i_1 = N_1$  and  $u_1 = v_1 = 0$ ). In all models (including `KYL1CR`) there is always no final circular polarisation (i.e.,  $v = \xi = 0$ ), which follows from the fact that the fourth local Stokes parameter is zero in each model.

## 6 MODELS FOR A RELATIVISTIC SPECTRAL LINE

Three general relativistic line models are included in the new set of XSPEC routines – non-axisymmetric Gaussian line model `KYG1LINE`, axisymmetric Gaussian line model `KYGLINE` and fluorescent lamp-post line model `KYFILL`.

### 6.1 Non-axisymmetric Gaussian line model KYG1LINE

The KYG1LINE model computes the integrated flux from the disc according to Eq. (11). It assumes that the local emission from the disc is

$$N_l(E_l) = \frac{1}{r^{\text{alpha}}} f(\mu_e) \exp \left[ - \left( 1000 \frac{E_l - E_{\text{rest}}}{\sqrt{2} \text{sigma}} \right)^2 \right] \quad (25)$$

for  $r \geq r_b$ ,

$$N_l(E_l) = \text{jump} r_b^{\text{beta}-\text{alpha}} \frac{1}{r^{\text{beta}}} f(\mu_e) \exp \left[ - \left( 1000 \frac{E_l - E_{\text{rest}}}{\sqrt{2} \text{sigma}} \right)^2 \right] \quad (26)$$

for  $r < r_b$ . The local emission is assumed to be a Gaussian line with its peak flux depending on the radius as a broken power law. The line is defined by nine points equally spaced with the central point at its maximum. The normalisation constant  $N_0$  in (11) is such that the total integrated flux of the line is unity. The parameters defining the Gaussian line are (see Table 4):

$E_{\text{rest}}$  – rest energy of the line in keV,

$\text{sigma}$  – width of the line in eV,

$\text{alpha}$  – radial power-law index for the outer region,

$\text{beta}$  – radial power-law index for the inner region,

$r_b$  – parameter defining the border between regions with different power-law indices,

$\text{jump}$  – ratio between flux in the inner and outer regions at the border radius,

$\text{limb}$  – switch for different limb darkening/brightening laws.

There are two regions with different power-law dependences with indices  $\text{alpha}$  and  $\text{beta}$ . The power law changes at the border radius  $r_b$  where the local emissivity does not need to be continuous (for  $\text{jump} \neq 1$ ). The  $r_b$  parameter defines this radius in the following way:

$$r_b = r_b \times r_{\text{ms}} \quad \text{for } r_b \geq 0, \quad (27)$$

$$r_b = -r_b + r_h \quad \text{for } r_b < 0, \quad (28)$$

where  $r_{\text{ms}}$  is the radius of the marginally stable orbit and  $r_h$  is the radius of the horizon of the black hole.

The function  $f(\mu_e) = f(\cos \delta_e)$  in (25) and (26) describes the limb darkening/brightening law, i.e., the dependence of the local emission on the local emission angle. Several limb darkening/brightening laws are implemented:

$$f(\mu_e) = 1 \quad \text{for } \text{limb} = 0, \quad (29)$$

$$f(\mu_e) = 1 + 2.06\mu_e \quad \text{for } \text{limb} = -1, \quad (30)$$

$$f(\mu_e) = \ln(1 + \mu_e^{-1}) \quad \text{for } \text{limb} = -2, \quad (31)$$

$$f(\mu_e) = \mu_e^{1.1\text{limb}} \quad \text{for } \text{limb} \neq 0, -1, -2. \quad (32)$$

Eq. (29) corresponds to the isotropic local emission, Eq. (30) corresponds to limb darkening in an optically thick electron scattering atmosphere (used by Laor [Laor et al., 1990, Laor, 1991, Phillips and Mészáros, 1986]), and Eq. (31) corresponds to limb brightening predicted

**Table 4.** Parameters of the non-axisymmetric Gaussian line model KYG1LINE. Model parameters that are not common for all non-axisymmetric models are denoted by asterisk.

Parameter	Unit	Default value	Minimum value	Maximum value
a/M	$GM/c$	0.9982	0.	1.
theta_o	deg	30.	0.	89.
rin-rh	$GM/c^2$	0.	0.	999.
ms	–	1.	0.	1.
rout-rh	$GM/c^2$	400.	0.	999.
phi	deg	0.	-180.	180.
dphi	deg	360.	0.	360.
nrad	–	200.	1.	10000.
division	–	1.	0.	1.
nphi	–	180.	1.	20000.
smooth	–	1.	0.	1.
zshift	–	0.	-0.999	10.
ntable	–	0.	0.	99.
*Erest	keV	6.4	1.	99.
*sigma	eV	2.	0.01	1000.
*alpha	–	3.	-20.	20.
*beta	–	4.	-20.	20.
*rb	$r_{ms}$	0.	0.	160.
*jump	–	1.	0.	1e6
*limb	–	-1.	-10.	10.
Stokes	–	0.	0.	6.

by some models of a fluorescent line emitted by an accretion disc due to X-ray illumination [Ghisellini et al., 1994, Haardt, 1993].

There is also a similar model KYG2LINE present among the new XSPEC models, which is useful when fitting two general relativistic lines simultaneously. The parameters are the same as in the KYG1LINE model except that there are two sets of those parameters describing the local Gaussian line emission. There is one more parameter present, `ratio21`, which is the ratio of the maximum of the second local line to the maximum of the first local line. Polarisation computations are not included in this model.

## 6.2 Axisymmetric Gaussian line model KYGLINE

This model uses Eq. (15) for computing the disc emission with local flux being

$$N_1(E_1) = \delta(E_1 - E_{\text{rest}}), \quad (33)$$

$$R(r) = r^{-\alpha}. \quad (34)$$

The function  $dF(\bar{g}) \equiv d\bar{g} F(\bar{g})$  in (16) was pre-calculated for three different limb darkening/brightening laws (29)–(31) and stored in corresponding FITS files `KBHline00.fits` to `KBHline02.fits`. The local emission is a delta function with its maximum depending

**Table 5.** Parameters of the axisymmetric Gaussian line model KYGLINE. Model parameters that are not common for all axisymmetric models are denoted by asterisk.

Parameter	Unit	Default value	Minimum value	Maximum value
a/M	$GM/c$	0.9982	0.	1.
theta_o	deg	30.	0.	89.
rin-rh	$GM/c^2$	0.	0.	999.
ms	–	1.	0.	1.
rout-rh	$GM/c^2$	400.	0.	999.
zshift	–	0.	-0.999	10.
ntable	–	1.	0.	99.
*Erest	keV	6.4	1.	99.
*alpha	–	3.	-20.	20.

on the radius as a power law with index `alpha` and also depending on the local emission angle. The normalisation constant  $N_0$  in (15) is such that the total integrated flux of the line is unity.

There are less parameters defining the line in this model than in the previous one (see Table 5):

`Erest` – rest energy of the line in keV,

`alpha` – radial power-law index.

Note that the limb darkening/brightening law can be chosen by means of the `ntable` switch.

This model is much faster than the non-axisymmetric KYGLINE model. Although it is not possible to change the resolution grid on the disc, it is hardly needed because the resolution is set to be very large, corresponding to `nrad` = 500, `division` = 1 and `nphi` = 20 000 in the KYGLINE model, which is more than sufficient in most cases. (These values apply if the maximum range of radii is selected, i.e., `rin`=0, `ms`=0 and `rout`=999; in case of a smaller range the number of points decreases accordingly.) This means that the resolution of the KYGLINE model is much higher than what can be achieved with the `laor` model, and the performance is still very good.

### 6.3 Non-axisymmetric fluorescent lamp-post line model KYF1LL

The line in this model is induced by the illumination of the disc from the primary power-law source located on the axis at `height` above the black hole. This model computes the final spectrum according to Eq. (11) with the local photon flux

$$\begin{aligned}
 N_1(E_1) = & g_L^{\text{PhoIndex}-1} \frac{\sin \theta_L d\theta_L}{r dr} \sqrt{1 - \frac{2\text{height}}{\text{height}^2 + a^2}} f(\mu_i, \mu_e) \\
 & \times \exp \left[ - \left( 1000 \frac{E_1 - E_{\text{rest}}}{\sqrt{2} \text{sigma}} \right)^2 \right].
 \end{aligned} \tag{35}$$

**Table 6.** Parameters of the fluorescent lamp-post line model KYFILL. Model parameters that are not common for all non-axisymmetric models are denoted by asterisk.

Parameter	Unit	Default value	Minimum value	Maximum value
a/M	$GM/c$	0.9982	0.	1.
theta_o	deg	30.	0.	89.
rin-rh	$GM/c^2$	0.	0.	999.
ms	–	1.	0.	1.
rout-rh	$GM/c^2$	400.	0.	999.
phi	deg	0.	-180.	180.
dphi	deg	360.	0.	360.
nrad	–	200.	1.	10000.
division	–	1.	0.	1.
nphi	–	180.	1.	20000.
smooth	–	1.	0.	1.
zshift	–	0.	-0.999	10.
ntable	–	0.	0.	99.
*PhoIndex	–	2.	1.5	3.
*height	$GM/c^2$	3.	-20.	100.
*Erest	keV	6.4	1.	99.
*sigma	eV	2.	0.01	1000.
Stokes	–	0.	0.	6.

Here,  $g_L$  is ratio of the energy of a photon received by the accretion disc to the energy of the same photon when emitted from a source on the axis,  $\theta_L$  is an angle under which the photon is emitted from the source (measured in the local frame of the source) and  $\mu_i \equiv \cos \delta_i$  is the cosine of the incident angle (measured in the local frame of the disc) – see Fig. 5. All of these functions depend on `height` above the black hole at which the source is located and on the rotational parameter `a/M` of the black hole. Values of  $g_L$ ,  $\theta_L$  and  $\mu_i$  for a given height and rotation are read from the lamp-post tables `lamp.fits` (see Appendix A3.3). At present, only tables for `a/M = 0.9987492` (i.e., for the horizon of the black hole  $r_h = 1.05$ ) and `height = 2, 3, 4, 5, 6, 8, 10, 12, 15, 20, 30, 50, 75` and `100` are included in `lamp.fits`, therefore, the `a/M` parameter is used only for the negative values of `height` (see below).

The factor in front of the function  $f(\mu_i, \mu_e)$  gives the radial dependence of the disc emissivity, which is different from the assumed broken power law in the KYG1LINE model. For the derivation of this factor, which characterises the illumination from a primary source on the axis see Appendix A2.

The function  $f(\mu_i, \mu_e)$  is a coefficient of reflection. It depends on the incident and reflection angles. Although the normalisation of this function also depends on the photon index of the power-law emission from a primary source, we do not need to take this into account because the final spectrum is always normalised to unity. Values of this function are read from a pre-calculated table which is stored in `fluorescent_line.fits` file (see [Matt et al., 1991] and Appendix A3.4).

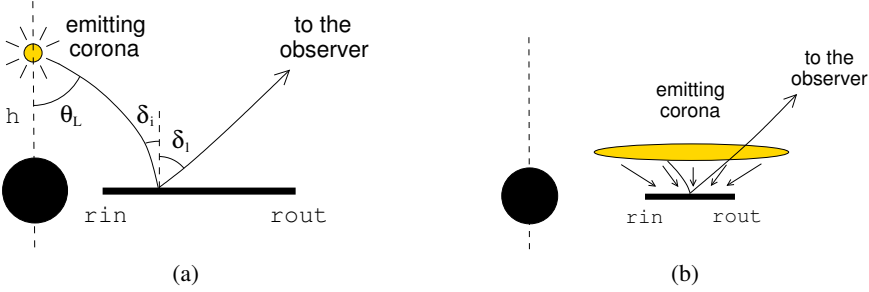


**Figure 5.** Reflection models: (a) lamp-post model; (b) diffuse corona model.

The local emission (35) is defined in nine points of local energy  $E_1$  that are equally spaced with the central point at its maximum. The normalisation constant  $N_0$  in the formula (11) is such that the total integrated flux of the line is unity. The parameters defining local emission in this model are (see Table 6):

PhoIndex – photon index of primary power-law illumination,  
height – height above the black hole where the primary source is located for  $\text{height} > 0$ , and radial power-law index for  $\text{height} \leq 0$ ,  
 $E_{\text{rest}}$  – rest energy of the line in keV,  
sigma – width of the line in eV.

If positive, the height parameter works as a switch – the exact value present in the tables `lamp.fits` must be chosen. If the height parameter is negative, then this model assumes that the local emission is the same as in the KYG1LINE model with the parameters  $\alpha = -\text{height}$ ,  $rb = 0$  and  $\text{limb} = -2$  (PhoIndex parameter is unused in this case).

## 7 COMPTON REFLECTION MODELS

We have developed two new relativistic continuum models – lamp-post Compton reflection model KYL1CR and the KYH1REFL model which is a relativistically blurred HREFL model that is already present in XSPEC. Both of these models are non-axisymmetric.

### 7.1 Non-axisymmetric lamp-post Compton reflection model KYL1CR

The emission in this model is induced by the illumination of the disc from the primary power-law source located on the axis at height above the black hole. As in every non-axisymmetric model the observed spectrum is computed according to Eq. (11). The local emission is

$$N_l(E_1) = g_L^{\text{PhoIndex}-1} \frac{\sin \theta_L d\theta_L}{r dr} \sqrt{1 - \frac{2\text{height}}{\text{height}^2 + (a/M)^2}} f(E_1; \mu_i, \mu_e) \quad (36)$$

for  $\text{height} > 0$ ,

$$N_1(E_1) = r^{\text{height}} \bar{f}(E_1; \mu_e) \quad (37)$$

for  $\text{height} \leq 0$ . For the definition of  $g_L$ ,  $\theta_L$  and  $\mu_i$  see Section 6.3 and Appendix A3.3, where pre-calculated tables of these functions in `lamp.fits` are described.

The function  $f(E_1; \mu_i, \mu_e)$  gives dependence of the locally emitted spectrum on the angle of incidence and the angle of emission, assuming a power-law illumination. This function depends on the photon index `PHOINDEX` of the power-law emission from a primary source. Values of this function for various photon indices of primary emission are read from the pre-calculated tables stored in `refspectra.fits` (see Appendix A3.5). These tables were calculated by the Monte Carlo simulations of Compton scattering [Matt et al., 1991]. At present, tables for `PHOINDEX` = 1.5, 1.6, ..., 2.9, 3.0 and for local energies in the range from 2 keV to 300 keV are available. The normalisation constant  $N_0$  in Eq.(11) is such that the final photon flux at an energy of 3 keV is equal to unity, which is different from what is usual for continuum models in XSPEC (where the photon flux is unity at 1 keV). The choice adopted is due to the fact that current tables in `refspectra.fits` do not extend below 2 keV.

The function  $\bar{f}(E_1; \mu_e)$ , which is used for negative `height`, is an averaged function  $f(E_1; \mu_i, \mu_e)$  over  $\mu_i$

$$\bar{f}(E_1; \mu_e) \equiv \int_0^1 d\mu_i f(E_1; \mu_i, \mu_e). \quad (38)$$

The local emission (37) can be interpreted as emission induced by illumination from clouds localised near above the disc rather than from a primary source on the axis (see Fig. 5). In this case photons strike the disc from all directions.

For positive values of `height` the KYL1CR model includes a physical model of polarisation based on Rayleigh scattering in single scattering approximation. The specific local Stokes parameters describing local polarisation of light are

$$i_1(E_1) = \frac{I_1 + I_r}{\langle I_1 + I_r \rangle} N_1(E_1), \quad (39)$$

$$q_1(E_1) = \frac{I_1 - I_r}{\langle I_1 + I_r \rangle} N_1(E_1), \quad (40)$$

$$u_1(E_1) = \frac{U}{\langle I_1 + I_r \rangle} N_1(E_1), \quad (41)$$

$$v_1(E_1) = 0, \quad (42)$$

where functions  $I_1$ ,  $I_r$  and  $U$  determine the angular dependence of the Stokes parameters in the following way

$$I_1 = \mu_e^2(1 + \mu_i^2) + 2(1 - \mu_e^2)(1 - \mu_i^2) - 4\mu_e\mu_i\sqrt{(1 - \mu_e^2)(1 - \mu_i^2)} \cos(\Phi_e - \Phi_i) - \mu_e^2(1 - \mu_i^2) \cos 2(\Phi_e - \Phi_i), \quad (43)$$

$$I_r = 1 + \mu_i^2 + (1 - \mu_i^2) \cos 2(\Phi_e - \Phi_i), \quad (44)$$

$$U = -4\mu_i\sqrt{(1 - \mu_e^2)(1 - \mu_i^2)} \sin(\Phi_e - \Phi_i) - 2\mu_e(1 - \mu_i^2) \sin 2(\Phi_e - \Phi_i), \quad (45)$$

**Table 7.** Parameters of the lamp-post Compton reflection model KYL1CR. Model parameters that are not common for all non-axisymmetric models are denoted by asterisk.

Parameter	Unit	Default value	Minimum value	Maximum value
a/M	$GM/c$	0.9982	0.	1.
theta_o	deg	30.	0.	89.
rin-rh	$GM/c^2$	0.	0.	999.
ms	–	1.	0.	1.
rout-rh	$GM/c^2$	400.	0.	999.
phi	deg	0.	-180.	180.
dphi	deg	360.	0.	360.
nrad	–	200.	1.	10000.
division	–	1.	0.	1.
nphi	–	180.	1.	20000.
smooth	–	1.	0.	1.
zshift	–	0.	-0.999	10.
ntable	–	0.	0.	99.
*PhoIndex	–	2.	1.5	3.
*height	$GM/c^2$	3.	-20.	100.
*line	–	0.	0.	1.
*E_cut	keV	300.	1.	1000.
Stokes	–	0.	0.	6.

Here  $\Phi_e$  and  $\Phi_i$  are the azimuthal emission and the incident angles in the local rest frame co-moving with the accretion disc (see Appendixes A1 and A2 for their definition). For the derivation of these formulae see the definitions (I.147) and eqs. (X.172) in [Chandrasekhar, 1960]. We have omitted a common multiplication factor, which would be cancelled anyway in eqs. (39)–(42). The symbol  $\langle \rangle$  in definitions of the local Stokes parameters means value averaged over the difference of the azimuthal angles  $\Phi_e - \Phi_i$ . We divide the parameters by  $\langle I_l + I_r \rangle$  because the function  $f(E_l; \mu_i, \mu_e)$ , and thus also the local photon flux  $N_l(E_l)$ , is averaged over the difference of the azimuthal angles.

The parameters defining local emission in this model are (see Table 7):

PhoIndex – photon index of primary power-law illumination,  
height – height above the black hole where the primary source is located for height > 0, and radial power-law index for height ≤ 0,  
line – switch whether to include the iron lines (0 – no, 1 – yes),  
E\_cut – exponential cut-off energy of the primary source in keV.

Tables `refspectra.fits` for the function  $f(E_l; \mu_i, \mu_e)$  also contain the emission in the iron lines  $K\alpha$  and  $K\beta$ . The two lines can be excluded from computations if the `line` switch is set to zero. The `E_cut` parameter sets the upper boundary in energies where the emission from a primary source ceases to follow a power-law dependence. If the `E_cut` parameter is lower than both the maximum energy of the considered dataset and the maximum energy

in the tables for  $f(E_1; \mu_i, \mu_e)$  in `refspectra.fits` (300 keV), then this model is not valid.

## 7.2 Non-axisymmetric Compton reflection model KYH1REFL

This model is based on an existing multiplicative HREFL model in combination with the POWERLAW model, both of which are present in XSPEC. Local emission in (11) is the same as the spectrum given by the model HREFL\*POWERLAW with the parameters `thetamin = 0` and `thetamax = 90` with a broken power-law radial dependence added:

$$N_1(E_1) = r^{-\text{alpha}} \text{HREFL*POWERLAW} \quad \text{for } r \geq r_b, \quad (46)$$

$$N_1(E_1) = \text{jump} r_b^{\text{beta-alpha}} r^{-\text{beta}} \text{HREFL*POWERLAW} \quad \text{for } r < r_b. \quad (47)$$

For a definition of the boundary radius  $r_b$  by the `rb` parameter see eqs. (27)–(28), and for a detailed description of the HREFL model see [Dovčiak et al., 2004] and the XSPEC manual. The KYH1REFL model can be interpreted as a Compton-reflection model for which the source of primary irradiation is near above the disc, in contrast to the lamp-post scheme with the source on the axis (see Fig. 5). The approximations for Compton reflection used in HREFL (and therefore also in KYH1REFL) are valid below  $\sim 15$  keV in the disc rest-frame. The normalisation of the final spectrum in this model is the same as in other continuum models in XSPEC, i.e., photon flux is unity at the energy of 1 keV.

The parameters defining the local emission in KYH1REFL (see Table 8) are

`PhoIndex` – photon index of the primary power-law illumination,  
`alpha` – radial power-law index for the outer region,  
`beta` – radial power-law index for the inner region,  
`rb` – parameter defining the border between regions with different power-law indices,  
`jump` – ratio between flux in the inner and outer regions at the border radius,  
`Feabun` – iron abundance relative to solar,  
`FeKedge` – iron K-edge energy,  
`Escfrac` – fraction of the direct flux from the power-law primary source seen by the observer,  
`covfac` – normalisation of the reflected continuum.

## 8 GENERAL RELATIVISTIC CONVOLUTION MODELS

We have also produced two convolution-type models, KY1CONV and KYCONV, which can be applied to any existing XSPEC model for the intrinsic X-ray emission from a disc around a Kerr black hole. We must stress that these models are substantially more powerful than the usual convolution models in XSPEC (these are commonly defined in terms of one-dimensional integration over energy bins). Despite the fact that our convolution models still use the standard XSPEC syntax in evaluating the observed spectrum (e.g., KYCONV(POWERLAW)), our code accomplishes a more complex operation. It still performs ray-tracing across the disc surface so that the intrinsic model contributions are integrated from different radii and azimuths on the disc.

There are several restrictions that arise from the fact that we use existing XSPEC models:

**Table 8.** Parameters of the reflection KYH1REFL model. Model parameters that are not common for all non-axisymmetric models are denoted by asterisk.

Parameter	Unit	Default value	Minimum value	Maximum value
a/M	$GM/c$	0.9982	0.	1.
theta_o	deg	30.	0.	89.
rin-rh	$GM/c^2$	0.	0.	999.
ms	–	1.	0.	1.
rout-rh	$GM/c^2$	400.	0.	999.
phi	deg	0.	-180.	180.
dphi	deg	360.	0.	360.
nrad	–	200.	1.	10000.
division	–	1.	0.	1.
nphi	–	180.	1.	20000.
smooth	–	1.	0.	1.
zshift	–	0.	-0.999	10.
ntable	–	0.	0.	99.
*PhoIndex	–	1.	0.	10.
*alpha	–	3.	-20.	20.
*beta	–	4.	-20.	20.
*rb	$r_{ms}$	0.	0.	160.
*jump	–	1.	0.	1e6
*Feabun	–	1.	0.	200.
*FeKedge	keV	7.11	7.0	10.
*Escfrac	–	1.	0.	1000.
*covfac	–	1.	0.	1000.
Stokes	–	0.	0.	6.

- by local XSPEC models only the energy dependence of the photon flux can be defined,
- only a certain type of radial dependence of the local photon flux can be imposed – we have chosen to use a broken power-law radial dependence,
- there is no azimuthal dependence of the local photon flux, except through limb darkening law,
- local flux depends on the binning of the data because it is defined in the centre of each bin, a large number of bins is needed for highly varying local flux.

For emissivities that cannot be defined by existing XSPEC models, or where the limitations mentioned above are too restrictive, one has to add a new user-defined model to XSPEC (by adding a new subroutine to XSPEC). This method is more flexible and faster than convolution models (especially when compared with the non-axisymmetric one), and hence it is recommended even for cases when these prefabricated models could be used. In any new model for XSPEC one can use the common ray-tracing driver for relativistic smearing of the local emission: `ide` for non-axisymmetric models and `idre` for axisymmetric ones. For a detailed description see Appendixes A4.1 and A4.2.

### 8.1 Non-axisymmetric convolution model KYC1ONV

The local emission in this model is computed according to Eq. (11) with the local emissivity equal to

$$N_l(E_l) = r^{-\text{alpha}} f(\mu_e) \text{MODEL} \quad \text{for } r > r_b, \quad (48)$$

$$N_l(E_l) = \text{jump} r_b^{\text{beta}-\text{alpha}} r^{-\text{beta}} f(\mu_e) \text{MODEL} \quad \text{for } r \leq r_b. \quad (49)$$

For a definition of the boundary radius  $r_b$  by the `rb` parameter see eqs. (27)–(28) and for definition of different limb darkening laws  $f(\mu_e)$  see eqs. (29)–(32). The local emission is given by the MODEL in the centre of energy bins used in XSPEC with the broken power-law radial dependence and limb darkening law added. Apart from the parameters of the MODEL, the local emission is defined also by the following parameters (see Table 9):

`normal` – switch for the normalisation of the final spectrum,  
 = 0 – total flux is unity (used usually for the line),  
 > 0 – flux is unity at the energy = `normal` keV (used usually for the continuum),  
 < 0 – flux is not normalised,  
`ne_loc` – number of points in the energy grid where the local photon flux is defined,  
`alpha` – radial power-law index for the outer region,  
`beta` – radial power-law index for the inner region,  
`rb` – parameter defining the border between regions with different power-law indices,  
`jump` – ratio between the flux in the inner and outer regions at the border radius,  
`limb` – switch for different limb darkening/brightening laws.

The local emission in each KY model has to be defined either on equidistant or exponential (i.e., equidistant in logarithmic scale) energy grid. Because the energy grid used in the convolution model depends on the binning of the data, which may be arbitrary, the flux has to be rebinned. It is always rebinned into an exponentially spaced energy grid in KY convolution models. The `ne_loc` parameter defines the number of points in which the rebinned flux will be defined.

### 8.2 Axisymmetric convolution model KYCONV

The local emission in this model is computed according to Eq. (15) with the local emissivity equal to

$$N_l(E_l) = \text{MODEL}, \quad (50)$$

$$R(r) = r^{-\text{alpha}}. \quad (51)$$

$$(52)$$

Except for the parameters of the MODEL, the local emission is defined also by the following parameters (see Table 10):

`alpha` – radial power-law index,  
`ne_loc` – number of points in energy grid where the local photon flux is defined,  
`normal` – switch for the normalisation of the final spectrum,  
 = 0 – total flux is unity (used usually for the line),

**Table 9.** Parameters of the non-axisymmetric convolution model KYC1ONV. Model parameters that are not common for all non-axisymmetric models are denoted by asterisk.

Parameter	Unit	Default value	Minimum value	Maximum value
a/M	$GM/c$	0.9982	0.	1.
theta_o	deg	30.	0.	89.
rin-rh	$GM/c^2$	0.	0.	999.
ms	–	1.	0.	1.
rout-rh	$GM/c^2$	400.	0.	999.
phi	deg	0.	-180.	180.
dphi	deg	360.	0.	360.
nrad	–	200.	1.	10000.
division	–	1.	0.	1.
nphi	–	180.	1.	20000.
smooth	–	1.	0.	1.
*normal	–	1.	-1.	100.
zshift	–	0.	-0.999	10.
ntable	–	0.	0.	99.
*ne_loc	–	100.	3.	5000.
*alpha	–	3.	-20.	20.
*beta	–	4.	-20.	20.
*rb	$r_{ms}$	0.	0.	160.
*jump	–	1.	0.	1e6
*limb	–	0.	-10.	10.
Stokes	–	0.	0.	6.

> 0 – flux is unity at the energy = normal keV (used usually for the continuum),  
 < 0 – flux is not normalised.

Note that the limb darkening/brightening law can be chosen through the `ntable` switch. This model is much faster than the non-axisymmetric convolution model KYC1ONV.

## 9 EXAMPLES AND COMPARISONS

In our new models we have concentrated ourselves mainly on two components that contribute to the X-ray spectra of active galactic nuclei and X-ray binaries with black-hole candidates – spectral line emission and its relativistic broadening, and the Compton reflection from an illuminated disc. Two basic types of illumination have been considered – the disc illuminated either from every direction by a nearby diffuse corona above the disc, or from a particular direction by a small source placed on the axis above the black hole (see Fig. 5). The illumination in the former case decreases with radius as a power law. Hence, this model is characterised by the radial power-law index  $\alpha$ . On the other hand, the illumination anisotropy in the latter (lamp-post) model depends mainly on the position of a primary source of emission characterised by height  $h$  where it is located. In both cases

**Table 10.** Parameters of the axisymmetric convolution model KYCONV. Model parameters that are not common for all axisymmetric models are denoted by asterisk.

Parameter	Unit	Default value	Minimum value	Maximum value
a/M	$GM/c$	0.9982	0.	1.
theta_o	deg	30.	0.	89.
rin-rh	$GM/c^2$	0.	0.	999.
ms	–	1.	0.	1.
rout-rh	$GM/c^2$	400.	0.	999.
zshift	–	0.	-0.999	10.
ntable	–	0.	0.	99.
*alpha	–	3.	-20.	20.
*ne_loc	–	100.	3.	5000.
*normal	–	1.	-1.	100.

it is assumed that the primary emission has a continuum power-law shape which can be characterised by a photon index  $\Gamma$  (PHOINDEX).

The emission from the disc depends on quite a number of parameters. It is influenced by the mass  $M$  and the rotation  $a$  of the central black hole, by the area from which the emission from disc comes (defined by inner radius  $r_{\text{in}}$ , outer radius  $r_{\text{out}}$  and azimuthal segment with boundaries at  $\varphi$  and  $\varphi + \Delta\varphi$ ), by the inclination  $\theta_o$  of the observer, by the radial power-law index  $\alpha$ , by the photon index  $\Gamma$  and by the position  $h$  of a primary source. Limb darkening/brightening law (dependence on the local emission angle) is another important factor that determines the final spectrum we observe.

Here, we will show several examples of emission for the lamp-post fluorescent line model and for the reflection models. For other examples and comparisons, see the accompanying paper (Dovčiak, Karas & Yaqoob [Dovčiak et al., 2004]). In all figures in this section, we

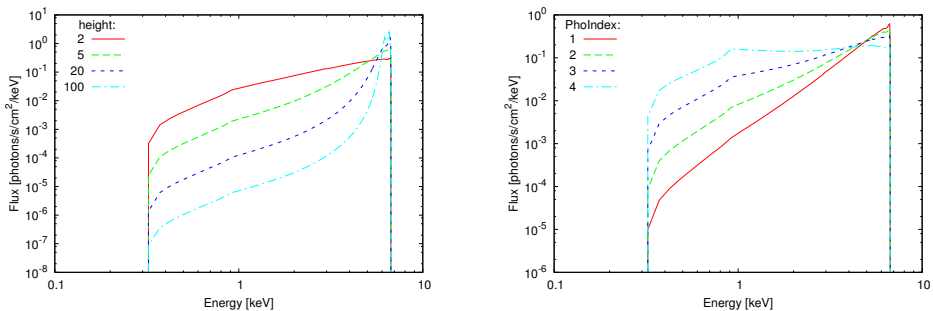


**Figure 6.** An example of a line profile originating from a disc in equatorial plane of a Kerr black hole ( $a = 0.9987 GM/c^2$ , i.e.,  $r_h = 1.05 GM/c^2$ ) due to the illumination from a primary source on the axis. The KYFILL model was used. **Left:** Dependence of the line profile on the height (in  $GM/c^2$ ) of a primary source with photon index  $\Gamma = 2$ . **Right:** Dependence of the line profile on the photon index of the primary emission with a source at height  $3 GM/c^2$  above the black hole.

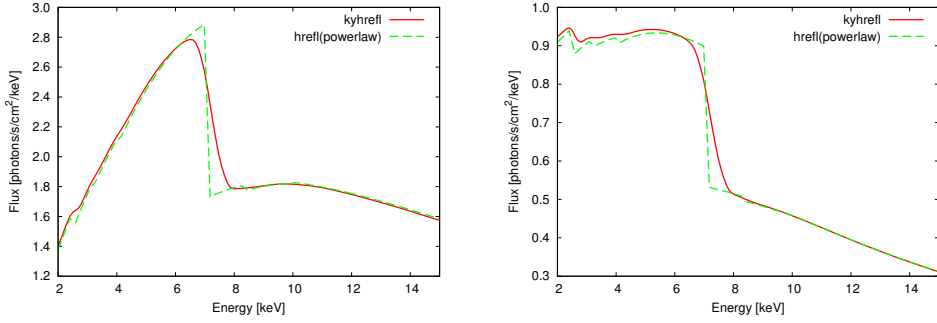


**Figure 7.** Comparison of the general relativistic KYH1REFL model with non-relativistic HREFL(POWERLAW). The relativistic blurring of the iron edge is clearly visible. The power-law index of the primary source is PhoIndex=2 (left) and PhoIndex=2.6 (right).

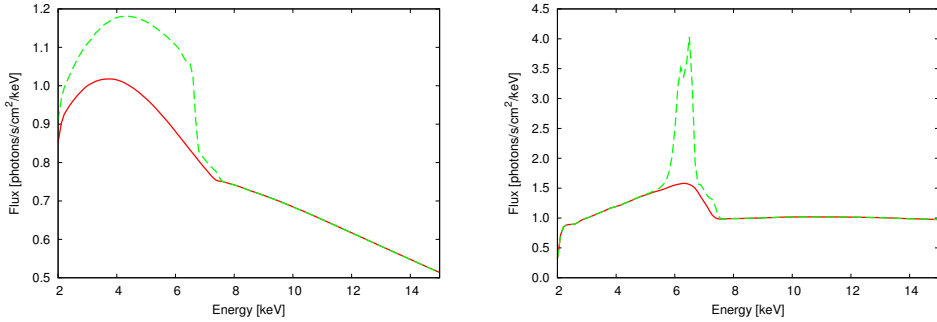


**Figure 8.** General relativistic lamp-post Compton reflection model KYL1CR with (dashed) and without (solid) iron lines  $K\alpha$  and  $K\beta$ . The emission from the disc is induced by illumination from a primary source placed  $2 GM/c^2$  (left) and  $100 GM/c^2$  (right) above the black hole.

assumed the inclination angle  $\theta_0 = 30^\circ$ , the rotational parameter  $a = 0.9987 GM/c^2$ , and an emitting ring extending from  $r_{\text{in}} = r_{\text{ms}}$  to  $r_{\text{out}} = 400 GM/c^2$ .

In Fig. 6 we demonstrate that the broad iron emission lines due to illumination from the source placed on the axis depend heavily on the height where the “lamp” is located (left), as well as on the photon index of the primary emission (right). It can be seen that the intrinsic width of the line (2 eV in this example) is much less than its subsequent relativistic broadening, and the local profile (assumed to be Gaussian) is thus smeared in the final spectrum. These graphs correspond to the iron  $K\alpha$  line with the rest energy of 6.4 keV.

Relativistic effects are demonstrated also in Fig. 7 where the non-relativistic reflection model HREFL(POWERLAW) is compared with our relativistic KYH1REFL. Blurring of the iron edge is clearly visible. Here, we set the radial power-law index  $\alpha = 1$  in KYH1REFL. Other parameters defining these models were set to their default values.

Examples of the Compton reflection emission component of the spectra with and without the fluorescent  $K\alpha$  and  $K\beta$  lines are shown in Fig. 8. It can be seen that originally narrow lines can contribute substantially to the continuum component.

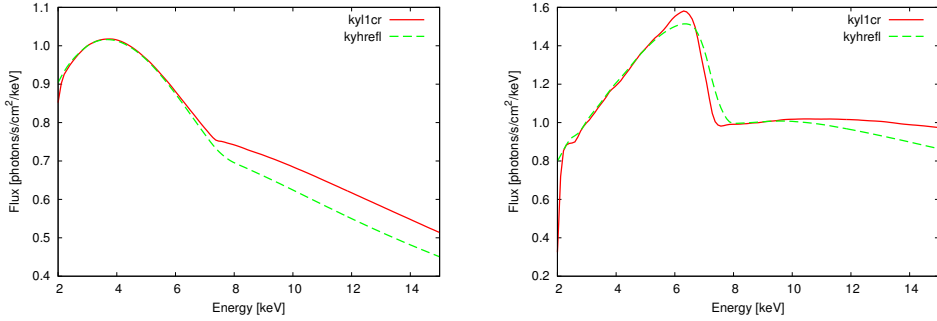


**Figure 9.** Comparison of the two new general relativistic Compton reflection models KYL1CR and KYH1REFL. The lamp-post KYL1CR model is characterised by the height  $h$  above the disc where a primary source of emission is placed, the reflection KYH1REFL model is characterised by the radial power-law index  $\alpha$ . **Left:**  $h = 2 GM/c^2$ ,  $\alpha = 3.4$ . **Right:**  $h = 100 GM/c^2$ ,  $\alpha = 1.5$ .

We compare the two new relativistic reflection models KYL1CR and KYH1REFL in Fig. 9. Note that the KYL1CR model is valid only above approximately 2 keV and the KYH1REFL model only below approximately 15 keV.

## 10 CONCLUSIONS

In this paper we described the main features of the newly developed set of routines. We have concentrated ourselves on various technical issues connected with fitting X-ray spectra using our model. In particular, we described several variants of the code which are suited for modelling relativistic spectral components originating in a Keplerian disc near a rotating black hole. Both axially symmetric and non-axisymmetric models were discussed. For further details and for exemplary analysis of *XMM-Newton* satellite data we refer to Dovčiak et al. [Dovčiak et al., 2004].

Our package offers a number of applications which could not be examined in the limited space of the present paper. In particular, timing analysis can be performed with the code, but we defer detailed description of this capability to subsequent papers. Also, we have only briefly touched the possibility of polarimetric analysis, which offers great possibilities for future X-ray spectroscopy but goes beyond routine capabilities of devices installed onboard present day satellites. Additional emissivity laws can be easily adopted. This can be achieved either by using the convolution component or by adding a new user-defined model. The latter method is more flexible and faster, and hence recommended. In both approaches, the ray-tracing routine is linked and used for relativistic blurring.

As general motivation for developing this project further, we remind the reader that various disc-like structures are almost ubiquitous in objects where the fluid orbits around and inflows onto a compact body. The central mass,  $M_{\bullet}$ , can vary by many orders of magnitude in different objects, and its value provides the basic classification for black-hole sources. Physical characteristics of accretion discs also scale roughly with  $M_{\bullet}$ . Indeed, accretion discs around supermassive black holes in active galactic nuclei and quasars share some properties with circumstellar discs in close binary systems, e.g., cataclysmic variable

stars and microquasars. However, there are important distinctions between the two kinds of objects which prohibit any simple scaling (for example, galactic nuclear discs tend to be colder and less dense compared to circumstellar discs). In both cases there is strong evidence suggesting that some spectral components (namely, the iron  $K\alpha$  line emission) originate, at least in part, within  $\sim 10$  gravitational radii of a central black-hole.

The central compact body governs gravitational field in which the medium of an accretion flow evolves. Since we consider a general relativistic description of the gravitational field, the rotation of the central body should not be ignored. An angular momentum is actually one of the model parameters which could in principle be measured by means of spectral analysis of observed radiation.

## ACKNOWLEDGEMENTS

The authors gratefully acknowledge kind invitation of the meeting organisers and financial support via the Czech Science Foundation grants 205/03/0902 (VK), 202/02/0735 (MD), and from the NASA grants NCC5-447 and NAG5-10769 (TY). Support from the Charles University is also acknowledged (GAUK 299/2004). AM acknowledges financial support from CNES and kind hospitality at the Astronomical Institute of the Czech Academy of Sciences.

## APPENDIX A: APPENDIX

### A1 Summary of equations

Before writing equations for the transfer functions let us summarise basic formulae defining the Kerr space-time, light geodesics and disc's motion. We remind the reader that units  $GM_{\bullet} = c = 1$  are used ( $M_{\bullet}$  is the mass of the central black hole).

The Kerr metric in Boyer–Lindquist coordinates is

$$g_{\mu\nu} = \begin{pmatrix} -\left(1 - \frac{2r}{\rho^2}\right) & 0 & 0 & -\frac{2ar \sin^2\theta}{\rho^2} \\ 0 & \frac{\rho^2}{\Delta} & 0 & 0 \\ 0 & 0 & \rho^2 & 0 \\ -\frac{2ar \sin^2\theta}{\rho^2} & 0 & 0 & \frac{\mathcal{A} \sin^2\theta}{\rho^2} \end{pmatrix},$$

where  $\rho^2 \equiv r^2 + a^2 \cos^2\theta$ ,  $\Delta \equiv r^2 - 2r + a^2$  and  $\mathcal{A} \equiv (r^2 + a^2)^2 - \Delta a^2 \sin^2\theta$ . We assume  $0 \leq a \leq 1$  everywhere in this paper.

The four-momentum of the photons emitted from the disc is (see e.g., [Carter, 1968] and [Misner et al., 1973])

$$p_e^t = [a(l - a) + (r^2 + a^2)(r^2 + a^2 - al)/\Delta]/r^2, \quad (\text{A1})$$

$$p_e^r = \mathbf{R}_{\text{sgn}}\{(r^2 + a^2 - al)^2 - \Delta[(l - a)^2 + q^2]\}^{1/2}/r^2, \quad (\text{A2})$$

$$p_e^\theta = -q/r^2, \quad (\text{A3})$$

$$p_e^\varphi = [l - a + a(r^2 + a^2 - al)/\Delta]/r^2. \quad (\text{A4})$$

Here  $l = \alpha \sin \theta_0$  and  $q^2 = \beta^2 + \cos^2(\alpha^2 - a^2)$  are constants of motion with  $\alpha$  and  $\beta$  being impact parameters measured perpendicular and parallel, respectively, to the spin axis of the black hole projected onto the observer's sky. Here we define  $\alpha$  to be positive when photon travels in the direction of the four-vector  $\frac{\partial}{\partial \varphi}$  at infinity, and  $\beta$  to be positive if it travels in the direction of  $-\frac{\partial}{\partial \theta}$  at infinity. Furthermore, we have denoted sign of the radial component of the momentum by  $R_{\text{sgn}}$ . We have chosen an affine parameter along light geodesics in such a way that the conserved energy is normalised to  $-p_{e t} = -p_{o t} = 1$ .

The Keplerian velocity of the co-rotating disc above the marginally stable orbit is

$$U^t = \frac{r^2 + a\sqrt{r}}{r\sqrt{r^2 - 3r + 2a\sqrt{r}}}, \quad (\text{A5})$$

$$U^r = 0, \quad (\text{A6})$$

$$U^\theta = 0, \quad (\text{A7})$$

$$U^\varphi = \frac{1}{\sqrt{r(r^2 - 3r + 2a\sqrt{r})}}. \quad (\text{A8})$$

We assume that the matter in the disc below the marginally stable orbit conserves its specific energy and its specific angular momentum, i.e.,  $U_t(r < r_{\text{ms}}) = U_t(r_{\text{ms}})$  and  $U_\varphi(r < r_{\text{ms}}) = U_\varphi(r_{\text{ms}})$ . We get the radial component  $U^r(r < r_{\text{ms}})$  from the normalisation of the four-velocity,  $U^\mu U_\mu = -1$ , and from the fact that the disc rotates in the equatorial plane even below the marginally stable orbit, i.e.,  $U^\theta(r < r_{\text{ms}}) = 0$ .

In our calculations we use the following local orthonormal tetrad connected with the matter in the disc

$$e_{(t)\mu} = U_\mu, \quad (\text{A9})$$

$$e_{(r)\mu} = \left( \frac{\sqrt{g_{rr}} U^r U_t}{\sqrt{1 + U^r U_r}}, \sqrt{g_{rr}(1 + U^r U_r)}, 0, \frac{\sqrt{g_{rr}} U^r U_\varphi}{\sqrt{1 + U^r U_r}} \right), \quad (\text{A10})$$

$$e_{(\theta)\mu} = (0, 0, \sqrt{g_{\theta\theta}}, 0), \quad (\text{A11})$$

$$e_{(\varphi)\mu} = \left( -\frac{\sqrt{\Delta} U^\varphi}{\sqrt{1 + U^r U_r}}, 0, 0, \frac{\sqrt{\Delta} U^t}{\sqrt{1 + U^r U_r}} \right). \quad (\text{A12})$$

The gravitational and Doppler shift ( $g$ -factor) is defined as the ratio of the energy of a photon received by an observer at infinity to the local energy of the same photon when emitted from an accretion disc

$$g = \frac{\nu_o}{\nu_e} = \frac{p_{o t}}{p_{e \mu} U^\mu} = -\frac{1}{p_{e \mu} U^\mu}. \quad (\text{A13})$$

Here  $\nu_o$  and  $\nu_e$  denote frequency of the observed and emitted photons, respectively.

We define lensing as the ratio of the area at infinity perpendicular to the light rays through which photons come to the proper area on the disc perpendicular to the light rays and corresponding to the same flux tube

$$\frac{dS_f}{dS_\perp} = \frac{1}{\sqrt{\|Y_{e1}\|^2 \|Y_{e2}\|^2 - \langle Y_{e1}, Y_{e2} \rangle^2}}. \quad (\text{A14})$$

The four-vectors  $Y_{e1}$  and  $Y_{e2}$  are transported along the geodesic according to the equation of the geodesic deviation from infinity where they are unit, space-like and perpendicular to each other and to the four-momentum of light. In (A14) we have denoted the magnitude of a four-vector by  $\| \cdot \|$  and the scalar product of two four-vectors by  $\langle \cdot, \cdot \rangle$ .

The cosine of the local emission angle is

$$\mu_e = \cos \delta_e = -\frac{p_{e\alpha} n^\alpha}{p_{e\mu} U^\mu}, \quad (\text{A15})$$

where  $n^\alpha = -e_{(\theta)}^\alpha$  is the normal to the disc with respect to the observer co-moving with the matter in the disc.

The relative time delay  $\Delta t$  is the Boyer–Lindquist time which elapses between the emission of a photon from the disc and its reception by an observer (plus a certain constant so that the delay is finite close to the black hole). We have integrated the equation of the geodesics in Kerr ingoing coordinates and thus we have calculated the delay in the Kerr ingoing time coordinate  $\Delta t_K$ . The Boyer–Lindquist time coordinate can be obtained from the Kerr ingoing one by the following equation

$$dt = dt_K - \left[ 1 + \frac{2r}{(r-r_+)(r-r_-)} \right] dr, \quad (\text{A16})$$

with  $r_\pm = 1 \pm \sqrt{1-a^2}$ . Then we define the delay as

$$\Delta t = \Delta t_K - \left[ r + \frac{2}{r_+ - r_-} \ln \frac{r - r_+}{r - r_-} + \ln [(r - r_+)(r - r_-)] \right] \quad \text{for } a < 1, \quad (\text{A17})$$

$$\Delta t = \Delta t_K - \left[ r - \frac{2}{r-1} + 2 \ln (r-1) \right] \quad \text{for } a = 1. \quad (\text{A18})$$

There is a minus in front of the brackets because the direction of integration is from infinity (represented by  $r_0 = 10^{11}$  in our computations) to the disc.

The change of the polarisation angle is (see [Connors and Stark, 1977], [Connors et al., 1980])

$$\tan \Psi = \frac{Y}{X}, \quad (\text{A19})$$

where

$$X = -(\alpha - a \sin \theta_0) \kappa_1 - \beta \kappa_2, \quad (\text{A20})$$

$$Y = (\alpha - a \sin \theta_0) \kappa_2 - \beta \kappa_1, \quad (\text{A21})$$

$$(\text{A22})$$

with  $\kappa_1$  and  $\kappa_2$  being components of the complex constant of motion  $\kappa_{pw}$  (see [Walker and Penrose, 1970])

$$\kappa_1 = ar p_e^\theta f^t - r [a p_e^t - (r^2 + a^2) p_e^\varphi] f^\theta - r(r^2 + a^2) p_e^\theta f^\varphi, \quad (\text{A23})$$

$$\kappa_2 = -r p_e^r f^t + r [p_e^t - a p_e^\varphi] f^r + ar p_e^r f^\varphi. \quad (\text{A24})$$

Here the polarisation vector  $f^\mu$  is a four-vector corresponding to the three-vector  $\mathbf{f}_1$  from Fig. 3 which is chosen in such a way that it is a unit vector parallel with  $\mathbf{n}'_1$  (i.e.,  $\Psi_1 = 0$ )

$$f^\mu = \frac{n^\mu - \mu_e (g p_e^\mu - U^\mu)}{\sqrt{1 - \mu_e^2}}. \quad (\text{A25})$$

We define the azimuthal emission angle as the angle between the projection of the three-momentum of the emitted photon into the disc (in the local rest frame co-moving with the disc) and the radial tetrad vector:

$$\Phi_e = -R_{\text{sgn}}^e \arccos \left( \frac{g p_{e\alpha} e_{(\varphi)}^\alpha}{\sqrt{1 - \mu_e^2}} \right) + \frac{\pi}{2}, \quad (\text{A26})$$

where  $R_{\text{sgn}}^e$  is positive if the emitted photon travels outwards ( $p_e^{(r)} > 0$ ) and negative if it travels inwards ( $p_e^{(r)} < 0$ ) in the local rest frame of the disc.

We conclude this section by the relationship between the Boyer–Lindquist coordinate  $\varphi$  and the Kerr ingoing coordinate  $\varphi_K$ , which we use when we interpolate between the pre-calculated tables

$$\varphi = \varphi_K + \frac{a}{r_+ - r_-} \ln \frac{r - r_+}{r - r_-} \quad \text{for } a < 1, \quad (\text{A27})$$

$$\varphi = \varphi_K - \frac{1}{r - 1} \quad \text{for } a = 1. \quad (\text{A28})$$

## A2 Local emission in lamp-post models

The local emission from a disc is proportional to the incident illumination from a power-law primary source placed on the axis at height  $h$  above the black hole. To calculate the incident illumination we need to integrate the geodesics from the source to the disc.

The four-momentum of the incident photons which were emitted by a primary source and which are striking the disc at radius  $r$  is (see e.g., [Carter, 1968] and [Misner et al., 1973])

$$p_i^t = 1 + 2/r + 4/\Delta, \quad (\text{A29})$$

$$p_i^r = R_{\text{sgn}}^i [(r^2 + a^2)^2 - \Delta(a^2 + q_L^2)]^{1/2}/r^2, \quad (\text{A30})$$

$$p_i^\theta = q_L/r^2, \quad (\text{A31})$$

$$p_i^\varphi = 2a/(r\Delta), \quad (\text{A32})$$

where  $q_L^2 = \sin^2\theta_L (h^2 + a^2)^2/\Delta_L - a^2$  is Carter's constant of motion with  $\Delta_L = h^2 - 2h + a^2$ , and with the angle of emission  $\theta_L$  being the local angle under which the photon is emitted from a primary source (it is measured in the rest frame of the source). We define this angle by  $\tan\theta_L = -p_L^{(\theta)}/p_L^{(r)}$ , where  $p_L^{(r)} = p_L^\mu e_{L\mu}^{(r)}$  and  $p_L^{(\theta)} = p_L^\mu e_{L\mu}^{(\theta)}$  with  $p_L^\mu$  and  $e_{L\mu}^{(a)}$  being the four-momentum of emitted photons and the local tetrad connected with a primary source, respectively. The angle is  $0^\circ$  when the photon is emitted downwards and  $180^\circ$  if the photon is emitted upwards.

We denoted the sign of the radial component of the momentum by  $R_{\text{sgn}}^i$ . We have chosen such an affine parameter for the light geodesic that the conserved energy of the light is  $-p_{it} = -p_{Lt} = 1$ . The conserved angular momentum of incident photons is zero ( $l_L = 0$ ).

The gravitational and Doppler shift of the photons striking the disc which were emitted by a primary source is

$$g_L = \frac{\nu_i}{\nu_L} = \frac{p_{i\mu} U^\mu}{p_{L\alpha} U_L^\alpha} = -\frac{p_{i\mu} U^\mu}{U_L^t}. \quad (\text{A33})$$

Here  $\nu_i$  and  $\nu_L$  denote the frequency of the incident and emitted photons, respectively and  $U_L^\alpha$  is a four-velocity of the primary source with the only non-zero component  $U_L^t = \sqrt{(h^2 + a^2)/\Delta_L}$ .

The cosine of the local incident angle is

$$\mu_i = |\cos \delta_i| = \frac{p_{i\alpha} n^\alpha}{p_{i\mu} U^\mu}, \quad (\text{A34})$$

where  $n^\alpha = -e_{(\theta)}^\alpha$  is normal to the disc with respect to the observer co-moving with the matter in the disc.

We further define the azimuthal incident angle as the angle between the projection of the three-momentum of the incident photon into the disc (in the local rest frame co-moving with the disc) and the radial tetrad vector,

$$\Phi_i = -R_{\text{sgn}}^i \arccos\left(\frac{-1}{\sqrt{1 - \mu_i^2}} \frac{p_{i\alpha} e_{(\varphi)}^\alpha}{p_{i\mu} U^\mu}\right) + \frac{\pi}{2}, \quad (\text{A35})$$

where  $R_{\text{sgn}}^i$  is positive if the incident photon travels outwards ( $p_i^{(r)} > 0$ ) and negative if it travels inwards ( $p_i^{(r)} < 0$ ) in the local rest frame of the disc.

In lamp-post models the emission of the disc will be proportional to the incident radiation  $N_i^S(E_i)$  which comes from a primary source

$$N_i^S(E_i) = N_L^{\Omega}(E_L) \frac{d\Omega_L}{dS_1}. \quad (\text{A36})$$

Here  $N_L^{\Omega}(E_L) = N_{0L} E_L^{-\Gamma}$  is an isotropic and stationary power-law emission from a primary source which is emitted into a solid angle  $d\Omega_L$  and which illuminates local area  $dS_1$  on the disc. The energy of the photon striking the disc (measured in the local frame co-moving with the disc) will be redshifted

$$E_i = g_L E_L. \quad (\text{A37})$$

The ratio  $d\Omega_L/dS_1$  is

$$\frac{d\Omega_L}{dS_1} = \frac{d\Omega_L}{dS} \frac{dS}{dS_1} = \frac{\sin \theta_L d\theta_L d\varphi}{dr d\varphi} \frac{dS}{dS_1}, \quad (\text{A38})$$

where (see eqs. (5) and (7))

$$dS = dr d\varphi = |d^2S_t{}^\theta| = -g^{\theta\theta} \frac{p_{it}}{p_1^\theta} dS_\perp = \frac{g^{\theta\theta}}{p_1^\theta} dS_\perp. \quad (\text{A39})$$

Here we used the same space-time slice as in the discussion above Eq. (4) and thus the element  $d^2S_{\alpha\beta}$  is defined as before, see Eq. (5). Note that here the area  $dS_\perp$  is defined by the incident flux tube as opposed to  $dS_\perp$  in Eq. (8) where it was defined by the emitted flux tube. The coordinate area  $dS$  corresponds to the proper area  $dS_\perp$  which is perpendicular to the incident light ray (in the local rest frame co-moving with the disc). The corresponding

proper area (measured in the same local frame) lying in the equatorial plane will be

$$\begin{aligned} dS_{\parallel} &= |d^2S_{(t)}^{(\theta)}| = |e_{(t)}^{\mu} e^{(\theta)\nu} d^2S_{\mu\nu}| = |g_{\theta\theta}^{-1/2} U^{\mu} d^2S_{\mu\theta}| = \\ &= -g_{\theta\theta}^{-1/2} \frac{p_{i\mu} U^{\mu}}{p_i^{\theta}} dS_{\perp} = g_{\theta\theta}^{-1/2} \frac{U_L^i}{p_i^{\theta}} g_L dS_{\perp}. \end{aligned} \quad (\text{A40})$$

Here we have used Eq. (4) for the tetrad components of the element  $d^2S_{\alpha\beta}$ , eqs. (6) and (A33).

It follows from eqs. (A36)–(A40) that the incident radiation will be again a power law with the same photon index  $\Gamma$  as in primary emission

$$N_i^S(E_{\parallel}) = N_{0i} E_{\parallel}^{-\Gamma}, \quad (\text{A41})$$

with the normalisation factor

$$N_{0i} = N_{0L} g_L^{\Gamma-1} \sqrt{1 - \frac{2h}{h^2 + a^2} \frac{\sin \theta_L d\theta_L}{r dr}}. \quad (\text{A42})$$

The emission of the disc due to illumination will be proportional to this factor.

### A3 Description of FITS files

#### A3.1 Transfer functions in `KBHtablesNN.fits`

The transfer functions are stored in the file `KBHtablesNN.fits` as binary extensions and parametrised by the value of the observer inclination angle  $\theta_o$  and the horizon of the black hole  $r_h$ . We found parametrisation by  $r_h$  more convenient than using the rotational parameter  $a$ , although the latter choice may be more common. Each extension provides values of a particular transfer function for different radii, which are given in terms of  $r - r_h$ , and for the Kerr ingoing axial coordinates  $\varphi_K$ . Values of the horizon  $r_h$ , inclination  $\theta_o$ , radius  $r - r_h$  and angle  $\varphi_K$ , at which the functions are evaluated, are defined as vectors at the beginning of the FITS file.

The definition of the file `KBHtablesNN.fits`:

0. All of the extensions defined below are binary.

(i) The first extension contains six integers defining which of the functions is present in the tables. The integers correspond to the delay,  $g$ -factor, cosine of the local emission angle, lensing, change of the polarisation angle and azimuthal emission angle, respectively. Value 0 means that the function is not present in the tables, value 1 means it is.

(ii) The second extension contains a vector of the horizon values in  $GM/c^2$  ( $1.00 \leq r_h \leq 2.00$ ).

(iii) The third extension contains a vector of the values of the observer's inclination angle  $\theta_o$  in degrees ( $0^\circ \leq \theta_o \leq 90^\circ$ ,  $0^\circ$  – axis,  $90^\circ$  – equatorial plane).

(iv) The fourth extension contains a vector of the values of the radius relative to the horizon  $r - r_h$  in  $GM/c^2$ .

(v) The fifth extension contains a vector of the values of the azimuthal angle  $\varphi_K$  in radians ( $0 \leq \varphi_K \leq 2\pi$ ). Note that  $\varphi_K$  is a Kerr ingoing axial coordinate, not the Boyer–Lindquist one!

(vi) All the previous vectors have to have values sorted in an increasing order.

(vii) In the following extensions the transfer functions are defined, each extension is for a particular value of  $r_h$  and  $\theta_o$ . The values of  $r_h$  and  $\theta_o$  are changing with each extension in the following order:

$$\begin{aligned}
 & r_h[1] \times \theta_o[1], \\
 & r_h[1] \times \theta_o[2], \\
 & r_h[1] \times \theta_o[3], \\
 & \dots \\
 & \dots \\
 & r_h[2] \times \theta_o[1], \\
 & r_h[2] \times \theta_o[2], \\
 & r_h[2] \times \theta_o[3], \\
 & \dots \\
 & \dots
 \end{aligned}$$

(viii) Each of these extensions has the same number of columns (up to six). In each column, a particular transfer function is stored – the delay,  $g$ -factor, cosine of the local emission angle, lensing, change of the polarisation angle and azimuthal emission angle, respectively. The order of the functions is important but some of the functions may be missing as defined in the first extension (see 1. above). The functions are:

delay – the Boyer–Lindquist time in  $GM/c^3$  that elapses between the emission of a photon from the disc and absorption of the photon by the observer’s eye at infinity plus a constant,

$g$ -factor – the ratio of the energy of a photon received by the observer at infinity to the local energy of the same photon when emitted from an accretion disc,

cosine of the emission angle – the cosine of the local emission angle between the emitted light ray and local disc normal,

lensing – the ratio of the area at infinity perpendicular to the light rays through which photons come to the proper area on the disc perpendicular to the light rays and corresponding to the same flux tube,

change of the polarisation angle in radians – if the light emitted from the disc is linearly polarised then the direction of polarisation will be changed by this angle at infinity – counter-clockwise if positive, clockwise if negative (we are looking towards the coming emitted beam); on the disc we measure the angle of polarisation with respect to the “up” direction perpendicular to the disc with respect to the local rest frame; at infinity we also measure the angle of polarisation with respect to the “up” direction perpendicular to the disc – the change of the polarisation angle is the difference between these two angles,

azimuthal emission angle in radians – the angle between the projection of the three-momentum of an emitted photon into the disc (in the local rest frame co-moving with the disc) and the radial tetrad vector.

For mathematical formulae defining the functions see eqs. (A13), (A14)–(A15), (A17)–(A19) and (A26) in Appendix A1.

(ix) Each row corresponds to a particular value of  $r - r_h$  (see 4. above).

(x) Each element corresponding to a particular column and row is a vector. Each element of this vector corresponds to a particular value of  $\varphi_K$  (see 5. above).

We have pre-calculated three sets of tables – `KBHtables00.fits`, `KBHtables50.fits` and `KBHtables99.fits`. All of these tables were computed for an accretion disc near a Kerr black hole with no disc corona present. Therefore, ray-tracing in the vacuum Kerr space-time could be used for calculating the transfer functions. When computing the transfer functions, it was supposed that the matter in the disc rotates on stable circular (free) orbits above the marginally stable orbit. The matter below this orbit is freely falling and has the same energy and angular momentum as the matter which is on the marginally stable orbit.

The observer is placed in the direction  $\varphi = \pi/2$ . The black hole rotates counter-clockwise. All six functions are present in these tables.

Tables are calculated for these values of the black-hole horizon:

- `KBHtables00.fits`: 1.00, 1.05, 1.10, 1.15, ..., 1.90, 1.95, 2.00 (21 elements),
- `KBHtables50.fits`: 1.00, 1.10, 1.20, ..., 1.90, 2.00 (11 elements),
- `KBHtables99.fits`: 1.05 (1 element),

and for these values of the observer’s inclination:

- `KBHtables00.fits`: 0.1, 1, 5, 10, 15, 20, ..., 80, 85, 89 (20 elements),
- `KBHtables50.fits`: 0.1, 1, 10, 20, ..., 80, 89 (11 elements),
- `KBHtables99.fits`: 0.1, 1, 5, 10, 15, 20, ..., 80, 85, 89 (20 elements).

The radii and azimuths at which the functions are evaluated are same for all three tables:

- radii  $r - r_h$  are exponentially increasing from 0 to 999 (150 elements),
- values of the azimuthal angle  $\varphi_K$  are equidistantly spread from 0 to  $2\pi$  radians with a much denser cover “behind” the black hole, i.e., near  $\varphi_K = 1.5\pi$  (because some of the functions are changing heavily in this area for higher inclination angles,  $\theta_o > 70^\circ$ ) (200 elements).

### A3.2 Tables in `KBHlineNN.fits`

Pre-calculated functions  $dF(g) \equiv dg F(g)$  defined in Eq.(16) are stored in FITS files `KBHlineNN.fits`. These functions are used by all axisymmetric models. They are stored as binary extensions and they are parametrised by the value of the observer inclination angle  $\theta_o$  and the horizon of the black hole  $r_h$ . Each extension provides values for different radii, which are given in terms of  $r - r_h$ , and for different  $g$ -factors. Values of the  $g$ -factor, radius  $r - r_h$ , horizon  $r_h$ , and inclination  $\theta_o$ , at which the functions are evaluated, are defined as vectors at the beginning of the FITS file.

The definition of the file `KBHlineNN.fits`:

0. All of the extensions defined below are binary.

(i) The first extension contains one row with three columns that define bins in the  $g$ -factor:

- integer in the first column defines the width of the bins (0 – constant, 1 – exponentially growing),
- real number in the second column defines the lower boundary of the first bin (minimum of the  $g$ -factor),
- real number in the third column defines the upper boundary of the last bin (maximum of the  $g$ -factor).

(ii) The second extension contains a vector of the values of the radius relative to the horizon  $r - r_h$  in  $GM/c^2$ .

(iii) The third extension contains a vector of the horizon values in  $GM/c^2$  ( $1.00 \leq r_h \leq 2.00$ ).

(iv) The fourth extension contains a vector of the values of the observer's inclination angle  $\theta_o$  in degrees ( $0^\circ \leq \theta_o \leq 90^\circ$ ,  $0^\circ$  – axis,  $90^\circ$  – equatorial plane).

(v) All the previous vectors have to have values sorted in an increasing order.

(vi) In the following extensions the functions  $dF(g)$  are defined, each extension is for a particular value of  $r_h$  and  $\theta_o$ . The values of  $r_h$  and  $\theta_o$  are changing with each extension in the same order as in tables in the `KBHtablesNN.fits` file (see the previous section, point 7.). Each extension has one column.

(vii) Each row corresponds to a particular value of  $r - r_h$  (see 2. above).

(viii) Each element corresponding to a particular column and row is a vector. Each element of this vector corresponds to a value of the function for a particular bin in the  $g$ -factor. This bin can be calculated from number of elements of the vector and data from the first extension (see 1. above).

We have pre-calculated several sets of tables for different limb darkening/brightening laws and with different resolutions. All of them were calculated from tables in the files `KBHtables00.fits` (see the previous section for details) and therefore these tables are calculated for the same values of the black-hole horizon and observer's inclination. All of these tables have equidistant bins in the  $g$ -factor which fall in the interval  $(0.001, 1.7)$ . Several sets of tables are available:

– `KBHline00.fits` for isotropic emission, see Eq. (29),

– `KBHline01.fits` for Laor's limb darkening, see Eq. (30),

– `KBHline02.fits` for Haardt's limb brightening, see Eq. (31).

All of these tables have 300 bins in the  $g$ -factor and 500 values of the radius  $r - r_h$  which are exponentially increasing from 0 to 999. We have produced also tables with a lower resolution – `KBHline50.fits`, `KBHline51.fits` and `KBHline52.fits` with 200 bins in the  $g$ -factor and 300 values of the radius.

### A3.3 *Lamp-post tables in lamp.fits*

This file contains pre-calculated values of the functions needed for the lamp-post model. It is supposed that a primary source of emission is placed on the axis at a height  $h$  above the Kerr black hole. The matter in the disc rotates on stable circular (free) orbits above the marginally stable orbit and it is freely falling below this orbit where it has the same energy and angular momentum as the matter which is on the marginally stable orbit. It is assumed that the corona between the source and the disc is optically thin, therefore ray-tracing in the vacuum Kerr space-time could be used for computing the functions.

There are five functions stored in the `lamp.fits` file as binary extensions. They are parametrised by the value of the horizon of the black hole  $r_h$ , and height  $h$ , which are defined as vectors at the beginning of the FITS file. Currently only tables for  $r_h = 1.05$  (i.e.,  $a \doteq 0.9987492$ ) and  $h = 2, 3, 4, 5, 6, 8, 10, 12, 15, 20, 30, 50, 75$  and 100 are available. The functions included are:

- angle of emission in degrees – the angle under which a photon is emitted from a primary source placed at a height  $h$  on the axis above the black hole measured by a local stationary observer ( $0^\circ$  – a photon is emitted downwards,  $180^\circ$  – a photon is emitted upwards),
- radius – the radius in  $GM/c^2$  at which a photon strikes the disc,
- $g$ -factor – the ratio of the energy of a photon hitting the disc to the energy of the same photon when emitted from a primary source,
- cosine of the incident angle – an absolute value of the cosine of the local incident angle between the incident light ray and local disc normal,
- azimuthal incident angle in radians – the angle between the projection of the three-momentum of the incident photon into the disc (in the local rest frame co-moving with the disc) and the radial tetrad vector.

For mathematical formulae defining the functions see eqs. (A33)–(A35) in Appendix A2.

The definition of the file `lamp.fits`:

0. All of the extensions defined below are binary.

(i) The first extension contains a vector of the horizon values in  $GM/c^2$ , though currently only FITS files with tables for one value of the black-hole horizon are accepted ( $1.00 \leq r_h \leq 2.00$ ).

(ii) The second extension contains a vector of the values of heights  $h$  of a primary source in  $GM/c^2$ .

(iii) In the following extensions the functions are defined. Each extension is for a particular value of  $r_h$  and  $h$ . The values of  $r_h$  and  $h$  are changing with each extension in the following order:

$$\begin{aligned}
 & r_h[1] \times h[1], \\
 & r_h[1] \times h[2], \\
 & r_h[1] \times h[3], \\
 & \dots \\
 & r_h[2] \times h[1], \\
 & r_h[2] \times h[2], \\
 & r_h[2] \times h[3],
 \end{aligned}$$

(iv) Each of these extensions has five columns. In each column, a particular function is stored – the angle of emission, radius,  $g$ -factor, cosine of the local incident angle and azimuthal incident angle, respectively. Extensions may have a different number of rows.

#### A3.4 Coefficient of reflection in `fluorescent_line.fits`

Values of the coefficient of reflection  $f(\mu_i, \mu_e)$  for a fluorescent line are stored for different incident and reflection angles in this file. For details on the model of scattering used for computations see [Matt et al., 1991]. It is assumed that the incident radiation is a power law with the photon index  $\Gamma = 1.7$ . The coefficient does not change its angular dependences for other photon indices, only its normalisation changes (see Fig. 14 in [George and Fabian, 1991]). The FITS file consists of three binary extensions:

- the first extension contains absolute values of the cosine of incident angles,
- the second extension contains values of the cosine of reflection angles,

– the third extension contains one column with vector elements, here values of the coefficient of reflection are stored for different incident angles (rows) and for different reflection angles (elements of a vector).

### A3.5 *Tables in refspectra.fits*

The function  $f(E_1; \mu_i, \mu_e)$  which gives dependence of a locally emitted spectrum on the angle of incidence and angle of emission is stored in this FITS file. The emission is induced by a power-law incident radiation. Values of this function were computed by the Monte Carlo simulations of Compton scattering, for details see [Matt et al., 1991]. The reflected radiation depends on the photon index  $\Gamma$  of the incident radiation. There are several binary extensions in this FITS file:

- the first extension contains energy values in keV where the function  $f(E_1; \mu_i, \mu_e)$  is computed, currently the interval from 2 to 300 keV is covered,
- the second extension contains the absolute values of the cosine of the incident angles,
- the third extension contains the values of the cosine of the emission angles,
- the fourth extension contains the values of the photon indices  $\Gamma$  of the incident power law, currently tables for  $\Gamma = 1.5, 1.6, \dots, 2.9$  and 3.0 are computed,
- in the following extensions the function  $f(E_1; \mu_i, \mu_e)$  is defined, each extension is for a particular value of  $\Gamma$ ; here values of the function are stored as a vector for different incident angles (rows) and for different angles of emission (columns), each element of this vector corresponds to a value of the function for a certain value of energy.

## A4 Description of the integration routines

Here we describe the technical details about the integration routines, which act as a common driver performing the ray-tracing for various models of the local emission. The description of non-axisymmetric and axisymmetric versions are both provided. An appropriate choice depends on the form of intrinsic emissivity. Obviously, non-axisymmetric tasks are computationally more demanding.

### A4.1 *Non-axisymmetric integration routine ide*

This subroutine integrates the local emission and local Stokes parameters for (partially) polarised emission of the accretion disc near a rotating (Kerr) black hole (characterised by the angular momentum  $a$ ) for an observer with an inclination angle  $\theta_0$ . The subroutine has to be called with ten parameters:

```
ide(ear, ne, nt, far, qar, uar, var, ide_param, emissivity, ne_loc)
```

*ear* – real array of energy bins (same as *ear* for local models in XSPEC),

*ne* – integer, number of energy bins (same as *ne* for local models in XSPEC),

*nt* – integer, number of grid points in time (*nt* = 1 means stationary model),

*far*(*ne*, *nt*) – real array of photon flux per bin (same as *photar* for local models in XSPEC but with the time resolution),

*qar*(*ne*, *nt*) – real array of the Stokes parameter  $Q$  divided by the energy,

uar(ne, nt) – real array of the Stokes parameter U divided by the energy,  
 var(ne, nt) – real array of the Stokes parameter V divided by the energy,  
 ide\_param – twenty more parameters needed for the integration (explained below),  
 emissivity – name of the external emissivity subroutine, where the local emission of  
 the disc is defined (explained in detail below),  
 ne\_loc – number of points (in energies) where local photon flux (per keV) in the emissivity  
 subroutine is defined.

The description of the ide\_param parameters follows:

ide\_param(1) – a/M – the black-hole angular momentum ( $0 \leq a/M \leq 1$ ),  
 ide\_param(2) – theta\_o – the observer inclination in degrees ( $0^\circ$  – pole,  $90^\circ$  –  
 equatorial plane),  
 ide\_param(3) – rin-rh – the inner edge of the non-zero disc emissivity relative to  
 the black-hole horizon (in  $GM/c^2$ ),  
 ide\_param(4) – ms – determines whether we also integrate emission below the margin-  
 ally stable orbit; if its value is set to zero and the inner radius of the disc is below the  
 marginally stable orbit then the emission below this orbit is taken into account, if set to  
 unity it is not,  
 ide\_param(5) – rout-rh – the outer edge of the non-zero disc emissivity relative to  
 the black-hole horizon (in  $GM/c^2$ ),  
 ide\_param(6) – phi – the position angle of the axial sector of the disc with non-zero  
 emissivity in degrees,  
 ide\_param(7) – dphi – the inner angle of the axial sector of the disc with non-zero  
 emissivity in degrees ( $dphi \leq 360^\circ$ ),  
 ide\_param(8) – nrad – the radial resolution of the grid,  
 ide\_param(9) – division – the switch for the spacing of the radial grid (0 – equidis-  
 tant, 1 – exponential),  
 ide\_param(10) – nphi – the axial resolution of the grid,  
 ide\_param(11) – smooth – the switch for performing simple smoothing (0 – no, 1 –  
 yes),  
 ide\_param(12) – normal – the switch for normalising the final spectrum,  
 if = 0 – total flux is unity (usually used for the line),  
 if > 0 – flux is unity at the energy = normal keV (usually used for the continuum),  
 if < 0 – final spectrum is not normalised,  
 ide\_param(13) – zshift – the overall redshift of the object,  
 ide\_param(14) – ntable – tables to be used, it defines a double digit number NN in  
 the name of the FITS file KBHtablesNN.fits containing the tables ( $0 \leq ntable \leq 99$ ),  
 ide\_param(15) – edivision – the switch for spacing the grid in local energies (0 –  
 equidistant, 1 – exponential),  
 ide\_param(16) – periodic – if set to unity then local emissivity is periodic if set to  
 zero it is not (need not be set if nt = 1),  
 ide\_param(17) – dt – the time step (need not be set if nt = 1),  
 ide\_param(18) – polar – whether the change of the polarisation angle and/or az-  
 imuthal emission angle will be read from FITS tables (0 – no, 1 – yes),  
 ide\_param(19) – r0-rh and

`ide_param(20) - phi0` – in dynamical computations the initial time will be set to the time when photons emitted from the point  $[r_0, \text{phi}0]$  on the disc (in the Boyer–Lindquist coordinates) reach the observer.

The `ide` subroutine needs an external emissivity subroutine in which the local emission and local Stokes parameters are defined. This subroutine has twelve parameters:

```
emissivity(ear_loc, ne_loc, nt, far_loc, qar_loc, uar_loc,
           var_loc, r, phi, cosine, phiphoton, first_emis)
```

`ear_loc(0:ne_loc)` – real array of the local energies where local photon flux `far_loc` is defined, with special meaning of `ear_loc(0)` – if its value is larger than zero then the local emissivity consists of two energy regions where the flux is non-zero; the flux between these regions is zero and `ear_loc(0)` defines the number of points in local energies with the zero local flux,

`ne_loc` – integer, the number of points (in energies) where the local photon flux (per keV) is defined,

`nt` – integer, the number of grid points in time (`nt = 1` means stationary model),

`far_loc(0:ne_loc, nt)` – real array of the local photon flux (per keV) – if the local emissivity consists of two separate non-zero regions (i.e., `ear_loc(0) > 0`) then `far_loc(0, it)` is the index of the last point of the first non-zero local energy region,

`qar_loc(ne_loc, nt)` – real array of the local Stokes parameter Q divided by the local energy,

`uar_loc(ne_loc, nt)` – real array of the local Stokes parameter U divided by the local energy,

`var_loc(ne_loc, nt)` – real array of the local Stokes parameter V divided by the local energy,

`r` – the radius in  $GM/c^2$  where the local photon flux `far_loc` at the local energies `ear_loc` is demanded

`phi` – the azimuth (the Boyer–Lindquist coordinate  $\varphi$ ) where the local photon flux `far_loc` at the local energies `ear_loc` is demanded,

`cosine` – the cosine of the local angle between the emitted ray and local disc normal,

`phiphoton` – the angle between the emitted ray projected onto the plane of the disc (in the local frame of the moving disc) and the radial component of the local tetrad (in radians),

`first_emis` – boolean, TRUE if we enter the emissivity subroutine from the `ide` subroutine for the first time, FALSE if this subroutine was already evaluated during the present run. This distinction is convenient to initialise some variables when calling the emissivity subroutine for the first time (e.g., calculation of the falling spot trajectory can be performed in this place).

#### A4.2 Axisymmetric integration routine `idre`

This subroutine integrates the local axisymmetric emission of an accretion disc near a rotating (Kerr) black hole (characterised by the angular momentum  $a$ ) for an observer with an inclination angle  $\theta_0$ . The subroutine has to be called with eight parameters:

```
idre(ear, ne, photar, idre_param, cmodel, ne_loc, ear_loc, far_loc)
```

`ear` – real array of energy bins (same as `ear` for local models in XSPEC),  
`ne` – integer, the number of energy bins (same as `ne` for local models in XSPEC),  
`photar` – real array of the photon flux per bin (same as `photar` for local models in XSPEC),  
`idre_param` – ten more parameters needed for the integration (explained below),  
`cmodel` – 32-byte string with a base name of a FITS file with tables for axisymmetric emission (e.g., “KBHline” for `KBHlineNN.fits`),  
`ne_loc` – the number of points (in energies) where the local photon flux (per keV) is defined in the emissivity subroutine,  
`ear_loc` – array of the local energies where the local photon flux `far_loc` is defined  
`far_loc` – array of the local photon flux (per keV).

The description of the `idre_param` parameters follows:

`idre_param(1)` – `a/M` – the black-hole angular momentum ( $0 \leq a/M \leq 1$ ),  
`idre_param(2)` – `theta_o` – the observer inclination in degrees ( $0^\circ$  – pole,  $90^\circ$  – equatorial plane),  
`idre_param(3)` – `rin-rh` – the inner edge of the non-zero disc emissivity relative to the black-hole horizon (in  $GM/c^2$ ),  
`idre_param(4)` – `ms` – determines whether we also integrate emission below the marginally stable orbit; if its value is set to zero and the inner radius of the disc is below the marginally stable orbit then the emission below this orbit is taken into account, if set to unity it is not,  
`idre_param(5)` – `rout-rh` – the outer edge of the non-zero disc emissivity relative to the black-hole horizon (in  $GM/c^2$ ),  
`idre_param(6)` – `smooth` – the switch for performing simple smoothing (0 – no, 1 – yes),  
`idre_param(7)` – `normal` – the switch for normalising the final spectrum,  
if = 0 – total flux is unity (usually used for the line),  
if > 0 – flux is unity at the energy = `normal` keV (usually used for the continuum),  
if < 0 – final spectrum is not normalised,  
`idre_param(8)` – `zshift` – the overall redshift of the object,  
`idre_param(9)` – `ntable` – tables to be used, it defines a double digit number NN in the name of the FITS file (e.g., in `KBHlineNN.fits`) containing the tables ( $0 \leq ntable \leq 99$ ),  
`idre_param(10)` – `alpha` – the radial power-law index.

The `idre` subroutine does not need for its operation any external emissivity subroutine.

## REFERENCES

- [Arnaud, 1996] Arnaud, K. A. (1996). XSPEC: The first ten years. In Jacoby, G. and Barnes, J., editors, *Astronomical Data Analysis Software and Systems V*, volume 101 of *ASP Conf. Series*, page 17.
- [Beckwith and Done, 2004] Beckwith, K. and Done, C. (2004). Iron line profiles in strong gravity. *Monthly Notices Roy. Astronom. Soc.*, 352:353.

- [Carter, 1968] Carter, B. (1968). Global structure of the Kerr family of gravitational fields. *Phys. Rev.*, 174:1559.
- [Chandrasekhar, 1960] Chandrasekhar, S. (1960). *Radiative Transfer*. Dover publications, New York.
- [Chandrasekhar, 1992] Chandrasekhar, S. (1992). *The Mathematical Theory of Black Holes*. Oxford University Press, New York.
- [Connors et al., 1980] Connors, P. A., Piran, T., and Stark, R. F. (1980). Polarization features of X-ray radiation emitted near black holes. *Astrophys. J.*, 235:224.
- [Connors and Stark, 1977] Connors, P. A. and Stark, R. F. (1977). Observable gravitational effects on polarised radiation coming from near a black hole. *Nature*, 269:128.
- [Dovčiak, 2004] Dovčiak, M. (2004). Phd thesis, Charles University at Prague, Prague. arXiv: astro-ph/0411605.
- [Dovčiak et al., 2004] Dovčiak, M., Karas, V., and Yaqoob, T. (2004). An extended scheme for fitting X-ray data with accretion disc spectra in the strong gravity regime. *Astrophys. J. Suppl.*, 153:205.
- [Fabian et al., 2000] Fabian, A. C., Iwasawa, K., Reynolds, C. S., and Young, A. J. (2000). Broad iron lines in active galactic nuclei. *Publ. Astronom. Soc. Pacific*, 112:1145.
- [Fanton et al., 1997] Fanton, C., Calvani, M., de Felice, F., and Čadež, A. (1997). Detecting accretion discs in active galactic nuclei. *Publ. Astronom. Soc. Japan*, 49:159.
- [George and Fabian, 1991] George, I. M. and Fabian, A. C. (1991). X-ray reflection from cold matter in active galactic nuclei and X-ray binaries. *Monthly Notices Roy. Astronom. Soc.*, 249:352.
- [Ghisellini et al., 1994] Ghisellini, G., Haardt, F., and Matt, G. (1994). The contribution of the obscuring torus to the X-ray spectrum of Seyfert galaxies – a test for the unification model. *Monthly Notices Roy. Astronom. Soc.*, 267:743.
- [Gierliński et al., 2001] Gierliński, M., Maciolek-Niedźwiecki, A., and Ebisawa, K. (2001). Application of a relativistic accretion disc model to X-ray spectra of LMC X-1 and GRO J1655-40. *Monthly Notices Roy. Astronom. Soc.*, 325:1253.
- [Haardt, 1993] Haardt, F. (1993). Anisotropic Comptonization in thermal plasmas – Spectral distribution in plane-parallel geometry. *Astrophys. J.*, 413:680.
- [Kato et al., 1998] Kato, S., Fukue, J., and Mineshige, S. (1998). Black-hole accretion disks. Kyoto, Japan. Kyoto University Press.
- [Krolik, 1999] Krolik, J. H. (1999). *Active galactic nuclei: from the central black hole to the galactic environment*. Princeton University Press, Princeton.
- [Laor, 1991] Laor, A. (1991). Line profiles from a disc around a rotating black hole. *Astrophys. J.*, 376:90.
- [Laor et al., 1990] Laor, A., Netzer, H., and Piran, T. (1990). Massive thin accretion discs. *Monthly Notices Roy. Astronom. Soc.*, 242:560.
- [Martocchia et al., 2000] Martocchia, A., Karas, V., and Matt, G. (2000). Kerr space-time on spectral features from X-ray illuminated accretion discs. *Monthly Notices Roy. Astronom. Soc.*, 312:817.
- [Matt et al., 1991] Matt, G., Perola, G. C., and Piro, L. (1991). The iron line and high energy bump as X-ray signatures of cold matter in Seyfert 1 galaxies. *Astronomy and Astrophysics*, 247:25.

- [Matt et al., 1992] Matt, G., Perola, G. C., Piro, L., and Stella, L. (1992). Iron K-alpha line from X-ray illuminated relativistic discs. *Astronomy and Astrophysics*, 257:63. Ibid. 1992, 263, 453.
- [Misner et al., 1973] Misner, C. W., Thorne, K. S., and Wheeler, J. A. (1973). *Gravitation*. Freeman, San Francisco.
- [Phillips and Mészáros, 1986] Phillips, K. C. and Mészáros, P. (1986). Polarization and beaming of accretion disc radiation. *Astrophys. J.*, 310:284.
- [Rauch and Blandford, 1994] Rauch, K. P. and Blandford, R. D. (1994). Optical caustics in a Kerr space-time and the origin of rapid X-ray variability in active galactic nuclei. *Astrophys. J.*, 421:46.
- [Reynolds and Nowak, 2003] Reynolds, C. S. and Nowak, M. A. (2003). Fluorescent iron lines as a probe of astrophysical black hole systems. *Phys. Rep.*, 377:389.
- [Schnittman and Bertschinger, 2004] Schnittman, J. D. and Bertschinger, E. (2004). The harmonic structure of high-frequency quasi-periodic oscillations in accreting black holes. *Astrophys. J.*, 606:1098.
- [Walker and Penrose, 1970] Walker, M. and Penrose, R. (1970). On quadratic first integrals of the geodesic equations for type {2,2} spacetimes. *Comm. Math. Phys.*, 18:265.



# Comparison of general relativistic polytropic and adiabatic fluid spheres with a repulsive cosmological constant

Stanislav Hledík, Zdeněk Stuchlík and Kristina Mrázová

*Institute of Physics, Faculty of Philosophy and Science, Silesian University in Opava  
Bezručovo nám. 13, CZ-746 01 Opava, Czech Republic*

## ABSTRACT

Solutions of general relativistic field equations for static, spherically symmetric, equilibrium perfect-fluid configurations obeying the polytropic and adiabatic equation of state in the presence of a repulsive cosmological constant are discussed. The influence of the cosmological constant on the total mass of the configurations, their radius and the profiles of energy density, rest energy density, pressure and metric coefficients is studied and compared for the polytropic and adiabatic case. The static equilibrium configurations are allowed for  $\sigma < \sigma_{\text{crit}}$  ( $\alpha < \alpha_{\text{crit}}$ ), where the critical values  $\sigma_{\text{crit}}$  ( $\alpha_{\text{crit}}$ ) of the relativity parameter  $\sigma(\alpha) \equiv p_c/\rho_c c^2$  of the polytropes (adiabates) depend on the cosmological constant and the polytropic index  $n$  of the equation of state and can be determined by a numerical procedure. The numerical results show that for sufficiently small values of the relativity parameter  $\sigma = \alpha \ll \sigma_{\text{crit}}$ , the polytropic spheres are more compact than the adiabatic ones. Increase of the cosmological constant causes increase of both the radius and mass of the spheres and makes the profiles of the metric coefficients flatter. For large values of the relativity parameter,  $\sigma = \alpha \lesssim \sigma_{\text{crit}}$ , the situation is more complex and depends also on the value of the polytropic parameter  $n$ . The mass of the adiabatic spheres can exceed the mass of the polytropes for  $n \gtrsim 2$ . In the case of  $n = 3$ , the adiabatic spheres can even be more compact than the polytropic ones. Generally, the role of the cosmological constant is suppressed with both  $\sigma = \alpha$  and  $n$  growing.

## 1 INTRODUCTION

Recent observations of the Hubble parameter, dynamical estimates of the present energy density, measurements of the cosmic relict radiation anisotropy, gravitational lensing of quasars statistics, galaxy number counts and high-redshift supernovae suggest that a nonzero (although very small) relict repulsive cosmological constant (or quintessence) must be invoked to explain the dynamics of the Universe (see [Linde, 1990, Krauss and Turner, 1995, Ostriker and Steinhardt, 1995, Krauss, 1998, Bahcall et al., 1999, Caldwell et al., 1998, Armendariz-Picon et al., 2000, Wang et al., 2000]).

The presence of a repulsive, i.e., positive, cosmological constant causes dramatical changes in black-hole backgrounds asymptotics, which become de Sitter, and the cosmologi-

cal event horizon, behind which the geometry is dynamic, appears [Stuchlík and Hledík, 1999, Stuchlík and Hledík, 2002b].

Besides vacuum black-hole (naked-singularity) spacetimes, unusual phenomena can also be expected in non-vacuum spacetimes (representing static mass configurations) with a nonzero cosmological constant.

Simple assumption of polytropic or adiabatic gas enables to obtain basic properties of configurations governed by the relativistic laws in a relatively simple way. Let us recall that the ultrarelativistic (nonrelativistic) degenerate Fermi gas is governed by the adiabatic equation of state with  $\Gamma = 4/3$  ( $\Gamma = 5/3$ ), or in terms of polytropic index  $n = 3$  ( $n = 3/2$ ).

Spherically symmetric equilibrium configurations of perfect fluid obeying the polytropic or adiabatic equation of state in spacetimes with a repulsive cosmological constant were discussed in [Stuchlík and Hledík, 2002a, Hledík et al., 2003], generalizing the well known results of Tooper [Tooper, 1964, Tooper, 1965]. In these papers, the profiles of the energy density, rest energy density, pressure and metric coefficients are given together with the gravitational potential energy and binding energy. Moreover, the spacetime structure of the polytropic and adiabatic spheres are represented by the embedding diagrams of both the ordinary geometry and optical geometry, reflecting some special properties of the geodetical motion [Stuchlík et al., 2000, Hledík, 2002]. Here we present a comparison of the polytropic and adiabatic spheres with common relativistic parameter  $\sigma = \alpha$ , and common polytropic index  $n$ . We compare profiles of the energy density, rest energy density, pressure and temporal and radial metric coefficients of the spacetimes.

## 2 EQUATIONS OF STRUCTURE

In standard Schwarzschild coordinates, the line element for a spherically symmetric, static equilibrium configuration reads

$$ds^2 = -e^{2\Phi} c^2 dt^2 + e^{2\Psi} dr^2 + r^2(d\theta^2 + \sin^2\theta d\phi^2). \quad (1)$$

The matter inside the sphere is described by the perfect-fluid stress-energy tensor

$$T^\mu_\nu = (p + \rho c^2)U^\mu U_\nu + p \delta^\mu_\nu \quad (2)$$

and is assumed to obey either the polytropic equation of state

$$p = K\rho^{1+\frac{1}{n}}, \quad (3)$$

where  $\rho$  and  $p$  denote the total mass-energy density and pressure, respectively, or

$$p = K\rho_g^{1+\frac{1}{n}}, \quad (4)$$

where  $\rho_g$  denotes the rest mass-energy density, being related to the total mass-energy density by [Tooper, 1964, Tooper, 1965]

$$\rho = \rho_g + np/c^2. \quad (5)$$

The polytropic (adiabatic) index  $n$  is assumed to be a given constant, not necessarily an integer,  $K$  is a constant that has to be determined by the thermal characteristics of a given fluid sphere.

The 4-velocity field of the fluid is given by

$$u^i = \frac{dx^i}{d\tau} = 0, \quad i = r, \theta, \phi, \quad u^t = \frac{dt}{d\tau} = e^{-\Phi}. \quad (6)$$

The energy-momentum tensor (2) is related to the spacetime geometry (1) by Einstein's gravitational equations in the standard form

$$G_{\mu\nu} \equiv R_{\mu\nu} - \frac{1}{2}Rg_{\mu\nu} + \Lambda g_{\mu\nu} = \frac{8\pi G}{c^4}T_{\mu\nu} \quad (7)$$

and the law of local energy-momentum conservation is described by

$$T^{\mu\nu}_{;\nu} = 0. \quad (8)$$

It is convenient to express the field equations in terms of the orthonormal tetrad components using 4-vectors carried by the fluid elements:

$$\vec{e}_{(t)} = \frac{1}{e^\Phi} \frac{\partial}{\partial t}, \quad \vec{e}_{(r)} = \frac{1}{e^\Psi} \frac{\partial}{\partial r}, \quad \vec{e}_{(\theta)} = \frac{1}{r} \frac{\partial}{\partial \theta}, \quad \vec{e}_{(\phi)} = \frac{1}{r \sin \theta} \frac{\partial}{\partial \phi}. \quad (9)$$

Projection of the conservation law  $T^{\mu\nu}_{;\nu} = 0$  to the hypersurface orthogonal to the 4-velocity  $u^\mu$  gives the equation of hydrostatic equilibrium in the form

$$(\rho c^2 + p) \frac{d\Phi}{dr} = -\frac{dp}{dr}. \quad (10)$$

There are two relevant structure equations – the  $(t)(t)$  and  $(r)(r)$  tetrad components of the field equations.

The  $(t)(t)$  component reads

$$G_{(t)(t)} = \frac{1}{r^2} - \frac{e^{-2\Psi}}{r^2} - \frac{1}{r} \frac{d}{dr} e^{-2\Psi} - \Lambda = \frac{8\pi G}{c^2} \rho \quad (11)$$

or, equivalently,

$$\frac{d}{dr} \left[ r \left( 1 - e^{-2\Psi} \right) - \frac{1}{3} \Lambda r^3 \right] = \frac{d}{dr} \frac{2G}{c^2} m(r), \quad (12)$$

where

$$m(r) = \int_0^r 4\pi r^2 \rho dr \quad \text{or} \quad \frac{dm(r)}{dr} = 4\pi \rho(r) r^2. \quad (13)$$

Integrating, one obtains [Misner et al., 1973, Stuchlík, 2000]

$$e^{2\Psi} = \left[ 1 - \frac{2Gm(r)}{c^2 r} - \frac{1}{3} \Lambda r^2 \right]^{-1}. \quad (14)$$

The  $(r)(r)$  component reads

$$G_{(r)(r)} = -\frac{1}{r^2} + \frac{e^{-2\Psi}}{r^2} + \frac{2e^{-2\Psi}}{r} \frac{d\Phi}{dr} + \Lambda = \frac{8\pi G}{c^4} p. \quad (15)$$

Using Eq. (14), we arrive to the relation

$$\frac{d\Phi}{dr} = \frac{\frac{G}{c^2} m(r) - \frac{1}{3} \Lambda r^3 + \frac{4\pi G}{c^4} p r^3}{r \left[ r - \frac{2G}{c^2} m(r) - \frac{1}{3} \Lambda r^3 \right]} \quad (16)$$

which enables to convert the equation of hydrostatic equilibrium (10) into the Tolman–Oppenheimer–Volkoff (TOV) form modified for the presence of a nonzero cosmological constant (see, e.g., [Stuchlík, 2000])

$$\frac{dp}{dr} = -(\rho c^2 + p) \frac{\frac{G}{c^2} m(r) - \frac{1}{3} \Lambda r^3 + \frac{4\pi G}{c^4} p r^3}{r \left[ r - \frac{2G}{c^2} m(r) - \frac{1}{3} \Lambda r^3 \right]}. \quad (17)$$

### 3 POLYTROPIC AND ADIABATIC SPHERES

The key equations, namely Eq. (3) for the polytropic case or Eq. (4) for the adiabatic case, together with mass conservation (13) and the equation of hydrostatical equilibrium (17), can conveniently be converted into dimensionless form by introducing appropriate new variables. In the subsequent treatment we have to distinguish the polytropic and adiabatic cases. The polytropic case is considered in detail in [Stuchlík and Hledík, 2002a] (see also [Stuchlík, 2002]). The adiabatic case is discussed in detail in [Hledík et al., 2003]. Here we concentrate our attention on comparison of the profiles for the polytropic and adiabatic spheres.

#### 3.1 The polytropic case

Let us introduce new variable  $\theta$  defined by the relation

$$\rho = \rho_c \theta^n, \quad (18)$$

which implies

$$p = K \rho_c^{1+\frac{1}{n}} \theta^{n+1} = p_c \theta^{n+1}, \quad (19)$$

and the following quantities: relativity parameter

$$\sigma = \frac{K}{c^2} \rho_c^{1/n} = \frac{p_c}{\rho_c c^2}, \quad (20)$$

scale factors

$$\mathcal{L}^* = \left[ \frac{(n+1)K\rho_c^{1/n}}{4\pi G\rho_c} \right]^{1/2} = \left[ \frac{\sigma(n+1)c^2}{4\pi G\rho_c} \right]^{1/2}, \quad (21)$$

$$\mathcal{M}^* = 4\pi \mathcal{L}^{*3} \rho_c = \frac{c^2}{G} \sigma(n+1) \mathcal{L}^* \quad (22)$$

and dimensionless radial coordinate, mass and cosmological parameter

$$\xi = \frac{r}{\mathcal{L}^*}, \quad v(\xi) = \frac{m(r)}{\mathcal{M}^*}, \quad \lambda = \frac{\rho_{\text{vac}}}{\rho_c}. \quad (23)$$

The cosmological constant  $\Lambda$  is related to the vacuum energy by the relation

$$\rho_{\text{vac}} c^2 = \frac{\Lambda c^4}{8\pi G} \quad (24)$$

or, explicitly to the cosmological parameter  $\lambda$ , by

$$\Lambda = \frac{8\pi G}{c^2} \rho_c \lambda, \quad (25)$$

$\rho_c$  and  $p_c$  being the central density and pressure, respectively.

Then the equations of structure can be rewritten in dimensionless form

$$\frac{d\theta}{d\xi} = \frac{\left(\frac{2}{3}\lambda\xi^3 - \sigma\xi^3\theta^{n+1} - v\right)(1 + \sigma\theta)}{\xi^2} g_{rr}(\xi, v; n, \sigma, \lambda), \quad (26)$$

$$\frac{dv}{d\xi} = \xi^2 \theta^n, \quad (27)$$

$$(28)$$

where the radial metric coefficient is given by

$$g_{rr}(\xi, v; n, \sigma, \lambda) \equiv \frac{1}{1 - 2\sigma(n+1)\left(\frac{v}{\xi} + \frac{1}{3}\lambda\xi^2\right)}. \quad (29)$$

The temporal metric coefficient for the polytropic case in the presence of a nonzero cosmological constant can be derived in analogous way as in [Tooper, 1964]

$$-g_{tt} = e^{2\Phi} = (1 + \sigma\theta)^{-2(n+1)} \left\{ 1 - 2\sigma(n+1) \left[ \frac{v(\xi_1)}{\xi_1} + \frac{1}{3}\lambda\xi_1^2 \right] \right\}. \quad (30)$$

### 3.2 The adiabatic case

Let us introduce new variable  $\theta$  defined as

$$\rho_g = \rho_{gc} \theta^n, \quad (31)$$

which implies

$$p = K \rho_{gc}^{1+\frac{1}{n}} \theta^{n+1} = p_c \theta^{n+1}, \quad (32)$$

and the following quantities: relativity parameter

$$\alpha = \frac{K}{c^2} \rho_{gc}^{1/n} = \frac{p_c}{\rho_{gc} c^2}, \quad (33)$$

scale factors

$$\mathcal{L}^* = \left[ \frac{(n+1)K\rho_{gc}^{1/n}}{4\pi G\rho_{gc}} \right]^{1/2} = \left[ \frac{\alpha(n+1)c^2}{4\pi G\rho_{gc}} \right]^{1/2}, \quad (34)$$

$$\mathcal{M}^* = 4\pi \mathcal{L}^{*3} \rho_{gc} = \frac{c^2}{G} \alpha(n+1) \mathcal{L}^* \quad (35)$$

and dimensionless radial coordinate, mass and cosmological parameter

$$\xi = \frac{r}{\mathcal{L}^*}, \quad v(\xi) = \frac{m(r)}{\mathcal{M}^*}, \quad \lambda = \frac{\rho_{vac}}{\rho_c}. \quad (36)$$

The cosmological constant  $\Lambda$  is related to the vacuum energy by the relation (24), or, explicitly to the cosmological parameter  $\lambda$ , by

$$\Lambda = \frac{8\pi G}{c^2} \rho_{\text{gc}} \lambda, \quad (37)$$

$\rho_{\text{gc}}$  being the central rest-energy density.

Then the equations of structure can be rewritten in dimensionless form

$$\frac{d\theta}{d\xi} = \frac{\left(\frac{2}{3}\lambda\xi^3 - \sigma\xi^3\theta^{n+1} - v\right) [1 + \alpha(n+1)\theta]}{\xi^2} g_{rr}(\xi, v; n, \alpha, \lambda), \quad (38)$$

$$\frac{dv}{d\xi} = \xi^2 \theta^n (1 + n\alpha\theta), \quad (39)$$

$$(40)$$

where the radial metric coefficient is given by

$$g_{rr}(\xi, v; n, \alpha, \lambda) \equiv \frac{1}{1 - 2\alpha(n+1) \left(\frac{v}{\xi} + \frac{1}{3}\lambda\xi^2\right)} \quad (41)$$

The temporal metric coefficient for the adiabatic case is given by the relation (see [Tooper, 1965])

$$-g_{tt} = e^{2\Phi} = [1 + \alpha(n+1)\theta]^{-2} \left\{ 1 - 2\alpha(n+1) \left[ \frac{v(\xi_1)}{\xi_1} + \frac{1}{3}\lambda\xi_1^2 \right] \right\}. \quad (42)$$

### 3.3 Boundary conditions and method of solution

Both the systems of two ODE's (26), (27) for the polytropic case and (38), (39) for the adiabatic case are subject to solution under the initial conditions:

$$\theta(0) = 1, \quad v(0) = 0. \quad (43)$$

It apparently follows from (27), (43) or (38), (39) that  $v(\xi) \propto \xi^3$  for  $\xi \rightarrow 0$  and, according to Eq. (26),

$$\lim_{\xi \rightarrow 0^+} \frac{d\theta}{d\xi} = 0. \quad (44)$$

Thus, for  $\xi = 0$ , the right-hand side of the equation (26) or (38) must be defined as zero by virtue of numerical solution.

The boundary of the fluid sphere ( $r = R$ ) is represented by the first zero point of  $\theta(\xi)$ , say at  $\xi_1$ :

$$\theta(\xi_1) = 0, \quad \theta(\xi) > 0 \quad \text{for} \quad 0 \leq \xi < \xi_1. \quad (45)$$

In the Newtonian limit ( $\sigma \ll 1$ ), for both the polytropic and adiabatic spheres, the structure equations can be transformed to one equation of second order

$$\frac{1}{\xi^2} \frac{d}{d\xi} \left( \xi^2 \frac{d\theta}{d\xi} \right) + \theta^n - 2\lambda = 0 \quad (46)$$

that is reduced to the well known Lane–Emden equation, if the cosmological term disappears.

The systems of ordinary differential equations (26), (27) and (38), (39) were integrated numerically using the Bulirsch–Stoer method. The solutions were started at the initial values (43) and proceeded forward until negative value of  $\theta$  is found. (Although negative value is unphysical, after redefining the power function  $x^n \equiv -|x|^n$  for negative  $x$ , it has a good mathematical sense.) This requires first estimate of the zero point (45), which can be adaptively decreased (increased) by the code developed if the estimate is overshoot (undershot). This procedure is repeated until the very last calculated point has  $\theta < 0$ . Then the last four points (the first three of them with positive  $\theta$ ) are interpolated by a cubic polynomial and the zero point (45) is established.

#### 4 RELEVANCE OF THE REPULSIVE COSMOLOGICAL CONSTANT IN THE NUMERICAL RESULTS

We shall concentrate on the influence of the repulsive cosmological constant on the structure of both the polytropic and adiabatic fluid spheres, and on the comparison with the  $\Lambda = 0$  case.

Numerical analysis reveals some interesting phenomena connected to the solutions of the systems (26), (27) and (38), (39). Fixing the polytropic (adiabatic) index  $n \leq 3$  and the relativity parameter  $\sigma$  or  $\alpha$ , the boundary of the fluid sphere exists only if the cosmological parameter  $\lambda$  does not exceed critical value  $\lambda_{\text{crit}}$ . If  $\lambda > \lambda_{\text{crit}}$  holds, the quantity  $\theta$  only drops to its minimum at certain  $\xi$  and starts to increase behind this point, i.e., there is no static, spatially limited equilibrium configuration.

The behaviour of the critical value of the cosmological constant for the polytropic case is shown in Fig. 1. With  $\lambda$  and  $n$  being fixed, the relativity parameter  $\sigma$  (or  $\alpha$ ) has to be limited. It follows from Fig. 1 that there can be more than one critical value of  $\sigma_{\text{crit}}$  ( $\alpha_{\text{crit}}$ ).

Numerical results for the profiles of both the metric coefficients, distribution of total mass-energy density (relative to the central one), distribution of rest mass-energy density (relative to the total mass-energy density at the centre), distribution of the pressure (relative to the central one), and the dimensionless mass  $m(r)/\mathcal{M}^*$  are graphically represented for five values of  $n = 1.0(0.5)3.0$ . For each value of  $n$ , four plots are constructed: the first pair of plots having small common value of relativity parameters,  $\sigma = \alpha = 0.1$ , the second pair of plots having the common value of relativity parameters  $\sigma = \alpha$  equal or slightly below  $n/(n + 1)$ , which corresponds to sound speed equal to  $c$  in the polytropic case (see [Tooper, 1964, Tooper, 1965]). Each pair of plots with common  $n$  and  $\sigma = \alpha$  consists of the plot for zero cosmological constant and the plot with  $\lambda$  slightly below the smaller of the polytropic and adiabatic critical  $\lambda$  to ensure the existence of the surface for both polytropic and adiabatic cases.

Although the normalised mass-energy density distribution  $\rho/\rho_c$  is natively  $\theta^n$  for the polytropic case, it should be emphasised that, due to (31), there is different formula in the adiabatic case, namely (see [Tooper, 1965])

$$\frac{\rho}{\rho_c} = \frac{\theta^n(1 + n\alpha\theta)}{1 + n\alpha}. \quad (47)$$

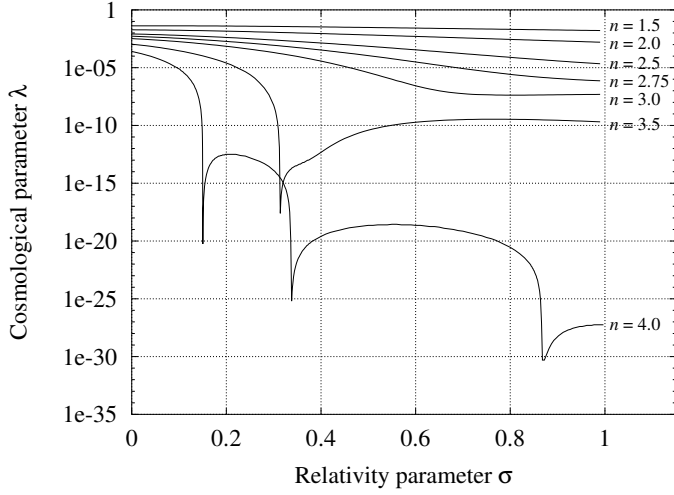


**Figure 1.** Dependence of  $\lambda_{\text{crit}}$  on  $\sigma$  for selected values of polytropic index  $n$ .

At the centre, where  $\theta = 1$ , both expressions (18) and (47) coincide.

Moreover, the distribution of rest mass-energy density relative to the total mass-energy density at the centre may be written as

$$\frac{\rho_g}{\rho_c} = \left( \frac{\theta}{1 + \sigma\theta} \right)^n \quad (48)$$

in the polytropic case (see [Tooper, 1964]), and as

$$\frac{\rho_g}{\rho_c} = \frac{\theta^n}{1 + n\alpha} \quad (49)$$

in the adiabatic case (see [Tooper, 1964]).

There is another subtle point concerning the plots. Even if we put the polytropic index and the relativity parameter for the polytropic case equal to the corresponding quantities for the adiabatic case, one may easily find out that the scale factors (21) and (34) differ, which subsequently leads to different values of dimensionless radius  $\xi$  for the same Schwarzschildian radius  $r$ . Since we intend to compare the Schwarzschildian radius  $r$ , let us rescale the adiabatic dimensionless radius as follows (we provide subscripts “p” and “a” to distinguish both cases):

$$\xi_a = \frac{r}{\mathcal{L}_a^*} = \frac{r}{\mathcal{L}_p^*} \frac{\mathcal{L}_p^*}{\mathcal{L}_a^*} = \xi_p \frac{\mathcal{L}_p^*}{\mathcal{L}_a^*} = k\xi_p, \quad (50)$$

where

$$k = \sqrt{\left( \frac{\rho_{gc}}{\rho_c} \right)_a} \quad (51)$$

(the subscript “a” emphasises the quantities in the fraction must be taken for adiabatic case). Substituting Eq. (49) with  $\theta = 0$  yields the final expression for the coefficient  $k$

$$k = \frac{1}{\sqrt{1+n\alpha}}. \quad (52)$$

The dimensionless radial coordinate corresponding to the same radius  $r$  is generally smaller for the adiabatic case. For this reason, the values of  $\xi$  corresponding to quantities related to the adiabatic case must be multiplied by

$$\kappa = k^{-1} = \sqrt{1+n\alpha} \quad (53)$$

to enable direct comparison. Because the mass scale factor  $\mathcal{M}^*$  can be written in the rightmost shape of (21) and (34), the same considerations may be applied to the values of  $m(r)/\mathcal{M}^*$ .

## 5 DISCUSSION AND CONCLUSIONS

We compare the properties of the polytropic and adiabatic spheres and discuss the influence of the repulsive cosmological constant on their structure profiles. We shall separate the discussion according the fixed values of the polytropic index. The values of the index are chosen in such a way that provides insight into physically interesting equations of state, i.e., we consider  $n = 1, 1.5, 2, 2.5, 3$ . Recall that  $n = 3$  ( $3/2$ ) corresponds to the adiabatic equation of state for ultrarelativistic (nonrelativistic) Fermi degenerate gas.

### 5.1 Case $n = 1$

The polytropic spheres have bigger mass and smaller radius than the adiabatic ones. The difference grows with both the relativistic parameter  $\sigma = \alpha$  and the cosmological parameter  $\lambda$  growing. Clearly, in this case the polytropes are more compact than the adiabates. With  $\sigma = \alpha$  growing, the profiles of the metric coefficients become more steeper, while with  $\lambda$  growing they become flatter. Notice that in this special case of  $n = 1$ , the relation  $\rho_{gc}/\rho_c$  is exactly the same for both polytropic and adiabatic spheres with any given  $\sigma = \alpha$  and  $\lambda$  (see Figs 2 and 3).

### 5.2 Case $n = 1.5$

The radius of the polytropic spheres have smaller radius than the adiabatic ones again. The difference is larger than in the case  $n = 1$  and grows with both  $\sigma = \alpha$  and  $\lambda$  growing. On the other hand, the total mass of the polytropic spheres is always greater than the mass of the adiabatic ones for small values  $\sigma = \alpha$ , independently of  $\lambda$ , but for large values of  $\sigma = \alpha \sim \sigma_{crit}$  the total mass becomes comparable; for  $\lambda$  large enough the adiabates can be even more massive (but not more compact) than the adiabates (see Figs 4 and 5).

The profiles of metric coefficients, energy density and pressure have the same properties as in the case  $n = 1$ .

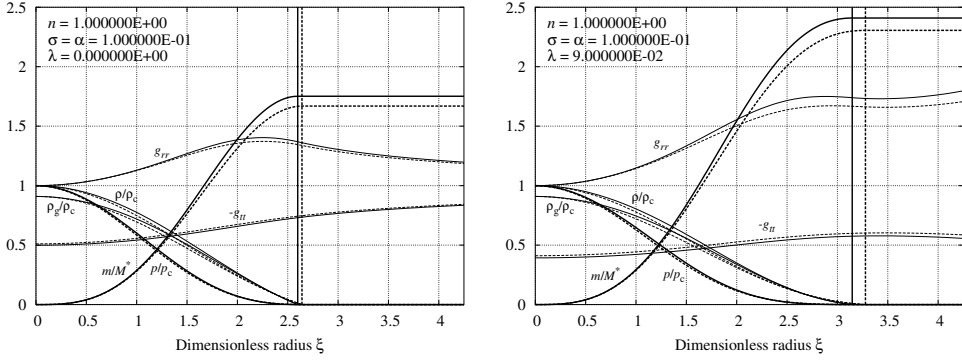


**Figure 2.** Profiles of metric coefficients, distribution of total mass-energy density, rest mass-energy density, pressure, and mass  $m(r)$  for polytropic index  $n = 1.0$  and common relativity parameter  $\sigma = \alpha = 0.1$ . The left plot describes the  $\lambda = 0$  case, the right one corresponds to  $\lambda = 0.09$ . The continuous (dashed) curves correspond to polytropic (adiabatic) case. The curves for pressure, mass and vertical lines marking the sphere boundary are drawn in bold.

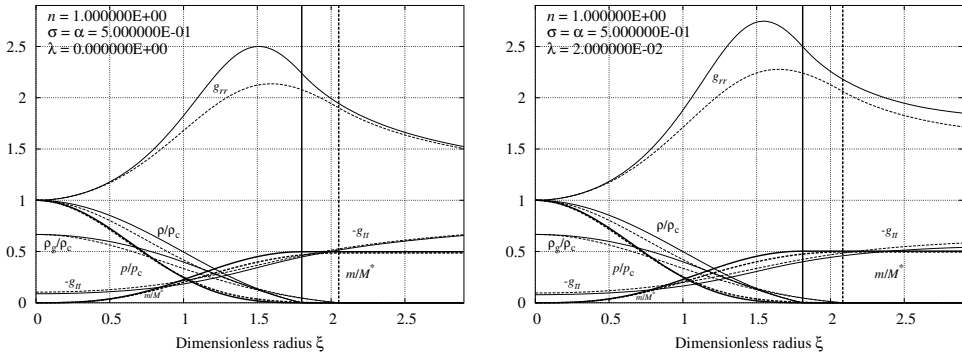


**Figure 3.** Profiles of metric coefficients, distribution of total mass-energy density, rest mass-energy density, pressure, and mass  $m(r)$  for polytropic index  $n = 1.0$  and common relativity parameter  $\sigma = \alpha = 0.5$ . The left plot describes the  $\lambda = 0$  case, the right one corresponds to  $\lambda = 0.02$ . The continuous (dashed) curves correspond to polytropic (adiabatic) case. The curves for pressure, mass and vertical lines marking the sphere boundary are drawn in bold.

### 5.3 Case $n = 2$

We can make the same conclusion as for the case of  $n = 1.5$ . Moreover, the adiabates can be more massive than the polytropes even for  $\lambda = 0$ , if  $\sigma = \alpha$  is large enough (see Figs 6 and 7).

### 5.4 Case $n = 2.5$

In this case we can observe qualitatively the same properties as in the case of  $n = 2$ , however, for large values  $\sigma = \alpha$ , the adiabatic spheres have larger mass than the polytropes almost

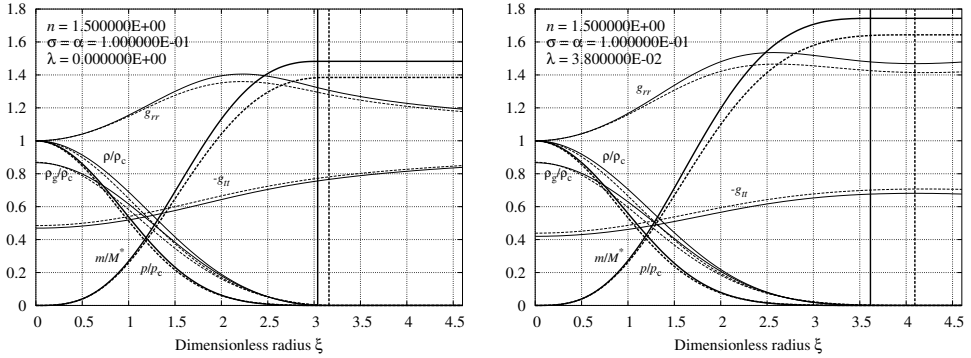


**Figure 4.** Profiles of metric coefficients, distribution of total mass-energy density, rest mass-energy density, pressure, and mass  $m(r)$  for polytropic index  $n = 1.5$  and common relativity parameter  $\sigma = \alpha = 0.1$ . The left plot describes the  $\lambda = 0$  case, the right one corresponds to  $\lambda = 0.038$ . The continuous (dashed) curves correspond to polytropic (adiabatic) case. The curves for pressure, mass and vertical lines marking the sphere boundary are drawn in bold.

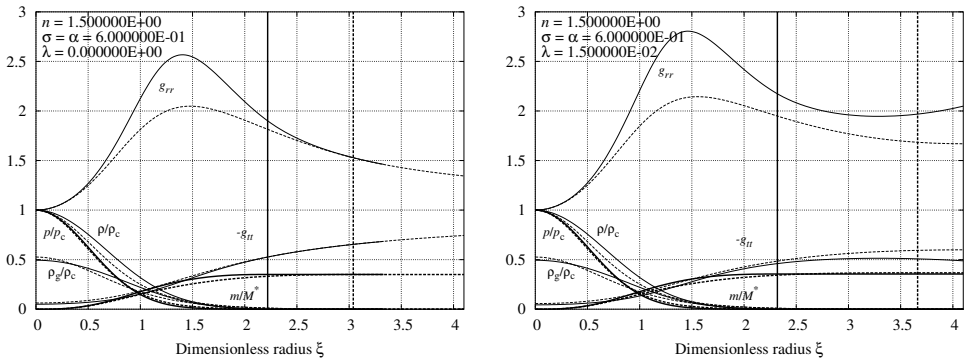


**Figure 5.** Profiles of metric coefficients, distribution of total mass-energy density, rest mass-energy density, pressure, and mass  $m(r)$  for polytropic index  $n = 1.5$  and common relativity parameter  $\sigma = \alpha = 0.6$ . The left plot describes the  $\lambda = 0$  case, the right one corresponds to  $\lambda = 0.015$ . The continuous (dashed) curves correspond to polytropic (adiabatic) case. The curves for pressure, mass and vertical lines marking the sphere boundary are drawn in bold.

independently on  $\lambda$ . The density and pressure profiles become close to a step character, with large values of relative density concentrated nearby the central part (see Figs 8 and 9).

### 5.5 Case $n = 3$

In this case, corresponding to the adiabatic spheres composed of ultrarelativistic Fermi gas, the role of  $\lambda$  is rather suppressed, and the profiles of density and pressure are qualitatively similar to the case  $n = 2, 5$  or  $n = 2$ . However, the adiabatic spheres can be more compact than the polytropes if  $\sigma = \alpha$  is large enough. The step-like character of the density and

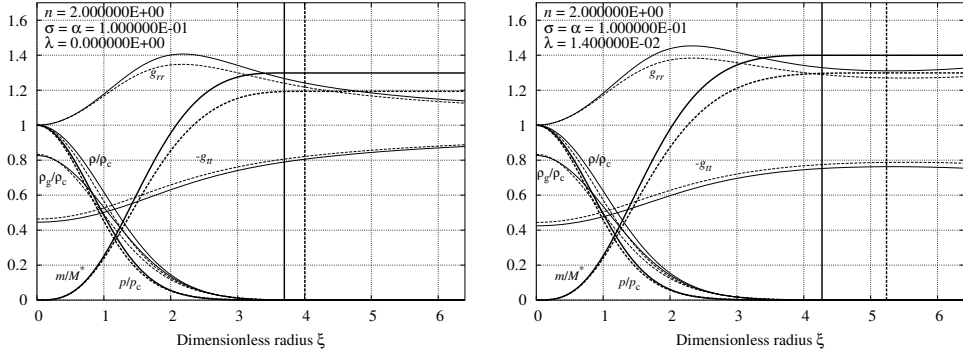


**Figure 6.** Profiles of metric coefficients, distribution of total mass-energy density, rest mass-energy density, pressure, and mass  $m(r)$  for polytropic index  $n = 2.0$  and common relativity parameter  $\sigma = \alpha = 0.1$ . The left plot describes the  $\lambda = 0$  case, the right one corresponds to  $\lambda = 0.014$ . The continuous (dashed) curves correspond to polytropic (adiabatic) case. The curves for pressure, mass and vertical lines marking the sphere boundary are drawn in bold.

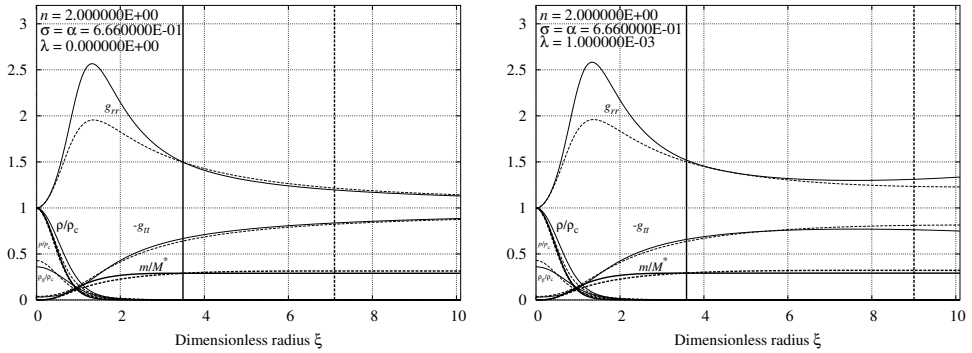


**Figure 7.** Profiles of metric coefficients, distribution of total mass-energy density, rest mass-energy density, pressure, and mass  $m(r)$  for polytropic index  $n = 2.0$  and common relativity parameter  $\sigma = \alpha = 0.666$ . The left plot describes the  $\lambda = 0$  case, the right one corresponds to  $\lambda = 0.001$ . The continuous (dashed) curves correspond to polytropic (adiabatic) case. The curves for pressure, mass and vertical lines marking the sphere boundary are drawn in bold.

pressure profiles is clearly evident (see Figs 10 and 11). In fact, for large values  $\sigma = \alpha$ , the energy density is exponentially in  $\sim 99\%$  of the radius of the equilibrium configuration.

The numerical results show that for sufficiently small values of the relativity parameter  $\sigma = \alpha \ll \sigma_{\text{crit}}$ , the polytropic spheres are more compact than the adiabatic ones. Increase of the cosmological constant causes increase of both the radius and mass of the spheres and makes the profiles of the metric coefficients flatter. For large values of the relativity parameter,  $\sigma = \alpha \lesssim \sigma_{\text{crit}}$ , the situation is more complex and depends also on the value of the polytropic parameter  $n$ . The mass of the adiabatic spheres can exceed the mass of the polytropes for  $n \gtrsim 2$ . In the case of  $n = 3$ , the adiabatic spheres can even be more compact

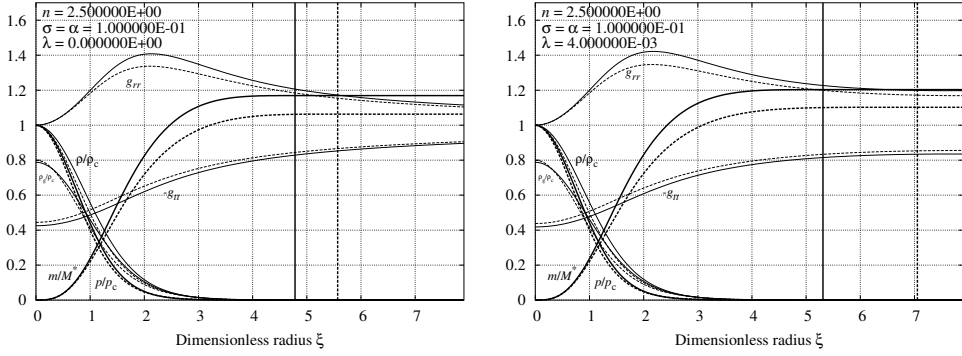


**Figure 8.** Profiles of metric coefficients, distribution of total mass-energy density, rest mass-energy density, pressure, and mass  $m(r)$  for polytropic index  $n = 2.5$  and common relativity parameter  $\sigma = \alpha = 0.1$ . The left plot describes the  $\lambda = 0$  case, the right one corresponds to  $\lambda = 0.004$ . The continuous (dashed) curves correspond to polytropic (adiabatic) case. The curves for pressure, mass and vertical lines marking the sphere boundary are drawn in bold.

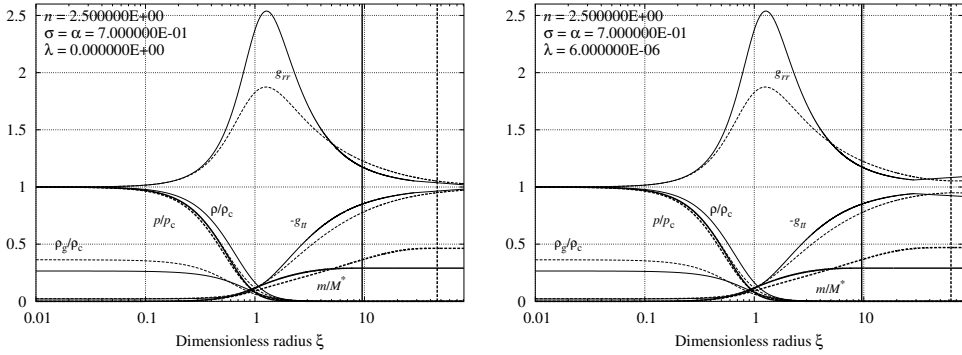


**Figure 9.** Profiles of metric coefficients, distribution of total mass-energy density, rest mass-energy density, pressure, and mass  $m(r)$  for polytropic index  $n = 2.5$  and common relativity parameter  $\sigma = \alpha = 0.7$ . The left plot describes the  $\lambda = 0$  case, the right one corresponds to  $\lambda = 6 \times 10^{-6}$ . The continuous (dashed) curves correspond to polytropic (adiabatic) case. The curves for pressure, mass and vertical lines marking the sphere boundary are drawn in bold.

than the polytropic ones. Generally, the role of the cosmological constant is suppressed with both  $\sigma = \alpha$  and  $n$  growing.

## ACKNOWLEDGEMENTS

The presented work was supported by the grants GAČR No. 205/03/1147 and GAČR No. 205/03/H144. The first two authors (S. H. and Z. S.) would like to thank to the Committee for Collaboration of the Czech Republic with CERN.

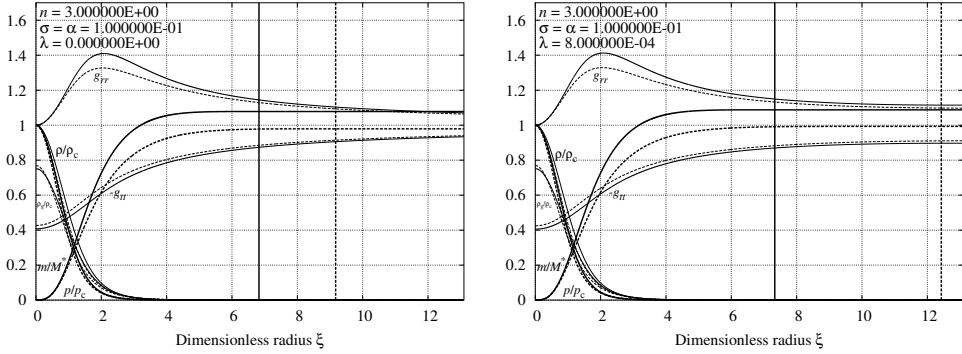


**Figure 10.** Profiles of metric coefficients, distribution of total mass-energy density, rest mass-energy density, pressure, and mass  $m(r)$  for polytropic index  $n = 3.0$  and common relativity parameter  $\sigma = \alpha = 0.1$ . The left plot describes the  $\lambda = 0$  case, the right one corresponds to  $\lambda = 8 \times 10^{-4}$ . The continuous (dashed) curves correspond to polytropic (adiabatic) case. The curves for pressure, mass and vertical lines marking the sphere boundary are drawn in bold.

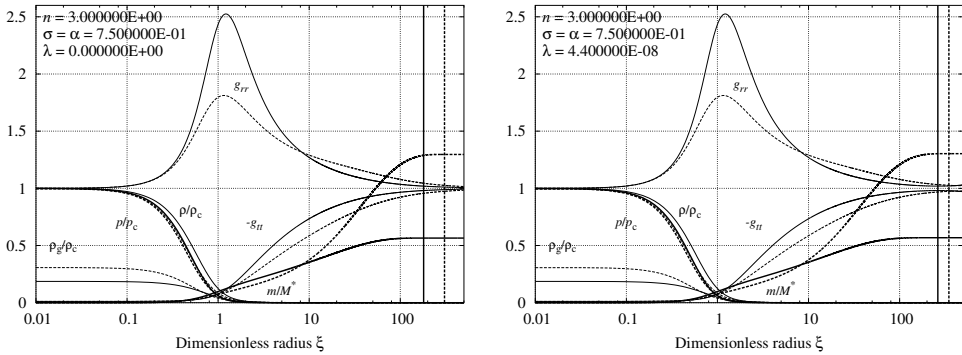


**Figure 11.** Profiles of metric coefficients, distribution of total mass-energy density, rest mass-energy density, pressure, and mass  $m(r)$  for polytropic index  $n = 3.0$  and common relativity parameter  $\sigma = \alpha = 0.75$ . The left plot describes the  $\lambda = 0$  case, the right one corresponds to  $\lambda = 4.4 \times 10^{-8}$ . The continuous (dashed) curves correspond to polytropic (adiabatic) case. The curves for pressure, mass and vertical lines marking the sphere boundary are drawn in bold.

## REFERENCES

- [Armendariz-Picon et al., 2000] Armendariz-Picon, C., Mukhanov, V., and Steinhardt, P. J. (2000). Dynamical solution to the problem of a small cosmological constant and late-time cosmic acceleration. *Phys. Rev. Lett.*, 85(21):4438.
- [Bahcall et al., 1999] Bahcall, N., Ostriker, J. P., Perlmutter, S., and Steinhardt, P. J. (1999). The cosmic triangle: Revealing the state of the universe. *Science*, 284:1481–1488.
- [Caldwell et al., 1998] Caldwell, R. R., Dave, R., and Steinhardt, P. J. (1998). Cosmological imprint of an energy component with general equation of state. *Phys. Rev. Lett.*, 80(8):1582.

- [Hledík, 2002] Hledík, S. (2002). Optical geometry, inertial forces, and embedding diagrams. In [Semerák et al., 2002], pages 161–192.
- [Hledík et al., 2003] Hledík, S., Stuchlík, Z., and Mrázovčá, K. (2003). General relativistic adiabatic fluid spheres with a repulsive cosmological constant. In preparation.
- [Krauss, 1998] Krauss, L. M. (1998). The end of the age problem, and the case for a cosmological constant revisited. *Astrophys. J.*, 501(2):461–466.
- [Krauss and Turner, 1995] Krauss, L. M. and Turner, M. S. (1995). *Gen. Relativity Gravitation*, 27:1137.
- [Linde, 1990] Linde, A. D. (1990). *Particle Physics and Inflationary Cosmology*. Gordon and Breach, New York.
- [Misner et al., 1973] Misner, C. W., Thorne, K. S., and Wheeler, J. A. (1973). *Gravitation*. Freeman, San Francisco.
- [Ostriker and Steinhardt, 1995] Ostriker, J. P. and Steinhardt, P. J. (1995). *Nature*, 377:600.
- [Semerák et al., 2002] Semerák, O., Podolský, J., and Žofka, M., editors (2002). *Gravitation: Following the Prague Inspiration (A Volume in Celebration of the 60th Birthday of Jiří Bičák)*, New Jersey, London, Singapore, Hong Kong. World Scientific.
- [Stuchlík, 2000] Stuchlík, Z. (2000). Spherically symmetric static configurations of uniform density in spacetimes with a non-zero cosmological constant. *Acta Phys. Slovaca*, 50(2):219–228.
- [Stuchlík, 2002] Stuchlík, Z. (2002). The role of a repulsive cosmological constant in astrophysical processes. In [Semerák et al., 2002], pages 27–83.
- [Stuchlík and Hledík, 1999] Stuchlík, Z. and Hledík, S. (1999). Some properties of the Schwarzschild–de Sitter and Schwarzschild–anti-de Sitter spacetimes. *Phys. Rev. D*, 60(4):044006 (15 pages).
- [Stuchlík and Hledík, 2002a] Stuchlík, Z. and Hledík, S. (2002a). General relativistic polytropes with a nonzero cosmological constant. In preparation.
- [Stuchlík and Hledík, 2002b] Stuchlík, Z. and Hledík, S. (2002b). Properties of the Reissner–Nordström spacetimes with a nonzero cosmological constant. *Acta Phys. Slovaca*, 52(5):363–407.
- [Stuchlík et al., 2000] Stuchlík, Z., Hledík, S., and Juráň, J. (2000). Optical reference geometry of Kerr–Newman spacetimes. *Classical Quantum Gravity*, 17(14):2691–2718.
- [Tooper, 1964] Tooper, R. F. (1964). General relativistic polytropic fluid spheres. *Astrophys. J.*, 140(2):434–459.
- [Tooper, 1965] Tooper, R. F. (1965). Adiabatic fluid spheres in general relativity. *Astrophys. J.*, 142(4):1541–1562.
- [Wang et al., 2000] Wang, L., Caldwell, R. R., Ostriker, J. P., and Steinhardt, P. J. (2000). Cosmic concordance and quintessence. *Astrophys. J.*, 530(1):17–35.



# General aspects of nonlinear resonance 3 : 2 in QPO context

Jiří Horák

*Faculty of Mathematics and Physics, Charles University, CZ-180 00 Prague, Czech Republic;  
Astronomical Institute, Academy of Science, Czech Republic*

## ABSTRACT

In the resonant model, quasi periodic oscillations (QPOs) are supposed to be consequence of a nonlinear resonance between modes of oscillations within innermost parts of an accretion disk. Several models with prescribed mode-mode interaction were proposed to examine characteristic properties of the resonance 3 : 2. In this paper I first review some general properties of nonlinear oscillations of the system having quadratic nonlinearity relevant for QPOs. Then I present very simple way how to study internal resonances of fully general system using the method of multiple scales. Finally, I concentrate to conservative systems and discuss their behaviour near the resonance 3 : 2.

## 1 INTRODUCTION

Recent observations made by RXTE discovered very rich phenomenology in light curves of more than 20 neutron stars and several black holes. The most attention is attracted to the two peaks which are often present in the kilohertz part of sources power spectra, because their frequency is comparable to the Keplerian orbital frequency in the innermost parts of an accretion disk.

The two peaks are present simultaneously in power spectra of neutron stars. Their positions vary considerably with time but remains almost linearly correlated. The slope of correlation is somewhat lower than 3 : 2 and is quite independent on the source. Although the frequency ratio does not remain constant, it is often close to 3 : 2 [Abramowicz et al., 2002].

Single QPOs were also reported in several black hole systems. Contrary to neutron stars, two peaks are not observed in the same time rather exceptionally, however in several cases both peaks were detected simultaneously. Their positions are constantly at the same frequencies which are in perfect rational ratio in all sources. This ratio is often 3 : 2, but can be also 5 : 3 [Remillard et al., 2002]. Several black holes exhibits only one QPO which properties are similar to upper peak.

The frequencies of QPO seem to scale with mass of compact object as  $1/M$ . This scaling is apparent between black hole sources, however rescaled frequencies to the one solar mass is also in good agreement with that observed in neutron stars. Since general relativity

effects are subject to the same scaling, kilohertz QPOs can be seen as good probe to strong gravitational fields.

The properties mentioned above found natural explanation in the resonant model which is briefly described in the next section. In section 3 I review general properties of nonlinear oscillations and introduce the method of multiple scales. The possible resonances in the oscillations of very general system having two degrees of freedom are discussed using this method in section 4. In section 4 we examine general properties of the oscillations of conservative systems near the resonance  $3 : 2$ .

## 2 ORBITAL RESONANCE

In the resonant model [Kluźniak and Abramowicz, 2000], a rational frequency ratios of high frequency QPOs can be produced as a result of nonlinear resonances between modes of oscillations within innermost parts of accretion disk (see also [Abramowicz and Kluźniak, 2001, Abramowicz et al., 2004]). Oscillations of the fluid in an accretion disk can be simply modelled by the epicyclic oscillations of test particle about circular orbit in an equatorial plane. Suppose that the particle angular momentum is fixed to a value  $\ell$ . The effective potential  $U_\ell(r, \theta)$  has a minimum at a radius  $r_0$ , corresponding to the location of stable circular orbit. Observer moving along this orbits sees radial, vertical and azimuthal epicyclic oscillations of the particle. Since the angular momentum of the particle is conserved, only two of them – radial and vertical – are independent.

The frequencies of epicyclic oscillations can be derived from the geodesic equations expanded to the linear order in deviations  $\delta r = r - r_0$  and  $\delta\theta = \theta - \pi/2$  from the circular orbit. We get two independent second order differential equations describing two uncoupled oscillators with frequencies  $\omega_r$  and  $\omega_\theta$ , which are given by the second derivatives of effective potential  $U_\ell(r, \theta)$ . In Newtonian theory  $\omega_r$  and  $\omega_\theta$  are equal to the Keplerian orbital frequency  $\Omega_K$ . This is in tune with the fact that orbits of particles are planar and closed curves. The degeneracy between two epicyclic frequencies can be seen as a result of scale-freedom of the Newtonian gravitational potential [Abramowicz and Kluźniak, 2003]. In Schwarzschild geometry this freedom is broken by introduction the gravitational radius  $r_g = 2GM/c^2$ . The degeneracy between the vertical epicyclic and orbital frequency is related to the spherical symmetry of the gravitational potential which assure the planar trajectories of particles. All the three frequencies are different in the vicinity of rotating Kerr black hole. In this case  $\omega_r < \omega_\theta \leq \Omega_K$ , which is a general property of epicyclic motion in Einstein gravity.

The above linear analysis is very useful in discussion of qualitative properties of particle orbits, but it does not provide any information about nonlinear effects such an epicyclic resonance. One should include higher terms than linear into the equations and solve them somehow. In the case of pure geodesic motion the exact equations can be solved analytically, however the solution does not show any resonance [Abramowicz et al., 2003]. It is necessary to include additional small forces of non-gravitational origin (pressure, magnetic field, viscosity, or other) which influence the motion of particles in accretion disk and excite a resonance. The precise determination of these forces require detail study of internal structure of an accretion disc which is beyond the scope of this paper. For the following discussion

it is sufficient to assume that this force has the form of nonlinear coupling between the modes of oscillations and thus that the particle oscillations are governed by the very general system of equations

$$\ddot{\delta r} + \omega_r^2 \delta r = \omega_r^2 f(\delta r, \delta\theta, \dot{\delta r}, \dot{\delta\theta}), \quad (1)$$

$$\ddot{\delta\theta} + \omega_\theta^2 \delta\theta = \omega_\theta^2 g(\delta r, \delta\theta, \dot{\delta r}, \dot{\delta\theta}), \quad (2)$$

where function  $f$  resp.  $g$  contains nonlinear part of geodesic equation and radial resp. vertical components of the non-geodesic forces. The nonlinearity of  $f$  and  $g$  means that the lowest term of their Taylor expansion is quadratic in deviations  $\delta r$ ,  $\delta\theta$  and their derivatives.

### 3 EFFECTS OF NONLINEARITIES

#### 3.1 Expansion method

Expansion method is very useful for solving nonlinear equations. In fact, our equations (1) and (2) cannot be solved exactly for arbitrary large amplitude of oscillations, but we can start with linear analysis and step-by-step include higher order terms. The main advantage of this method is that although the original equation is nonlinear we solve linear equations in each step. Typical procedure is apparent from the following example. Let us consider simple algebraic equation

$$x = 1 + \epsilon x^3, \quad (3)$$

for  $\epsilon \ll 1$ . When  $\epsilon = 0$  we solve linear equation with the solution  $x_0 = 1$ . For nonzero, but small  $\epsilon$  we seek the solution in the form of an expansion

$$x(\epsilon) = x_0 + \epsilon x_1 + \epsilon^2 x_2 + \dots \quad (4)$$

When we substitute (4) into (3) and equate terms of the same power of  $\epsilon$ , we get a system of linear algebraic equations for  $x_n$  which can be solved successively. Since the series converges one can approximate it by a finite number of terms (i.e., for a sufficient approximation one solves finite number of equations).

#### 3.2 Quadratic nonlinearity

The situation is a bit more complicated in case of nonlinear ordinary differential equations. Let us consider the case of small but finite oscillation of a single-degree-of-freedom system with quadratic nonlinearity governed by equation

$$\ddot{x} + \omega^2 x = \alpha \omega^2 x^2. \quad (5)$$

The strength of the nonlinearity is parametrised by the constant  $\alpha$ . When  $\alpha = 0$  one obtain governing equation of the corresponding linear system. We seek a perturbation expansion of the form

$$x(t, \epsilon) = \epsilon x_1(t) + \epsilon^2 x_2(t) + \dots, \quad (6)$$

The expansion parameter  $\epsilon$  express the order of amplitude of oscillations. For a practical purpose it is necessary to require this series to be uniformly convergent for all times of

interest. In that case the higher order terms are small compared to lower order terms and a sufficient approximation is reached concerning finite number of terms in expansion. The expansion (6) can represent periodic solutions as well as unbounded solutions with exponential growth. The uniformity of the expansion means that the higher order approximations are not larger than lower order term itself.

We substitute expansion (6) into governing equation (5) and, since the  $x_k$  are independent of  $\epsilon$ , equate the coefficient of corresponding powers of  $\epsilon$  at both hand-sides. This leads to the following system of equations (up to the third order):

$$\ddot{x}_1 + \omega^2 x_1 = 0, \quad (7)$$

$$\ddot{x}_2 + \omega^2 x_2 = \alpha \omega^2 x_1^2, \quad (8)$$

$$\ddot{x}_3 + \omega^2 x_3 = 2\alpha \omega^2 x_1 x_2. \quad (9)$$

The general solution of (7) can be written in the form  $x_1(t) = Ae^{i\omega t} + cc$ , where  $cc$  denotes complex conjugate. The complex constant  $A$  contains information about initial amplitude and phase of oscillations. Substituting it into (8) we find linear equation for the first approximation  $x_2(t)$

$$\ddot{x}_2 + \omega^2 x_2 = \alpha \left( A^2 e^{2i\omega t} + |A|^2 \right) + cc. \quad (10)$$

A general solutions contains solution of homogeneous equation and one particular solution.

$$x_2(t) = A_2 e^{i\omega t} - \alpha \left( \frac{1}{3} A_1^2 e^{2i\omega t} - |A_1|^2 \right) + cc, \quad (11)$$

where  $A_1$  denotes a constant  $A$  of solution of (7). Therefore the solution of governing equation up to the second order of approximation is given by

$$x(t) = \left( \epsilon A_1 + \epsilon^2 A_2 \right) e^{i\omega t} - \alpha \left( \frac{1}{3} A_1^2 e^{2i\omega t} - |A_1|^2 \right) + cc. \quad (12)$$

In fact, there are two possible ways how to satisfy a general initial conditions  $x(0) = \epsilon x_0$  and  $\dot{x}(0) = \epsilon \dot{x}_0$  imposed on equation (5). One is to compare them with the general solution (12) and find constant  $A_1, A_2$ . This procedure should be repeated in each order of approximation which involves quite complicated algebra especially in higher orders. The second equivalent and apparently much easier way is to include only particular solutions to the higher approximations and treat the constant  $A$  as a function of  $\epsilon$  which expansion is  $A_1 + \epsilon A_2 + \dots$ . Then a given initial condition are satisfied if one expands the solution for  $x_1$  via  $\epsilon$  and choose the coefficients  $A_n$  such that the initial condition is satisfied.

According to this discussion we express the solution of (10) as

$$x_2(t) = -\alpha \left( \frac{1}{3} A^2 e^{2i\omega t} - |A|^2 \right) + cc. \quad (13)$$

Substituting  $x_1$  and  $x_2$  into (9) we obtain

$$\ddot{x}_3 + \omega^2 x_3 = \frac{2\alpha^2 \omega^2}{3} \left( 5A|A|^2 e^{i\omega t} - A^3 e^{3i\omega t} \right) + cc. \quad (14)$$

Since the right hand-side of this equation contains term  $\propto e^{i\omega t}$  any solution contain secular term proportional to  $t e^{i\omega t}$ , which becomes unbounded as  $t \rightarrow \infty$ . However, this fact has

nothing to do with true physical behaviour of the system for large times. The meaning is rather mathematical. Starting from time when  $(\omega t) \sim 1/(\epsilon\alpha)$ , the higher order approximation  $x_3$ , which contains the secular term, does not provide a small correction to  $x_1$  and  $x_2$  and the expansion (6) becomes singular. The presence of the secular term in the third approximation reflects very general feature of the nonlinear oscillations – dependence of the observed frequency on the actual amplitude. For larger amplitude the actual frequency of oscillations differs from the eigenfrequency  $\omega$  and the higher order terms in the expansion (6) always oscillating with an integer multiples of  $\omega$  must quickly increase as time grows. There are several methods taking into account this amplitude-frequency interaction such Lindstedt–Poincaré method developed in the nineteenth century or the method of multiple scales.

### 3.3 The method of multiple scales

Is it possible to find an expansion representing a solution of equation (5) which is uniformly valid even for larger time then  $\sim \epsilon^{-1}$ ? The answer is yes, if one considers more general form of the expansion than (6). In the method of multiple scales more general dependence of coefficients  $x_i$  on the time is reached by introducing several time scales  $T_\mu$ , instead of one physical time  $t$ . The time scales are introduced as

$$T_\mu \equiv \epsilon^\mu t, \quad \mu = 0, 1, 2, \dots \quad (15)$$

and they are treated as independent. It follows that instead of the single time derivation we have an expansion of partial derivatives with respect to the  $T_\mu$

$$\frac{d}{dt} = D_0 + \epsilon D_1 + \epsilon^2 D_2 + \dots, \quad (16)$$

$$\frac{d^2}{dt^2} = D_0^2 + 2\epsilon D_0 D_1 + \epsilon^2 (D_1^2 + 2D_0 D_2) + \dots, \quad (17)$$

where  $D_\mu = \partial/\partial T_\mu$ .

We assume that the solution can be represented by an expansion having the form

$$x(t, \epsilon) = \epsilon x_1(T_\mu) + \epsilon^2 x_2(T_\mu) + \epsilon^3 x_3(T_\mu) + \dots \quad (18)$$

The number of time scales is the same as the order at which the expansion is truncated. Here we carry out the expansion to the third order and thus first three scales  $T_0$ ,  $T_1$  and  $T_2$  are sufficient.

Substituting (18) and (17) into the governing equation (5) and equating the coefficients of  $\epsilon$ ,  $\epsilon^2$  and  $\epsilon^3$  to zero we obtain

$$(D_0^2 + \omega^2)x_1 = 0, \quad (19)$$

$$(D_0^2 + \omega^2)x_2 = -2D_0 D_1 x_1 + \alpha \omega^2 x_1, \quad (20)$$

$$(D_0^2 + \omega^2)x_3 = -2D_0 D_1 x_2 - D_1^2 x_1 - 2D_0 D_2 x_1 + \alpha \omega^2 x_1 x_2. \quad (21)$$

Note that although these equations are more complicated than (7)–(9), they are still linear and can be solved successively. The solution of the equation (19) is the same as the solution of corresponding linear system, the only difference is that constant  $A$  generally depends on the other scales

$$x_1 = A(T_1, T_2)e^{i\omega T_0} + \text{cc}. \quad (22)$$

Substituting of  $x_1$  to the equation (20) we obtain

$$(D_0^2 + \omega^2)x_2 = -2i\omega(D_1A)e^{i\omega T_0} + \alpha\omega^2 \left( A^2e^{2i\omega T_0} + |A|^2 \right) + \text{cc}. \quad (23)$$

The first term on the right hand-side produce secular term in the second order approximation which cause the non-uniformity of the expansion (18). In case of method of multiple scales these terms can be eliminated by imposing additional conditions<sup>1</sup> on the function  $A(T_\mu)$ . Actually, the reason why the same number of scales as the order of approximation is needed is that we eliminate one secular term and thus specify one additional condition on  $A(T_\mu)$  in each step. The secular term is eliminated if we require  $D_1A = 0$  and thus we assume that  $A$  does not depend on the first time scale. One particular solution of equation (23) is

$$x_2(t) = -\alpha \left( \frac{1}{3}A^2(T_2)e^{2i\omega T_0} - |A(T_2)|^2 \right) + \text{cc}. \quad (24)$$

Using the condition  $D_1A = 0$  the equation (21) takes much simpler form

$$(D_0^2 + \omega^2)x_3 = - \left( 2i\omega D_2A + \frac{10\alpha^2\omega^2}{3}A|A|^2 \right) e^{i\omega T_0} - \frac{2\alpha^2\omega^2}{3}A^3e^{3i\omega T_0} + \text{cc}. \quad (25)$$

The secular term is eliminated if we equal the terms in the bracket to zero

$$2i\omega D_2A + \frac{10\alpha^2\omega^2}{3}A|A|^2 = 0. \quad (26)$$

This second additional condition fully determines (excepting initial conditions) time behaviour of “constant”  $A$ . For this purpose, it is convenient to write it in polar form  $A = \frac{1}{2}\tilde{a}e^{i\phi}$  and then separate real and imaginary parts. We obtain

$$D_2\tilde{a} = 0 \quad \text{and} \quad D_2\phi = -\frac{5\alpha^2}{12}\omega\tilde{a}^2. \quad (27)$$

The solutions of this equations are

$$\tilde{a} = \tilde{a}_0 \quad \text{and} \quad \phi = -\frac{5}{12}\alpha^2\tilde{a}_0^2\omega T_2 + \phi_0, \quad (28)$$

where  $\tilde{a}_0$  and  $\phi_0$  are constants which are determined from the initial condition.

It follows from (22) that  $A(T_2)$  slowly modulate the amplitude and the phase of oscillations. Since  $\tilde{a}$  is constant, the amplitude is constant all the time. Since  $\phi$  depends on  $T_2 = \epsilon^2t$  linearly, also the frequency of the oscillations is constant but not equal to eigenfrequency  $\omega$ .

Substituting (28) and (24) into (18) we obtain solution of (5) up to the second order

$$x(t) = a_0 \cos(\omega^*t + \phi_0) - \frac{\alpha}{6}a_0^2 \cos[2(\omega^*t + \phi_0)] + \frac{\alpha}{2}a_0^2 + \mathcal{O}(a_0^3), \quad (29)$$

where  $a_0 = \epsilon\tilde{a}_0 \ll 1$  and  $\omega^*$  is the observable frequency of oscillation given by

$$\omega^* = \omega \left( 1 - \frac{5\alpha^2}{12}a_0^2 \right). \quad (30)$$

<sup>1</sup> These conditions are sometimes called conditions of solvability or consistency.

### 3.4 Essential properties of nonlinear oscillations

We close this section summarising main properties of nonlinear oscillations. The equation (29) is very helpful for this purpose.

The leading term of the expansion (29) describes oscillations with frequency close to eigenfrequency of the system. Both the amplitude and the frequency are constant in time, but they are not independent (as in case of the linear approximation). The frequency correction given by (30) is proportional to the square of the amplitude. This fact is sometimes called the amplitude-frequency interaction and, as was mention above, it causes the non-uniformity of the expansion (6) (see Fig. 1).

The second term oscillates with double frequency and provide a second-order correction to the leading term. The presence of higher harmonics is another particular feature of nonlinear oscillations and the fact that it has been reported in several sources of QPOs, points to nonlinear nature of this phenomena.

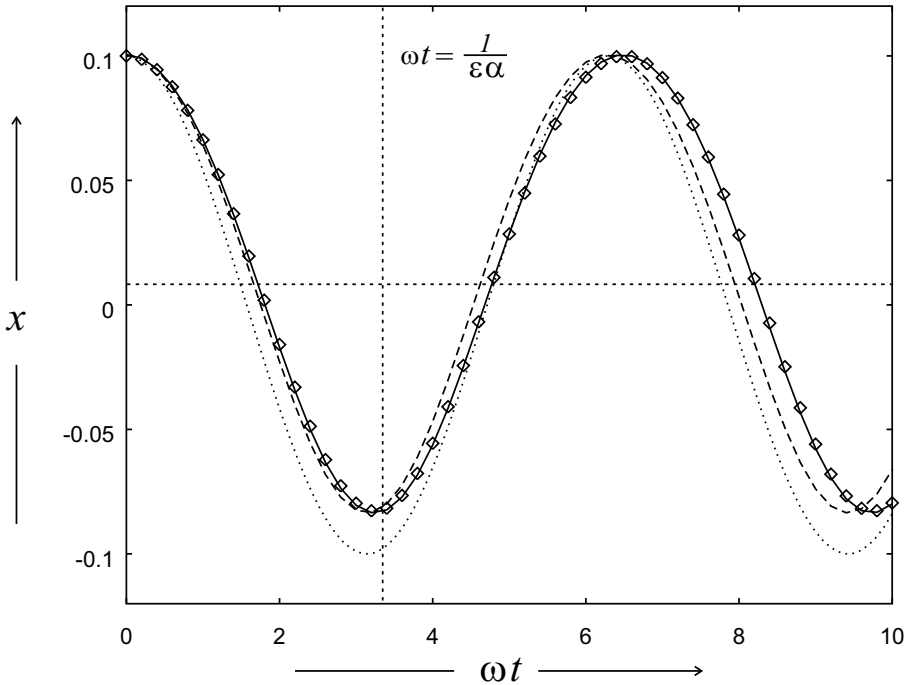


**Figure 1.** Oscillations of the system with quadratic nonlinearity governed by the equation (5). We compare results of the multiple scales method (solid curve), simple straight forward-expansion method (dashed curve) and using a direct numerical integration (points). The initial condition are  $x(0) = 0.1$  and  $\dot{x}(0) = 0$  and the strength of nonlinearity is  $\alpha = 3$ . The horizontal dotted line shows the shifted “equilibrium position” and the vertical one denotes value  $(\omega t) = (\epsilon\alpha)^{-1}$  at which the straight-forward expansion becomes nonuniform. Note the excellent agreement between the multiple scales expansion and the numerical integration. The solution corresponding to the linear system is also shown (dotted curve).

The third term describes constant shift from the equilibrium position and is related to asymmetry of the potential energy about the point  $x = 0$ . In the linear case, this effect miss because the potential depends on  $x^2$ . Hence, the drift or steady-streaming, is the third characteristic feature of nonlinear oscillations.

#### 4 INTERNAL RESONANCES OF CONSERVATIVE SYSTEMS

Let us study nonlinear oscillations of the system having two degree of freedom  $\delta r$  and  $\delta\theta$ . The oscillations are described by two coupled differential equations of the very general form

$$\ddot{\delta r} + \omega_r^2 \delta r = \omega_r^2 f_r(\delta r, \delta\theta, \dot{\delta r}, \dot{\delta\theta}), \quad (31)$$

$$\ddot{\delta\theta} + \omega_\theta^2 \delta\theta = \omega_\theta^2 f_\theta(\delta r, \delta\theta, \dot{\delta r}, \dot{\delta\theta}). \quad (32)$$

Suppose that the functions  $f_r$  and  $f_\theta$  are nonlinear, i.e., their Taylor expansion starts in the second order. Other assumption is that these function are invariant under a reflection of time (i.e., that the Taylor expansion does not contain odd powers of time derivatives of  $r$  and  $\theta$ ). As we see later this assumption is related to the conservation of energy in the system. Many authors studied such systems with a particular form of functions  $f$  and  $g$ , however in this paper we keep discussion fully general.

We seek the solutions of the governing equations in the form of the multiple scales expansions

$$\delta r(t, \epsilon) = \sum_{n=1}^N \epsilon^n r_n(T_\mu), \quad \delta\theta(t, \epsilon) = \sum_{n=1}^N \epsilon^n \theta_n(T_\mu), \quad (33)$$

where  $T_\mu = \epsilon^\mu t$  are independent time scales,  $\mu = 0, 1, 2, N-1$  (we finish this discussion in the fourth order, however it is possible to proceed to higher orders in suggested way). We expand the time derivatives according to (16) and (16) and equate terms of the same order in  $\epsilon$  on the both sides of the governing equations.

In the first order we obtain equations corresponding to the linear approximation

$$(D_0^2 + \omega_r^2)r_1 = 0, \quad (D_0^2 + \omega_\theta^2)\theta_1 = 0. \quad (34)$$

with the solutions

$$x_1 = \widehat{A}_r + \widehat{A}_{-r}, \quad \theta_1 = \widehat{A}_\theta + \widehat{A}_{-\theta}. \quad (35)$$

where we denoted  $\widehat{A}_x = A_x e^{i\omega_x T_0}$  and  $\widehat{A}_{-x} = A_x^* e^{-i\omega_x T_0}$ . The complex functions  $\widehat{A}_x$  generally depends on higher time-scales  $T_1, T_2, T_3, \dots$  and  $x = r, \theta$  respectively (since many considerations are independent of the mode of oscillations we keep this notation through the whole paper).

Having solved the linear approximation, we can proceed to higher orders. The terms proportional to  $\epsilon^2$  in the expanded left-hand side of the governing equation (31) resp. (31) are

$$\left[ \ddot{\delta x} + \omega_x^2 x \right]_2 = (D_0^2 + \omega_x^2)x_2 + 2i\omega_x D_1 \widehat{A}_x - 2i\omega_x D_1 \widehat{A}_{-x}, \quad (36)$$

On the right hand side there are second order terms of the Taylor expansion of the nonlinearity  $f(\delta r, \delta\theta, \dot{\delta r}, \dot{\delta\theta})$ , with  $r_1, \theta_1, D_0 r_1$  and  $D_0 \theta_1$  on the place of  $\delta r, \delta\theta, \dot{\delta r}$  and  $\dot{\delta\theta}$ . Since the derivation  $D_0$  only adds coefficient  $i\omega$  the second-order terms on the right hand-side can be expressed as the linear combination of quadratic terms constructed from  $\widehat{A}_{\pm r}$  and  $\widehat{A}_{\pm\theta}$

$$[f_x(\delta r, \delta\theta, \dot{\delta r}, \dot{\delta\theta})]_2 = \omega_x^2 \sum_{|\alpha|=2} C_\alpha^{(2,x)} \widehat{A}_r^{\alpha_1} \widehat{A}_\theta^{\alpha_2} \widehat{A}_{-r}^{\alpha_3} \widehat{A}_{-\theta}^{\alpha_4}, \quad (37)$$

where  $\alpha = (\alpha_1, \dots, \alpha_4)$  and  $|\alpha| = \alpha_1 + \dots + \alpha_4$ . The constants  $C_\alpha^{(2,x)}$  are combinations of the coefficients of the Taylor expansion and  $\omega_x$ . The coefficients coming from the terms containing time derivatives are generally complex, since each time derivation produce one  $i$ . However, if we suppose that the Taylor expansion does not contain odd powers of time derivatives, all of the constants  $C_\alpha^{(2,x)}$  are real. Equating (36) and (37) we have

$$(D_0^2 + \omega_x^2)x_2 = -2i\omega_x D_1 \widehat{A}_x + 2i\omega_e D_1 \widehat{A}_{-x} + \omega_x^2 \sum_{|\alpha|=2} C_\alpha^{(2,x)} \widehat{A}_r^{\alpha_1} \widehat{A}_\theta^{\alpha_2} \widehat{A}_{-r}^{\alpha_3} \widehat{A}_{-\theta}^{\alpha_4}. \quad (38)$$

The right hand-side of the equation (38) contains one secular term independently of the eigenfrequencies  $\omega_r$  and  $\omega_\theta$ . We call it strictly secular term. However, in some particular cases, additional secular terms appears. For example, when  $\omega_r \approx 2\omega_\theta$  the terms proportional to  $\widehat{A}_\theta^2$  in the radial equation and  $\widehat{A}_r \widehat{A}_{-\theta}$  in the meridional equation becomes nearly secular and they should be included in the solvability conditions. The analogical situation happens when  $\omega_r \approx \omega_\theta/2$ . The solutions in these cases shows qualitatively different behaviour and we speak about *internal* or *parametric resonance*. Possible resonances in the second order of approximation and appropriate solvability conditions are listed in the Table 1. At this moment, let us keep the discussion general and require.

$$D_1 A_x = 0. \quad (39)$$

**Table 1.** Possible resonances and appropriate solvability conditions in the second order of approximation. We substitute constants  $C_\alpha^{(n,x)}$  by  $K$  and  $L$  for simplicity. The first record is related to the case when the system is far from any listed resonance. In this case only strictly secular terms are present. The first resp. second row in the record of each resonance is related to the equation for the radial resp. vertical oscillations. In that case, we list only nearly secular terms in the 2nd column, however strictly secular terms are included in the solvability conditions.

$\omega_\theta : \omega_r$	Secular terms	Solvability condition
any	$D_1 \widehat{A}_r$ $D_1 \widehat{A}_\theta$	$D_1 \widehat{A}_r = 0$ $D_1 \widehat{A}_\theta = 0$
1 : 2	$\widehat{A}_{-r} \widehat{A}_\theta$ $\widehat{A}_r^2$	$-2iD_1 \widehat{A}_r + \omega_r K \widehat{A}_{-r} \widehat{A}_\theta = 0$ $-2iD_1 \widehat{A}_\theta + \omega_\theta L \widehat{A}_r^2 = 0$
2 : 1	$\widehat{A}_\theta^2$ $\widehat{A}_r \widehat{A}_{-\theta}$	$-2iD_1 \widehat{A}_r + \omega_r K \widehat{A}_\theta^2 = 0$ $-2iD_1 \widehat{A}_\theta + L \widehat{A}_r \widehat{A}_{-\theta} = 0$

**Table 2.** Possible resonances in the third order of approximation.

$\omega_\theta : \omega_r$	Secular terms	Solvability condition
	$D_2 \widehat{A}_r,  A_r ^2 \widehat{A}_r,  A_\theta^2  \widehat{A}_r$	$2iD_2 \widehat{A}_r - \omega_r \left[ \kappa_r  A_r ^2 + \kappa_\theta  A_\theta ^2 \right] \widehat{A}_r = 0$
	$D_2 \widehat{A}_\theta,  A_r ^2 \widehat{A}_\theta,  A_\theta^2  \widehat{A}_\theta$	$2iD_2 \widehat{A}_\theta - \omega_\theta \left[ \lambda_r  A_r ^2 + \lambda_\theta  A_\theta ^2 \right] \widehat{A}_\theta = 0$
1 : 3	$\widehat{A}_\theta^3$	$2iD_2 \widehat{A}_r - \omega_r \left[ \kappa_r  A_r ^2 + \kappa_\theta  A_\theta ^2 \right] \widehat{A}_r + \omega_r K \widehat{A}_\theta^3 = 0$
	$\widehat{A}_r \widehat{A}_{-\theta}^2$	$2iD_2 \widehat{A}_\theta - \omega_\theta \left[ \lambda_r  A_r ^2 + \lambda_\theta  A_\theta ^2 \right] \widehat{A}_\theta + \omega_\theta L \widehat{A}_r \widehat{A}_{-\theta}^2 = 0$
1 : 1	$ A_r ^2 \widehat{A}_\theta,  A_\theta ^2 \widehat{A}_\theta,$ $\widehat{A}_r^2 \widehat{A}_{-\theta}, \widehat{A}_{-r} \widehat{A}_\theta^2$	$2iD_2 \widehat{A}_r - \omega_r \left[ \kappa_r  A_r ^2 + \kappa_\theta  A_\theta ^2 \right] \widehat{A}_r + \omega_r (K_1  A_r ^2 \widehat{A}_\theta +$ $+ K_2  A_\theta ^2 \widehat{A}_\theta + K_3 \widehat{A}_r^2 \widehat{A}_{-\theta} + K_4 \widehat{A}_{-r} \widehat{A}_\theta^2) = 0$
	$ A_r ^2 \widehat{A}_r,  A_\theta ^2 \widehat{A}_\theta,$ $\widehat{A}_{-r} \widehat{A}_\theta^2, \widehat{A}_r^2 \widehat{A}_{-\theta}$	$2iD_2 \widehat{A}_\theta - \omega_\theta \left[ \lambda_r  A_r ^2 + \lambda_\theta  A_\theta ^2 \right] \widehat{A}_\theta + \omega_\theta (L_1  A_r ^2 \widehat{A}_r +$ $+ L_2  A_\theta ^2 \widehat{A}_\theta + L_3 \widehat{A}_{-r} \widehat{A}_\theta^2 + L_4 \widehat{A}_r^2 \widehat{A}_{-\theta}) = 0$
3 : 1	$\widehat{A}_{-r}^2 \widehat{A}_\theta$	$2iD_2 \widehat{A}_r - \omega_r \left[ \kappa_r  A_r ^2 + \kappa_\theta  A_\theta ^2 \right] \widehat{A}_r + \omega_r K \widehat{A}_{-r}^2 \widehat{A}_\theta = 0$
	$\widehat{A}_r^3$	$2iD_2 \widehat{A}_\theta - \omega_\theta \left[ \lambda_r  A_r ^2 + \lambda_\theta  A_\theta ^2 \right] \widehat{A}_\theta + \omega_\theta L \widehat{A}_r^3 = 0$

Far from the resonances, the frequencies and the amplitudes are constant and the behaviour of the system is almost same as in the linear approximation. The only difference is the presence of the higher harmonics oscillating with the frequencies  $2\omega_r$ ,  $2\omega_\theta$  and  $|\omega_r \pm \omega_\theta|$ . They are given by a particular solution of equation (38) after elimination of secular term and can be expressed as a linear combination

$$x_2 = \sum_{|\alpha|=2} Q_\alpha^{(2,x)} \widehat{A}_r^{\alpha_1} \widehat{A}_\theta^{\alpha_2} \widehat{A}_{-r}^{\alpha_3} \widehat{A}_{-\theta}^{\alpha_4}. \quad (40)$$

Under the assumption of the invariance under the time reflection, constants  $Q_\alpha^{(2,x)}$  are real and their relation to  $C_\alpha^{(2,x)}$  becomes obvious, if one substitute (40) into (38).

When we proceed to the higher order, the discussion is analogical in many respects. The terms proportional to  $\epsilon^3$  which appear on the left hand-side of the governing equations are given by

$$\left[ \delta \ddot{x} + \omega_x^2 x \right]_3 = (D_0^2 + \omega_x^2) x_3 + 2i\omega_x D_2 \widehat{A}_x - 2i\omega_e D_2 \widehat{A}_{-x}. \quad (41)$$

The terms containing  $D_1 x_1$  and  $D_1 x_2$  vanishes in consequence of the solvability conditions (39). The right hand-side contains cubic terms of the Taylor expansion combined using first-order approximations  $r_1$ ,  $\theta_1$  and quadratic terms combined using one first-order,  $r_1$  or  $\theta_1$ , and one second-order approximation,  $r_2$  or  $\theta_2$ . Since the second order approximation  $x_2$  is given by a linear combination of  $\widehat{A}_{\pm r}$  and  $\widehat{A}_{\pm \theta}$ , the governing equations take the form

$$(D_0^2 + \omega_x^2) x_3 = -2i\omega_x D_2 \widehat{A}_x + 2i\omega_e D_2 \widehat{A}_{-x} + \omega_x^2 \sum_{|\alpha|=3} C_\alpha^{(3,x)} \widehat{A}_r^{\alpha_1} \widehat{A}_\theta^{\alpha_2} \widehat{A}_{-r}^{\alpha_3} \widehat{A}_{-\theta}^{\alpha_4}, \quad (42)$$

where all constants  $C_\alpha^{(3,x)}$  are real. The secular terms together with possible resonances are summarised in the Table 2. Far from any listed resonance we eliminate only strictly secular

terms. Multiplying by  $e^{-i\omega_x t}$ , the solvability conditions take the form

$$D_2 A_r = -\frac{i\omega_r}{2} \left[ \kappa_r |A_r|^2 + \kappa_\theta |A_\theta|^2 \right] A_r, \quad (43)$$

$$D_2 A_\theta = -\frac{i\omega_\theta}{2} \left[ \lambda_r |A_r|^2 + \lambda_\theta |A_\theta|^2 \right] A_\theta, \quad (44)$$

where we denoted  $\kappa_r = C_{2010}^{(3,r)}$ ,  $\kappa_\theta = C_{1101}^{(3,r)}$ ,  $\lambda_r = C_{1110}^{(3,\theta)}$  and  $\lambda_\theta = C_{0201}^{(3,\theta)}$  because of simpler notation. A particular solution of equations (42) is given by linear combination of cubic terms constructed from  $\widehat{A}_{\pm r}$  and  $\widehat{A}_{\pm\theta}$

$$x_3 = \sum_{|\alpha|=3} Q_\alpha^{(3,x)} \widehat{A}_r^{\alpha_1} \widehat{A}_\theta^{\alpha_2} \widehat{A}_{-r}^{\alpha_3} \widehat{A}_{-\theta}^{\alpha_4}, \quad (45)$$

where all coefficients  $Q_\alpha^{(3,x)}$  are real.

The terms proportional to  $\epsilon^4$  in the expanded left hand-side of the equations (31) and (32) are

$$\left[ \delta \ddot{x} + \omega_x^2 x \right]_4 = (D_0^2 + \omega_x^2) x_3 + 2D_3 D_0 x_1 + 2D_0 D_2 x_2, \quad (46)$$

The operator  $D_0 D_2$  acts on  $x_2$  given by (40). The result is found using the solvability conditions (43), (44) and can be written in the form

$$2D_0 D_2 x_2 = \omega_x^2 \sum_{|\alpha|=4} J_\alpha^{(x)} \widehat{A}_r^{\alpha_1} \widehat{A}_\theta^{\alpha_2} \widehat{A}_{-r}^{\alpha_3} \widehat{A}_{-\theta}^{\alpha_4}. \quad (47)$$

where constants  $J_\alpha^{(x)}$  are real because both  $D_0$  and  $D_2$  produce one  $i$ . The right hand-side is expanded in a similar way. We obtain

$$(D_0^2 + \omega_x^2) x_4 = -2i\omega_x D_3 \widehat{A}_x + 2i\omega_e D_3 \widehat{A}_{-x} + \omega_x^2 \sum_{|\alpha|=4} C_\alpha^{(4,x)} \widehat{A}_r^{\alpha_1} \widehat{A}_\theta^{\alpha_2} \widehat{A}_{-r}^{\alpha_3} \widehat{A}_{-\theta}^{\alpha_4}, \quad (48)$$

with real  $C_\alpha^{(4,x)}$ . On the right hand-side there is only one strictly secular term  $-2i\omega_x D_3 \widehat{A}_x$ , the sum contains only terms which becomes nearly secular in case of a resonance. These terms and solvability conditions are listed in the Table 3.

One general feature of a internal resonance  $k : l$  is that  $k\omega_r$  and  $l\omega_\theta$  need not to be infinitesimally close. Consider, for example, resonance 1 : 2. The resonance occurs when  $\omega_\theta \approx 2\omega_r$ . Suppose that the system departs from this exact ratio by small (first-order) deviation  $\omega_\theta = 2\omega_r + \epsilon\sigma$ , where  $\sigma$  is often called detuning parameter. The terms  $\widehat{A}_{-r} \widehat{A}_\theta$  and  $\widehat{A}_r^2$  in the equations (38) remain still secular in  $T_0$  since

$$\widehat{A}_{-r} \widehat{A}_\theta = A_r^* A_\theta e^{i(\omega_\theta - \omega_r)T_0} = A_r^* A_\theta e^{i(\omega_r + \epsilon\sigma)T_0} = A_r^* A_\theta e^{i\sigma T_1} e^{i\omega_r T_0} \quad (49)$$

and analogically for  $\widehat{A}_r^2$ .

Let us study oscillations of the conservative system with eigenfrequencies close to resonance 3 : 2. The time behaviour of frequency and amplitude is given by solvability conditions (39), (43) and (44). In the fourth order we also eliminate terms which become nearly secular. For this purpose let us introduce a detuning parameters  $\sigma_2$  and  $\sigma_3$  according to

$$3\omega_r = 2\omega_\theta + \epsilon^2 \sigma_2 + \epsilon^3 \sigma_3, \quad (50)$$

**Table 3.** Possible resonances in the fourth order of approximation.

$\omega_\theta : \omega_r$	Secular terms	Solvability condition
	$D_3 \widehat{A}_r$	$D_3 \widehat{A}_r = 0$
	$D_3 \widehat{A}_\theta$	$D_3 \widehat{A}_\theta = 0$
1 : 4	$\widehat{A}_\theta^4$ $\widehat{A}_r \widehat{A}_\theta^3$	$2iD_3 \widehat{A}_r - \omega_r K \widehat{A}_\theta^4 = 0$ $2iD_3 \widehat{A}_\theta - \omega_\theta L \widehat{A}_r \widehat{A}_\theta^3 = 0$
2 : 3	$\widehat{A}_r \widehat{A}_{-\theta}^3$ $\widehat{A}_r^2 \widehat{A}_{-\theta}^2$	$2iD_3 \widehat{A}_r - \omega_r K \widehat{A}_r \widehat{A}_{-\theta}^3 = 0$ $2iD_3 \widehat{A}_\theta - \omega_\theta L \widehat{A}_r^2 \widehat{A}_{-\theta}^2 = 0$
3 : 2	$\widehat{A}_{-r}^2 \widehat{A}_\theta^2$ $\widehat{A}_r^3 \widehat{A}_{-\theta}$	$2iD_3 \widehat{A}_r - \omega_r K \widehat{A}_{-r}^2 \widehat{A}_\theta^2 = 0$ $2iD_3 \widehat{A}_\theta - \omega_\theta L \widehat{A}_r^3 \widehat{A}_{-\theta} = 0$
4 : 1	$\widehat{A}_r^3 \widehat{A}_\theta$ $\widehat{A}_r^4$	$2iD_3 \widehat{A}_r - \omega_r K \widehat{A}_r^3 \widehat{A}_\theta$ $2iD_3 \widehat{A}_\theta - \omega_\theta L \widehat{A}_r^4 = 0$

where the term  $\epsilon\sigma_1$  misses because the complex amplitude  $A$  depend on  $T_2$  and  $T_3$ . The secular terms in (48) is eliminated if (see Table 3)

$$2iD_3 A_r - \omega_r \alpha (A_r^2)^* A_\theta^2 e^{-i(\sigma_2 T_2 + \sigma_3 T_3)} = 0, \quad (51)$$

$$2iD_3 A_\theta - \omega_\theta \beta A_r^3 A_\theta^* e^{i(\sigma_2 T_2 + \sigma_3 T_3)} = 0, \quad (52)$$

where  $\alpha$  and  $\beta$  are real constant which depend on properties of the system. Since  $A_r$  and  $A_\theta$  are complex, the conditions (51) and (52) together with (39) and (43) represents 8 real equations. This can be seen, if we substitute polar forms  $A_r = \frac{1}{2} \tilde{a}_r e^{i\phi_r}$  and  $A_\theta = \frac{1}{2} \tilde{a}_\theta e^{i\phi_\theta}$  and separate real and imaginary parts. We obtain

$$D_2 \tilde{a}_r = 0, \quad (53)$$

$$D_2 \tilde{a}_\theta = 0, \quad (54)$$

$$D_2 \phi_r = -\frac{\omega_r}{8} \left[ \kappa_r \tilde{a}_r^2 + \kappa_\theta \tilde{a}_\theta^2 \right], \quad (55)$$

$$D_2 \phi_\theta = -\frac{\omega_\theta}{8} \left[ \lambda_r \tilde{a}_r^2 + \lambda_\theta \tilde{a}_\theta^2 \right], \quad (56)$$

$$D_3 \tilde{a}_r = \frac{\alpha \omega_r}{16} \tilde{a}_r^2 \tilde{a}_\theta^2 \sin(-3\phi_r + 2\phi_\theta - \sigma_2 T_2 - \sigma_3 T_3), \quad (57)$$

$$D_3 \tilde{a}_\theta = \frac{\beta \omega_\theta}{16} \tilde{a}_r^3 \tilde{a}_\theta \sin(3\phi_r - 2\phi_\theta + \sigma_2 T_2 + \sigma_3 T_3), \quad (58)$$

$$D_3 \phi_r = -\frac{\alpha \omega_r}{16} \tilde{a}_r \tilde{a}_\theta^2 \cos(-3\phi_r + 2\phi_\theta - \sigma_2 T_2 - \sigma_3 T_3), \quad (59)$$

$$D_3 \phi_\theta = -\frac{\beta \omega_\theta}{16} \tilde{a}_r^3 \cos(3\phi_r - 2\phi_\theta + \sigma_2 T_2 + \sigma_3 T_3). \quad (60)$$

The amplitudes  $\tilde{a}_r$  and  $\tilde{a}_\theta$  of the oscillations change slowly, because they depend only on  $T_3$ . Phases of oscillations  $\phi_r$  and  $\phi_\theta$  are modified on both time scales  $T_2$  and  $T_3$ . The number of equations can be if we introduce the phase function  $\gamma(T_2, T_3) = 2\phi_\theta - 3\phi_r - \sigma_2 T_2 - \sigma_3 T_3$ .

Then we get

$$D_3 \tilde{a}_r = \frac{\alpha \omega_r}{16} \tilde{a}_r^2 \tilde{a}_\theta^2 \sin \gamma, \quad (61)$$

$$D_3 \tilde{a}_\theta = -\frac{\beta \omega_\theta}{16} \tilde{a}_r^3 \tilde{a}_\theta \sin \gamma, \quad (62)$$

$$D_2 \gamma = -\sigma_2 + \frac{\omega_\theta}{4} (\mu_r \tilde{a}_r^2 + \mu_\theta \tilde{a}_\theta^2), \quad (63)$$

$$D_3 \gamma = -\sigma_3 + \frac{\omega_\theta}{8} \tilde{a}_r (\alpha \tilde{a}_\theta^2 - \beta \tilde{a}_r^2) \cos \gamma, \quad (64)$$

where we used the fact that near the resonance  $\omega_r \approx (2/3)\omega_\theta$  and then we defined  $\mu_r = \kappa_r - \lambda_r$  and  $\mu_\theta = \kappa_\theta - \lambda_\theta$ . The situation can be further simplified if we come back to the one physical time  $t$ . Then equations for evolution of  $\gamma$  are merged using  $d/dt = \epsilon^2 D_2 + \epsilon^3 D_3$  and we obtain

$$\dot{a}_r = \frac{\alpha \omega_r}{16} a_r^2 a_\theta^2 \sin \gamma, \quad (65)$$

$$\dot{a}_\theta = -\frac{\beta \omega_\theta}{16} a_r^3 a_\theta \sin \gamma, \quad (66)$$

$$\dot{\gamma} = -\sigma + \frac{\omega_\theta}{4} \left[ \mu_r a_r^2 + \mu_\theta a_\theta^2 + \frac{a_r}{2} (\alpha a_\theta^2 - \beta a_r^2) \cos \gamma \right], \quad (67)$$

where we defined  $a = \epsilon \tilde{a}$  and  $\sigma = \epsilon^2 \sigma_2 + \epsilon^3 \sigma_3$ .

#### 4.1 The steady-state solutions

For the steady-state solutions amplitudes and frequencies of oscillations remain constant in time. It is obvious from the equations (65) and (66) that, the condition  $\dot{a}_r = \dot{a}_\theta = 0$  can be for nonzero amplitudes satisfied only if  $\sin \gamma = 0$  constantly and thus also  $\dot{\gamma} = 0$ . Under this conditions equation (67) becomes

$$-\frac{\sigma}{\omega_\theta} = \frac{1}{4} \left[ \mu_r a_r^2 + \mu_\theta a_\theta^2 \pm \frac{a_r}{2} (\alpha a_\theta^2 - \beta a_r^2) \right], \quad (68)$$

which is an algebraic equation. The left hand-side can be expressed using the eigenfrequency ratio  $R = \omega_\theta / \omega_r$  as

$$\frac{\sigma}{\omega_\theta} = -\frac{2}{R} \left( R - \frac{3}{2} \right). \quad (69)$$

Then we get

$$R = \frac{3}{2} + \frac{3}{16} (\mu_r a_r^2 + \mu_\theta a_\theta^2) \pm \frac{3}{32} a_r (\alpha a_\theta^2 - \beta a_r^2), \quad (70)$$

where we neglected terms of order  $a^4$ . Note that the lowest correction to eigenfrequencies is of order  $a^2$ . Thus for a given amplitudes  $a_r, a_\theta$  steady state oscillations occur when the ratio of eigenfrequencies departs from  $3/2$  by deviations of order  $a^2$ .

The relation between observed frequencies of oscillations  $\omega_r^*, \omega_\theta^*$  and eigenfrequencies  $\omega_r, \omega_\theta$  are given by the time derivation of phases  $\phi_r$  and  $\phi_\theta$

$$\omega_r^* = \omega_r + \dot{\phi}_r, \quad \omega_\theta^* = \omega_\theta + \dot{\phi}_\theta. \quad (71)$$

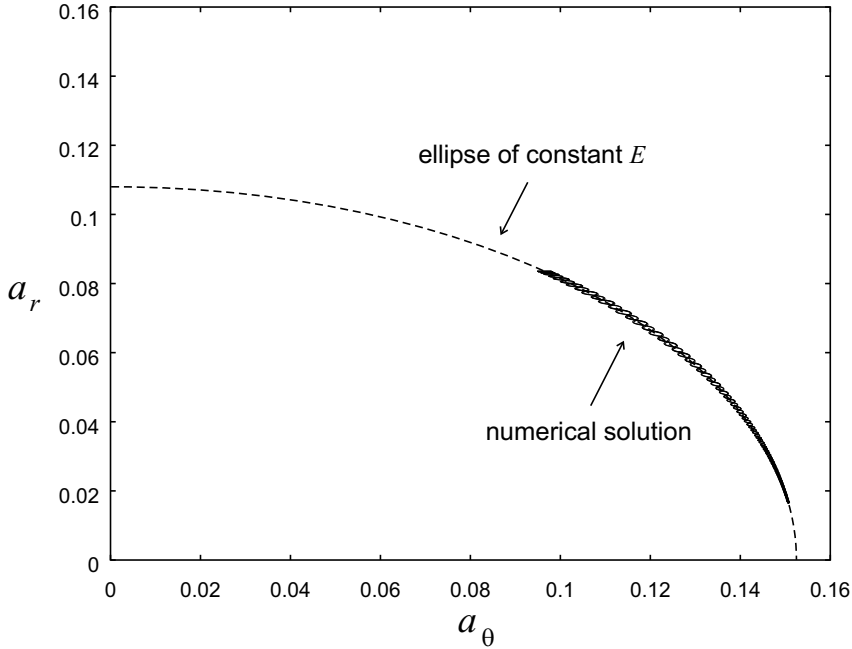


**Figure 2.** Comparison of an analytical constraint on the behaviour of the system studied in [Abramowicz et al., 2003] and the numerical solution. Numerical solution is plotted by the solid curve. Each point of the curve corresponds to the amplitudes of the oscillations in one time. On the other hand, from the discussion of equation (75) we know that these points must lay on a ellipse. This ellipse is plotted by dashed line.

Then we can find simple relation between observed frequencies and the phase function

$$3\omega_r^* - 2\omega_\theta^* = 3\omega_r - 2\omega_\theta + (3\dot{\phi}_r - 2\dot{\phi}_\theta) = \sigma + (3\dot{\phi}_r - 2\dot{\phi}_\theta) = -\dot{\gamma}. \tag{72}$$

For steady state solutions  $\dot{\gamma} = 0$ , and thus observed frequencies are adjusted to exact 3 : 2 ratio even if eigenfrequencies depart from it.

Finally, let us derive explicit relations for  $\omega_r^*$  and  $\omega_\theta^*$  up to to the second order in amplitudes. Using the equations (55) and (56) we obtain

$$\omega_r^* = \omega_r \left[ 1 - \frac{1}{8} (\kappa_r a_r^2 + \kappa_\theta a_\theta^2) \right], \quad \omega_\theta^* = \omega_\theta \left[ 1 - \frac{1}{8} (\lambda_r a_r^2 + \lambda_\theta a_\theta^2) \right]. \tag{73}$$

### 4.2 Integrals of motion

The time-dependent solution is described by three variables  $a_r(t)$ ,  $a_\theta(t)$  and  $\gamma(t)$  and three first-order differential equations (65), (66) and (67). However, the number of differential equations can be reduced to one because it is possible two find two integrals of motion of the system.

Consider equations (65) and (66). Eliminating of  $\sin \gamma$  from both equations we find

$$\frac{d}{dt}(a_r^2 + \nu a_\theta^2) = 0 \quad (74)$$

and thus

$$a_r^2 + \nu a_\theta^2 = \text{const} = E, \quad (75)$$

where we defined

$$\nu = \frac{\alpha \omega_r}{\beta \omega_\theta} \approx \frac{2\alpha}{3\beta}. \quad (76)$$

When  $\nu > 0$ , the both amplitudes of oscillations are bounded. The curve  $[(a_r(t), a_\theta)]$  is a segment of an ellipse. The constant  $E$  is proportional to the energy of the system. On the other hand, when  $\nu < 0$ , one amplitude of oscillations can grows without bounds while the second amplitude vanish. This case correspond to the presence of an regenerative element in the system [Nayev and Mook, 1979]. The corresponding curve in the  $[(a_r(t), a_\theta)]$  plane is hyperbola. In further discussion we assume that  $\nu > 0$ .

In order to verify that the the energy of the system is conserved, I numerically integrated governing equation (31) and (32) for the one particular system discussed in [Abramowicz et al., 2003]. The comparison is in Fig. 2. Note that numerical and analytical results are in very good agreement.

The second integral of motion is found in following way. Let us multiply the equation (67) by  $a_\theta$ . Then we obtain

$$a_\theta \dot{\gamma} = -\sigma a_\theta + \frac{\omega_\theta}{4} \mu_r a_r^2 a_\theta + \frac{\omega_\theta}{4} \mu_\theta a_\theta^3 + \frac{\omega_\theta}{8} \alpha a_r a_\theta^3 \cos \gamma - \frac{\omega_\theta}{8} \beta a_r^3 a_\theta \cos \gamma. \quad (77)$$

Changing the independent variable from  $t$  to  $a_\theta$  and multiplying the whole equation by  $da_\theta$  we find

$$a_r^3 a_\theta^2 d(\cos \gamma) + \frac{8\sigma}{\beta \omega_\theta} d(a_\theta^2) - \frac{4\mu_r}{\beta} a_r^2 a_\theta d(a_\theta^2) - \frac{\mu_\theta}{\beta} d(a_\theta^4) - \frac{2\alpha}{\beta} a_r a_\theta^3 \cos \gamma da_\theta + 2a_r^3 a_\theta \cos \gamma da_\theta = 0. \quad (78)$$

The equation (75) implies

$$a_\theta da_\theta = -\frac{a_r da_r}{\nu}. \quad (79)$$

With aid of this relation the equation (78) takes the form

$$3a_r^2 a_\theta^2 \cos \gamma da_r + 2a_r^3 a_\theta \cos \gamma da_\theta + a_r^3 a_\theta^2 d(\cos \gamma) + \frac{8\sigma}{\beta \omega_\theta} d(a_\theta^2) + \frac{\mu_r}{\beta \nu} d(a_r^4) - \frac{\mu_\theta}{\beta} d(a_\theta^4) = 0. \quad (80)$$

The first three terms express the differential of function  $-a_r^3 a_\theta^2 \cos \gamma$ . Using this the above equation can be arranged to the form

$$d\left(a_r^3 a_\theta^2 \cos \gamma + \frac{8\sigma}{\beta \omega_\theta} a_\theta^2 + \frac{\mu_r}{\beta \nu} a_r^4 - \frac{\mu_\theta}{\beta} a_\theta^4\right) = 0. \quad (81)$$

In other words,

$$a_r^3 a_\theta^2 \cos \gamma + \frac{8\sigma}{\beta \omega_\theta} a_\theta^2 + \frac{\mu_r}{\beta \nu} a_r^4 - \frac{\mu_\theta}{\beta} a_\theta^4 = \text{const} = L \quad (82)$$

is another integral of equations (65)–(67).

### 4.3 Analytical results

Knowing two integral of motion, we should find one differential equation which governs behaviour of the system.

First, the amplitudes  $a_r$  and  $a_\theta$  are not independent because they are related by equation (75). To satisfied this relation manifestly, let us define new variable  $\xi(t)$  by

$$a_r^2 = \xi E, \quad a_\theta^2 = (1 - \xi) \frac{E}{\nu}. \quad (83)$$

The equation describing an evolution of  $\xi(t)$  is derived as follows. Let us multiply the equation (65) by  $2a_r$  and integrate it. Then we obtain

$$\frac{d(a_r^2)}{dt} = \frac{\alpha}{8} \omega_r a_r^3 a_\theta^2 \sin \gamma. \quad (84)$$

Since  $\dot{E} = 0$ , we can change  $a_r^2$  and  $\xi$  and then square it. Then we find

$$\left( \frac{8E}{\alpha \omega_r} \right)^2 \dot{\xi}^2 = \left( a_r^3 a_\theta^2 \sin \gamma \right)^2. \quad (85)$$

The right hand-side of this equation can be expressed using (82)

$$\left( a_r^3 a_\theta^2 \sin \gamma \right)^2 = \left( a_r^3 a_\theta^2 \right)^2 - \left( L - \frac{8\sigma}{\beta \omega_\theta} a_\theta^2 - \frac{\mu_r}{\beta \nu} a_r^4 + \frac{\mu_\theta}{\beta} a_\theta^4 \right)^2. \quad (86)$$

After the substitution into the equation (85) and using the relations (83) and (83) we get

$$\frac{\dot{\xi}^2}{E^3} \left( \frac{8}{\beta \omega_\theta} \right)^2 = (1 - \xi)^2 \xi^3 - \frac{\nu^2}{E^5} \left[ L - \frac{8\sigma E}{\beta \nu \omega_\theta} (1 - \xi) - \frac{\mu_r E^2}{\beta \nu} \xi^2 + \frac{\mu_\theta E^2}{\beta \nu^2} (1 - \xi)^2 \right]^2. \quad (87)$$

The equation of motion has very familiar form.

$$\mathcal{K}^2 \dot{\xi}^2 = F^2(\xi) - G^2(\xi), \quad (88)$$

where the  $\mathcal{K}^2$  is a positive constant,  $F(\xi) = (1 - \xi)\xi^{3/2}$  and  $G(\xi)$  is a quadratic function which coefficients depend on initial condition through  $E$  and  $L$ . For example, the same form has the equation containing an effective potential which governs motion of test particle around the massive body in both Newtonian and Einstein gravity. Therefore the following discussion is same as in that case.

In general, the motion occurs only when  $\dot{\xi}^2$  is positive and thus for  $\xi$  which satisfy  $|F(\xi)| \geq |G(\xi)|$ . The turning points, where  $\dot{\xi}$  changes its signature, are determined by the condition

$$|F(\xi)| = |G(\xi)|. \quad (89)$$

The functions  $\pm F(\xi)$  and  $G(\xi)$  are plotted together in the Fig. 3. Generally, the function  $G$  intersects functions  $\pm F$  in two points which corresponds to  $\xi(t)$  oscillating between two bounds  $\xi_1$  and  $\xi_2$  given by condition (89). That means, the radial and vertical mode of oscillations will periodically exchange the energy. The exchanged energy is given by  $\Delta E/E = \xi_2 - \xi_1$ . However, for some particular values of  $L$  and  $E$  only one intersection of  $\pm F$  and  $G$  can be found. These stationary oscillations correspond to the steady state solutions which were discussed in the previous section.

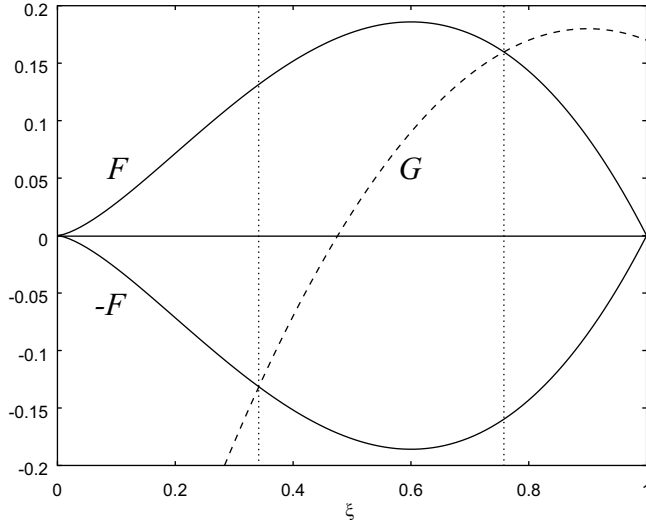


**Figure 3.** The functions  $\pm F(\xi) = \pm(1 - \xi)\xi^{3/2}$  and the quadratic function  $G(\xi)$  which second power is the second term on the right hand-side of the equation (87). The behaviour of the system corresponds to  $\xi$  in the interval  $[\xi_1, \xi_2]$  (denoted by the two dotted vertical lines) where the condition  $|F(\xi)| \geq |G(\xi)|$  is satisfied.

The period of the energy exchange can be find by integration of the equation (87)

$$T = \frac{16}{\beta\omega_\theta} E^{-3/2} \int_{\xi_1}^{\xi_2} \frac{d\xi}{\sqrt{F^2(\xi) - G^2(\xi)}}. \quad (90)$$

The integral on the right hand-side can be estimated in the following way. Since  $P_5 = F^2(\xi) - G^2(\xi)$  is a polynomial of the fifth order in  $\xi$  having two roots  $\xi_1$  and  $\xi_2$  in the interval  $[0, 1]$ , we can write it as  $-(\xi - \xi_1)(\xi - \xi_2)P_3(\xi)$ , where  $P_3(\xi)$  is a polynomial of the third order positive in the interval  $[0, 1]$ . Using the mean-value theorem we get

$$\int_{\xi_1}^{\xi_2} \frac{d\xi}{\sqrt{-(\xi - \xi_1)(\xi - \xi_2)P_3(\xi)}} = \frac{1}{p} \int_{\xi_1}^{\xi_2} \frac{d\xi}{\sqrt{-(\xi - \xi_1)(\xi - \xi_2)}} = \frac{\pi}{p}, \quad (91)$$

where  $p > 0$  is a value of  $P_3$  for some  $\xi$  in the interval  $[\xi_1, \xi_2]$ . Since  $P_5 \sim F^2 \sim 0.01$  and  $(\xi_2 - \xi_1)^2 \sim 0.01$  typically, the values of  $P_3(\xi)$  are of order of 1 and thus  $p \sim 1$ . The period of the energy exchange can be roughly approximated by

$$T \sim \frac{16\pi}{\beta\omega_\theta} E^{-3/2}. \quad (92)$$

However, near the steady state  $(\xi_2 - \xi_1)^2$  is near to zero and the period becomes much longer.

The observed frequencies  $\omega_r^*$  and  $\omega_\theta^*$ , given by relations (73), depend on squares of amplitudes  $a_r$  and  $a_\theta$ . Since the both  $a_r^2$  and  $a_\theta^2$  are parametrised by  $\xi(t)$ , observed frequencies are linear functions of  $\xi$  and are linearly correlated each other. The slope of this correlation

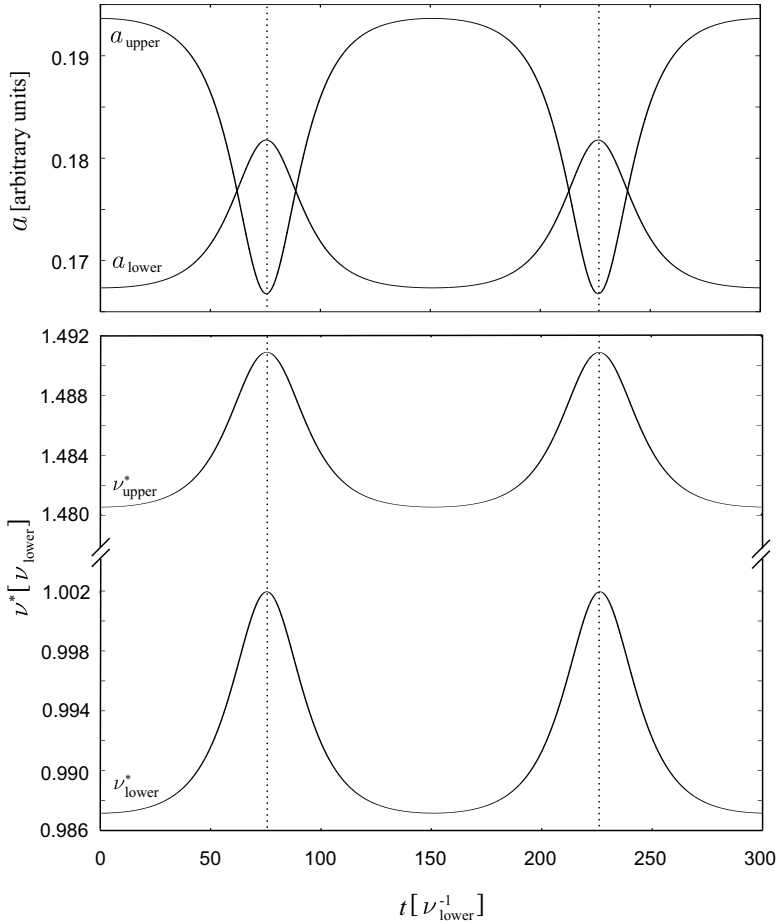


**Figure 4.** Amplitudes and observed frequencies of oscillations versus time in units of one over the lower eigenfrequency. The lower and upper mode corresponds to the radial and vertical oscillations.

$\omega_\theta^* = K \omega_r^* + Q$  is independent of the energy of oscillations and is given only by parameters of the system

$$K = \frac{\omega_\theta \lambda_r \nu - \lambda_\theta}{\omega_r \kappa_r \nu - \kappa_\theta}. \quad (93)$$

The slope of the correlation differs from  $3/2$ , however the observed frequencies are still close to it.

#### 4.4 Numerical results

The equations (65)–(67) were solved numerically using the 5th order Runge–Kutta method with an adaptive step size. One of the solutions is in the Fig. 4. It is in agreement with the

general results obtained analytically in the last section. The top panel of the Fig. 4 shows the time behaviour of the amplitudes of two modes of oscillations. Since energy of the system is constant, amplitudes are anticorrelated and the two modes exchanges some amount of energy. The bottom panel shows observed frequencies which are correlated each other and they are also correlated to one of the amplitudes. The frequency ratio varies with time and it differs from exact  $3/2$ , however it is still very close to it.

## 5 CONCLUSIONS

Although this discussion was originally motivated by observations and models connected to QPO, the results are very general and can be applied to any system with governing equations of the form (31) and (32). Moreover, the solvability conditions, which are derived for all resonances up to the 4th order and summarised in tables 1, 2 and 3, are valid also for nonconservative systems. The only difference is that constants  $C_\alpha^{(n,x)}$  which appears in the multiple scale expansion are generally complex. However, the results discussed in the previous section are derived under the assumption that the system is conservative and thus all the constants  $C_\alpha^{(n,x)}$  are real. In future I plane to include also nonconservative systems into the discussion.

The main result of this calculation is prediction of the low frequency modulation of the amplitudes and frequencies of oscillations. The characteristic timescale is approximately given by equation (92). In separate paper [Horák et al., 2004] we pointed to possible connection of this modulation to the “normal branch oscillations” (NBOs) often observed together with QPOs. Specially, the correlation between higher frequency and lower amplitude apparent from Fig. 4 is the same as was recently seen in SCO X-1 [Yu et al., 2001].

## ACKNOWLEDGEMENT

It is a pleasure to acknowledge the support of my supervisor Vladimír Karas. I also thank Marek Abramowicz, Wlodek Kluźniak, Paola Rebusco, Michal Bursa and Michal Dovčiak for helpful discussion. This work was supported by the GAČR grant 205/03/0902 and GAUK grant 2004.

## REFERENCES

- [Abramowicz et al., 2002] Abramowicz, M. A., Bulik, T., Bursa, M., and Kluźniak, W. (2002). *Astronomy and Astrophysics*, 404:L21–L24.
- [Abramowicz et al., 2003] Abramowicz, M. A., Karas, V., Kluźniak, W., Lee, W. H., and Rebusco, P. (2003). *Publ. Astronom. Soc. Japan*, 55:467.
- [Abramowicz and Kluźniak, 2001] Abramowicz, M. A. and Kluźniak, W. (2001). *Astronomy and Astrophysics Lett.*, 374:L19.
- [Abramowicz and Kluźniak, 2003] Abramowicz, M. A. and Kluźniak, W. (2003). *Gen. Relativity Gravitation*, 35,1,69 18:4725.

- [Abramowicz et al., 2004] Abramowicz, M. A., Kluźniak, W., Stuchlík, Z., and Török, G. (2004). arXiv: astro-ph/0401464.
- [Horák et al., 2004] Horák, J., Abramowicz, M. A., Karas, V., and Kluźniak, W. (2004). In preparation.
- [Kluźniak and Abramowicz, 2000] Kluźniak, W. and Abramowicz, M. A. (2000). *Phys. Rev. Lett. (submitted), Acta Phys. Polon. B*, B32:3605.
- [Nayev and Mook, 1979] Nayev, A. H. and Mook, D. T. (1979). *Nonlinear oscillations*. John Wiley & sons, New York.
- [Remillard et al., 2002] Remillard, R. A., Muno, M. P., McClintock, J. E., and Orosz, J. A. (2002). *Astrophys. J.*, 580:1030.
- [Yu et al., 2001] Yu, W., van der Klis, M., and Jonker, P. G. (2001). *Astrophys. J.*, 559:L29.

# Inertial forces in Kerr–de Sitter spacetimes

Jiří Kovář<sup>1</sup> and Zdeněk Stuchlík<sup>2</sup>

<sup>1</sup>*Department of Physics, Faculty of Science, Palacký University, Olomouc, Czech Republic*

<sup>2</sup>*Institute of Physics, Faculty of Philosophy and Science, Silesian University in Opava  
Bezručovo nám. 13, CZ-746 01 Opava, Czech Republic*

## ABSTRACT

Definition of the inertial forces in the framework of the optical reference geometry is applied to the stationary and axially symmetric Kerr–de Sitter spacetimes. The attention is restricted to the inertial forces acting on particles moving along circular orbits in the equatorial plane of these spacetimes. It is shown, where the gravitational force vanishes, and where the centrifugal force vanishes independently of velocities of test particles. The Coriolis force does not vanish for a non-zero velocity.

## 1 INTRODUCTION

The covariant definition of the inertial forces in the framework of the optical reference geometry was introduced by M. Abramowicz and his co-workers [Abramowicz et al., 1988, Abramowicz et al., 1995, Abramowicz et al., 1993b]. This definition provides a description of relativistic dynamics in accordance with our natural Newtonian intuition. It is its main advantage in comparison with a number of other definitions of inertial forces in the framework of general relativity [Jantzen et al., 1992].

The inertial forces related to the optical reference geometry were extensively exploited in many papers describing properties of black-hole spacetimes [Abramowicz, 1990, Abramowicz and Miller, 1990, Abramowicz et al., 1993a]. Moreover, it has been shown that many important properties of relativistic dynamics in terms of inertial forces can be effectively illustrated by properties of embedding diagrams of the optical reference geometry [Hledík, 2001, Hledík, 2002]. Black-hole spacetimes with a non-zero cosmological constant were treated in terms of the optical reference geometry in the simplest, spherically symmetric cases of the Schwarzschild–de Sitter and Reissner–Nordström–de Sitter spacetimes [Stuchlík and Hledík, 1999b, Stuchlík et al., 2001, Stuchlík and Hledík, 2002]. In the later case, naked-singularity spacetimes appear along with the black-hole spacetimes. Here, we shall consider the Kerr–de Sitter black-hole and naked-singularity spacetimes.

In Section 2, a brief summary of the Abramowicz definition of the gravitational, Coriolis, centrifugal, and Euler forces is given in general stationary spacetimes. In Section 3, we focus on the forces acting on particles stationary moving along circular orbits in equatorial planes of stationary and axially symmetric spacetimes. Basic properties of the forces in the Kerr–de Sitter spacetimes and its limit cases, i.e., in the Kerr spacetimes and Schwarzschild–de Sitter spacetimes are discussed in Section 5. Basic features of the

Kerr–de Sitter spacetimes are summarized in Section 4. In Section 6, some concluding remarks are presented.

## 2 INERTIAL FORCES IN STATIONARY SPACETIMES

### 2.1 Special observers

Let us consider a stationary spacetime described by the metric  $g_{ik}$  (with signature +2) containing a timelike vector field  $n^i$ . We can identify this vector field with 4-velocity field of family of special observers related to the spacetime. Let [Abramowicz et al., 1993b]

$$n^k n_k = -1, \quad n^i \nabla_i n_k = \nabla_k \Phi, \quad (1)$$

where  $\Phi$  is a scalar function called *gravitational potential*. It is useful (but not necessary for the definition of inertial forces) to require that the vector field  $n^i$  satisfies the condition of hypersurface orthogonality

$$n_{[i} \nabla_j n_{k]} = 0. \quad (2)$$

We can find at least two solutions of Eq. (1):  $\Phi = \text{const}$  and  $n^i$  corresponding to the 4-velocity field of free-falling (geodesic) observers is the first solution.  $\Phi = \frac{1}{2} \ln(-\iota^i \iota_i)$  and  $n^i = e^{-\Phi} \iota^i$  corresponding to the 4-velocity of stationary observer is the second one. In the second case,  $n^i$  is the unit vector field parallel to the timelike Killing vector  $\iota^i$ , which exists due to the spacetime stationarity ( $e^\Phi$  is the norm coefficient). The equation

$$n^i \nabla_i \Phi = 0, \quad (3)$$

following from (1), suggests that the special observers with 4-velocity  $n^i$  observe no change in the gravitational potential as their proper time passes. It means the observers are fixed with respect to the *gravitational field*. The local instantaneous 3-dimensional space of the observer, which is orthogonal to  $n^i$ , is described by the metric

$$h_{ik} = g_{ik} + n_i n_k, \quad (4)$$

the so-called *directly projected geometry*. It is useful to define the conformally adjusted metric of the spacetime

$$\tilde{g}_{ik} = e^{-2\Phi} g_{ik} \quad (5)$$

and the conformally adjusted metric of the directly projected geometry

$$\tilde{h}_{ik} = e^{-2\Phi} h_{ik}, \quad (6)$$

the so-called *optical reference geometry*.

### 2.2 Inertial forces

The 4-velocity  $u^i$  of a particle with a rest mass  $m$  can be decomposed into the time part and spatial part ( $n^i$  orthogonal) in the reference frame of the special observer with the 4-velocity  $n^i$  by using the relation

$$u^i = \gamma(n^i + v\tau^i), \quad (7)$$

where  $\tau^i$  is the unit spacelike vector parallel to the 3-velocity  $v^i$  of the particle in the 3-dimensional space ( $n^i$  orthogonal) and  $\gamma = (1 - v^2)^{-1/2}$  is the Lorentz factor (the speed of light  $c = 1$ ). Note that  $\gamma v\tau^k = \gamma v^k = u^i h_i^k$  and  $\gamma = -n^i u_i$ ;  $h_k^i = \delta_k^i + n^i n_k$  is the projection tensor allowing the special observer to define 3-dimensional quantities by projecting 4-dimensional quantities into his local instantaneous 3-dimensional space ( $n^i$  orthogonal).

The 4-acceleration of the particle is defined by the relation  $a_k = u^i \nabla_i u_k$ . Using (7), we can easily derive the following formula for the 4-acceleration (in which the terms are arranged according to the powers of the speed and its derivate)

$$a_k = \gamma^2 \nabla_k \Phi + \gamma^2 v (n^i \nabla_i \tau_k + \tau^i \nabla_i n_k) + \gamma^2 v^2 \tau^i \nabla_i \tau_k + (v\dot{\gamma}) \tau_k + \dot{\gamma} n_k, \quad (8)$$

where  $(v\dot{\gamma}) \equiv u^i \nabla_i (\gamma v)$ . By using  $\tilde{\tau}^i = e^\Phi \tau^i$  (the spacelike unit vector in the optical reference geometry, parallel to  $\tau^i$ ), its covariant form  $\tilde{\tau}_i = e^{-\Phi} \tau_i$ , the scalar  $E = -v^i u_i$ , the identity  $\gamma^2 = 1 + v^2 \gamma^2$  and by denoting  $\tilde{v} = \gamma v$ , we obtain (after amount of simple but tedious algebra)

$$a_k = \nabla_k \Phi + \gamma^2 v (n^i \nabla_i \tau_k + \tau^i \nabla_i n_k) + \tilde{v}^2 \tilde{\tau}^i \tilde{\nabla}_i \tilde{\tau}_k + (-E\dot{v}) \tilde{\tau}_k + \dot{\gamma} n_k. \quad (9)$$

By projecting (9) (using the projection tensor  $h_j^k$ ) into the 3-dimensional space (orthogonal to  $n^i$ ) and by using the condition of hypersurface orthogonality (2), we arrive at

$$a_j^\perp = h_j^k a_k = \nabla_j \Phi + \tilde{v}^2 \tilde{\tau}^i \tilde{\nabla}_i \tilde{\tau}_j + \gamma^2 v X_j + \dot{V} \tilde{\tau}_j, \quad (10)$$

where  $X_j \equiv n^i (\nabla_i \tau_j - \nabla_j \tau_i)$  and  $\dot{V} \equiv u^i \nabla_i (-E v)$ .

The real force acting on the particle (for example a thrust of a rocket orbiting a black hole) in the 3-dimensional space of the comoving frame of the particle can be expressed by the relation  $F_k^\perp = m a_k^\perp$ . This equation can be rewritten to the form  $F_k^\perp - m a_k^\perp = 0$ , which suggests that the particle is not accelerated and the real force is balanced by the inertial force  $F_k'^\perp = -m a_k^\perp$ , i.e.,  $F_k^\perp + F_k'^\perp = 0$ . Due to the Eq. (10), we can decompose this inertial force into the sum of (subsequently) the gravitational, centrifugal, Coriolis, and Euler forces [Abramowicz et al., 1993b]

$$\begin{aligned} F_k'^\perp &= -m a_k^\perp \\ &= -m \nabla_k \Phi - m \tilde{v}^2 \tilde{\tau}^i \tilde{\nabla}_i \tilde{\tau}_k - m \gamma^2 v X_k - m \dot{V} \tilde{\tau}_k \\ &= G_k^\perp + Z_k^\perp + C_k^\perp + E_k^\perp. \end{aligned} \quad (11)$$

Finally, we obtain the following expressions for the different kinds of inertial forces, which are familiar from the Newtonian physics. (Notice that in the context of the optical geometry relativistic approach, the gravitational force belongs to the inertial forces.)

$$G_k^\perp = -m \nabla_k \Phi, \quad (12)$$

$$C_k^\perp = -m \gamma^2 v X_k, \quad (13)$$

$$Z_k^\perp = -m \tilde{v}^2 \tilde{\tau}^i \tilde{\nabla}_i \tilde{\tau}_k, \quad (14)$$

$$E_k^\perp = -m \dot{V} \tilde{\tau}_k. \quad (15)$$

(In the following text, the superscript symbol  $\perp$  is dropped.)

### 3 CIRCULAR MOTION IN STATIONARY AND AXIALLY SYMMETRIC SPACETIMES

Consider a spacetime with a timelike Killing vector field  $\eta^i$  and axial Killing vector field  $\xi^i$ . We can denote  $m^i$  as the 4-velocity of the special stationary observer who was defined in the subsection 2.1. According to this, the 4-velocity  $m^i$  should be the unit vector parallel to an arbitrary timelike Killing vector  $v^i = C\eta^i + D\xi^i$ , where  $C, D$  are coefficients of the linear combination. After normalising  $v^i$ , we arrive at  $m^i = e^{-\Phi}[\eta^i + (D/C)\xi^i]$ , where  $\Phi = \frac{1}{2} \ln \{-[\eta^i + (D/C)\xi^i][\eta_i + (D/C)\xi_i]\}$ . If we introduce the new timelike Killing vector  $l^i = \eta^i + (D/C)\xi^i$  and  $D/C \equiv \Omega$ , we obtain the relation

$$m^i = e^{-\Phi} l^i = e^{-\Phi} (\eta^i + \Omega \xi^i), \quad (16)$$

which corresponds to the well-known unit 4-velocity of the stationary observer in axially symmetric and stationary spacetimes moving at  $r = \text{const}$  with the angular 3-velocity  $\Omega = d\phi/dt$ . In general, this 4-velocity is not hypersurface orthogonal, but the case corresponding to the locally non-rotating frames with  $\Omega \equiv \Omega_{\text{LNRF}} = -\eta^i \eta_i / \eta^i \xi_i$  is hypersurface orthogonal. Therefore we can choose the 4-velocity

$$n^i \equiv e^{-\Phi} l^i = e^{-\Phi} (\eta^i + \Omega_{\text{LNRF}} \xi^i) \quad (17)$$

as the 4-velocity field of the special family of locally non-rotating observers.

The 4-velocity of the particle moving along a circular orbit ( $r = \text{const}$ ) in the equatorial plane can be written in the form

$$u^i = A(\eta^i + \Omega \xi^i). \quad (18)$$

Due to the choice of locally non-rotating observers (with  $n^i$  being hypersurface orthogonal), the unit vector  $\tau^i$  is located in the hypersurface and it is directed along the Killing vector  $\xi^i$ , because we consider the circular orbits, i.e.,

$$\tau^i = (\xi^k \xi_k)^{-1/2} \xi^i. \quad (19)$$

From this fact and from (18) and (7), we obtain relations

$$\gamma = Ae^{\Phi}, \quad (20)$$

$$v = e^{-\Phi} (\xi^i \xi_i)^{1/2} (\Omega - \Omega_{\text{LNRF}}). \quad (21)$$

By using the general form of the inertial forces (12)–(15) and the equations (18)–(21), we arrive at the expressions for components of the gravitational, Coriolis, and centrifugal forces acting on the particle moving along the circular orbit with  $\Omega = \text{const}$  [Abramowicz et al., 1995]

$$G_k = -m \frac{1}{2} \partial_k (\ln e^{2\Phi}), \quad (22)$$

$$C_k = m\gamma^2 v g_{\phi\phi}^{-3/2} e^{-\Phi} (g_{\phi\phi} \partial_k g_{t\phi} - g_{t\phi} \partial_k g_{\phi\phi}), \quad (23)$$

$$Z_k = m(\gamma v)^2 \frac{1}{2} g_{\phi\phi}^{-1} e^{-2\Phi} (e^{2\Phi} \partial_k g_{\phi\phi} - g_{\phi\phi} \partial_k e^{2\Phi}). \quad (24)$$

Note that the Euler force  $E_k$  appears in the case of  $\Omega \neq \text{const}$ . Due to the axial symmetry and stationarity of the spacetimes the  $t$  and  $\phi$ -components vanish. Moreover the  $\theta$ -components

vanish in the case of the motion in the equatorial plane, which we shall focus on. Then the only non-vanishing  $r$ -components of the forces can be rewritten in the form

$$G_r = -m\nabla_r\Phi, \quad (25)$$

$$C_r = -m(1 + \tilde{v}^2)^{1/2}\tilde{v}\tilde{R}\nabla_r\Omega_{\text{LNRF}}, \quad (26)$$

$$Z_r = m\tilde{v}^2\tilde{R}^{-1}\nabla_r\tilde{R}, \quad (27)$$

where

$$\tilde{v} = \gamma v, \quad \tilde{r} = (\xi^i \xi_i)^{1/2}, \quad \tilde{R} = \tilde{r}e^{-\Phi}. \quad (28)$$

Note that by using  $\tilde{\Omega} = \Omega - \Omega_{\text{LNRF}}$ , we obtain from (21) the relation  $v = \tilde{\Omega}\tilde{R}$  having the familiar Newtonian form. From these expressions, it is really obvious that the inertial forces have the Newtonian character. The gravitational force is velocity-independent, the Coriolis force depends on the first power of the velocity, and the centrifugal force depends on the second power of the velocity. We can also give the mass and velocity independent parts of the forces [Abramowicz et al., 1995]

$$g_r = \frac{G_r}{m} = -m \frac{1}{2} \partial_r (\ln e^{2\Phi}) = -\nabla_r \Phi, \quad (29)$$

$$c_r = \frac{C_r}{m\gamma^2 v} = g_{\phi\phi}^{-3/2} e^{-\Phi} (g_{\phi\phi} \partial_r g_{t\phi} - g_{t\phi} \partial_r g_{\phi\phi}) = -\tilde{R} \nabla_r \Omega_{\text{LNRF}}, \quad (30)$$

$$z_r = \frac{Z_r}{m(\gamma v)^2} = \frac{1}{2} g_{\phi\phi}^{-1} e^{-2\Phi} (e^{2\Phi} \partial_r g_{\phi\phi} - g_{\phi\phi} \partial_r e^{2\Phi}) = \tilde{R}^{-1} \nabla_r \tilde{R}. \quad (31)$$

#### 4 KERR–DE SITTER SPACETIMES

The Kerr–de Sitter spacetime is a stationary and axially symmetric solution of Einstein's vacuum equations with a positive (repulsive) cosmological constant. This solution describes the geometry of a spacetime around an isolated Kerr (rotating and uncharged) black hole or naked singularity determined by a mass  $M$  and a specific angular momentum  $a$  in the universe with a repulsive cosmological constant  $\Lambda > 0$ .

The line element of the Kerr–de Sitter geometry (in the standard Boyer–Lindquist coordinates, geometric units with  $c = G = 1$ , and signature +2) is given by the relation

$$ds^2 = -\frac{\Delta_r}{I^2 \rho^2} (dt - a \sin^2 \theta d\phi)^2 + \frac{\Delta_\theta \sin^2 \theta}{I^2 \rho^2} [a dt - (r^2 + a^2) d\phi]^2 + \frac{\rho^2}{\Delta_r} dr^2 + \frac{\rho^2}{\Delta_\theta} d\theta^2, \quad (32)$$

where

$$\Delta_r = r^2 - 2Mr + a^2 - \frac{1}{3}\Lambda r^2(r^2 + a^2), \quad (33)$$

$$\Delta_\theta = 1 + \frac{1}{3}\Lambda a^2 \cos^2 \theta, \quad (34)$$

$$I = 1 + \frac{1}{3}\Lambda a^2, \quad (35)$$

$$\rho^2 = r^2 + a^2 \cos^2 \theta. \quad (36)$$

It is convenient to use the following dimensionless quantities  $s/M \rightarrow s$ ,  $t/M \rightarrow t$ ,  $r/M \rightarrow r$ ,  $a/M \rightarrow a$  and to introduce a dimensionless cosmological parameter

$$y = \frac{1}{3} \Lambda M^2. \quad (37)$$

The Kerr–de Sitter geometry, being stationary and axially symmetric, admits two Killing vector fields: the timelike vector field  $\eta = \partial/\partial t$  and the spacelike vector field  $\xi = \partial/\partial \phi$ , which are not orthogonal in general. In addition note that  $g_{tt} = (\eta^i \eta_i)$ ,  $g_{t\phi} = (\eta^i \xi_i)$ , and  $g_{\phi\phi} = (\xi^i \xi_i)$ .

#### 4.1 Black-hole and naked-singularity spacetimes

The stationary regions of the Kerr–de Sitter spacetimes are determined by the relation

$$\Delta_r(r; a, y) = r^2 - 2r + a^2 - yr^2(r^2 + a^2) \geq 0, \quad (38)$$

and bounded by the horizons:  $r = r_{h-}$  (the inner black-hole horizon),  $r = r_{h+}$  (the outer black-hole horizon), and  $r = r_c$  (the cosmological horizon), which are the real roots of the equality in (38). We can express the condition for the positions of the horizons in the form [Stuchlík and Hledík, 2000, Stuchlík and Slaný, 2004]

$$y = y_h(r; a^2) \equiv \frac{r^2 - 2r + a^2}{r^2(r^2 + a^2)}. \quad (39)$$

In addition note that in the Kerr–de Sitter spacetimes

$$y > 0 \quad (40)$$

Using (39), we can now discuss the number of horizons. The asymptotic behaviour of the function  $y_h(r; a^2)$  is given by  $y_h(r \rightarrow \infty; a^2) \rightarrow 0$  and  $y_h(r \rightarrow 0; a^2) \rightarrow \infty$ . The stationary points of the function  $y_h(r; a^2)$  are determined (due to the condition  $\partial_r y_h(r; a^2) = 0$ ) by the relation

$$a^2(r) = a_{\text{he}}^2(r) \equiv \frac{1}{2}(-2r^2 + \sqrt{8r + 1} + r), \quad (41)$$

which determines the curve in the plane  $(r^+ \times a^2)$  (see Fig. 1a). From the condition  $\partial_r a_{\text{he}}^2(r) = 0$  and relation (41), it follows that the maximum  $a_{\text{he,max}}^2$  of this function is located at

$$r_{\text{he,max}} = \frac{1}{4}(3 + 2\sqrt{3}) \doteq 1.62, \quad (42)$$

and takes the value

$$a_{\text{he,max}}^2 \doteq 1.21. \quad (43)$$

Using this point, we can divide the curve  $a_{\text{he}}^2(r)$  into the “left” and “right” parts denoted by  $a_{\text{he1}}^2(r)$  and  $a_{\text{he2}}^2(r)$ . By using second partial derivate of the function  $y_h(r; a^2)$  at the points of this curve, we can convince ourselves that the function  $y_h(r; a^2)$  has local maximum at  $a_{\text{he2}}^2(r)$  and local minimum at  $a_{\text{he1}}^2(r)$  for a specific value of the parameter  $a^2$ . The point  $a_{\text{he,max}}^2$  corresponds to an inflexion point of  $y_h(r; a)$  (see Fig. 1b). It is also useful to

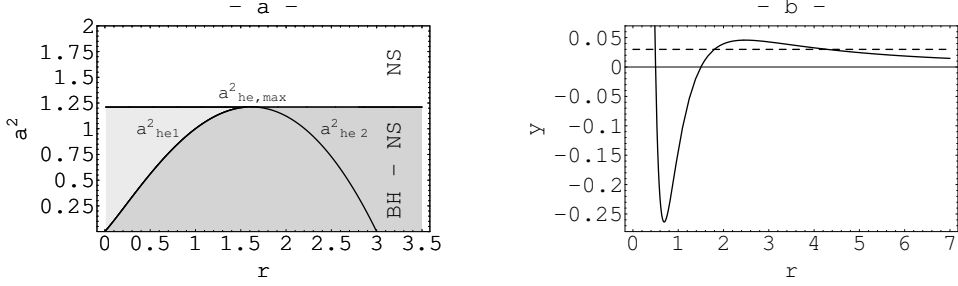


**Figure 1.** (a) Curve  $a_{\text{he}}^2(r)$  and its parts, regions NS-BH and NS (separated by the line  $a^2 = a_{\text{he,max}}^2 \doteq 1.21$ ) corresponding to the classification of the Kerr–de Sitter spacetimes. Notice that the outer black-hole stationary region can not occur in the light-gray part and the inner black-hole region can not occur in the dark-gray part of the NS-BH region. (b) Behaviour of the function  $y_h(r, a^2)$  (solid) for the specific value of the parameter  $a^2 = 0.75$ . Intersections of the dashed line  $y = 0.03$  and the function  $y_h(r; a^2)$  determine the inner black-hole, outer black-hole, and cosmological horizons of the Kerr–de Sitter spacetimes with these rotational and cosmological parameters.

introduce  $y_{\text{he1}}$  and  $y_{\text{he2}}$  as the values of the function  $y_h(r; a^2)$  at the points of the “left” and “right” parts of the curve  $a_{\text{he}}^2(r)$ .

By using the rotational parameter  $a^2$ , we can now give the following classification of the Kerr–de Sitter spacetimes (see Fig. 1a).

**Class BH-NS:**  $0 < a^2 < 1.21$ . In these spacetimes,

- there is 1 horizon in the case of  $y < y_{\text{he1}}$ ,
- there is 1 horizon in the case of  $y > y_{\text{he2}}$ ,
- there are 2 horizons in the case of  $y = y_{\text{he1}}$ ,
- there are 2 horizons in the case of  $y = y_{\text{he2}}$ ,
- there are 3 horizons in the case of  $y_{\text{he1}} < y < y_{\text{he2}}$ .

**Class NS:**  $a^2 \geq 1.21$ . In these spacetimes, there is one horizon in the case of any value of  $y$ .

The class NS contains only the Kerr–de Sitter naked-singularity spacetimes, whereas the class BH-NS contains the Kerr–de Sitter black-hole spacetimes and naked-singularity spacetimes as well, in dependence on the value of the cosmological parameter  $y$ . Spacetimes containing 3 or 2 horizons are black-hole spacetimes and spacetimes containing 1 horizon are naked-singularity spacetimes (see Fig.1). Thereinafter we use “BH” instead of the word “black-hole” and “NS” instead of the word “naked-singularity”.

## 5 INERTIAL FORCES IN KERR–DE SITTER SPACETIMES

By using (32), we can express the inertial forces (22)–(24) in the following form

$$G_r = m \left\{ r \Delta_r [r a^4 y + (y r^3 + r + 2) a^2 + r^3] \right\}^{-1} \times \left\{ r^3 a^2 (a^2 + r^2)^2 y^2 \right.$$

$$+ r^2(a^2 + r^2)[r^3 + a^2(r + 4)]y - r^4 - 2r^2a^2 + 4ra^2 - a^4\}, \quad (44)$$

$$Z_r = m(\gamma v)^2 \left\{ r \Delta_r [ra^4y + (yr^3 + r + 2)a^2 + r^3] \right\}^{-1} \times \left\{ r^3 a^4 (a^2 + r^2) y^2 + r^2 a^2 [(2r + 5)a^2 + r^2(2r + 3)]y + r^4(r - 3) + ra^2[r(r - 3) + 6] - 2a^4 \right\}, \quad (45)$$

$$C_r = m\gamma^2 v \frac{2a(a^2 + r^2)}{r\sqrt{\Delta_r} [ra^4y + (yr^3 + r + 2)a^2 + r^3]}. \quad (46)$$

The behaviour of the gravitational, centrifugal, and Coriolis forces acting on a particle stationary moving along a circular orbit in the equatorial plane of the Kerr–de Sitter spacetimes (see Fig. 2) can be elucidated by studying the following basic problems.

**(a) Range of definition:** The forces are defined only in the stationary regions of the Kerr–de Sitter spacetimes where

$$r > 0, \quad y > 0, \quad \Delta_r(r; a^2, y) > 0 \quad \Leftrightarrow \quad y < y_h(r; a^2). \quad (47)$$

**(b) Divergence:** The forces diverge at points where their denominator equals to zero, i.e., at the singularity and horizons.

**(c) Vanishing of forces:** The velocity dependent forces, i.e., the centrifugal and Coriolis forces, naturally vanish for  $v = 0$ . It is, however much more interesting to establish where the forces vanish independently of the velocity, as well as to establish where the gravitational force force vanishes. Each of forces vanishes on the circular orbit with the radius  $r$  satisfying the condition of their numerator equal to zero. It means the gravitational force vanishes on circular orbits with the radius determined by the relation

$$y = y_G(r; a^2) \equiv \frac{-r[r^3 + a^2(r + 4)] + \sqrt{r(a^2 + r^2)[r^5 + r^2a^2(r + 12) + 4a^4]}}{2r^2a^2(a^2 + r^2)}, \quad (48)$$

and the centrifugal force vanishes independently of the velocity on circular orbits with the radius determined by the relation

$$y = y_Z(r; a^2) \equiv \left[ 2a^2r^2(a^2 + r^2) \right]^{-1} \times \left\{ -(2r + 5)ra^2 - r^3(2r + 3) + \sqrt{r(a^2 + 3r^2)[8a^4 + ra^2(16r + 1) + r^3(8r + 3)]} \right\}. \quad (49)$$

The Coriolis force vanishes only in the case of the velocity equal to zero, therefore we shall restrict our attention only to the circular orbits where the gravitational and centrifugal forces vanish. The discussion of the existence and number of such orbits is then based on the study of the behaviour of the functions  $y_G(r; a^2)$  and  $y_Z(r; a^2)$ .

**(d) Change of orientation of forces:** At the radii of circular orbits where the forces vanish independently of the velocity, the forces can change their orientation. It only happens in the case of no local extrema of the forces at these radii.

The problem (c) is discussed in the following part of the article in detail.

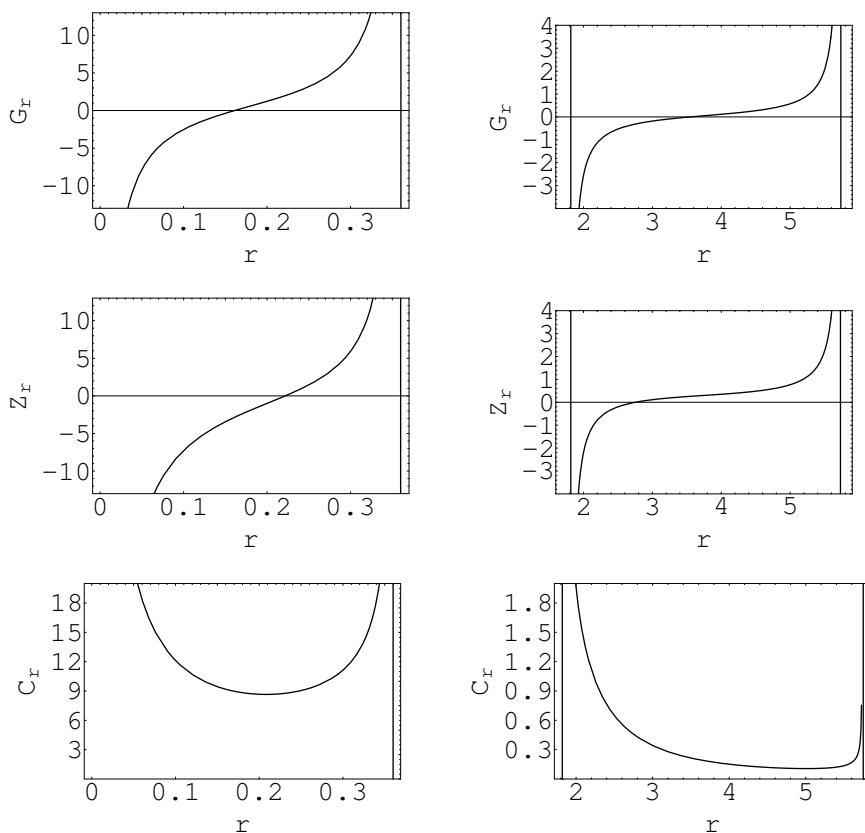


**Figure 2.** Behaviour of velocity independent parts of gravitational, Coriolis, and centrifugal forces for the specific values of the parameters  $a^2 = 0.77$  and  $y = 0.02$ . The intersections of the vertical lines and  $r$  – axis determine the positions of horizons. The intersections of these functions, denoted as  $\mathcal{G}_r$ ,  $\mathcal{Z}_r$ , and  $\mathcal{C}_r$  with  $r$  – axes determine the radii of circular orbits, where the gravitational, centrifugal, and Coriolis forces vanish independently of the velocity.

## 5.1 Gravitational force

### 5.1.1 Existence of circular orbits with $G_r = 0$

The relevant part of the function  $y_G(r; a^2)$  must satisfy the conditions (47) for the range of definition of forces, i.e., the relations

$$y_G(r; a^2) < y_h(r; a^2), \quad (50)$$

$$y_G(r; a^2) > 0. \quad (51)$$

We start with the determination of the region where  $y_G(r; a^2) < y_h(r; a^2)$ . The asymptotic behaviour of the function  $y_G(r; a^2)$  is given by  $y_G(r \rightarrow \infty; a^2) \rightarrow +0$  and

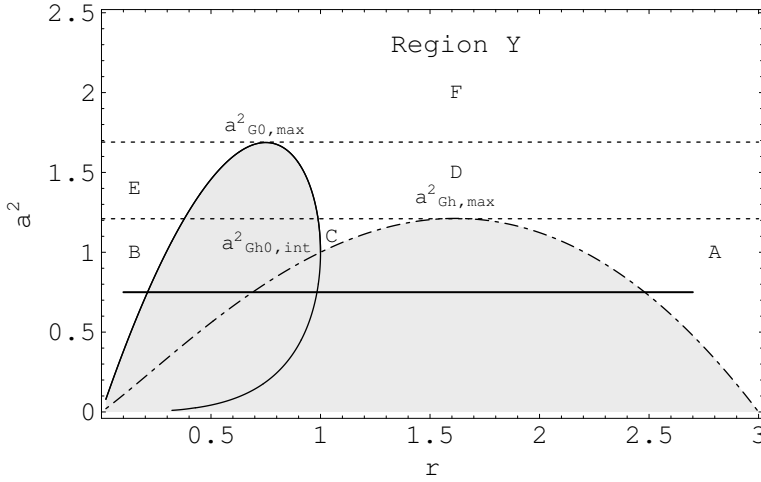


**Figure 3.** Regions  $Y$  (white),  $N$  (gray), regions  $A, B, C, D, E$ , and  $F$  (separated by curves and dashed lines), curve  $a_{Gh}^2(r)$  (dashed and dotted) enclosing the area where  $y_G(r; a^2) > y_h(r; a^2)$ , and curve  $a_{G0}^2(r)$  (solid) enclosing the area where  $y_G(r; a^2) < 0$ . The intersections of the thick line  $a^2 = 0.75$  and the curve  $a_{G0}^2(r)$  determine the points where  $y_G(r; a^2) = 0$ , and the intersections with the curve  $a_{Gh}^2(r)$  determine the points where  $y_G(r; a^2) = y_h(r; a^2)$ , for the specific value of the parameter  $a^2 = 0.75$  (compare with Fig. 4).

$y_G(r \rightarrow 0; a^2) \rightarrow \infty$ , whereas  $y_G(r \rightarrow 0; a^2) < y_h(r \rightarrow 0; a^2)$  and  $y_G(r \rightarrow \infty; a^2) < y_h(r \rightarrow \infty; a^2)$ .

The points where  $y_G(r; a^2) = y_h(r; a^2)$  are given by the relation

$$a^2 = a_{Gh}^2(r) \equiv \frac{1}{2}(-2r^2 + \sqrt{8r + 1}r + r), \quad (52)$$

which determines the curve in the plane  $(r^+ \times a^2)$  (see Fig. 3).

Note that the function  $a_{Gh}^2(r)$  is identical with the function  $a_{he}^2(r)$  and that the local maximum  $a_{Gh,max}^2 \doteq 1.21$  of this function is located at  $r_{Gh,max} \doteq 1.62$ . In addition, this point divides the curve  $a_{Gh}^2(r)$  into the “left” and “right” parts denoted by  $a_{Gh1}^2(r)$  and  $a_{Gh2}^2(r)$ . By using the asymptotic behaviour of the function  $y_G(r; a^2)$  and (52), we can determine the region in the plane  $(r^+ \times a^2)$  where  $y_G(r; a^2) < y_h(r; a^2)$  (see Fig. 3). It is also useful to introduce  $y_{Gh1}$  and  $y_{Gh2}$  as the values of the function  $y_G(r; a^2)$  at the points of the “left” and “right” parts of the curve  $a_{Gh}^2(r)$ .

Next, we determine the region where  $y_G(r; a^2) > 0$ . The points where  $y_G(r; a^2) = 0$  are given by the relation

$$r^4 + 2r^2a^2 - 4ra^2 + a^4 = 0, \quad (53)$$

which we denote as the implicit form of the function  $a_{G0}^2(r)$ . Note that in the plane  $(r^+ \times a^2)$ , this function determine the curve (see Fig. 3), which consists of two parts determined by the solution of (53), i.e. by the relation

$$a^2 = a_{G0\pm}^2(r) \equiv 2r - r^2 \pm 2\sqrt{r^2 - r^3}. \quad (54)$$

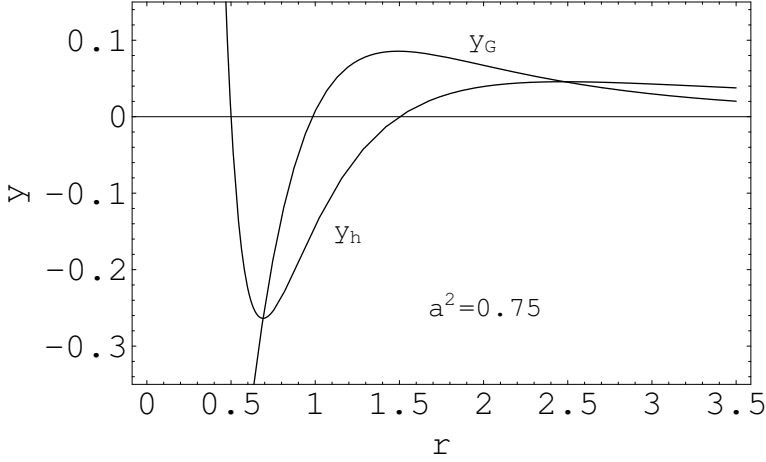


**Figure 4.** Behaviour of functions  $y_G(r; a^2)$  and  $y_h(r; a^2)$  for the specific value of the parameter  $a^2 = 0.75$ .

The maximum  $a_{G0, \max}^2 \doteq 1.69$  of this function is located at  $r_{G0, \max} \doteq 0.75$ . In addition, this point divides the curve into the “left” and “right” parts denoted by  $a_{G01}^2(r)$  and  $a_{G02}^2(r)$ . The asymptotic behaviour of the function  $y_G(r; a^2)$  and (53) determine the region in the plane  $(r^+ \times a^2)$  where  $y_G(r; a^2) > 0$  (see Fig. 3).

The plane  $(r^+ \times a^2)$  can be divided into two regions: the region  $Y$  where the function fulfils the conditions (50) and (51), i.e., where the existence of the circular orbits with  $G_r = 0$  is possible and the region  $N$  where the existence of the circular orbits with  $G_r = 0$  is not possible. We can also divide the region  $Y$  into six subregions with respect to the radial coordinate  $r$ : *A*-region ( $r > r_{Gh2}$ ), *B*-region ( $0 < r < r_{G01}$ ), *C*-region ( $r_{G02} < r < r_{Gh1}$ ), *D*-region ( $r > r_{G02}$ ), *E*-region ( $0 < r < r_{G01}$ ), and *F*-region ( $r > 0$ ) (see Fig. 3). It is also useful to introduce  $y_{G01}$  and  $y_{G02}$  as values of the function  $y_G(r; a^2)$  at the “left” and “right” parts of the curve  $a_{G0}^2(r)$ . The common point of the functions  $a_{Gh}^2(r)$  and  $a_{G0}^2(r)$  takes the value  $a_{Gh0, \text{int}}^2 = 1$  and is located at  $r_{Gh0, \text{int}} = 1$ .

### 5.1.2 Number of circular orbits with $G_r = 0$

The number of the circular orbits with  $G_r = 0$  depends on the number of local extrema of the function  $y_G(r; a^2)$ . The stationary points of the function  $y_G(r; a^2)$  are determined (due to the condition  $\partial_r y_G(r; a^2) = 0$ ) by the relation

$$6r^2 + 2a^2 - \frac{(r^2 + a^2)(9r^4 + 8a^2r^2 + 3a^4)}{\sqrt{r(r^2 + a^2)[r^5 + r^2a^2(r + 12) + 4a^2]}} = 0, \quad (55)$$

which we denote as the implicit form of the function  $a_{Ge}^2(r)$ . This function also determines the curve in the plane  $(r^+ \times a^2)$  (see Fig 5a). The maximum  $a_{Ge, \max}^2 \doteq 2.44$  of this function divides the curve into the “left” and “right” parts denoted by  $a_{Ge1}^2(r)$  and  $a_{Ge2}^2(r)$ . The “right” part of this curve corresponds to local maxima of the function  $y_G(r; a^2)$ , the “left”

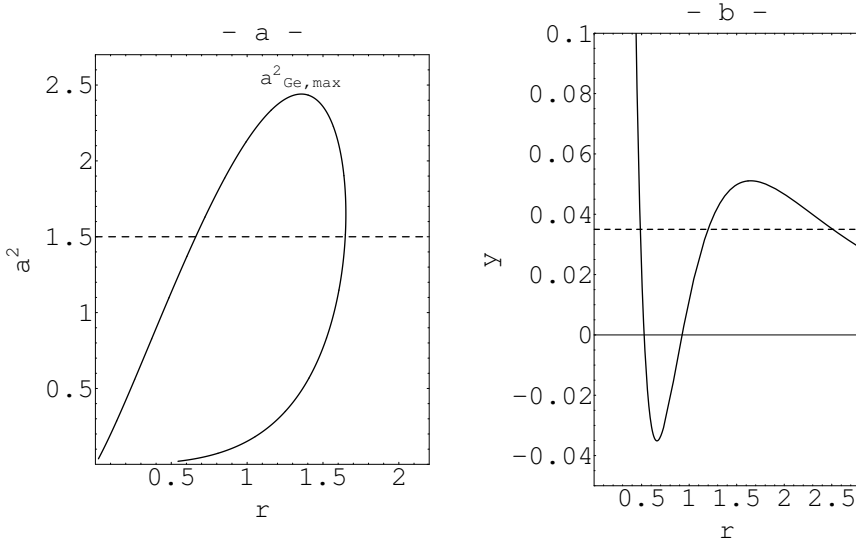


**Figure 5.** (a) Curve  $a^2_{\text{Ge}}(r)$ . The intersections of the dashed line  $a^2 = 1.5$  with this curve determine the stationary points of the function  $y_G(r; a^2)$  for the specific value of the parameter  $a^2 = 1.5$  (compare with the next part of the figure). (b) Behaviour of function  $y_G(r; a^2)$  for the specific value of the parameter  $a^2 = 1.5$ . Intersections of the dashed line  $y = 0.035$  with the graph of the function  $y_G(r; 1.5)$  determine radii of circular orbits with  $G_r = 0$  in the Kerr–de Sitter spacetimes with the parameters  $a^2 = 1.5$  and  $y = 0.035$ .

part corresponds to the local minima, whereas these extrema coalesce at  $r_{\text{Ge,max}} \doteq 1.36$  (see Fig. 5). Notice that in the Kerr–de Sitter spacetimes, even three circular orbits with  $G_r = 0$  can occur in the case of two local extrema of the function  $y_G(r; a^2)$ . It is also useful to introduce  $y_{\text{Ge1}}$  and  $y_{\text{Ge2}}$  as the values of the function  $y_G(r; a^2)$  at the points of the “left” and “right” parts of the curve  $a^2_{\text{Ge}}(r)$ .

The common point of the functions  $a^2_{\text{Gh}}(r)$  and  $a^2_{\text{Ge}}(r)$  is identical with the maximum of the function  $a^2_{\text{Gh}}(r)$ .

### 5.1.3 Classification of Kerr–de Sitter spacetimes

Using the rotational and cosmological parameters, we can give the following classification of the Kerr–de Sitter spacetimes (see Fig. 6).

**Class GI:** ( $0 < a^2 \leq 1$ )

In these spacetimes, there are 2 regions of  $r$  where the existence of the orbits with  $G_r = 0$  is possible: *A*-region and *B*-region.

(a) spacetimes with  $0 < y < y_{\text{Gh2}}$  are BH spacetimes containing:

- 1 orbit in the *A*-region (in the outer BH region),
- 1 orbit in the *B*-region (in the inner BH region).

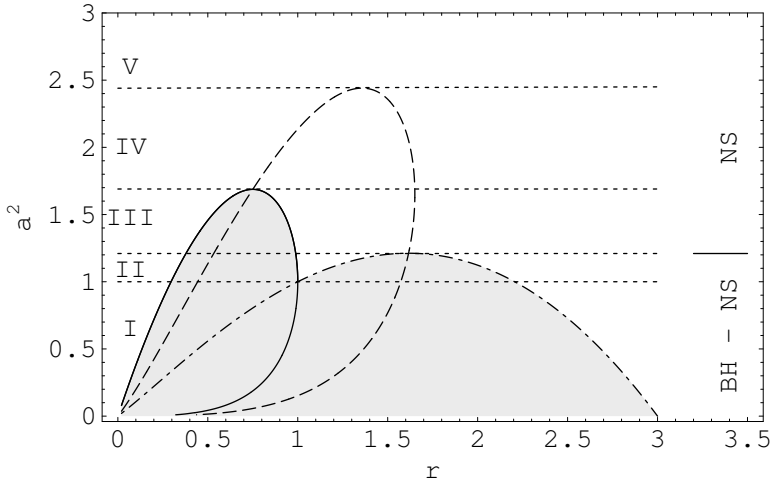


**Figure 6.** Curves  $a_{\text{Gh}}^2(r)$  (dashed and dotted),  $a_{\text{G0}}^2(r)$  (solid),  $a_{\text{Ge}}^2(r)$  (dashed), and regions *I*, *II*, *III*, *IV*, and *V* (separated by dashed lines) corresponding to the classification of the Kerr–de Sitter spacetimes.

(b) spacetimes with  $y \geq y_{\text{Gh2}}$  are NS spacetimes containing:

- 1 orbit in the *B*-region

**Class GII:** ( $1 < a^2 < 1.21$ )

In these spacetimes, there are 3 regions of  $r$  where the existence of the orbits with  $G_r = 0$  is possible: *A*-region, *B*-region, and *C*-region.

(a) spacetimes with  $0 < y < y_{\text{Gh1}}$  are NS spacetimes containing:

- 1 orbit in the *A*-region,
- 1 orbit in the *B*-region,
- 1 orbit in the *C*-region.

(b) spacetimes with  $y_{\text{Gh1}} \leq y < y_{\text{Gh2}}$  are BH spacetimes containing:

- 1 orbit in the *A*-region (in the outer BH region),
- 1 orbit in the *B*-region (in the inner BH region)

(c) spacetimes with  $y \geq y_{\text{Gh2}}$  are NS spacetimes containing:

- 1 orbit in the *B*-region

**Class GIII:** ( $1.21 \leq a^2 \leq 1.69$ )

These spacetimes are NS spacetimes. There are 2 regions of  $r$  where the existence of the orbits with  $G_r = 0$  is possible: *D*-region and *E*-region. They can be divided into 2 subclasses.

**Subclass GIIIa:** ( $a^2 = 1.21$ )(a) spacetimes with  $0 < y < y_{\text{Ge}2}$  contain:

- 2 orbits in the  $D$ -region,
- 1 orbit in the  $E$ -region.

(b) spacetimes with  $y \geq y_{\text{Ge}2}$  contain:

- 1 orbit in the  $E$ -region

**Subclass GIIIb:** ( $1.21 < a^2 \leq 1.69$ )(a) spacetimes with  $0 < y < y_{\text{Ge}2}$  contain:

- 2 orbits in the  $D$ -region,
- 1 orbit in the  $E$ -region.

(b) spacetimes with  $y = y_{\text{Ge}2}$  contain:

- 1 orbit in the  $D$ -region,
- 1 orbit in the  $E$ -region.

(c) spacetimes with  $y > y_{\text{Ge}2}$  contain:

- 1 orbit in the  $E$ -region

**Class GIV:** ( $1.69 < a < 2.44$ )

These spacetimes are NS spacetimes.

(a) spacetimes with  $0 < y < y_{\text{Ge}1}$  contain: 1 orbit(b) spacetimes with  $y = y_{\text{Ge}1}$  contain: 2 orbits(c) spacetimes with  $y_{\text{Ge}1} < y < y_{\text{Ge}2}$  contain: 3 orbits(d) spacetimes with  $y = y_{\text{Ge}2}$  contain: 2 orbits(e) spacetimes with  $y > y_{\text{Ge}2}$  contain: 1 orbit**Class GV:** ( $a^2 \geq 2.44$ )These spacetimes are NS spacetimes and contain 1 circular orbit with  $G_r = 0$  for any  $y > 0$ .*5.1.4 Schwarzschild-de Sitter and Kerr case*In the Schwarzschild-de Sitter spacetimes ( $a^2 = 0, y > 0$ ), we obtain from (44) that the gravitational force is given by the relation

$$G_r = m \frac{1 - r^3 y}{r(2 - r + r^3 y)}. \quad (56)$$

Notice that the force vanishes at the static radius  $r_s = y^{-1/3}$ , where the gravitational attraction of the black hole is balanced by the cosmological repulsion. The gravitational force also changes its orientation on the circular orbit with this radius. The circular orbit

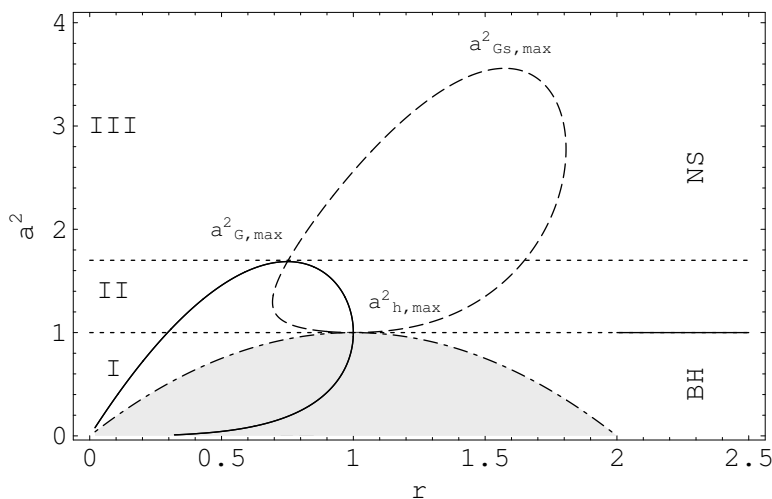


**Figure 7.** Curves  $a_G^2(r)$  (solid),  $a_{G_s}^2(r)$  (dashed),  $a_h^2(r)$  (dashed and dotted) enclosing dynamic area (gray), and regions *I*, *II*, and *III* corresponding to the classification of the Kerr spacetimes. The intersections of a line  $a^2 = \text{const}$  with the curve  $a_G^2(r)$  determine the radii of the circular orbits with  $G_r = 0$ , the intersections with the curve  $a_{G_s}^2(r)$  determine the radii where the gravitational force  $G_r$  has stationary points, and the intersections with the curve  $a_h^2(r)$  determine the positions of black-hole horizons in the Kerr spacetimes with the parameter  $a$ .

with the radius  $r_s = y^{-1/3}$  has an important meaning even in the Kerr–de Sitter spacetimes. It is the outer limit for the existence of circular geodesics where two families of the geodesic circular stationary motion coalesce. (We can express the velocity  $v$  of the particle from the condition of the stationary circular geodesic motion, i.e., from the condition  $G_r + C_r + Z_r = 0$ , and convince ourselves that the relation  $r \leq y^{-1/3}$  is the condition for the velocity  $v$  to be real. It means it is the necessary condition for the stationary circular geodesic motion in the equatorial plane.)

In the Kerr spacetimes ( $a > 0$ ,  $y = 0$ ), we obtain from (44) that the gravitational force is given by the relation

$$G_r = m \frac{-r^4 - 2r^2a^2 + 4ra^2 - a^4}{r \Delta_r [(r+2)a^2 + r^3]}. \quad (57)$$

Clearly, in the Kerr spacetimes, this force is also defined only in the region determined by  $\Delta_r > 0$ , i.e., in the region determined by the condition  $a^2 > r(2-r)$ . The equality in this equation determines the function  $a_h^2(r)$  (with the maximum  $a_{h,\text{max}}^2 = 1$  at  $r_{h,\text{max}} = 1$ ), which divides the plane ( $r^+ \times a^2$ ) into the stationary and dynamic regions (see Fig. 7). The gravitational force vanishes on the circular orbit with radii determined by the relation

$$r^4 + 2r^2a^2 - 4ra^2 + a^4 = 0. \quad (58)$$

We denote this equation as the implicit form of the function  $a_G^2(r)$ , which determines the curve in the the plane ( $r^+ \times a^2$ ) (see Fig. 7). Note that the function  $a_G^2(r)$  is identical

with the function  $a_{G_0}^2(r)$  and that the maximum  $a_{G,\max}^2 \doteq 1.69$  of this function is located at  $r_{G,\max} \doteq 0.75$ . By using the condition  $\partial_r G_r = 0$ , we obtain the function  $a_{G_s}^2(r)$ , which determines the stationary points of the gravitational force (see Fig. 7). The maximum  $a_{G_s,\max}^2$  and the minimum  $a_{G_s,\min}^2 \equiv a_{h,\max}^2$  of this function are the only inflexion points of the gravitational force. The other points determined by the function  $a_{G_s}^2$  corresponds to local extrema.

Using the rotational parameter, we can now give the following classification of the Kerr spacetimes (see Fig. 7).

**Class GI:** ( $0 < a^2 \leq 1$ )

These spacetimes are BH spacetimes. In the inner stationary region, there is only 1 orbit with  $G_r = 0$ . On this orbit the gravitational force also changes its orientation. In the outer stationary region, there is no such orbit.

**Class GII:** ( $1 < a^2 \leq 1.69$ )

These spacetimes are NS spacetimes. There are 2 orbits with  $G_r = 0$  for  $a^2 < 1.69$  and there is 1 such orbit for  $a^2 = 1.69$ , but on this orbit the gravitational force does not change its orientation.

**Class GIII:** ( $a^2 > 1.69$ )

These spacetimes are NS spacetimes. There is no orbit with  $G_r = 0$ .

## 5.2 Centrifugal force

### 5.2.1 Existence of circular orbits with $Z_r = 0$

The relevant part of the function  $y_Z(r; a^2)$  must satisfy the conditions (47) for the range of definition of forces, i.e., the relations

$$y_Z(r; a^2) < y_h(r; a^2), \quad (59)$$

$$y_Z(r; a^2) > 0. \quad (60)$$

Again, we start with the determination of the region where  $y_Z(r; a^2) < y_h(r; a^2)$ . The asymptotic behaviour of the function  $y_Z(r; a^2)$  is given by  $y_Z(r \rightarrow \infty; a^2) \rightarrow -\infty$  and  $y_Z(r \rightarrow 0; a^2) \rightarrow \infty$ , whereas  $y_Z(r \rightarrow 0; a^2) < y_h(r \rightarrow 0; a^2)$  and  $y_Z(r \rightarrow \infty; a^2) < y_h(r \rightarrow \infty; a^2)$ .

The points where  $y_Z(r; a^2) = y_h(r; a^2)$  are given by the relation

$$a^2 = a_{Z_h}^2(r) \equiv \frac{1}{2}(-2r^2 + \sqrt{8r + 1}r + r), \quad (61)$$

which determines the curve in the plane  $(r^+ \times a^2)$  (see Fig. 8). Note that the function  $a_{Z_h}^2(r)$  is identical with the function  $a_{G_h}^2(r)$  and that the local maximum  $a_{Z_h,\max}^2 \doteq 1.21$  of this function is located at  $r_{Z_h,\max} \doteq 1.62$ . In addition, this point divides the curve  $a_{Z_h}^2(r)$  into the “left” and “right” parts denoted by  $a_{Z_{h1}}^2(r)$  and  $a_{Z_{h2}}^2(r)$ . By using the asymptotic behaviour of the function  $y_Z(r; a^2)$  and (61), we can determine the region in the plane  $(r^+ \times a^2)$  where  $y_Z(r; a^2) < y_h(r; a^2)$  (see Fig. 8). It is also useful to introduce  $y_{Z_{h1}}$  and  $y_{Z_{h2}}$  as the values of the function  $y_Z(r; a^2)$  at the points of the “left” and “right” parts of the curve  $a_{Z_h}^2(r)$ .

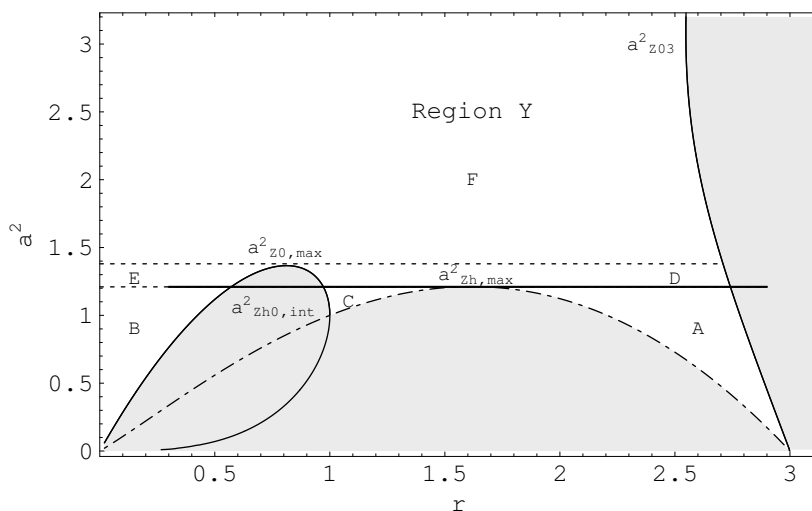


**Figure 8.** Regions  $Y$  (white),  $N$  (gray), regions  $A$ ,  $B$ ,  $C$ ,  $D$ ,  $E$ , and  $F$  (separated by curves and dashed lines), curve  $a^2_{Z_0}(r)$  (dashed and dotted) enclosing the area where  $y_Z(r; a^2) > y_h(r; a^2)$ , and curve  $a^2_{Z_0}(r)$  (solid) enclosing the area where  $y_Z(r; a^2) < 0$ . The intersections of the thick line  $a^2 = 1.21$  and the curve  $a^2_{Z_0}(r)$  determine the points where  $y_Z(r; a^2) = 0$  and the intersections with the curve  $a^2_{Z_h}(r)$  determine the points where  $y_Z(r; a^2) = y_h(r; a^2)$ , for the specific value of the parameter  $a^2 = 1.21$  (compare with Fig. 9).

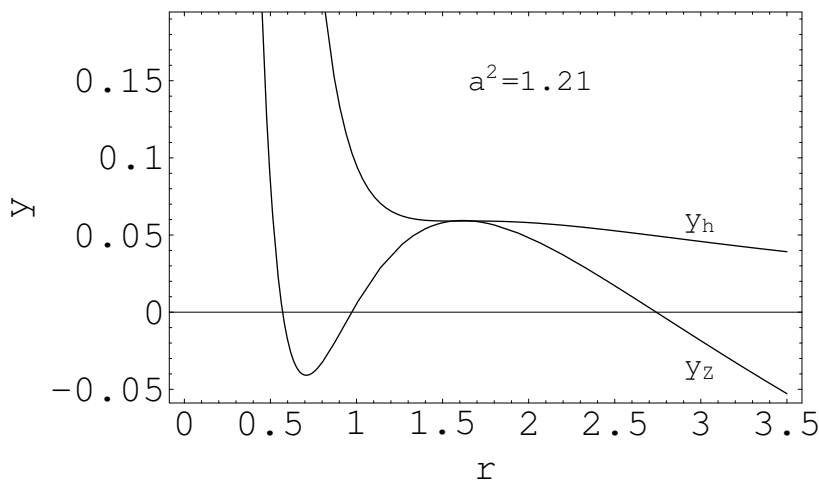


**Figure 9.** Behaviour of functions  $y_Z(r; a^2)$  and  $y_h(r; a^2)$  for the specific value of the parameter  $a^2 = 1.21$ .

Next, we determine the region where  $y_Z(r; a^2) > 0$ . The points where  $y_Z(r; a^2) = 0$  are given by the relation

$$r^4(r-3) + ra^2[r(r-3) + 6] - 2a^4 = 0, \quad (62)$$

which we denote as the implicit form of the function  $a_{Z0}^2(r)$ . Note that in the plane  $(r^+ \times a^2)$ , this function determine the curve (see Fig. 8), which consists of two parts determined by the solution of (62), i.e., by the relation

$$a^2 = a_{Z0\pm}^2(r) \equiv \frac{1}{4}r\{6 + r(r-3) \pm \sqrt{(r-1)[r^2(r+3) - 36]}\} \quad (63)$$

The maximum  $a_{Z0,\max}^2 \doteq 1.37$  of this function is located at  $r_{Z0,\max} \doteq 0.81$ . In addition, this point divides one part of the curve into the “left” and “right” parts denoted by  $a_{Z01}^2(r)$  and  $a_{Z02}^2(r)$ . We denote the other part of this curve as  $a_{Z03}^2(r)$ . The asymptotic behaviour of the function  $y_Z(r; a^2)$  and (62) determine the region in the plane  $(r^+ \times a^2)$  where  $y_Z(r; a^2) > 0$  (see Fig. 8).

The plane  $(r^+ \times a^2)$  can be divided into two regions: the region  $Y$  where the function fulfils the conditions (59) and (60), i.e., where the existence of the circular orbits with  $Z_r = 0$  is possible, and the region  $N$  where the existence of the circular orbits with  $Z_r = 0$  is not possible. We can also divide the region  $Y$  into six subregions with respect to the radial coordinate  $r$ :  $A$ -region ( $r_{Zh2} < r < r_{Z03}$ ),  $B$ -region ( $0 < r < r_{Z01}$ ),  $C$ -region ( $r_{Z02} < r < r_{Zh1}$ ),  $D$ -region ( $r_{Z02} < r < r_{Z03}$ ),  $E$ -region ( $0 < r < r_{Z01}$ ), and  $F$ -region ( $0 < r < r_{Z03}$ ) (see Fig. 8). It is useful to introduce  $y_{Z01}$  and  $y_{Z02}$  as the values of the function  $y_Z(r; a^2)$  at the “left” and “right” parts of the curve  $a_{Z0}^2(r)$ . The common point of the functions  $a_{Zh}^2(r)$  and  $a_{Z0}^2(r)$  takes the value  $a_{Zh0,\text{int}}^2 = 1$  and is located at  $r_{Zh0,\text{int}} = 1$ .

### 5.2.2 Number of circular orbits with $Z_r = 0$

The number of the circular orbits with  $Z_r = 0$  depends on the number of local extrema of the function  $y_Z(r; a^2)$ . The stationary points of the function  $y_Z(r; a^2)$  are determined (due to the condition  $\partial_r y_Z(r; a^2) = 0$ ) by the relation

$$0 = 5a^4 + 12r^2a^2 + 3r^4 - \left\{ \sqrt{a^4r^3(a^2 + 3r^2)[8a^4 + r(16r + 1)a^2 + r^3(8r + 3)]} \right\}^{-1} \\ \times \left\{ r[12a^8 + r(48r + 1)a^6 + 3r^3(24r + 1)a^4 \right. \\ \left. + 3r^5(16r + 1)a^2 + 3r^7(4r + 3)]a^2 \right\}, \quad (64)$$

which we denote as the implicit form of the function  $a_{Ze}^2(r)$ . This function also determines the curve in the plane  $(r^+ \times a^2)$  (see Fig. 10a). The maximum  $a_{Ze,\max}^2 \doteq 1.81$  of this function divides the curve into the “left” and “right” parts denoted by  $a_{Ze1}^2(r)$  and  $a_{Ze2}^2(r)$ . The “right” part of this curve corresponds to the local maxima of the function  $y_Z(r; a^2)$ , the left part corresponds to the local minima, whereas these extrema coalesce at  $r_{Ze,\max} \doteq 1.33$  (see Fig. 10b). Notice that in the Kerr–de Sitter spacetimes, even three circular orbits with  $Z_r = 0$  can occur in the case of two local extrema of the function  $y_Z(r; a^2)$ . It is also useful to introduce  $y_{Ze1}$  and  $y_{Ze2}$  as the values of the function  $y_Z(r; a^2)$  at the points of the “left” and “right” parts of the curve  $a_{Ze}^2(r)$ .

The common point of the functions  $a_{Zh}^2(r)$  and  $a_{Ze}^2(r)$  is identical with the maximum of the function  $a_{Zh}^2(r)$ .

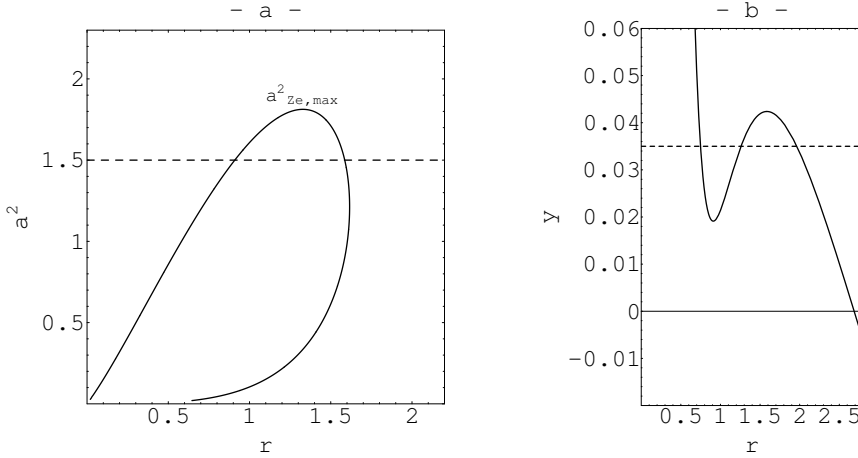


**Figure 10.** (a) Curve  $a^2_{Ze}(r)$ . The intersections of the dashed line  $a^2 = 1.5$  with this curve determine the stationary points of the function  $y_Z(r; a^2)$  for the specific value of the parameter  $a^2 = 1.5$  (compare with the next part of the figure). (b) Behaviour of function  $y_Z(r; a^2)$  for the specific value of the parameter  $a^2 = 1.5$ . Intersections of the dashed line  $y = 0.035$  with the graph of the function  $y_Z(r; 1.5)$  determine radii of circular orbits with  $Z_r = 0$  in the Kerr–de Sitter spacetimes with the parameters  $a^2 = 1.5$  and  $y = 0.035$ .

### 5.2.3 Classification of Kerr–de Sitter spacetimes

Using the rotational and cosmological parameters, we can give the following classification of the Kerr–de Sitter spacetimes (see Fig. 11).

**Class ZI:** ( $0 < a^2 \leq 1$ )

In these spacetimes, there are 2 regions of  $r$  where the existence of the orbits with  $Z_r = 0$  is possible: *A*-region and *B*-region.

(a) spacetimes with  $0 < y < y_{Zh2}$  are BH spacetimes containing:

- 1 orbit in the *A*-region (in the outer BH region),
- 1 orbit in the *B*-region (in the inner BH region).

(b) Spacetimes with  $y \geq y_{Zh2}$  are NS spacetimes containing:

- 1 orbit in the *B*-region.

**Class ZII:** ( $1 < a^2 < 1.21$ )

In these spacetimes, there are 3 regions of  $r$  where the existence of the orbits with  $Z_r = 0$  is possible: *A*-region, *B*-region, and *C*-region

(a) spacetimes with  $0 < y < y_{Zh1}$  are NS spacetimes containing:

- 1 orbit in the *A*-region,
- 1 orbit in the *B*-region,

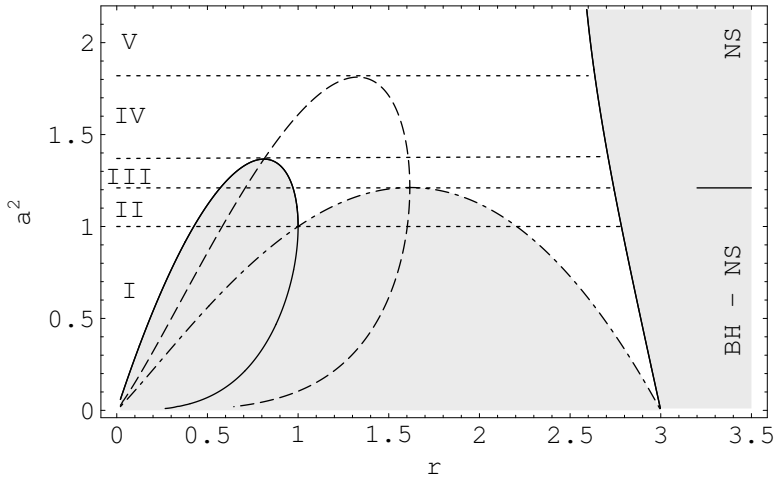


**Figure 11.** Curves  $a_{Zh}^2(r)$  (dashed and dotted),  $a_{Z0}^2(r)$  (solid),  $a_{Ze}^2(r)$  (dashed), and regions *I*, *II*, *III*, *IV*, and *V* (separated by dashed lines) corresponding to the classification of the Kerr–de Sitter spacetimes.

- 1 orbit in the *C*-region
- (b) spacetimes with  $y_{Zh1} \leq y < y_{Zh2}$  are BH spacetimes containing:
  - 1 orbit in the *A*-region (in the outer BH region),
  - 1 orbit in the *B*-region (in the inner BH region).
- (c) Spacetimes with  $y \geq y_{Zh2}$  are NS spacetimes containing:
  - 1 orbit in the *B*-region

**Class ZIII:** ( $1.21 \leq a^2 \leq 1.37$ )

These spacetimes are NS spacetimes. There are 2 regions of  $r$  where the existence of the orbits with  $Z_r = 0$  is possible: *D*-region and *E*-region. They can be divided into 2 subclasses.

**Subclass ZIIIa:** ( $a^2 = 1.21$ )

- (a) spacetimes with  $0 < y < y_{Ze2}$  contain:
  - 2 orbits in the *D*-region,
  - 1 orbit in the *E*-region
- (b) spacetimes with  $y \geq y_{Ze2}$  contain:
  - 1 orbit in the *E*-region

**Subclass ZIIIb:** ( $1.21 < a^2 \leq 1.37$ )

- (a) spacetimes with  $0 < y < y_{Ze2}$  contain:

- 2 orbits in the  $D$ -region,
  - 1 orbit in the  $E$ -region
- (b) spacetimes with  $y = y_{Ze2}$  contain:
- 1 orbit in the  $D$ -region,
  - 1 orbit in the  $E$ -region
- (c) spacetimes with  $y > y_{Ze2}$  contain:
- 1 orbit in the  $E$ -region

**Class ZIV:** ( $1.37 < a < 1.81$ )

These spacetimes are NS spacetimes.

- (a) spacetimes with  $0 < y < y_{Ze1}$  contain: 1 orbit
- (b) spacetimes with  $y = y_{Ze1}$  contain: 2 orbits
- (c) spacetimes with  $y_{Ze1} < y < y_{Ze2}$  contain: 3 orbits
- (d) spacetimes with  $y = y_{Ze2}$  contain: 2 orbits
- (e) spacetimes with  $y > y_{Ze2}$  contain: 1 orbit

**Class ZV:** ( $a^2 \geq 1.81$ )

These spacetimes are NS spacetimes and contain 1 circular orbit with  $Z_r = 0$  for any  $y > 0$ .

#### 5.2.4 Schwarzschild-de Sitter and Kerr case

In the Schwarzschild-de Sitter spacetimes ( $a^2 = 0, y > 0$ ), we obtain from (45) that the centrifugal force is given by the relation

$$Z_r = m(\gamma v)^2 \frac{(3 - r)}{r(2 - r + r^3 y)}. \quad (65)$$

Notice that the centrifugal force vanishes on the circular orbit with the radius  $r = 3$  independently of the value of the cosmological parameter and the velocity. The centrifugal force also changes its orientation on this orbit.

In the Kerr spacetimes ( $a > 0, y = 0$ ), we obtain from (45) that the centrifugal force is given by the relation

$$Z_r = m(\gamma v)^2 \frac{-r^4(r - 3) + ra^2[r(r - 3) + 6] - 2a^4}{r \Delta_r [(r + 2)a^2 + r^3]}. \quad (66)$$

Clearly, in the Kerr spacetimes, this force is also defined only in the region determined by  $\Delta_r > 0$ , i.e., in the region determined by  $a^2 > r(2 - r)$ . The equality in this equation determines the function (with the maximum  $a_{h,\max}^2 = 1$  at  $r_{h,\max} = 1$ ), which divides the plane ( $r^+ \times a^2$ ) into the stationary and dynamic regions (see Fig. 12). The centrifugal force vanishes independently of the velocity on the circular orbit with radii determined by the relation

$$r^4(r - 3) + ra^2[r(r - 3) + 6] - 2a^4 = 0. \quad (67)$$

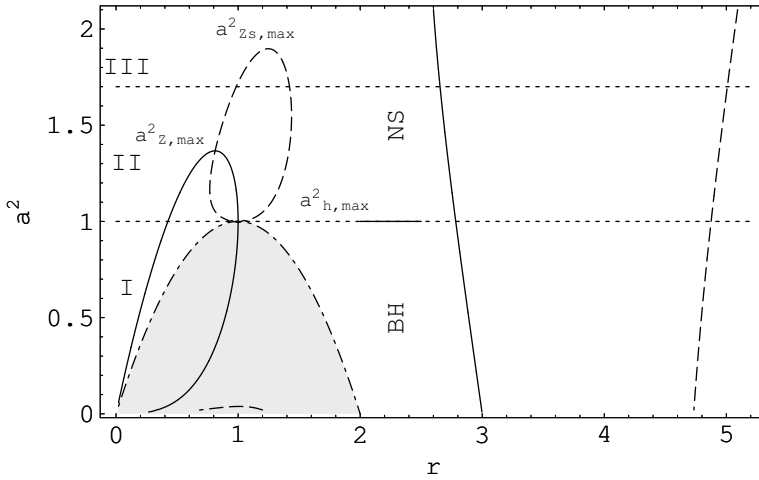


**Figure 12.** Curves  $a_Z^2(r)$  (solid),  $a_{Zs}^2(r)$  (dashed),  $a_h^2(r)$  (dashed and dotted) enclosing dynamic area (gray), and regions *I*, *II*, and *III* corresponding to the classification of the Kerr spacetimes. The intersections of a line  $a^2 = \text{const}$  with the curve  $a_Z^2(r)$  determine the radii of the circular orbits with  $Z_r = 0$ , the intersections with the curve  $a_{Zs}^2(r)$  determine the radii where the centrifugal force  $Z_r$  has stationary points, and the intersections with the curve  $a_h^2(r)$  determine the positions of black-hole horizons in the Kerr spacetimes with the parameter  $a$ .

We denote this equation as the implicit form of the function  $a_Z^2(r)$  which determines the curve in the plane  $(r^+ \times a^2)$  (see Fig. 12). Note that the function  $a_Z^2(r)$  is identical with the function  $a_{Z0}^2(r)$  and that the maximum  $a_{Z,\text{max}}^2 \doteq 1.38$  of this function is located at  $r_{Z,\text{max}} \doteq 0.81$ . By using the condition  $\partial_r Z_r = 0$  we obtain the function  $a_{Zs}^2(r)$ , which determines the stationary points of the centrifugal force (see Fig. 12). The maximum  $a_{Zs,\text{max}}^2$  and the minimum  $a_{Zs,\text{min}}^2 \equiv a_{h,\text{max}}^2$  of this function are the only inflexion points of the centrifugal force. The other points determined by the function  $a_{Zs}^2$  corresponds to local extrema.

Using the rotational parameter, we can now give the following classification of the Kerr spacetimes (see Fig. 12).

**Class ZI:** ( $0 < a^2 \leq 1$ )

These spacetimes are BH spacetimes. In the inner stationary region, there is only 1 orbit with  $Z_r = 0$ . On this orbit, the centrifugal force also changes its orientation. In the outer stationary region, there is also only 1 such orbit.

**Class ZII:** ( $1 < a^2 \leq 1.38$ )

These spacetimes are NS spacetimes. There are 3 orbits with  $Z_r = 0$  for  $a^2 < 1.38$  and there are 2 such orbits for  $a^2 = 1.38$ , but on the first of these orbits, the centrifugal force does not change its orientation.

**Class ZIII:** ( $a^2 > 1.38$ )

These spacetimes are NS spacetimes. There is only 1 orbit with  $Z_r = 0$ . On this orbit the centrifugal force changes its orientation.

## 6 CONCLUSIONS

The Kerr–de Sitter black-hole spacetimes contain two stationary regions in the equatorial plane. The inner region is limited by the singularity ( $r = 0$ ) and by the inner black-hole horizon ( $r = r_{h-}$ ). The outer region is limited by the outer horizon ( $r = r_{h+}$ ) and by the cosmological horizon ( $r = r_c$ ). For any given values of the rotational parameter  $a$  and the cosmological parameter  $y$ , in each of these regions, there is only one circular orbit where the gravitational force vanishes, and the only one orbit, where the centrifugal force vanishes independently of the velocity. Both the gravitational and centrifugal forces change their orientations on these orbits. The same situation occurs in the Kerr black-hole spacetimes [Stuchlík and Hledík, 1999a], except the outer stationary region, where there is no circular orbit where the gravitational force vanishes, in contrast to the Kerr–de Sitter outer stationary region. In the only one stationary region of the Schwarzschild–de Sitter spacetimes [Stuchlík and Hledík, 1999b], there is also only one such circular orbit.

The Kerr–de Sitter naked-singularity spacetimes contain one stationary region between the singularity ( $r = 0$ ) and the cosmological horizon ( $r = r_c$ ). In these spacetimes, even three circular orbits where the gravitational force vanishes and three circular orbits where the centrifugal force vanishes independently of the velocity can occur, indicating a relatively complex structure of these spacetimes as a result of mixed influence of rotation of the source and the cosmological repulsion. It is more complicated situation than in the Kerr naked-singularity spacetimes [Stuchlík and Hledík, 1999a, de Felice, 1974], where the maximum number of the orbits where the gravitational vanishes is only two. There are also most three circular orbits where the centrifugal force vanishes independently of the velocity.

## Acknowledgements

The work was supported by the grant GAČR No. 205/03/1147 and by the Committee for collaboration of the Czech Republic with CERN. One author (Z. S.) would like to thank Theory Division of CERN for perfect hospitality.

## REFERENCES

- [Abramowicz, 1990] Abramowicz, M. A. (1990). Centrifugal force – a few surprises. *Monthly Notices Roy. Astronom. Soc.*, 245(4):733–746.
- [Abramowicz et al., 1988] Abramowicz, M. A., Carter, B., and Lasota, J. (1988). *Gen. Relativity Gravitation*, 20:1173.
- [Abramowicz et al., 1993a] Abramowicz, M. A., Miller, J., and Stuchlík, Z. (1993a). Concept of radius of gyration in general relativity. *Phys. Rev. D*, 47(4):1440–1447.
- [Abramowicz and Miller, 1990] Abramowicz, M. A. and Miller, J. C. (1990). Ellipticity behaviour of relativistic Maclaurin spheroids. *Monthly Notices Roy. Astronom. Soc.*, 245(4):729.
- [Abramowicz et al., 1993b] Abramowicz, M. A., Nurowski, P., and Wex, N. (1993b). Covariant definition of inertial forces. *Classical Quantum Gravity*, 10(10):L183.

- [Abramowicz et al., 1995] Abramowicz, M. A., Nurowski, P., and Wex, N. (1995). Optical reference geometry for stationary and axially symmetric spacetimes. *Classical Quantum Gravity*, 12(6):1467.
- [de Felice, 1974] de Felice, F. (1974). Repulsive phenomena and energy emission in the field of a naked singularity. *Astronomy and Astrophysics*, 34:15–19.
- [Hledík, 2001] Hledík, S. (2001). Embedding diagrams of the ordinary and optical reference geometry of black-hole spacetimes and their astrophysical relevance. In Hledík, S. and Stuchlík, Z., editors, *Proceedings of RAGtime 2/3: Workshops on black holes and neutron stars, Opava, 11–13/8–10 October 2000/01*, pages 25–52, Opava. Silesian University in Opava.
- [Hledík, 2002] Hledík, S. (2002). Optical geometry, inertial forces, and embedding diagrams. In Semerák, O., Podolský, J., and Žofka, M., editors, *Gravitation: Following the Prague Inspiration (A Volume in Celebration of the 60th Birthday of Jiří Bičák)*, pages 161–192, New Jersey, London, Singapore, Hong Kong. World Scientific.
- [Jantzen et al., 1992] Jantzen, R. T., Carini, P., and Bini, D. (1992). The many faces of gravitoelectromagnetism. *Ann. Physics*, 215(1):1–50.
- [Stuchlík and Hledík, 1999a] Stuchlík, Z. and Hledík, S. (1999a). Embedding diagrams of the optical geometry of Kerr backgrounds. *Acta Phys. Slovaca*, 49(5):795–803.
- [Stuchlík and Hledík, 1999b] Stuchlík, Z. and Hledík, S. (1999b). Some properties of the Schwarzschild–de Sitter and Schwarzschild–anti-de Sitter spacetimes. *Phys. Rev. D*, 60(4):044006 (15 pages).
- [Stuchlík and Hledík, 2000] Stuchlík, Z. and Hledík, S. (2000). Equatorial photon motion in the Kerr–Newman spacetimes with a non-zero cosmological constant. *Classical Quantum Gravity*, 17(21):4541–4576.
- [Stuchlík and Hledík, 2002] Stuchlík, Z. and Hledík, S. (2002). Properties of the Reissner–Nordström spacetimes with a nonzero cosmological constant. *Acta Phys. Slovaca*, 52(5):363–407.
- [Stuchlík et al., 2001] Stuchlík, Z., Hledík, S., Šoltés, J., and Østgaard, E. (2001). Null geodesics and embedding diagrams of the interior Schwarzschild–de Sitter spacetimes with uniform density. *Phys. Rev. D*, 64(4):044004 (17 pages).
- [Stuchlík and Slaný, 2004] Stuchlík, Z. and Slaný, P. (2004). Equatorial circular orbits in the Kerr–de Sitter spacetimes. *Phys. Rev. D*, 69:064001.

# Astrophysical clouds in galactic nuclei. Monte Carlo simulations

Petr Nováček

*Faculty of Mathematics and Physics, Charles University, CZ-180 00 Prague, Czech Republic;  
Astronomical Institute, Academy of Sciences, Prague, Czech Republic*

## ABSTRACT

This article deals with the numerical simulations of the astrophysical systems located in the inner most parts of the galaxies – so called Active Galactic Nuclei (AGNs). Our simulation we are going to describe in this paper is treated in the Monte Carlo way and is used to solve the Fokker-Planck equation of our system to obtain its time evolution while taking into account all the relevant physical mechanisms involved in the system evolution. In the beginning of the paper we outline the system we would like to study in our simulations and then we summarise the physical ingredients involved in our model of the system. The largest part of the paper will be devoted to the description of the simulation method used to simulate a spherical star cluster as one part of the model of our system. Finally we present some results of such a simulation and draw an outline of the future prospects of our research.

**Keywords:** Monte Carlo – numerical simulations – Active Galactic Nuclei – star clusters – clouds

## 1 INTRODUCTION

The aim of this work is to develop a numerical code capable to simulate an accretion disk surrounding a massive black hole located in the galactic nucleus taking into account the gravitational effects caused by a stellar cluster around the galactic nucleus. The numerical code used to simulate this system should be based on Monte Carlo numerical scheme. We would like to concentrate on the interaction between the surrounding star cluster and the accretion disk in order to study the behaviour of outer parts of the accretion disk. The result of this study should be the model of so called Broad Line Regions (BLR) that were observed in AGNs. The model we would like to prove using our simulations describes the existence of BLRs in AGNs as the result of the fragmentation of outer parts of the accretion due to gravitation of the surrounding stellar cluster – these regions where broad lines of AGNs spectra are formed comprise of the fragments (clouds) of the accretion disk. Having these clouds in the outer parts of our system it is easy to describe the formation of broad lines in the active galactic nuclei spectra as they are observed. Thus the main aim of the work is to simulate this system and create the fragments of the accretion disk in some reasonable physical way.

## 2 MODEL OF THE SYSTEM

The system we are going to simulate consists of three crucial subsystems:

(i) Central black hole. This black hole is the massive one with the mass equal to  $10^6$ – $10^9$  sun masses. We do not take care about the formation of such a massive black hole. But we just suppose there is such a massive object with strong tidal gravitational field and we take into account the effects connected with the presence of such an object in our system – overall gravitational field, tidal disruption, growth of the central massive object due to matter inflow from the accretion disk.

(ii) Accretion disk. We assume an axial symmetric accretion disk surrounding the central black hole. We employ a model of thin self-gravitating accretion disk. In this paper we do not discuss in detail the properties of accretion disk and its interaction with other subsystems. We will focus on the third component of our system – the stellar cluster.

(iii) Stellar cluster. We consider a spherical symmetric stellar cluster surrounding the subsystem of central black hole and the accretion disk that extends up to several parsecs far from the centre of our system. The central cluster is rich and comprises of several  $10^6$  of stars. In addition we suppose the system is in a dynamical equilibrium – we do not want to handle an initial phase of the system evolution when the rapid collective motions occur frequently. The evolution of the star cluster itself is driven mainly by 2-body relaxation but we would like to consider also another physical mechanisms like stellar collisions.

Having an idea how the system looks like we turn to the physics that is involved in our system and to physical mechanisms we want to take into account in the system evolution. The physical processes that influence significantly the system evolution are the following ones [Freitag and Benz, 2001]:

- Relaxation. The relaxation drives the evolution of the stellar cluster in our system for the significant fraction of live time (simulation time) of the system. We simulate the relaxation as 2-body distant encounters (weak encounters) of the stars in the cluster when only the orbital energy and angular momentum of interacting stars are redistributed. When the same model of relaxation is applied to a standard globular cluster it leads to a gravo-thermal catastrophe of the cluster when the central dense core and diffuse halo forms after several billions of years.
- Stellar collisions. The collisions influence significantly the evolution of the stellar cluster in the final phase of its evolution when the central dense core is built. The collisions become as important as the relaxation when the velocity dispersion of the cluster is about  $1000 \text{ km s}^{-1}$ . Thus the collisions are important only in the central parts of the cluster.
- Stellar evolution. Because we would like to simulate the system evolution during several  $10^9$  of years we must allow stars to evolve during this time. The stars lose their mass and also change their diameter during their evolution. These changes affect the strength of other processes we are taking into account especially stellar collisions – stars in giant phase have higher cross section than the star remnants.
- Tidal disruptions. The tidal field generated by the massive central black hole destroys the stars that come too close to the centre and also it causes a systematic depletion of some stellar orbits in the cluster. These stars then become a fuel for the continuous growth of the central black hole.

- Growth of the central black hole. As the stars come too close to the centre they are destroyed by the tidal field of the black hole and they become a part of an accretion disk surrounding the black hole. So there is a continuous accretion of gas to the central black hole leading to a continuous growth of its mass. The higher the mass of the black hole is the deeper is the potential generated by the black hole and so the higher is the tidal disruption rate and the higher are the stellar velocities in the cluster.

If we want to cope with all these physical processes in our simulation the code we are going to develop must meet some important requirements. First it must be able to simulate our system evolution for several billions of years. It implies the time step of the evolution cannot be of order of orbital time of a star but rather of a relaxation time of the system. The second requirement arises from the necessity to simulate the star evolution so the code must allow an arbitrary mass distribution of stars in the cluster. Third important requirement is the non-isotropic velocity distribution that should be handled in the simulation in order to simulate a tidal disruption in a realistic way.

Having all these requirements and having in mind we should use a Monte Carlo approach we turn our attention to the algorithm developed by Hénon in 1960s [Hénon, 1971]. This algorithm was originally developed to simulate the evolution of spherical stellar system such a globular cluster so we use it to simulate the evolution of the third part of our system – the surrounding star cluster. The biggest advantage of this algorithm is its speed - it uses the fraction of relaxation time as a time step and gains a lot from the spherical symmetry of the system so the simulation of the medium size system can be performed on a standard personal computer taking acceptable CPU time.

### 3 ASSUMPTIONS AND FOUNDATION STONES OF THE METHOD

Our algorithm used to simulate a stellar cluster surrounding the central black hole with the accretion disk is based on Hénon Monte Carlo algorithm for globular clusters [Hénon, 1971].

The algorithm relies on several assumptions about the simulated system. The first assumption is the spherical symmetry of the simulated system. Having the system exactly spherical symmetric it allows us to simplify the computation of potential and of the distant encounters significantly (see later). It also allow us to represent the system structure easily. We will treat the stellar cluster as the set of  $n$  concentric spherical shells (so called superstars) where each shell consists of  $K$  stars. The individual stars in a certain shell have the similar orbital and stellar parameters and all the processes affect them at the same time. Parameter  $K$  is the free parameter if the proper physical units are chosen. The individual stars are randomly distributed within one superstar (on the shell surface) so the only coordinates is the radial distance of the superstar  $R$ . Similarly the transverse velocity of individual stars is assumed to be distributed randomly. Thus we characterise each superstar with radial distance  $R$ , angular momentum  $A$ , energy  $E$ , radial and transverse velocities  $v_r$ ,  $v_t$  and mass  $M$ .

The algorithm can handle only well relaxed systems, i.e., the system must be in dynamical equilibrium. The method can simulate only old systems where all the collective motions from the initial evolution phase disappeared. The first advantage is that we can take a fraction

of the system relaxation time as the simulation time step because only the relaxation drives the evolution of the cluster (rapid motions disappeared). The relaxation time of the self-gravitating system is given by:

$$t_r = C_1 \frac{N}{\ln N} t_c, \quad (1)$$

where  $t_c$  is the system crossing time that can be computed as:

$$t_c = C_2 \frac{GM^{\frac{5}{2}}}{\epsilon^{\frac{3}{2}}}. \quad (2)$$

$\epsilon$  is the total system energy and  $M$  is its total mass. As the time step for the simulation we take a fraction of the relaxation time:

$$\Delta t = b \frac{GN}{\ln N} \frac{M^{\frac{5}{2}}}{\epsilon^{\frac{3}{2}}}. \quad (3)$$

where  $b$  is the small proportional constant. We take 0.005 for  $b$  in our simulations.

The second advantage of the system equilibrium is that the distribution function of the particles has a form of discretised one-particle distribution function and depends only on integrals of motion:

$$f = F(E, A, m), \quad (4)$$

where  $E$  is the energy per unit mass and  $A$  is the angular momentum per unit mass

$$E = U(r) + \frac{1}{2}(v_r^2 + v_t^2), \quad (5)$$

$$A = r v_t, \quad (6)$$

where  $U(r)$  is the gravitational potential at  $r$  and  $v_r$  and  $v_t$  are radial and transverse velocities of a star.

The third assumption is the local approximation assumption. This assumption is based on the simplification made to the distant encounters treatment. Because the perturbation caused by the field star to the test star is proportional to

$$\sim \ln \frac{Nl}{R}, \quad (7)$$

the biggest perturbation comes from the star from the closest vicinity of the test star. Thus we can say the mass and velocity distribution of field stars is everywhere the same and we can take instead of it the local mass and velocity distribution function of the test star that does not depend on the position of the field star (is space-independent). It allows us to select the position of the field star in the first step independently on its mass and velocity that can be selected in the second step of the algorithm.

The initial conditions, i.e., the initial distribution function can be arbitrary but must fulfil the requirement of dynamical equilibrium of the system. In our simulations we use Plummer's model (polytrope of index 5) where the density distribution function is given by:

$$\rho(r, 0) = \frac{3}{4}\pi \frac{M}{R^3 \left(1 + \left(\frac{r}{R}\right)^2\right)^{\frac{5}{2}}}, \quad (8)$$

where  $M$  is the total system mass and  $R$  is the dimensional parameter. The corresponding potential is then:

$$U(r, 0) = -\frac{GM}{R \left[1 + \left(\frac{r}{R}\right)^2\right]^{1/2}}. \quad (9)$$

The generation of initial conditions is done in Monte Carlo way using random numbers and von Neumann's rejection techniques to sample the given initial distribution of velocities. The detailed description of the algorithm for generation of Plummer's mass distribution can be found in [Aarseth and Hénon, 1974].

#### 4 MAIN ALGORITHM

In order to simulate a relaxation within the cluster we need a background potential of the system in which the test star will move when it is being perturbed. The background potential is generated by all the stars in the cluster and also there is the contribution from the central black hole. Because the cluster is far from the central black hole we can treat the black hole potential in a Newtonian approximation.

The potential of the stellar cluster can be computed as the potential of  $n$  spherical concentric shells (superstars) according to our representation of the cluster. Using Newton's theorems we can write for the potential at any distance  $r$  from the centre between superstar of rank  $k$  and  $k + 1$ :

$$U(r) = U_{\text{BH}} + KG \left( -\frac{1}{r} \sum m_i - \sum \frac{m_i}{r_i} \right). \quad (10)$$

During the simulation it is necessary to compute and store the values of potential only at the positions of the superstars:

$$U_k = U_{k+1} - GM_k \left( \frac{1}{r_k} - \frac{1}{r_{k+1}} \right), \quad (11)$$

$$M_k = M_k - Km_k, \quad (12)$$

$$k = n, \dots, 1, \quad (13)$$

$$U_n = 0, \quad (14)$$

$$M_{n+1} = M. \quad (15)$$

The potential at any other radial distance, if needed, is then computed using the stored potential at two nearest shells and the linear interpolation.

Having the potential computed we can simulate the distant encounter of the test star to a field star. The simulation of 2-body relaxation through distant (weak) encounters can be done in the Monte Carlo manner, i.e., the effect of the encounter can be estimated by sampling. But here the mean perturbation of the test star caused by the field star can be easily computed exactly. Thus we compute the effect exactly and then we choose such a

field star whose effect to a test star will equal to the computed one. It is correct to do so because as we discussed above we can use local approximation assumption and select the position of the field star independently on its mass and velocity. These latter two quantities can be selected separately and we take them from the nearest field star.

Considering weak encounters and using a reference frame co-moving with the centre of mass of the test and field star we can derive for the weak encounter the following equation for the impact parameter  $l$  and deflection angle  $\beta$ :

$$l = \sqrt{\frac{2r^2 \Delta r}{(p-1)K w \Delta t \ln N}}, \quad (16)$$

$$\beta = 2 \arctan \frac{G(m+m')}{w^2 l} \quad (17)$$

where  $w$  stays for the relative velocity of the field and test star,  $\Delta r$  is the relative radial distance of these two stars,  $m$  and  $m'$  are the masses of the test and field star and  $\Delta t$  is the time step given by (3). According to this equation we choose the second nearest star ( $p = 2$ ) as the field star. In this way we create the superstar pairs: 1-3, 2-4, 5-7 etc. and compute the encounter for all these pairs where each star acts as a field star and then as a test star. The result of each encounter is the redistribution of the orbital energy and the angular momentum between test and field star, i.e., the velocities of the test star and the field star are perturbed accordingly.

In order to compute new perturbed velocities for both stars we need to know the angle  $\psi$  between the co-moving plane and some reference plane. We compute angle  $\psi$  as a random number between 0 and  $2\pi$  because the distribution of field stars is homogenous. Generating random angle  $\psi$  and computing the deflection angle for a pair of superstars using (16) we compute new perturbed relative velocity of these two superstars  $w^*$ :

$$w^* = w \cos \beta + w_1 \sin \beta \cos \psi + w_2 \sin \beta \sin \psi, \quad (18)$$

$$w_1 = \left( \frac{w_y w}{w_p}, -\frac{w_x w}{w_p}, 0 \right), \quad (19)$$

$$w_2 = \left( -\frac{w_x w_z}{w_p}, -\frac{w_y w_z}{w_p}, w_p \right), \quad (20)$$

$$w_p = \sqrt{w_x^2 + w_y^2}, \quad (21)$$

where  $w_x$ ,  $w_y$  and  $w_z$  are the components of original relative velocity  $w$ .

Having new relative velocity we calculate new velocities  $v^*$  and  $v'^*$  of both test and field star after encounter:

$$v^* = v - \frac{m'}{m+m'} (w^* - w), \quad (22)$$

$$v'^* = v' + \frac{m}{m+m'} (w^* - w). \quad (23)$$

Finally we compute new radial velocity  $v_r^*$ , transverse velocity  $v_t^*$ , energy  $E^*$  and angular momentum  $A^*$  for both stars:

$$v_r^* = v_z^*, \quad (24)$$

$$v_t^* = \sqrt{v_x^{*2} + v_y^{*2}}, \quad (25)$$

$$E^* = U(r) + \frac{1}{2}(v_r^{*2} + v_t^{*2}), \quad (26)$$

$$A^* = r v_t^*. \quad (27)$$

The second step in the simulation of the encounter between a test star and a field star is the selection of new positions for each star according to the velocity perturbation induced by the encounter. To select a new radial distance for the star we use orbital equation of the star rosette orbit:

$$Q(r) = v_r^2 = 2E - 2U(r) - \frac{A^2}{r^2} = 0, \quad (28)$$

where  $E$  and  $A$  are the new perturbed energy and angular momentum of the star (test or field star). By solving the orbital equation we obtain the minimal and maximal radial distance  $r_{\min}$  and  $r_{\max}$  at which the star can occur.

The new position of the star must be selected with the probability distribution proportional to the function that describes the dependence of a time period the star spends at the different radii when moving on its rosette orbit. To sample this distribution  $f(r) = \frac{1}{|v_r|}$  we use von Neumann's rejection technique. Because of divergence of  $f(r)$  we introduce more suitable sampling function  $g(s)$ :

$$g(s) = \frac{1}{|v_r|} \frac{dr}{ds}, \quad (29)$$

that turns to a new function for  $r$ :

$$r = \frac{1}{2}(r_{\min} + r_{\max}) + \frac{1}{4}(r_{\max} - r_{\min})(3s - s^3). \quad (30)$$

Using this new function and normalising it we derive an empiric formula for the upper limit  $F$  of function  $g_s$  used for the rejection method:

$$F = 1.2 \max \left[ \frac{3(r_{\max} - r_{\min})}{Q'(r_{\min})}, \frac{-3(r_{\max} - r_{\min})}{Q'(r_{\max})} \right], \quad (31)$$

where  $Q'(r)$  is the derivation of (28). Computing this value we can proceed with the rejection algorithm: we generate two random numbers  $X$  and  $Y$  and compute the pair  $(s_0, g_0)$ :

$$s_0 = -1 + 2X, \quad (32)$$

$$g_0 = YF. \quad (33)$$

The corresponding value of  $r$  is taken as a new position of the star if the generated pair  $(s_0, g_0)$  satisfies the inequality:

$$g_0 < g(s_0), \quad (34)$$

otherwise new pair  $(s_0, g_0)$  must be generated. The pair  $(s_0, g_0)$  that satisfies the inequality is used to compute a new radial velocity  $v_r$  using (29) and the new position  $r$  using (30) for the given star. According to (28) we must select the sign of the radial velocity – it is selected randomly with the uniform probability. Finally we compute a new transverse velocity for the star as

$$v_t = Ar. \quad (35)$$

This procedure is repeated for all the pairs of superstars in order to obtain a new positions and velocities for each superstar after one time step  $\Delta t$ . Having new positions we can compute a new potential of the cluster using (11). The cycle is repeated until the given evolution time is not reached.

## 5 SIMULATION RESULTS

Because of the Monte Carlo nature of the simulation method the simulation results are never the same for the identical initial conditions. Therefore for one set of initial conditions the simulation is repeated several times (10–100 times) and the results of all the "sub-simulation" are then joined and averaged in the statistical way. Thus the results of the simulation has the statistical behaviour – the larger the number of sub-simulations is the more smoothed, averaged and realistic results are obtained.

The basic quantity that comes from the simulation is the time evolution of radii of each superstar. But these raw data alone are not too useful so we use them to compute better quantities - Lagrangian radii and particle density. Lagrangian radius is defined as the radius of the sphere that contains the given fraction of total cluster mass, e.g., Lagrangian radii  $R_{30}$  is the radius within 30% of the total cluster mass is concentrated.

First we done some code testing simulations. Such a simulation does not simulate relaxation driven evolution of the cluster, simply we switch off the relaxation algorithm. The only thing that the algorithm does is the re-positioning of the stars after each time step. We expect that the cluster does not evolve in sense of continuous changes of the radial distance of all the superstar, i.e., we suppose the Lagrangian radii remain roughly the same during the evolution of the cluster. This could be seen at Figs 1 and 2. As discussed above the figures show that when the relaxation is switched off the Lagrangian radii for the cluster do not evolve merely. But you can see a small slope of all the Lagrangian radii - this slope is caused by the spurious relaxation produced by the algorithm itself. This relaxation can be neglected because it is really small comparing the real relaxation or it can be filtered out by some modifications of the algorithm.

Second we performed simulations of 2 stellar clusters – one comprised of 5 000 superstars and the second formed by 10 000 superstars. The simulation time of the system was 5 billions years and 1 billion years respectively. The Lagrangian radii for each simulation are plotted in Figs 3, 4, 5 and 6.

First these figures illustrate the statistical behaviour of the simulation results. The more stars the cluster contains the more smoothed and averaged the results are and the larger the number of simulation repetitions is the more flattened the results are. It means the greater number of superstars is involved in the simulation the more realistic and precise the results of the simulation are.

The second noticeable thing shown on these 4 figures is the evolution of the cluster itself. As obtained in many other simulations the system evolves in the way it continuously forms a central dense core and builds up the diffuse extended halo. Thus also our simulation brings a gravo-thermal catastrophe to the cluster evolution as discussed in the beginning of this paper.

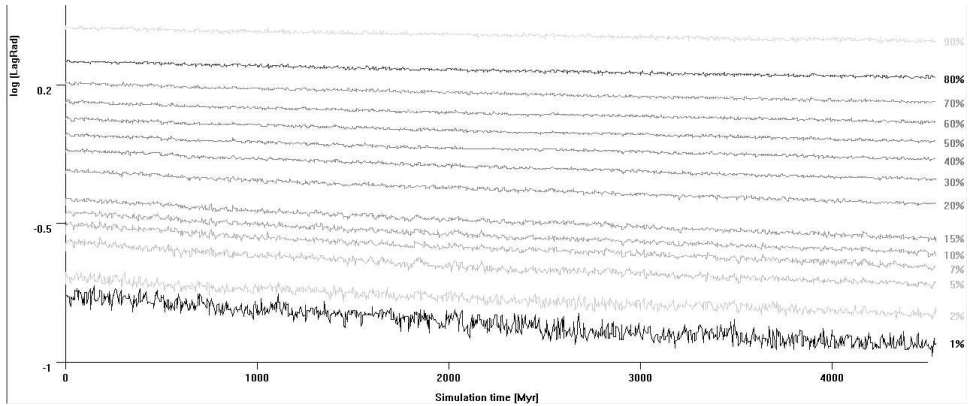


**Figure 1.** Lagrangian radii for cluster of 5000 superstars when the relaxation is switched off. The number of simulation repetitions is 1 and the evolution time is 5 billions years.

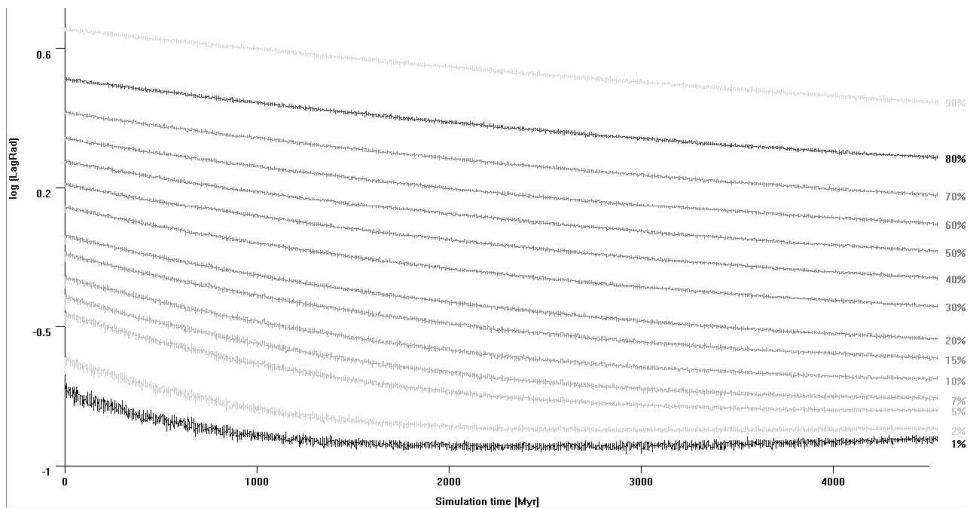


**Figure 2.** Lagrangian radii for cluster of 5000 superstars when the relaxation is switched off. The number of simulation repetitions is 10 and the evolution time is 5 billions years.

## 6 CONCLUSION

We developed a Monte Carlo code based on Hénon algorithm capable to treat a spherical symmetric stellar cluster whose evolution is driven by 2-body relaxation. The code is fast and optimised enough to perform a simulation of medium-sized cluster on a standard computer consuming realistic amount of CPU time. The results of our test simulations are promising because we obtained more or less realistic evolution of the cluster demonstrating the physical effects shown in many other simulations.

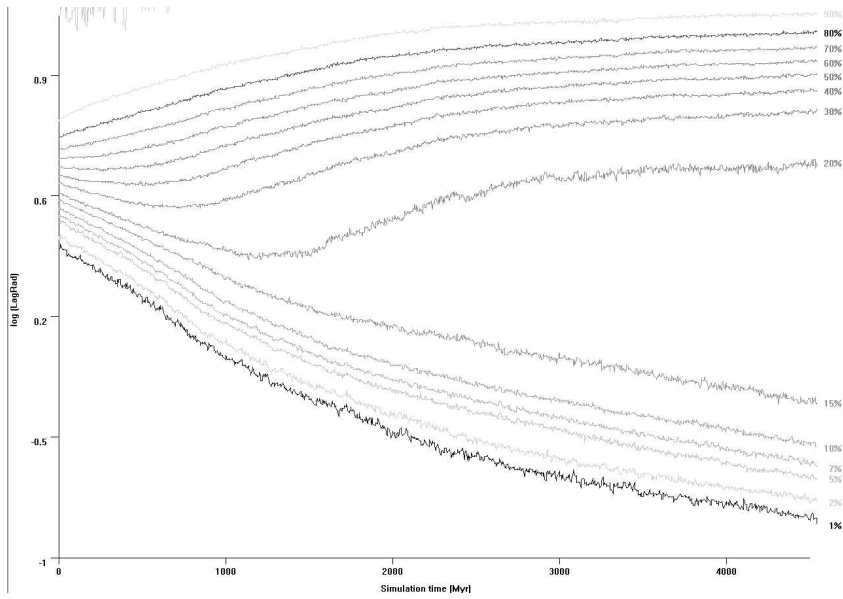


**Figure 3.** Lagrangian radii for cluster of 5000 superstars. The number of simulation repetitions is 1 and the evolution time is 5 billions years.

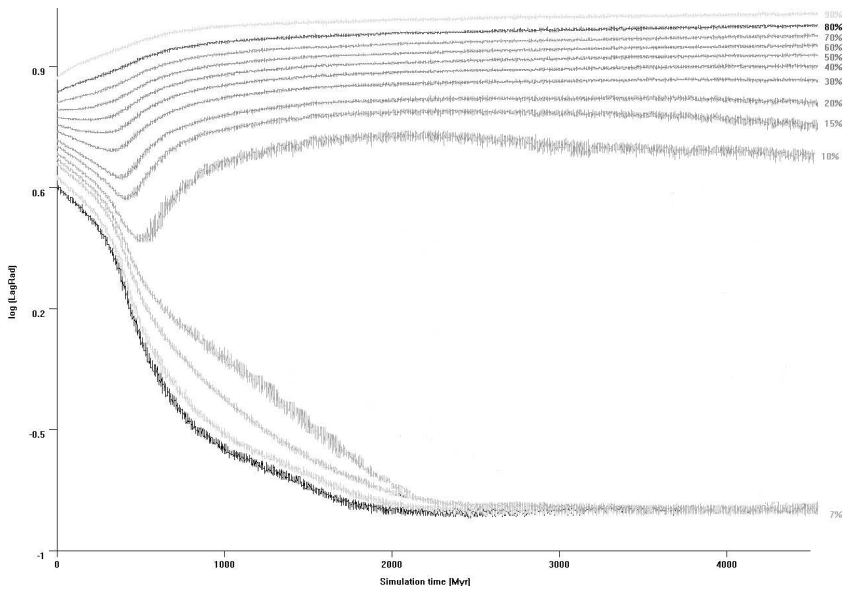


**Figure 4.** Lagrangian radii for cluster of 5000 superstars. The number of simulation repetitions is 10 and the evolution time is 5 billions years.

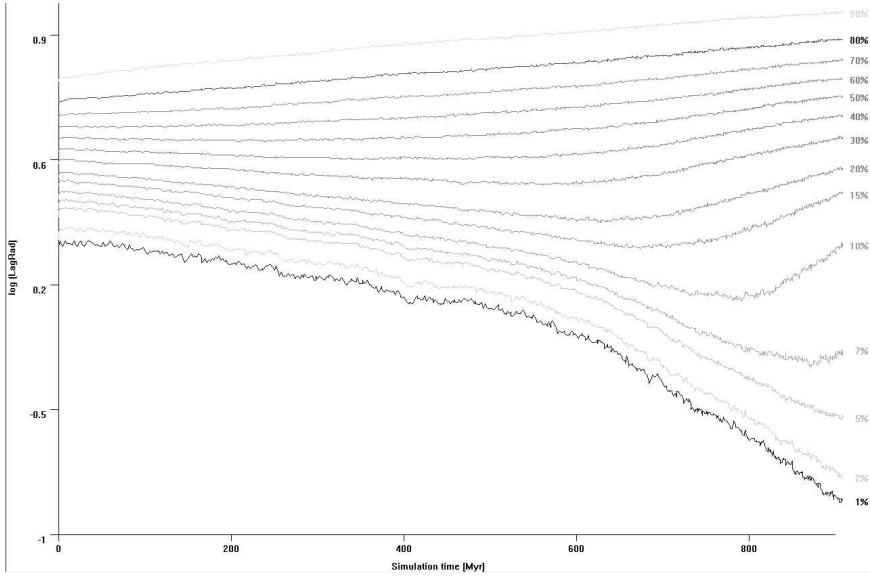


**Figure 5.** Lagrangian radii for cluster of  $10^4$  superstars. The number of simulation repetitions is 1 and the evolution time is 1 billion years.

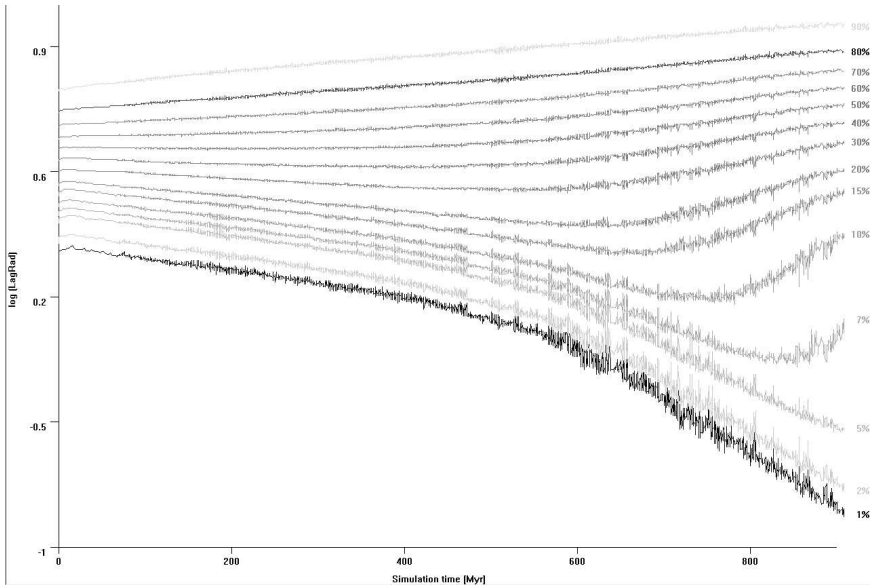


**Figure 6.** Lagrangian radii for cluster of  $10^4$  superstars. The number of simulation repetitions is 10 and the evolution time is 1 billion years.

In the future we are planning to involve other physical ingredients listed in the very beginning of this paper in order to treat the system evolution in more realistic way and in order to inspect the influence of these physical effect on the system, especially on the accretion disk. The big task for us will be the integration of the accretion disk into our simulation – it means to get rid of the spherical symmetry dependence of the algorithm or to incorporate somehow the axial symmetry into the algorithm in order to cope with the accretion disk.

## REFERENCES

- [Aarseth and Hénon, 1974] Aarseth, S. J. and Hénon, M. (1974). *Astronomy and Astrophysics*, 37:183.
- [Freitag and Benz, 2001] Freitag, M. and Benz, W. (2001). *Astronomy and Astrophysics*, 375:711.
- [Hénon, 1971] Hénon, M. (1971). *Astrophysics and Space Science*, 14:151.

# Decaying orbits near a rotating black hole

Tomáš Pecháček<sup>1</sup> and Vladimír Karas<sup>2</sup>

<sup>1</sup>*Faculty of Mathematics and Physics, Charles University, CZ-180 00 Prague, Czech Republic*

<sup>2</sup>*Astronomical Institute, Academy of Sciences, Prague, Czech Republic*

## ABSTRACT

We consider orbits of a test body near a rotating black hole. The orbits are perturbed by two effects which drive them away from purely geodesic motion: (i) dissipative interaction with an accretion disc, and (ii) variable driving force, magnitude of which depends on position of the body. The effect of dissipative interaction with the disc medium is proportional to its density, resulting in gradual orbital decay. The origin of the latter term, i.e., the driving force, is also linked to the presence of gas medium: it can be seen as a second order effect modulating the orbital decay. Hence, this effect is important when subsequent transits of the body through the disc medium occur at (almost) the same place during short time span. This kind of a variable perturbation is important because it adds new ingredients to the well-known properties of the geodesic motion.

In this note we consider a toy-model for decaying forced orbits in (non-axisymmetric) gravitational field of a rotating (Kerr) black hole [Chandrasekhar, 1992]. Geometrical setup of the system is as follows. Firstly, a central black hole determines the gravitational field in which motion takes place. Secondly, an accretion disc forms dissipative gaseous environment around the black hole; a Keplerian, geometrically thin non-selfgravitating disc is assumed. A particle in free-fall motion is followed outside the disc plane. It experiences small kicks when passing across the disc slab. In other words, when crossing the disc plane, instantaneous change of orbital parameters affects the trajectory and causes its gradual evolution (energy and angular momentum losses). A dissipative force acts against the particle velocity three-vector ( $\mathbf{v}$  when expressed locally in the disc co-rotating frame, “dcf”) at the moments of successive transits:

$$\Delta \mathbf{v} = -A_{\text{eff}} K \mathbf{v}, \quad (1)$$

where  $A_{\text{eff}}$  is effective cross-section of the body. It is only a starting motivation that  $A_{\text{eff}}$  should be roughly equal to the geometrical cross-sectional area of the body in hypersonic motion (for further details see, e.g., [Šubr and Karas, 2004] in this Volume, and references cited therein). Function  $K$  contains other parameters on which we do not concentrate our attention in the present discussion, e.g., density profile and geometrical height of the disc ( $\rho_d(r)$ ,  $h_d(r)$ ), the orbit inclination  $\theta_*$ , mass of the body  $m_*$ , etc. In order to draw specific examples we use the same form for  $K$  as in ref. [Karas et al., 2002], namely,  $K = \rho_d h_d (\gamma_{\text{dcf}} - 1) m_*^{-1} \gamma_{\text{dcf}}^{-3} v^{-2} \sin^{-1} \theta_*$ . Here, the Lorentz factor,  $\gamma_{\text{dcf}}$ , and sine of inclination angle,  $\sin \theta_*(r_*)$ , characterise the orbit at the point of its intersection with the disc, i.e.,  $r = r_*$ ,  $\theta = \pi/2$ .

Back-reaction of the disc due to transiting body can be included via secular modulation of the term  $A_{\text{eff}}$ . The modulation reflects feedback due to the disturbed disc and it effectively acts as a tiny driving force. It should be quite obvious that a simple analytical formula can hardly describe this process. Indeed, at this stage we do not specify the exact physical mechanism for the driving, which must depend on the detailed description of the medium and the body. It can be interpreted either as radiation force (cf. [Chandrasekhar, 1960]) or the gravitational effect of the perturbed disc [Karas et al., 2002]. In general, points of transition are scattered across the disc area in the whole range between the orbit pericentre and apocentre. Under special circumstances, however, subsequent transits occur close to each other. This assumption requires a special value of orbital parameters determining the orbit shape and precession.

Hence, we assume that the disc medium is disturbed more at those locations where the body transitions are repeated in a continuous sequence. When this happens? The orbit crosses the disc at specific values of radii if the corresponding epicyclic frequency is in rational relation to the frequency of latitudinal oscillations. The two frequencies are defined for small oscillations of an almost circular orbit. (In case of a general orbit one may have to use an appropriate definition of averaged values of the frequencies.) This motivates us to adopt the effective cross-section in the form

$$A_{\text{eff}}(r_\star) = A_i \cos \frac{2\pi\omega_r(r_\star)}{\omega_z(r_\star)}, \quad A_i = \text{const}, \quad \theta_\star = \frac{\pi}{2}. \quad (2)$$

An exact numerical value of the constant factor,  $A_i$ , is not important for the present discussion: total time on which the orbit decays is simply proportional to  $A_i$ . Naturally,  $A_i$  must be small enough to assure that the trajectory is only slightly perturbed on each transit through the disc medium; i.e., the orbital decay must proceed on time-scale much longer than the dynamical time.

We show two examples of the long-term orbital evolution in which the above-mentioned effects are visible. In particular, the gradual orbital decay towards low-eccentricity, low-

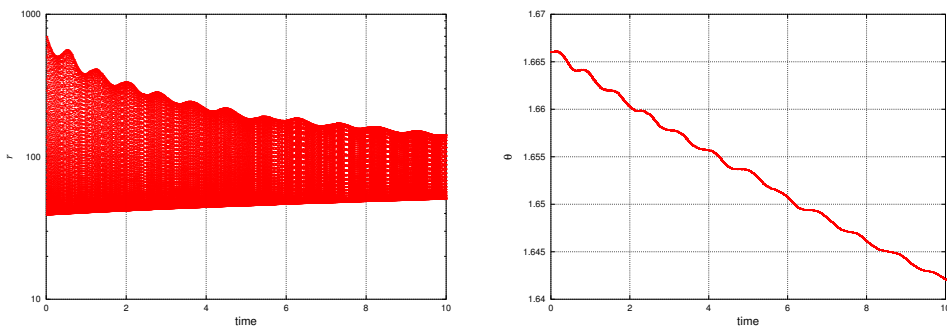


**Figure 1.** Intersection of the orbit around a maximally rotating Kerr black hole ( $a = M$ ). **Left:** radius is measured in units of  $GM/c^2$ , time is scaled by  $10^4 GM/c^3$ . The whole time span of the figure captures  $\approx 10^5$  orbits. Notice that radii of intersection points are scattered in a range between the pericentre and apocentre. Only occasionally, when a resonance occurs, the orbit crosses the disc plane at few distinct values of  $r$ . **Right:** graph of oscillations in inclination.

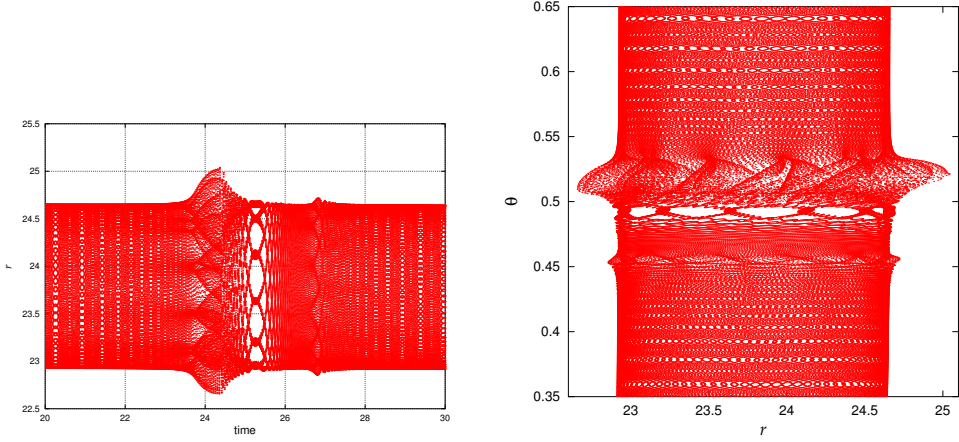


**Figure 2.** **Left:** time evolution of radius for another orbit. This case has low eccentricity ( $22.9M \leq r \leq 24.6M$ ) and it co-rotates with the disc ( $\theta \approx 30$  deg). **Right:** oscillations in  $(r, \theta)$ -projection.

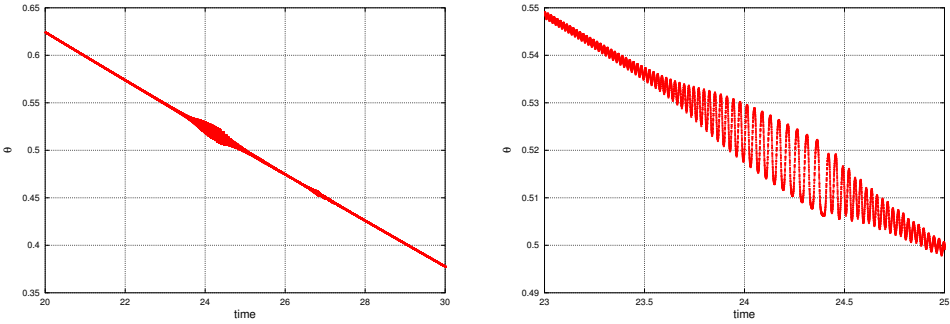


**Figure 3.** **Left:** temporal oscillations of inclination (the same orbit as in previous figure). **Right:** a detail of the graph on left.

inclination trajectory can be recognised clearly. Furthermore, one can observe low-frequency periodical component that originates due to  $A_{\text{eff}}$  dependence on orbital parameters and modulates the orbital evolution.

Fig. 1 shows two different projections of an eccentric orbit that, initially, intersects the disc between  $r_{\text{min}} = 40M$  and  $r_{\text{max}} = 700M$  (we set  $G = c = 1$ ), and has a large (almost polar) inclination. Intersections with equatorial plane are represented by dots. Two plots show these points of intersection in  $(r, t)$ -plane (time evolution of the orbit radius), and  $(\theta, t)$  (time evolution of inclination), respectively. Eccentricity oscillates and decreases, as well as the orbit inclination. Figs 2 and 3 give another example of the orbital decay. Also in this case, the gradual decay is coupled with oscillations. However, the initial eccentricity and inclination were both chosen rather small.

We have illustrated how an interplay between the dissipative orbital decay and the periodic driving term can lead to oscillations at certain stages of the orbit evolution. In conclusion,

it may be worth to repeat the motivation for the adopted prescription (2): We employed an *ad hoc* term for the perturbing force, which has been inspired by the assumption than this force arises due to collisions between the gaseous disc and the orbiter crashing on the disc periodically. Repetitive collisions may drill a hole in the disc slab and change the interaction if collisions happen in the same place of the disc several times after each other. Therefore, the interaction was assumed to depend on the ratio of epicyclic and vertical oscillations. The satellites enters into the resonant state because of its long-term orbital decay, which is also caused by the gaseous medium of the disc.

## ACKNOWLEDGEMENTS

The authors gratefully acknowledge support from Charles University in Prague (GAUK 299/2004) and from the Czech Science Foundation (the research grant No. 205/03/0902).

## REFERENCES

- [Chandrasekhar, 1960] Chandrasekhar, S. (1960). *Radiative Transfer*. Dover publications, New York.
- [Chandrasekhar, 1992] Chandrasekhar, S. (1992). *The Mathematical Theory of Black Holes*. Oxford University Press, New York.
- [Karas et al., 2002] Karas, V., Šubr, L., and Šlechta, M. (2002). Stellar dynamics in a galactic centre surrounded by an accretion disc. In Semerák, O., Podolský, J., and Žofka, M., editors, *Gravitation: Following the Prague Inspiration (A Volume in Celebration of the 60th Birthday of Jiří Bičák)*, pages 85–110, New Jersey, London, Singapore, Hong Kong. World Scientific.
- [Šubr and Karas, 2004] Šubr, L. and Karas, V. (2004). Stellar orbits in the gravitational field of a massive torus near a galactic centre. In Hledík, S. and Stuchlík, Z., editors, *Proceedings of RAGtime 4/5: Workshops on black holes and neutron stars, Opava, 14–16/13–15 October 2002/03*, Opava. Silesian University in Opava. This volume.

# Nonlinear dynamics of thick discs in Schwarzschild–de Sitter spacetimes

Luciano Rezzolla

*SISSA, International School for Advanced Studies, Trieste, Italy;*  
*INFN, Trieste, Italy*

## ABSTRACT

We consider the effects of a cosmological constant on the dynamics of constant angular momentum discs orbiting Schwarzschild–de Sitter black holes. The motivation behind this study is to investigate whether the presence of a radial force contrasting the black hole’s gravitational attraction can influence the occurrence of the runaway instability, a robust feature of the dynamics of constant angular momentum tori in Schwarzschild and Kerr spacetimes. In addition to the inner cusp near the black hole horizon through which matter can accrete onto the black hole, in fact, a positive cosmological constant introduces also an outer cusp through which matter can leave the torus without accreting onto the black hole. To assess the impact of this outflow on the development of the instability we have performed time-dependent and axisymmetric hydrodynamical simulations of equilibrium initial configurations in a sequence of background spacetimes of Schwarzschild–de Sitter black holes with increasing masses. The simulations have been performed with an unrealistic value for the cosmological constant which, however, yields sufficiently small discs to be resolved accurately on numerical grids and thus provides a first qualitative picture of the dynamics. The calculations, carried out for a wide range of initial conditions, show that the mass-loss from the outer cusp can have a considerable impact on the instability, with the latter being rapidly suppressed if the outflow is large enough.

## 1 INTRODUCTION

Relativistic accretion tori orbiting around stellar-mass black holes have been the subject of renewed interest over the last few years in connection with the different astrophysical scenarios where these objects are expected to form, such as the core collapse of a massive star leading to a “failed” supernova explosion (a collapsar), or in the catastrophic merger of two (unequal mass) neutron stars in a close binary system. However, thick accretion discs are probably present at much larger scales as well, surrounding quasars and other active galactic nuclei, and feeding their central supermassive black holes. One of the major issues about such systems concerns their dynamical stability. This has important implications on the most favoured current models for the central engines of  $\gamma$ -ray bursts, either collapsars or binary neutron star mergers, for long and short bursts, respectively (see, e.g., [Mészáros, 2002] for a recent review).

Discs around black holes may suffer from a number of instabilities produced either by axisymmetric or by non-axisymmetric perturbations and further triggered by the presence of magnetic fields. A type of instability that has been studied in a number of works and that could take place when the discs are geometrically thick and axisymmetric is the so-called *runaway instability* (see [Font and Daigne, 2002a, Zanotti et al., 2003] and references therein). To appreciate the mechanism leading to the development of this instability, consider an inviscid fluid torus with a vertical structure and internal pressure gradients orbiting around a black hole (either Schwarzschild or Kerr). If the fluid is non self-gravitating, it will be contained within isopotential surfaces which generically possess a cusp on the equatorial plane [Fishbone and Moncrief, 1976, Kozłowski et al., 1978, Abramowicz et al., 1978]. As a result, material from the disc can accrete onto the black hole through the cusp as the result of small deviations from hydrostatic equilibrium.

Any amount of matter lost by the disc and captured by the black hole will increase its mass (and angular momentum), resulting in a modification of the equipotential surfaces which may cause the cusp to move deeper inside the torus more rapidly than the inner edge of the torus. When this happens, additional disc material will be allowed to fall into the black hole in an increasingly accelerated manner leading to the runaway instability.

Although this instability was first studied in the '80s [Abramowicz et al., 1983, Wilson, 1984], time-dependent hydrodynamical simulations have been performed only recently, either with SPH techniques and pseudo-Newtonian potentials [Masuda and Eriguchi, 1997, Masuda et al., 1998], or with high-resolution shock-capturing (HRSC hereafter) techniques in general relativity ([Font and Daigne, 2002a, Zanotti et al., 2003]). These investigations have shown that, under the (idealised) assumption of constant specific angular momentum distributions, relativistic tori around Schwarzschild and Kerr black holes are generically unstable to the runaway instability, if non self-gravitating. The inclusion of more generic initial conditions, however, can disfavour the occurrence of the instability. Recently, [Font and Daigne, 2002b] (see also [Daigne and Font, 2003]) have shown through numerical simulations that the runaway instability is suppressed when a non-constant distribution of the angular momentum is assumed for the torus (increasing as a power-law of the radius), a result which is in agreement with studies based on a recent perturbative analysis [Rezzolla et al., 2003a, Rezzolla et al., 2003b]. While a similar stabilizing effect has been shown to be provided by the black hole if this is rotating [Abramowicz et al., 1998, Wilson, 1984], [Masuda and Eriguchi, 1997] were able to show that the inclusion of the self-gravity of the torus effectively favours the instability. Clearly, a final conclusion on the occurrence of this instability has not been reached yet and will have to wait for fully general relativistic simulations. However, the increasingly realistic investigations performed recently have addressed several important aspects and the prospects are that we may be close to reaching a detailed description of the dynamics of the instability.

A further physical process acting against the instability and which has not been investigated so far, is provided by the existence of a repulsive force pointing in the direction opposite to the black hole's gravitational attraction. Such a force could disturb and even balance the standard outflow of mass through the inner cusp, thus potentially suppressing the runaway instability. As suggested recently by [Stuchlík et al., 2000], such conditions could arise naturally in a black hole spacetime with a positive cosmological constant, i.e., in a Schwarzschild–de Sitter spacetime. In such a spacetime, in fact, a second cusp appears in

the outer parts of the equilibrium tori, near the so-called “static radius”. Assuming a value for the relict cosmological constant  $\Lambda \sim 10^{-56} \text{ cm}^{-2}$  as deduced from recent cosmological observations of the vacuum energy density [Krauss, 1998] and compatible with a sample of observational estimates provided by the analysis of a large number of high redshift supernovae [Perlmutter, 1999, Riess, 1998, Stuchlík et al., 2000] find that the location of this outer cusp for the largest stationary discs which can be built in a Schwarzschild–de Sitter spacetime is at about 50–100 kpc for supermassive black holes with masses in the range  $\sim 10^8 M_\odot$ – $10^9 M_\odot$ . As for the inner one, a slight violation of the hydrostatic equilibrium at the outer cusp would induce a mass outflow from the disc and away from the black hole, which could affect the overall dynamics of the torus.

However, this is not the only way in which a cosmological constant could modify the dynamics of a disc orbiting around a Schwarzschild–de Sitter black hole. As argued by [Stuchlík et al., 2000], in fact, a cosmological constant could produce a sensible modification in the accretion processes onto primordial black holes during the very early stages of expansion of the Universe, when phase transitions could take place, and the effective cosmological constant can have values in many orders exceeding its present value [Kolb and Turner, 1990]. Furthermore, a positive cosmological constant could also result into strong collimation effects on jets escaping along the rotation axis of the central black hole [Stuchlík et al., 2000].

The aim of this paper is to investigate one of these intriguing possibilities through numerical simulations. More precisely, we present a comprehensive study of the nonlinear hydrodynamics of constant angular momentum relativistic tori evolving in a sequence of background Schwarzschild–de Sitter spacetimes with increasing black holes masses. Our study clarifies the dynamical impact of a mass outflow on the occurrence of the runaway instability in such relativistic tori.

The organization of the paper is as follows. In Sect. 2 we briefly review the main properties of relativistic tori in a Schwarzschild–de Sitter spacetime. Next, in Sect. 3 we present the hydrodynamics equations and the numerical methods implemented in our axisymmetric evolution code. The material presented in this Section is rather limited, since the details have previously been reported in a number of papers. The last part of this Section is devoted to a discussion of the initial data we use for the simulations. The numerical results are then described in Sect. 4 and, finally, Sect. 5 contains our conclusions. Throughout the paper we use a space-like signature  $(-, +, +, +)$  and a system of geometrized units in which  $c = G = 1$ . The unit of length is chosen to be the gravitational radius of the black hole,  $r_g \equiv GM/c^2$ , where  $M$  is the mass of the black hole. Greek indices run from 0 to 3 and Latin indices from 1 to 3.

## 2 STATIONARY CONFIGURATIONS IN A SCHWARZSCHILD–DE SITTER SPACETIME

Building on a wide literature discussing equilibrium configurations of perfect fluid relativistic tori orbiting around Schwarzschild or Kerr black holes, [Stuchlík et al., 2000] have recently extended these results to the case of a Schwarzschild–de Sitter black hole. In spherical coordinates  $(t, r, \theta, \phi)$  the line element of this spacetime reads

$$ds^2 = - \left( 1 - \frac{2M}{r} - y \frac{r^2}{M^2} \right) dt^2 + \left( 1 - \frac{2M}{r} - y \frac{r^2}{M^2} \right)^{-1} dr^2 + r^2 (d\theta^2 + \sin^2 \theta d\phi^2), \quad (1)$$

where  $M$  is the mass of the black hole and the cosmological constant  $\Lambda$  is incorporated in the dimensionless parameter  $y$  defined as

$$y \equiv \frac{1}{3} \Lambda M^2. \quad (2)$$

This parameter has to be smaller than a critical value  $y < y_c \equiv 1/27$  in order to produce static regions of the spacetime where equilibrium configurations can be found. We note that a negative cosmological constant, corresponding to a Schwarzschild–anti-de Sitter black hole, does not introduce new qualitative features in the development of the runaway instability when compared to a Schwarzschild spacetime and will not be considered here.

Consider therefore a perfect fluid with four-velocity  $u^\mu$  and described by the stress-energy tensor

$$T^{\mu\nu} \equiv (e + p)u^\mu u^\nu + pg^{\mu\nu} = \rho h u^\mu u^\nu + pg^{\mu\nu}, \quad (3)$$

where  $g^{\mu\nu}$  are the coefficients of the metric (1) in which, however, the black hole mass  $M$  could be a function of time to account for the mass accreted onto the black hole [cf. the discussion of Eq. (11) below]. The fluid variables  $e$ ,  $p$ ,  $\rho$ , and  $h = (e + p)/\rho$  are the proper energy density, the isotropic pressure, the rest mass density, and the specific enthalpy, respectively. An equation of state (EOS) of polytropic type,  $p = \kappa \rho^\gamma = \rho \epsilon (\gamma - 1)$ , completes the thermodynamical description of the fluid. Here,  $\kappa$  is the polytropic constant,  $\gamma$  is the adiabatic index and  $\epsilon = e/\rho - 1$  is the specific internal energy. As shown by [Kozłowski et al., 1978] (see also [Fishbone and Moncrief, 1976]), the pressure gradients can balance the gravitational and centrifugal forces, allowing for the existence of stationary configurations of matter in non-geodesic circular motion and contained within closed “constant pressure” equipotential surfaces. Under the conditions of hydrostatic equilibrium and of axisymmetry (i.e.,  $\partial_t = \partial_\phi = 0$ ) the relativistic Euler equations for a fluid with four-velocity  $u^\alpha = (u^t, 0, 0, u^\phi)$  take the simple Bernoulli-type form

$$\frac{\nabla_i p}{e + p} = -\nabla_i W + \frac{\Omega \nabla_i \ell}{1 - \Omega \ell}, \quad i = r, \theta, \quad (4)$$

where  $W = W(r, \theta) \equiv \ln(u_t)$  is the effective potential,  $\ell \equiv -u_\phi/u_t$  is the specific angular momentum, and  $\Omega \equiv u^\phi/u^t$  is the coordinate angular velocity as measured by an observer near the static radius, where the spacetime geometry is very close to a flat one [Stuchlík et al., 2000]. Note that an explicit relation exists between the angular velocity and the specific angular momentum, which is given by  $\Omega = -\ell(g_{tt}/g_{\phi\phi})$ .

Once  $M$  and  $\Lambda$  have been prescribed, the explicit expression for the potential  $W(r, \theta)$  in the Schwarzschild–de Sitter spacetime is simply given by [Stuchlík et al., 2000]

$$W(r, \theta) = \frac{1}{2} \ln \left[ \frac{(1 - 2M/r - yr^2/M^2)r^2 \sin^2 \theta}{r^2 \sin^2 \theta - (1 - 2M/r - yr^2/M^2)\ell^2} \right]. \quad (5)$$

It is apparent from Eq. (4) that the simplest and indeed best studied configurations are obtained when the distribution of specific angular momentum  $\ell$  is prescribed to be constant. In this case, which is also the one considered here,  $W(r, \theta)$  shows three local extrema in

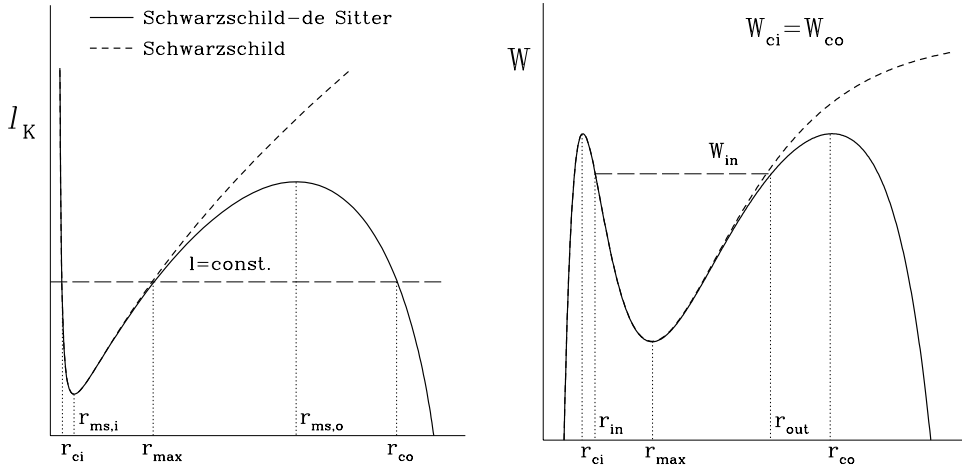


**Figure 1.** Schematic diagram for the Keplerian specific angular momentum  $\ell_K$  in a Schwarzschild–de Sitter spacetime (left panel) and the corresponding effective potential  $W$  (right panel) once a constant value for  $\ell$  has been chosen. The figure reports the different radial locations that are relevant for our discussion: the inner and outer cusp points  $r_{ci}, r_{co}$ , the inner and outer radii for the torus  $r_{in}, r_{out}$ , the inner and outer marginally stable orbits  $r_{ms,i}, r_{ms,o}$ , and the location of the maximum pressure in the torus  $r_{max}$  (see text for details). Note that  $r_{ci}, r_{co}$  and  $r_{max}$  are determined once a value for the constant specific angular momentum has been chosen (this is shown with the long-dashed line in the left panel) and that the inner and outer radii need not coincide with the corresponding locations of the cusps but are set by the value chosen for the potential  $W_{in}$  (this is shown with the long-dashed line in the right panel). Reported for comparison with a short-dashed line are  $\ell_K$  and  $W$  in a Schwarzschild spacetime; the radial coordinate is shown on a logarithmic scale.

the equatorial plane, one more than in the case of a Schwarzschild spacetime (cf. Fig. 1). Ordering these points with increasing values of  $r$ , the first extremum corresponds to the position of the inner cusp,  $r_{ci}$ , where the equipotential surface has a self-crossing point in the  $(r, \theta)$  plane. The second extremum corresponds to the position of the “centre” of the torus,  $r_{max}$ , where the internal pressure of the torus has its maximum. The third extremum, finally, marks the position of the outer cusp,  $r_{co}$ , which is not present in the Schwarzschild spacetime and represents the distinctive contribution of the non-zero cosmological constant (see Fig. 1 for a schematic diagram). Note that for a configuration with constant  $\ell$ , a local extremum of  $W$  is also a point of vanishing pressure gradients [cf. Eq. (4)]. As a result, the fluid motion on a circular orbit of radius  $r_{ci}, r_{max}$  or  $r_{co}$  is a purely geodesic one, with the specific angular momentum being given by the Keplerian one  $\ell_K$  for a point-like particle at that radius. In a Schwarzschild–de Sitter spacetime this is given by

$$\ell_K^2(r, y) \equiv \frac{r^3 M(1 - yr^3/M^3)}{(r - 2M - yr^3/M^2)^2}. \quad (6)$$

Once a value for the cosmological parameter and for the angular momentum have been fixed, Eq. (4), supplemented by the polytropic EOS, can be integrated analytically for any  $r \leq r_s$ , to yield the rest-mass density distribution inside the torus

$$\rho(r, \theta) = \left\{ \frac{\gamma - 1}{\kappa\gamma} [\exp(W_{\text{in}} - W) - 1] \right\}^{1/(\gamma-1)}, \quad (7)$$

where  $W_{\text{in}} \equiv W(r_{\text{in}}, \pi/2)$  and  $r_{\text{in}}$  is the inner edge of the torus. The latter is assumed to be a free parameter and is effectively controlled by the potential gap  $\Delta W_i \equiv W(r_{\text{in}}, \pi/2) - W(r_{\text{ci}}, \pi/2)$ .

Hereafter, we will focus on tori built in a parameter space that is smaller than the one discussed so far. In particular, we will consider tori with constant specific angular momentum in the range  $\ell_{\text{ms},i} \leq \ell \leq \ell_{\text{ph}} < \ell_{\text{ms},o}$ , where  $\ell_{\text{ph}}^2 \equiv r^3/(r - 2M - yr^3/M^2)$  is the angular momentum of the unstable photon circular geodesic [Stuchlík et al., 2000]. Furthermore, the hydrodynamical evolution of these tori will be followed in Schwarzschild–de Sitter spacetimes with dimensionless cosmological constant  $0 \leq y \leq y_e = 1/118125 \sim 8.46 \times 10^{-6}$ , where  $y_e$  corresponds to the value of  $y$  for which the minimum of  $\ell_{\text{ph}}$  is equal to the Keplerian angular momentum of the outer marginally stable orbit [Stuchlík et al., 2000].

### 3 NUMERICAL APPROACH AND INITIAL DATA

#### 3.1 Numerical approach

The numerical code we use is the same employed by [Zanotti et al., 2003] to study the dynamics of constant angular momentum relativistic discs around a Schwarzschild black hole. For the present investigation the code has been extended to account for the modifications introduced by the Schwarzschild–de Sitter geometry. The general relativistic hydrodynamics equations are solved by means of a HRSC scheme based on Marquina’s flux formula (see, e.g., [Font, 2000] for a review of these methods in numerical general relativistic hydrodynamics).

In order to cover optimally the large spatial extent of the equilibrium configurations and yet reach a satisfactory spatial resolution in the regions closer to the two cusps where the fluid motion needs to be calculated most accurately, we have introduced an important technical modification in the handling of the radial-coordinate grid. More precisely, we use a non-uniform radial grid with a logarithmic spacing, which is double-varied in the vicinities of the inner and outer cusps. The coordinate mapping used for this purpose is reminiscent of a tortoise coordinate mapping but it has been extended to a Schwarzschild–de Sitter metric as

$$r_* = \pm \int \left( 1 - \frac{2M}{r} - y \frac{r^2}{M^2} \right)^{-1} dr, \quad (8)$$

where the  $\pm$  sign distinguishes whether the mapping is made for increasing or decreasing values of the coordinate  $r$ , respectively.

As a result of this mapping, a radial grid of  $N_r = 300$  zones allows to cover a spatial domain going from  $r_{\text{MIN}} = 2.1$  to  $r_{\text{MAX}} = 100$  with a minimum radial spacing of the innermost part of the grid  $\Delta r = 10^{-4}$  and, correspondingly, a minimum radial spacing  $\Delta r = 10^{-3}$  for the outermost part of the radial grid. The two grids join smoothly at  $r = 48.6$ , where the resolution is  $\Delta r = 2.72$ . The angular grid, on the other hand, is more

straightforward to build and consists of  $N_\theta = 70$  equally spaced zones extending from 0 to  $\pi$  (cf. [Zanotti et al., 2003]).

As in [Zanotti et al., 2003], a low density “atmosphere” is introduced in those parts of the numerical domain outside the torus. The initial atmosphere model chosen corresponds to the spherically symmetric accretion solution of non-interacting test fluid particles. The maximum density of the atmosphere is typically 5 to 6 orders of magnitude smaller than the density at the centre of the torus. In all of the validating tests performed, the hydrodynamical evolution of the torus was found to be unaffected by the presence of this atmosphere, which is evolved as the bulk of the fluid.

Finally, the mass outflows at the innermost and outermost radial points are computed respectively as

$$\dot{m}_i(r_{\text{MIN}}) \equiv -2\pi \int_0^\pi \sqrt{-g} Dv^r d\theta \Big|_{r_{\text{MIN}}}, \quad (9)$$

and

$$\dot{m}_o(r_{\text{MAX}}) \equiv 2\pi \int_0^\pi \sqrt{-g} Dv^r d\theta \Big|_{r_{\text{MAX}}}, \quad (10)$$

where  $g$  is the determinant of the metric and  $\sqrt{-g} = r^2 \sin \theta$ .

Note that the mass outflow given by Eq. (9) corresponds effectively to the mass accretion rate onto the black hole and is used to account for the instantaneous increase of the black hole mass at every time step. This, in turn, provides information about the changes in the background spacetime, fundamental for the appearance of the runaway instability [Font and

**Table 1.** Main properties of the tori considered in the numerical calculations. From left to right the columns report: the name of the model, the specific angular momentum  $\ell$  (normalised to  $M$ ), the polytropic constant  $\kappa$ , the inner and outer cusps of the torus,  $r_{\text{ci}}$  and  $r_{\text{co}}$ , the radial position of the pressure maximum  $r_{\text{max}}$  (all radii are in units of the gravitational radius  $r_g$ ), the potential gaps  $\Delta W_i \equiv W_{\text{in}} - W_{\text{ci}}$  and  $\Delta W_o \equiv W_{\text{in}} - W_{\text{co}}$ , where  $W_{\text{in}}$  is the potential at the inner edge of the disc. The last column reports the orbital period at the centre of the torus,  $t_{\text{orb}}$ , expressed in milliseconds. All of the models share the same value of the cosmological parameter  $y = 10^{-6}$ , the same mass for the black hole,  $M = 10M_\odot$ , the same adiabatic index  $\gamma = 4/3$ , and the same torus-to-hole mass ratio  $M_t/M = 0.2$ .

Model	$\ell$	$\kappa$ (cgs)	$r_{\text{ci}}$	$r_{\text{co}}$	$r_{\text{max}}$	$\Delta W_i$	$\Delta W_o$	$t_{\text{orb}}$ (ms)
$A_1$	3.84	$8.970 \times 10^{14}$	4.419	94.866	8.822	0.010	-0.010	8.11
$A_2$	3.84	$2.568 \times 10^{15}$	4.419	94.866	8.822	0.025	0.005	8.11
$A_3$	3.84	$4.372 \times 10^{15}$	4.419	94.866	8.822	0.032	0.012	8.11
$B_1$	3.94	$2.295 \times 10^{15}$	4.133	94.564	9.876	0.004	0.004	9.61
$B_2$	3.94	$3.775 \times 10^{15}$	4.133	94.564	9.876	0.010	0.010	9.61
$B_2$	3.94	$6.740 \times 10^{15}$	4.133	94.564	9.876	0.020	0.020	9.61
$C_1$	4.00	$3.025 \times 10^{15}$	4.000	94.373	10.489	-0.007	0.007	10.51
$C_2$	4.00	$7.120 \times 10^{15}$	4.000	94.373	10.489	0.007	0.021	10.51
$C_2$	4.00	$1.125 \times 10^{16}$	4.000	94.373	10.489	0.020	0.034	10.51

Daigne, 2002a, Zanotti et al., 2003]. As mentioned in the Introduction, since we neglect the self-gravity of the torus, the hydrodynamics equations are solved in a sequence of background Schwarzschild–de Sitter spacetimes with increasing black hole masses. In practice, the spacetime evolution is achieved through a remapping of the metric functions at each time level of the type

$$g_{\mu\nu}(r, M^n, y) \longrightarrow \tilde{g}_{\mu\nu}(r, M^{n+1}, y), \quad (11)$$

where  $M^{n+1} = M^n + \Delta t \dot{m}_i^n(r_{\text{MIN}})$  is the mass of the black hole at the new timelevel  $t^{n+1}$ . A detailed discussion on the validity of this approximation can be found in [Font and Daigne, 2002a] and in [Zanotti et al., 2003]. The prescription (11) is justified and can be regarded as a very good approximation when the variation of the black hole mass per unit time,  $\dot{m}_i^n$ , is very small. This is certainly the case for the small disc-to-hole mass ratios  $M_t/M$  considered here (cf. Table 1).

### 3.2 Initial Data

As shown by [Font and Daigne, 2002a, Zanotti et al., 2003], the runaway instability is a robust feature of constant angular momentum relativistic tori in Schwarzschild and Kerr spacetimes, if these are non self-gravitating. This result does not depend on the way the instability is triggered, i.e., by either artificially expanding the torus over the potential barrier at the inner cusp [Font and Daigne, 2002a], or by introducing perturbations in an otherwise stable torus [Zanotti et al., 2003]. As discussed above, however, the presence of an outer cusp in a Schwarzschild–de Sitter spacetime is likely to affect the robustness of this conclusion. In order to investigate to what extent an outflow of mass can interfere with the development of the runaway instability we have studied the behaviour of three different classes of models, which we refer to as *A*, *B* and *C*. These models are distinguished on whether the effective potential at the inner cusp,  $W_{\text{ci}}$ , is less than, equal to, or larger than the effective potential  $W_{\text{co}}$  at the outer cusp, respectively. Furthermore, for each of these classes of models we have considered three different initial configurations, with the potential at the inner edge of the torus,  $W_{\text{in}}$ , being different from the potential barrier,  $W_{\text{ci}}$ , by the adjustable amount  $\Delta W_i$ .

Note that for all of the models of the class *A*, the hydrostatic equilibrium is always violated at the inner cusp, i.e.,  $W_{\text{in}} > W_{\text{ci}}$ , and a mass outflow will necessarily take place at the inner edge of the disc once the initial data is evolved. Furthermore, a mass loss will take place also at the outer cusp for models  $A_2$  and  $A_3$ , which have  $W_{\text{in}} > W_{\text{co}} > W_{\text{ci}}$ . For all of the models of the class *B*, on the other hand, the hydrostatic equilibrium is violated at both cusps and by the same amount, i.e.,  $W_{\text{in}} > W_{\text{ci}} = W_{\text{co}}$  and, again, the mass outflows are regulated by the potential jump  $\Delta W_i$ . Finally, for all of the models of the class *C*, the hydrostatic equilibrium is always violated at the outer cusp, i.e.,  $W_{\text{in}} > W_{\text{co}}$ , and also at the inner cusp for models  $C_2$  and  $C_3$ , for which  $W_{\text{in}} > W_{\text{ci}} > W_{\text{co}}$ .

Summarised in Table 1 are the potential jumps  $\Delta W_i$  and  $\Delta W_o$ , as well as the most relevant parameters of the various initial models considered here. Note that we have used a polytropic index  $\gamma = 4/3$  and adjusted the polytropic constant so as to have a small torus-to-hole mass ratio  $M_t/M = 0.2$ , thus minimising the error introduced by neglecting the self-gravity of the torus.

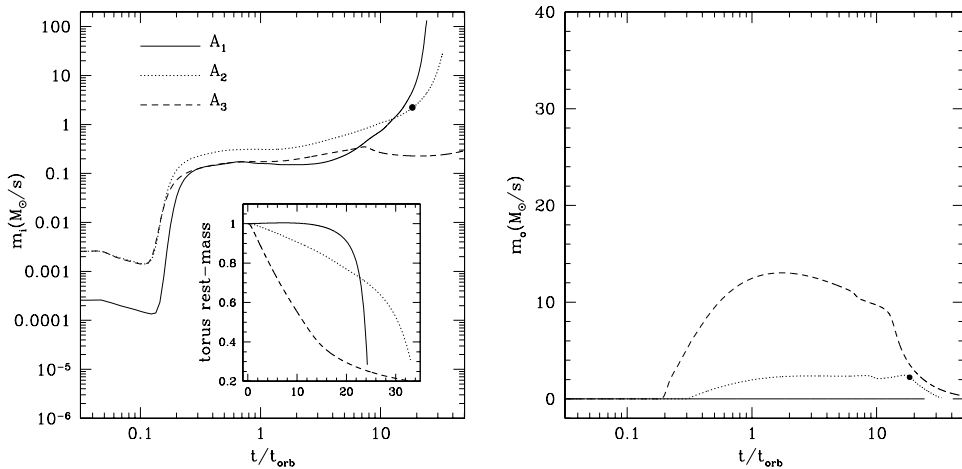


**Figure 2.** Time evolution of the inner (left panel) and of the outer (right panel) mass outflows for the models of class *A*. The data is shown in units of solar masses per second, while the time is expressed in units of the orbital period. Note that only models *A*<sub>1</sub> (solid line) and *A*<sub>2</sub> (dotted line) are runaway unstable. The solid circles in the two panels indicate the time at which  $\dot{m}_i > \dot{m}_o$  for model *A*<sub>2</sub>.

## 4 RESULTS

As mentioned above, the development of the runaway instability appears to be a robust feature of the dynamics of non self-gravitating tori orbiting around Schwarzschild or Kerr black holes with constant distributions of specific angular momentum. This conclusion has been reached after numerous simulations have been performed for a large range of torus-to-hole mass ratios  $M_t/M$  and under a number of different initial conditions [Font and Daigne, 2002a, Zanotti et al., 2003]. In all of these simulations, the onset and full development of the instability was observed when the spacetime geometry was suitably modified to account for the black hole’s mass-increase due to accretion. As a result of the instability, the torus is very rapidly accreted onto the black hole and this is most clearly signalled by the exponential growth in time of the rest-mass accretion rate at the innermost radial grid point. The growth-time for the instability is inversely proportional to the ratio  $M_t/M$  and is comparable with the dynamical (i.e., orbital) timescale when  $M_t/M \sim 1$ .

In the case of a Schwarzschild–de Sitter black hole, however, the rest-mass of the torus can change not only because of losses through the inner cusp leading to accretion onto the black hole, but also because of outflows from the outer cusp and away from the black hole. While both allowed, the impact that these two mass outflows could have on the dynamics of the torus is very different. The first one, in fact, induces changes in the black hole mass and could therefore lead to the runaway instability. The second one, on the other hand, does not produce changes of the background spacetime and cannot therefore produce an instability. Nevertheless, it can affect the hydrodynamical evolution in a number of different ways: firstly, by reducing the amount of rest-mass in the torus available for accretion and, secondly, by producing significant alterations of the velocity field, especially in the outer regions of the torus.

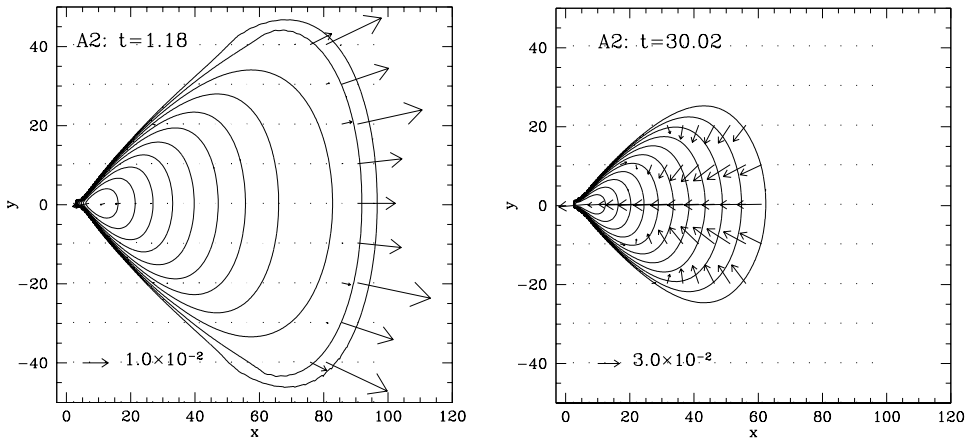


**Figure 3.** Velocity field and equally spaced isocontours of the logarithm of the rest-mass density for model  $A_2$  at an early time (left panel) and at a later time (right panel); the times reported are in units of the orbital period. Initially the outer mass flux dominates the dynamics of the torus. However, the gravitational attraction of the black hole eventually overcomes the effect of the cosmological constant and the runaway instability takes place. This leads to the large inward-directed fluxes and to the disappearance of the torus inside the black hole in a few orbital periods.

We have followed the hydrodynamical evolution of the models described in Table 1 over a number of orbital periods sufficiently large to reveal the impact of a positive cosmological constant on the occurrence of the runaway instability. In Figs 2 and 4 we show the two mass outflows  $\dot{m}_i$  and  $\dot{m}_o$  as a function of the orbital period  $t_{\text{orb}} = 2\pi/\Omega_{\text{max}}$  at the centre of the torus, and for the three classes of models listed in Table 1. The three small insets shown in the panels for  $\dot{m}_i$  offer a view of the evolution of the rest-mass of the torus after this has been normalised to its initial value. The description of the dynamics of the tori is also completed with Figs 3 and 5, which show equally spaced isocontours of the logarithm of the rest-mass density and, superimposed, the velocity field for models  $A_2$  and  $B_2$ , respectively, at two different times during the evolution.

As it is apparent from a rapid look at these figures, the runaway instability is no longer the only possible evolution of the system, whose dynamics is instead the result of the interplay between the inner and the outer mass outflows. The occurrence of the runaway instability is clearly visible in the left panel of Fig. 2 for model  $A_1$  (solid line). Model  $A_1$ , in fact, has initial conditions that resemble those encountered for a Schwarzschild black hole, with the outer radius of the torus located far from the outer cusp (cf. Fig. 1). As a result, the right panel of Fig. 2, shows that the outer mass outflow is in this case very small (indeed slightly negative as a result of accretion onto the torus of the infalling atmosphere), while the mass accretion rate onto the black hole (left panel) grows exponentially and undisturbed until the full development of the runaway instability at  $t \sim 24.2 t_{\text{orb}}$ . The dynamical evolution is different for models  $A_2$  (dotted line) and  $A_3$  (dashed line), where the competition between the two outflows at the inner and outer edges of the disc is closer to a balance and the initial outer mass-loss is non-negligible. For model  $A_2$ , in particular, this is clearly visible in the left panel of Fig. 3, which shows that at early times ( $t \sim 1.2 t_{\text{orb}}$ ) the largest fluid velocities

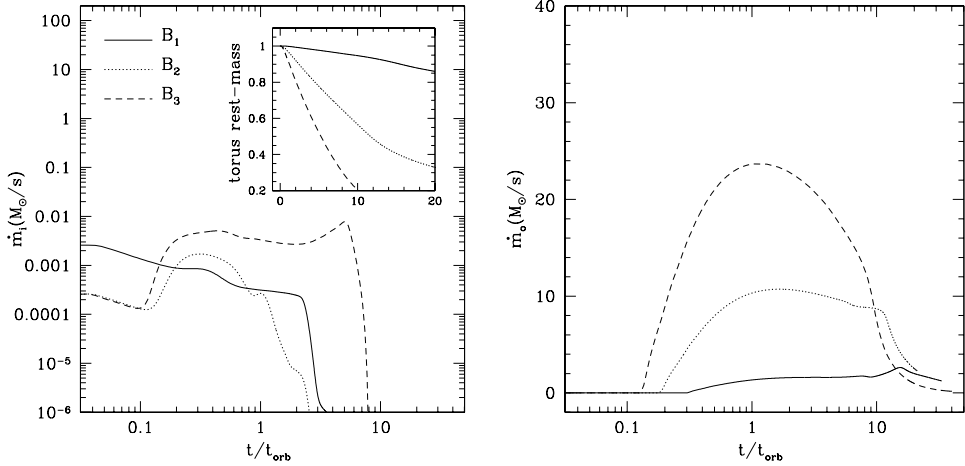


**Figure 4.** Same as Fig. 2 but for the models of class *B*.

( $v \sim 4 \times 10^{-3}$ ) are reached in the outer regions of the torus and are outwardly directed. However, the outer mass-loss eventually becomes insufficient to prevent the development of the runaway instability, which takes place after  $t \sim 33 t_{\text{orb}}$ . The corresponding velocity field (with all vectors pointing towards the black hole) and the isocontours of the logarithm of the rest-mass density displayed in the right panel of Fig. 3 (at time  $t \sim 30.0 t_{\text{orb}}$ ) show the important reduction in size undergone by the torus, which is about to disappear entirely inside the black hole after a few more orbital periods. This type of evolution does not take place for model  $A_3$ , whose dynamics is completely dominated by the mass outflow through the outer cusp and for which the runaway instability does not develop (cf. Fig. 2).

To better interpret the dynamics behind these simulations it is useful to compare the amount of rest-mass in the torus after the first 10 orbital periods of the evolution for the three models of class *A* (see inset in the left panel of Fig. 2). The residual rest-mass of the torus is 99%, 90%, and 55% of the initial one for the models  $A_1$ ,  $A_2$ , and  $A_3$ , respectively. This may appear somewhat surprising given the fact that the mass outflow from the inner cusp is smaller in the case of model  $A_3$  than it is for model  $A_2$ , despite  $A_3$  having a larger initial potential jump  $\Delta W_i$ . The explanation for this comes from looking at the right panel of Fig. 2 which shows that the mass outflow from the outer cusp is however larger for model  $A_3$  than it is for model  $A_2$ . As a result, the torus is emptied more efficiently, and this happens mostly through the outer cusp.

It is also very instructive to compare the mass outflows at the inner and outer edges of the disc for the three models of class *A*. Doing so leads to the important result that  $\dot{m}_i > \dot{m}_o$  at all times for model  $A_1$  and that  $\dot{m}_i < \dot{m}_o$  at all times for model  $A_3$ . In other words, the unstable and the stable models seem to differ from each other on whether the mass outflow from the inner edge is larger or smaller than the corresponding mass-loss from the outer edge. In the case of model  $A_2$ , on the other hand, the two mass outflows are closer to a balance and  $\dot{m}_i > \dot{m}_o$  only for  $t \gtrsim 18 t_{\text{orb}}$ , after which the runaway instability clearly develops; the time when this happens is shown with the filled circles in the two panels of

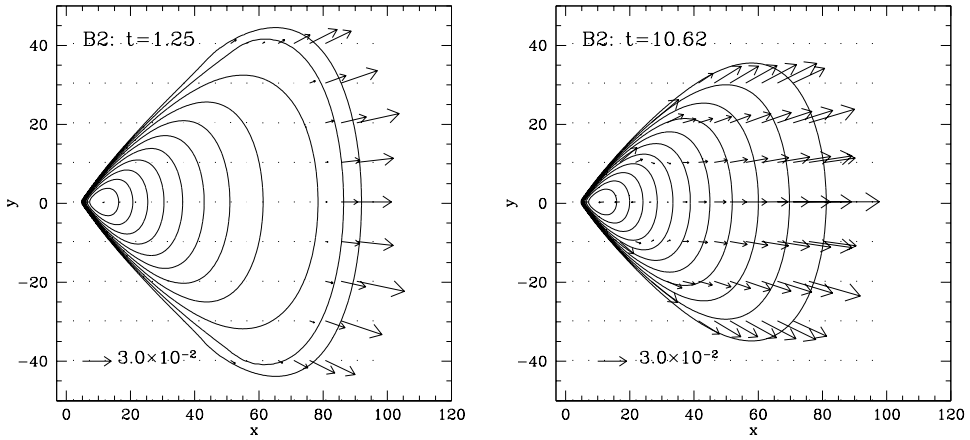


**Figure 5.** Same as Fig. 3 but for model  $B_2$ . The intense mass outflow across the outer edge of the disc removes a large fraction of its mass, and suppresses the runaway instability. The final disc reaches a quasi-steady state.

Fig. 2. It appears, therefore, that an increasing potential gap at the outer edge of the torus *favours* the outflow of mass from the *outer* cusp but it also *disfavours* (and to a larger extent) the mass outflow from the *inner* cusp, with the corresponding accretion onto the black hole being severely suppressed. As a result, the feed-back of the black hole spacetime onto the overall dynamics of the system is considerably reduced and the runaway instability suppressed. Stated differently, the development of the runaway instability appears to be related to the efficiency of the mass-loss through the edges of the disc and, in particular, the instability is effectively “extinguished” whenever the mass outflow from the *outer edge* of the disc and away from the black hole is *larger* than the mass outflow from the *inner edge* of the disc and onto the black hole. The condition  $\dot{m}_i < \dot{m}_o$  can thus be used as a simple sufficient condition for the suppression of the runaway instability in a thick disc orbiting around a Schwarzschild–de Sitter black hole.

The role played by a positive cosmological constant on the dynamics of the discs and described so far for the models of class  $A$  is present also for the models of class  $B$  and  $C$ , although with some slight differences. As discussed in Sect. 3.2, the models of class  $B$  are built with the outer and inner edges having the same effective potential. One would therefore expect that this would yield to very similar mass outflows at the two boundaries of the disc. However, the two panels of Fig. 4 show that the mass fluxes through the outer edges of the discs to infinity are always larger than the ones towards the black hole (i.e.,  $\dot{m}_i < \dot{m}_o$ ). As a result, the models of class  $B$  are all stable to the runaway instability. This is particularly apparent in models  $B_2$  and  $B_3$ , for which the outer mass outflows are at least a couple of orders of magnitude larger than the corresponding mass outflows onto the black hole, and which become negligibly small (i.e.,  $\dot{m}_i < 10^{-8} M_\odot/\text{s}$ ) well before 10 orbital periods. As a result, a large amount of the matter in those discs is not accreted onto the black hole, but escapes to infinity. This is illustrated in the small inset of the left panel of

Fig. 4 which shows that after about 20 orbital periods more than 60% of the torus rest-mass is lost for model  $B_2$  and more than 90% for model  $B_3$ .

Once the outflows die off in the tori of class  $B$ , the remaining matter reaches a quasi-stable equilibrium, accreting onto the black hole on a timescale which is essentially controlled by the rate of mass-loss through the inner cusp. The importance of the mass outflow at the outer edges of the discs of class  $B$  is also apparent from Fig. 5, which shows the velocity field and isocontours of the logarithm of the rest-mass density of model  $B_2$  at an early and a later stage of the evolution. Note how the left panels of Fig. 3 and 5 have velocity fields that differ mostly in modulus but are equally oriented, while the right panels are substantially different with velocity fields that have opposite orientations leading to the disappearance of the torus into the black hole and to infinity, respectively. We also note that while the difference between the inner and outer mass outflows remains large also in the case of model  $B_1$ , the dynamics is in this case much closer to an equilibrium, with the torus being still progressively emptied to infinity, but on a much larger timescale. No runaway instability was observed for this model over the time for which the calculations were carried out ( $t \sim 33 t_{\text{orb}}$ ).

Finally, for models  $C$ , the dynamics of the discs is particularly simple and the final result is rather clear to interpret. In this case, in fact, all the discs are built with an effective potential which is larger at the outer edge and represent, therefore, initial conditions that are conceptually the opposite of those in models  $A$ . Because of the high potential barrier at the inner edge of the disc, the inner mass outflow is always rather minute and several orders of magnitude smaller than the corresponding mass outflow from the outer edge. As a result, the mass in the torus is lost very rapidly to infinity and very little is accreted onto the black hole. In particular, in the most dramatic case of model  $C_3$ , the residual rest-mass in the torus is less than 20% after only 6 orbital periods.

## 5 CONCLUSIONS

We have investigated the effect of a positive cosmological constant on the dynamics of non self-gravitating thick accretion discs orbiting Schwarzschild–de Sitter black holes with constant distributions of specific angular momentum. The motivation behind this investigation has been that of assessing the role played by an effective repulsive force in the onset and development of the runaway instability, which represents a robust feature in the dynamics of constant angular momentum tori. In addition to the inner cusp near the black hole horizon, through which matter can accrete onto the black hole when small deviations from the hydrostatic equilibrium are present, thick discs in a Schwarzschild de-Sitter spacetime also possess an outer cusp through which matter can leave the torus without accreting onto the black hole. As a result of this mass-loss to infinity, the changes in the background metric (which are responsible for the development of the runaway instability) may be altered considerably and the instability thus suppressed.

As a simple way to evaluate this effect we have considered a sequence of Schwarzschild–de Sitter spacetimes differing only in their total mass and have performed time-dependent general relativistic hydrodynamical simulations in these background metrics of thick discs which are initially slightly out of hydrostatic equilibrium. In doing this we have adopted an

unrealistically high value for the cosmological constant which however yields sufficiently small discs (extending up to about a few hundred gravitational radii) to be accurately resolved with fine enough axisymmetric numerical grids.

We have performed a number of simulations involving initial configurations of constant specific angular momentum discs differing both for the relative amplitude of the peaks in the effective potential and for the potential jump at the inner and outer cusps. The results obtained indicate that the runaway instability is no longer the only possible evolution of these systems but that their dynamics is rather the end-result of the interplay between the inner and the outer mass outflows. On the one hand, in fact, we have evolved initial models for which the cosmological constant has a weak influence; these models have negligible mass outflows to infinity while maintaining large mass outflows onto the black hole, which then lead to the development of the runaway instability. On the other hand, we have evolved initial models which are significantly influenced by the cosmological constant; these models develop mass outflows through the outer cusp which are much larger than those appearing at the inner cusp and, hence, do not develop the runaway instability. Placed somewhere between these two classes of initial configurations there exist initial models for which the mass outflows from the inner and outer cusps are more closely balanced. In these cases the runaway instability may or may not develop and we have noticed that a simple comparison between the mass outflows can be used to deduce the fate of the accreting disc. More specifically, we have found that the condition  $\dot{m}_i < \dot{m}_o$  provides a simple sufficient condition for the suppression of the runaway instability in a thick disc orbiting around a Schwarzschild–de Sitter black hole.

In spite of the idealised setup used, the simulations performed here provide a first qualitative description of the complex nonlinear dynamics of thick discs in Schwarzschild–de Sitter spacetimes and we expect that most of the results obtained will continue to hold also when more realistic values for the cosmological constant are used. As a final comment we note that besides providing a qualitative description of the role that a cosmological constant could play on the dynamics of relativistic tori, these calculations also offer a way of assessing, at least qualitatively, the inertial role that the self-gravity of the torus plays in the development of the runaway instability. This will be very useful when studying the dynamics of relativistic tori with numerical codes solving also the full Einstein equations.

## ACKNOWLEDGEMENTS

The work presented in this talk is in collaboration with Olindo Zanotti and Toni Font. Financial support for this research has been provided by the Italian MIUR and by the EU Network Programme (Research Training Network Contract HPRN-CT-2000-00137). The computations were performed on the Beowulf Cluster for numerical relativity “*Albert100*”, at the University of Parma.

## REFERENCES

- [Abramowicz et al., 1983] Abramowicz, M. A., Calvani, M., and Nobili, L. (1983). *Nature*, 302:597.

- [Abramowicz et al., 1978] Abramowicz, M. A., Jaroszyński, M., and Sikora, M. (1978). Relativistic accreting disks. *Astronomy and Astrophysics*, 63(1–2):221–224.
- [Abramowicz et al., 1998] Abramowicz, M. A., Karas, V., and Lanza, A. (1998). *Astronomy and Astrophysics*, 331:1143.
- [Daigne and Font, 2003] Daigne, F. and Font, J. A. (2003). In preparation.
- [Fishbone and Moncrief, 1976] Fishbone, L. G. and Moncrief, V. (1976). *Astrophys. J.*, 207:962.
- [Font, 2000] Font, J. A. (2000). Living reviews in relativity, 3, 2.
- [Font and Daigne, 2002a] Font, J. A. and Daigne, F. (2002a). *Monthly Notices Roy. Astronom. Soc.*, 334:383.
- [Font and Daigne, 2002b] Font, J. A. and Daigne, F. (2002b). On the Stability of Thick Accretion Disks around Black Holes. *Astrophys. J.*, 581:L23–L26.
- [Kolb and Turner, 1990] Kolb, E. W. and Turner, M. S. (1990). *The Early Universe*. Addison-Wesley, Redwood City, California. The Advanced Book Program.
- [Kozłowski et al., 1978] Kozłowski, M., Jaroszyński, M., and Abramowicz, M. A. (1978). The analytic theory of fluid disks orbiting the Kerr black hole. *Astronomy and Astrophysics*, 63:209–220.
- [Krauss, 1998] Krauss, L. M. (1998). The end of the age problem, and the case for a cosmological constant revisited. *Astrophys. J.*, 501(2):461–466.
- [Masuda and Eriguchi, 1997] Masuda, N. and Eriguchi, Y. (1997). Three-dimensional Simulations of Runaway Instability of Self-gravitating Accretion Disks. *Astrophys. J.*, 489:804818.
- [Masuda et al., 1998] Masuda, N., Nishida, S., and Eriguchi, Y. (1998). The runaway instability of self-gravitating tori with non-constant specific angular momentum around black holes. *Monthly Notices Roy. Astronom. Soc.*, 297(4):1139–1144.
- [Mészáros, 2002] Mészáros, P. (2002). *Annual Review of Astronomy and Astrophysics*, 40:137.
- [Perlmutter, 1999] Perlmutter, S. (1999). *Astrophys. J.*, 517:565.
- [Rezzolla et al., 2003a] Rezzolla, L., Yoshida, S., Maccarone, T. J., and Zanotti, O. (2003a). A new simple model for high-frequency quasi-periodic oscillations in black hole candidates. *Monthly Notices Roy. Astronom. Soc.*, 344(3):L37–L41.
- [Rezzolla et al., 2003b] Rezzolla, L., Yoshida, S., and Zanotti, O. (2003b). *Monthly Notices Roy. Astronom. Soc.*, 344:978.
- [Riess, 1998] Riess, A. G. (1998). *Astronom. J.*, 116:1009.
- [Stuchlík et al., 2000] Stuchlík, Z., Slaný, P., and Hledík, S. (2000). Equilibrium configurations of perfect fluid orbiting Schwarzschild–de Sitter black holes. *Astronomy and Astrophysics*, 363(2):425–439.
- [Wilson, 1984] Wilson, D. B. (1984). *Nature*, 312:620.
- [Zanotti et al., 2003] Zanotti, O., Rezzolla, L., and Font, J. A. (2003). *Monthly Notices Roy. Astronom. Soc.*, 341:832.



# Optical appearance of isotropically radiating sphere in the Schwarzschild–de Sitter spacetime

Zdeněk Stuchlík and Kamila Plšková

*Institute of Physics, Faculty of Philosophy and Science, Silesian University in Opava  
Bezručovo nám. 13, CZ-746 01 Opava, Czech Republic*

## ABSTRACT

We consider appearance of isotropically radiating sources located at a sphere at the static radius of the Schwarzschild–de Sitter spacetimes to static observers in vicinity of the black hole horizon and the cosmological horizon and to radially moving observers. We expect these observers to follow geodesics starting from the static radius. It is shown that the observed flux diverges at both the horizons for both classes of observers. Nevertheless the frequency shift remains finite at the horizons for the radially moving observers.

## 1 INTRODUCTION

Optical effects in the field of black holes are of great interest from the very beginning of the black hole investigations [Podurets, 1964, Ames and Thorne, 1968]. Appearance of distant sources to observers in vicinity of the black hole horizon was studied by [Bardeen, 1973, Cunningham and Bardeen, 1972, Cunningham, 1975]. Recently, the existence of repulsive cosmological constant ( $\Lambda > 0$ ) is indicated by many cosmological tests [Krauss and Turner, 1995, Ostriker and Steinhardt, 1995]. Therefore, it is interesting to study the influence of  $\Lambda > 0$  on the optical effect nearby the horizons.

In this paper we compute the appearance of distant objects (sphere of isotropically radiating sources) to an observer near the black hole or an observer near the cosmological horizon. We will study this problem for the spherically symmetric Schwarzschild–de Sitter spacetime with repulsive (positive) cosmological constant.

We consider two classes of observers for which we will compute the appearance of sources in the external universe. The first class are static observers, i.e., observers who (for example thanks to its rocket) sit at rest in the external field of the hole (with world lines of constant  $r, \theta, \phi = \text{const}$ ). The second class are radially moving observers, i.e., observers who fall freely from a given radius onto the black hole or who recede from a given radius to the cosmological horizon.

It is useful to choose the starting point for the radially moving observers at the static radius, where the gravitational attraction of the hole is balanced by the cosmological repulsion. Hereafter, we assume that the stationary, isotropically radiating background is generated by sources located on the static radius.

## 2 SCHWARZSCHILD–DE SITTER GEOMETRY

The line element of the Schwarzschild–de Sitter spacetime in the standard Schwarzschild coordinates in geometric units ( $c = G = 1$ ) has the form

$$ds^2 = - \left( 1 - \frac{2M}{r} - \frac{\Lambda}{3} r^2 \right) dt^2 + \left( 1 - \frac{2M}{r} - \frac{\Lambda}{3} r^2 \right)^{-1} dr^2 + r^2 (d\theta^2 + \sin^2 \theta d\phi^2), \quad (1)$$

where  $M$  is mass of the central black hole,  $\Lambda \sim 10^{-56} \text{ cm}^{-2}$  is the repulsive cosmological constant. It is advantageous to introduce dimensionless cosmological parameter  $y$  by the relation

$$y = \frac{1}{3} \Lambda M^2. \quad (2)$$

### 2.1 The horizons

The event horizons of the spacetime are given by condition

$$g_{tt} \equiv - \left( 1 - \frac{2}{r} - yr^2 \right) = 0. \quad (3)$$

The location of events horizons is determined by the relation

$$y = y_h(r) \equiv \frac{r-2}{r^3}. \quad (4)$$

In the Schwarzschild–de Sitter spacetimes there exists a critical value of the parameter  $y$ , given by the relation  $y_{\text{crit}} = y_h(r=3) = 1/27$ , corresponding to the local maximum of  $y_h(r)$ . For  $0 < y < y_{\text{crit}}$ , there exists two events horizons. The black-hole horizon and the cosmological horizon are located at

$$r_h = \frac{2}{\sqrt{3y}} \cos \frac{\pi + \xi}{3}, \quad r_c = \frac{2}{\sqrt{3y}} \cos \frac{\pi - \xi}{3}, \quad (5)$$

respectively, where

$$\xi = \cos^{-1} 3\sqrt{3y}. \quad (6)$$

The spacetime is dynamic at  $r < r_h$  and  $r > r_c$ . If  $y = y_{\text{crit}} = 1/27$ , the horizons coincide at  $r_h = 3$ . If  $y > 1/27$ , the spacetime is dynamic at  $r > 0$  and describes a naked singularity [Stuchlík and Hledík, 1999].

The motion of test particles and photons is given by geodesic structure of the spacetime. The equation of geodetical motion reads

$$\frac{Dp^\mu}{d\lambda} = 0, \quad (7)$$

where  $p^\mu \equiv dx^\mu/d\lambda$  is the 4-momentum of the particle (photon) and  $\lambda$  is an affine parameter. It has to be completed by the condition

$$p^\mu p_\mu = -m^2, \quad (8)$$

where  $m$  is the rest mass of the test particle. (For photons  $m = 0$ .)

It follows from the central symmetry of the geometry (1) that the geodetical motion of test particles and photons is allowed in the central planes only. Due to the existence of the Killing vector fields  $\xi_{(t)} = \partial/\partial t$  and  $\xi_{(\phi)} = \partial/\partial\phi$ , there must exist two constants of the geodetical motion:

$$p_t = g_{t\mu}p^\mu = -\mathcal{E}, \quad p_\phi = g_{\phi\mu}p^\mu = \Phi. \tag{9}$$

We can introduce the specific energy  $E$ , specific angular momentum  $L$  and impact parameter  $l$  by the relations

$$E = \frac{\mathcal{E}}{m}, \quad L = \frac{\Phi}{m}, \quad l = \frac{\Phi}{\mathcal{E}}. \tag{10}$$

If we choose the plane of the motion as the equatorial plane ( $\theta = \pi/2$ ), the motion of the test particles ( $m \neq 0$ ) will be given by the effective potential

$$V_{\text{eff}}^2(r, L, y) \equiv \left(1 - \frac{2}{r} - yr^2\right) \left(1 + \frac{L^2}{r^2}\right). \tag{11}$$

The motion is allowed in the regions where

$$E^2 \geq V_{\text{eff}}^2(r, L, y). \tag{12}$$

The turning points of the radial motion are given by the condition

$$E^2 = V_{\text{eff}}^2(r, L, y). \tag{13}$$

Radial motion of photons ( $m = 0$ ) can be determined by the generalised effective potential related to the impact parameter  $l$ . The motion is allowed in regions where

$$l^2 \leq l_{\text{R}}^2(r, y) \equiv \frac{r^3}{r - 2 - yr^3}. \tag{14}$$

The condition  $l^2 = l_{\text{R}}^2(r, y)$  holds for the turning points of the radial motion.

In the Schwarzschild–de Sitter spacetimes,  $V_{\text{eff}}^2(r, L, y)$  and  $l_{\text{R}}^2(r, y)$  are well defined between the black hole horizon and the cosmological horizon.

The circular orbits of test particles correspond to a local extreme of the effective potential ( $\partial V_{\text{eff}}^2/\partial r = 0$ ). Its maxima ( $\partial^2 V_{\text{eff}}^2/\partial^2 r < 0$ ) determine unstable orbits, minima ( $\partial^2 V_{\text{eff}}^2/\partial^2 r > 0$ ) determine stable circular orbits. Specific energy and specific angular momentum of the particle on a circular geodesic are given by relation

$$E_c(r, y) = \left(1 - \frac{2}{r} - yr^2\right) \left(1 - \frac{3}{r}\right)^{-1/2}, \tag{15}$$

$$L_c(r, y) = \left[r(1 - yr^3)\right]^{1/2} \left(1 - \frac{3}{r}\right)^{-1/2}. \tag{16}$$

The circular orbits may exist only in regions restricted by the condition

$$3 \leq r \leq r_s \equiv y^{-1/3}. \tag{17}$$

The lower limit of this region is connected with divergences of the functions  $E_c$  and  $L_c$  at  $r = 3$ . The photon circular orbit, which is given by the local minimum of the function

$l_{\text{R}}^2$ , exist there. This minimum is located at  $r = 3$  for arbitrary values of dimensionless parameter  $y$ . However the impact parameter of the photon circular orbit depends on  $y$  by the relation

$$l_{\text{c}}^2(y) = \frac{27}{1 - 27y}. \quad (18)$$

The upper limit of the region, where the circular orbits may exist, is called static radius and denoted  $r_{\text{s}}$ . The gravitational attraction of the hole is just balanced by the cosmological repulsion there. The static radius is given by the condition

$$y = y_{\text{s}}(r) \equiv \frac{1}{r^3}. \quad (19)$$

The position of the particle on the static radius with specific energy

$$E_{\text{s}}(y) = \left(1 - 3y^{1/3}\right)^{1/2}, \quad (20)$$

and  $L = 0$  is unstable relative to radial perturbations.

Stable circular orbits exist on radii simultaneously satisfying the conditions  $\partial V_{\text{eff}}^2/\partial r = 0$  and  $\partial^2 V_{\text{eff}}^2/\partial^2 r \geq 0$  that imply

$$4yr^4 - 15yr^3 - r + 6 \geq 0. \quad (21)$$

Marginally stable circular orbits are given by the relation

$$y = y_{\text{ms}}(r) \equiv \frac{r - 6}{r^3(4r - 15)}. \quad (22)$$

The curve  $y_{\text{ms}}(r)$  has its maximum located at  $r_{\text{crit}} = 15/2$  corresponding to a critical value of the cosmological parameter for the spacetimes that permit the existence of stable circular orbits

$$y_{\text{crit(ms)}} = \frac{12}{15^4} \simeq 0.000237. \quad (23)$$

### 3 STATIC OBSERVERS

Let us consider static observers who are located at rest at  $r = \text{const}$ ,  $\theta = \text{const}$ ,  $\phi = \text{const}$ . The observers are endowed by a proper reference system with an orthonormal tetrad of one-forms

$$\omega^{(t)} = B(r, y) dt, \quad (24)$$

$$\omega^{(r)} = \frac{1}{B(r, y)} dr, \quad (25)$$

$$\omega^{(\theta)} = r d\theta, \quad (26)$$

$$\omega^{(\phi)} = r \sin \theta d\phi, \quad (27)$$

and an orthonormal tetrad of 4-vectors

$$e_{(t)} = \frac{1}{B(r, y)} \frac{\partial}{\partial t}, \quad (28)$$

$$e_{(r)} = B(r, y) \frac{\partial}{\partial r}, \quad (29)$$

$$e_{(\theta)} = \frac{1}{r} \frac{\partial}{\partial \theta}, \quad (30)$$

$$e_{(\phi)} = \frac{1}{r \sin \theta} \frac{\partial}{\partial \phi}, \quad (31)$$

where we denote

$$B^2(r, y) \equiv 1 - \frac{2}{r} - yr^2. \quad (32)$$

Recall that

$$\omega_{\mu}^{(\alpha)} e_{\beta}^{\mu} = \delta_{(\beta)}^{(\alpha)}, \quad e_{(\alpha)}^{\mu} \omega_{\nu}^{(\alpha)} = \delta_{\nu}^{\mu}, \quad (33)$$

where  $\delta_{\nu}^{\mu}$  is the Kronecker delta. The general relations between the locally measured 4-momentum  $p^{(\alpha)}$  and the coordinate 4-momentum  $p^{\mu}$  are given by

$$p^{(\alpha)} = \omega_{\mu}^{(\alpha)} p^{\mu}, \quad p_{(\alpha)} = e_{(\alpha)}^{\mu} p_{\mu}, \quad (34)$$

$$p^{\alpha} = e_{(\mu)}^{\alpha} p^{(\mu)}, \quad p_{\alpha} = \omega_{\alpha}^{(\mu)} p_{(\mu)}. \quad (35)$$

Hereafter, we consider (for simplicity) the observers located on axis of symmetry ( $\theta = 0$ ).

The source (a radiating sphere) will be assumed to be at rest on the static radius  $r_s$ . The source emits photons that are entrapped by the observers. The photon world line, a null geodesic, is characterised by the impact parameter  $l$ . Covariant components of the 4-momentum of a photon in the coordinate system are (we express the motion in latitudinal coordinate and assume  $\phi = \text{const}$ ) [Cunningham, 1975]

$$p_t = -\mathcal{E}, \quad (36)$$

$$p_r = \frac{A(r, y; l)}{B^2(r, y)} \mathcal{E}, \quad (37)$$

$$p_{\theta} = l \mathcal{E} = \Phi, \quad (38)$$

where

$$A(r, y; l) = \pm \sqrt{1 - B^2(r, y) \frac{l^2}{r^2}}. \quad (39)$$

The ‘+’ sign corresponds to photons receding from the black hole, the ‘-’ sign corresponds to photons infalling into the black hole. The components of 4-momentum of the photon measured by a static observer located at a given  $r$  ( $p^{(\alpha)} = \omega_{\mu}^{(\alpha)} p^{\mu}$ ) are given by the relations

$$p_{\text{obs}}^{(t)} = \frac{\mathcal{E}}{B(r, y)}, \quad (40)$$

$$p_{\text{obs}}^{(r)} = \frac{A(r, y; l)}{B(r, y)} \mathcal{E}, \quad (41)$$

$$p_{\text{obs}}^{(\theta)} = \frac{l \mathcal{E}}{r} = \frac{\Phi}{r}. \quad (42)$$

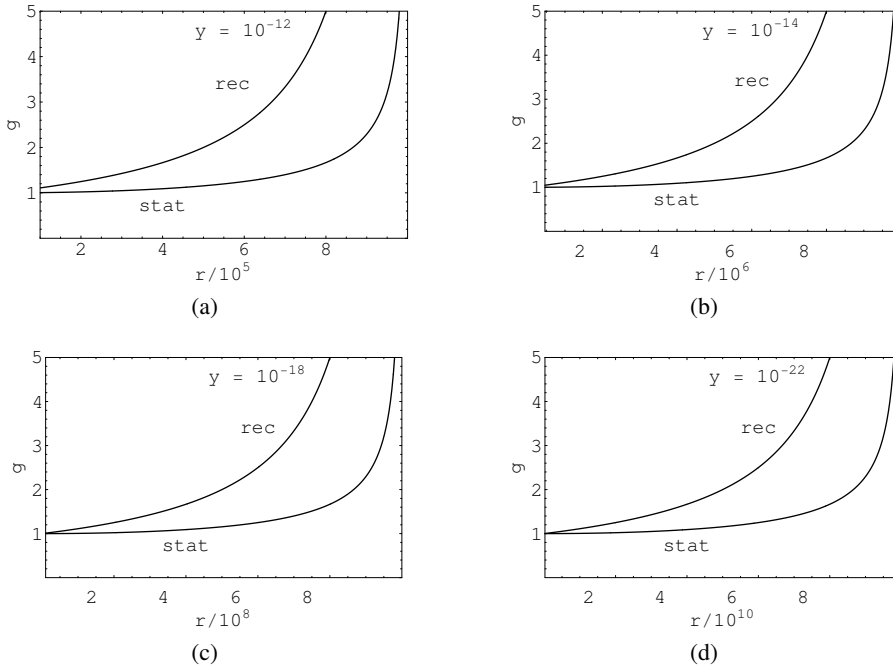


**Figure 1.** The frequency shift for two types of observers, static, and receding ones. The smallest value of  $r$  corresponds to  $10r_s$ , the largest one to the cosmological horizon. The corresponding values of the dimensionless parameter  $y$  are given in the figures.

Index ‘obs’ (observer) denotes the components measured by a static observer located on a given  $r$ . The time component of the photon 4-momentum, measured by a static observer located on the static radius  $r_s$ ,  $p_{\text{em}}^{(t)}$  satisfies the relation

$$p_{\text{em}}^{(t)} = \frac{\mathcal{E}}{B_s(y)}. \quad (43)$$

We introduce here a new parameter

$$B_s(y) \equiv B(r = r_s, y) = (1 - 3y^{1/3}). \quad (44)$$

The frequency shift of the photon (the ratio of observed and emitted energy) is given by the relation

$$g \equiv \frac{p_{\text{obs}}^{(t)}}{p_{\text{em}}^{(t)}} = \frac{B_s(y)}{B(r, y)}. \quad (45)$$

Behaviour of the frequency shift is illustrated in Figs 1 and 6.

An observer (located at  $r < r_s$ ) will see the photons coming from the directional angle  $\alpha$  related to the outward radial direction as given by the general relation

$$\cos \alpha = -\frac{P_{\text{obs}}^{(r)}}{P_{\text{obs}}^{(t)}}. \quad (46)$$

In the Schwarzschild–de Sitter spacetimes we arrive at

$$\cos \alpha = -A(r, y; l) = \pm \sqrt{1 - \left(1 - \frac{2}{r} - yr^2\right) \frac{l^2}{r^2}}. \tag{47}$$

The maximum angle  $\alpha_{\max}$  corresponds to the geodesic with  $l^2 = l_c^2 = 27/(1 - 27y)$ . In the area with  $\alpha > \alpha_{\max}$ , the sky seems to be black. Any radiation observed in this region must originate at a close vicinity of the black hole. The black region grows when the observer approaches the black hole.

Very near the horizon,  $\alpha_{\max} \approx 0$ , and all the radiation from the sky is concentrated into a tiny cone around the radial axis, (see Fig. 2).

Now we determine what the observer will see. First of all we determine the relation between the angle coordinates of the emitter  $(\theta_{em}, \phi_{em})$  and angles, in which the static observer located on the axis receives the incoming photon  $(\alpha, \beta)$ . We denote as  $\beta$  the azimuthal angle round the radial axis in the observer’s rest system. We assume null geodesics observed in directions  $(\alpha, \beta)$ , which for large distance  $r$  corresponds to angles  $(\theta_{em}, \phi_{em})$ , see Fig. 3, [Cunningham, 1975]. Then the following relations must hold

$$\theta_{em} = |\Delta\theta - 2n\pi| \quad \text{if} \quad (2n - 1)\pi < \Delta\theta < (2n + 1)\pi, \tag{48}$$

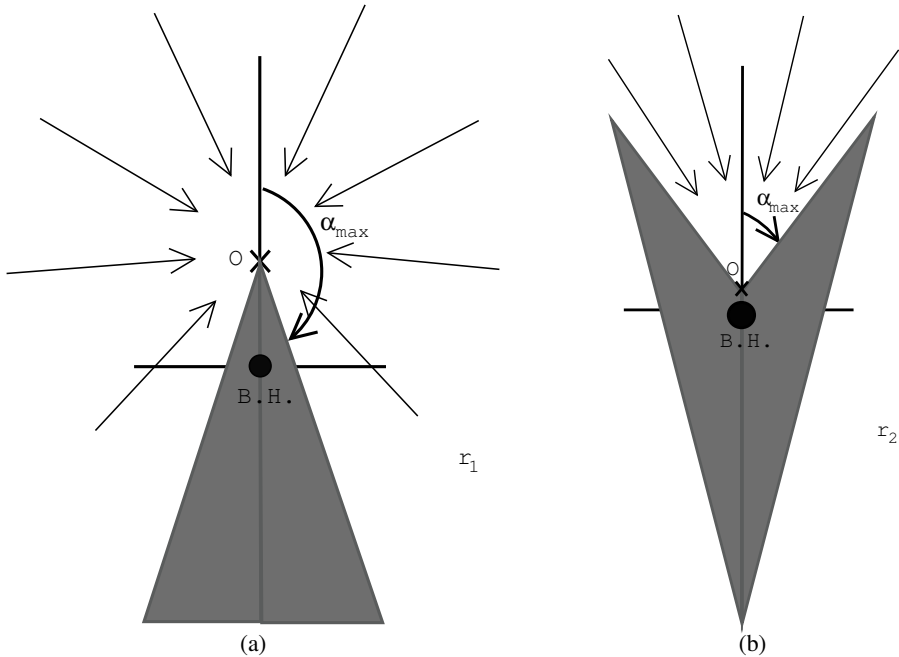


**Figure 2.** Trapping of photons by the black hole. The unshaded area characterised by the angle  $\alpha \in (0, \alpha_{\max})$ , from which the radiation hits to the observer O. The area decreases when the observer approaches the black hole ( $r_1 > r_2$ ).

$$\phi_{em} = \beta + \begin{cases} 0 & \text{if } 2n\pi < \Delta\theta < (2n+1)\pi, \\ \pi & \text{if } (2n-1)\pi < \Delta\theta < 2n\pi, \end{cases} \quad (49)$$

where the total angle  $\Delta\theta$ , spanned by the photon trajectory between the emitter and observer, is given by the relations

$$\Delta\theta = \int_{r_{obs}}^{r_s} \frac{p^\theta}{p^r} dr = \int_{r_{obs}}^{r_s} \frac{l}{r^2 A(r, y; l)} dr, \quad (50)$$

with  $l$  being determined by the angle  $\alpha$  and the location of the observer through (47). These equations give  $(\theta_{em}, \phi_{em})$  as a function of  $(\alpha, \beta)$ .

The radiation field travelling between a source and an observer is governed by the Boltzmann equation which can be given in the form [Misner et al., 1973]

$$\frac{I_\nu}{\nu^3} = \text{const}, \quad (51)$$

where  $\nu$  is the frequency of the photon and  $I_\nu$  is the specific intensity of the radiating field corresponding to the given frequency. For a bundle of photons with nearly the same values of constants of the motion  $\mathcal{E}$  and  $l$ , we can express the Boltzmann equation in the form

$$\frac{I_{\nu_{obs}}}{\nu_{obs}^3} = \frac{I_{\nu_{em}}}{\nu_{em}^3}. \quad (52)$$

For the ratio of the observed and emitted specific intensities we then obtain

$$\frac{I_{\nu_{obs}}}{I_{\nu_{em}}} = \left( \frac{p_{obs}^{(t)}}{p_{em}^{(t)}} \right)^3 = \left( \frac{B_s(y)}{B(r, y)} \right)^3. \quad (53)$$

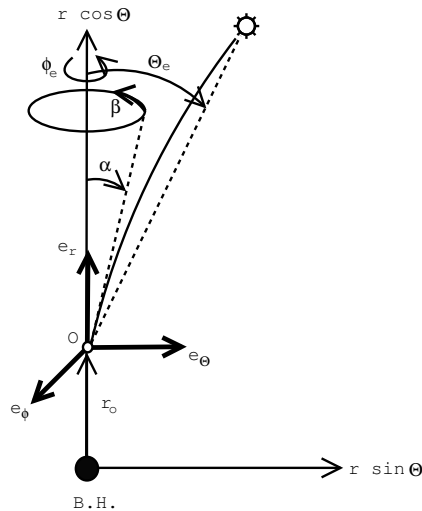


**Figure 3.** Photon trajectory and observed angles. The schematic representation of setting angles. The observer is located on the polar axis ( $\theta = 0$ ) at distance  $r_{obs}$  from the black hole. The photons, which he observes, are characterised by a couple of angles  $(\alpha, \beta)$ .

Suppose that the radiating sphere located at  $r_s$  generates an isotropic radiation field with the intensity  $I_{\text{em}}$  ( $\text{erg cm}^{-2} \text{sec}^{-1} \text{sr}^{-1}$ ) given by the relation

$$I_{\text{em}} = \int I_{\nu_{\text{em}}} d\nu_{\text{em}}. \tag{54}$$

The observed energy flux  $F$  ( $\text{erg cm}^{-2} \text{sec}^{-1}$ ) will be given by the equation

$$\begin{aligned} \frac{F}{4\pi I_{\text{em}}} &= \iint \frac{I_{\nu_{\text{obs}}}}{4\pi I_{\text{em}}} d\nu_{\text{obs}} d\Omega = \frac{1}{2} \left[ \frac{B_s(y)}{B(r, y)} \right]^4 (1 - \cos \alpha_{\text{max}}) \\ &= \frac{1}{2} B_s^4(y) \left( 1 - \frac{2}{r} - yr^2 \right)^{-2} \\ &\quad \times \left[ 1 \pm \sqrt{1 - \left( 1 - \frac{2}{r} - yr^2 \right) \left( \frac{27}{1 - 27y} \right) \frac{1}{r^2}} \right]. \end{aligned} \tag{55}$$

Dependence of the flux on the radius of the observer is illustrated in Fig.4 for different values of parameter  $y$ .

It makes sense in real situation to consider only direct photons. Multiple images, created by photons orbiting the black hole several times, will be so weak that it will be very difficult to observe them, see [Cunningham, 1975]. Therefore we do not consider the multiple images here.

Now we determine the flux in the limit of  $y \rightarrow 0$ . Taking the first terms of the Taylor expansion, we obtain the following results

$$\xi \simeq \frac{\pi}{2} - \sqrt{27y}, \tag{56}$$

and

$$r_h \simeq 2 - y, \tag{57}$$

for the black hole horizon, and

$$r_c \simeq \frac{1}{\sqrt{y}}(1 - \sqrt{y}), \tag{58}$$

for the cosmological horizon.

In this approximation the flux near the black hole horizon ( $r \rightarrow r_h$ ) has the form

$$\frac{F}{4\pi I_{\text{em}}} \simeq \frac{27(1 - 3y^{1/3})^2}{4} \left( 1 - \frac{2}{r} - yr^2 \right)^{-1} \frac{27}{(1 - 27y)} \frac{1}{(2 - y)^2}. \tag{59}$$

If we consider in limit for  $y \rightarrow 0$  only the linear members, we obtain

$$\frac{F}{4\pi I_{\text{em}}} \simeq \frac{1}{16} \left( 1 - \frac{2}{r} - yr^2 \right)^{-1} (1 - 6y^{2/3} + 28y). \tag{60}$$

The situation will be different for the static observers located on  $r > r_s$ . Here we consider only the situations with  $r \gg r_s$ , when the radiating sphere at  $r = r_s$  can be considered as a small radiating spot observed at a small angle  $\Delta\theta$ . This approximation is possible only in spacetimes, where  $r_c \gg r_s$ . Since  $r_c \sim 1/\sqrt{y}$  a  $r_s \sim 1/y^{1/3}$ , it is clear that we have to assume  $y \lesssim 10^{-12}$ .

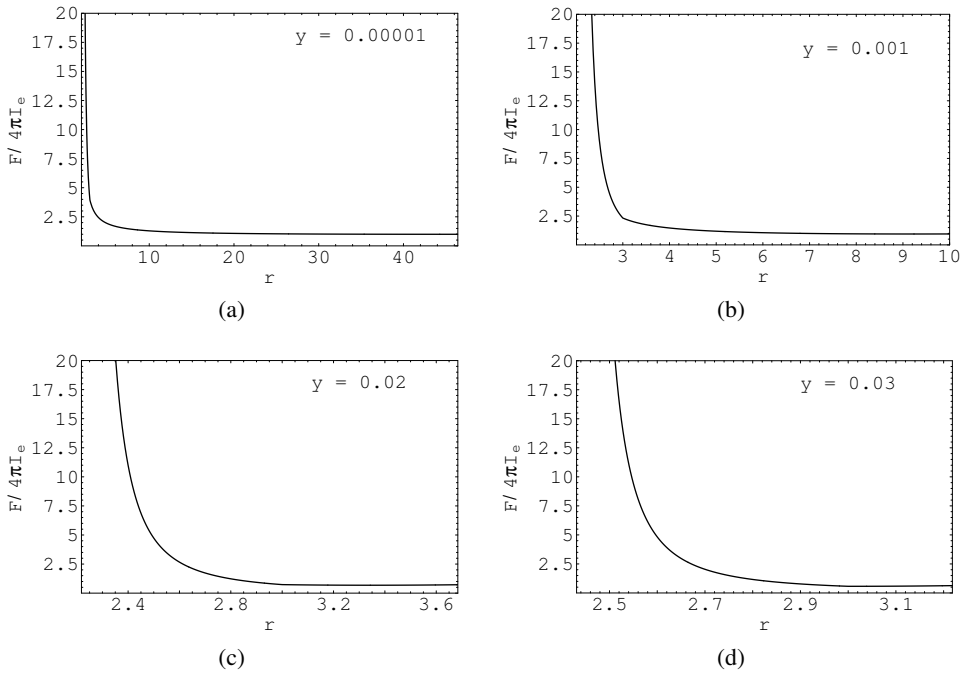


**Figure 4.** The flux of radiation measured by the static observer located at  $r_h < r < r_s$ . Extension of the  $r$  axis corresponds to the black hole horizon  $r_h$  and the static radius  $r_s$ . The corresponding values of the dimensionless parameter  $y$  are given in the figure.

The radiation flux, measured by the static observer is then given by the relation

$$\frac{F}{4\pi I_{\text{em}}} \simeq \frac{1}{2} B_s^4(y) \left(1 - \frac{2}{r} - yr^2\right)^{-2} \Delta\theta. \quad (61)$$

For small angles  $\Delta\theta$  we can use approximate relation

$$\Delta\theta \simeq \frac{r_s}{r - r_s}. \quad (62)$$

Dependence of the resulting flux on  $r$  is illustrated in Fig. 5. We can see that for  $r \rightarrow r_c$  the observed radiation flux will diverge, since  $\Delta\theta \sim r_s/(r_c - r_s)$  is nonzero and the frequency shift diverges nearby the cosmological horizon for the static observers.

#### 4 RADIALLY FALLING OBSERVERS

When approaching the black hole horizon the static observers must be kept at rest by diverging trust. Clearly, the static observers are rather unnatural observers in vicinity of the horizons. On the other hand, as natural observers could be considered falling radially onto the black hole, or receding to the cosmological horizon. Here we consider family of observers freely moving from the static radius  $r_s$ , with the specific energy  $E_s = \sqrt{1 - 3y^{1/3}}$ .

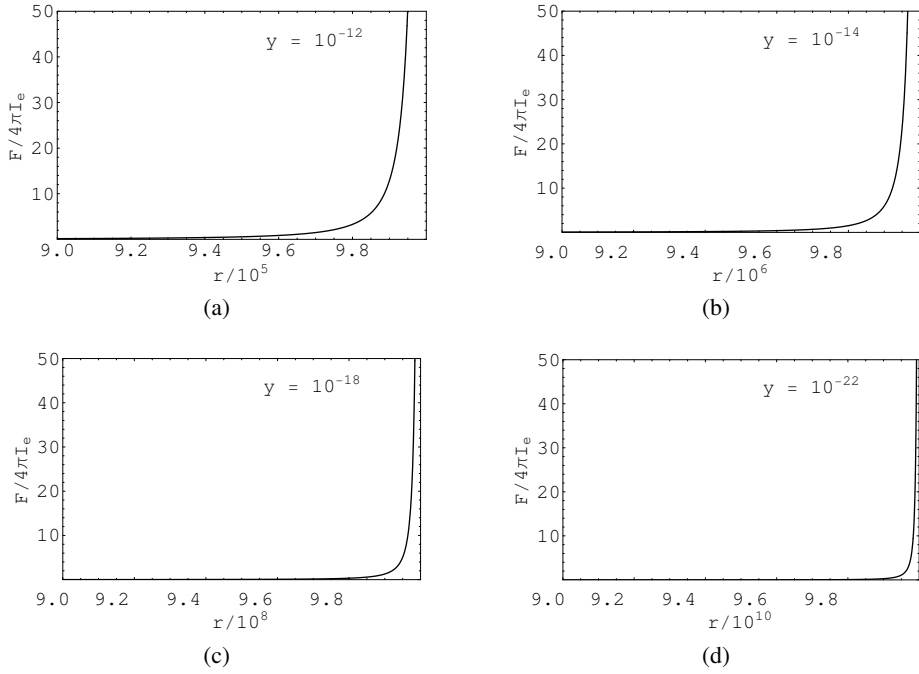


**Figure 5.** The flux of radiation measured by the static observer located at  $r_s < r < r_c$ . The smallest value at the axis  $r$  corresponds  $r = 0.9 r_c$ , the largest one to the cosmological horizon  $r_c$ . The corresponding values of the dimensionless parameter  $y$  are given in the figure.

Values of physical quantities locally measured by such radially falling (or receding) observers we will denote by index in round brackets with a tilde. First, we determine the orthonormal tetrad of 1-forms for the radially falling observer by using relations

$$e_{(\tilde{\nu})} = \Lambda_{(\tilde{\nu})}^{(\mu)} e_{(\mu)}, \quad \omega^{(\tilde{\nu})} = \Lambda_{(\mu)}^{(\tilde{\nu})} \omega^{(\mu)}. \quad (63)$$

$\Lambda$  is matrix of the Lorentz transformation between the static observer and radially moving observer on given  $r$

$$\Lambda_{(\tilde{\nu})}^{(\mu)} = \begin{pmatrix} \cosh \psi & \sinh \psi & 0 & 0 \\ \sinh \psi & \cosh \psi & 0 & 0 \\ 0 & 0 & 1 & 0 \\ 0 & 0 & 0 & 1 \end{pmatrix},$$

$$\Lambda_{(\nu)}^{(\tilde{\mu})} = \begin{pmatrix} \cosh \psi & -\sinh \psi & 0 & 0 \\ -\sinh \psi & \cosh \psi & 0 & 0 \\ 0 & 0 & 1 & 0 \\ 0 & 0 & 0 & 1 \end{pmatrix},$$

where  $\cosh \psi$ ,  $\sinh \psi$  are given by the relations

$$\cosh \psi = \gamma = \frac{1}{\sqrt{1 - v^2}}, \quad (64)$$

$$\sinh \psi = \frac{v}{\sqrt{1-v^2}}, \quad (65)$$

with  $v$  being the velocity of the freely falling observer as measured by the static observer. This locally measured velocity is determined by the standard formula

$$v = \frac{dl}{d\tau} = \sqrt{\frac{g_{rr}}{g_{tt}}} \frac{dr}{dt} = \sqrt{\frac{g_{rr}}{g_{tt}}} \frac{dr}{d\tau} \frac{d\tau}{dt}, \quad (66)$$

where  $dl$  is an element of proper distance,  $d\tau$  is an element of proper time of the static observer and  $dr/dt$  is the radial coordinate velocity of radially falling observer. The motion of the radially falling observer from the static radius is given by the coordinate components of 4-momentum

$$p^t = \frac{dt}{d\lambda} = g^{tt} p_t = \mathcal{E} B^{-2}(r, y), \quad (67)$$

$$p^r = \frac{dr}{d\lambda} = -\sqrt{\mathcal{E}^2 - V_{\text{eff}}^2} = -m \sqrt{\frac{\mathcal{E}^2}{m^2} - B^2(r, y)}, \quad (68)$$

where  $\mathcal{E}$  is the constant energy of the motion and  $\lambda = \tau/m$  is an affine parameter. For the velocity  $v$  we obtain the relation

$$v = -\frac{Z(r, y)}{\sqrt{1-3y^{1/3}}}, \quad (69)$$

where we introduced a new variable

$$Z(r, y) \equiv \sqrt{\frac{2}{r} + yr^2 - 3y^{1/3}}, \quad (70)$$

which characterises the observer radially falling from the static radius. Then the parameters of the Lorentz transformation are given by

$$\cosh \psi = \frac{\sqrt{1-3y^{1/3}}}{B(r, y)}, \quad \sinh \psi = -\frac{Z(r, y)}{B(r, y)}, \quad (71)$$

and the orthonormal tetrad of 1-forms of the radially falling observers has the form

$$\omega^{(\tilde{t})} = \sqrt{1-3y^{1/3}} dt + Z(r, y) B^{-2}(r, y) dr, \quad (72)$$

$$\omega^{(\tilde{r})} = Z(r, y) dt + \sqrt{1-3y^{1/3}} B^{-2}(r, y) dr, \quad (73)$$

$$\omega^{(\tilde{\theta})} = r d\theta, \quad (74)$$

$$\omega^{(\tilde{\phi})} = r \sin \theta d\phi. \quad (75)$$

The locally measured 4-momentum is related to the coordinate 4-momentum by

$$p^{(\tilde{\mu})} = \omega^{(\tilde{\mu})}_{(v)} p^{(v)}. \quad (76)$$

The components of 4-momentum of the photons, measured locally by the observers radially falling along the axis of symmetry are given by the relations

$$p_{\text{obs}}^{(\tilde{t})} = \frac{\mathcal{E}}{B^2(r, y)} \left( \sqrt{1-3y^{1/3}} + Z(r, y) A(r, y; l) \right), \quad (77)$$

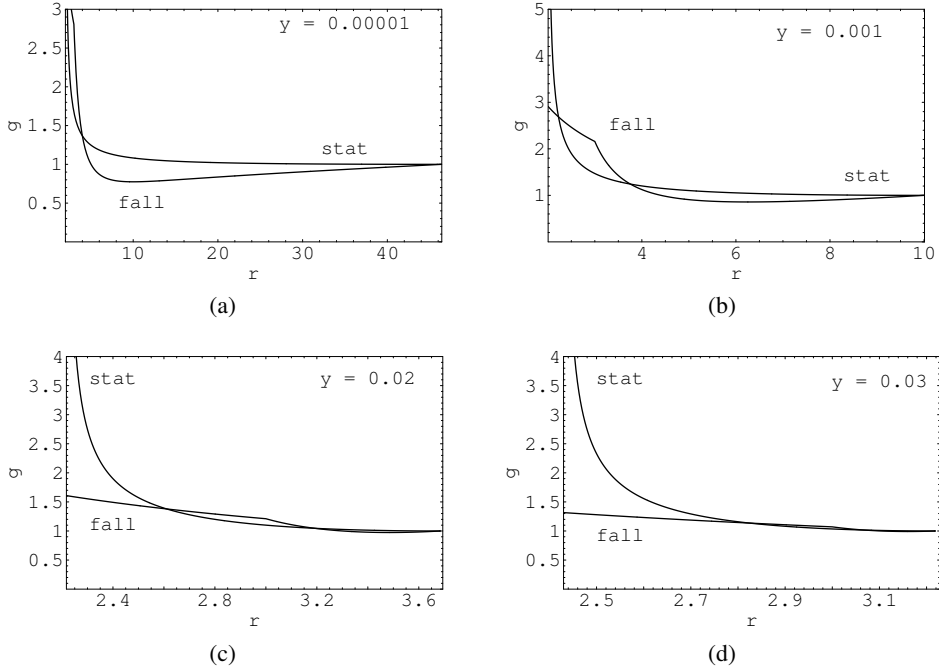


**Figure 6.** The frequency shift of photons emitted at  $r_s$  and observed by static and radially falling observers. The sign + for falling observers means, that they observe radiation coming from their “own” space. For both types of observers  $r_h < r < r_s$ . The corresponding values of the dimensionless parameter  $y$  are given in the figures.

$$p_{\text{obs}}^{(\tilde{r})} = \frac{\mathcal{E}}{B^2(r, y)} \left( Z(r, y) + \sqrt{1 - 3y^{1/3}A(r, y; l)} \right), \quad (78)$$

$$p_{\text{obs}}^{(\tilde{\theta})} = \frac{\mathcal{E}l}{r} = \frac{\Phi}{r}. \quad (79)$$

Again we assume the motion with  $\phi = \text{const}$ .

#### 4.1 Frequency shift

The frequency shift of the photon measured by the radially falling observer is given by the relation

$$\tilde{g} \equiv \frac{p_{\text{obs}}^{(\tilde{r})}}{p_{\text{em}}^{(\tilde{r})}} = \frac{B_s(y)}{B^2(r, y)} \left( \sqrt{1 - 3y^{1/3}} + Z(r, y)A(r, y; l) \right) \quad (80)$$

$$= \frac{B_s(y)}{Z(r, y) \cos \tilde{\alpha} + \sqrt{1 - 3y^{1/3}}}, \quad (81)$$

and its dependence on  $r$  is illustrated in Fig. 6.

## 4.2 Directional angles

The directional angle  $\tilde{\alpha}$  (related to the outward radial direction), in which the falling observer will see the incoming photon with impact parameter  $l$  is given by the relations

$$\cos \tilde{\alpha} = -\frac{\left(Z(r, y) + \sqrt{1 - 3y^{1/3}}A(r, y; l)\right)}{\left(\sqrt{1 - 3y^{1/3}} + Z(r, y)A(r, y; l)\right)}, \quad (82)$$

$$\frac{l}{r} = \frac{\sin \tilde{\alpha}}{\left(Z(r, y) \cos \tilde{\alpha} + \sqrt{1 - 3y^{1/3}}\right)}. \quad (83)$$

As in the case of the static observers, the radially falling observers will see the dark sky at the angles  $\tilde{\alpha} > \tilde{\alpha}_{\max}$ . The angle  $\tilde{\alpha}_{\max}$  corresponds to the photons incoming from the unstable circular photon orbit located on  $r = 3$  with  $l^2 \equiv l_c^2 = 27/(1 - 27y)$ . It is clear from the equation (81) that the observed frequency shift depends upon the direction, in which the photon arrives to the observer.

## 4.3 Photons from the parallel region of the spacetime

Until the observer does not cross the horizon, he sees only its proper region of the spacetime. The situation will change after crossing the horizon, if we consider the extended Schwarzschild–de Sitter spacetime with “parallel” static regions [Gibbons and Hawking, 1977], which will also influence the observer below the black hole horizon. The photons from the “other side”, i.e., from the “parallel” region of the spacetime, have the conserved energy  $p_t = +\mathcal{E}$ , in contrast to the photons from observer’s own space with  $p_t = -\mathcal{E}$ . The components of the 4-momentum of the photons from the “other side”, measured by the radially falling observer are given by the relations

$$p_{\text{obs}}^{(\tilde{r})} = \frac{\mathcal{E}}{B^2(r, y)} \left(-\sqrt{1 - 3y^{1/3}} + Z(r, y)A(r, y; l)\right), \quad (84)$$

$$p_{\text{obs}}^{(\tilde{r})} = \frac{\mathcal{E}}{B^2(r, y)} \left(-Z(r, y) + \sqrt{1 - 3y^{1/3}}A(r, y; l)\right), \quad (85)$$

$$p_{\text{obs}}^{(\tilde{\theta})} = \frac{\mathcal{E}l}{r} = \frac{\Phi}{r}. \quad (86)$$

In analogy with equations (80), (81), (82), (83) the following relations hold for the photons from the “other side”

$$\begin{aligned} \tilde{g} &\equiv \frac{p_{\text{obs}}^{(\tilde{r})}}{p_{\text{em}}^{(\tilde{r})}} = \frac{B_s(y)}{B^2(r, y)} \left(-\sqrt{1 - 3y^{1/3}} + Z(r, y)A(r, y; l)\right) \\ &= -\frac{B_s(y)}{Z(r, y) \cos \tilde{\alpha} + \sqrt{1 - 3y^{1/3}}}, \end{aligned} \quad (87)$$

$$\cos \tilde{\alpha} = \frac{\left(A(r, y; l)\sqrt{1 - 3y^{1/3}} - Z(r, y)\right)}{\left(\sqrt{1 - 3y^{1/3}} - Z(r, y)A(r, y; l)\right)}, \quad (88)$$

$$\frac{l}{r} = -\frac{\sin \tilde{\alpha}}{\left( Z(r, y) \cos \tilde{\alpha} + \sqrt{1 - 3y^{1/3}} \right)}. \quad (89)$$

#### 4.4 Energy flux

The flux of radiation from the isotropically radiating source located at  $r_s$  and observed by the freely falling observers is given by the relation

$$\frac{F}{4\pi I_{em}} = \frac{B_s^4(y)}{6Z(r, y)} \times \left[ \left( Z(r, y) \cos \tilde{\alpha}_{max} + \sqrt{1 - 3y^{1/3}} \right)^{-3} - \left( Z(r, y) + \sqrt{1 - 3y^{1/3}} \right)^{-3} \right], \quad (90)$$

for the radiation from the “observers side” of the spacetime (Fig. 7) and by the relation

$$\frac{F}{4\pi I_{em}} = \frac{B_s^4(y)}{6Z(r, y)} \times \left[ -\left( Z(r, y) - \sqrt{1 - 3y^{1/3}} \right)^{-3} - \left( \sqrt{1 - 3y^{1/3}} + Z(r, y) \cos \tilde{\alpha}_{min} \right)^{-3} \right]. \quad (91)$$

for the radiation from the “other side” (Fig. 8).

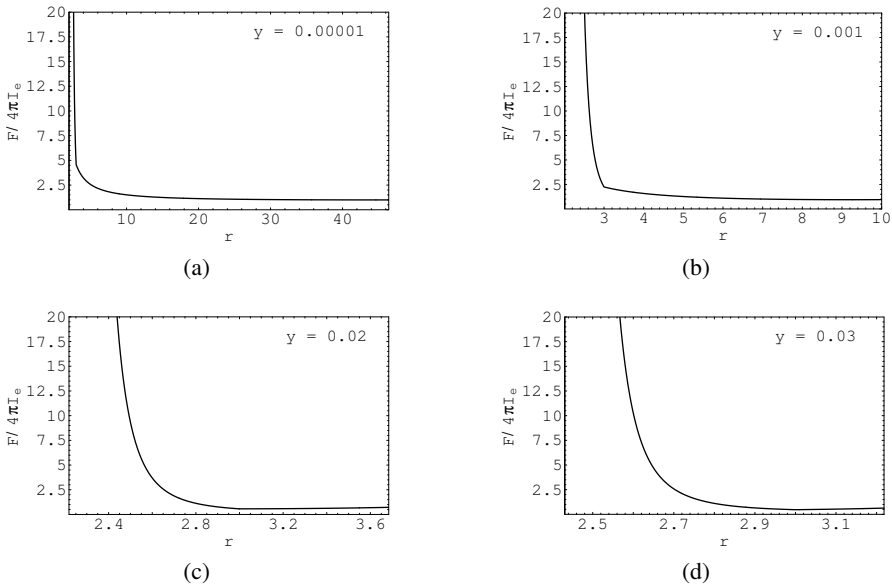


**Figure 7.** The flux of radiation from the observer’s side, measured by the radially falling observer located at  $r_h < r < r_s$ . Extension of  $r$  axis corresponds to the black hole horizon  $r_h$  and the static horizon  $r_s$ . The corresponding values of the dimensionless parameter  $y$  are given in the figure.

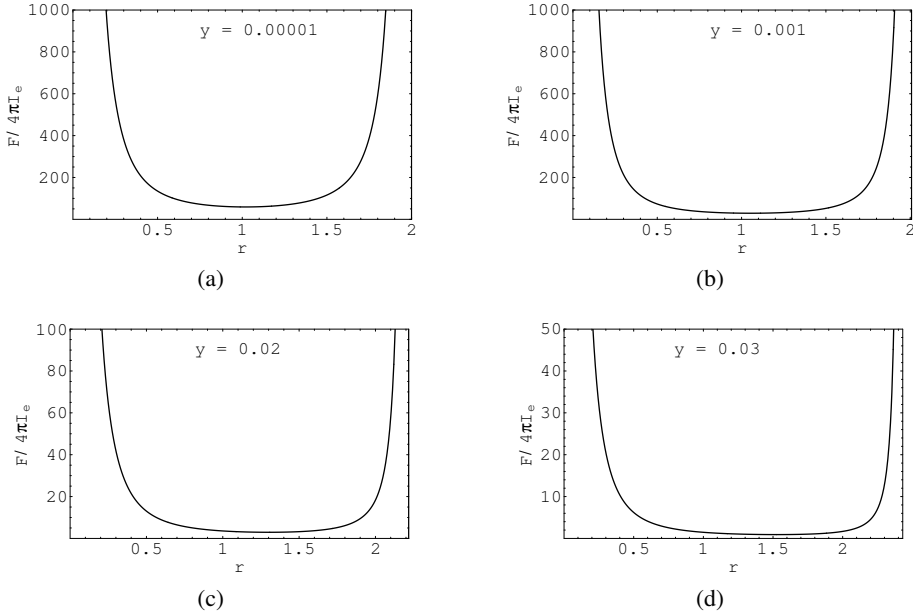


**Figure 8.** The flux of radiation from the “other” side, measured by the radially falling observer located at  $r < r_h$ . The smallest value at the axis  $r$  corresponds to  $r = 0$ , the largest one to the black hole horizon  $r_h$ . The corresponding values of the dimensionless parameter  $y$  are given in the figures.

## 5 RADIALLY RECEDING OBSERVERS

Let consider the observers freely receding from the static radius  $r_s$  to the cosmological horizon. The situation will be similar to the case of the static observer at  $r > r_s$ . The observer will see the radiation coming from an area, which (if the observer recedes on  $r \gg r_s$ ) we can be considered in a rough approximation as a spot observed under the angle  $\Delta\theta$ . The velocity of the freely receding observer is given by (we take here  $p^r$  with positive sign)

$$v = \frac{Z(r, y)}{\sqrt{1 - 3y^{1/3}}}. \quad (92)$$

The parameters of the Lorentz transformation have the form

$$\cosh \psi = \frac{\sqrt{1 - 3y^{1/3}}}{B(r, y)}, \quad (93)$$

$$\sinh \psi = \frac{Z(r, y)}{B(r, y)}. \quad (94)$$

The tetrad of 1-forms of radially receding observer has the form

$$\omega^{(\tilde{t})} = \sqrt{1 - 3y^{1/3}} dt - Z(r, y)B^{-2}(r, y) dr, \quad (95)$$

$$\omega^{(\tilde{r})} = -Z(r, y) dt + \sqrt{1 - 3y^{1/3} B^{-2}(r, y)} dr, \quad (96)$$

$$\omega^{(\tilde{\theta})} = r d\tilde{\theta}, \quad (97)$$

$$\omega^{(\tilde{\phi})} = r \sin \tilde{\theta} d\phi. \quad (98)$$

The photons are emitted in the outward direction from the source situated on  $r_s$ , therefore we must consider for the component of the 4-momentum  $p_r$

$$A(r, y; l) = +\sqrt{1 - B^2(r, y) \frac{l^2}{r^2}}. \quad (99)$$

The components of the photon's 4-momentum, measured by the freely receding observer located on the axis of symmetry, have the form

$$p_{\text{obs}}^{(\tilde{r})} = \frac{\mathcal{E}}{B^2(r, y)} \left( \sqrt{1 - 3y^{1/3}} - Z(r, y) A(r, y; l) \right), \quad (100)$$

$$p_{\text{obs}}^{(\tilde{r})} = \frac{\mathcal{E}}{B^2(r, y)} \left( -Z(r, y) + \sqrt{1 - 3y^{1/3}} A(r, y; l) \right), \quad (101)$$

$$p_{\text{obs}}^{(\tilde{\theta})} = \frac{\mathcal{E} l}{r} = \frac{\Phi}{r}. \quad (102)$$

For the frequency shift of the photon, we obtain

$$\tilde{g} \equiv \frac{p_{\text{obs}}^{(\tilde{r})}}{p_{\text{em}}^{(\tilde{r})}} = \frac{B_s(y)}{\sqrt{1 - 3y^{1/3}} - Z(r, y) \cos \Delta\tilde{\theta}}. \quad (103)$$

The frequency shift is illustrated in Fig. 1.

Now we must express the angle  $\Delta\tilde{\theta}$ , in which the radially receding observer located on  $r \gg r_s$  sees the radiating sphere. We can estimate this angle by using the of special relativistic transformation of the angle  $\Delta\theta \simeq r_s/(r - r_s)$  measured by the static observer. We transfer this angle to the system, which moves relative to the static observer with the velocity  $v$  of the receding observers as measured by the static observer. The Lorentz transformation gives

$$\cos \Delta\tilde{\theta} = \frac{\cos \Delta\theta + v}{1 + v \cos \Delta\theta}, \quad (104)$$

where  $v$  is given by the relation (92).

Note that this is an approximative result only; to obtain exact result, a fully general relativistic computation is necessary taking into account the gravitational focusing. But this needs a relatively complex computational code. Therefore, we use here the special-relativistic estimate. For small angle we can expand  $\cos \Delta\tilde{\theta}$  to the series and we obtain

$$\Delta\tilde{\theta}^2 \simeq \Delta\theta^2 \frac{1 - v}{1 + v}, \quad (105)$$

whereas  $\Delta\theta$  is given by (62).

The observed flux of the radiation has then the form

$$\frac{F}{4\pi I_{\text{em}}} = \frac{1}{2} \frac{B_s^4(y)}{\left( \sqrt{1 - 3y^{1/3}} - Z(r, y) \cos \Delta\tilde{\theta} \right)^4} \Delta\tilde{\theta}. \quad (106)$$

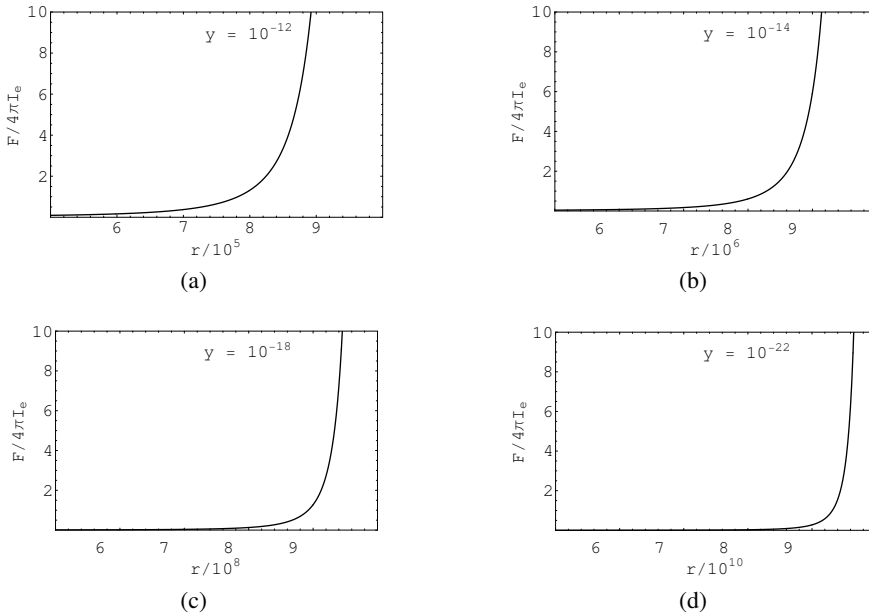


**Figure 9.** The flux of radiation measured by the radially receding observer located at  $r_s < r < r_c$ . The smallest value at the axis  $r$  corresponds to  $r = 0.5 r_c$ , the largest value to the cosmological horizon  $r_c$ . The corresponding values of the dimensionless parameter  $y$  are given in the figures.

Its radial dependence is presented in Fig. 9.

## 6 CONCLUSION

In the case of the Schwarzschild–de Sitter spacetime we discussed properties of the flux of radiation coming from the isotropically radiating sources distributed continuously on the sphere at the static radius  $r_s$ , as observed in vicinity of the horizons of the spacetime. We considered three families of observers: the static ones, observers radially falling from  $r_s$  to the hole, and observers radially receding from  $r_s$  to the cosmological horizon  $r_c$ .

For the static and receding observers located above the static radius we give only approximative results, considering the radiating sphere as an radiating spot observed at a small angle  $\Delta\theta$ . We assume position of the observer  $r \gg r_s$ .

The observed flux for the static observers near the black hole and cosmological horizon diverges. It is influenced by the gravitational blue shift and the gravitational focusing.

The observed flux for falling observers near the black hole horizon diverges, too. In this case the gravitational focusing is important. The gravitational blue shift is finite at the horizon. For completeness, we investigated also the radiation coming from the “parallel” universe of the Schwarzschild–de Sitter spacetime as observed by the radially falling observer under the black hole horizon. In this case, the flux diverges near both the horizon and the singularity at  $r = 0$ .

## ACKNOWLEDGEMENTS

The work was supported by the grants GAČR No 203/03/1147 and 205/03/H 144 and by the committee for collaboration of the Czech Republic with CERN. One author (Z. S.) would like to thank Theory Division of CERN for perfect hospitality.

## REFERENCES

- [Ames and Thorne, 1968] Ames, W. L. and Thorne, K. S. (1968). *Astrophys. J.*, 151:659–670.
- [Bardeen, 1973] Bardeen (1973). *Astrophys. J.*, 173:137.
- [Cunningham, 1975] Cunningham, C. (1975). Optical appearance of distant objects to observer near and inside a Schwarzschild black hole. *Phys. Rev.*, 12:323–328.
- [Cunningham and Bardeen, 1972] Cunningham, C. and Bardeen, J. (1972). *Astrophys. J.*, 173:L137.
- [Gibbons and Hawking, 1977] Gibbons, G. W. and Hawking, S. W. (1977). Cosmological event horizons, thermodynamics, and particle creation. *Phys. Rev. D*, 15:2738–2751.
- [Krauss and Turner, 1995] Krauss, L. M. and Turner, M. S. (1995). *Gen. Rel. Grav.*, 27:1137.
- [Misner et al., 1973] Misner, C. W., Thorne, K. S., and Wheeler, J. A. (1973). *Gravitation*. Freeman, San Francisco.
- [Ostriker and Steinhardt, 1995] Ostriker, J. P. and Steinhardt, P. J. (1995). *Nature*, 377:600.
- [Podurets, 1964] Podurets, M. A. (1964). *Astronomicheskii Zhurnal*, 41:1090–1096.
- [Stuchlík and Hledík, 1999] Stuchlík, Z. and Hledík, S. (1999). Some properties of the Schwarzschild–de Sitter and Schwarzschild–anti-de Sitter spacetimes. *Phys. Rev. D*, 60(4):044006 (15 pages).



# Influence of relict vacuum energy on the Rees–Sciama effect

Zdeněk Stuchlík and Jan Schee

*Institute of Physics, Faculty of Philosophy and Science, Silesian University in Opava  
Bezručovo nám. 13, CZ-746 01 Opava, Czech Republic*

## ABSTRACT

The role of the observed relict vacuum energy on the fluctuations of CMBR going through cosmological matter condensations is studied in the framework of the Einstein–Strauss–de Sitter vakuola model. It is shown that refraction of light at the matching surface of the vakuola and the expanding Friedman universe can be very important during the accelerated expansion of the universe when the velocity of the matching surface relative to static Schwarzschildian observers becomes relativistic.

## 1 INTRODUCTION

Temperature fluctuations of the Cosmic Microwave Background Radiation (CMBR), recently measured by sophisticated observational methods (COBE, WMAP, etc.), are observed on the level of  $\Delta T/T \sim 10^{-5}$  [Spergel et al., 2003]. These fluctuations could be explained in two ways. First, by the Sachs–Wolfe effect [Sachs and Wolfe, 1967], i.e., as an imprint of energy density fluctuations related to the CMBR temperature fluctuations at the cosmological redshift  $z \sim 1300$  during the era of recombination, when effective interaction of matter and CMBR is ceased [Börner, 1993]. Second, by the Rees–Sciama effect [Rees and Sciama, 1968], i.e., as a result of influence of large-scale inhomogeneities (both large galaxies or their clusters, and large voids) evolved in the expanding universe due to the gravitational instability of matter at the era characterised by  $z \lesssim 10$ . In the case of spherically symmetric clusters and voids, the Rees–Sciama effect was considered in detail by Mészáros and Molnár [Mészáros and Molnár, 1996]. They describe the clusters by the standard Einstein–Strauss vakuola model, while the voids they model in an approximative way that does not meet the full general-relativistic junction conditions. Further, they do not consider the effect of refraction of light at the boundary surface matching the cluster (void) with the expanding universe. However, this effect could be of great importance in an accelerating universe, indicated by many of recent cosmological tests predicting present value of the vacuum energy density  $\rho_{\text{vac}} \sim 0.67\rho_{\text{crit}}$  ( $\rho_{\text{crit}} \equiv 3H/8\pi G$  is the critical energy density corresponding to the flat universe predicted by the inflationary paradigm [Linde, 1990, Spergel et al., 2003]). The vacuum energy density (or energy of a quintessence field) is related to the (effective) cosmological constant by

$$\Lambda = \frac{8\pi G}{c^2} \rho_{\text{vac}}. \quad (1)$$

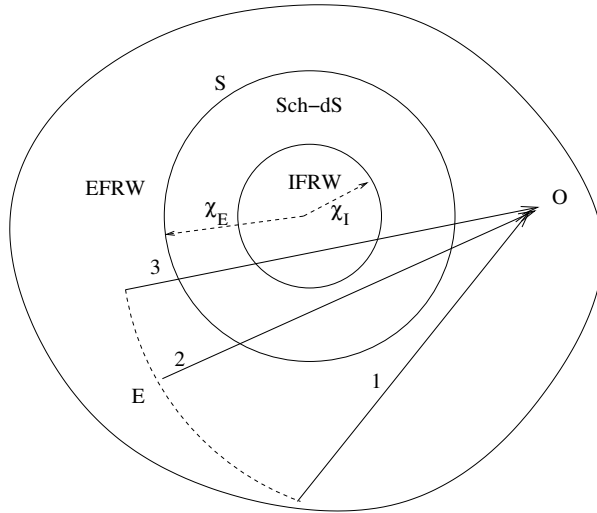


**Figure 1.** A schematic picture of a cluster represented as a spherical symmetric inhomogeneity immersed in the dust filled Friedman universe. At the centre of the cluster could be a Schwarzschild black hole or a dust sphere described by Friedman–Robertson–Walker (FRW) metric with parameters different then those characterising the external FRW universe. The central region is related to the EFRW universe through the intermediate vacuum Schwarzschild–de Sitter region;  $\chi_E = \chi_b$  is the comoving radius of the cluster,  $\chi_I$  is the comoving radius of the internal dust filled universe.

Here we present a study of the influence of the relict repulsive cosmological constant, indicated by observations to be equal  $\Lambda \approx 10^{-56} \text{ cm}^{-2}$ , on the Rees–Sciama effect. We use the Einstein–Strauss–de Sitter vakuola model in which the inhomogeneity is represented by a spherically symmetric cluster which is immersed into the Friedmanian dust-filled universe (see Fig. 1). We determine temperature fluctuations of the CMBR passing the vakuola described by the Einstein–Strauss–de Sitter model and give estimations of the relevance of the effect of refraction at the matching surface. We show, how the influence of the refraction effect grows with the velocity of the matching surface. Note that in the standard Friedman models with  $\Lambda = 0$ , the velocity of the matching surface falls in the expanding universe and the refraction effects are suppressed. However, in the accelerated universe, the velocity grows, and the refraction effect becomes significant. Such effect could serve as another test of the presence of the cosmological constant; it could have strong observational consequences in future, when the velocity of the matching surface becomes to be relativistic.

Throughout our computations, we use the geometric units with  $c = G = 1$ .

## 2 EINSTEIN–STRAUSS–DE SITTER VAKUOLA MODEL

In the construction of the Einstein–Strauss–de Sitter model with a repulsive cosmological constant, we remove at a fixed value of the comoving Robertson–Walker coordinate  $\chi_b$  a spherical ball of dust of the mass  $M$  from the dust-filled universe and replace it by

the Schwarzschild–de Sitter spacetime of the same mass  $M$ . Its expanding boundary surface coincides with expanding surface  $\chi = \chi_b = \text{const}$  of the Friedman universe. The Schwarzschild–de Sitter spacetime can be completely vacuum, i.e., black-hole spacetime, or, as used frequently, it can have a spherical source represented by a part of an internal dusty Friedman universe with parameters different than those of the external Friedman universe outside of the vacuum Schwarzschild–de Sitter spacetime.

The vacuum Schwarzschild–de Sitter spacetime of mass  $M$  is described in the standard Schwarzschild coordinates by the line element

$$ds^2 = -\mathcal{A}^2(r) dt^2 + \mathcal{A}^{-2}(r) dr^2 + r^2 d\Omega, \tag{2}$$

where

$$\mathcal{A}^2(r) = 1 - \frac{2M}{r} - \frac{\Lambda}{3}r^2. \tag{3}$$

The external Friedman universe is described by the Robertson–Walker geometry. In the standard comoving coordinates its line element reads

$$ds^2 = -dT^2 + R^2(T) \left[ d\chi^2 + \Sigma_k^2(\chi) d\Omega \right], \tag{4}$$

where

$$\Sigma_k(\chi) = \begin{cases} \sin \chi & \text{for } k = +1, \\ \chi & \text{for } k = 0, \\ \sinh \chi & \text{for } k = -1. \end{cases} \tag{5}$$

The Robertson–Walker metric describes the external Friedman universe at  $\chi \geq \chi_b$ , while at  $\chi < \chi_b$  it is replaced by the expanding part of the Schwarzschild–de Sitter spacetime. The particles with  $\chi = \chi_b$  follow radial geodesics of the Schwarzschild–de Sitter spacetime.

The evolution of the Friedman universe is given by the evolution of the scale factor  $R$  and the energy density  $\rho$  in dependence on the cosmic time  $T$ . The scale factor fulfils the Friedman equation

$$\left( \frac{dR}{dT} \right)^2 = \frac{8\pi\rho}{3R} + \frac{\Lambda}{3}R^2 - k \tag{6}$$

and the energy density  $\rho$  satisfies the energy conservation equation in the form

$$\frac{8\pi\rho}{3}R^3 = \text{const} = R_0. \tag{7}$$

It is necessary to synchronise the proper time of a dust particle on the matching hypersurface (MH hereinafter)  $\chi = \chi_b$  as measured from the both sides of the hypersurface of junction. Therefore, the proper time of the radial geodesics  $\tau$  of the particle as measured in the Schwarzschild–de Sitter spacetime must be equal to the cosmic time  $T$  as measured in the Friedman–Robertson–Walker spacetime. The junction conditions have the following form [Stuchlík, 1983]

$$r_b = R(T) \Sigma_k(\chi_b), \tag{8}$$

$$\tilde{R} = R_0 \Sigma_k(\chi_b), \tag{9}$$

and

$$\tilde{R}\sqrt{\tilde{R}/2M} = R_0, \tag{10}$$

where the parameter  $\tilde{R}$  is related to the covariant energy of the radial geodesic  $\mathcal{E}_b$  of the test particles on the MH by the relation

$$\mathcal{E}_b = \sqrt{1 - \frac{2kM}{\tilde{R}}}. \tag{11}$$

The internal 3-geometry of the MH measured from the Friedman universe side is given by the line element

$$ds_+^2 = -dT^2 + R^2(T) \Sigma_k^2(\chi_b) \left( d\theta^2 + \sin^2 \theta d\phi^2 \right). \tag{12}$$

From the side of the Schwarzschild–de Sitter spacetime it is given by the line element

$$ds_-^2 = -dT^2 + r_b^2(T) \left( d\theta^2 + \sin^2 \theta d\phi^2 \right). \tag{13}$$

Both geometries are identical due to the junction conditions. One can show that the same statement holds for the extrinsic curvature of the MH [Stuchlík, 1984].

### 3 THE GEODESICS INTERSECTING THE MATCHING HYPERSURFACE

Let us consider geodesics crossing the MH. We have to find the relation between the directional angle as measured by the comoving Friedman observers,  $\psi_F$ , and the directional angle as measured by the Schwarzschild–de Sitter static observers,  $\psi_S$ .

The segments of the geodesics in the Friedman and Schwarzschild–de Sitter geometry must be smoothly connected on the MH. We are looking for the Lorentz transformation which relates the comoving Friedman and static Schwarzschild–de Sitter observers on the MH.

In the Robertson–Walker metric, the geodesic equations can be integrated and expressed in the form [Stuchlík, 1984]

$$p^T = \frac{dT}{d\lambda} = \left( m^2 + \frac{p^2}{R^2} \right)^{1/2}, \tag{14}$$

$$p^\chi = \frac{d\chi}{d\lambda} = \pm \frac{1}{R^2} \left( p^2 - \frac{L^2}{\Sigma_k^2} \right)^{1/2}, \tag{15}$$

$$p^\theta = \frac{d\theta}{d\lambda} = \pm \frac{1}{R^2 \Sigma_k^2} \left( L^2 + \frac{\ell^2}{\sin^2 \theta} \right)^{1/2}, \tag{16}$$

$$p^\phi = \frac{d\phi}{d\lambda} = \frac{\ell}{R^2 \Sigma_k^2 \sin^2 \theta}. \tag{17}$$

where  $\lambda$  is an affine parameter and  $m$  is mass of the particle; the proper time  $\tau = m\lambda$ . The constants of motion are

$$\ell = p_\phi, \tag{18}$$

$$L^2 = p_\theta^2 + \frac{p_\phi^2}{\sin^2 \theta}, \tag{19}$$

$$p^2 = p_\chi^2 + \frac{L^2}{\Sigma_k^2}, \tag{20}$$

where  $\ell(L)$  represent the azimuthal (total) angular momentum. Geodesic equations in the Schwarzschild–de Sitter spacetime are in the integrated form expressed by the formulae

$$p^t = \frac{dt}{d\lambda} = E \mathcal{A}^{-2}(t), \tag{21}$$

$$p^r = \frac{dr}{d\lambda} = \pm \left( E^2 - V_{\text{eff}}^2 \right)^{1/2}, \tag{22}$$

$$p^\theta = \frac{d\theta}{d\lambda} = \pm \frac{1}{r^2} \left( L^2 + \frac{\ell^2}{\sin^2 \theta} \right)^{1/2}, \tag{23}$$

$$p^\phi = \frac{d\phi}{d\lambda} = \frac{\ell}{r^2 \sin^2 \theta}. \tag{24}$$

where

$$V_{\text{eff}}^2 = \mathcal{A}^2(r) \left( m^2 + \frac{L^2}{r^2} \right) \tag{25}$$

is the effective potential. The constants of motion  $\ell$  and  $L$  have the same meaning as in the Friedman case.  $E$  is the covariant energy

$$E = -p_t. \tag{26}$$

Let us consider coordinate systems with coincidentally oriented coordinate axes, moving mutually in the direction of the radial axis. The orthonormal base vectors are related by the standard Lorentz transformation

$$\mathbf{e}_{(\mu')} = \Lambda_{\mu'}{}^\nu \mathbf{e}_{(\nu)} \tag{27}$$

with the Lorentz matrix

$$\Lambda_{\mu'}{}^\nu = \begin{pmatrix} \cosh \alpha & \sinh \alpha & 0 & 0 \\ \sinh \alpha & \cosh \alpha & 0 & 0 \\ 0 & 0 & 1 & 0 \\ 0 & 0 & 0 & 1 \end{pmatrix}. \tag{28}$$

The orthonormal basis of the static Schwarzschild-de Sitter observers is given by the relations

$$\mathbf{e}_{(t)} = \mathcal{A}^{-1}(r) \frac{\partial}{\partial t}, \tag{29}$$

$$\mathbf{e}_{(r)} = \mathcal{A}(r) \frac{\partial}{\partial r}, \tag{30}$$

$$\mathbf{e}_{(\theta)} = r^{-1} \frac{\partial}{\partial \theta}, \tag{31}$$

$$\mathbf{e}_{(\phi)} = (r \sin \theta)^{-1} \frac{\partial}{\partial \phi} \tag{32}$$

while in the case of the comoving Friedmannian observers it is given by

$$\mathbf{e}_{(T)} = \frac{\partial}{\partial T}, \tag{33}$$

$$\mathbf{e}_{(\chi)} = R^{-1} \frac{\partial}{\partial \chi}, \tag{34}$$

$$\mathbf{e}_{(\theta)} = (R \Sigma_k)^{-1} \frac{\partial}{\partial \theta}, \tag{35}$$

$$\mathbf{e}_{(\phi)} = (R \Sigma_k \sin \theta)^{-1} \frac{\partial}{\partial \phi}. \tag{36}$$

We obtain the parameter of the Lorentz transformation from the fact that the 4-velocity of the test particles comoving with the MH can be expressed in the Friedman and Schwarzschild–de Sitter spacetimes by the relations

$$\begin{aligned} \mathbf{u}_{(b)} &= \frac{\partial}{\partial T} = \mathbf{e}_T \\ &= \mathcal{A}^{-1}(r_b) \mathcal{E}_b \mathbf{e}_t + \left[ \mathcal{E}_b^2 - \mathcal{A}^2(r_b) \right]^{1/2} \mathcal{A}^{-1}(r_b) \mathbf{e}_r. \end{aligned} \tag{37}$$

Therefore, we arrive at the Lorentz transformation parameter in the form

$$\begin{aligned} \cosh \alpha &= \Lambda_T^t = \Lambda_\chi^r = \mathcal{E}_b \mathcal{A}^{-1}(r_b) \\ &= \sqrt{1 - \frac{2kM}{\tilde{R}}} \left( 1 - \frac{2M}{r_b} - \frac{\Lambda r_b^2}{3} \right)^{-1/2}. \end{aligned} \tag{38}$$

The velocity parameter of the Lorentz shift

$$V(r_b) = \sqrt{1 - \frac{\mathcal{A}^2(r_b)}{\mathcal{E}_b^2}} \tag{39}$$

specifies the speed of the expansion of the MH as measured by the static Schwarzschild–de Sitter observers; the Lorentz factor is then given by the relation

$$\gamma = \cosh \alpha = \left[ 1 - V(r_b)^2 \right]^{-1/2}. \tag{40}$$

#### 4 REFRACTION OF LIGHT AT THE MATCHING HYPERSURFACE

Denoting the directional angles (related to the outward radial direction defined for observers at the radius, where the MH is located momentarily) of a photon entering (leaving) the Friedman universe from (into) the Schwarzschild–de Sitter vakuola as  $\psi_F^+$ ,  $\psi_S^+$  ( $\psi_F^-$ ,  $\psi_S^-$ ), we arrive at the formulae

$$\cos \psi_F^+ = \frac{\cos \psi_S^+ - V_r}{1 - V_r \cos \psi_S^+}, \tag{41}$$

$$\sin \psi_F^+ = \frac{\sin \psi_S^+ \sqrt{1 - V_r^2}}{1 - V_r \cos \psi_S^+} \tag{42}$$

for the photons entering the Friedman universe, and formulae

$$\cos \psi_F^- = \frac{\cos \psi_S^- + V_r}{1 + V_r \cos \psi_S^-}, \tag{43}$$

$$\sin \psi_F^- = \frac{\sin \psi_S^+ \sqrt{1 - V_r^2}}{1 + V_r \cos \psi_S^+} \tag{44}$$

for the photons leaving the Friedman universe. The analysis of these formulae can be given in a quite simple form.

#### 4.1 Photons entering the Friedman universe

First, we discuss Eq. (41). Introducing variables

$$y \equiv \cos \psi_F^+, \quad x \equiv \cos \psi_S^+, \tag{45}$$

with  $x \in [0, 1]$  and  $V_r \in [0, 1)$ , we determine  $y' \equiv dy/dx$  in the form

$$y' = \frac{1 - V_r^2}{(1 - V_r x)^2}. \tag{46}$$

Clearly, there is  $y' > 0$  for  $x \in [0, 1]$  and  $V_r \in [0, 1)$ . The function  $y(x)$  grows monotonically for  $x \in [0, 1]$ . It has its minimum  $y_{\min} = -V_r$  for  $x = 0$ , and its maximum  $y_{\max} = 1$  for  $x = 1$ . We can write

$$\frac{d\cos \psi_F^+}{d\cos \psi_S^+} > 0 \tag{47}$$

for  $\cos \psi_F^+ \in [-V_r, 1]$ . For  $\cos \psi_S^+ = V_r$ , there is  $\cos \psi_F^+ = 0$  and we can conclude that

$$\cos \psi_F^+ \leq 0 \tag{48}$$

for  $\cos \psi_S^+ \in [0, V_r]$  and

$$\cos \psi_F^+ > 0 \tag{49}$$

for  $\cos \psi_S^+ \in (V_r, 1]$ . Now, we analyse the formula (42). Introducing

$$\bar{y} \equiv \sin \psi_F^+, \quad \bar{x} \equiv \sin \psi_S^+, \tag{50}$$

we express the derivative  $\bar{y}' = d\bar{y}/d\bar{x}$  in the form

$$\bar{y}' = \sqrt{\frac{1 - V_r^2}{1 - \bar{x}^2} \frac{(1 - V_r \sqrt{1 - \bar{x}^2}) \sqrt{1 - \bar{x}^2} - V_r \bar{x}^2}{(1 - V_r \sqrt{1 - \bar{x}^2})^2}}. \tag{51}$$

Its local extrema  $\bar{y}' = 0$  are given by the condition

$$(1 - V_r \sqrt{1 - \bar{x}^2}) \sqrt{1 - \bar{x}^2} - V_r \bar{x}^2 = 0. \tag{52}$$

In the intervals  $\bar{x} \in [0, 1]$  and  $V_r \in [0, 1)$ , we obtain solution of (52)

$$\bar{y}_{\text{ex}} = 1 \tag{53}$$

**Table 1.** Total reflection angle  $\psi_{S(T)}^+$ , calculated for four different values of the speed parameter  $V_r$ .

$V_r$	0.1	0.3	0.7	0.9
$\psi_{S(T)}^+$	84°15'	72°32'	45°34'	25°50'

for  $\bar{x}_{\text{ex}} = \sqrt{1 - V_r^2}$ .

Since there is one local extremum of  $\bar{y}(\bar{x})$  for  $\bar{x} \in [0, 1]$ , we can divide  $\bar{y}(\bar{x})$  into two monotonously varying parts. There is  $\bar{y}(0) = 0$  and  $\bar{y}(1) = \sqrt{1 - V_r^2}$ , and we conclude that for  $\bar{x} \in [0, \bar{x}_{\text{ex}}]$ ,  $\bar{y} \in [0, 1]$ , while for  $\bar{x} \in [\bar{x}_{\text{ex}}, 1]$ ,  $\bar{y} \in [\sqrt{1 - V_r^2}, 1]$ .

Using equation (42), we can say that

$$\sin \psi_F^+ > 0 \quad \text{for} \quad \sin \psi_S^+ \in [0, 1]. \tag{54}$$

Putting relations (48), (49) and (54) together, we arrive at the final statement

$$\sin \psi_F^+ > 0 \quad \text{for} \quad \psi_S^+ \in [0, \pi/2], \tag{55}$$

$$\cos \psi_F^+ > 0 \quad \text{for} \quad \psi_S^+ \in [0, \arccos V_r], \tag{56}$$

$$\cos \psi_F^+ \leq 0 \quad \text{for} \quad \psi_S^+ \in [\arccos V_r, \pi/2]. \tag{57}$$

Further, there is

$$\cos \psi_F^+ - \cos \psi_S^+ = -\frac{V_r \sin^2 \psi_S^+}{1 - V_r \cos \psi_S^+}, \tag{58}$$

and this difference is always negative. With the fact that  $\cos \psi_F^+ \in [-V_r, 1]$ , the relation (58) implies

$$\psi_F^+ > \psi_S^+ \quad \text{for} \quad \psi_S^+ \in [0, \pi/2]; \tag{59}$$

we can conclude that for photons crossing the MH from the Schwarzschild–de Sitter region to the Friedman universe, the refraction angle is always larger than the impact angle. The total reflection occurs for angles

$$\psi_S^+ > \psi_{S(T)}^+ \equiv \arccos V_r \tag{60}$$

In Table 1, we give the critical angles of the total refraction  $\psi_{S(T)}^+$  for some values of the expansion velocity of the MH. In Fig. 2, we present the dependence  $\psi_F^+ = \psi_F^+(\psi_S^+; V_r)$  for some representatively chosen values of the expansion velocity.

## 4.2 Photons entering the Schwarzschild–de Sitter region

Because the relations (43) and (44) can be transformed into the form

$$\cos \psi_S^- = \frac{\cos \psi_F^- - V_r}{1 - V_r \cos \psi_F^-}, \tag{61}$$

$$\sin \psi_S^- = \frac{\sin \psi_F^- \sqrt{1 - V_r^2}}{1 - V_r \cos \psi_F^-}, \tag{62}$$

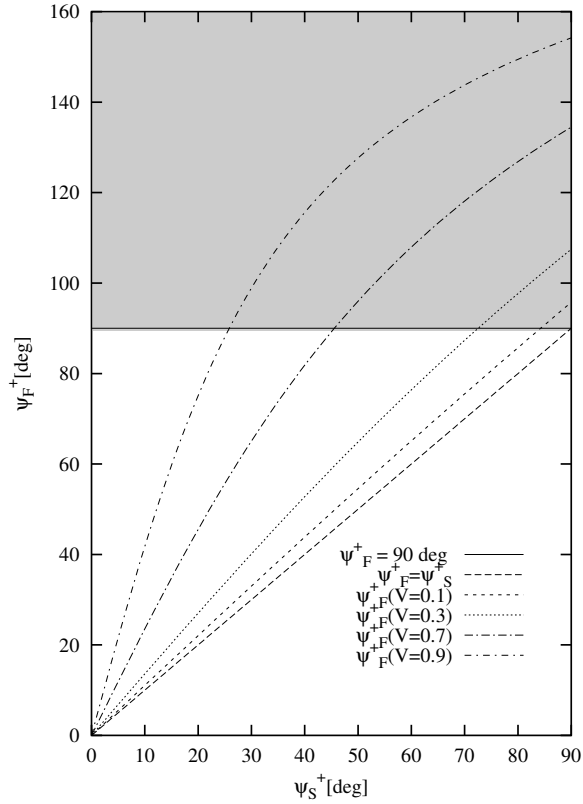


**Figure 2.** The refraction angle  $\psi_F^+$ , for fixed speed parameter  $V_r$ , as a function of the impact angle  $\psi_S^+$  from the interval  $[0, \pi/2]$ . The shaded area corresponds to the total reflexion of the light.

the analysis of the relations (41) and (42) can be repeated, with the following change

$$\psi_F^+ \rightarrow \psi_S^-, \quad \psi_S^+ \rightarrow \psi_F^-. \quad (63)$$

We can conclude that  $\psi_S^- > \psi_F^-$  for  $\psi_F^- \in [0, \pi/2]$ , i.e., for photons crossing the MH from the Friedman region into the Schwarzschild–de Sitter region, the refraction angle is again always larger than the impact angle, and the total reflection occurs for.

$$\psi_F^- > \psi_{F(T)}^- \equiv \arccos V_r \quad (64)$$

### 4.3 The expansion velocity of the matching hypersurface

We shall consider the simplest case of the expansion velocity for the hypersurface matching the spatially flat universe ( $k = 0$ ). Then [Stuchlík, 1984]

$$V_r = \sqrt{\frac{2M}{r_b} + \frac{\Lambda r_b^2}{3}}. \quad (65)$$

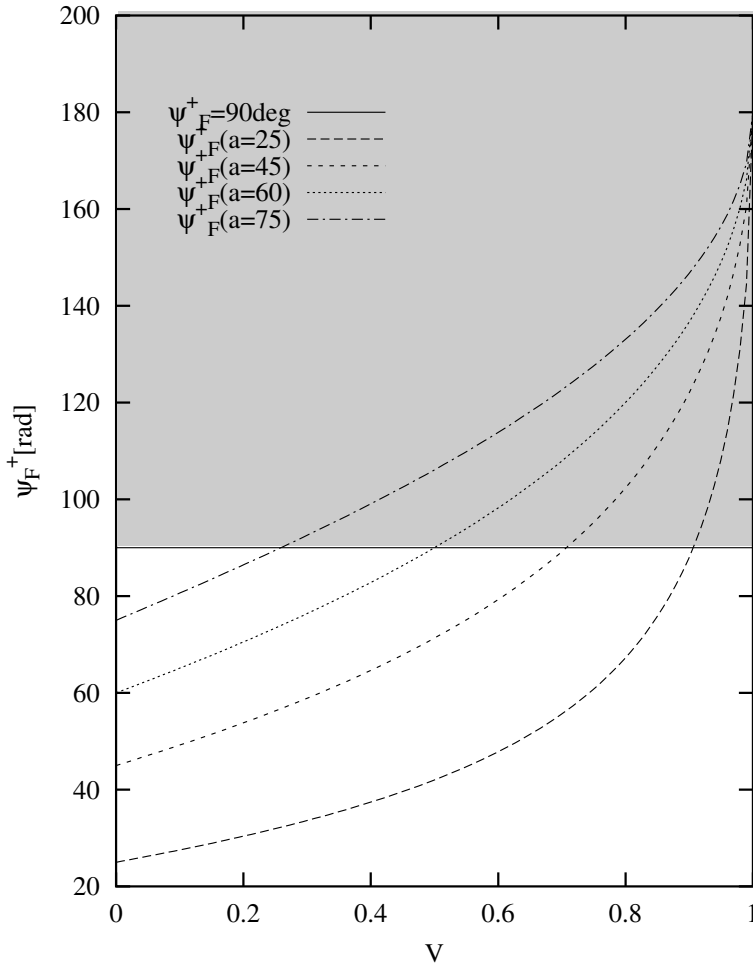


**Figure 3.** The behaviour of the refraction angle  $\psi_F^+$ , for the impact angle  $\psi_S^+$  fixed and the speed parameter  $V_r$  from the interval  $[0, 1)$ . The shaded area corresponds to the total reflection.

It is convenient to define  $y \equiv \frac{1}{3}\Lambda r^2$  and to express  $r_b$  in units of  $M$ , i.e.,  $r_b/M \rightarrow r_b$ . Then

$$V_r = \sqrt{\frac{2}{r_b} + yr_b^2}. \tag{66}$$

First, we follow the dependence  $V_r = V_r(\Lambda)$  with  $r_b$  fixed. Since

$$\frac{dV_r}{dy} = r_b^2 \sqrt{\frac{r_b}{2M + yr_b^3}}, \tag{67}$$

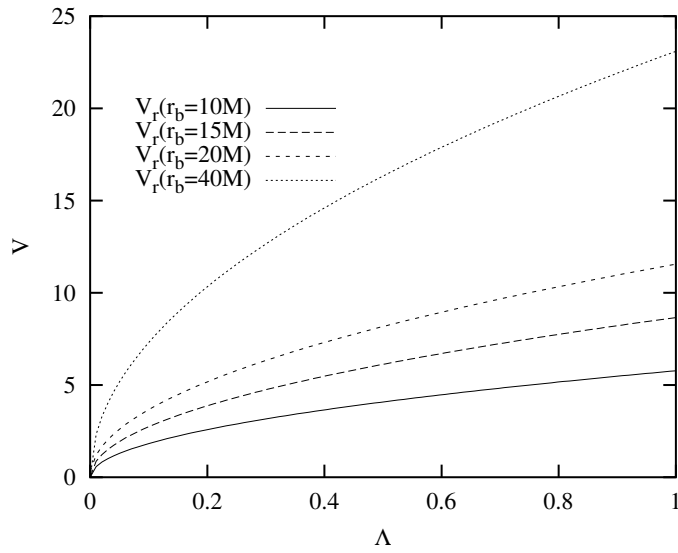


**Figure 4.** The dependence  $V_r = V_r(\Lambda)$  for fixed vakuola radius  $r_b$  and  $\Lambda$  from the interval  $[0,1]$ .

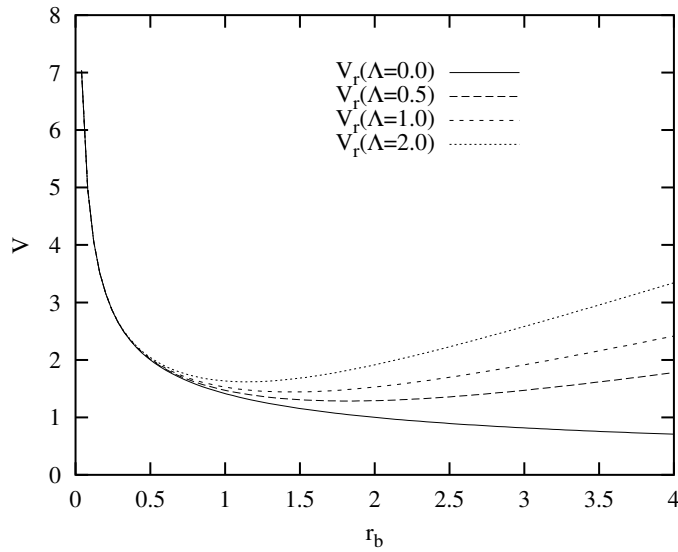


**Figure 5.** The dependence  $V_r = V_r(r_b)$  for fixed  $\Lambda$  and vakuola radius  $r_b$  from the interval  $[0, 20M]$ . The function  $V_r$  reaches its local minimum as it approaches to the static radius  $r_s$ .

and assuming  $r_b > 0$ ,  $\Lambda \in [0, \infty)$ , we conclude that

$$\frac{dV_r}{dy} > 0 \tag{68}$$

and therefore,  $V_r = V_r(\Lambda)$  monotonically grows for  $\Lambda \in [0, \infty)$  (see Fig. 4). Nevertheless, it is more relevant to study the dependence  $V_r = V_r(r_b)$  with  $y$  fixed. There is

$$\frac{dV_r}{dr_b} = \frac{2(yr_b^3 - 1)}{r_b^{3/2}(2 + yr_b^3)^{1/2}}. \quad (69)$$

The local extremum of  $V_r(r_b)$  ( $dV_r/dr_b = 0$ ) is located at so called static radius of the Schwarzschild–de Sitter region

$$r_s \equiv y^{-1/3}, \quad (70)$$

where the gravitational attraction of the central mass condensation (or a black hole) is just balanced by the cosmological repulsion [Stuchlík and Hledík, 1999]. We can see that  $V_r(r_b)$  falls down for  $r_b < r_s$ , it reaches its minimum at the static radius ( $r_b = r_s$ ), where

$$V_{r(\min)} = V_r(r_b = r_s) = \frac{3}{r_s} = 3y^{1/3}, \quad (71)$$

and the expansion speed is accelerated at  $r_b > r_s$ , approaching velocity of light ( $V_r \rightarrow 1$ ) when  $r_b$  approaches the cosmological horizon of the Schwarzschild–de Sitter region ( $r_b \rightarrow r_c$ ). Notice that for  $y \ll 1$  the cosmological horizon is approximately given by

$$r_c \sim y^{1/2}. \quad (72)$$

For the exact relationship between  $r_c$  and  $r_h$  in the Schwarzschild–de Sitter spacetimes see [Stuchlík and Hledík, 1999].

## 5 INFLUENCE OF THE REFRACTION EFFECT ON TEMPERATURE FLUCTUATIONS OF THE CMBR

Here, we shall study the influence of the refraction effect on the CMBR in the framework of the Einstein–Strauss–de Sitter model using the simplified approach developed by Mészáros and Molnár (for more detailed model, considering also deflection of light by the mass condensation, see [Dyer and Roeder, 1973]). We do not consider the model of void used in [Mészáros and Molnár, 1996], since it is not self-consistent from the point of view of general relativity. It was shown in [Mészáros and Molnár, 1996] that the temperature fluctuations are fully determined by the length of the photon ray spanned in the vakuola region, i.e., it is determined by the angle  $\psi_S$  giving the impact angle of photon on the MH with the Friedman region. Therefore, the effect of refraction can be incorporated into the model in a very simple way, namely, by substituting the angle  $\psi_S^+$  influenced by the refraction effect directly into the formula determining the temperature fluctuation. For simplicity, we shall consider here photon trajectories which do not enter the internal Friedman region, and, as usual in the model, we abandon deflection of light in the Schwarzschild-de Sitter spacetime. The impact angle  $\psi_S^+$  then has to be related to the view angle  $\beta$  of observer through the angle of refraction  $\psi_F^+$  (see Fig. 6).

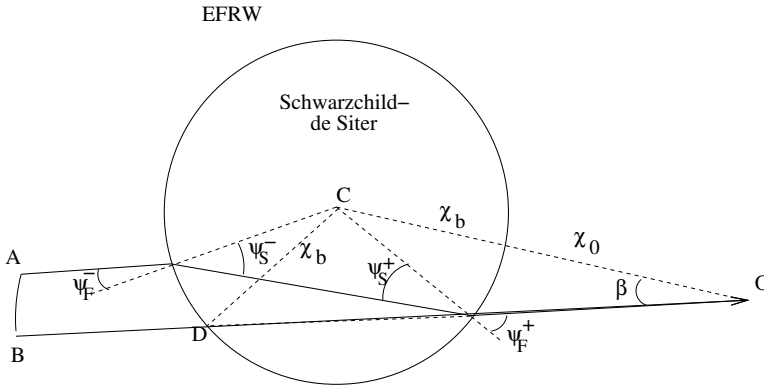


**Figure 6.** Refraction of a photon ray going through the vakuola.  $\chi_b$  is the comoving coordinate of the vakuola boundary,  $\chi_0$  is the comoving ‘radial’ distance of the observer from vakuola,  $\chi = \chi_b + \chi_0$ . The ray  $BO$ , with no refraction effect considered in accord with [Mészáros and Molnár, 1996], is included for comparison with previous results in order to clear up the relevance of the refraction on the Rees–Sciama effect.

### 5.1 Temperature fluctuation formulae

The temperature fluctuation (frequency shift) of a CMBR photon due to transversing the vakuola region is given by the relation [Mészáros and Molnár, 1996]

$$\Delta T = \frac{2c^3 Y^3}{H^3} \left\{ \frac{\Omega}{2} \sin^2 \psi \cos \psi + \frac{1 + 2\Omega}{3} \cos^3 \psi \right\}, \quad (73)$$

where  $\psi = \psi_S^+$  determines the length of the ray in the vakuola; here  $Y = R(\eta)\chi$  is the actual physical extension of the vakuola and  $H = \dot{R}/R$  is the actual value of the Hubble parameter;  $R(\eta)$  is the scale factor,  $\dot{R} \equiv dR/dT$ ,  $\eta$  is the conformal time defined by  $d\eta = dT/R$ .

Refraction effect will change the length of light ray spanning the vakuola region (see Fig. 6). Influence of the refraction on the photon frequency (temperature) will be given by the angle  $\psi_F^+$  related to the viewing angle  $\beta$  of the Friedmannian comoving observer. For vanishing refraction effect, there is

$$\psi_S^+ = \psi_F^+ \quad (74)$$

in agreement with the Mészáros–Molnár model [Mészáros and Molnár, 1996].

The refraction formulae imply the relations

$$\cos \psi_S^+ = \frac{\cos \psi_F^+ + V_r}{1 + V_r \cos \psi_F^+}, \quad (75)$$

$$\sin \psi_S^+ = \frac{\sin \psi_F^+ \sqrt{1 - V_r^2}}{1 + V_r \cos \psi_F^+}, \quad (76)$$

and the temperature fluctuation with refraction effect included is given by the relation

$$\Delta T_r = \frac{2c^3 Y^3}{H^3} \left[ \frac{\cos \psi_F^+ + V(r_b)}{1 + V(r_b) \cos \psi_F^+} \right] \times \left\{ \frac{\Omega}{2} \left[ \frac{\sin \psi_F^+}{\gamma (1 + V(r_b) \cos \psi_F^+)} \right]^2 + \frac{1 + 2\Omega}{3} \left[ \frac{\cos \psi_F^+ + V(r_b)}{1 + V(r_b) \cos \psi_F^+} \right]^2 \right\}. \quad (77)$$

The relevance of the refraction effect is given by the difference of the temperature fluctuations  $\Delta T_r$  and  $\Delta T$ . Using (77) and (73), we find

$$\Delta T_r - \Delta T = \frac{2c^3 Y^3}{H^3} \times \left\{ \frac{\Omega}{2} \left[ \frac{\cos \psi_F^+ + V_r}{1 + V_r \cos \psi_F^+} \left( \frac{\sin \psi_F^+}{\gamma [1 + V_r \cos \psi_F^+]} \right)^2 - \cos \psi_F^+ \sin^2 \psi_F^+ \right] + \frac{1 + 2\Omega}{3} \left[ \left( \frac{\cos \psi_F^+ + V_r}{1 + V_r \cos \psi_F^+} \right)^3 - \cos^3 \psi_F^+ \right] \right\} \quad (78)$$

In the limit of non-relativistic velocities,  $V_r \ll 1$ , the relations (75) and (76) imply

$$\cos \psi_S^+ \sim \cos \psi_F^+ + V_r \sin^2 \psi_F^+, \quad \sin \psi_S^+ \sim \sin \psi_F^+ (1 - V_r \cos \psi_F^+), \quad (79)$$

so that up to the first order of  $V_r$ , the temperature difference is given by the formula

$$\Delta T_r - \Delta T \sim \frac{2c^3 Y^3}{H^3} V_r \cos^2 \psi_F^+ \sin^2 \psi_F^+ \left( 1 + \Omega + \frac{\Omega}{2} \tan^2 \psi_F^+ \right). \quad (80)$$

Clearly, as we expected intuitively, the influence of the refraction effect vanishes linearly with  $V_r \rightarrow 0$ .

Now we have to express the relevance of the refraction effect in terms of the viewing angle  $\beta$  (see Fig. 6). It follows directly from the sine rule that

$$\sin \psi_F^+ = \frac{\chi_0 + \chi_b}{\chi_b} \sin \beta. \quad (81)$$

For the MH, relation between the Schwarzschild coordinate  $r_b$ , and the Robertson–Walker comoving coordinate  $\chi_b$  is given by

$$r_b = R(t_b) \chi_b = \frac{R_0}{1+z} \chi_b, \quad (82)$$

where  $R_0$  is recent value of  $R$ , and  $z$  is the cosmological redshift, being the measure of the cosmic time. Introducing new variables

$$A(\beta) = \frac{\sqrt{1 - \left( \frac{\chi_0 + \chi_b}{\chi_b} \right)^2} + V_r}{1 + V_r \sqrt{1 - \left( \frac{\chi_0 + \chi_b}{\chi_b} \right)^2}}, \quad (83)$$

$$B(\beta) = \frac{\frac{\chi_0 + \chi_b}{\chi_b} \sin \beta}{\gamma \left[ 1 + V_r \sqrt{1 - \left( \frac{\chi_0 + \chi_b}{\chi_b} \right)^2} \right]}, \quad (84)$$

$$C(\beta) = \sqrt{1 - \left( \frac{\chi_0 + \chi_b}{\chi_b} \right)^2} \left( \frac{\chi_0 + \chi_b}{\chi_b} \sin \beta \right), \quad (85)$$

the temperature difference (78) can be expressed as a function of  $\beta$  in the form

$$\begin{aligned} \Delta T_r - \Delta T = \frac{2c^3 Y^3}{H^3} & \left\{ \frac{\Omega}{2} \left[ A(\beta) B^2(\beta) - C(\beta) \right] \right. \\ & \left. + \frac{1 + 2\Omega}{3} \left[ A^3(\beta) - \left( \sqrt{1 - \left( \frac{\chi_0 + \chi_b}{\chi_b} \right)^2} \right)^3 \right] \right\}. \end{aligned} \quad (86)$$

## 5.2 Relevance of the refraction effect

We express the relevance of the refraction effect by considering the influence of the expansion velocity  $V_r$  on the temperature difference

$$\Delta = \Delta T_r - \Delta T. \quad (87)$$

Introducing the functions and relations

$$A(V_r) = \frac{\cos \psi_F^+ + V_r}{1 + V_r \cos \psi_F^+}, \quad (88)$$

$$B(V_r) = \frac{\sin \psi_F^+ \sqrt{1 - V_r^2}}{1 + V_r \cos \psi_F^+}, \quad (89)$$

$$K = \frac{2c^3 Y^3}{H^3}, \quad (90)$$

$$()^\prime = \frac{d}{dV_r}, \quad (91)$$

we can express the temperature difference by the relation

$$\Delta = K \left\{ \frac{\Omega}{2} \left[ AB^2 - \cos \psi_F^+ \sin^2 \psi_F^+ \right] + \frac{1 + 2\Omega}{3} \left[ A^3 - \cos^3 \psi_F^+ \right] \right\}. \quad (92)$$

Its derivative is given by

$$\Delta^\prime = K \left\{ \frac{\Omega}{2} \left[ A^\prime B^2 + 2BB^\prime A \right] + (1 + 2\Omega) A^2 A^\prime \right\}, \quad (93)$$

where

$$A^\prime = \frac{\sin^2 \psi_F^+}{(1 + V_r \cos \psi_F^+)^2}, \quad (94)$$

$$B' = -\sin \psi_F^+ \frac{\cos \psi_F^+ + V_r}{(1 + V_r \cos \psi_F^+)^2 \sqrt{1 - V_r^2}}. \quad (95)$$

Finally, we obtain

$$\Delta' = K \left\{ \frac{\sin^2 \psi_F^+}{(1 + V_r \cos \psi_F^+)^4} \left[ \frac{\Omega}{2} (1 - V_r^2) \sin^2 \psi_F^+ + (1 + \Omega)(\cos \psi_F^+ + V_r)^2 \right] \right\}. \quad (96)$$

Clearly, for  $V_r = 0$ , there is  $\Delta T_r - \Delta T = 0$ . For  $V_r > 0$ , there is  $\Delta' > 0$  for each  $\sin \psi_F^+ \neq 0$ . Therefore,  $\Delta T_r - \Delta T$  grows with  $V_r$  growing.

## 6 CONCLUDING REMARKS

We conclude that there are two basic phenomena related to the importance of the refraction effect in the Einstein–Strauss–de Sitter model explaining the temperature fluctuations of CMBR.

(i) The total reflection phenomenon implies that some part of the vakuola region will not be visible to the external observer. This part will be enlarged with expansion velocity  $V_r$  growing.

(ii) The refraction effects on the temperature fluctuations (in the case of spatially flat universe) will fall, if the boundary of the MH  $r_b$  approaches the static radius  $r_s$  of the Schwarzschild–de Sitter region, and it starts to grow after crossing the static radius. The effect becomes to be extremely strong when  $r_b$  approaches the cosmological horizon  $r_c$  and  $V_r \rightarrow c$ .

We can expect that in the accelerated universe the influence of the relict vacuum energy on the fluctuations of CMBR due to the Rees–Sciama effect could be very important, especially the refraction effect has the tendency to rise up the fluctuations. At present, we make our model more precise, and we estimate conditions under which observable effect could be expected.

## ACKNOWLEDGEMENTS

This work has been supported by the GAČR grant No. 205/03/1147 and by the Committee for Collaboration of Czech Republic with CERN. One of the authors (Z. S.) would like to acknowledge the perfect hospitality at the CERN Theory Division.

## REFERENCES

- [Börner, 1993] Börner, G. (1993). *The Early Universe*. Springer-Verlag, Berlin–Heidelberg–New York.
- [Dyer and Roeder, 1973] Dyer, C. C. and Roeder, R. C. (1973). *ASTRJ2*, 180:L31.
- [Linde, 1990] Linde, A. D. (1990). *Particle Physics and Inflationary Cosmology*. Gordon and Breach, New York.

- [Mészáros and Molnár, 1996] Mészáros, A. and Molnár, Z. (1996). On the alternative origin of the dipole anisotropy of microwave background due to the Rees–Sciama effect. *Astrophys. J.*, 470:49.
- [Rees and Sciama, 1968] Rees, M. J. and Sciama, D. W. (1968). *Nature*, 217:511.
- [Sachs and Wolfe, 1967] Sachs, R. K. and Wolfe, A. M. (1967). *Astrophys. J.*, 147:73.
- [Spergel et al., 2003] Spergel, D. N., Verde, L., Peiris, H. V., Komatsu, E., Nolta, M. R., Bennett, C. L., Halpern, M., Hinshaw, G., Jarosik, N., Kogut, A., Limon, M., Meyer, S. S., Page, L., Tucker, G. S., Weiland, J. L., Wollack, E., and Wright, E. L. (2003). First Year Wilkinson Microwave Anisotropy Probe (WMAP) Observations: Determination of Cosmological Parameters. arXiv: astro-ph/0302209v3, accepted by the ApJ.
- [Stuchlík, 1983] Stuchlík, Z. (1983). The motion of test particles in black-hole backgrounds with non-zero cosmological constant. *Bull. Astronom. Inst. Czechoslovakia*, 34(3):129–149.
- [Stuchlík, 1984] Stuchlík, Z. (1984). An Einstein–Strauss–de Sitter model of the universe. *Bull. Astronom. Inst. Czechoslovakia*, 35(4):205–215.
- [Stuchlík and Hledík, 1999] Stuchlík, Z. and Hledík, S. (1999). Some properties of the Schwarzschild–de Sitter and Schwarzschild–anti-de Sitter spacetimes. *Phys. Rev. D*, 60(4):044006 (15 pages).



# Accretion disks in the Kerr–de Sitter spacetimes

Zdeněk Stuchlík and Petr Slaný

*Institute of Physics, Faculty of Philosophy and Science, Silesian University in Opava  
Bezručovo nám. 13, CZ-746 01 Opava, Czech Republic*

## ABSTRACT

We consider basic properties of both the geometrically thin and thick accretion disks in the Kerr–de Sitter black-hole and naked-singularity spacetimes. The properties are determined by character of the equatorial circular geodesics of these spacetimes and by the equilibrium configurations of a perfect fluid rotating around their symmetry axis. Transformation of a Kerr–de Sitter naked singularity into an extreme black hole due to accretion in the thin disks is briefly discussed for both the plus-family and minus-family disks. It is shown that such a conversion leads to an abrupt instability of the innermost parts of the plus-family accretion disks that can have strong observational consequences.

**Keywords:** Accretion, accretion disks – black-hole physics – relativity – cosmological constant – galaxies: jets, radii

## 1 INTRODUCTION

The energy sources of quasars and active galactic nuclei are most probably accretion disks around central massive black holes [Abramowicz and Percival, 1997, Blandford, 1990]. Basic properties of geometrically thin accretion disks (with negligible pressure) are determined by the circular geodesic motion in the black-hole backgrounds [Novikov and Thorne, 1973]. Basic properties of geometrically thick disks are determined by the equilibrium configurations of perfect fluid orbiting in the black-hole backgrounds, however, the geodesic structure of the backgrounds is relevant also for the properties of the thick disks [Jaroszyński et al., 1980].

Because Penrose’s cosmic censorship hypothesis [Penrose, 1969] is far from being proved, naked singularity spacetimes related to the black-hole spacetimes with a non-zero charge and/or rotational parameter could still be considered conceivable models of quasars and active galactic nuclei and deserve some attention. Of particular interest are those effects that could distinguish a naked singularity from black holes.

Recent cosmological tests indicate convincingly that in the framework of the inflationary cosmology a non-zero, although very small, repulsive cosmological constant  $\Lambda > 0$  has to be invoked in order to explain the dynamics of the recent Universe [Bahcall et al., 1999, Kolb and Turner, 1990]. Therefore, it is relevant to clarify the influence of the repulsive cosmological constant on the astrophysically interesting properties of black-hole or naked-singularity backgrounds. For these purposes, analysis of the geodesic motion of

test particles and photons is among the most important techniques. (Moreover, it could be noted that the optical reference geometry reflects in an illustrative and intuitive way some hidden properties of the geodesic motion [Abramowicz and Prasanna, 1990, Stuchlík and Hledík, 2000, Hledík, 2002].) Of particular interest are circular geodesics being relevant for the accretion disks.

Properties of the geodesic motion in the Schwarzschild–(anti-)de Sitter and Reissner–Nordström–(anti-)de Sitter spacetimes were discussed in [Stuchlík and Hledík, 1999, Stuchlík and Hledík, 2002]. Properties of the circular orbits of test particles show that due to the presence of a repulsive cosmological constant the thin disks have not only an inner edge determined (approximately) by the radius of the innermost stable circular orbit, but also an outer edge given by the radius of the outermost stable circular orbit, located nearby so called static radius, where the gravitational attraction of a black hole (naked singularity) is just compensated by the cosmological repulsion.

A similar analysis of equilibrium configurations of perfect fluid orbiting in the Schwarzschild–de Sitter black-hole backgrounds allowing existence of stable circular orbits, which is a necessary condition for the existence of accretion disks, shows that also thick accretion disks has both the inner and outer edge located nearby the inner (outer) marginally bound circular geodesic. The accretion through the inner cusp and the outflow of matter through the outer cusp of the equilibrium configurations are driven by the Paczyński mechanism. It is a mechanical non-equilibrium process when the matter of the disk slightly overfills the critical equipotential surface with the cusp and thus violates the hydrostatic equilibrium [Stuchlík et al., 2000].

In the case of Reissner–Nordström–(anti-)de Sitter backgrounds [Stuchlík and Hledík, 2002], the discussion has been enriched for the case of the naked-singularity spacetimes. However, it is crucial to understand the role of a non-zero cosmological constant in astrophysically most relevant, rotating, Kerr backgrounds. Here, attention will be focused on the circular equatorial motion of test particles in the Kerr–de Sitter backgrounds, which is relevant for geometrically thin disks, and on the equilibrium configurations of perfect fluid rotating in the background, which are relevant for thick accretion disks.

## 2 KERR–DE SITTER BLACK-HOLE AND NAKED-SINGULARITY SPACETIMES

In the standard Boyer–Lindquist coordinates  $(t, r, \theta, \phi)$  and the geometric units ( $c = G = 1$ ), the Kerr–(anti-)de Sitter geometry is given by the line element

$$ds^2 = -\frac{\Delta_r}{I^2 \rho^2} (dt - a \sin^2 \theta d\phi)^2 + \frac{\Delta_\theta \sin^2 \theta}{I^2 \rho^2} [adt - (r^2 + a^2) d\phi]^2 + \frac{\rho^2}{\Delta_r} dr^2 + \frac{\rho^2}{\Delta_\theta} d\theta^2, \quad (1)$$

where

$$\Delta_r = -\frac{1}{3} \Lambda r^2 (r^2 + a^2) + r^2 - 2Mr + a^2, \quad (2)$$

$$\Delta_\theta = 1 + \frac{1}{3} \Lambda a^2 \cos^2 \theta, \quad (3)$$

$$I = 1 + \frac{1}{3}\Lambda a^2, \quad (4)$$

$$\rho^2 = r^2 + a^2 \cos^2 \theta. \quad (5)$$

The parameters of the spacetime are: mass ( $M$ ), specific angular momentum ( $a$ ), cosmological constant ( $\Lambda$ ). It is convenient to introduce a dimensionless cosmological parameter

$$y = \frac{1}{3}\Lambda M^2. \quad (6)$$

For simplicity, we put  $M = 1$  hereafter. Equivalently, also the coordinates  $t$ ,  $r$ , the line element  $ds$ , and the parameter of the spacetime  $a$  being expressed in units of  $M$  become dimensionless.

We focus our attention to the case  $y > 0$  corresponding to the repulsive cosmological constant; then (1) describes a Kerr–de Sitter spacetime.

The event horizons of the spacetime are given by the pseudosingularities of the line element (1), determined by the condition  $\Delta_r = 0$ . The loci of the event horizons are determined by the relation

$$a^2 = a_h^2(r; y) \equiv \frac{r^2 - 2r - yr^4}{yr^2 - 1}. \quad (7)$$

The asymptotic behaviour of the function  $a_h^2(r; y)$  is given by  $a_h^2(r \rightarrow 0, y) \rightarrow 0$ ,  $a_h^2(r \rightarrow \infty, y) \rightarrow -\infty$ . For  $y = 0$ , the function  $a_h^2(r) = 2r - r^2$  determines loci of the horizons of Kerr black holes. The divergent points of  $a_h^2(r; y)$  are determined by

$$y = y_{d(h)}(r) \equiv \frac{1}{r^2}, \quad (8)$$

its zero points are given by

$$y = y_{z(h)}(r) \equiv \frac{r - 2}{r^3}, \quad (9)$$

and its local extrema are determined by the relation

$$y = y_{e(h)\pm}(r) \equiv \frac{2r + 1 \pm \sqrt{8r + 1}}{2r^3}. \quad (10)$$

The function  $y_{e(h)-}(r)$  has its maximum at  $r_{\text{crit}} = (3 + 2\sqrt{3})/4$ , where the value of the cosmological parameter takes a critical value

$$y_{c(\text{KdS})} = \frac{16}{(3 + 2\sqrt{3})^3} \doteq 0,05924; \quad (11)$$

for  $y > y_{c(\text{KdS})}$ , only naked-singularity backgrounds exist for  $a^2 > 0$ . A common point of the functions  $y_{z(h)}(r)$  and  $y_{e(h)-}(r)$  is located at  $r = 3$ , where is the maximum of  $y_{z(h)}(r)$  taking a critical value

$$y_{c(\text{SdS})} = \frac{1}{27} \doteq 0.03704, \quad (12)$$

which is the limiting value for the existence of Schwarzschild–de Sitter black holes [Stuchlík and Hledík, 1999]. In the Reissner–Nordström–de Sitter spacetimes, the critical value of

the cosmological parameter limiting the existence of black-hole spacetimes is [Stuchlík and Hledík, 2002]

$$y_{c(\text{RNdS})} = \frac{2}{27} \doteq 0.07407. \tag{13}$$

If  $y = y_{c(\text{KdS})}$ , the function  $a_h^2(r; y)$  has an inflex point at  $r = r_{\text{crit}}$ , corresponding to a critical value of the rotation parameter of the Kerr–de Sitter spacetimes

$$a_{\text{crit}}^2 = \frac{3}{16}(3 + 2\sqrt{3}) \doteq 1, 21202. \tag{14}$$

Kerr–de Sitter black holes can exist for  $a^2 < a_{\text{crit}}^2$  only, while Kerr–de Sitter naked singularities can exist for both  $a^2 < a_{\text{crit}}^2$  and  $a^2 > a_{\text{crit}}^2$ .

For  $y > 0$ , the function  $y_{e(h)-}(r)$  determines two local extrema of  $a_h^2(r; y)$  at  $y < y_{c(\text{KdS})}$ , denoted as  $a_{\text{max}(h)}^2(r_1, y)$ ,  $a_{\text{min}(h)}^2(r_2, y)$ , with  $r_1 < r_2$ . If  $y < y_{c(\text{SdS})}$ ,  $a_{\text{min}(h)}^2(r_2, y) < 0$ , and the minimum is unphysical. The function  $a_h^2(r)$  diverges at  $r_d = 1/\sqrt{y}$ , and it is discontinuous there. The function  $y_{e(h)+}(r)$  determines a maximum of  $a_h^2(r; y)$  at a negative value of  $a^2$  which is, therefore, physically irrelevant (see Fig. 1 giving typical behaviour of  $a_h^2(r; y)$ ).

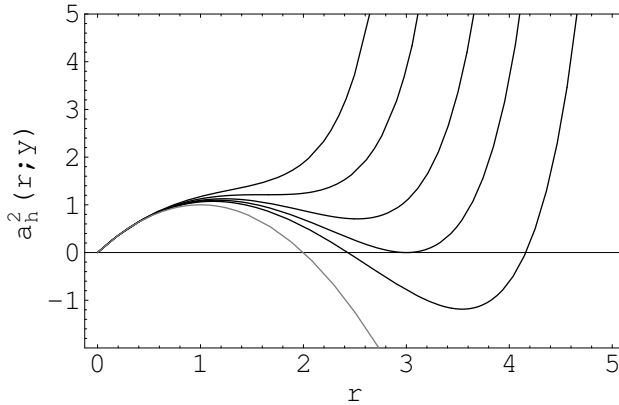


**Figure 1.** Horizons of the Kerr–de Sitter spacetimes. They are given for five typical values of the cosmological parameter  $y$  by the function  $a_h^2(r; y)$ . For  $y > y_{c(\text{KdS})} \doteq 0.05924$  ( $y = 0.08$ ) the function has no local extrema and only naked-singularity spacetimes are allowed (the only horizon is the cosmological horizon). For  $y = y_{c(\text{KdS})}$ , the function has an inflex point where the black-hole and the cosmological horizons coincide. For  $y_{c(\text{SdS})} = 1/27 < y < y_{c(\text{KdS})}$  ( $y = 0.045$ ) the function has two local extrema in positive values and the black-hole spacetimes exist for  $a^2$  between those extrema. For  $y = y_{c(\text{SdS})}$  the local minimum resides on axis  $a^2 = 0$ . The critical value  $y_{c(\text{SdS})}$  represents the limiting value of cosmological parameter for which the Schwarzschild–de Sitter black holes can exist; the Kerr–de Sitter black holes again exist for  $a^2$  between those extrema. For  $0 < y < y_{c(\text{SdS})}$  ( $y = 0.03$ ) the local minimum resides in the non-physical region  $a^2 < 0$  and the black holes exist for  $a^2$  up to the local maximum. For completeness, we present the gray curve determining horizons of the Kerr ( $y = 0$ ) black holes. In all cases, the local extrema correspond to the extreme black holes. (Taken from [Stuchlík and Slaný, 2004].)

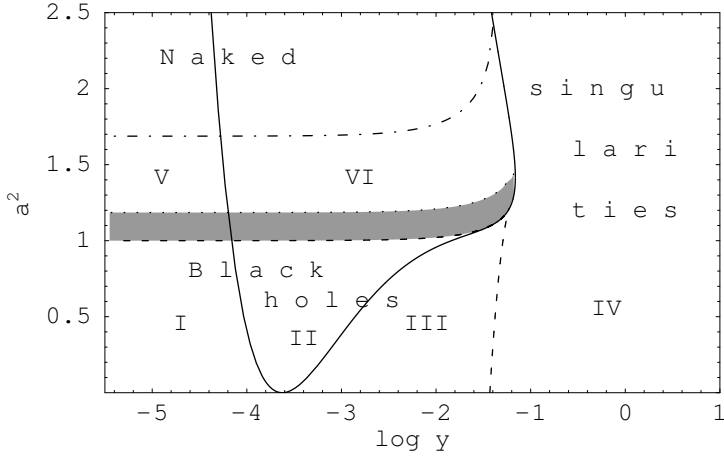


**Figure 2.** Classification of the Kerr–de Sitter spacetimes. The space of parameters  $a^2$  and  $y$  is separated into six regions. Dashed curves separate regions of black holes and naked singularities. Full curves divide the parametric space into spacetimes differing by properties of the stable circular orbits relevant for Keplerian accretion disks. For large values of  $a^2$  both the full lines tend to the  $a^2$ -axis. **I** black-hole spacetimes with both co-rotating and counter-rotating stable or bound circular orbits, **II** black-hole spacetimes with no counter-rotating stable or bound circular orbits, **III** black-hole spacetimes with no co-rotating and counter-rotating stable or bound circular orbits, **IV** naked-singularity spacetimes with no co-rotating and counter-rotating stable or bound circular orbits, **V** naked-singularity spacetimes with both co-rotating and counter-rotating stable or bound circular orbits, **VI** naked-singularity spacetimes with no counter-rotating stable or bound circular orbits of the minus-family. Dashed-dotted curve defines the subregion of the naked-singularity spacetimes, where the plus-family circular orbits could be stable and counter-rotating (from the point of view of a locally non-rotating observer), shaded is the subregion allowing stable circular orbits with  $E_+ < 0$ ! (Taken from [Stuchlík and Slaný, 2004].)

If  $0 < y < y_{c(\text{SdS})}$ , the black-hole spacetimes exist for  $a^2 \leq a^2_{\text{max}(h)}(y)$ , and the naked-singularity spacetimes exist for  $a^2 > a^2_{\text{max}(h)}(y)$ . If  $y_{c(\text{SdS})} < y \leq y_{c(\text{KdS})}$ , the black-hole spacetimes exist for  $a^2_{\text{min}(h)}(y) \leq a^2 \leq a^2_{\text{max}(h)}(y)$ , while the naked-singularity spacetimes exist for  $a^2 < a^2_{\text{min}(h)}(y)$  and  $a^2 > a^2_{\text{max}(h)}(y)$ . The functions  $a^2_{\text{min}(h)}(y)$ ,  $a^2_{\text{max}(h)}(y)$  are implicitly given by Eqs (7) and (10); the separation of the Kerr–de Sitter black-hole and naked-singularity spacetimes in the parameter space  $y$ – $a^2$  is shown in Fig. 2. In the black-hole spacetimes, there are two black-hole horizons and the cosmological horizon, with  $r_{h-} < r_{h+} < r_c$ . In the naked-singularity spacetimes, there is the cosmological horizon  $r_c$  only.

The extreme cases, when two (or all three) horizons coalesce, were discussed in detail for the case of Reissner–Nordström–de Sitter spacetimes [Brill and Hayward, 1994, Hayward and Nakao, 1994]. In the Kerr–de Sitter spacetimes, the situation is analogical. If  $r_{h-} = r_{h+} < r_c$ , the extreme black-hole case occurs, if  $r_{h-} < r_{h+} = r_c$ , the marginal naked-singularity case occurs, if  $r_{h-} = r_{h+} = r_c$ , the “ultra-extreme” case occurs corresponding to a naked singularity.

### 3 EQUATORIAL MOTION

Basic properties of thin accretion disks are determined by equatorial circular motion of test particles. Note that due to the dragging of inertial frames any tilted disk has to be driven to the equatorial plane of the rotating spacetimes [Bardeen and Petterson, 1975].

The motion of a test particle with rest mass  $m$  is given by the geodesic equations. In a separated and integrated form, the equations were obtained by Carter [Carter, 1973]. For the motion restricted to the equatorial plane ( $d\theta/d\lambda = 0$ ,  $\theta = \pi/2$ ) the Carter equations take the following form

$$r^2 \frac{dr}{d\lambda} = \pm R^{1/2}(r), \quad (15)$$

$$r^2 \frac{d\phi}{d\lambda} = -IP_\theta + \frac{aIP_r}{\Delta_r}, \quad (16)$$

$$r^2 \frac{dt}{d\lambda} = -aIP_\theta + \frac{(r^2 + a^2)IP_r}{\Delta_r}, \quad (17)$$

where

$$R(r) = P_r^2 - \Delta_r (m^2 r^2 + K), \quad (18)$$

$$P_r = I\mathcal{E} (r^2 + a^2) - Ia\Phi, \quad (19)$$

$$P_\theta = I(a\mathcal{E} - \Phi), \quad (20)$$

$$K = I^2(a\mathcal{E} - \Phi)^2. \quad (21)$$

The proper time of the particle  $\tau$  is related to the affine parameter  $\lambda$  by  $\tau = m\lambda$ . The constants of motion are: energy ( $\mathcal{E}$ ), related to the stationarity of the geometry, axial angular momentum ( $\Phi$ ), related to the axial symmetry of the geometry, ‘total’ angular momentum ( $K$ ), related to the hidden symmetry of the geometry. For the equatorial motion,  $K$  is restricted through Eq. (21) following from the conditions on the latitudinal motion [Stuchlík, 1983]. Notice that  $\mathcal{E}$  and  $\Phi$  cannot be interpreted as energy and axial angular momentum at infinity, since the spacetime is not asymptotically flat.

The equatorial motion is governed by the constants of motion  $\mathcal{E}$ ,  $\Phi$ . Its properties can be conveniently determined by an “effective potential” given by the condition  $R(r) = 0$  for turning points of the radial motion. It is useful to define specific energy and specific angular momentum by the relations

$$E \equiv \frac{I\mathcal{E}}{m}, \quad L \equiv \frac{I\Phi}{m}. \quad (22)$$

Solving the equation  $R(r) = 0$ , we find the effective potential in the form

$$\begin{aligned} E_{(\pm)}(r; L, a, y) \equiv & \left[ (1 + ya^2) r (r^2 + a^2) + 2a^2 \right]^{-1} \\ & \times \left\{ a \left[ yr (r^2 + a^2) + 2 \right] L \right. \\ & \left. \pm \Delta_r^{1/2} \left\{ r^2 L^2 + r \left[ (1 + ya^2) r (r^2 + a^2) + 2a^2 \right] \right\}^{1/2} \right\}. \end{aligned} \quad (23)$$

In the stationary regions ( $\Delta_r \geq 0$ ), the motion is allowed where

$$E \geq E_{(+)}(r; L, a, y), \quad (24)$$

or

$$E \leq E_{(-)}(r; L, a, y). \quad (25)$$

Conditions  $E = E_{(+)}(r, L, a, y)$  (or  $E = E_{(-)}(r; L, a, y)$ ) give the turning points of the radial motion; at the dynamic regions ( $\Delta_r < 0$ ), the turning points are not allowed. In the region between the outer black-hole horizon and the cosmological horizon, the motion of particles in the positive-root states, i.e., particles with positive energy as measured by local observers, being future-directed ( $dt/d\lambda > 0$ ) and having a direct “classical” physical meaning, is determined by the effective potential  $E_{(+)}(r; L, a, y)$ . The character of the motion in the whole Kerr–de Sitter background, and relevance of the effective potential  $E_{(-)}(r; L, a, y)$ , determining the motion of particles in the negative-root states between the black-hole and cosmological horizons, is qualitatively the same as discussed in [Bičák et al., 1989]. In the following we restrict attention to the positive-root states determined by the effective potential  $E_{(+)}(r; L, a, y)$ .

It is convenient to redefine the axial angular momentum by the relation

$$X \equiv L - aE; \quad (26)$$

for an analogous redefinition in the case of equatorial photon motion see [Stuchlík and Hledík, 2000]. With the constant of motion  $X$ , instead of  $L$ , the effective potential takes the simple form

$$E_{(+)}(r; X, a, y) \equiv \frac{1}{r^2} \left[ aX + \Delta_r^{1/2} (r^2 + X^2)^{1/2} \right]. \quad (27)$$

#### 4 EQUATORIAL CIRCULAR ORBITS

The equatorial circular orbits can most easily be determined by solving simultaneously the equations

$$R(r) = r^4 E^2 - 2ar^2 EX + (a^2 - \Delta_r) X^2 - r^2 \Delta_r = 0, \quad (28)$$

$$\frac{dR}{dr} = 4r^3 E^2 - 4ar EX - \Delta'_r X^2 - \Delta'_r r^2 - 2r \Delta_r = 0, \quad (29)$$

where  $\Delta'_r \equiv d\Delta_r/dr$ . Combining the Eqs (28) and (29), we arrive at a quadratic equation

$$A(r) \left( \frac{X}{E} \right)^2 + B(r) \left( \frac{X}{E} \right) + C(r) = 0, \quad (30)$$

with

$$A(r) = 2\Delta_r (a^2 - \Delta_r) + a^2 \Delta'_r r, \quad (31)$$

$$B(r) = -2a \Delta'_r r^3, \quad (32)$$

$$C(r) = r^4 (\Delta'_r r - 2\Delta_r). \quad (33)$$

Its solution can be expressed in the following relatively simple form

$$\left(\frac{X}{E}\right)_{\pm}(r; a, y) = \frac{r^2(r - a^2 - yr^4)}{ar[r - 1 - yr(2r^2 + a^2)] \pm \Delta_r[r(1 - yr^3)]^{1/2}}. \quad (34)$$

Assuming now

$$X_+ = E_+ \left(\frac{X}{E}\right)_+, \quad X_- = E_- \left(\frac{X}{E}\right)_-, \quad (35)$$

substituting into Eq. (28) and solving for the specific energy of the orbit, we obtain

$$E_{\pm}(r; a, y) = \frac{1 - \frac{2}{r} - (r^2 + a^2)y \pm a\left(\frac{1}{r^3} - y\right)^{1/2}}{\left[1 - \frac{3}{r} - a^2y \pm 2a\left(\frac{1}{r^3} - y\right)^{1/2}\right]^{1/2}}. \quad (36)$$

The related constant of motion  $X$  of the orbit is then given by the expression

$$X_{\pm}(r; a, y) = \frac{-a \pm r^2\left(\frac{1}{r^3} - y\right)^{1/2}}{\left[1 - \frac{3}{r} - a^2y \pm 2a\left(\frac{1}{r^3} - y\right)^{1/2}\right]^{1/2}}, \quad (37)$$

while the specific angular momentum of the circular orbits is determined by the relation

$$L_{\pm}(r; a, y) = -\frac{2a + ar(r^2 + a^2)y \mp r(r^2 + a^2)\left(\frac{1}{r^3} - y\right)^{1/2}}{r\left[1 - \frac{3}{r} - a^2y \pm 2a\left(\frac{1}{r^3} - y\right)^{1/2}\right]^{1/2}}. \quad (38)$$

The relations (36)–(38) determine two families of the circular orbits. We call them plus-family orbits and minus-family orbits according to the  $\pm$  sign in the relations (36)–(38). Typical behaviour of the functions  $E_{\pm}(r; a, y)$  and  $L_{\pm}(r; a, y)$  giving the specific energy and specific angular momentum is illustrated in Fig. 3 and Fig. 4, respectively, for Kerr–de Sitter black-hole spacetimes with appropriately taken parameters. Fig. 5 shows typical behaviour of these functions for some Kerr–de Sitter naked-singularity spacetimes.

In the limit of  $y \rightarrow 0$ , the relations (36) and (38) reduce to the expression given by Chandrasekhar (in units of  $M$ ) [Chandrasekhar, 1983] for circular orbits in the Kerr backgrounds

$$E_{\pm}(r; a) = \frac{1 - \frac{2}{r} \pm \frac{a}{r^{3/2}}}{\left[1 - \frac{3}{r} \pm \frac{2a}{r^{3/2}}\right]^{1/2}}, \quad (39)$$

$$L_{\pm}(r; a) = \pm r^{1/2} \frac{1 + \frac{a^2}{r^2} \mp \frac{2a}{r^{3/2}}}{\left[1 - \frac{3}{r} \pm \frac{2a}{r^{3/2}}\right]^{1/2}}. \quad (40)$$

In the limit of  $a \rightarrow 0$  we arrive at the formulae determining the specific energy and the specific angular momentum of circular orbits in the field of Schwarzschild–de Sitter black

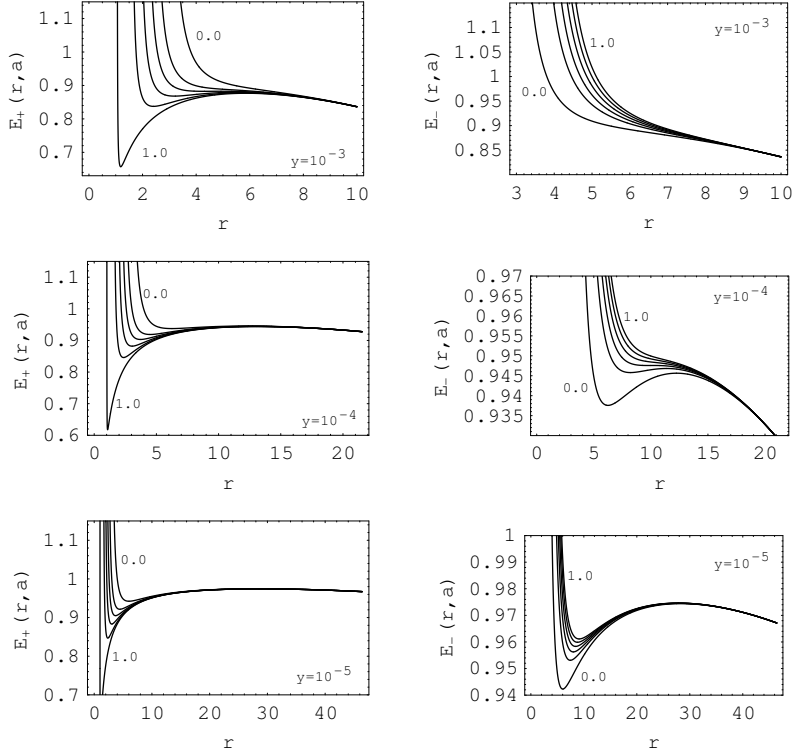


**Figure 3.** Specific energy of the equatorial circular orbits in the Kerr–de Sitter black-hole spacetimes. The spacetimes are specified by the cosmological parameter  $y$  and the rotational parameter  $a$  ( $a^2$  varies from 0.0 to 1.0 in steps of 0.2). The left column corresponds to the plus-family orbits, the right column corresponds to the minus-family orbits. The local extrema of the curves correspond to the marginally stable orbits, the rising parts correspond to stable orbits, the descending parts correspond to unstable ones. Behaviour of the curves for the spacetimes with  $y < 10^{-5}$  is similar to the case of  $y = 10^{-5}$ . (Taken from [Stuchlík and Slaný, 2004].)

holes [Stuchlík and Hledík, 1999]:

$$E(r; y) = \frac{r - 2 - yr^3}{[r(r - 3)]^{1/2}}, \quad (41)$$

$$L(r; y) = \frac{r(1 - yr^3)^{1/2}}{(r - 3)^{1/2}}; \quad (42)$$

here, we do not give  $E$  and  $L$  for the minus-family orbits as these are equivalent to the plus-family orbits in spherically symmetric spacetimes.

Inspecting expressions (36) and (38), we find two reality conditions on the circular orbits. The first restriction on the existence of circular orbits is given by the relation

$$y \leq y_s \equiv \frac{1}{r^3}, \quad (43)$$

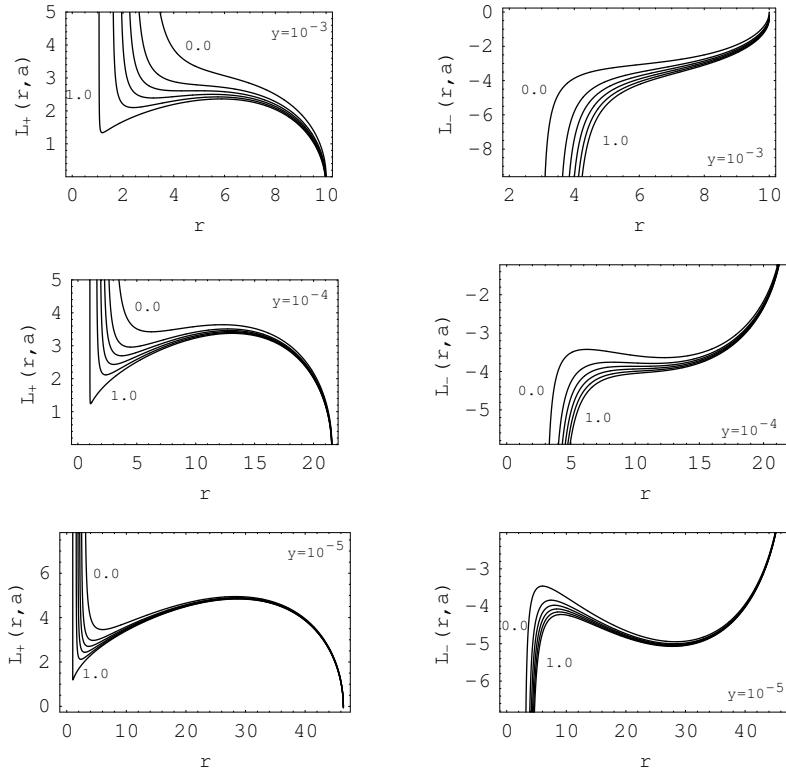


**Figure 4.** Specific angular momentum of the equatorial circular orbits in the Kerr–de Sitter black-hole spacetimes. The spacetimes are specified by the cosmological parameter  $y$  and the rotational parameter  $a$  ( $a^2$  varies from 0.0 to 1.0 in steps of 0.2). The left column corresponds to the plus-family orbits, the right column corresponds to the minus-family orbits. The local extrema of the curves correspond to the marginally stable orbits, the rising parts of  $L_+$  and the descending parts of  $L_-$  correspond to the stable orbits, the descending parts of  $L_+$  and the rising parts of  $L_-$  correspond to the unstable ones. Behaviour of the curves for the spacetimes with  $y < 10^{-5}$  is similar to the case of  $y = 10^{-5}$ . (Taken from [Stuchlík and Slaný, 2004].)

which introduces the notion of the “static radius”, given by the formula  $r_s = y^{-1/3}$  independently of the rotational parameter  $a$ . It can be compared with formally identical result in the Schwarzschild–de Sitter spacetimes [Stuchlík and Hledík, 1999]. A “free” or “geodetical” observer on the static radius has only  $U^t$  component of 4-velocity non-zero. The position on the static radius is unstable relative to radial perturbations, as follows from the discussion on stability of the circular orbits performed below.

The second restriction on the existence of the circular orbits is given by the condition

$$1 - \frac{3}{r} - a^2 y \pm 2a \left( \frac{1}{r^3} - y \right)^{1/2} \geq 0; \quad (44)$$

the equality determines radii of photon circular orbits, where both  $E \rightarrow \infty$  and  $L \rightarrow \pm\infty$ .

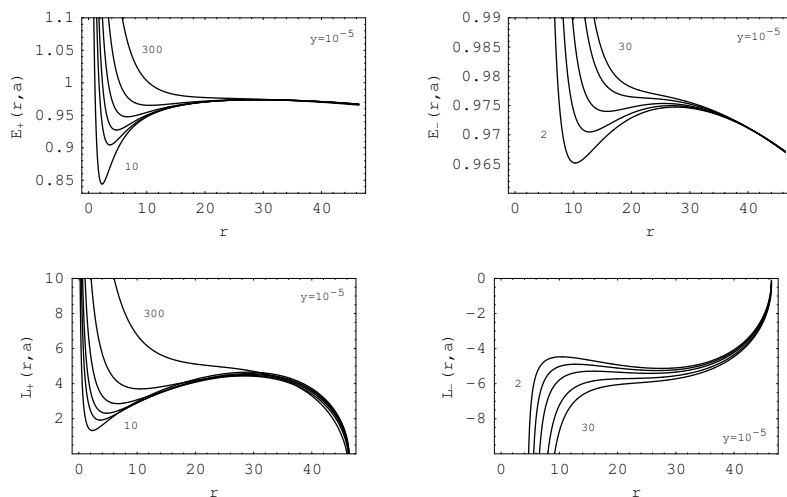


**Figure 5.** Specific energy and specific angular momentum of the equatorial circular orbits in the Kerr–de Sitter naked-singularity spacetimes. The plus-family curves are plotted for the rotational parameter  $a^2 = 10, 20, 30, 50, 100, 300$ , the minus-family curves are plotted for  $a^2 = 2, 5, 10, 20, 30$ . Meaning of particular parts of the curves is the same as in the black-hole spacetimes. (Taken from [Stuchlík and Slaný, 2004].)

The photon circular orbits of the plus-family are given by the relation

$$a = a_{\text{ph}(1,2)}^{(+)}(r; y) \equiv \frac{(1 - yr^3)^{1/2} \pm (1 - 3yr^2)^{1/2}}{yr^{3/2}}, \quad (45)$$

while for the minus-family orbits they are given by the relation

$$a = a_{\text{ph}(1,2)}^{(-)}(r; y) \equiv \frac{-(1 - yr^3)^{1/2} \pm (1 - 3yr^2)^{1/2}}{yr^{3/2}}. \quad (46)$$

A detailed discussion of the photon circular orbits can be found in [Stuchlík and Hledík, 2000, Stuchlík and Slaný, 2004].

The behaviour of circular orbits in the field of Kerr black holes ( $y = 0$ ) suggests that the plus-family orbits correspond to the co-rotating orbits, while the minus-family circular orbits correspond to the counter-rotating ones. However, this statement is not generally correct even in some of the Kerr naked-singularity spacetimes, namely in the spacetimes with the rotational parameter low enough, where counter-rotating plus-family orbits could exist nearby the ring singularity [Stuchlík, 1980]. In the Kerr–de Sitter spacetimes, the situation is more complicated and we cannot identify the plus-family circular orbits with purely co-rotating orbits even in the black-hole spacetimes. Moreover, in the rotating spacetimes with a nonzero cosmological constant it is not possible to define the co-rotating (counter-rotating) orbits in relation to stationary observers at infinity, as can be done in the Kerr spacetimes, since these spacetimes are not asymptotically flat.

Natural way of defining the orientation of the circular orbits in the Kerr–de Sitter spacetimes is to use the point of view of locally non-rotating frames that is used in the asymptotically flat Kerr spacetimes too. The tetrad of 1-forms corresponding to these frames in the Kerr–de Sitter backgrounds is given by [Stuchlík and Hledík, 2000]:

$$\omega^{(t)} \equiv \left( \frac{\Delta_r \Delta_\theta \varrho^2}{I^2 A} \right)^{1/2} dt, \quad (47)$$

$$\omega^{(\phi)} \equiv \left( \frac{A \sin^2 \theta}{I^2 \varrho^2} \right)^{1/2} (d\phi - \Omega dt), \quad (48)$$

$$\omega^{(r)} \equiv \left( \frac{\varrho^2}{\Delta_r} \right)^{1/2} dr, \quad (49)$$

$$\omega^{(\theta)} \equiv \left( \frac{\varrho^2}{\Delta_\theta} \right)^{1/2} d\theta, \quad (50)$$

where

$$A \equiv (r^2 + a^2)^2 - a^2 \Delta_r, \quad (51)$$

$$\Delta_\theta \equiv 1 + ya^2 \cos^2 \theta, \quad (52)$$

and the angular velocity of the locally non-rotating frames

$$\Omega \equiv \frac{d\phi}{dt} = \frac{a}{A} \left[ -\Delta_r + (r^2 + a^2) \Delta_\theta \right]. \quad (53)$$

Note that  $\Delta_\theta = 1$  in the equatorial plane.

Locally measured components of 4-momentum are given by the projection of a particle's 4-momentum onto the tetrad

$$p^{(\alpha)} = p^\mu \omega_\mu^{(\alpha)}, \quad (54)$$

where

$$p^\mu = m \frac{dx^\mu}{d\tau} \equiv m \dot{x}^\mu = \frac{dx^\mu}{d\lambda} \quad (55)$$

are the coordinate components of particle's 4-momentum, the affine parameter  $\lambda = \tau/m$ ,  $m$  denotes the rest mass of the particle, and  $\tau$  is its proper time.

In the equatorial plane,  $\theta = \pi/2$ , the azimuthal component of the 4-momentum measured in the locally non-rotating frames is given by the relation

$$p^{(\phi)} = \frac{mA^{1/2}}{Ir} (\dot{\phi} - \Omega i), \quad (56)$$

where the temporal and azimuthal components of the 4-momentum, determined by the geodesic equations, can be expressed in the form containing the specific constants of motion  $E$ ,  $X$ :

$$i = \frac{I}{r^2} \left[ aX + \frac{(r^2 + a^2)(r^2 E - aX)}{\Delta_r} \right], \quad (57)$$

$$\dot{\phi} = \frac{I}{r^2} \left[ X + \frac{a}{\Delta_r} (r^2 E - aX) \right]. \quad (58)$$

A simple calculation reveals

$$p^{(\phi)} = \frac{mr}{A^{1/2}}(aE + X) \tag{59}$$

and using Eq. (26) we obtain intuitively anticipated relation

$$p^{(\phi)} = \frac{mr}{A^{1/2}}L. \tag{60}$$

We can see that the sign of the azimuthal component of the 4-momentum measured in the locally non-rotating frames is given by the sign of the specific angular momentum of a particle on the orbit of interest. Therefore, the circular orbits with  $p^{(\phi)} > 0$ , ( $L > 0$ ), we call co-rotating, and the circular orbits with  $p^{(\phi)} < 0$ , ( $L < 0$ ) we call counter-rotating, in agreement with the approach used in the case of asymptotically flat Kerr spacetimes.

The circular geodesics can be astrophysically relevant, if they are stable with respect to radial perturbations.

The loci of the stable circular orbits are given by the condition

$$\frac{d^2R}{dr^2} \geq 0 \tag{61}$$

that have to be satisfied simultaneously with the conditions  $R(r) = 0$  and  $dR/dr = 0$  determining the specific energy and the specific angular momentum of the circular orbits. Using the relations (36) and (37), we find that radii of the stable orbits of both families are restricted by the condition

$$r \left[ 6 - r + r^3(4r - 15)y \right] \mp 8a \left[ r \left( 1 - yr^3 \right)^3 \right]^{1/2} + a^2 \left[ 3 + r^2y \left( 1 - 4yr^3 \right) \right] \geq 0. \tag{62}$$

The marginally stable orbits of both families can be described together by the relation

$$\begin{aligned} a^2 = a_{\text{ms}(1,2)}^2(r; y) \equiv & \left[ 3 + r^2y \left( 1 - 4yr^3 \right) \right]^{-2} r \left\{ \left[ r - 6 - r^3(4r - 15)y \right] \right. \\ & \times \left[ 3 + r^2y \left( 1 - 4yr^3 \right) \right] + 32 \left( 1 - yr^3 \right)^3 \pm 8 \left( 1 - yr^3 \right)^{3/2} \left( 1 - 4yr^3 \right)^{1/2} \\ & \left. \times \left\{ r \left[ 3 - ry \left( 6 + 10r - 15yr^3 \right) \right] - 2 \right\}^{1/2} \right\}. \end{aligned} \tag{63}$$

The ( $\pm$ ) sign in Eq. (63) is not directly related to the plus-family and the minus-family orbits. The function  $a_{\text{ms}(1)}^2$ , corresponding to the + sign in Eq. (63), determines marginally stable orbits of the plus-family, while the function  $a_{\text{ms}(2)}^2$ , corresponding to the – sign in Eq. (63), is relevant for both the plus-family and minus-family orbits. The reality conditions for the functions  $a_{\text{ms}(1,2)}^2(r; y)$  are directly given by the Eq. (63). The standard condition  $y \leq y_s(r) \equiv 1/r^3$ , is guaranteed by the first relevant condition

$$y \leq y_{\text{ms}}(r) \equiv \frac{1}{4r^3}. \tag{64}$$

The other two conditions can be given in the form

$$y \leq y_{\text{ms}-}(r) \quad \text{or} \quad y \geq y_{\text{ms}+}(r), \tag{65}$$

where the functions  $y_{\text{ms}\pm}(r)$  are given by the relation

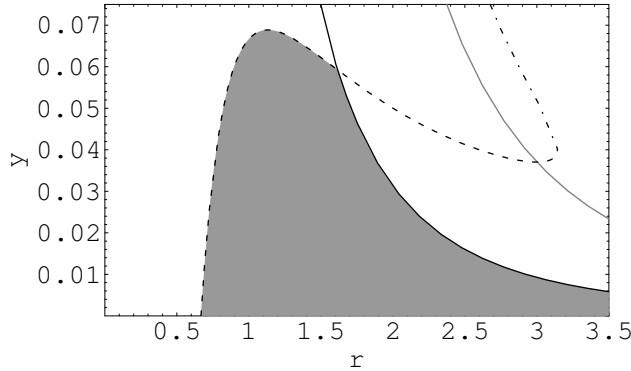


**Figure 6.** Reality conditions for the existence of the stable circular orbits. Black and gray solid curves correspond to the functions  $y_{ms}(r)$  and  $y_s(r)$ , respectively, dashed-dotted and dashed curves correspond to the functions  $y_{ms+}(r)$  and  $y_{ms-}(r)$ , respectively. Stable orbits can exist only in the shaded region, where the local maximum corresponds to the critical value of the cosmological parameter  $y_{crit(ms+)} \doteq 0.06886$ . (Taken from [Stuchlík and Slaný, 2004].)

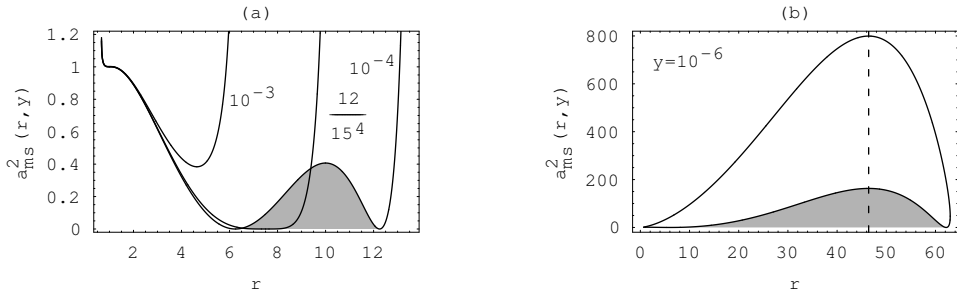


**Figure 7.** Marginally stable circular orbits in the Kerr-de Sitter spacetimes. The relevant functions are given for some typical values of the cosmological parameter  $y$ . **(a)** The black-hole region of the Kerr-de Sitter spacetimes. For  $y < 12/15^4$  there exist spacetimes containing four marginally stable (ms) orbits. For a given spacetime, the innermost and the outermost ms-orbits belong to the plus-family, the two orbits in between belong to the minus-family orbits. **(b)** In the naked-singularity region there exist spacetimes with no stable orbits for a fixed value of  $y$  (spacetimes with  $a^2$  greater than the global maximum of function  $a_{ms}^2(r; y)$  for a given  $y$ ). Stable counter-rotating (minus-family) orbits exist only in shaded regions of presented spacetimes. But some naked-singularity spacetimes contain counter-rotating plus-family orbits, for more details see the text. The dashed line corresponds to the radius  $(10y)^{-1/3}$  where both maxima of  $a_{ms}^2(r; y)$  are located. (Taken from [Stuchlík and Slaný, 2004].)

$$y_{ms\pm}(r) = \frac{3 + 5r \pm (60r - 20r^2 + 9)^{1/2}}{15r^3}. \tag{66}$$

The behaviour of the functions  $y_s(r)$ ,  $y_{ms}(r)$  and  $y_{ms\pm}(r)$  is illustrated in Fig. 6. The function  $y_{ms+}(r)$  is irrelevant, the relevant function  $y_{ms-}(r)$  intersects the function  $y_s(r)$  at  $r = 3$ , where  $y = y_{c(sDs)} = 1/27$ , and the function  $y_{ms}(r)$  at  $r = (3 + 2\sqrt{3})/4$ , where

$y = y_i = 16/(3+2\sqrt{3})^3$ . The critical value of the cosmological parameter for the existence of the stable (plus-family) orbits, corresponding to the local maximum of  $y_{\text{ms}(-)}(r)$ , is given by

$$y_{\text{crit}(\text{ms}+)} = \frac{100}{(5+2\sqrt{10})^3} \doteq 0.06886. \quad (67)$$

The related critical value of the rotational parameter is

$$a_{\text{crit}(\text{ms}+)}^2 = \frac{955+424\sqrt{10}}{1620} \doteq 1.41716. \quad (68)$$

The plus-family stable circular orbits are allowed for  $y < y_{\text{ms}}(r)$ , if  $y < y_i$ , and for  $y < y_{\text{ms}(-)}(r)$ , if  $y_i < y < y_{\text{crit}(\text{ms}+)}$ .

The condition determining the local extrema of  $a_{\text{ms}(1,2)}^2(r; y)$

$$\frac{\partial a_{\text{ms}(1,2)}^2(r; y)}{\partial r} = 0 \quad (69)$$

implies very complicated relations, however, they lead to one simple relevant relation

$$y = y_{\text{e}(\text{ms})}(r) \equiv \frac{1}{10r^3} \quad (70)$$

determining important local extrema of both  $a_{\text{ms}(1,2)}^2(r; y)$  simultaneously, both located on the radius

$$r = r_{\text{e}(\text{ms})}(y) \equiv \frac{1}{(10y)^{1/3}}. \quad (71)$$

The critical value of the cosmological parameter for the existence of the minus-family stable circular orbits, determined by the condition  $a_{\text{ms}(2)}^2(r_{\text{e}(\text{ms})}; y) = 0$ , is given by

$$y_{\text{crit}(\text{ms}-)} = \frac{12}{154}. \quad (72)$$

It coincides with the limit on the existence of the stable circular orbits in the Schwarzschild–de Sitter spacetimes [Stuchlík and Hledík, 1999].

Properties of the functions  $a_{\text{ms}(1,2)}^2(r; y)$  can be summarised in the following way.

(i)  $y > y_{\text{crit}(\text{ms}+)}$

No stable circular orbits are allowed for any value of the rotational parameter.

(ii)  $y_{\text{crit}(\text{ms}+)} > y > y_{\text{crit}(\text{ms}-)}$

At  $r = r_{\text{e}(\text{ms})}$ , the function  $a_{\text{ms}(1)}^2(r; y)$  has a local maximum ( $a_{\text{ms}(\text{max})}^2$ ), and the function  $a_{\text{ms}(2)}^2(r; y)$  has a local minimum ( $a_{\text{ms}(\text{min})}^2$ ). For  $a_{\text{ms}(\text{min})}^2 < a^2 < a_{\text{ms}(\text{max})}^2$ , the equation  $a^2 = a_{\text{ms}(1,2)}^2(r; y)$  determines two marginally stable plus-family circular orbits (the inner one and the outer one). For  $0 < a^2 < a_{\text{ms}(\text{min})}^2$  and  $a^2 > a_{\text{ms}(\text{max})}^2$ , no stable circular orbits are allowed.

(iii)  $y < y_{\text{crit}(\text{ms}-)}$

There are two zero points of the function  $a_{\text{ms}(2)}^2(r; y)$  corresponding to its local minima, while it has a local maximum  $a_{\text{ms}(\text{max}2)}^2$  at  $r = r_{\text{e}(\text{ms})}$ , where the maximum of the function  $a_{\text{ms}(1)}^2(r; y)$  is located too. For  $a^2 > a_{\text{ms}(\text{max})}^2$ , there is no stable circular orbit. For  $a_{\text{ms}(\text{max}2)}^2 < a^2 < a_{\text{ms}(\text{max})}^2$ , there are two marginally stable plus-family circular orbits. For

$a^2 < a_{\text{ms(max2)}}^2$ , there are four marginally stable orbits. The innermost and the outermost orbits belong to the plus-family, the two orbits in between belong to the minus-family.

The functions  $a_{\text{ms}(1,2)}^2$  are illustrated for typical values of the cosmological parameter in Fig. 7. In the parameter space  $y$ - $a^2$ , separation of the Kerr-de Sitter spacetimes according to the existence of stable circular orbits, determined by the functions  $a_{\text{ms}(1,2)}^2(r; y)$  and  $y_{\text{e(ms)}}(r)$ , is given in Fig. 2.

In theory of thick accretion disks, another type of circular orbits plays a very important role.

Behaviour of the effective potential (27) enables us to introduce the notion of the marginally bound orbits, i.e., unstable circular orbits where a small radial perturbation causes infall of a particle from the orbit to the centre, or its escape to the cosmological horizon. For some special value of the axial parameter  $X$ , denoted as  $X_{\text{mb}}$ , the effective potential has two local maxima related by the condition

$$E_{(+)}(r_{\text{mb(i)}}; X_{\text{mb}}, a, y) = E_{(+)}(r_{\text{mb(o)}}; X_{\text{mb}}, a, y), \quad (73)$$

and corresponding to both the inner and outer marginally bound orbits, see Fig. 8. For completeness, the figure include the effective potentials defining both the inner and outer marginally stable orbits (corresponding to special values of the parameter  $X$ :  $X_{\text{ms(i)}}$ ,  $X_{\text{ms(o)}}$ ). The search for the marginally bound orbits in a concrete Kerr-de Sitter spacetime must be realized in a numerical way and can be successful only in the spacetimes admitting stable circular orbits. Clearly, in the spacetimes with  $y \geq 12/15^4$ , the minus-family marginally bound orbits do not exist. Fig. 2 offers insight into the possibility of existence of both the stable and bound circular orbits of both the families. The limiting (full) curves are obtained from the conditions (63), (70) that have to be solved simultaneously.

Location of the astrophysically important circular orbits (photon orbits, marginally stable and marginally bound orbits) in dependence on the rotational parameter  $a$  is given in Fig. 9 for three appropriately chosen values of the cosmological parameter  $y$ . The values of  $y$  reflect the dependence of existence of stable minus-family orbits on  $y$ . The stable plus-family orbits exist for all of the chosen values of  $y$  in the relevant range of the parameter  $a$ . Spacetimes without stable circular orbits or without any circular orbits are discussed in [Stuchlík and Slaný, 2004].

In comparison with the asymptotically flat Kerr spacetimes, where the effect of space-time rotation vanishes for asymptotically large values of the radius, in the Kerr-de Sitter spacetimes the properties of the circular orbits must be treated more carefully, because the rotational effect is relevant in whole the region where the circular orbits are allowed and it survives even at the cosmological horizon.

The minus-family orbits have specific angular momentum negative,  $L_- < 0$ , in every Kerr-de Sitter spacetime and such orbits are counter-rotating from the point of view of locally non-rotating frames.

In the black-hole spacetimes, the plus-family orbits are co-rotating in almost all radii where the circular orbits are allowed except some region in vicinity of the static radius, where they become to be counter-rotating, as their specific angular momentum  $L$  is slightly negative there. However, these orbits are unstable. In the naked-singularity spacetimes, the plus-family orbits behave in a more complex way. They are always counter-rotating

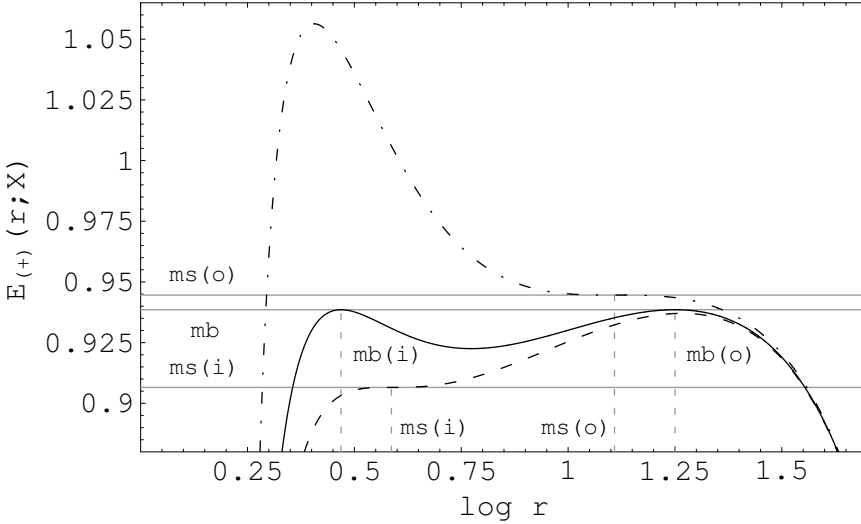


**Figure 8.** Effective potential of the equatorial radial motion of test particles in an appropriately chosen Kerr–de Sitter black-hole spacetime ( $y = 10^{-4}$ ,  $a^2 = 0.36$ ) allowing stable circular orbits for co-rotating particles. Marginally bound (mb) orbits are given by the solid curve corresponding to the angular momentum parameter  $X = X_{mb+} \doteq 2.38445$ . The curve has two local maxima of the same value,  $E_{mb} \doteq 0.93856$ , corresponding to the inner (mb(i)) and the outer (mb(o)) marginally bound orbits. The dashed effective potential defines the inner marginally stable orbit (ms(i)) by coalescing the local minimum and the (inner) local maximum. It corresponds to the parameter  $X = X_{ms(i)+} \doteq 2.20307$  with specific energy  $E_{ms(i)+} \doteq 0.90654$ . In an analogous manner, the dashed-dotted potential defines the outer marginally stable orbit (ms(o)) with specific energy  $E_{ms(o)+} \doteq 0.94451$  corresponding to the parameter  $X = X_{ms(o)+} \doteq 2.90538$ . (Taken from [Stuchlík and Slaný, 2004].)

in vicinity of the static radius. Moreover, in the naked singularity spacetimes, with the rotational parameter low enough, the stable counterrotating plus-family circular orbits exist.

The specific angular momentum of particles located at the static radius, where the plus-family orbits and the minus-family orbits coalesce, is given by the relation

$$L(r_s; y, a) = L_s \equiv -a \frac{3y^{1/3} + a^2 y}{(1 - 3y^{1/3} - a^2 y)^{1/2}}, \quad (74)$$

and their specific energy is

$$E(r_s; y, a) = E_s \equiv (1 - 3y^{1/3} - a^2 y)^{1/2}. \quad (75)$$

The motion along the stable plus-family circular geodesics counter-rotating relative to locally non-rotating frames is discussed in detail in [Stuchlík and Slaný, 2004]. A special attention is focused on stable circular orbits with negative energy which could exist in Kerr–de Sitter naked-singularity spacetimes with the rotational parameter sufficiently close to unity.

## 5 BASIC PROPERTIES OF THIN DISKS

Both the black-hole and naked-singularity Kerr–de Sitter spacetimes can be separated into three classes according to the existence of stable (and, equivalently, marginally bound) circular orbits (see Fig. 2). The stable orbits of both the plus-family and minus-family exist in the spacetimes of class I (black holes) and class V (naked singularities). Solely stable orbits of the plus-family exist in the spacetimes of classes II (black holes) and VI (naked singularities). No stable orbits exist in the spacetimes of classes III and IV. In dependence on the cosmological parameter, there are three qualitatively different types of the behaviour of the loci of the marginally stable, marginally bound, and photon circular orbits as functions of the rotational parameter. These functions are illustrated for three representative values of  $y$  in Fig. 9 enabling to make in a straightforward way separation of the Kerr–de Sitter

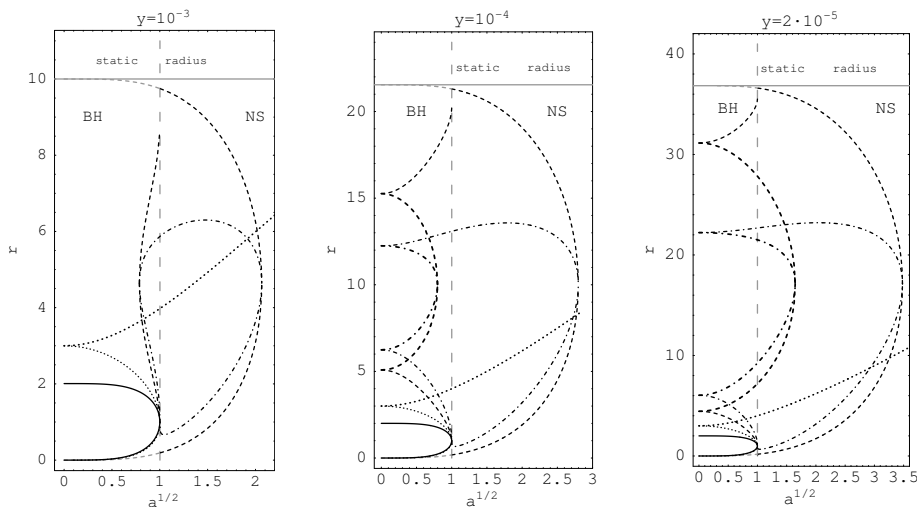


**Figure 9.** Mutual positions of the astrophysically important circular orbits in the Kerr–de Sitter spacetimes. The figures are constructed for three representative values of  $y$ . The radii of the special equatorial circular orbits are plotted as functions of the rotational parameter  $a$ . Widely dashed line is given by the value of rotational parameter corresponding to the extreme black hole and it splits up the Kerr–de Sitter spacetimes into the black-hole (BH) and naked-singularity (NS) regions. Thin curves are used for the plus-family orbits (in the most cases they correspond to the co-rotating orbits from the point of view of the locally non-rotating observers, but there are exceptions described in the text). Bold curves are used for the minus-family orbits (in all spacetimes under consideration: counter-rotating orbits). Full curves determine the inner and the outer black-hole horizons. Dotted curves determine the photon circular orbits, dashed curves determine the marginally bound (mb) circular orbits, there is a disconnection between BH and NS regions for the plus-family orbits. Lower gray dashed curves determine the marginally bound orbits hidden under the inner black-hole horizon, the upper one, approaching the static radius for small  $a$ , is its outer analogy. Dashed-dotted curves determine the marginally stable (ms) orbits. For  $y \geq 12/15^4$  there are no minus-family mb and ms orbits. (Taken from [Stuchlík and Slaný, 2004].)

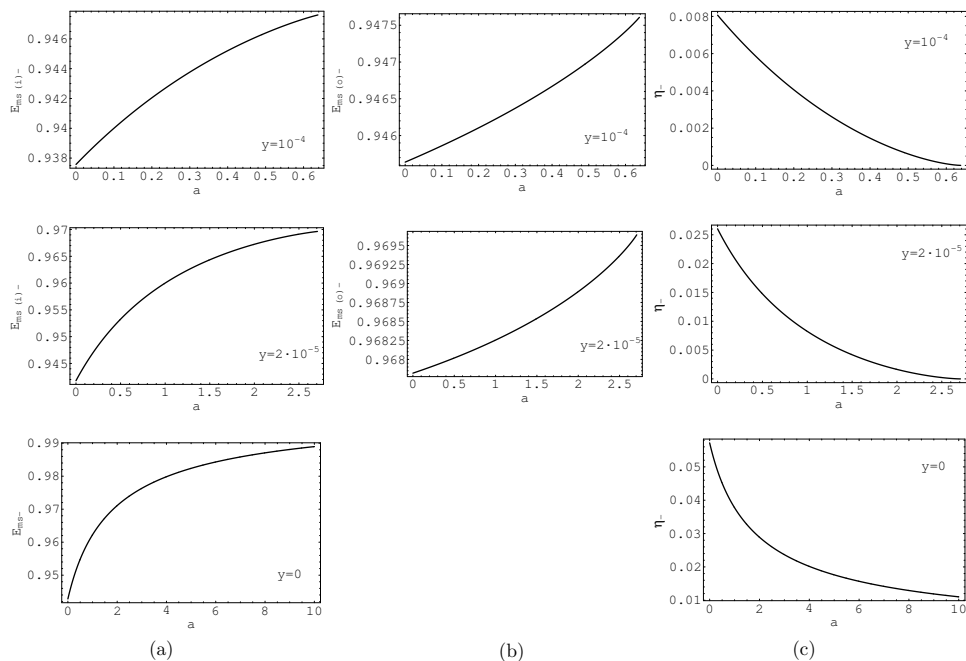


**Figure 10.** Specific energy of the marginally stable minus-family orbits ((a)–inner, (b)–outer) and (c) the accretion efficiency  $\eta_- \equiv E_{\text{ms}(o)-} - E_{\text{ms}(i)-}$  given as a function of the rotational parameter for three representative values of the cosmological parameter. For the Kerr spacetimes,  $y = 0$ , we assume  $E_{\text{ms}(o)-} = 1$ . (Taken from [Stuchlík and Slaný, 2004].)

spacetimes into the classes I–VI. In the special case of the Kerr spacetimes ( $y = 0$ ), these functions can be found in [Bardeen, 1973, Stuchlík, 1980].

The marginally stable circular orbits are crucial in the context of Keplerian (geometrically thin) accretion disks as these orbits determine the efficiency of conversion of rest mass into heat energy of any element of matter transversing the disks from their outer edge located on the outer marginally stable orbit to their inner edge located on the inner marginally stable orbit:

$$\eta \equiv E_{\text{ms}(o)} - E_{\text{ms}(i)}. \quad (76)$$

The accretion disks constituted from the minus-family orbits are everywhere counter-rotating relative to the locally non-rotating frames. For the minus-family disks, the specific energy of both the outer and inner marginally stable circular orbits, and the efficiency parameter  $\eta_- = E_{\text{ms}(o)-} - E_{\text{ms}(i)-}$ , are given for three typical values of  $y$  as functions of  $a$  in Fig. 10. In the limit of  $a \rightarrow 0$  with  $y$  being fixed, we obtain the known values of the specific energy  $E_{\text{ms}(o)}$ ,  $E_{\text{ms}(i)}$ , and the efficiency parameter of the accretion process  $\eta$  for the Schwarzschild-de Sitter black holes [Stuchlík and Hledík, 1999]. Both the specific energy parameters  $E_{\text{ms}(o)-}(a)$ ,  $E_{\text{ms}(i)-}(a)$  and the efficiency  $\eta_-(a)$  vary smoothly at values of the rotational parameter corresponding to the extreme black holes.

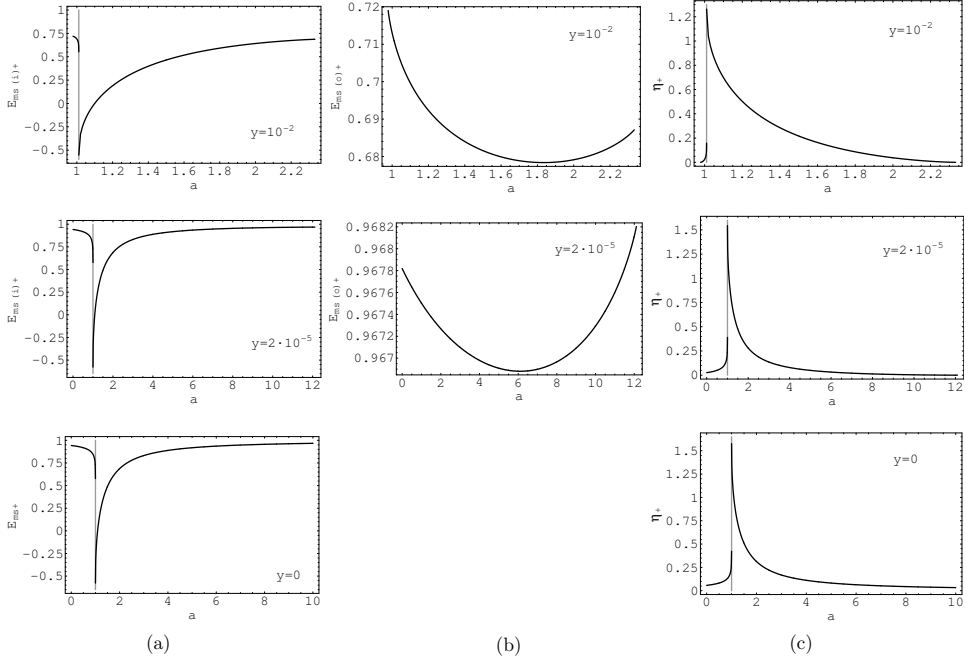


**Figure 11.** Specific energy of the marginally stable plus-family orbits **(a)**–inner, **(b)**–outer and **(c)** the accretion efficiency  $\eta_+ \equiv E_{\text{ms}(o)+} - E_{\text{ms}(i)+}$  (right column) as a function of the rotational parameter for three representative values of the cosmological parameter. Gray line corresponds to the extreme black hole. We can see a strong discontinuity of the specific energy of the inner marginally stable orbits and the accretion efficiency when black holes and naked singularities approach the extreme black-hole state. For the Kerr spacetimes,  $y = 0$ , we assume  $E_{\text{ms}(o)+} = 1$ . (Taken from [Stuchlík and Slaný, 2004].)

The accretion disks constituted from the plus-family orbits behave in much more complex way in comparison with those of the minus-family orbits. First, usually these disks could be considered as co-rotating relative to the locally non-rotating frames; recall that in the asymptotically flat Kerr black-hole spacetimes the plus-family disks are co-rotating at all radii down to the marginally stable orbit, while in the field of naked singularities with  $a/M < \frac{3}{4}\sqrt{3}$  the stable circular orbits co-rotating at large distances are transformed into counter-rotating orbits in vicinity of the marginally stable orbit [Stuchlík, 1980]. A similar behaviour occurs in the Kerr–de Sitter spacetimes, however, in the spacetimes with  $y \rightarrow y_{\text{c}(KdS)}$ , the stable plus-family orbits can be counter-rotating even at all allowed radii [Stuchlík and Slaný, 2004]. Moreover, there are always counter-rotating plus-family orbits in vicinity of the static radius, where the plus-family orbits and the minus-family orbits coalesce; these orbits are, however, unstable relative to radial perturbations and cannot be related to accretion disks.

Second, the specific energy  $E_{\text{ms}(i)+}(y, a)$  of the inner marginally stable plus-family orbit can be negative. Recall that  $E_{\text{ms}(i)+} < 0$  in the asymptotically flat Kerr naked-singularity

spacetimes with the rotational parameter  $a/M < \frac{4}{3}\sqrt{\frac{2}{3}}$ , indicating the efficiency of the accretion process  $\eta_+ = E_{\text{ms}(o)+} - E_{\text{ms}(i)+} > 1$ , because in the asymptotically flat Kerr spacetimes the outer edge of the accretion disks can be at arbitrarily large radii implying thus  $E_{\text{ms}(o)+} = 1$ . In the Kerr–de Sitter spacetimes allowing  $E_{\text{ms}(i)+} < 0$ , the efficiency of the accretion process can be both  $\eta > 1$  and  $\eta < 1$ , as it depends strongly on  $E_{\text{ms}(o)+}$ , which for  $y \sim y_{\text{c(KdS)}}$  can be even negative. For three typical values of  $y$ , the functions  $E_{\text{ms}(o)+}(a)$ ,  $E_{\text{ms}(i)+}(a)$ ,  $\eta_+(a)$  are illustrated in Fig. 11. The specific energy function  $E_{\text{ms}(i)+}(a)$  falls for  $a$  growing in the black-hole region, and for  $a$  descending in the naked-singularity region. The specific energy function  $E_{\text{ms}(o)+}(a)$  has a local minimum at some value of the rotational parameter  $a$  strongly dependent on the cosmological parameter  $y$ . For  $y$  being fixed, the accretion efficiency  $\eta_+(a)$  grows for  $a$  growing in the black-hole sector up to the critical value corresponding to the extreme black-hole spacetime, and it also grows for  $a$  descending in the naked-singularity sector down to the critical value.

Third, there is a strong discontinuity of the specific energy function  $E_{\text{ms}(i)+}(a)$  for the spacetimes approaching the extreme black hole state from the black-hole and the naked-singularity sectors. For the extreme Kerr black holes ( $y = 0, a/M = 1$ ), there is the limiting value of the specific energy  $E_{\text{ms}(bh)} = 1/\sqrt{3}$ , while for naked singularities approaching the extreme hole states ( $a/M \rightarrow 1$  from above), there is  $E_{\text{ms}(ns)} = -1/\sqrt{3}$ . For the extreme Kerr–de Sitter spacetimes, the dependence of the specific energy of the inner marginally stable orbit on the cosmological parameter is shown in Fig. 12a. Clearly, there is  $E_{\text{ms}(ns)}(y) = -E_{\text{ms}(bh)}(y)$ , where, for a given cosmological parameter  $y$  the rotational parameter  $a$  of the corresponding extreme black hole is determined by the upper branch of the limiting line separating black-hole and naked-singularity states in Fig. 2. For  $y \rightarrow y_{\text{c(KdS)}}$ , there is  $E_{\text{ms}(bh)}(y) \rightarrow 0$ . For the specific energy function  $E_{\text{ms}(o)+}(y, a)$  of the outer marginally stable orbits there is no discontinuity at the states corresponding to the extreme black-hole spacetimes (see Fig. 12b). The accretion efficiency  $\eta_+(y)$  in the field of extreme black holes ( $\eta_{\text{bh}}(y)$ ) and in the field of the naked singularities infinitesimally close to the extreme hole states ( $\eta_{\text{ns}}(y)$ ) is shown in Fig. 12c. For  $y = 0$  their difference takes the maximum ( $\eta_{\text{ns}} = 1 + 1/\sqrt{3}$ ,  $\eta_{\text{bh}} = 1 - 1/\sqrt{3}$ ), while at  $y = y_{\text{c(KdS)}}$  the difference vanishes ( $\eta_{\text{ns}} = 0$ ,  $\eta_{\text{bh}} = 0$ ).

## 6 EQUILIBRIUM CONFIGURATIONS OF PERFECT FLUID

The stress-energy tensor of perfect fluid is given by the relation

$$T^\mu_\nu = (p + \epsilon)U^\mu U_\nu + p \delta^\mu_\nu \tag{77}$$

where  $\epsilon$  and  $p$  denote total energy density and pressure of the fluid,  $U^\mu$  is its four velocity. We shall consider test perfect fluid rotating in the  $\phi$  direction, i.e.,  $U^\mu = (U^t, U^\phi, 0, 0)$ . The rotating fluid can be characterised by the vector fields of the angular velocity  $\Omega(r, \theta)$  and the angular momentum density  $\ell(r, \theta)$ , defined by

$$\Omega = \frac{U^\phi}{U^t}, \quad \ell = -\frac{U_\phi}{U_t}. \tag{78}$$

The vector fields are related by the metric coefficients of the Kerr–de Sitter spacetime

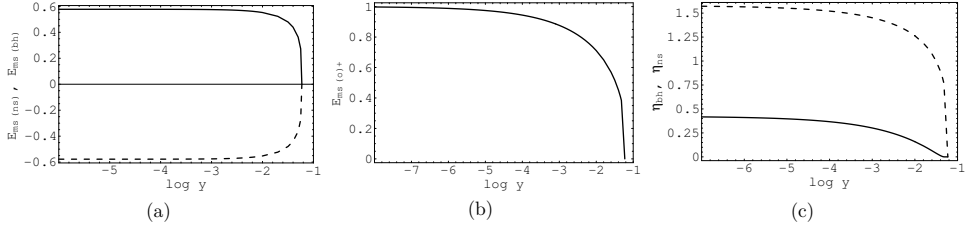


**Figure 12.** Specific energy of the marginally stable orbits and accretion efficiency near the extreme black-hole states. **(a)** Specific energy of the inner marginally stable plus-family orbit in the extreme black-hole and the related limiting naked-singularity spacetimes approaching the extreme hole states as a function of the cosmological parameter  $y$ . Solid curve corresponds to the extreme black holes, dashed curve corresponds to the limiting naked singularities. The curves are symmetric around the zero-energy-axis and tend to zero for  $y = y_{c(\text{KdS})}$ . In the extreme Kerr spacetimes ( $y = 0$ ), the specific energy in the black-hole and naked-singularity cases are  $1/\sqrt{3}$  and  $-1/\sqrt{3}$ , respectively. **(b)** Specific energy of the outer marginally stable plus-family orbit in the extreme Kerr–de Sitter black-hole spacetimes is the same as for the naked-singularity spacetimes approaching the extreme hole state, i.e., there is no discontinuity in this case. The specific energy tends to zero for  $y \rightarrow y_{c(\text{KdS})}$ . **(c)** Accretion efficiency for the extreme black holes  $\eta_{\text{bh}}$  (the solid curve) and for the limiting naked singularities  $\eta_{\text{ns}}$  (the dashed curve). For  $y = 0$  (pure Kerr spacetimes) we obtain the maximum value 0.42 for black holes and 1.58 for naked singularities. For  $y \rightarrow y_{c(\text{KdS})}$  the efficiency tends to zero for both black holes and naked singularities. (Taken from [Stuchlík and Slaný, 2004].)

$$\Omega = -\frac{g_{t\phi} + \ell g_{tt}}{g_{\phi\phi} + \ell g_{t\phi}}. \quad (79)$$

Projecting the energy-momentum conservation law  $T^{\mu\nu}{}_{;v} = 0$  onto the hypersurface orthogonal to the four velocity  $U^\mu$  by the projection tensor  $h_{\mu\nu} = g_{\mu\nu} + U_\mu U_\nu$ , we obtain the relativistic Euler equation in the form

$$\frac{\partial_\mu p}{p + \epsilon} = -\partial_\mu (\ln U_t) + \frac{\Omega \partial_\mu \ell}{1 - \Omega \ell}, \quad (80)$$

where

$$(U_t)^2 = \frac{g_{t\phi}^2 - g_{tt} g_{\phi\phi}}{g_{\phi\phi} + 2\ell g_{t\phi} + \ell^2 g_{tt}}. \quad (81)$$

For barytropic perfect fluid, i.e., the fluid with an equation of state  $p = p(\epsilon)$ , the solution of the relativistic Euler equation can be given by Boyer’s condition determining the surfaces of constant pressure through the “equipotential surfaces” of the potential  $W(r, \theta)$  by the relations [Abramowicz et al., 1978]

$$\int_0^p \frac{dp}{p + \epsilon} = W_{\text{in}} - W, \quad (82)$$

$$W_{\text{in}} - W = \ln(U_t)_{\text{in}} - \ln(U_t) + \int_{\ell_{\text{in}}}^\ell \frac{\Omega d\ell}{1 - \Omega \ell}; \quad (83)$$

the subscript “in” refers to the inner edge of the disk. For an alternative definition of Boyer’s condition see [Abramowicz et al., 1978, Fishbone and Moncrief, 1976, Fishbone, 1977]. The equipotential surfaces are determined by the condition

$$W(r, \theta) = \text{const}, \tag{84}$$

and in a given spacetime can be found from Eq. (83), if a rotation law  $\Omega = \Omega(\ell)$  is given.

Equilibrium configurations of test perfect fluid are determined by the equipotential surfaces which can be closed or open. Moreover, there is a special class of critical, self-crossing surfaces (with a cusp), which can be either closed or open. The closed equipotential surfaces determine stationary toroidal configurations. The fluid can fill any closed surface – at the surface of the equilibrium configuration pressure vanishes, but its gradient is non-zero [Kozłowski et al., 1978]. On the other hand, the open equipotential surfaces are important in dynamical situations, e.g., in modelling of jets [Lynden-Bell, 1969, Blandford, 1987]. The critical, self-crossing closed equipotential surfaces  $W_{\text{cusp}}$  are important in the theory of thick accretion disks, because accretion onto the black hole through the cusp of the equipotential surface located in the equatorial plane is possible due to the Paczyński mechanism.

According to Paczyński, the accretion into the black hole proceeds in the vicinity of the cusp due to a little overcoming of the critical equipotential surface,  $W = W_{\text{cusp}}$ , by the surface of the disk. The accretion is thus driven by a violation of the hydrostatic equilibrium, rather than by viscosity of the accreting matter [Kozłowski et al., 1978].

It is well known that all characteristic properties of the equipotential surfaces for a general rotation law are reflected by the equipotential surfaces of the simplest configurations with uniform distribution of the angular momentum density  $\ell$  – see [Jaroszyński et al., 1980]. Moreover, these configurations are very important astrophysically, being marginally stable [Seguin, 1975]. Under the condition

$$\ell(r, \theta) = \text{const}, \tag{85}$$

holding in the rotating fluid, a simple relation for the equipotential surfaces follows from Eq. (83):

$$W(r, \theta) = \ln U_t(r, \theta), \tag{86}$$

with  $U_t(r, \theta)$  being determined by  $\ell = \text{const}$ , and the metric coefficients only.

The equipotential surfaces are described by the formula  $\theta = \theta(r)$ , which can be given by the differential equation

$$\frac{d\theta}{dr} = -\frac{\partial p / \partial r}{\partial p / \partial \theta}, \tag{87}$$

which for the configurations with  $\ell = \text{const}$  reduces to

$$\frac{d\theta}{dr} = -\frac{\partial U_t / \partial r}{\partial U_t / \partial \theta}. \tag{88}$$

In the Kerr–de Sitter spacetimes there is

$$U_t(r, \theta; \ell) = \frac{\rho}{I} \cdot \frac{\Delta_r^{1/2} \Delta_\theta^{1/2} \sin \theta}{\left[ \Delta_\theta \sin^2 \theta (r^2 + a^2 - a\ell)^2 - \Delta_r (\ell - a \sin^2 \theta)^2 \right]^{1/2}} \quad (89)$$

and

$$W(r, \theta) = \ln \left\{ \frac{\rho}{I} \cdot \frac{\Delta_r^{1/2} \Delta_\theta^{1/2} \sin \theta}{\left[ \Delta_\theta \sin^2 \theta (r^2 + a^2 - a\ell)^2 - \Delta_r (\ell - a \sin^2 \theta)^2 \right]^{1/2}} \right\}. \quad (90)$$

The best insight into the  $\ell = \text{const}$  configurations is given by properties of  $W(r, \theta)$  in the equatorial plane ( $\theta = \pi/2$ ).

The reality conditions of  $W(r, \theta = \pi/2)$  can be put in the following way.

- a)  $\Delta_r > 0$ ; naturally, we have to consider stationary parts of the Kerr–de Sitter geometry,
- b) for  $\Delta_r > a^2$  (outside the ergosphere), the condition

$$\ell_{\text{ph-}} < \ell < \ell_{\text{ph+}} \quad (91)$$

must be satisfied. For  $a^2 > \Delta_r$  (inside the ergosphere), the condition

$$\ell < \ell_{\text{ph-}} \quad \text{or} \quad \ell > \ell_{\text{ph+}} \quad (92)$$

must be satisfied, where the functions  $\ell_{\text{ph}\pm}(r; a, y)$ , given by

$$\ell_{\text{ph}\pm}(r; a, y) \equiv \frac{a \left[ \Delta_r - (r^2 + a^2) \right] \pm r^2 \Delta_r^{1/2}}{\Delta_r - a^2}, \quad (93)$$

determine the photon geodesic motion (see [Stuchlík and Hledík, 2000, Stuchlík and Slaný, 2004]). Notice that for the photon motion, it is useful to redefine the impact parameter by

$$\ell \rightarrow X = \ell - a. \quad (94)$$

The “effective potential” of the equatorial photon motion then takes the simple form

$$X_{\text{ph}\pm}(r; a, y) = \frac{r^2}{a \pm \Delta_r^{1/2}}. \quad (95)$$

The functions  $\ell_{\text{ph}\pm}$  are finite on the horizons. However,  $\ell_{\text{ph-}}$  diverges on the surface of static limit:  $\ell_{\text{ph-}}(r \rightarrow r_{\text{s.l.}+}) \rightarrow -\infty$ ,  $\ell_{\text{ph-}}(r \rightarrow r_{\text{s.l.-}}) \rightarrow +\infty$ , while the function  $\ell_{\text{ph+}}(r = r_{\text{s.l.}}) = a + r_{\text{s.l.}}^2/2a$ , being continuous there.

Condition for the local extrema of the potential  $W(r, \theta = \pi/2)$  is identical with the condition of vanishing of the pressure gradient ( $\partial U_t / \partial r = 0 = \partial U_t / \partial \theta$ ). Since in the equatorial plane there is  $\partial U_t / \partial \theta = 0$ , independently of  $\ell = \text{const}$ , the only relevant condition is

$$\frac{\partial U_t}{\partial r} = 0, \quad (96)$$

which implies the relation

$$\ell = \ell_{\text{K}\pm}(r; a, y) \quad (97)$$

with  $\ell_{\text{K}\pm}$  being the angular momentum density of the geodetical Keplerian orbits

$$\ell_{\text{K}\pm}(r; a, y) \equiv \frac{(r^2 + a^2)(1 - yr^3)^{1/2} \mp ar^{1/2}[2 + yr(r^2 + a^2)]}{r^{3/2}[1 - y(r^2 + a^2)] - 2r^{1/2} \pm a(1 - yr^3)^{1/2}}. \quad (98)$$

The closed equipotential surfaces and surfaces with a cusp allowing the outflow of matter from the disk, are permitted in those parts of the functions  $\ell_{K\pm}(r; a, y)$  enabling the existence of stable circular geodesics corresponding to the centre of the equilibrium configurations.

We present some typical sequences of equipotential surfaces in both the Kerr–de Sitter black-hole and naked-singularity spacetimes. In the black-hole spacetimes, both the Boyer–Lindquist (Fig. 13) and Kerr–Schild (Fig. 14) coordinates could be used, giving similar picture of the behaviour of the equipotential surfaces due to restriction to the region above the outer horizon. In the naked-singularity spacetimes, however, the Kerr–Schild coordinate system is more suitable, because it enables to describe the region very close to the ring singularity in proper way, see Fig. 15.

Influence of a repulsive cosmological constant on the structure of thick accretion disks consists in two main features: the existence of the outer cusp and the collimation of the open equipotential surfaces near the rotational axis being evident in the vicinity of the static radius and further. Outer cusp, also located near the static radius, gives an upper limit on the extension of accretion disks due to the violation of hydrostatic equilibrium when a matter overfills the critical equipotential surface with a cusp. However, these features were known from the analysis of equilibrium configurations of a perfect fluid orbiting in the Schwarzschild–de Sitter backgrounds. Influence of the rotation of a spacetime remains in the fact that the collimation is stronger and the disks can be larger than in non-rotating backgrounds. Comparison of the shapes of marginally bound thick accretion disks in the Schwarzschild–de Sitter and Kerr–de Sitter black-hole background of the same central mass  $M$  reveals that the corotating disk is thicker and its funnel is narrower than the Schwarzschild–de Sitter case which is thicker with narrower funnel than the counterrotating disk. More detailed analysis of the structure of equilibrium disk-like configurations of perfect fluid orbiting in the Kerr–de Sitter background is prepared for the original paper [Slaný and Stuchlík, 2004].

## 7 CONCLUDING REMARKS

Due to accretion in a plus-family or a minus-family Keplerian disk, a hypothetical naked singularity can be converted into an extreme black hole. In the case of Kerr naked singularities their evolution into an extreme hole state was discussed in [Calvani and Nobili, 1979, Stuchlík, 1981, Stuchlík et al., 2002]. Such a conversion can be a rather dramatic process in the case of the plus-family accretion disks because of the discontinuity of the plus-family orbits at the extreme black-hole state. We can understand this process, if we show how the stable circular orbits are distributed in the naked-singularity spacetimes approaching the extreme black-hole state (Fig. 16). We can see that all the orbits with the specific energy ranging from  $E_{ms(ns)}(y)$  up to  $E_{ms(bh)}(y)$  are distributed at an infinitesimally small range of the radial coordinate in vicinity of the radius corresponding to the event horizon of the extreme black hole. Of course, it is well known that at these radii the physically relevant proper radial length, along which the accretion disk is distributed, becomes very (almost infinitely) long (see [Bardeen, 1973]). If the conversion of a hypothetical naked singularity into an extreme black hole is realized, the part of the accretion disk located under the marginally stable

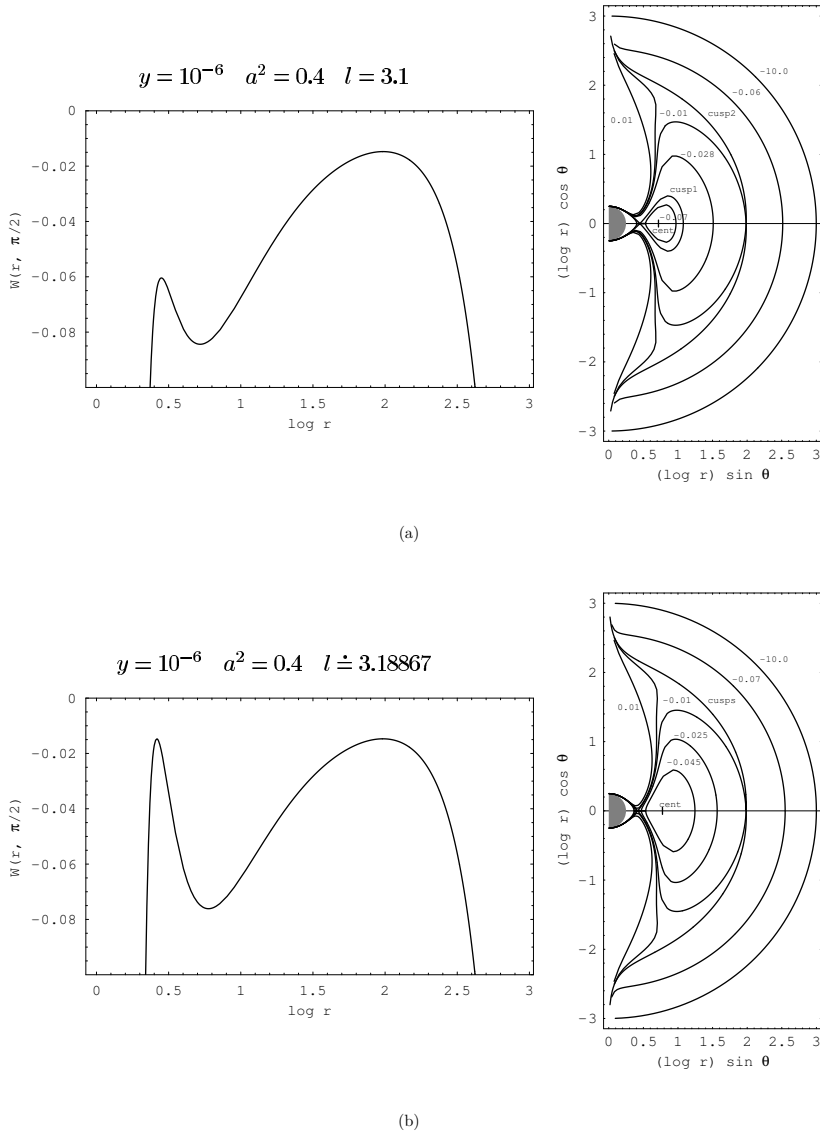


**Figure 13.** Behaviour of the potential in the equatorial plane and the meridional sections through the structure of equipotential surfaces in the cases corresponding to accretion disks in the black-hole backgrounds described in Boyer–Lindquist (B–L) coordinates. (a) Typical behaviour for the angular momentum density  $\ell_{\text{ms}(i)} < \ell < \ell_{\text{mb}}$  leading to the system of closed equipotential surfaces where the last one contains the (inner) cusp enabling the accretion onto the central black hole (the gray surface). (b) Marginally bound accretion disk corresponding to the angular momentum density  $\ell = \ell_{\text{mb}}$ . The critical closed equipotential surface contains both the cusps. The inner one enables an accretion onto the black hole, the outer one makes possible an outflow from the disk.

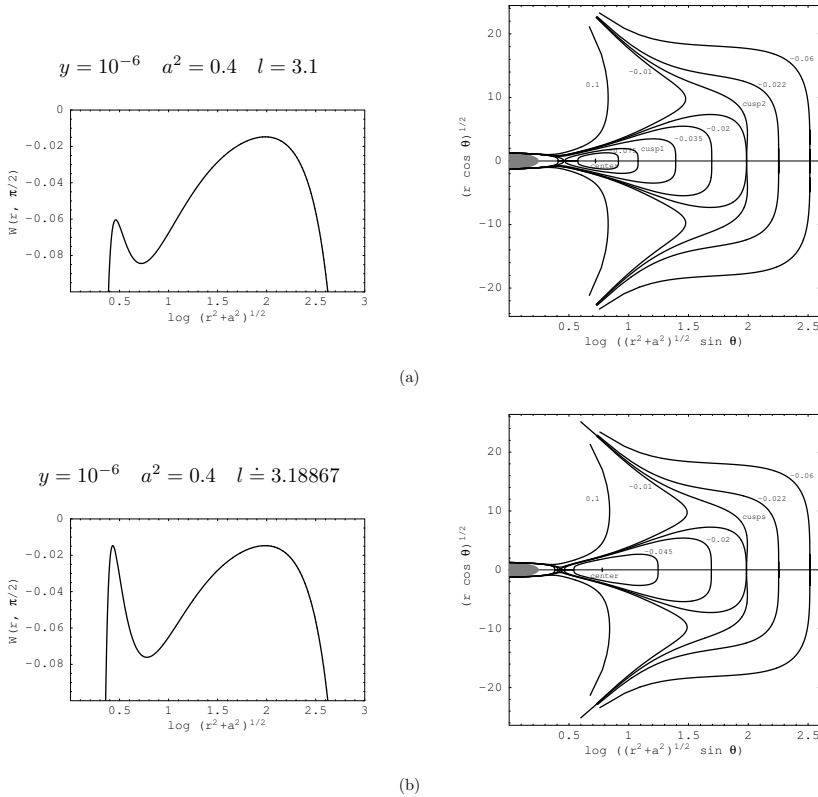


**Figure 14.** The same situation as in Fig. 13 described in Kerr–Schild coordinates now. The black-hole case is almost identical with the picture in Boyer–Lindquist coordinates. Behaviour of the open equipotential surfaces near the rotational axis demonstrates the strong collimation effect of a repulsive cosmological constant.

circular orbit of the created black hole becomes unstable relative to radial perturbations and will be immediately swallowed by the black hole. It can be expected that the collapse of the unstable internal part of the disk with the specific energy ranging from  $E_{\text{ms}(\text{ns})}(y)$  up to  $E_{\text{ms}(\text{bh})}(y)$  could be observationally important, leading to an abrupt fall down of observable luminosity of the accretion disk.

In the case of thick accretion disks around Kerr–de Sitter naked singularities we expect a similar dramatic process. Moreover, the inner edge of an accretion disk is located very close to the ring singularity and the outer edge can be extended almost up to the static radius (even closer than in any black-hole case). A gravitational pit, the difference of energies on the inner edge and in the centre of an accretion disk around a naked singularity can be many times deeper than in the disks orbiting black holes. A collimation effect, which could play an important role in the formation and propagation of jets, is much stronger in the naked-singularity backgrounds in accordance with the geodesic collimation in Kerr naked-singularity spacetimes discovered by Bičák et al. [Bičák et al., 1993]. However, in

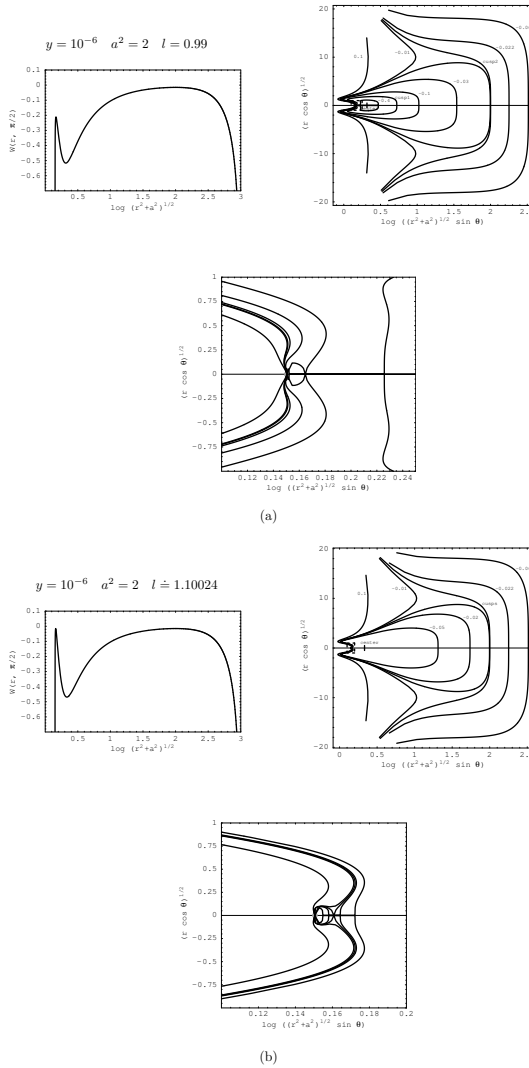


**Figure 15.** Behaviour of the potential in the equatorial plane and the meridional sections through the structure of equipotential surfaces in the cases corresponding to accretion disks in naked-singularity backgrounds described in Kerr–Schild (K–S) coordinates. (a) Typical behaviour for the angular momentum density  $\ell_{\text{ms}(i)} < \ell < \ell_{\text{mb}}$  leading to the system of closed equipotential surfaces where the last one contains the (inner) cusp enabling the accretion onto the central ring singularity (the grey point in the equatorial plane). (b) Marginally bound accretion disk corresponding to the angular momentum density  $\ell = \ell_{\text{mb}}$ . The critical closed equipotential surface contains both the cusps. The inner one enables an accretion onto the ring singularity, the outer one makes possible an outflow from the disk. Behaviour of the open equipotential surfaces near the rotational axis demonstrates the strong collimation effect of a repulsive cosmological constant.

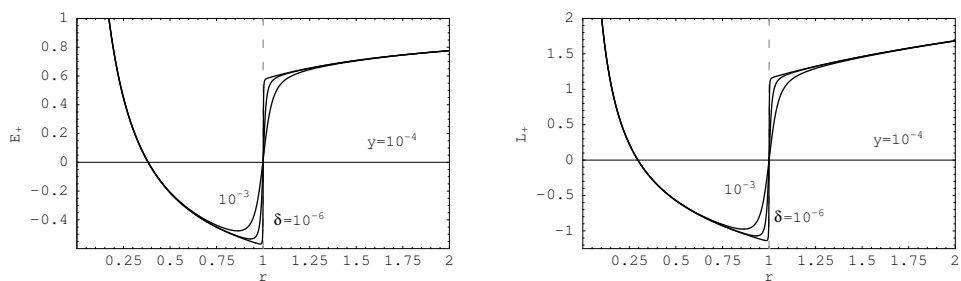


**Figure 16.** Distribution of the specific energy and the specific angular momentum of the equatorial circular orbits in the naked-singularity spacetimes approaching the extreme black-hole state. The orbits with the specific energy in the interval  $E_{\text{ms}(\text{ns})} < E < E_{\text{ms}(\text{bh})}$  are located in an extremely small interval of the radial coordinate having, however, an extremely long proper length [Bardeen, 1973]. After conversion of a hypothetical naked singularity into an extreme black hole all these circular orbits become unstable relative to radial perturbations and will be immediately swallowed by the black hole. The figures are drawn for  $a = a_0(1 + \delta)$  and  $y = y_0(1 - \delta)$ , where  $y_0 = 10^{-4}$  and  $a_0 = 1.0001$  are chosen to correspond to an extreme black hole, and, subsequently,  $\delta = 10^{-3}, 10^{-4}, 10^{-6}$ . (Taken from [Stuchlík and Slaný, 2004].)

Kerr–de Sitter backgrounds the collimation is stronger than in corresponding Kerr spacetime because of the existence of the static radius where a cosmological repulsion starts to dominate.

We can give to our results proper astrophysical relevance by presenting numerical estimates for observationally established current value of the cosmological constant. Wide range of recent cosmological observations give strong “concordance” indication [Krauss, 1998] that the observed value of the vacuum energy density is

$$\varrho_{\text{vac}(0)} \approx 0.66 \varrho_{\text{crit}(0)} \quad (99)$$

with present values of the critical energy density  $\varrho_{\text{crit}(0)}$ , and the Hubble parameter  $H_0$  given by

$$\varrho_{\text{crit}(0)} = \frac{3H_0^2}{8\pi}, \quad H_0 = 100h \text{ km s}^{-1} \text{ Mpc}^{-1}. \quad (100)$$

Taking value of the dimensionless parameter  $h \approx 0.7$ , we obtain the “relict” repulsive cosmological constant to be

$$\Lambda_0 = 8\pi\varrho_{\text{vac}(0)} \approx 1.1 \times 10^{-56} \text{ cm}^{-2}. \quad (101)$$

Having this value of  $\Lambda_0$ , we can determine the mass parameter of the spacetime corresponding to any value of  $y$ , parameters of the equatorial circular geodesics and basic characteristics of both the thin and thick accretion disks. For extreme black holes (we have chosen some typical values of the black-hole mass), dimensions of the static radius and the outer marginally stable circular orbit of the plus-family accretion disk are given in Table 1. For more detailed information in the case of thick disks around Schwarzschild–de Sitter black holes see [Stuchlík et al., 2000], where the estimates for primordial black holes in the early universe with a repulsive cosmological constant related to a hypothetical vacuum

**Table 1.** Mass parameter, the static radius and radius of the outer marginally stable circular orbit determining the outer edge of corotating Keplerian disks in extreme Kerr–de Sitter black-hole spacetimes are given for the relict repulsive cosmological constant indicated by recent cosmological observations:  $\Lambda_0 \approx 1.1 \times 10^{-56} \text{ cm}^{-2}$ . Outer edge of the corotating marginally bound thick accretion disk is determined by the outer marginally bound circular orbit which is located very close to, and for presented values of  $y$  almost at the static radius of a given spacetime. (Taken from [Stuchlík and Slaný, 2004].)

$y$	$M$ [ $M_\odot$ ]	$r_s$ [kpc]	$r_{\text{ms}(o)+}$ [kpc]
$10^{-46}$	1.1	0.1	0.07
$10^{-44}$	11.1	0.2	0.15
$10^{-42}$	111.4	0.5	0.3
$10^{-40}$	$1.1 \times 10^3$	1.1	0.7
$10^{-34}$	$1.1 \times 10^6$	11.4	7.2
$10^{-32}$	$1.1 \times 10^7$	24.5	15.5
$10^{-30}$	$1.1 \times 10^8$	52.8	33.3
$10^{-28}$	$1.1 \times 10^9$	113.8	71.7
$10^{-26}$	$1.1 \times 10^{10}$	245.2	154.5
$10^{-24}$	$1.1 \times 10^{11}$	528.3	332.9
$10^{-22}$	$1.1 \times 10^{12}$	1138.4	717.1

energy density connected with the electroweak symmetry breaking or the quark confinement are presented.

It is well known (see, e.g., [Carroll and Ostlie, 1996]) that dimensions of accretion disks around stellar-mass black holes ( $M \sim 10M_\odot$ ) in binary systems are typically  $10^{-3}$  pc, dimensions of large galaxies with central black-hole mass  $M \sim 10^8M_\odot$ , of both spiral and elliptical type, are in the interval 50–100 kpc, and the extremely large elliptical galaxies of cD type with central black-hole mass  $M \sim 3 \times 10^9M_\odot$  extend up to 1 Mpc. Therefore, we can conclude that the influence of the relict cosmological constant is quite negligible in the accretion disks in binary systems of stellar-mass black holes as the static radius exceeds in many orders dimension of the binary systems. But it can be relevant for accretion disks in galaxies with large active nuclei as the static radius puts limit on the extension of the disks well inside of the galaxies. Moreover, the agreement (up to one order) of the dimension of the static radius related to the mass parameter of central black holes at nuclei of large or extremely large galaxies with extension of such galaxies suggests that the relict cosmological constant could play an important role in formation and evolution of such galaxies. Of course, the first step in confirming such a suggestion is modelling of the influence of the repulsive cosmological constant on self-gravitating accretion disks. Some hints on this way could be given by recent results of Rezzolla et al. [Rezzolla et al., 2003], based on sophisticated numerical hydrodynamic methods developed by Font [Font and Daigne, 2002a, Font and Daigne, 2002b], who showed that mass outflow from the outer

edge of thick accretion disks, induced by the relict cosmological constant, could efficiently stabilise the accretion disks against the runaway dynamical instability.

## ACKNOWLEDGEMENTS

The present work was supported by the grants GAČR No. 205/03/1147, IGS SU No. 2/2003 (P.S.) and by Bergen Computational Physics Laboratory project, an EU Research Infrastructure at the University of Bergen, Norway, supported by the European Community Access to Research Infrastructure Action of the Improving Human Potential Programme. The authors would like to express their gratitude to Prof. L. P. Csernai for perfect hospitality at the University of Bergen. Z. S. and P. S. would like to acknowledge the excellent working conditions at the CERN's Theory Division and SISSA's Astrophysics Sector, respectively.

## REFERENCES

- [Abramowicz et al., 1978] Abramowicz, M. A., Jaroszyński, M., and Sikora, M. (1978). Relativistic accreting disks. *Astronomy and Astrophysics*, 63(1–2):221–224.
- [Abramowicz and Percival, 1997] Abramowicz, M. A. and Percival, M. J. (1997). *Classical Quantum Gravity*, 14:2003.
- [Abramowicz and Prasanna, 1990] Abramowicz, M. A. and Prasanna, A. R. (1990). Centrifugal force reversal near a Schwarzschild black-hole. *Monthly Notices Roy. Astronom. Soc.*, 245(4):720–728.
- [Bahcall et al., 1999] Bahcall, N., Ostriker, J. P., Perlmutter, S., and Steinhardt, P. J. (1999). The cosmic triangle: Revealing the state of the universe. *Science*, 284:1481–1488.
- [Bardeen, 1973] Bardeen, J. M. (1973). Timelike and null geodesics in the Kerr metric. In Witt, C. D. and Witt, B. S. D., editors, *Black Holes*, page 215, New York–London–Paris. Gordon and Breach.
- [Bardeen and Petterson, 1975] Bardeen, J. M. and Petterson, J. A. (1975). The Lense–Thirring effect and accretion disks around Kerr black holes. *Astrophys. J. Lett.*, 195:L65.
- [Bičák et al., 1993] Bičák, J., Semerák, O., and Hadrava, P. (1993). Collimation Effects of the Kerr Field. *Monthly Notices Roy. Astronom. Soc.*, 263(3):545–559.
- [Bičák et al., 1989] Bičák, J., Stuchlík, Z., and Balek, V. (1989). The motion of charged particles in the field of rotating charged black holes and naked singularities – I. The general features of the radial motion and the motion along the axis of symmetry. *Bull. Astronom. Inst. Czechoslovakia*, 40(2):65–92.
- [Blandford, 1987] Blandford, R. D. (1987). Astrophysical black holes. In Hawking, S. W. and Israel, W., editors, *Three hundred years of gravitation*, page 277, Cambridge. Cambridge University Press.
- [Blandford, 1990] Blandford, R. D. (1990). Physical processes in active galactic nuclei. In Courvoisier, T. and Mayor, M., editors, *Active Galactic Nuclei. Saas-Fee Advanced Course 20, Lectures Notes 1990*, page 161, Berlin. Swiss Society for Astrophysics and Astronomy, Springer-Verlag.
- [Brill and Hayward, 1994] Brill, D. R. and Hayward, S. A. (1994). Global structure of a black hole cosmos and its extremes. *Classical Quantum Gravity*, 11(2):359–370.

- [Calvani and Nobili, 1979] Calvani, M. and Nobili, L. (1979). Dressing up a Kerr naked singularity. *Nuovo Cimento B*, 51:247–261.
- [Carroll and Ostlie, 1996] Carroll, B. W. and Ostlie, D. A. (1996). *An Introduction to Modern Astrophysics*. Addison-Wesley, Reading, Massachusetts.
- [Carter, 1973] Carter, B. (1973). Black hole equilibrium states. In Witt, C. D. and Witt, B. S. D., editors, *Black Holes*, page 57, New York–London–Paris. Gordon and Breach.
- [Chandrasekhar, 1983] Chandrasekhar, S. (1983). *The Mathematical Theory of Black Holes*. Oxford University Press, Oxford.
- [Fishbone, 1977] Fishbone, L. G. (1977). *Astrophys. J.*, 205:323.
- [Fishbone and Moncrief, 1976] Fishbone, L. G. and Moncrief, V. (1976). *Astrophys. J.*, 207:962.
- [Font and Daigne, 2002a] Font, J. A. and Daigne, F. (2002a). *Monthly Notices Roy. Astronom. Soc.*, 334:383.
- [Font and Daigne, 2002b] Font, J. A. and Daigne, F. (2002b). *Astrophys. J. Lett.*, 581:L23–L26.
- [Hayward and Nakao, 1994] Hayward, S. A. and Nakao, K.-I. (1994). A cosmological constant limits the size of black holes. *Phys. Rev. D*, 49(10):5080–5085.
- [Hledík, 2002] Hledík, S. (2002). Optical geometry, inertial forces, and embedding diagrams. In Semerák, O., Podolský, J., and Žofka, M., editors, *Gravitation: Following the Prague Inspiration (A Volume in Celebration of the 60th Birthday of Jiří Bičák)*, pages 161–192, New Jersey, London, Singapore, Hong Kong. World Scientific.
- [Jaroszyński et al., 1980] Jaroszyński, M., Abramowicz, M. A., and Paczyński, B. (1980). *Acta Astronom.*, 30:1.
- [Kolb and Turner, 1990] Kolb, E. W. and Turner, M. S. (1990). *The Early Universe*. Addison-Wesley, Redwood City, California. The Advanced Book Program.
- [Kozłowski et al., 1978] Kozłowski, M., Jaroszyński, M., and Abramowicz, M. A. (1978). The analytic theory of fluid disks orbiting the Kerr black hole. *Astronomy and Astrophysics*, 63:209–220.
- [Krauss, 1998] Krauss, L. M. (1998). The end of the age problem, and the case for a cosmological constant revisited. *Astrophys. J.*, 501(2):461–466.
- [Lynden-Bell, 1969] Lynden-Bell, D. (1969). *Nature*, 223:690.
- [Novikov and Thorne, 1973] Novikov, I. D. and Thorne, K. S. (1973). Black hole astrophysics. In Witt, C. D. and Witt, B. S. D., editors, *Black Holes*, page 343, New York–London–Paris. Gordon and Breach.
- [Penrose, 1969] Penrose, R. (1969). Gravitational collapse: The role of general relativity. *Nuovo Cimento B*, 1(special number):252–276.
- [Rezzolla et al., 2003] Rezzolla, L., Zanotti, O., and Font, J. A. (2003). Dynamics of thick discs around Schwarzschild-de Sitter black holes. *Astronomy and Astrophysics*, 412:603.
- [Seguin, 1975] Seguin, F. H. (1975). *Astrophys. J.*, 197:745.
- [Slaný and Stuchlík, 2004] Slaný, P. and Stuchlík, Z. (2004). Relativistic thick disks in Kerr–de Sitter backgrounds. In preparation.
- [Stuchlík, 1980] Stuchlík, Z. (1980). Equatorial circular orbits and the motion of the shell of dust in the field of a rotating naked singularity. *Bull. Astronom. Inst. Czechoslovakia*, 31(3):129–144.

- [Stuchlík, 1981] Stuchlík, Z. (1981). Evolution of Kerr naked singularities. *Bull. Astronom. Inst. Czechoslovakia*, 32(2):68–72.
- [Stuchlík, 1983] Stuchlík, Z. (1983). The motion of test particles in black-hole backgrounds with non-zero cosmological constant. *Bull. Astronom. Inst. Czechoslovakia*, 34(3):129–149.
- [Stuchlík and Hledík, 1999] Stuchlík, Z. and Hledík, S. (1999). Some properties of the Schwarzschild–de Sitter and Schwarzschild–anti-de Sitter spacetimes. *Phys. Rev. D*, 60(4):044006 (15 pages).
- [Stuchlík and Hledík, 2000] Stuchlík, Z. and Hledík, S. (2000). Equatorial photon motion in the Kerr–Newman spacetimes with a non-zero cosmological constant. *Classical Quantum Gravity*, 17(21):4541–4576.
- [Stuchlík and Hledík, 2002] Stuchlík, Z. and Hledík, S. (2002). Properties of the Reissner–Nordström spacetimes with a nonzero cosmological constant. *Acta Phys. Slovaca*, 52(5):363–407.
- [Stuchlík et al., 2002] Stuchlík, Z., Pišková, K., and Hledík, S. (2002). Evolution of Kerr naked singularities due to accretion in counterrotating thin disks. *Perseus*, Volumes not numbered(4). <http://var.astro.cz/brno/perseus.html#archiv>.
- [Stuchlík and Slaný, 2004] Stuchlík, Z. and Slaný, P. (2004). Equatorial circular orbits in the Kerr–de Sitter spacetimes. *Phys. Rev. D*, 69:064001.
- [Stuchlík et al., 2000] Stuchlík, Z., Slaný, P., and Hledík, S. (2000). Equilibrium configurations of perfect fluid orbiting Schwarzschild–de Sitter black holes. *Astronomy and Astrophysics*, 363(2):425–439.



# Marginally stable thick discs with gradient inversion of orbital velocity measured in locally non-rotating frames

## A mechanism for excitation of oscillations in accretion discs?

Zdeněk Stuchlík, Petr Slaný and Gabriel Török

*Institute of Physics, Faculty of Philosophy and Science, Silesian University in Opava  
Bezučovo nám. 13, CZ-746 01 Opava, Czech Republic*

### ABSTRACT

[Aschenbach, 2004] has shown that in Kerr black-hole spacetimes with rotation parameter  $a > 0.9953$ , the Keplerian orbital velocity measured in locally non-rotating frames (LNRF) has a positive radial gradient in a small region in the vicinity of the event horizon and proposed that excitation of oscillations in Keplerian thin discs can be related to this fact. Similarly, we show that in the equatorial plane of marginally stable thick discs (with uniformly distributed specific angular momentum  $\ell(r, \theta) = \text{const}$ ) the orbital velocity relative to the LNRF has a positive radial gradient in the vicinity of black holes with  $a > 0.99979$ . The change of sign of the velocity gradient occurs just above the centre of the thick toroidal discs, in the region where stable circular geodesics of the Kerr spacetime are allowed. Therefore, the same mechanism as in the Keplerian discs could trigger oscillations in thick discs, but the rotational parameter of the Kerr spacetime must be much closer to the extreme-hole state with  $a = 1$ . The global character of the phenomenon is given in terms of topology changes of the von Zeipel surfaces (equivalent to equivelocity surfaces in the tori with  $\ell(r, \theta) = \text{const}$ ). Toroidal von Zeipel surfaces exist around the circle corresponding to the minimum of the equatorial LNRF velocity profile, indicating a possibility of development of some vertical instabilities in those parts of marginally stable tori with positive gradient of the LNRF velocity.

**Keywords:** accretion, accretion discs – QPOs – black hole physics – relativity

## 1 INTRODUCTION

High frequency (kHz) quasi-periodic oscillations (QPOs) with frequency ratios 3:2 (and sometimes 3:1) are observed in microquasars (see, e.g., [van der Klis, 2000, McClintock and Remillard, 2004]). The same frequency ratios of QPOs in mHz are observed in the Galactic Centre black hole Sgr A\* [Genzel et al., 2003, Aschenbach, 2004]. It is commonly accepted now that the QPOs are related to the parametric or forced resonance [Landau and

Lifshitz, 1973] of the radial and vertical epicyclic oscillations in accretion discs [Nowak and Lehr, 1998, Kluźniak and Abramowicz, 2000, Abramowicz and Kluźniak, 2000, Kluźniak and Abramowicz, 2001, Abramowicz and Kluźniak, 2003].

In the Kerr black-hole spacetimes, the frequencies of the radial and latitudinal (vertical) epicyclic oscillations around an equatorial Keplerian circular orbit at given  $r$  are given by the formulae (e.g., [Nowak and Lehr, 1998])

$$\omega_r^2 = \Omega_K^2(1 - 4ax^{-3/2} + 3a^2x^{-2}), \quad (1)$$

$$\omega_\theta^2 = \Omega_K^2(1 - 6x^{-1} + 8ax^{-3/2} - 3a^2x^{-2}), \quad (2)$$

where

$$\Omega_K = \left( \frac{GM}{r_g^3} \right)^{1/2} (x^{3/2} + a)^{-1} \quad (3)$$

is the Keplerian angular frequency of the Keplerian orbit;  $x \equiv r/r_g$ ,  $r_g \equiv GM/c^2$ ,  $a \equiv Jc/GM^2$  with  $M$ ,  $J$  being the mass and internal angular momentum of the black hole. Then  $x$  and  $a$  are dimensionless radius and black-hole rotational parameter.

The oscillations could be related to both the thin Keplerian discs [Abramowicz et al., 2003, Kato, 2001] or the thick, toroidal accretion discs [Rezzolla et al., 2003, Kluźniak et al., 2004]. The parametric resonance of the radial and vertical oscillations in the thin discs can explain the QPOs with the  $\omega_\theta/\omega_r = 3 : 2$  frequency ratio observed in all the microquasars and can put strong limits on the rotational parameter of their central black holes related to the limits on their mass [Török et al., 2004].

[Aschenbach, 2004] conjectured relation between the 3:2 and 3:1 resonance orbits by relating their Keplerian orbital velocities at  $r_{3:2}$  and  $r_{3:1}$  to be  $\Omega_K(r_{3:1}; a) = 3\Omega_K(r_{3:2}; a)$ , fixing thus the rotational parameter of black holes at the value of  $a = a_f = 0.99616$ . Further, he proposed that excitation of the oscillations at  $r = r_{3:1}$  can be related to two changes of sign of the radial gradient of the Keplerian orbital velocity as measured in the LNRF that occurs in vicinity of  $r = r_{3:1}$  for black holes with  $a > 0.9953$  (see Fig. 1).

While the assumption of frequency commensurability of Keplerian orbits at  $r_{3:1}$  and  $r_{3:2}$  seems to be rather artificial because distant parts of the Keplerian disc have to be related, we consider the positive radial gradient of orbital velocity in LNRF nearby the  $r_{3:1}$  orbit around black holes with  $a > 0.9953$  to be a physically very interesting phenomenon that could be related to a mechanism for triggering the excitation of radial and vertical epicyclic oscillations. (By an accident, the physical mechanism starts to work for values of  $a$  close to the number of  $a = a_f = 0.99616$  given by the assumption of commensurability of Keplerian orbits.) Therefore, we consider that it is important to investigate further the proposed mechanism based on the existence of a small region of radii where the gradient of locally defined orbital velocity is positive, as it could lead to *locally triggered instabilities* and disc oscillations<sup>1</sup>. Because the accretion-disc regime will vary from thin Keplerian disc to thick toroidal disc with variations of accretion flow, we shall study here, without addressing details of the mechanism, whether the orbital velocity in LNRF can have positive

<sup>1</sup> Of course, details of the proposed mechanism are not known at present and have to be carefully treated in future.

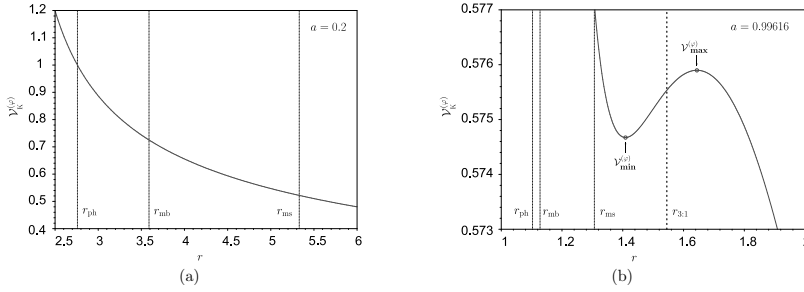


**Figure 1.** The Keplerian orbital velocity as measured in the LNRF, Eq. (29), for two illustrative cases. (a) For  $a < 0.9953$ , the curve is monotonic everywhere above the event horizon. (b) For  $a > 0.9953$ , two local extrema exist above the marginally stable orbit. Dashed line denotes the location of 3:1 resonance orbit. We choose the value of  $a$  in accordance with [Aschenbach, 2004]. Note that in this case  $\Delta V_K^{(\phi)} = V_{\max}^{(\phi)} - V_{\min}^{(\phi)} \approx 0.001$ . For values of  $a$  much closer to the extreme-hole state  $a = 1$ ,  $\Delta V_K^{(\phi)}$  is much higher reaching values of  $\sim 0.07$ .

gradient also for matter orbiting black holes in marginally stable thick discs with uniform distribution of the specific angular momentum ( $\ell(r, \theta) = \text{const}$ ), leading to a possibility to excite oscillations in the thick-disc accretion regime. Note that the assumption of uniform distribution of the specific angular momentum can be relevant at least at the inner parts of the thick disc and that matter in the disc follows nearly geodesic circular orbits nearby the centre of the disc and in the vicinity of its inner edge determined by the cusp of its critical equipotential surface, see [Abramowicz et al., 1978, Kozłowski et al., 1978].

Indeed, we will show that the positive gradients of the LNRF velocity exist for thick discs around black holes with rotational parameter  $a > a_{c(\text{thick})} \doteq 0.99979$  which is remarkably higher than the critical value of the rotational parameter  $a_{c(\text{thin})} \doteq 0.9953$  when the positive gradients occur in Keplerian discs. In thick tori, it is necessary to have information about the character of the phenomenon also outside the equatorial plane. We shall obtain such information by introducing the notion of von Zeipel radius  $\mathcal{R}$ , analogical to the radius of gyration  $\tilde{\rho}$  introduced for the case of Kerr spacetimes in the framework of optical geometry by [Abramowicz et al., 1995], generalising in one special way the definition used for static spacetimes [Abramowicz et al., 1993]. The von Zeipel radius is defined in such a way that for the marginally stable tori the von Zeipel surfaces, i.e., the surfaces of constant values of  $\mathcal{R}$ , coincide with surfaces of constant orbital velocity relative to the LNRF.

In Section 2, we summarise basic relations characterising marginally stable thick discs. In Section 3, the orbital velocity relative to the LNRF is given and its properties are determined. In Section 4, the notion of von Zeipel radius is introduced and properties of the von Zeipel surfaces are analysed. In Section 5, we present discussion and some concluding remarks.

## 2 TOROIDAL MARGINALLY STABLE ACCRETION DISCS

In general, stationary and axially symmetric spacetimes with the line element

$$ds^2 = g_{tt} dt^2 + 2g_{t\phi} dt d\phi + g_{\phi\phi} d\phi^2 + g_{rr} dr^2 + g_{\theta\theta} d\theta^2, \quad (4)$$

the stationary and axisymmetric toroidal discs with stress-energy tensors

$$T^{\mu\nu} = (\rho + p)U^\mu U^\nu + pg^{\mu\nu} \quad (5)$$

are characterised by 4-velocity field

$$U^\mu = (U^t, 0, 0, U^\phi) \quad (6)$$

with  $U^t = U^t(r, \theta)$ ,  $U^\phi = U^\phi(r, \theta)$ , and by the distribution of specific angular momentum

$$\ell = -\frac{U_\phi}{U_t}. \quad (7)$$

The angular velocity of orbiting matter,  $\Omega = U^\phi/U^t$ , is then related to  $\ell$  by the formula

$$\Omega = -\frac{\ell g_{tt} + g_{t\phi}}{\ell g_{t\phi} + g_{\phi\phi}}. \quad (8)$$

The marginally stable toroids are characterised by the uniform distribution of specific angular momentum

$$\ell = \ell(r, \theta) = \text{const} \quad (9)$$

and they are fully determined by the spacetime structure through equipotential surfaces of the potential  $W = W(r, \theta)$  defined by the relation [Abramowicz et al., 1978]

$$W - W_{\text{in}} = \ln \frac{U_t}{(U_t)_{\text{in}}} \quad (10)$$

with

$$(U_t)^2 = \frac{g_{t\phi}^2 - g_{tt}g_{\phi\phi}}{g_{tt}\ell^2 + 2g_{t\phi}\ell + g_{\phi\phi}}; \quad (11)$$

the subscript “in” refers to the inner edge of the disc.

In the Kerr spacetimes with the rotational parameter assumed to be  $a > 0$ , the relevant metric coefficients in the standard Boyer–Lindquist coordinates read:

$$g_{tt} = -\frac{\Delta - a^2 \sin^2 \theta}{\Sigma}, \quad (12)$$

$$g_{t\phi} = -\frac{2ar \sin^2 \theta}{\Sigma}, \quad (13)$$

$$g_{\phi\phi} = \frac{A \sin^2 \theta}{\Sigma}, \quad (14)$$

where

$$\Delta = r^2 - 2r + a^2, \quad (15)$$

$$\Sigma = r^2 + a^2 \cos^2 \theta, \quad (16)$$

$$A = (r^2 + a^2)^2 - \Delta a^2 \sin^2 \theta. \quad (17)$$

The geometrical units,  $c = G = 1$ , together with putting the mass of the black hole equal to one,  $M = 1$ , are used to obtain completely dimensionless formulae hereafter. The relation (8) for the angular velocity of matter orbiting the black hole acquires the form

$$\Omega = \Omega(r, \theta; a, \ell) = \frac{(\Delta - a^2 \sin^2 \theta)\ell + 2ar \sin^2 \theta}{(A - 2\ell ar) \sin^2 \theta} \quad (18)$$

and the potential  $W$ , defined in Eq. (10), has the explicit form

$$W = W(r, \theta; a, \ell) = \frac{1}{2} \ln \frac{\Sigma \Delta \sin^2 \theta}{(r^2 + a^2 - a\ell)^2 \sin^2 \theta - \Delta(\ell - a \sin^2 \theta)^2}. \quad (19)$$

### 3 THE ORBITAL VELOCITY IN LNRF

The locally non-rotating frames are given by the tetrad of 1-forms (see, e.g., [Bardeen et al., 1972, Misner et al., 1973])

$$\mathbf{e}^{(t)} = \left( \frac{\Sigma \Delta}{A} \right)^{1/2} \mathbf{d}t, \quad (20)$$

$$\mathbf{e}^{(r)} = \left( \frac{\Sigma}{\Delta} \right)^{1/2} \mathbf{d}r, \quad (21)$$

$$\mathbf{e}^{(\theta)} = \Sigma^{1/2} \mathbf{d}\theta, \quad (22)$$

$$\mathbf{e}^{(\phi)} = \left( \frac{A}{\Sigma} \right)^{1/2} \sin \theta (\mathbf{d}\phi - \omega \mathbf{d}t) \quad (23)$$

where the angular velocity of LNRF,  $\omega = -g_{t\phi}/g_{\phi\phi}$ , is given by the relation

$$\omega = \frac{2ar}{A}. \quad (24)$$

The azimuthal component of 3-velocity in LNRF reads

$$\mathcal{V}_{\text{LNRF}}^{(\phi)} = \frac{U^\mu \mathbf{e}_\mu^{(\phi)}}{U^\nu \mathbf{e}_\nu^{(t)}} = \frac{A \sin \theta}{\Sigma \sqrt{\Delta}} (\Omega - \omega). \quad (25)$$

Substituting for the angular velocities  $\Omega$  and  $\omega$  from the relations (18) and (24), respectively, we arrive at the formula

$$\mathcal{V}_{\text{LNRF}}^{(\phi)} = \frac{A(\Delta - a^2 \sin^2 \theta) + 4a^2 r^2 \sin^2 \theta}{\Sigma \sqrt{\Delta} (A - 2a\ell r) \sin \theta} \ell. \quad (26)$$

We focus our investigation to the motion in the equatorial plane,  $\theta = \pi/2$ , where (26) reduces to

$$\mathcal{V}^{(\phi)}(r, \theta = \pi/2; a, \ell) = \frac{r \sqrt{\Delta}}{r(r^2 + a^2) - 2a(\ell - a)} \ell. \quad (27)$$

Formally, this velocity vanishes for  $r \rightarrow \infty$  and  $r \rightarrow r_+ = 1 + \sqrt{1 - a^2}$ , where the event horizon is located, i.e., there must be a change of its radial gradient for any case of values of the parameters  $a$  and  $\ell$ , contrary to the case of Keplerian orbits where the azimuthal component of the 3-velocity in LNRF, after substituting of the angular velocity formula [Bardeen et al., 1972]

$$\Omega = \Omega_{\text{K}}(r; a) = \frac{1}{(r^{3/2} + a)} \quad (28)$$

into Eq. (25), and restricting on the equatorial plane,  $\theta = \pi/2$ , reads

$$\mathcal{V}_K^{(\phi)}(r; a) = \frac{(r^2 + a^2)^2 - a^2 \Delta - 2ar(r^{3/2} + a)}{r^2(r^{3/2} + a)\sqrt{\Delta}} \tag{29}$$

that formally diverges at  $r = r_+$ . The profile of Keplerian specific angular momentum in the thin discs is given by

$$\ell_K(r; a) = \frac{r^2 - 2ar^{1/2} + a^2}{r^{3/2} - 2r^{1/2} + a}. \tag{30}$$

This function is very important in the theory of thick discs too, as it determines both the inner edge of the disc on its part with negative radial gradient (corresponding to unstable circular geodesics), and the centre of the disc on its part with positive radial gradient (corresponding to stable circular geodesics). The minimum of  $\ell_K(r; a)$  corresponds to the marginally stable circular geodesic.

Of course, for both thick tori and Keplerian discs we must consider the limit on the disc extension given by the innermost stable orbit. For Keplerian discs this is the marginally stable geodesical orbit, while for the thick tori this is an unstable circular geodesic kept stable by pressure gradients and located between the marginally bound and the marginally stable geodesical orbits, with the radius being determined by the specific angular momentum  $\ell = \text{const} \in (l_{\text{ms}}, l_{\text{mb}})$  through the equation  $\ell = \ell_K(r; a)$ ;  $\ell_{\text{ms}}$  ( $\ell_{\text{mb}}$ ) denotes specific angular momentum of the circular marginally stable (marginally bound) geodesic.

The radial gradient of the equatorial orbital velocity of thick discs reads

$$\frac{\partial \mathcal{V}^{(\phi)}}{\partial r} = \frac{[\Delta + (r - 1)r][r(r^2 + a^2) - 2a(\ell - a)] - r(3r^2 + a^2)\Delta}{[r(r^2 + a^2) - 2a(\ell - a)]^2 \sqrt{\Delta}} \ell, \tag{31}$$

so that it changes its orientation at radii determined for a given  $\ell \in (l_{\text{ms}}, l_{\text{mb}})$  by the condition

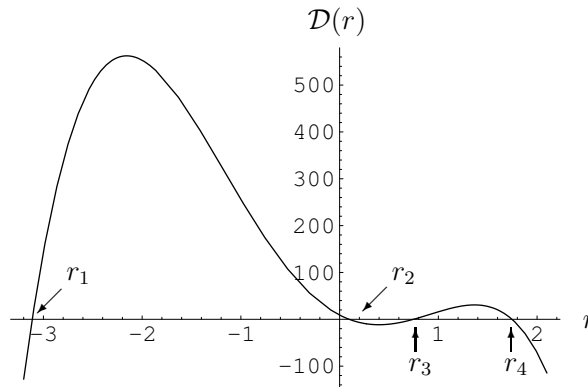


**Figure 2.** Reality condition for the existence of local extrema of the function  $\ell_{\text{ex}}(r; a)$ . The extrema are allowed, if  $\mathcal{D}(r) > 0$ . Clearly, the physically relevant extrema, located above the outer horizon, can exist in the interval  $r \in (1, r_4)$ .

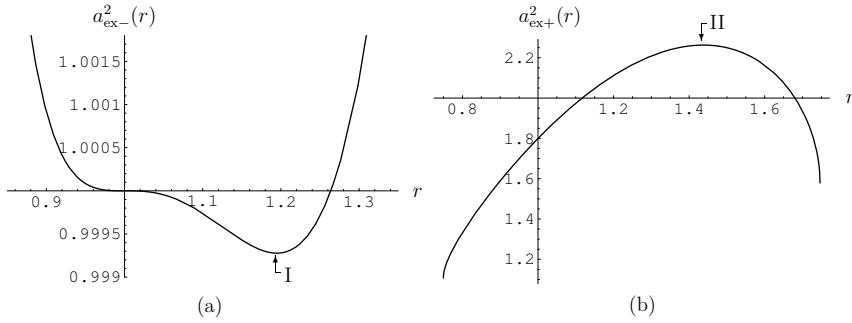


**Figure 3.** Loci of local extrema of the function  $\ell_{\text{ex}}(r; a)$ . They are determined by the functions  $a_{\text{ex}\pm}^2(r)$ . (a) The function  $a_{\text{ex}-}^2(r)$  is relevant for both black holes and naked singularities; its local minimum is denoted I. (b) The function  $a_{\text{ex}+}^2(r)$  is relevant for naked singularities only; its local maximum is denoted II.

$$\ell = \ell_{\text{ex}}(r; a) \equiv a + \frac{r^2[(r^2 + a^2)(r - 1) - 2r\Delta]}{2a[\Delta + r(r - 1)]}. \quad (32)$$

We have to discuss properties of  $\ell_{\text{ex}}(r; a)$  above the event horizon  $r_+$  taking into account the limits on the inner boundary of the tori. The local extrema of  $\ell_{\text{ex}}(r; a)$  are given by the relation

$$a^2 = a_{\text{ex}\pm}^2(r) \equiv r \frac{3 + 18r - 7r^2 \pm \sqrt{\mathcal{D}(r)}}{2(3r + 2)}, \quad (33)$$

with

$$\mathcal{D}(r) = 9 - 108r + 150r^2 - 12r^3 - 23r^4 = -23(r - r_1)(r - r_2)(r - r_3)(r - r_4), \quad (34)$$

where

$$r_1 \doteq -3.11363, \quad r_2 \doteq 0.09602, \quad r_3 \doteq 0.74939, \quad r_4 \doteq 1.74648. \quad (35)$$

The situation is illustrated in Fig. 2 which implies that only the interval  $r \in (r_3, r_4)$  is relevant for the region outside of the black-hole event horizon. Behaviour of the functions  $a_{\text{ex}\pm}^2(r)$  is given in Fig. 3. Clearly, only  $a_{\text{ex}-}^2(r)$  is relevant for black holes. The minimum of  $a_{\text{ex}-}^2(r)$ , denoted I, is located at radius  $r_{\text{min}} \doteq 1.19466$  and the critical value of the rotational parameter is

$$a_{\text{c(bh)}} \doteq \sqrt{0.99928} \doteq 0.99964. \quad (36)$$

Note that both the functions  $a_{\text{ex}\pm}^2(r)$  are relevant for Kerr naked singularities. The maximum of  $a_{\text{ex}+}^2(r)$ , denoted II, is located at radius  $r_{\text{max}} \doteq 1.43787$  and the critical value of the rotational parameter is

$$a_{\text{c(ns)}} \doteq \sqrt{2.26289} \doteq 1.50429. \quad (37)$$

Therefore, the possibility to have three changes of the sign of  $\partial \mathcal{V}^{(\phi)} / \partial r$  in marginally stable thick discs is limited from below for black holes, and from above for naked singularities. Here we restrict our attention to the Kerr black holes.

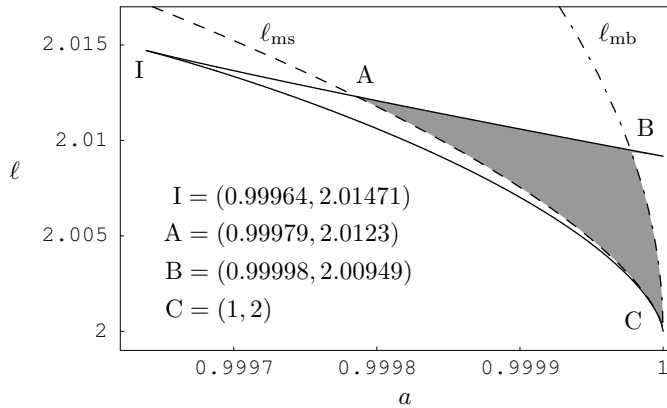


**Figure 4.** Kerr spacetimes with the change of sign of the gradient of LNRF velocity. In the  $\ell$ – $a$  plane, the functions  $\ell_{\text{ex(max)}}(a)$  (upper solid curve),  $\ell_{\text{ex(min)}}(a)$  (lower solid curve),  $\ell_{\text{ms}}(a)$  (dashed curve) and  $\ell_{\text{mb}}(a)$  (dashed-dotted curve) are given. For pairs of  $(a, \ell)$  from the shaded region, the gradient of the orbital velocity changes its sign twice inside the marginally stable tori. Between the points A, B, the  $\ell_{\text{ex(max)}}(a)$  curve determines an inflex point of  $\mathcal{V}^{(\phi)}(r; a, \ell)$ . The inflex points determined by the curve  $\ell_{\text{ex(min)}}(a)$  are irrelevant being outside of the definition region for marginally stable toroids,  $\ell \in (\ell_{\text{ms}}(a), \ell_{\text{mb}}(a))$ . The point I corresponds to the inflex point of  $\ell_{\text{ex}}(r; a)$ ; cf. Fig. 3a.

Now, we have to compare the local extrema of the function  $\ell_{\text{ex}}(r; a)$ , determined by the condition (33), with the functions characterising the marginally stable,  $\ell_{\text{ms}}(a)$ , and the marginally bound,  $\ell_{\text{mb}}(a)$ , circular geodesics as these determine the limits of allowance of accreting toroidal structures in the Kerr spacetimes [Abramowicz et al., 1978]. For each given value of  $a$ , location of both the marginally stable and marginally bound circular geodesics is uniquely given by the functions  $r_{\text{ms}} = r_{\text{ms}}(a)$ ,  $r_{\text{mb}} = r_{\text{mb}}(a)$  (see, e.g., [Bardeen et al., 1972]), and  $\ell_{\text{ms}}(a)$ ,  $\ell_{\text{mb}}(a)$  can then be determined using the formulae for  $\ell_{\text{K}}(r; a)$  and  $r_{\text{ms}}(a)$ ,  $r_{\text{mb}}(a)$ , respectively. In Fig. 4, behaviour of the local extrema  $\ell_{\text{ex(min)}}(a)$ ,  $\ell_{\text{ex(max)}}(a)$  and the functions  $\ell_{\text{ms}}(a)$ ,  $\ell_{\text{mb}}(a)$  is illustrated. It is clear immediately that the sign's change of  $\partial\mathcal{V}^{(\phi)}/\partial r$  is relevant only for thick discs orbiting the Kerr black holes with the rotational parameter

$$a > a_{\text{c(thick)}} \doteq 0.99979, \quad (38)$$

which is much higher than the critical value  $a_{\text{c(thin)}} \doteq 0.9953$  determined by Aschenbach for thin Keplerian discs [Aschenbach, 2004]. For  $a > a_{\text{c(thick)}}$  the relevance of  $\ell_{\text{ex}}(r; a)$  is limited from below by  $\ell_{\text{ms}}(a)$ . There is another critical value of the rotational parameter,  $a = a_{\text{c(mb)}} \doteq 0.99998$ , where  $\ell_{\text{mb}}(a) = \ell_{\text{ex(max)}}(a)$ ; for  $a > a_{\text{c(mb)}}$  the relevance of  $\ell_{\text{ex}}(r; a)$  is limited from above by  $\ell_{\text{mb}}(a)$ .

The character of the region, where  $\partial\mathcal{V}^{(\phi)}/\partial r$  changes sign, can be properly illustrated by considering the functions  $\ell_{\text{ex}}(r; a)$  and  $\ell_{\text{K}}(r; a)$  simultaneously. First, we show that there is no common point of those functions in black-hole spacetimes with  $a < 1$ . Indeed, the condition  $\ell_{\text{ex}}(r; a) = \ell_{\text{K}}(r; a)$  implies an equation quartic in  $a$ , which has four solutions

$$a = a_1(r) \equiv r\sqrt{r}, \quad a = a_2(r) \equiv -\sqrt{r(2-r)},$$

$$a = a_h(r) \equiv \sqrt{r(2-r)}, \quad a = a_{\text{ph}+}(r) \equiv \frac{\sqrt{r}}{2}(3-r). \quad (39)$$

The solution  $a_1(r) > 1$  at  $r > 1$ , i.e., it corresponds to naked singularities at  $r > 1$ , the solution  $a_2(r)$  is negative everywhere, the solution  $a_3 = a_h(r)$  determines radius of the event horizon, while the solution  $a_4 = a_{\text{ph}+}(r)$  determines the radius of the corotating photon circular geodesic. None of the solutions is relevant for the accretion discs. We can conclude that above the photon circular orbit there is always  $\ell_K(r; a) > \ell_{\text{ex}}(r; a)$ ; therefore, the innermost local maximum of  $\mathcal{V}^{(\phi)}(r; a)$  for  $a > a_{\text{c}(\text{bh})}$ , and the only local maximum of  $\mathcal{V}^{(\phi)}(r; a)$  for  $a < a_{\text{c}(\text{bh})}$ , is always physically irrelevant in marginally stable thick tori.

For black-hole spacetimes, behaviour of the functions  $\ell_{\text{ex}}(r; a)$  and  $\ell_K(r; a)$  can then be classified into six classes which are illustrated in Fig. 5:

- (i)  $0 < a < a_{\text{c}(\text{bh})}$ : No extrema of  $\ell_{\text{ex}}(r; a)$  (Fig. 5a).
- (ii)  $a = a_{\text{c}(\text{bh})}$ : An inflex point of  $\ell_{\text{ex}}(r; a)$  (Fig. 5b).
- (iii)  $a_{\text{c}(\text{bh})} < a < a_{\text{c}(\text{thick})}$ : Two local extrema of  $\ell_{\text{ex}}(r; a)$  present, but out of the region allowing the existence of thick discs (Fig. 5c).
- (iv)  $a_{\text{c}(\text{thick})} < a < a_{\text{c}(\text{mb})}$ : Two local extrema of  $\ell_{\text{ex}}(r; a)$  allowed in the region of  $\ell \in (\ell_{\text{ms}}, \ell_{\text{ex}(\text{max})})$  (Fig. 5d).
- (v)  $a_{\text{c}(\text{mb})} < a < 1$ : Two local extrema of  $\ell_{\text{ex}}(r; a)$  allowed in the region  $\ell \in (\ell_{\text{ms}}, \ell_{\text{mb}})$  (Fig. 5e).
- (vi)  $a = 1$ : The minimum of  $\ell_{\text{ex}}(r; a)$  coincides with the marginally bound geodesic with  $\ell_{\text{mb}} = 2$  at  $r_{\text{mb}} = 1$ . The curves  $\ell_{\text{ex}}(r; a = 1)$  and  $\ell_K(r; a = 1)$  intersect at  $r = 1$  (Fig. 5f).

Clearly, two changes of sign of  $\partial \mathcal{V}^{(\phi)} / \partial r$  can occur for Kerr black holes with the rotational parameter  $a > a_{\text{c}(\text{thick})} \doteq 0.99979$ . The interval of relevant values of the specific angular momentum  $\ell \in (\ell_{\text{ms}}(a), \ell_{\text{ex}(\text{max})}(a))$  grows with  $a$  growing up to the critical value of  $a_{\text{c}(\text{mb})} \doteq 0.99998$ . For  $a > a_{\text{c}(\text{mb})}$ , the interval of relevant values of  $\ell \in (\ell_{\text{ms}}(a), \ell_{\text{mb}}(a))$  is narrowing with growing of the rotational parameter up to  $a = 1$ , which corresponds to a singular case where  $\ell_{\text{ms}}(a = 1) = \ell_{\text{mb}}(a = 1) = 2$ . Notice that the situation becomes to be singular only in terms of the specific angular momentum; it is shown (see [Bardeen et al., 1972]) that for  $a = 1$  both the total energy  $E$  and the axial angular momentum  $L$  differ at  $r_{\text{ms}}$  and  $r_{\text{mb}}$ , respectively, but their combination,  $\ell \equiv L/E$ , giving the specific angular momentum, coincides at these radii.

#### 4 VON ZEIPEL SURFACES

It is useful to obtain global characteristics of the phenomenon that is shown to be manifested in the equatorial plane as the existence of a small region with positive gradient of the LNRF velocity.

It is well known that rotational properties of perfect fluid equilibrium configurations in strong gravity are well represented by the radius of gyration  $\tilde{\rho}$ , introduced in the case of spherically symmetric Schwarzschild spacetimes by [Abramowicz et al., 1993], as the direction of increase of  $\tilde{\rho}$  defines a local outward direction of the dynamical effects of rotation of the fluid.

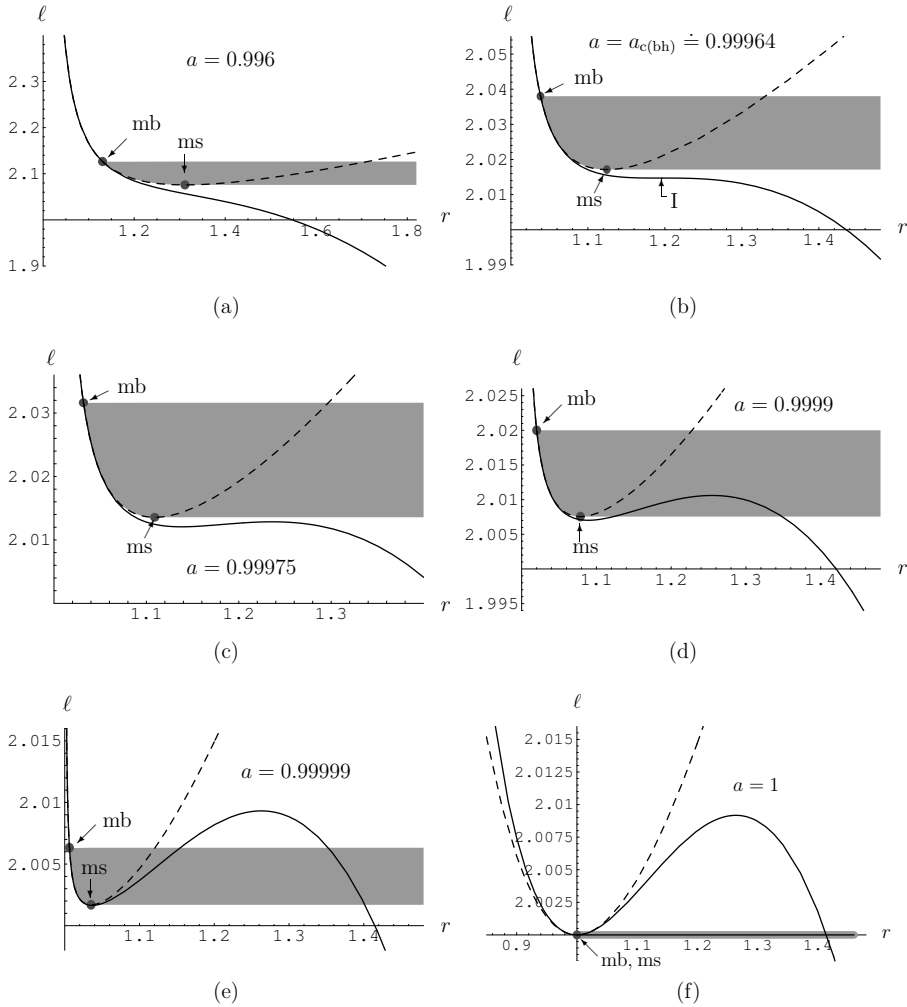


**Figure 5.** Classification of the Kerr black-hole spacetimes according to the properties of the functions  $\ell_{\text{ex}}(r; a)$  (solid curves) and  $\ell_{\text{K}}(r; a)$  (dashed curves). The functions are plotted for six cases corresponding to the classification. The marginally stable tori can exist in the shaded region only along  $\ell = \text{const}$  lines. Their inner edge (centre) is determined by the decreasing (increasing) part of  $\ell_{\text{K}}(r; a)$ . The local extrema of the orbital velocity relative to LNRF relevant for thick discs are given by the intersections of  $\ell = \text{const}$  line with the curve of  $\ell_{\text{ex}}(r; a)$  in the shaded region. Notice that the region corresponding to the allowed values of  $\ell$  for the discs is narrowing with  $a \rightarrow 1$ , it is degenerated into the  $\ell = 2$  line for  $a = 1$  as  $\ell_{\text{ms}} = \ell_{\text{mb}} = 2$  in this case. In the case (e), the gradient  $\partial \mathcal{V}^{(\phi)} / \partial r$  changes sign for all values of  $\ell \in (\ell_{\text{ms}}, \ell_{\text{mb}})$  allowed for the tori, while in the case (d), it is allowed for a region restricted from above by the value  $\ell_{\text{ex}(\text{max})}(a)$ . In the cases (a)–(c), the change of sign of  $\partial \mathcal{V}^{(\phi)} / \partial r$  cannot occur in the disc. It is directly seen from cases (d)–(f) that the gradient  $\partial \mathcal{V}^{(\phi)} / \partial r$  changes the sign closely above the centre of the disc.

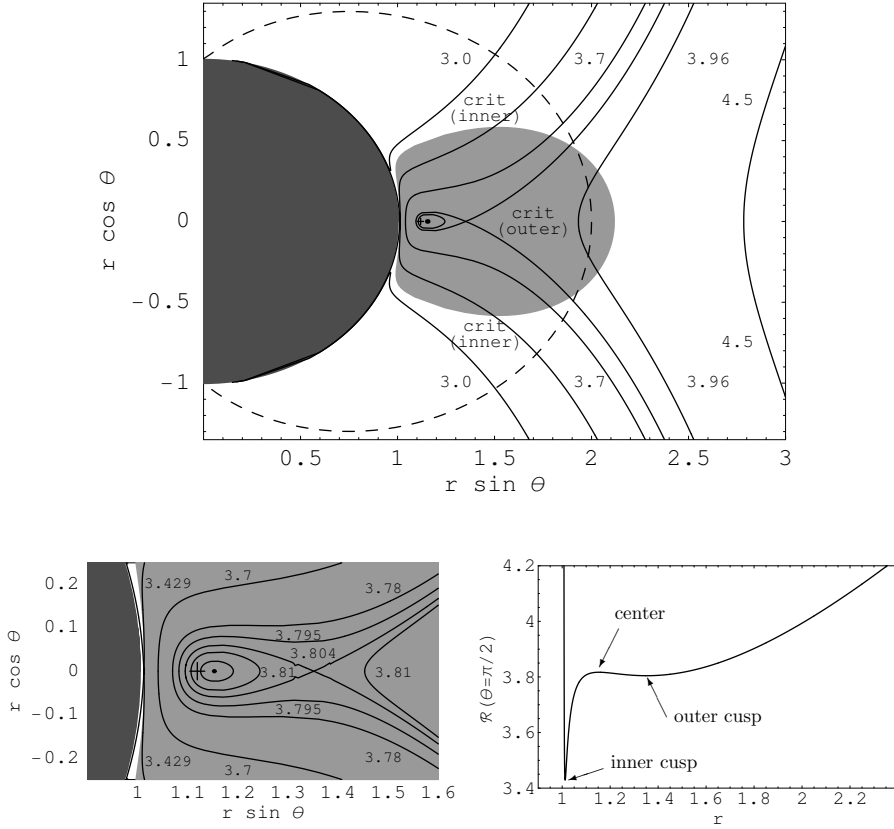


**Figure 6.** Von Zeipel surfaces (meridional sections). For  $a < a_{c(\text{bh})}$  and any  $\ell$ , only one surface with a cusp in the equatorial plane and no closed (toroidal) surfaces exist. The cusp is, however, located outside the toroidal equilibrium configurations of perfect fluid. For  $a > a_{c(\text{bh})}$  and  $\ell$  appropriately chosen, two surfaces with a cusp, or one surface with both the cusps, together with closed (toroidal) surfaces, exist located always inside the ergosphere (dashed surface) of a given spacetime. Moreover, if  $a > a_{c(\text{thick})}$ , both the outer cusp and the central ring of closed surfaces are located inside the toroidal equilibrium configurations corresponding to marginally stable thick discs (light-gray region; its shape is determined by the critical self-crossing *equipotential surface* of the potential  $W$  given by (19)). The cross (+) denotes the centre of the torus. Dark region corresponds to the black hole. Figures illustrating all possible configurations of the von Zeipel surfaces are presented in [Stuchlík et al., 2004]. Here we present the figure plotted for the parameters  $a = 0.99998$ ,  $\ell = 2.0065$ . Critical value of the von Zeipel radius corresponding to the inner and the outer self-crossing surface is  $\mathcal{R}_{c(\text{in})} \doteq 3.429$  and  $\mathcal{R}_{c(\text{out})} \doteq 3.804$ , respectively, the central ring of toroidal surfaces corresponds to the value  $\mathcal{R}_{\text{center}} \doteq 3.817$ . Interesting region containing both the cusps and the toroidal surfaces is plotted in detail at the left lower figure. Right lower figure shows the behaviour of the von Zeipel radius in the equatorial plane. The resonance between the radial and vertical epicyclic oscillations is possible in the region where stable circular geodesics are allowed – right to the centre of the disc.

A physically reasonable way of defining a global quantity characterising rotating fluid configurations in terms of the LNRF orbital velocity is to introduce, so-called, von Zeipel radius defined by the relation

$$\mathcal{R} \equiv \frac{\ell}{\mathcal{V}_{\text{LNRF}}^{(\phi)}} \quad (40)$$

which generalises the Schwarzschildian definition of gyration radius. For more details see [Stuchlík et al., 2004], where full discussion of the properties of the von Zeipel surfaces is presented and illustrated.

In the case of marginally stable tori with  $\ell(r, \theta) = \text{const}$ , the von Zeipel surfaces, i.e., the surfaces of  $\mathcal{R}(r, \theta; a, \ell) = \text{const}$ , coincide with the constant velocity surfaces  $\mathcal{V}_{\text{LNRF}}^{(\phi)}(r, \theta; a, \ell) = \text{const}$ . For the tori in the Kerr spacetimes, there is

$$\mathcal{R}(r, \theta; a, \ell) = \frac{\Sigma \sqrt{\Delta} (A - 2alr) \sin \theta}{A(\Delta - a^2 \sin^2 \theta) + 4a^2 r^2 \sin^2 \theta}. \quad (41)$$

Topology of the von Zeipel surfaces can be directly determined by the behaviour of the von Zeipel radius (41) in the equatorial plane

$$\mathcal{R}(r, \theta = \pi/2; a, \ell) = \frac{r(r^2 + a^2) - 2a(\ell - a)}{r\sqrt{\Delta}}. \quad (42)$$

The local minima of the function (42) determine loci of the cusps of the von Zeipel surfaces, while its local maximum (if it exists) determines a circle around which closed toroidally shaped von Zeipel surfaces are concentrated (see Fig. 6). Notice that the minima (maximum) of  $\mathcal{R}(r, \theta = \pi/2; a, \ell)$  correspond(s) to the maxima (minimum) of  $\mathcal{V}_{\text{LNRF}}^{(\phi)}(r, \theta = \pi/2; a, \ell)$ , therefore, the inner cusp is always physically irrelevant being located outside of the toroidal configuration of perfect fluid, cf. Fig. 5. Behaviour of the von Zeipel surfaces nearby the centre and the inner edge of the thick tori orbiting Kerr black holes with  $a > a_{\text{c(thick)}} \doteq 0.99979$ , i.e., the existence of the von Zeipel surface with an outer cusp or the surfaces with toroidal topology, suggests possibility of strong instabilities in both the vertical and radial direction and a tendency for development of some vortices crossing the equatorial plane. We plan studies of these expected phenomena in future.

## 5 DISCUSSION AND CONCLUSIONS

It is useful to discuss both the qualitative and quantitative aspects of the phenomenon of the positive gradient of the LNRF orbital velocity. In the Kerr spacetimes with  $a > a_{\text{c(thick)}}$ , changes of sign of the gradient of  $\mathcal{V}^{(\phi)}(r; a)$  must occur closely above the centre of relevant toroidal discs, at radii corresponding to stable circular geodesics of the spacetime, where the radial and vertical epicyclic frequencies are well defined<sup>2</sup> (cf. Fig. 5).

<sup>2</sup> It is a question, to which an extent the notion of the epicyclic frequencies, basically related to Keplerian, geodetical circular orbits, and usually considered in the framework of Keplerian, thin discs, can be used for marginally stable toroidal discs. Nevertheless, we expect that the epicyclic frequencies could be, to some extent, relevant at least for marginally stable tori having  $\ell \gtrsim \ell_{\text{ms}}$ , with their structure being close to the one of Keplerian discs.

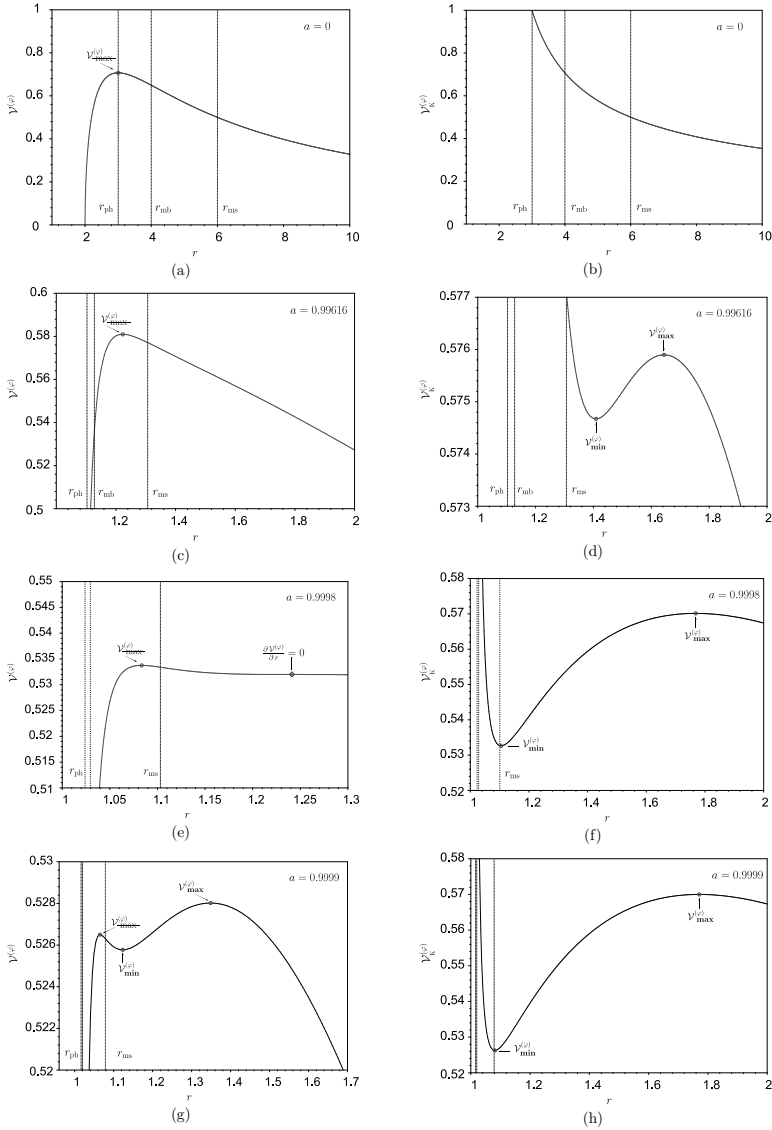


**Figure 7.** Profiles of the equatorial orbital velocity of marginally stable tori in LNRF in terms of the radial Boyer–Lindquist coordinate. The profiles are given for typical values of  $a$  corresponding to the classification of the Kerr black-hole spacetimes. For comparison, the profiles are given for the orbital velocity of Keplerian discs in Kerr spacetimes with the same rotational parameter  $a$ . For thick discs, values of  $\ell = \text{const}$  are appropriately chosen; commonly,  $\ell = \ell_{\text{ms}}$  is used giving the maximal value of the velocity difference in between the local extrema, and representing the limiting case of marginally stable thick discs.

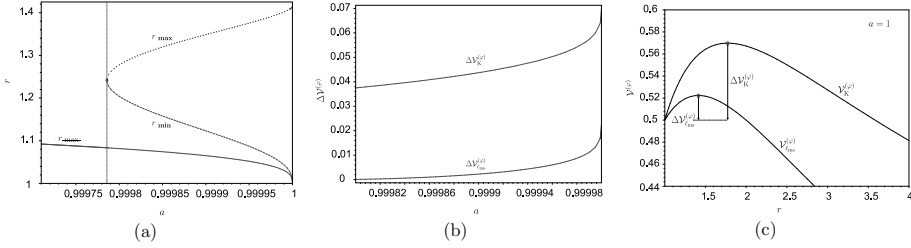


**Figure 8.** (a) Positions of local extrema of  $\mathcal{V}_{\text{LNRF}}^{(\phi)}$  (in B-L coordinates) for the marginally stable discs with  $\ell = \ell_{\text{ms}}$  in dependence on the rotational parameter  $a$  of the black hole. (b) Velocity difference  $\Delta\mathcal{V}^{(\phi)} = \mathcal{V}_{\text{max}}^{(\phi)} - \mathcal{V}_{\text{min}}^{(\phi)}$  as a function of the rotational parameter  $a$  of the black hole for both the thin (Keplerian) disc and the marginally stable (non-Keplerian) disc with  $\ell = \ell_{\text{ms}}$ . (c) Orbital-velocity curves in the limiting case of the extreme black hole. At  $r = 1$ , the Keplerian orbital velocity  $\mathcal{V}_{\text{K}}^{(\phi)}$  has a local minimum, whereas the orbital velocity  $\mathcal{V}_{\ell_{\text{ms}}}^{(\phi)}$  of the marginally stable disc has an inflex point. In both cases, the velocity difference  $\Delta\mathcal{V}^{(\phi)}$  reaches its maximal values:  $\Delta\mathcal{V}_{\text{K}}^{(\phi)} \doteq 0.06986$ ,  $\Delta\mathcal{V}_{\ell_{\text{ms}}}^{(\phi)} \doteq 0.02241$ .

For  $a = a_{\text{c(bh)}}$ , an inflex point of  $\mathcal{V}^{(\phi)}(r; a_{\text{c(bh)}})$  occurs at  $r_{\text{min}} \doteq 1.19466$  for the disc with  $\ell \doteq 2.01471$ . With rotational parameter growing ( $a > a_{\text{c(bh)}}$ ), the local maximum of  $\mathcal{V}^{(\phi)}(r; a, \ell)$  is successively shifted up to values of  $r \sim 1.4$ , while the local minimum of  $\mathcal{V}^{(\phi)}(r; a, \ell)$  is shifted down to  $r = 1$  in the limit of  $a = 1$ . Of course, the local extrema of  $\mathcal{V}^{(\phi)}(r; a, \ell)$  become to be relevant till for the rotational parameter  $a > a_{\text{c(thick)}}$ , when the specific angular momentum,  $\ell = \text{const}$ , enters the interval corresponding to the marginally stable tori,  $\ell \in (\ell_{\text{ms}}, \ell_{\text{mb}})$ . The loci of these extreme points can be directly inferred from Fig. 5, where the regions corresponding to marginally stable tori are shaded.

For all the relevant cases of the classification of Kerr spacetimes given in the previous section, behaviour of  $\mathcal{V}^{(\phi)}(r; a, \ell)$  is illustrated in Fig. 7, which enables us to make some conclusions on the quantitative properties of the orbital velocity and its gradient. For comparison, profiles of the Keplerian velocity  $\mathcal{V}_{\text{K}}^{(\phi)}(r; a)$  are included. With  $a$  growing in the region of  $a \in (a_{\text{c(thick)}}, 1)$ , the difference  $\Delta\mathcal{V}^{(\phi)} \equiv \mathcal{V}_{\text{max}}^{(\phi)} - \mathcal{V}_{\text{min}}^{(\phi)}$  grows as well as the difference of radii,  $\Delta r \equiv r_{\text{max}} - r_{\text{min}}$ , where the local extrema of  $\mathcal{V}^{(\phi)}(r; a, \ell)$  occur, see Figs 8a, b. Recall that the innermost local maximum of  $\mathcal{V}^{(\phi)}(r; a, \ell)$  must be located, necessarily, under the disc structure. The value of  $\mathcal{V}^{(\phi)}(r = r_{\text{in}}; a, \ell)$  at the inner edge of the toroid (where  $\ell = \ell_{\text{K}}(r; a)$ ) is located closer and closer to the local minimum of  $\mathcal{V}^{(\phi)}(r; a, \ell)$  when  $a \rightarrow 1$ . For  $a = 1$ , there is an inflex point of  $\mathcal{V}^{(\phi)}(r; a = 1, \ell)$  at  $r = 1$  where the local minimum and the “forbidden” local maximum of  $\mathcal{V}^{(\phi)}(r; a, \ell)$  for  $\ell = 2$  coincide, Fig. 8c.

We can conclude that the changes of sign of gradient of the LNRF orbital velocity of marginally stable thick discs occur for discs orbiting Kerr black holes with the rotational parameter  $a > a_{\text{c(thick)}} \doteq 0.99979$ . In terms of the redefined rotational parameter,  $1 - a$ , its value of  $1 - a_{\text{c(thick)}} \doteq 2.1 \times 10^{-4}$  is more than one order lower than the value  $1 - a_{\text{c(thin)}} \doteq 4.7 \times 10^{-3}$  found by Aschenbach for the changes of sign of the gradient of orbital velocity in Keplerian, thin discs. Moreover, the velocity difference,  $\Delta\mathcal{V}^{(\phi)} = \mathcal{V}_{\text{max}}^{(\phi)} - \mathcal{V}_{\text{min}}^{(\phi)}$ , is smaller but comparable in the thick discs in comparison with thin discs (see Fig. 8b). In fact, we

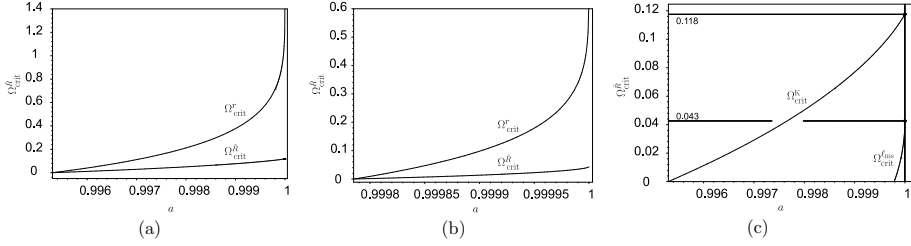


**Figure 9.** Critical “oscillatory” frequency for excitation of epicyclic oscillations, introduced by [Aschenbach, 2004], as a function of the rotational parameter of the black hole in terms of both the B–L coordinate radius ( $\Omega_{\text{crit}}^r$ ) and the proper radial distance ( $\Omega_{\text{crit}}^R$ ). (a) Keplerian discs. (b) Marginally stable (non-Keplerian) discs with constant specific angular momentum  $\ell = \ell_{\text{ms}}$ . (c) Comparison of critical frequencies for Keplerian  $\Omega_{\text{crit}}^K$ , and non-Keplerian  $\Omega_{\text{crit}}^{\ell_{\text{ms}}}$  discs in terms of the proper radius.

can see that for  $a \rightarrow 1$ , the velocity difference in the thick discs  $\Delta \mathcal{V}_{(\text{thick})}^{(\phi)} \approx 0.02$ , while for the Keplerian discs it goes even up to  $\Delta \mathcal{V}_{(\text{thin})}^{(\phi)} \approx 0.07$ , Fig. 8c. These are really huge velocity differences, being expressed in units of  $c$ .

Moreover, we can conclude that in constant specific angular momentum tori, the effect discovered by Aschenbach is elucidated by topology changes of the von Zeipel surfaces. In addition to one self-crossing von Zeipel surface existing for all values of the rotational parameter  $a$ , for  $a > a_{\text{c(thick)}}$  the second self-crossing surface together with toroidal surfaces occur. Toroidal von Zeipel surfaces exist under the newly developing cusp, being centred around the circle corresponding to the minimum of the equatorial LNRF velocity profile. Further, the behaviour of von Zeipel surfaces in marginally stable tori orbiting Kerr black holes with  $a > a_{\text{c(thick)}}$  strongly suggests a possibility of development of both the vertical and vortical instabilities because of the existence of the critical surface with a cusp, located above the centre of the torus and the toroidal von Zeipel surfaces located under the cusp.

As [Aschenbach, 2004], we can define the typical frequency of the mechanism for excitation of oscillations by the maximum slope of the positive gradient of  $\partial \mathcal{V}^{(\phi)} / \partial r$  in between of its sign,

$$\Omega_{\text{crit}}^r = 2\pi \left. \frac{\partial \mathcal{V}^{(\phi)}}{\partial r} \right|_{\text{max}}. \quad (43)$$

The “oscillatory” frequency has to be determined numerically. We have done it for both Keplerian discs and the marginally stable discs with  $\ell = \ell_{\text{ms}} = \text{const}$ , see Fig. 9. However, it is more appropriate to consider the gradient of  $\partial \mathcal{V}^{(\phi)} / \partial \tilde{R}$  where  $\tilde{R}$  is the proper radial distance defined by

$$d\tilde{R} = \sqrt{g_{rr}} dr = \sqrt{\frac{\Sigma}{\Delta}} dr, \quad (44)$$

as  $\tilde{R}$ , giving the physically relevant distance (coordinate-independent), is more convenient for estimation of physically realistic characteristic frequencies related to local physics in

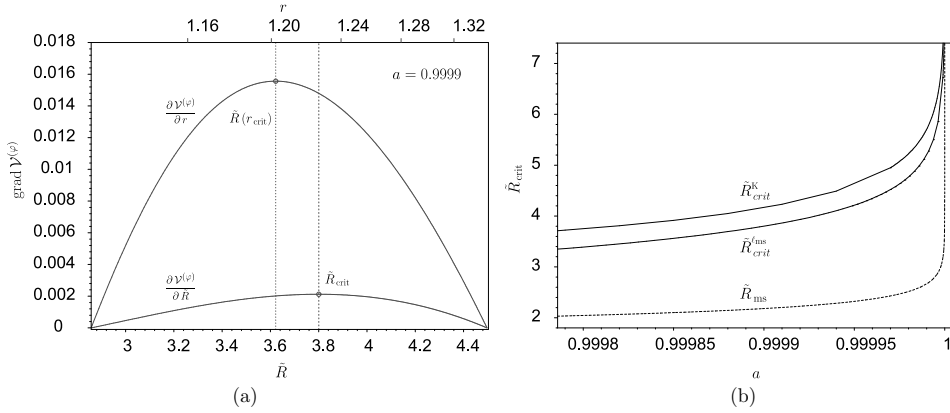


**Figure 10.** (a) Positive parts of the “coordinate” and “proper” radial gradient  $\partial \mathcal{V}(\phi)/\partial r$  and  $\partial \mathcal{V}(\phi)/\partial \tilde{R}$  for given value of the rotational parameter  $a$ . (c) Proper radial distance of the loci of  $(\partial \mathcal{V}(\phi)/\partial \tilde{R})_{\text{max}}$  measured from the marginally bound orbit for both the Keplerian disc ( $\tilde{R}_{\text{crit}}^{\text{K}}$ ) and the marginally stable (non-Keplerian) disc with  $\ell = \ell_{\text{ms}}$  ( $\tilde{R}_{\text{crit}}^{\text{ms}}$ ). Dashed curve corresponds to the loci of marginally stable equatorial circular geodesic determining, in this case, the inner edge of both types of discs.

the disc<sup>3</sup>. In terms of the proper radial distance, the critical frequency for possible excitation of oscillations is given by the relation

$$\Omega_{\text{crit}}^{\tilde{R}} = 2\pi \left. \frac{\partial \mathcal{V}(\phi)}{\partial \tilde{R}} \right|_{\text{max}}. \quad (45)$$

Because the velocity gradients related to the proper distance are suppressed in comparison with those related to the coordinate (unphysical) distance, there is  $\Omega_{\text{crit}}^{\tilde{R}} < \Omega_{\text{crit}}^r$ . The situation is illustrated in Fig. 9. Moreover, Fig. 10a shows mutual behaviour of the “coordinate” and “proper” radial gradient  $\partial \mathcal{V}(\phi)/\partial r$  and  $\partial \mathcal{V}(\phi)/\partial \tilde{R}$  in region between the local minimum and the outer local maximum of the orbital velocity  $\mathcal{V}(\phi)$  for an appropriately chosen value of the rotational parameter  $a$ . Location of the orbit  $\tilde{R}_{\text{crit}}$  corresponding to the maximal positive value of the orbital velocity gradient, in terms of its proper radial distance from the marginally bound orbit, is depicted for both the thin discs and the marginally stable toroidal configurations with  $\ell = \ell_{\text{ms}}$  in Fig. 10b. Note that in marginally stable tori with constant specific angular momentum  $\ell = \ell_{\text{ms}}$ , the inner edge is located at the marginally stable equatorial circular geodesic, like in thin (Keplerian) discs. Fig. 10b enables to give an idea on the mutual positions of the critical orbit  $\tilde{R}_{\text{crit}}$  in the disc and the inner edge of the disc  $\tilde{R}_{\text{ms}}$ .

The effect of “velocity gradient sign changes” can be very important as a trigger instability mechanism for oscillations observed in QPOs. Of course, further studies directed both to the theoretically well founded, detailed physical mechanisms for triggering of oscillations

<sup>3</sup> Of course, such a locally defined “oscillatory” frequency, confined to the orbiting disc, should be further related to distant observers by an appropriate coordinate transformation involving the time metric coefficient and the motion of the disc.

in the equilibrium tori with general specific angular momentum distribution, and the link to observations, are necessary and planned for the future.

Finally, we would like to call attention to the fact that signs' changes of the radial gradient of orbital velocity in LNRF occur nearby the  $r = r_{3:1}$  orbit, while in the vicinity of the  $r = r_{3:2}$  orbit,  $\partial \mathcal{V}_{\text{LNRF}}^{(\phi)} / \partial r < 0$  for all values of  $a$  for both the Keplerian discs and the marginally stable toroidal discs with all allowed values of  $\ell$ . Clearly, the parametric resonance, which is the strongest one for ratios of the epicyclic frequencies  $\Omega_V / \Omega_R = 3/2$  works at the  $r = r_{3:2}$  orbit, while its effect is much smaller at the radius  $r = r_{3:1}$  with  $\Omega_V / \Omega_R = 3/1$  [Abramowicz et al., 2003]. Therefore, the forced resonance, triggered by the changes of  $\partial \mathcal{V}_{\text{LNRF}}^{(\phi)} / \partial r$ , will be important for the 3:1 resonance. Notice that the forced resonance at  $r = r_{3:1}$  can generally result in observed QPOs frequencies with 3:2 ratio due to the beat frequencies allowed for the forced resonance [Abramowicz et al., 2004]; however it seems to be irrelevant in the case of microquasars, as all observed frequencies lead to the values of the rotational parameter  $a < a_{\text{c(thick)}}$  as shown in [Török et al., 2004].

## ACKNOWLEDGEMENTS

Authors are supported by the GAČR grants 202/02/0735, 205/03/1147 and 205/03/H144. The main parts of the work were done at the Department of Astrophysics of Chalmers University at Göteborg and at Nordita at Copenhagen. The authors would like to express their gratitude to the staff of the Chalmers University and Nordita for perfect hospitality. Special thanks belong to Prof. Marek A. Abramowicz for stimulating discussion and advice to analyse the von Zeipel surfaces.

## REFERENCES

- [Abramowicz et al., 1978] Abramowicz, M. A., Jaroszyński, M., and Sikora, M. (1978). Relativistic accreting disks. *Astronomy and Astrophysics*, 63(1–2):221–224.
- [Abramowicz et al., 2003] Abramowicz, M. A., Karas, V., Kluźniak, W., Lee, W., and Rebusco, P. (2003). Non-Linear Resonance in Nearly Geodesic Motion in Low-Mass X-Ray Binaries. *Publ. Astronom. Soc. Japan*, 55(2):467.
- [Abramowicz and Kluźniak, 2000] Abramowicz, M. A. and Kluźniak, W. (2000). *Astronomy and Astrophysics Letters*, 374:L19.
- [Abramowicz and Kluźniak, 2003] Abramowicz, M. A. and Kluźniak, W. (2003). *General Relativity and Gravitation*, 35:69.
- [Abramowicz et al., 2004] Abramowicz, M. A., Kluźniak, W., Stuchlík, Z., and Török, G. (2004). In Hledík, S. and Stuchlík, Z., editors, *Proceedings of RAGtime 4/5: Workshops on black holes and neutron stars, Opava, 13–15/16–18 Oct/Sep 2002/03*, Opava. Silesian University in Opava. in press.
- [Abramowicz et al., 1993] Abramowicz, M. A., Miller, J., and Stuchlík, Z. (1993). Concept of radius of gyration in general relativity. *Phys. Rev. D*, 47(4):1440–1447.
- [Abramowicz et al., 1995] Abramowicz, M. A., Nurowski, P., and Wex, N. (1995). Optical reference geometry for stationary and axially symmetric spacetimes. *Classical Quantum Gravity*, 12(6):1467.

- [Aschenbach, 2004] Aschenbach, B. (2004). Measuring mass and angular momentum of black holes with high-frequency quasi-periodic oscillations. *Astronomy and Astrophysics*, 425:1075–1082.
- [Bardeen et al., 1972] Bardeen, J. M., Press, W. H., and Teukolsky, S. A. (1972). Rotating black holes: locally nonrotating frames, energy extraction, and scalar synchrotron radiation. *Astrophys. J.*, 178:347–369.
- [Genzel et al., 2003] Genzel, R., Schoedel, R., Ott, T., Eckart, A., Alexander, T., Lacombe, F., Rouan, D., and Aschenbach, B. (2003). *Nature*, 425:934.
- [Kato, 2001] Kato, S. (2001). *Publ. Astronom. Soc. Japan*, 53:1.
- [Kluźniak and Abramowicz, 2000] Kluźniak, W. and Abramowicz, M. A. (2000). The physics of khz qpos—strong gravity’s coupled anharmonic oscillators. *astro-ph/0105057*. (submitted to Phys. Rev. Lett.).
- [Kluźniak and Abramowicz, 2001] Kluźniak, W. and Abramowicz, M. A. (2001). *Acta Phys. Polon. B*, 32:3605.
- [Kluźniak et al., 2004] Kluźniak, W., Abramowicz, M. A., and Lee, W. H. (2004). High-frequency qpos as a problem in physics: non-linear resonance. In Kaaret, P., Lamb, F. K., and Swank, J. H., editors, *X-Ray Timing 2003: Rossi and Beyond*, Melville, NY. AIP. astro-ph/0402013.
- [Kozłowski et al., 1978] Kozłowski, M., Jaroszyński, M., and Abramowicz, M. A. (1978). The analytic theory of fluid disks orbiting the Kerr black hole. *Astronomy and Astrophysics*, 63:209–220.
- [Landau and Lifshitz, 1973] Landau, L. D. and Lifshitz, J. M. (1973). *Mechanika*, volume I of *Teoretičeskaja fizika*. Nauka, Moskva, 3rd edition.
- [McClintock and Remillard, 2004] McClintock, J. E. and Remillard, R. A. (2004). In Lewin, W. H. G. and van der Klis, M., editors, *Compact Stellar X-Ray Sources*, Cambridge. Cambridge University Press. astro-ph/0306213.
- [Misner et al., 1973] Misner, C. W., Thorne, K. S., and Wheeler, J. A. (1973). *Gravitation*. Freeman, San Francisco.
- [Nowak and Lehr, 1998] Nowak, M. A. and Lehr, D. E. (1998). Stable oscillations of black hole accretion discs. In Abramowicz, M. A., Björnsson, G., and Pringle, J. E., editors, *Theory of Black Hole Accretion Disks*, pages 233–253, Cambridge. Cambridge University Press.
- [Rezzolla et al., 2003] Rezzolla, L., Yoshida, S., Maccarone, T. J., and Zanotti, O. (2003). A new simple model for high-frequency quasi-periodic oscillations in black hole candidates. *Monthly Notices Roy. Astronom. Soc.*, 344(3):L37–L41.
- [Stuchlík et al., 2004] Stuchlík, Z., Slaný, P., Török, G., and Abramowicz, M. A. (2004). *gr-qc/0411091*. (submitted to Phys. Rev. D).
- [Török et al., 2004] Török, G., Abramowicz, M. A., Kluźniak, W., and Stuchlík, Z. (2004). *astro-ph/0401464*. (submitted to Astronomy and Astrophysics).
- [van der Klis, 2000] van der Klis, M. (2000). Millisecond Oscillations in X-ray Binaries. *Annual Review of Astronomy and Astrophysics*, 38:717–760.

# Trapping of neutrinos in extremely compact stars

Zdeněk Stuchlík, Gabriel Török and Stanislav Hledík

*Institute of Physics, Faculty of Philosophy and Science, Silesian University in Opava,  
Bezručovo nám. 13, CZ-746 01 Opava, Czech Republic*

## ABSTRACT

Extremely compact objects ( $9GM/4c^2 < R < 3GM/c^2$ ) contain trapped null geodesics that cannot escape the objects. Certain part of neutrinos produced in their interior will therefore be trapped, thus influencing neutrino luminosity of the objects and consequently their thermal evolution. The existence of trapped neutrinos also indicates possibility of “two-temperature” cooling regime of extremely compact objects. It is shown that the trapping of neutrinos can be relevant even for moderately extremely compact stars.

## 1 INTRODUCTION

It is well known that in the internal Schwarzschild spacetimes of uniform energy density [Schwarzschild, 1916] with radius  $R < 3GM/c^2$ , bound null geodesics must exist being concentrated around the stable circular null geodesic [Stuchlík et al., 2001, Abramowicz et al., 1993]. It follows immediately from the behaviour of the effective potential of null geodesics in the exterior, vacuum Schwarzschild spacetimes, determining the unstable null circular geodesics at the radius  $r_{\text{ph}} = 3GM/c^2$  (see, e.g., [Misner et al., 1973]), that any spherically symmetric, static non-singular interior spacetime with radius  $R < r_{\text{ph}}$  admits existence of bound null geodesics. We call objects (stars) satisfying this condition – extremely compact objects (stars). The equations of state admitting existence of the extremely compact objects were investigated, e.g., in [Nilsson and Ugla, 2000, Stuchlík and Hledík, 2001, Hledík et al., 2004].

The existence of bound null geodesics in extremely compact objects has interesting astrophysical consequences. For example, trapped modes of gravitational waves were studied extensively by M. Abramowicz and his collaborators [Abramowicz et al., 1997, Abramowicz, 1999] using the optical reference geometry which brings a new insight into the properties of extremely compact objects. Clearly, the existence of trapped gravitational waves could influence some instability modes in these objects.

We shall consider another interesting problem related to the existence of bound null geodesics – namely, the problem of neutrinos trapped by the strong gravitational field of extremely compact objects. The trapped neutrinos can be important at least for two reasons. First, they will suppress the neutrino flow from extremely compact stars; such a suppression

could have observable consequences. Second, trapped neutrinos, being restricted to a layer extending from some radius, depending on details of the structure of extremely compact stars, up to their surface, can strongly influence cooling of the extremely compact stars. Moreover, the cooling process could be realized in a “two-temperature” regime, when the temperature profile in the interior of the star with no trapped neutrinos differs from the profile established in the external layer with trapped neutrinos. For the neutrino dominated period of the cooling process, one can even speculate that some part of the external layer will reach a higher temperature than its interior near the radius of the stable null circular geodesic, where the trapping of neutrinos reaches highest efficiency. This effect can lead to an inflow of heat from the “overheated” external layer to the interior of the star through other “agents” than the neutrino flows. Such a heat flow could influence the structure of extremely compact stars, maybe, even some special “self-organized” structures could develop due to the assumed heat flow. Then properties of the extremely compact stars could be modified substantially.

Of course, all of these ideas deserve very detailed and sophisticated analytical estimates and numerical simulations. Here, we restrict our attention to the first step in considering the role of trapped neutrinos in extremely compact stars. We shall estimate the relative number of trapped neutrinos in comparison to all neutrinos produced in the extremely compact objects, giving this estimate in both local and global relations. For simplicity, we shall consider the internal Schwarzschild spacetime with uniform distribution of energy density (but a nontrivial pressure profile) when all the calculations can be realized in terms of elementary functions only and the geometric units can be effectively used. We would like to recall that this spacetime can well represent spacetime properties of realistic extremely compact stars [Glendenning, 2000]. It is important that the trapping of neutrinos is shown to be relevant even for the internal Schwarzschild spacetimes with radius only moderately smaller than  $r_{\text{ph}} = 3GM/c^2$ . Therefore, it is worth to continue in detailed studies of trapped neutrinos in realistic models of extremely compact neutron stars or quark stars, when we usually expect radii  $R$  moderately smaller than  $r_{\text{ph}}$ . (Of course, some models admit existence of objects with radii  $R$  close to the critical value of  $9GM/4c^2$ , see, e.g., [Nilsson and Uglia, 2000].) Recently, we extend the estimates of the trapping process to the cases of the polytropic and adiabatic spherical objects and realistic models of extremely compact neutron stars and quark stars.

## 2 INTERNAL SCHWARZSCHILD METRIC

In the standard Schwarzschild coordinates and the geometric units with  $c = G = 1$ , the line element for the internal Schwarzschild spacetime of uniform energy density  $\rho$  reads

$$ds^2 = -e^{2\Phi(r)} dt^2 + e^{2\Psi(r)} dr^2 + r^2(d\theta^2 + \sin^2\theta d\phi^2). \quad (1)$$

The temporal and radial components of the metric tensor are given by the formulae

$$(-g_{tt})^{1/2} = e^\Phi = \frac{3}{2}Y_1 - \frac{1}{2}Y(r), \quad (g_{rr})^{1/2} = e^\Psi = 1/Y(r), \quad (2)$$

where

$$Y(r) = \sqrt{1 - \frac{r^2}{a^2}}, \quad Y_1 \equiv Y(R) = \sqrt{1 - \frac{R^2}{a^2}}, \quad (3)$$

$$\frac{1}{a^2} = \frac{8}{3}\pi\rho = \frac{2M}{R^3}, \quad (4)$$

$R$  is the radius of the internal spacetime,  $M$  is the mass parameter of the internal spacetime, which coincides with the mass parameter of the external, vacuum Schwarzschild spacetime. It can be shown that the internal Schwarzschild spacetimes are allowed for  $R > 9M/4$  only, see, e.g., [Stuchlík et al., 2001] for details.

The metric (1) in terms of the tetrad formalism reads

$$ds^2 = -[\omega^{(t)}]^2 + [\omega^{(r)}]^2 + [\omega^{(\theta)}]^2 + [\omega^{(\phi)}]^2, \quad (5)$$

where

$$\omega^{(t)} = e^\Phi dt, \quad \omega^{(r)} = e^\Psi dr, \quad \omega^{(\theta)} = r d\theta, \quad \omega^{(\phi)} = r \sin\theta d\phi. \quad (6)$$

Tetrad of 4-vectors  $e_{(\alpha)}^\mu = [\omega_{\mu}^{(\alpha)}]^{-1}$  is then given by

$$\vec{e}_{(t)} = \frac{1}{e^\Phi} \frac{\partial}{\partial t}, \quad \vec{e}_{(r)} = \frac{1}{e^\Psi} \frac{\partial}{\partial r}, \quad \vec{e}_{(\theta)} = \frac{1}{r} \frac{\partial}{\partial \theta}, \quad \vec{e}_{(\phi)} = \frac{1}{r \sin\theta} \frac{\partial}{\partial \phi}. \quad (7)$$

Tetrad components of 4-momentum of a test particle or a photon are determined by projections  $p_{(\alpha)} = p_\mu e_{(\alpha)}^\mu$ .

### 3 NULL GEODESICS AND EFFECTIVE POTENTIAL

We assume the period of cooling of extremely compact stars when their temperature falls down enough that the motion of neutrinos can be considered free, i.e., geodetical. This period starts at the moment when mean free path of neutrinos becomes to be comparable to the radius  $R$ . Weak interaction of ultrarelativistic neutrinos thus implies their motion along null geodesics obeying the equations ( $\lambda$  is affine parameter):

$$\frac{Dp^\mu}{d\lambda} = 0, \quad p^\mu p_\mu = 0. \quad (8)$$

Due to the existence of two Killing vector fields: the temporal  $\partial/\partial t$  one, and the azimuthal  $\partial/\partial \phi$  one, two conserved components of the 4-momentum must exist:

$$E = -p_t \quad (\text{energy}), \quad L = p_\phi \quad (\text{axial angular momentum}). \quad (9)$$

Moreover, the motion plane is central. For a single-particle motion, one can set  $\theta = \pi/2 = \text{const}$ , choosing the equatorial plane.

The null-geodetical motion can conveniently be described in terms of the impact parameter

$$\ell = \frac{L}{E}. \quad (10)$$

Then (8) yields the equation governing the radial motion in the form

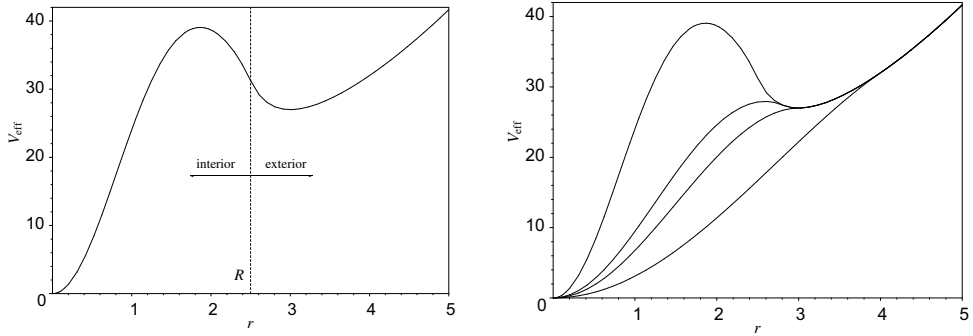


**Figure 1.** Effective potential ( $M = 1$ ) for  $R = 2.5$  (left) and for several values of  $R$  (right). The inner bound geodesics exist for  $R < 3$  only.

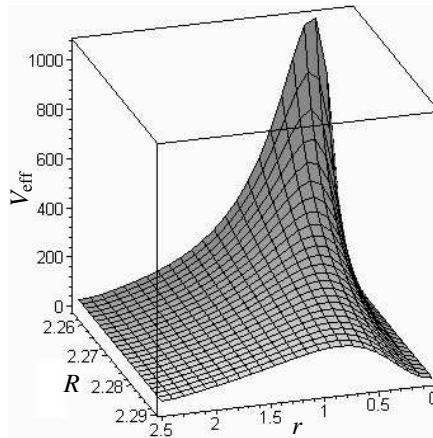


**Figure 2.** Segment of 3D plot of  $V_{\text{eff}}^{\text{int}}$  ( $M = 1$ ) for  $9/4 < R < 2.3$  and  $0 \leq r \leq 2.5$ . The maximum of the effective potential diverges when  $R \rightarrow 9M/4$  and shifts to  $r = 0$ .

$$(p^r)^2 = e^{-2(\Phi+\Psi)} E^2 \left( 1 - e^{2\Phi} \frac{\ell^2}{r^2} \right). \tag{11}$$

The radial motion is restricted by an effective potential defined by the relations

$$\ell^2 \leq V_{\text{eff}} = \begin{cases} V_{\text{eff}}^{\text{int}} = \frac{4a^2[1 - Y^2(r)]}{[3Y_1 - Y(r)]^2} & \text{for } r \leq R \\ V_{\text{eff}}^{\text{ext}} = \frac{r^3}{r - 2M} & \text{for } r > R \end{cases} \tag{12}$$

Notice that  $V_{\text{eff}}^{\text{ext}}$  is the effective potential of the null-geodesical motion in the vacuum Schwarzschild spacetime [Misner et al., 1973].

Circular null geodesics are given by local extrema of the effective potential ( $\partial V_{\text{eff}}/\partial r = 0$ ), which in the internal spacetime yields for their radius and their impact parameter the relations

$$Y(r_c) = \frac{1}{3Y_1}, \quad \ell_{c(i)}^2 = \frac{4a^2}{9Y_1^2 - 1}. \tag{13}$$

Typical behaviour of  $V_{\text{eff}}$  is illustrated in Figs 1 and 2.

#### 4 TRAPPING OF NEUTRINOS

In the case of extremely compact objects ( $R < 3$ ), stable bound null geodesics exist (see, e.g., [Stuchlík et al., 2001]) that prevent some part of produced neutrinos from escaping these static objects. The relation (13) reduces for unit mass  $M = 1$  (we shall assume that in the following) to

$$\ell_{c(i)}^2 = \frac{R^4}{4R - 9}, \tag{14}$$

which corresponds to the local maximum of the effective potential  $V_{\text{eff}}^{\text{int}}$  at  $r_{c(i)}$ , where the stable circular null geodesics of the internal spacetime are located. The local minimum of  $V_{\text{eff}}^{\text{ext}}$  at  $r_{c(e)} = 3$  corresponds to the unstable circular null geodesics of the external spacetime, with  $\ell_{c(e)}^2 = 27$  (see Fig. 3).

##### 4.1 Regions of trapping

Bound neutrinos (depicted by the shaded area in Fig. 3) may generally appear outside the extremely compact object, but they are trapped by the strong gravitational field of these objects and they enter them again. Therefore, we divide the trapped neutrinos into two families:

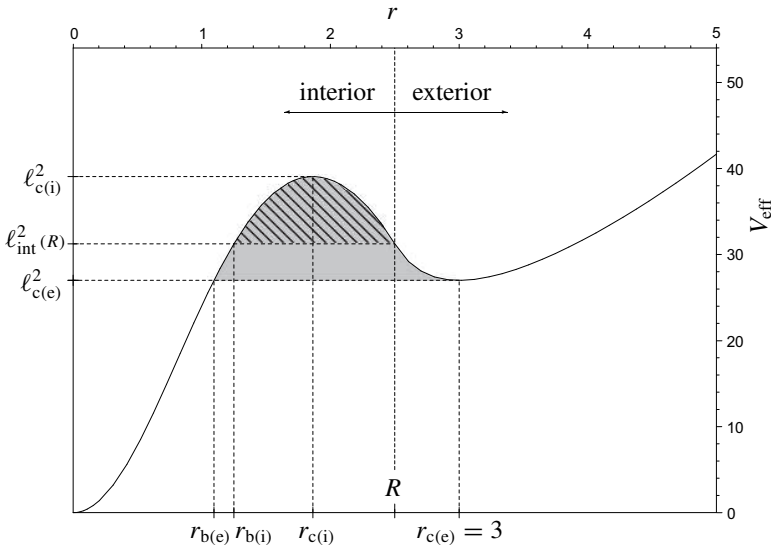
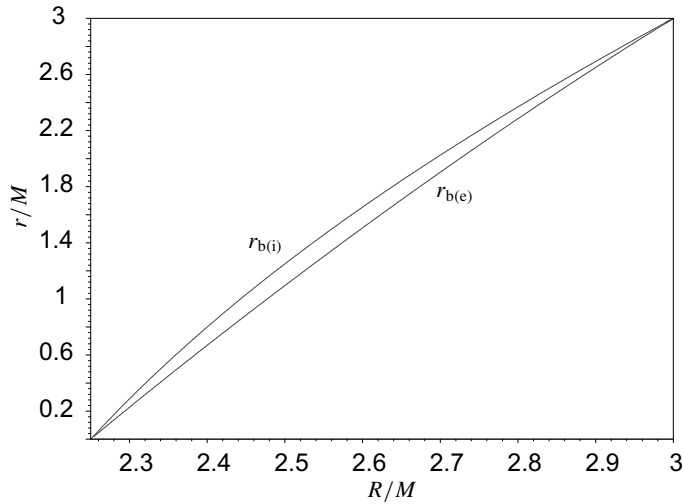


Figure 3. Detailed behaviour of  $V_{\text{eff}}$  ( $M = 1$ ) for  $R = 2.5$ .



**Figure 4.** The dependence of  $r_{b(e)}$  and  $r_{b(i)}$  on the radius  $R$ . The relations for the variable  $Y(r)$  are converted into relations for  $r$ .

- “Internal” bound neutrinos (upper (shaded) part of the shadow area with impact parameter between  $\ell_{int}^2(R)$  and  $\ell_{c(i)}^2$ ): their motion is restricted inside the object.
- “External” bound neutrinos (lower part of the shadow area with impact parameter between  $\ell_{c(e)}^2$  and  $\ell_{int}^2(R)$ ): may leave the object, but they re-enter the object.

Pericentra for both the marginally bound ( $r_{b(e)}$ ) and “internal” marginally bound neutrinos ( $r_{b(i)}$ ) can then be expressed in the form

$$Y_{\pm}(r_{b(e)}) = \frac{81\sqrt{1 - \frac{2}{R}} \pm 2R\sqrt{R^4 - 108R + 243}}{2R^3 + 27} \tag{15}$$

$$Y(r_{b(i)}) = \sqrt{1 - \frac{2}{R}} \left( \frac{9 - 2R}{2R - 3} \right), \tag{16}$$

see Fig. 4 for graphical representation.

Bound neutrinos with mean free path  $\gg R$  (this condition can be fulfilled in a few days old neutron star, see [Shapiro and Teukolsky, 1983, Weber and Glendenning, 1992]) will slow down the cooling although they will be re-scattered due to finiteness of the mean free path. An eventual scattering of trapped neutrinos will cause change of their impact parameter, therefore, some of them will escape the extremely compact star, suppressing thus the slow down of the cooling process. Moreover, the “external” bound neutrinos have certain portion of their orbit outside the configuration without any interaction; this fact the other hand “suppress the suppression” of the cooling timescale retardation. Clearly, the re-scattering effect on the trapped neutrinos is a very complex process deserving sophisticated numerical code based on the Monte Carlo method. Only neutrinos produced above or at  $r_{b(e)}$  are subject to this effect; those produced below  $r_{b(e)}$  freely escape to infinity.

### 4.2 Directional angles

Considering (without loss of generality, as stated just above Eq. (10)) an equatorial motion, we can define the *directional angle* relative to an outward pointed radial direction measured in the emitter system by the standard relations

$$\sin \psi = \frac{p^{(\phi)}}{p^{(t)}}, \quad \cos \psi = \frac{p^{(r)}}{p^{(t)}}, \quad (17)$$

where

$$p^{(\alpha)} = p^\mu \omega_\mu^{(\alpha)}, \quad p_{(\alpha)} = p_\mu e_{(\alpha)}^\mu. \quad (18)$$

Besides conserving components (9), and  $p_\theta = 0$ , Eq. (11) implies

$$p_r = \pm E e^{\psi - \phi} \left( 1 - e^{2\phi} \frac{\ell^2}{r^2} \right). \quad (19)$$

For the directional angles we thus obtain relations

$$\sin \psi = \alpha(r, R) \frac{\ell}{r}, \quad \cos \psi = \pm \sqrt{1 - \sin^2 \psi}, \quad (20)$$

where

$$\alpha(r, R) = \frac{3}{2} \sqrt{1 - \frac{2}{R}} - \frac{1}{2} \sqrt{1 - \frac{2}{R} \left( \frac{r}{R} \right)^2}. \quad (21)$$

The directional angle limit for the bound neutrinos is determined by the impact parameter  $\ell_{c(e)}^2 = 27$ . We arrive at relations

$$\sin \psi_e(r, R) = \alpha(r, R) \frac{3\sqrt{3}}{r}, \quad \cos \psi_e(r, R) = \pm \sqrt{1 - \frac{27\alpha^2(r, R)}{r^2}}. \quad (22)$$

The directional angle limit for the “internal” bound neutrinos is determined by Eq. (14) and yields the relations

$$\sin \psi_i(r, R) = \alpha(r, R) \frac{R^{3/2}}{r\sqrt{R-2}}, \quad \cos \psi_i(r, R) = \pm \sqrt{1 - \frac{\alpha^2(r, R)R^3}{(R-2)r^2}} \quad (23)$$

Apparently, the condition  $\psi_i > \psi_e$  holds at any given radius  $r < R$ .

### 4.3 Escaped to produced neutrinos ratio

We assume that neutrinos are locally produced by isotropically emitting sources. Then escaped-to-produced-neutrinos ratio depends on a geometrical argument only. It is determined by the solid angle  $2\Omega$  corresponding to escaping neutrinos (also inward emitted neutrinos must be involved because even these neutrinos can be radiated away), see Fig. 5.

Let  $N_p$ ,  $N_e$  and  $N_b$  denote, respectively, the number of produced, escaped and trapped neutrinos per unit time of an external static observer at infinity. In order to determine the global correction factors

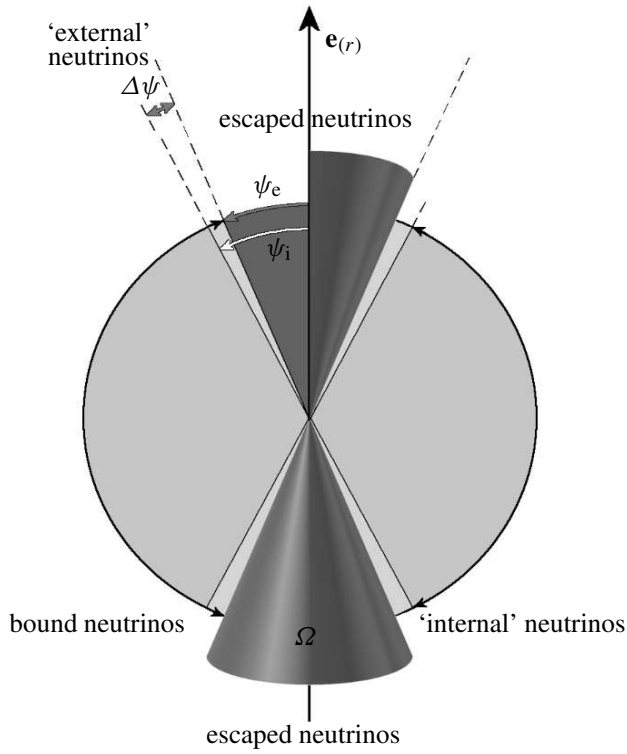


**Figure 5.** Overview of the geometry of neutrino radiation.

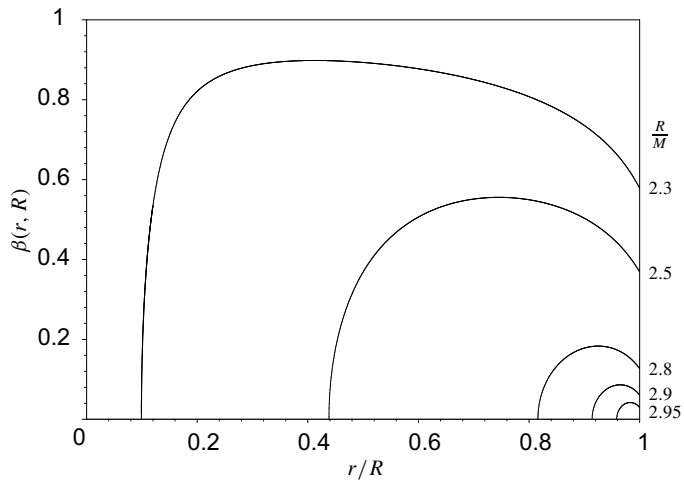


**Figure 6.**  $\beta(r, R)$  for several values of  $R$ .

$$\mathcal{E}(R) \equiv \frac{N_e(R)}{N_p(R)}, \quad \mathcal{B}(R) \equiv \frac{N_b(R)}{N_p(R)} = 1 - \mathcal{E}(R) \quad (24)$$

it is necessary to introduce the local correction factor for escaping neutrinos (notice that we consider production and escaping rates at a given radius  $r$ , but the radius  $R$  of the compact object enters the relation as it determines the escaping directional angle)

$$\epsilon(r, R) = \frac{dN_e(r)}{dN_p(r)} = \frac{2\Omega(\psi_e(r, R))}{4\pi} = 1 - \cos \psi_e(r, R) \quad (25)$$

and the complementary factor for trapped neutrinos

$$\beta(r, R) = 1 - \epsilon(r, R) = \frac{dN_b(r)}{dN_p(r)} = \cos \psi_e(r, R). \quad (26)$$

The coefficient  $\beta(r, R)$ , determining local efficiency of the neutrino trapping, i.e., the ratio of the trapped and produced neutrinos at any given radius, is shown for some representative values of  $R$  in Fig. 6.

#### 4.4 Neutrino production rates

Generally, the neutrino production is a very complex process depending on detailed structure of an extremely compact object. We can express the neutrino production rate in the form

$$\mathcal{I}(r\{\mathcal{A}\}) = \frac{dN(r\{\mathcal{A}\})}{d\tau(r)}, \quad (27)$$

where  $dN$  is the number of interactions at radius  $r$ ,  $\tau$  is the proper time of the static observer at the given  $r$ ,  $\{\mathcal{A}\}$  is the full set of quantities relevant for the production rate. We can write that

$$dN(r) = n(r)\Gamma(r)dV(r), \quad (28)$$

where  $n(r)$ ,  $\Gamma(r)$  and  $dV(r)$  are the number density of particles entering the neutrino production processes, the neutrino production rate and the proper volume element at the radius  $r$ , respectively. Both  $n(r)$  and  $\Gamma(r)$  are given by detailed structure of the extremely compact stars,  $dV(r)$  is given by the spacetime geometry.

Here, considering the uniform energy density Schwarzschild stars (for requirements of more realistic model see, e.g., [Østgaard, 2001]), we shall assume the local production rate to be proportional to the energy density, i.e., we assume uniform production rate as measured by the local static observers; of course, from the point of view of static observers at infinity, the production rate will not be distributed uniformly. (According to [Glendenning, 2000], such toy model could be reasonable good starting point for more realistic calculations.)

Therefore. we write the local neutrino production rate in the form

$$\mathcal{I}(r) \propto \rho = \text{const} \quad (29)$$

or

$$\mathcal{I} = \frac{d\mathcal{N}}{d\tau}, \quad \frac{d\mathcal{N}(r)}{d\tau} \propto n(r) \propto \rho(r) \propto \text{const}. \quad (30)$$

The local neutrino production rate related to the distant static observers is then given by the relation including the time-delay factor

$$I = \frac{dN}{dt} = \mathcal{L}e^{\Phi(r)}. \tag{31}$$

Now, the number of neutrinos produced in a proper volume  $dV$  per unit time of a distant static observer is

$$dN_p(r) = I(r) dV(r) = 4\pi \mathcal{L} e^{\Phi(r)+\Psi(r)} r^2 dr. \tag{32}$$

Integrating through whole the compact object (from 0 to  $R$ ) and using (2), we arrive to the global neutrino production rate in the form

$$N_p(R) = 4\pi \mathcal{L} \int_0^R \left[ \frac{3R\sqrt{R-2}}{\sqrt{R^3-2r^2}} - 1 \right] r^2 dr. \tag{33}$$

In an analogical way, we can give the expressions for the global rates of escaping and trapping of the produced neutrinos:

$$N_e(R) = 4\pi \mathcal{L} \int_0^R (1 - \cos \psi_e(r, R)) \left[ \frac{3R\sqrt{R-2}}{\sqrt{R^3-2r^2}} - 1 \right] r^2 dr, \tag{34}$$

$$N_b(R) = 4\pi \mathcal{L} \int_{r_{b(e)}}^R \cos \psi_e(r, R) \left[ \frac{3R\sqrt{R-2}}{\sqrt{R^3-2r^2}} - 1 \right] r^2 dr. \tag{35}$$

The coefficients giving the global efficiency of trapping (escaping) of neutrinos generated in whole the compact object are hence given by the relations

$$\mathcal{B}(R) = \frac{\int_{r_{b(e)}}^R \gamma(r, R) \sqrt{1 - \frac{27\alpha^2(r, R)}{r^2}} r^2 dr}{\int_0^R \gamma(r, R) r^2 dr}, \tag{36}$$

$$\mathcal{E}(R) = 1 - \mathcal{B}(R), \tag{37}$$

where

$$\gamma(R, r) = \frac{3R\sqrt{R-2}}{\sqrt{R^3-2r^2}} - 1, \tag{38}$$

and  $\alpha(r, R)$  is given by (21).

We can, moreover, define other global characteristic coefficients. For the “internal” neutrinos, we introduce

$$\mathcal{Q} = \frac{N_i}{N_p} = \frac{\int_{r_{b(i)}}^R \gamma(r, R) \sqrt{1 - \alpha^2(r, R) \frac{R^3}{(R-2)r^2}} r^2 dr}{\int_0^R \gamma(r, R) r^2 dr} \tag{39}$$

and for the “external” neutrinos, we can use a complementary coefficient

$$\mathcal{X} = \frac{N_{ext}}{N_p} = \mathcal{B} - \mathcal{Q} \tag{40}$$

Numerical results for the coefficients  $\mathcal{E}$ ,  $\mathcal{B}$ ,  $\mathcal{Q}$  and  $\mathcal{X}$  in dependence on  $R$  are depicted in Fig. 7.

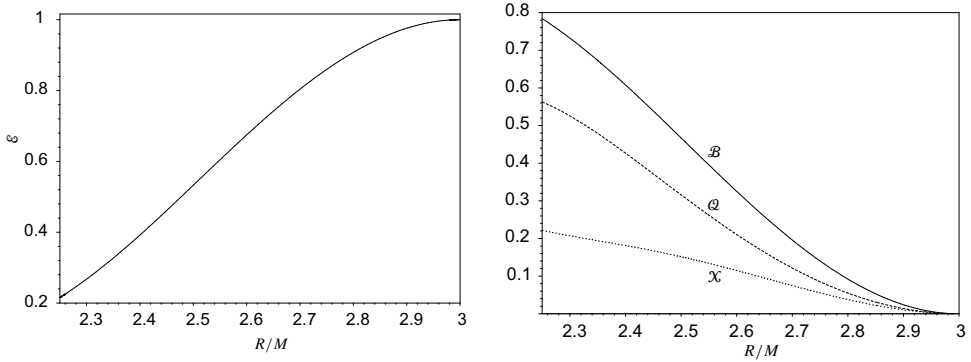


Figure 7. Dependence of  $\mathcal{E}$ ,  $\mathcal{B}$ ,  $\mathcal{Q}$  and  $\mathcal{X}$  on total radius  $R$ .

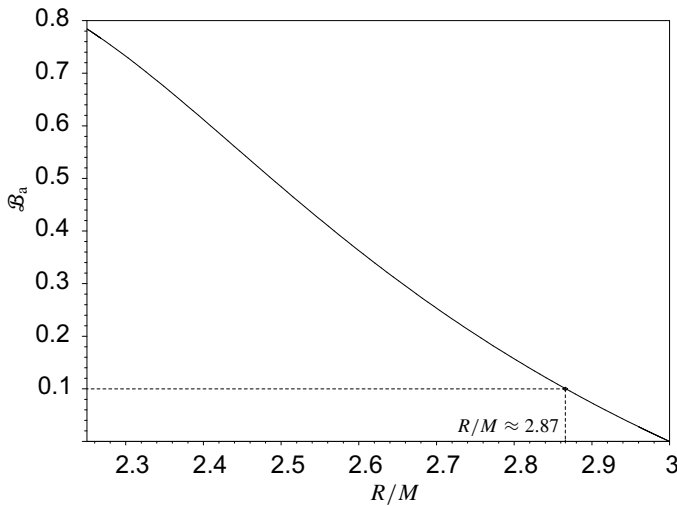


Figure 8. Behaviour of the coefficient  $\mathcal{B}_a$ . It is explicitly shown that  $\mathcal{B}_a \sim 10\%$  for  $R = 2.87M$ .

It can also be useful to have an information on the global efficiency of the trapping process related to the “active” zone of the extremely compact objects. This efficiency is expressed by the global efficiency coefficient defined by the relation

$$\mathcal{B}_a(R) = \frac{\int_{r_{b(e)}}^R \gamma(r, R) \sqrt{1 - \frac{27\alpha^2(r, R)}{r^2}} r^2 dr}{\int_{r_{b(e)}}^R \gamma(r, R) r^2 dr} \tag{41}$$

$$\tag{42}$$

Behaviour of the function  $\mathcal{B}_a(R)$  is depicted in Fig. 8. In fact, the coefficient  $\mathcal{B}_a(R)$  yields better intuitive insight into the influence of the trapped neutrinos on the cooling process than the coefficient  $\mathcal{B}(R)$  can, because it is restricted purely to the active zone, where the trapping occurs.

## 5 CONCLUSIONS

Efficiency of the neutrino trapping in the extremely compact objects described by the internal Schwarzschild spacetime grows with radius  $R$  descending from  $R = 3M$  down to the limiting critical value of  $R = 9M/4$ . The local efficiency factor  $\beta(r, R)$  has its maximum at the radius of the stable null circular geodesic. Notice that  $\beta_{\max}(R = 2.9M) \sim 0.1$ , and it grows strongly with descending  $R$ , as  $\beta_{\max}(R = 2.5M) \sim 0.5$  and  $\beta_{\max}(R \rightarrow 9M/4) \rightarrow 1$ . Therefore, the trapping can be locally important at even slightly extremely compact objects with  $R \sim 2.9M$ .

The global efficiency factor of the trapping  $\mathcal{B}(R)$  grows almost linearly with  $R$  descending from the limiting value of  $R = 3M$ . We can see that the value of the global trapping factor  $\mathcal{B} = 0.1$  is reached for  $R \sim 2.8M$ , and  $\mathcal{B} > 0.2$  for  $R < 2.7M$ . We can conclude that globally the trapping of neutrinos becomes relevant for moderately extreme compact objects. Moreover, considering the active zone of the trapping only, we obtain even higher values of the global trapping factor. For example, we deduce from Fig. 8 that  $\mathcal{B}_a > 0.1$  for  $R < 2.87M$ .

Because the effect of trapping of neutrinos is a cumulative one, we can expect its relevance in realistic models of extreme compact objects. It is under study now, how the trapping will really influence the cooling process in some simple models of quark stars with a relatively simple “bag” equation of state, and how the cooling of such a quark star will be modified by cumulation of neutrinos in the zone of trapping.

## ACKNOWLEDGEMENTS

The present work was supported by grants GAČR 202/02/0735 and GAČR 205/03/H144. Two of authors (S. H. and Z. S.) would like to express their gratitude to the Bergen Computational Physics Laboratory (BCPL), an EU Research Infrastructure, for support and hospitality during their stay at the University of Bergen in the framework of the BCPL Project 58, and to the Theory Division of CERN for perfect hospitality.

## REFERENCES

- [Abramowicz, 1999] Abramowicz, M. A. (1999). Gravitational radiation in optical geometry applied to supercompact stars. *Phys. Rep.*, 311:325.
- [Abramowicz et al., 1997] Abramowicz, M. A., Anderson, N., Bruni, M., Ghosh, P., and Sonego, S. (1997). Gravitational waves from ultracompact stars: the optical geometry view of trapped modes. *Classical Quantum Gravity*, 14:L189.
- [Abramowicz et al., 1993] Abramowicz, M. A., Miller, J., and Stuchlík, Z. (1993). Concept of radius of gyration in general relativity. *Phys. Rev. D*, 47(4):1440–1447.
- [Glendenning, 2000] Glendenning, N. K. (2000). *Compact Stars: Nuclear Physics, Particle Physics, and General Relativity*. Springer-Verlag, New York.
- [Hledík et al., 2004] Hledík, S., Stuchlík, Z., and Mrázová, K. (2004). Comparison of general relativistic polytropic and adiabatic fluid spheres with a repulsive cosmological constant. In Hledík, S. and Stuchlík, Z., editors, *Proceedings of RAGtime 4/5: Workshops*

- on black holes and neutron stars, Opava, 14–16/13–15 October 2002/03, Opava. Silesian University in Opava.
- [Misner et al., 1973] Misner, C. W., Thorne, K. S., and Wheeler, J. A. (1973). *Gravitation*. Freeman, San Francisco.
- [Nilsson and Ugla, 2000] Nilsson, U. S. and Ugla, C. (2000). General Relativistic Stars: Polytropic Equations of State. arXiv: gr-qc/0002022.
- [Østgaard, 2001] Østgaard, E. (2001). Internal structure of neutron stars. In Hledík, S. and Stuchlík, Z., editors, *Proceedings of RAGtime 2/3: Workshops on black holes and neutron stars, Opava, 11–13/8–10 October 2000/01*, pages 73–102, Opava. Silesian University in Opava.
- [Schwarzschild, 1916] Schwarzschild, K. (1916). Über das Gravitationsfeld einer Kugel aus inkompressibler Flüssigkeit nach der Einsteinschen Theorie. *Sitzber. Deut. Akad. Wiss. Berlin, Kl. Math.-Phys. Tech.*, pages 424–434.
- [Shapiro and Teukolsky, 1983] Shapiro, S. L. and Teukolsky, S. A. (1983). *Black Holes, White Dwarfs and Neutron Stars: The Physics of Compact Objects*. John Wiley & Sons, New York.
- [Stuchlík and Hledík, 2001] Stuchlík, Z. and Hledík, S. (2001). Bound neutrinos in extremely compact stars. In preparation.
- [Stuchlík et al., 2001] Stuchlík, Z., Hledík, S., Šoltés, J., and Østgaard, E. (2001). Null geodesics and embedding diagrams of the interior Schwarzschild–de Sitter spacetimes with uniform density. *Phys. Rev. D*, 64(4):044004 (17 pages).
- [Weber and Glendenning, 1992] Weber, F. and Glendenning, N. K. (1992). *Astrophys. J.*, 390:541.



# Stellar orbits in the gravitational field of a massive torus near a galactic centre

Ladislav Šubr<sup>1</sup> and Vladimír Karas<sup>2</sup>

<sup>1</sup>*Faculty of Mathematics and Physics, Charles University, CZ-180 00 Prague, Czech Republic*

<sup>2</sup>*Astronomical Institute, Academy of Sciences, Prague, Czech Republic*

## ABSTRACT

We further examine orbits of satellite stars in the gravitational field of a dark super-massive compact body, which is surrounded by a self-gravitating accretion disc or a massive molecular torus. The disc extends to several hundred gravitational radii from the core and its mass can reach a significant fraction of the central mass, causing a non-negligible perturbation of the orbits. We demonstrate that resonances occur for orbits exhibiting epicyclic and latitudinal oscillations whose periods are in rational ratios. As a result, episodic changes of orbital eccentricity and inclination take place. Some of the satellite stars may populate highly eccentric orbits with an increased chance of being damaged by tidal forces at the moment of their close approach to the central black hole, or they may be even set on an unstable trajectory and captured by the hole. This effect influences the long-term evolution of the system which would otherwise exhibit only very slow orbital decay and gradual sinking of the satellites toward the core. It may be therefore relevant for the structure of an inner cluster residing in galactic nuclei.

## 1 INTRODUCTION

Active galactic nuclei (AGN) and quasars are fed by accretion process onto a super-massive black hole [Kato and Fukue, 1980]. An accretion disc is essential ingredient of the model, however, the role of stars is also crucial and cannot be neglected in a picture of the system which aims to be astrophysically realistic. Both sub-systems, i.e., stars and diluted interstellar environment, are mutually interconnected and they influence each other. Very near the centre, stars move under dominating influence of the central black hole, but its attraction is less prominent further out. If the interstellar gas is sufficiently dense, which is the case of luminous AGN, then it provides dissipative environment causing a long-term orbital decay of satellite orbits towards the centre, jointly with action of dynamical friction. In the end, satellites are captured and destroyed by the hole.

In early papers on this subject (e.g., [Syer et al., 1991]), when the effect of stellar transits across the disc was taken into account, it was found that gradual circularisation takes place and stellar satellites are eventually brought into the disc plane after  $\sim 10^4$ – $10^7$  orbits, depending on the stellar type of the satellite and surface density of the disc [Karas et al., 2002]. However, it was argued [Vokrouhlický and Karas, 1998] that the disc self-gravity

should not be ignored, because taking the disc mass into consideration may significantly change the orbit evolution even if the disc is very light, i.e.,  $M_d \ll M_\bullet$ .

Galactic nuclei host central dark objects with the mass in range  $10^6 M_\odot \lesssim M_\bullet \lesssim 10^8 M_\odot$ . They are very compact and traditionally interpreted in terms of a super-massive black hole (e.g., [Kormendy and Richstone, 1995]). Relevant length-scale is therefore the black hole gravitational radius,  $R_g = GM_\bullet/c^2 \sim 1.5 \times 10^{13} M_8 \text{ cm}$  (where  $M_8 \equiv M_\bullet/10^8 M_\odot$ ). A compact nuclear cluster can be also present in nuclei of some galaxies [Lauer et al., 1998, Schinnerer et al., 2001], where its members must inevitably undergo mutual interaction with the central mass and with gas in the accretion disc. In its innermost region, the cluster structure should reflect the presence of the massive black hole which eventually dominates the gravitational field of the centre. Hereby we will discuss the region of its dynamical influence,  $R_h = GM_\bullet \sigma_c^{-2} \sim 0.5 M_8 (\sigma_c/[10^3 \text{ km/s}])^{-2} \text{ pc}$ , where  $\sigma_c$  denotes velocity dispersion in the core.

Although we concentrate our attention on AGN, assuming a sufficiently large accretion rate in this paper, there is also an interesting possibility of a cold disc residing even in the centre of the Milky Way [Levin and Beloborodov, 2003, Nayakshin, 2004]. Similar approach could be thus applied to the discussion of stellar motion in Sagittarius A\*. Former interaction between the disc and stars could be essential for the present structure of the Galactic centre, although its existence is still questionable. On the other hand, it is worth noting that the mass ratio  $M_d/M_\bullet$  need not be much less than unity, i.e., the disc mass can reach the value comparable with the black hole mass in systems like NGC 1068 [Greenhill et al., 1996, Huré, 2003]. Gravitation of the disc medium manifests itself in several ways which we discuss below.

## 2 MOTION OF SATELLITE STARS IN A GALACTIC NUCLEUS

We examine stellar orbits by means of dissipative dynamics in an axially symmetric gravitational field. Stars are treated as test-mass orbiters, which form a family of satellites encircling the super-massive black hole in its region of dominance. We want to explore how the mutual action of gravity (due to the centre plus the disc) and dissipation (due to gaseous environment) may set satellites on eccentric trajectories with a small pericentre, bringing them this way near the core.

We employ Newtonian description of the gravitational field, which is constructed as a superposition of the field of two main components, i.e., the central mass and the gaseous disc. Several models of the disc gravity were used. We start from an analytical potential for a ring of radius  $R_d$  and mass  $M_d$ :

$$\Sigma_d(R) = \frac{M_d}{2\pi R_d} \delta(R - R_d), \quad V_d(R, z) = -\frac{2GM_d}{\pi} \frac{K(k)}{B}, \quad (1)$$

where  $K$  is the complete elliptic integral of the first kind,  $B^2(R, z) \equiv z^2 + (R + R_d)^2$  and  $k(R, z) \equiv 4RR_d/B^2(R, z)$ . We further considered analytical potential of razor-thin Kuzmin's disc:

$$\Sigma_d(R) = \frac{M_d}{2\pi} \frac{\kappa}{(\kappa^2 + R^2)^{3/2}}, \quad V_d(R, z) = -\frac{GM_d}{\sqrt{R^2 + (\kappa + |z|)^2}}, \quad (2)$$

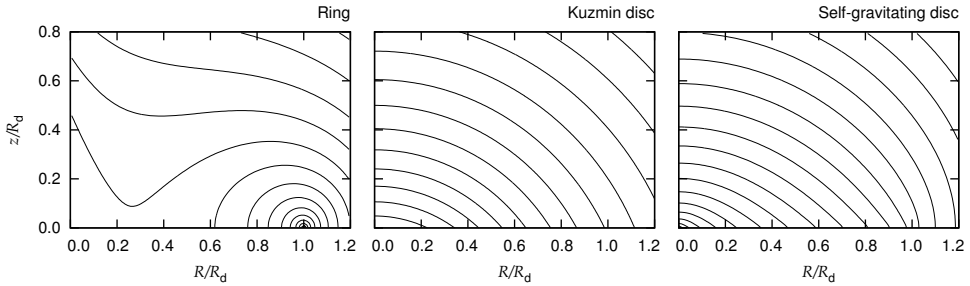


**Figure 1.** Comparison of the gravitational potential of a ring, Kuzmin’s disc ( $\kappa = 0.5R_d$ ), and one of the numerical models of a self-gravitating disc (see the text). Equipotentials are shown (with a logarithmic step) in a meridional section across the disc, which is located in  $z = 0$  plane.

where  $\kappa$  is a constant. This disc has infinite radius but finite mass  $M_d$  (55% of the total mass is concentrated within the distance  $R = 2\kappa$ ).

Finally, we proceed to more complicated numerical solutions for axially symmetric accretion discs. In particular, we calculate the gravitational field corresponding to a gas-pressure dominated standard-type model [Shakura and Sunyaev, 1973] with opacity due to free–free scattering, and radiation pressure dominated disc with electron scattering opacity. In outer regions of the system we employ a marginally unstable solution for a self-gravitating disc with either zero or solar metallicity [Huré, 1998, Huré, 2000, Goodman, 2003]. In both cases gaseous discs are geometrically thin and their density distribution can be described by means of vertically integrated quantities. The particular model used in this paper consists of radiation pressure dominated standard model switched to marginally unstable solution with solar metallicity at  $\sim 10^3 R_g$ .

Even if the gravitational field of the disc is treated as a perturbation in comparison to the dominating central field, the vertical component of the disc field may successfully compete with that of the centre in certain regions. This fact is known to be essential for the structure of self-gravitating discs, but here we demonstrate its importance also for the satellite long-term motion. We demonstrate structure of the gravitational potential of different axi-symmetric sources in Fig. 1. One can see that gravitational potential of a self-consistent (numerical) model is approximated by Kuzmin’s potential rather accurately. On the other hand, the potential of a narrow ring provides less satisfactory approximation at small radii.

We used a Runge–Kutta integrator with adaptable step-size for tracking individual orbits. The field components for a ring and for Kuzmin’s potential can be evaluated analytically, however, in other cases which we considered, evaluation requires to compute one- or two-dimensional integrals numerically (with a diverging integrand in some cases). Therefore, in order to reduce time consumption to an acceptable level, we have pre-computed the potential and the field at a discrete grid. We found the values among mesh points by interpolation.

Oscillatory evolution of the orbital radius  $r$  from the centre (spherical coordinate) and height  $z$  above equatorial plane (vertical coordinate) is shown in Fig. 2. We present this case as an exemplary orbit evolving in the gravitational field of the central mass  $M_\bullet$  and a narrow ring ( $M_d = 0.1M_\bullet$ ). Here we see that the power spectra have non-trivial profiles. We thus introduce frequencies of radial and vertical oscillations  $\omega_r$  and  $\omega_z$  in a usual way.

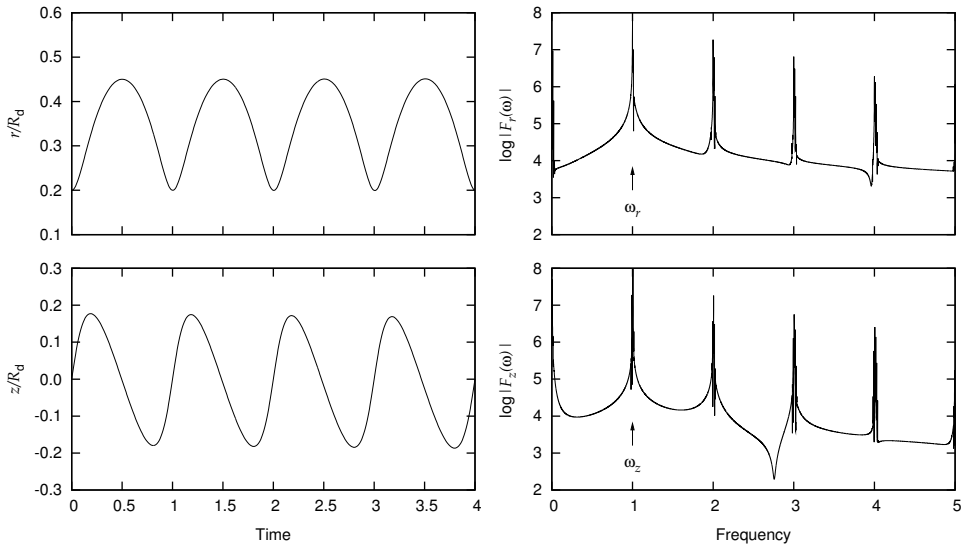


**Figure 2.** Satellite motion in the superposed gravitational field of a central mass and an infinitesimally thin ring of radius  $R_d = 5000R_g$  and mass  $M_d = 0.1M_\bullet$ . **Left:** a short piece of orbital oscillations (radial and vertical) in time domain; time unit is normalised to the orbital period. **Right:** corresponding Fourier power spectra of the oscillations, which consist of narrow peaks located at frequencies  $\omega_r$  and  $\omega_z$  (indicated by arrows), and their harmonics. The radial epicyclic and the corresponding vertical frequencies come out almost identical. They are the basic oscillations in this case. Frequencies are scaled with respect to the mean orbital frequency.

The two frequencies correspond to maxima in the Fourier power spectrum. It should be quite obvious that, in the non-spherical field of a ring, these two frequencies may differ from each other. For a ring or, more generally, a disc-type field, the vertical frequency is typically higher than the radial one (although we have also found trajectories with  $\omega_z/\omega_r$  considerably smaller than unity, depending on details of the orbit and density distribution in the disc).

When the time domain is extended over several hundreds of revolutions, we observe slow periodic variations in both  $r$  and  $z$  coordinates. Corresponding frequencies  $\Omega_r$  and  $\Omega_z$  can be also identified in the power spectrum but their nature is distinct from epicyclic oscillations. In contrary to  $\omega_r$  and  $\omega_z$ , the long-term amplitude oscillations stay in ratio 1 : 2, and this feature can be understood by energy conservation arguments: the amplitudes tell us how the total energy is periodically interchanged between radial and vertical oscillations. It derives from the energy conservation that these long periods are interconnected to each other. Twice as long period of vertical amplitude oscillations arises from the fact that these oscillations switch between two states, symmetric with respect to the equatorial plane. This feature is clearly visible in Fig. 3 where we show the evolution of radius and altitude over several hundreds of revolutions for the same initial conditions as in Fig. 2. Although this feature appears quite generic, the long-term oscillations may be difficult to distinguish in the power spectrum. Either their amplitude is considerably suppressed or the frequency

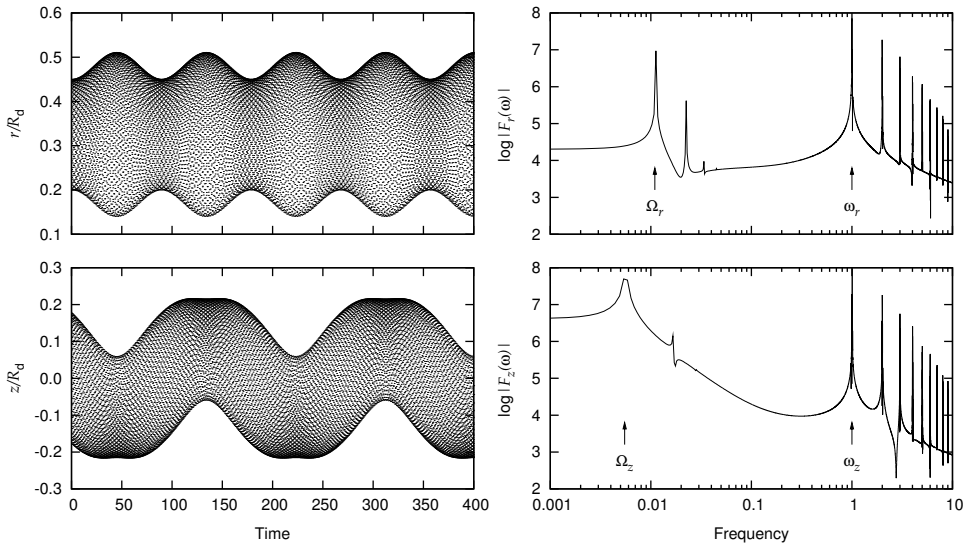


**Figure 3.** Similar to previous figure, the long-term orbital evolution is shown in the combined field of the centre and the ring. Parameters of the system and initial conditions of the orbit are the same as in Fig. 2, but time span is longer by two orders of magnitude. Frequency domain is shown in the logarithmical scale in order to emphasise low frequency oscillations  $\Omega_r$  and  $\Omega_z$ .

is hidden in a complicated spectrum. On the other hand,  $\Omega_r$  and/or  $\Omega_z$  may eventually dominate in the power spectra, which makes mechanical identification of resonances rather complicated.

An increasing complexity of the gravitational field leads to additional structure of the Fourier spectrum. Fig. 4 represents example of an orbit evolving in the gravity of a centre and rather massive self-consistent disc with  $M_d = 0.77M_\bullet$  and  $R_d = 4 \times 10^4 R_g$ . Now, we show orbit with remarkably different values of radial and vertical oscillations, in particular,  $13\omega_r \approx 15\omega_z$ . We remark, that such a low ratio of  $\omega_z : \omega_r$  is exceptional. Already on a short time-scale we notice remarkable differences with respect to the motion in the central potential, which would be characterised by a unique value of oscillation frequency,  $\omega_r = \omega_z$ , common for both directions. Compared to the previous case, amplitude oscillations are much faster, however, their frequencies are still locked at the same constant ratio of 1 : 2.

For the purpose of further analysis, it is useful to parametrise trajectories by a set of three parameters (implied by the number of integrals of motion). We found it convenient to define the orbit semi-major axis and eccentricity by means of the trajectory geometrical properties:

$$a \equiv \lim_{t \rightarrow \infty} \frac{1}{2}(r_{\max} + r_{\min}) \quad \text{and} \quad e \equiv \lim_{t \rightarrow \infty} \frac{r_{\max} - r_{\min}}{r_{\max} + r_{\min}}. \quad (3)$$

Orbital elements defined in this way stand as unchanging parameters of individual orbits (which would not be the case of definition emerging from instantaneous position and velocity, i.e., in terms of Laplace's vector). Moreover, in the case of eccentricity, its value is ensured to lie within the interval (0, 1). Let us remark that, according to Eqs (3), semi-major

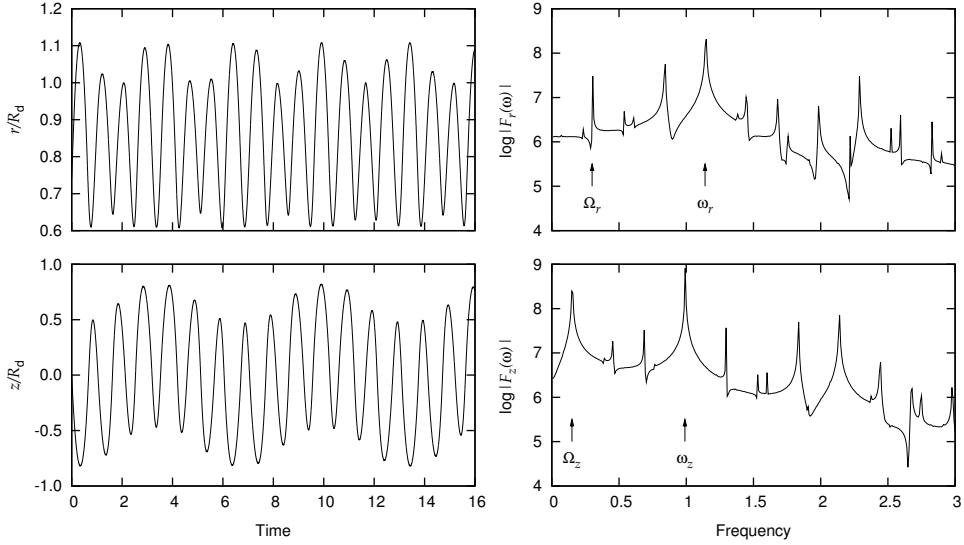


**Figure 4.** **Left:** satellite trajectory in the field of the central body and the massive self-gravitating disc. Difference in the periods of radial and vertical oscillations,  $\omega_r$  and  $\omega_z$ , are clearly visible in this case. Furthermore, frequencies  $\Omega_r$  and  $\Omega_z$  get considerably closer to  $\omega_r$  and  $\omega_z$ . **Right:** Fourier power spectrum is shown and the corresponding frequencies are indicated.

axis and eccentricity are equal to  $3.63 R_g$  and  $0.93$  in Figs 2 and 3. Considering only a limited interval of time would lead to eccentricity values oscillating periodically. In particular, at the initial phase, covered by Fig. 2, we would obtain eccentricity  $e \approx 0.43$ .

Due to considerable distortion of the orbital trajectory, it is not possible to define the orbital inclination directly on basis of its geometrical shape; the perturbation cannot be assumed to be small. Hence, we define cosine of the inclination in terms of the mean of the ratio of  $z$ -component and total angular momentum:

$$x \equiv \lim_{t \rightarrow \infty} \frac{1}{t} \int_0^t \frac{L_z}{L} dt'. \quad (4)$$

Definition (4) also ensures that the cosine of inclination stays always within interval  $(-1, 1)$ .

### 3 THE HYDRODYNAMICAL DRAG

In order to simulate a long-term orbital evolution, we further considered the impact of hydrodynamical interaction between the satellite and the disc medium. For this purpose we adopted approximation of instantaneous changes of the orbiter's velocity components after each crossing the equatorial plane:

$$\delta \mathbf{v} \equiv \mathbf{v}' - \mathbf{v} = -\frac{A}{A+1} (\mathbf{v} - \mathbf{v}_d), \quad (5)$$

where  $\mathbf{v}_d$  is the disc local velocity and

$$A \equiv \frac{\pi R_*^2 \Sigma_d v_{\text{rel}}}{M_* |v_\vartheta|}. \quad (6)$$

This approach is adequate in the situation when the disc is geometrically thin ( $H \ll R$ ) and the relative velocity of satellite and the disc medium exceeds speed of sound in the surrounding environment. Under these assumptions we can work with vertically integrated quantities.

The disc column density influences the pace of evolution, while its rotation law determines the satellite trajectory in the phase space of osculating elements. Neglecting the disc gravity and assuming Keplerian rotation, one can show that the drag of the disc causes a gradual decay towards circular orbit co-rotating with the disc at radius  $a_f = \frac{1}{4}a_0(1 - e_0^2)(1 + x_0)^2$  (see e.g., [Šubr and Karas, 1999]). Taking the disc gravity into consideration, it appears that the overall tendency to low eccentricity is retained, however, new significant features

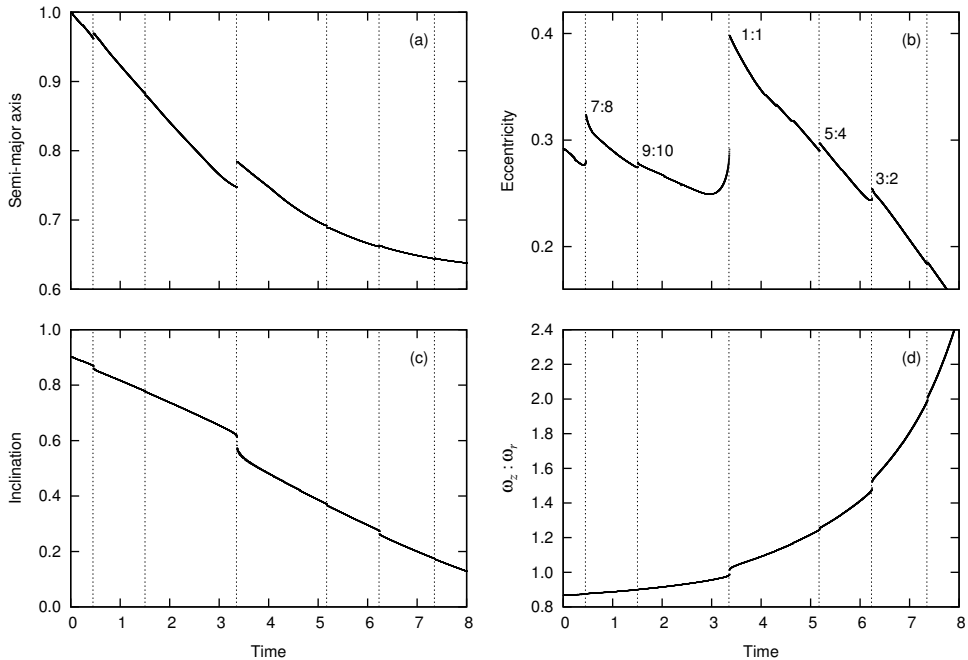


**Figure 5.** Long-term evolution of three orbital (osculating) elements is shown (panels a–c) for a satellite star under the influence of a self-consistent disc plus the central super-massive body. The evolution is driven by repetitive collisions with the disc. Jumps occur at various resonances between vertical and radial frequencies of epicyclic oscillations. In panel (b) we mark major resonances with corresponding their ratios of  $\zeta \equiv \omega_z : \omega_r$ . In panel (d),  $\zeta$  is plotted as a function of time. Vertical dotted lines indicate moments when  $\zeta(t)$  attains a rational value, equal to a ratio of small natural numbers. Rapid oscillations of the orbital elements are present in the numerical integration of the orbit, but they were filtered out for better clarity of the graph. Here we use time units of  $\tau \equiv 10^{12} M_8 \sim 16 \text{ Myr}$  as a fiducial time-scale of our problem.

in the form of occasional jumps of osculating elements are observed. Again, we found that these jumps are related to resonances between radial and vertical excursions.

An example of a typical trajectory is presented in Fig. 5. For the sake of better comparison, we employed the same type of a massive disc as previously in Fig. 4 ( $M_d = 0.77M_\bullet$ ,  $R_d = 4 \times 10^4 R_g$ ). The trajectory was integrated numerically in a superposed gravitational field of central mass and the disc. According to the prescription (5) velocity was changed after each passage through the equatorial plane. In equally spaced time intervals, the collisional interaction with the disc was switched off and the orbit was integrated for several hundreds of revolutions in order to obtain orbital parameters and the frequencies  $\omega_r$  and  $\omega_z$ . Fig. 4 represents a snapshot resulting from this procedure, providing the starting point of trajectory shown in Fig. 5.

As we have already mentioned above, the osculating elements exhibit sudden jumps when  $\omega_z/\omega_r$  reaches a rational number. The effect of resonance is the strongest for ratios satisfying empirical relation

$$\frac{\omega_z}{\omega_r} = \frac{2N \pm 1}{2N}, \tag{7}$$

preferably with small natural values of  $N$ . The single (and important) exception from this rule is represented by the resonance 1 : 1, which is clearly visible in our example. The relative strength of three different resonances is compared in Fig. 6 by means of the eccentricity evolution. We found it convenient to demonstrate the effect of resonances on eccentricity which appears to be the most sensitive parameter. While the first two cases comply with the rule (7), in the case of 2 : 1 ratio the jump is considerably smaller and comparable to the resonance 7 : 6.

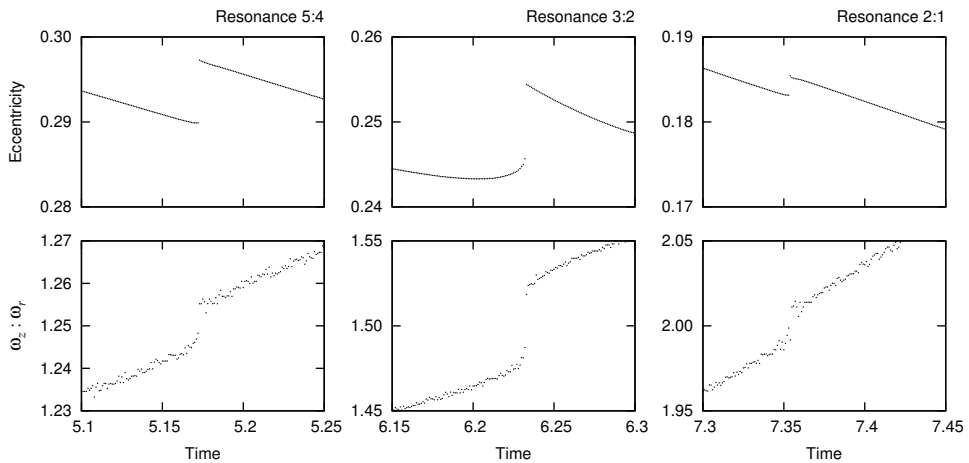


**Figure 6.** Detailed plots of eccentricity jumps which occur in three different resonances. In order to give a true picture of relative magnitudes of the steps, we set equal ranges on horizontal axes and, in the case of eccentricity, also on the vertical axes of the individual frames.

#### 4 CONCLUSIONS

The problem of stellar motion near a galactic centre is very timely because its understanding can help in finding super-massive black holes and measuring their parameters. It is however a demanding problem that poses various challenges; here we tackled the question of long-term orbital evolution in a combined gravitational field of a central compact mass surrounded by a massive disc or a torus. The relevant length-scale is of the order of  $\sim 10^3 R_g$ , and hence it is in sub-parsec region near the black hole, which is difficult to resolve with present-day techniques in distant galaxies. However, these scales are perfectly accessible in the case of Milky Way centre, and they will be resolved also in other galaxies in future. We were able to show how a massive disc can induce variations and jumps in orbital parameters of the satellite star. Notice that the assumed ratio  $M_d/M_\bullet$  was a fraction of unity, a sensible value as far as the mass of molecular tori is concerned.

In conclusion, it may be worth mentioning various issues that need to be addressed in future work. First of all it is hydrodynamics of hypersonic stellar transitions across the disc medium which should be explored in more detail. The disc affects passing satellites either directly at the point of their transitions through the disc, or indirectly, via induced waves and gap formation in the disc. Case of crossing as well as embedded trajectories need to be considered.

Further, gravitational interaction due to occasional grazing encounters of satellites should be taken into account (only rather simplistic approaches have been considered so far) and also the drag force due to dynamical friction. These effects should act selectively on different stellar types present in the nuclear cluster, resulting in their growing segregation. For example, very massive satellites tend to open a gap in the disc. Once this happens, a qualitatively different mode of radial motion takes place, which is typically orders of magnitude slower than the orbital decay proceeding under the regime of density waves. The latter case is relevant for low-mass satellites. Introducing the distribution of satellite masses in the cluster, one can observe how the initial (Salpeter-type) mass function changes its slope in the course of evolution (see [Šubr et al., 2004]).

Finally, the problem of orbital decay of stellar satellites near a black hole is relevant for forthcoming gravitational wave experiments, because the effect of gas-dynamical drag needs to be taken into account in order to compute predicted waveforms with sufficient accuracy. [Narayan, 2000] estimated that this effect can be safely ignored at late stages, before the satellite plunges into the hole, if accretion takes place in the mode of a (very diluted) advection dominated flow. However, the situation is rather different in the case of massive and dense gaseous discs [Šubr and Karas, 1999].

Normally, non-gravitational forces, such as hydrodynamical drag, tidal forces, radiation pressure and gravitational waves, exert only mild influence on individual stellar trajectories inside the sphere of black hole gravitational dominance. However one should not neglect them when exploring the overall cluster evolution on long time scales. Here we assumed that most of gas is concentrated in the disc, but we expect that a less flat distribution will have similar impact as far as the gaseous system maintains the assumed toroidal geometry. Nevertheless, details of star-disc interaction should leave their imprints in the system. It is most likely that non-standard dissipation operates in self-gravitating regions of the disc. Therefore, disc models should switch to a different viscosity prescription near  $\sim 0.01$  pc,

thereby creating additional features in the distribution function of a stellar cluster interacting with the disc. Last but not least, the modified structure of the nuclear cluster is relevant for studies of the relationship between black hole masses and velocity dispersions in AGN, for estimating the ratio of the black hole mass to the bulge mass, and it may be even pertinent for the discussion of black-hole feeding problem.

## ACKNOWLEDGEMENTS

We gratefully acknowledge financial support from the postdoctoral grant 205/02/P089 and the research grant 205/03/0902 of the Czech Science Foundation (GAČR), and from the project 2004 of the Charles University Prague (GAUK 299).

## REFERENCES

- [Goodman, 2003] Goodman, J. (2003). Self-gravity and quasi-stellar object discs. *Monthly Notices Roy. Astronom. Soc.*, 339(4):937.
- [Greenhill et al., 1996] Greenhill, L. J., Gwinn, C. R., Antonucci, R., and Barvainis, R. (1996). VLBI Imaging of Water Maser Emission from the Nuclear Torus of NGC 1068. *Astrophys. J. Lett.*, 472:L21–L24.
- [Huré, 1998] Huré, J.-M. (1998). Properties of self-gravitating  $\alpha$ -discs in AGN revisited General scaling laws. *Astronomy and Astrophysics*, 337(2):625.
- [Huré, 2000] Huré, J.-M. (2000). On the transition to self-gravity in low mass AGN and YSO accretion discs. *Astronomy and Astrophysics*, 358(1):378–394.
- [Huré, 2003] Huré, J.-M. (2003). Origin of non-Keplerian motions of masers in NGC 1068. *Astronomy and Astrophysics*, 395(2):L21.
- [Karas et al., 2002] Karas, V., Šubr, L., and Šlechta, M. (2002). Stellar dynamics in a galactic centre surrounded by an accretion disc. In Semerák, O., Podolský, J., and Žofka, M., editors, *Gravitation: Following the Prague Inspiration (A Volume in Celebration of the 60th Birthday of Jiří Bičák)*, pages 85–110, New Jersey, London, Singapore, Hong Kong. World Scientific.
- [Kato and Fukue, 1980] Kato, S. and Fukue, J. (1980). Trapped Radial Oscillations of Gaseous Disks around a Black Hole. *Publ. Astronom. Soc. Japan*, 32(3):377–388.
- [Kormendy and Richstone, 1995] Kormendy, J. and Richstone, D. (1995). *AR&AA*, 33:581.
- [Lauer et al., 1998] Lauer, R., Faber, M., Ajhar, A., Grillmair, J., and Scowen, A. (1998).
- [Levin and Beloborodov, 2003] Levin, Y. and Beloborodov, A. M. (2003). Stellar Disk in the Galactic Center: A Remnant of a Dense Accretion Disk? *Astrophys. J.*, 590(1):L33–L36.
- [Narayan, 2000] Narayan, R. (2000). Hydrodynamic Drag on a Compact Star Orbiting a Supermassive Black Hole. *Astrophys. J.*, 536(2):663.
- [Nayakshin, 2004] Nayakshin, S. (2004). Feeding the black hole with condensing accretion flows: radiatively efficient and radiatively inefficient cases. arXiv: astro-ph/0402469.

- [Schinnerer et al., 2001] Schinnerer, E., Eckart, A., and Tacconi, J. (2001). The Nuclear Stellar Cluster in the Seyfert 1 Galaxy NGC 3227: High Angular Resolution Near-Infrared Imaging and Spectroscopy. *Astrophys. J.*, 549(1):254.
- [Shakura and Sunyaev, 1973] Shakura, N. I. and Sunyaev, R. A. (1973). Black holes in binary systems. Observational appearance. *Astronomy and Astrophysics*, 24:337.
- [Šubr and Karas, 1999] Šubr, L. and Karas, V. (1999). An orbiter crossing an accretion disc. *Astronomy and Astrophysics*, 352:452–458.
- [Šubr et al., 2004] Šubr, L., Karas, V., and Huré, J.-M. (2004).
- [Syer et al., 1991] Syer, D., Clarke, C. J., and Rees, M. J. (1991). Star-disc interactions near a massive black hole. *Monthly Notices Roy. Astronom. Soc.*, 250:505–512.
- [Vokrouhlický and Karas, 1998] Vokrouhlický, D. and Karas, V. (1998). Stellar dynamics in a galactic centre surrounded by a massive accretion disc – I. Newtonian description. *Monthly Notices Roy. Astronom. Soc.*, 298(1):53–66.



Title: **Proceedings of RAGtime 4/5: Workshops on black holes and neutron stars,  
14–16/13–15 October 2002/2003, Opava, Czech Republic**

Published by: Silesian University in Opava  
Faculty of Philosophy and Science  
Institute of Physics  
Bezručovo nám. 13  
CZ-746 01 Opava  
Czech Republic

Editors: S. Hledík and Z. Stuchlík

Cover design: Otakar Karlas

Copyright © 2004 by Silesian University in Opava

All rights reserved. No part of this publication may be reproduced, stored in a retrieval system or transmitted in any form or by any means, electronic, mechanical, photocopying, recording or otherwise, without the prior permission of the Publisher.

1st edition

Printed by Ediční středisko FPF SU, Opava, Czech Republic

Published in December 2004

ISBN 80-7248-242-4

Typeset in L<sup>A</sup>T<sub>E</sub>X



Název: **Proceedings of RAGtime 4/5: Workshops on black holes and neutron stars,  
14–16/13–15 October 2002/2003, Opava, Czech Republic**

Nakladatel: Slezská univerzita v Opavě  
Filozoficko-přírodovědecká fakulta  
Ústav fyziky  
Bezručovo nám. 13  
CZ-746 01 Opava  
Česká republika

Editoři: S. Hledík and Z. Stuchlík

Obálka: Otakar Karlas

Copyright © 2004 by Silesian University in Opava  
Všechna práva vyhrazena. Žádná část této publikace nesmí být reprodukována, přenášena  
jakoukoli formou, elektronicky, mechanicky, kopírováním, nahráváním nebo jakýmkoli  
systémy pro skladování informací bez předchozího souhlasu nakladatele.

První vydání

Tisk: Ediční středisko FPF SU, Opava, Česká republika

Vydáno v prosinci 2004

ISBN 80-7248-242-4

Vysázeno systémem L<sup>A</sup>T<sub>E</sub>X

